

Design of Quantum Dot and Smartphone-based Luminescent Bioassay Platforms for Prospective Point-of-Care Diagnostics

by

ELEONORA PETRYAYEVA

Hon.B.Sc., The University of Toronto, 2011

M.Sc., The University of Toronto, 2012

A THESIS SUBMITTED IN PARTIAL FULFILLMENT OF
THE REQUIREMENTS FOR THE DEGREE OF

DOCTOR OF PHILOSOPHY

in

THE FACULTY OF GRADUATE AND POSTDOCTORAL STUDIES
(Chemistry)

THE UNIVERSITY OF BRITISH COLUMBIA
(Vancouver)

December 2016

© Eleonora Petryayeva 2016

Abstract

Smartphones are essential components of daily life. These devices feature built-in cameras and light sources, data storage, and wireless data transmission, making them emerging devices for optical imaging and diagnostic bioassays. To date, the majority of smartphone-based diagnostics have been developed for colourimetric assays, which often suffer from limited multiplexing capability and poor sensitivity. In general, fluorescence-based assays offer greater sensitivity and multiplexing capacity, and in combination with smartphone platform may help to overcome these limitations. This thesis describes research toward the development of smartphone platforms for fluorescence-based bioassays using quantum dots (QDs) and Förster resonance energy transfer (FRET), and addresses two critical challenges: multiplexing and analysis of biological sample matrices. Multiplexing was achieved by matching the built-in RGB (red-green-blue) channels of smartphone cameras with the narrow, bright, and tunable emission of QDs. The QDs provided superior brightness in comparison to traditional fluorescent dyes and proteins, and served as excellent FRET donors in assays that used proteases as model analytes. Up to three-plex assays were demonstrated for the detection of trypsin, chymotrypsin, and enterokinase. The analytical performance of the smartphone-based platform matched that of a bench-top spectrofluorimeter, where the smartphone was a fraction of the cost and size. A smartphone-based platform was also developed for detection of analytes in serum and whole blood. Most clinical samples will take this form and necessitate careful assay design to overcome challenges associated with physical, optical and chemical properties of whole blood. Blood is strongly absorbing, scattering, autofluorescent, and contains high concentrations of proteins and small molecules. A well-thought-out combination of QDs, FRET, and a paper-in-PDMS chip enabled direct, single-step and quantitative fluorescence-based detection of thrombin activity in whole

blood. The research in this thesis is a foundation for the development of novel point-of-care diagnostics assays with consumer electronics that could help enable personalized health care.

Preface

Chapter 1 is an adaptation of two published works. Section 1.1 is reproduced in part from Petryayeva, E.; Algar, W. R., Toward point-of-care diagnostics with consumer electronic devices: the expanding role of nanoparticles. *RSC Adv.* **2015**, *5* (28), 22256-22282 with permission from The Royal Society of Chemistry (Copyright 2015 The Royal Society of Chemistry). Sections 1.3.1–1.3.5 are reproduced in part from Petryayeva, E.; Algar, W. R.; Medintz, I. L., Quantum Dots in Bioanalysis: A Review of Applications Across Various Platforms for Fluorescence Spectroscopy and Imaging. *Appl. Spectrosc.* **2013**, *67* (3), 215-252 with permission from the Society of Applied Spectroscopy (Copyright under Creative Commons Attribution - NonCommercial 4.0 International licence). These review articles were written by Eleonora Petryayeva with input and editing from Dr. Algar. Sections 1.2 and 1.3.6 contain unpublished work.

Chapter 2 is an adaptation of published work, and is reproduced from Petryayeva, E.; Algar, W. R., A Job for Quantum Dots: Use of a Smartphone and 3D-Printed Accessory for All-In-One Excitation and Imaging of Photoluminescence. *Anal. Bioanal. Chem.* **2016**, *408* (11), 2913-2925, with permission of Springer (Copyright 2016 Springer). Eleonora Petryayeva and Dr. Algar conceived the research. Eleonora Petryayeva designed, completed, and analyzed the experiments and data presented. Pritesh Padhiar in the UBC Department of Chemistry Mechanical Engineering Shop assisted with 3D printing based on the device designs created by Eleonora Petryayeva. The manuscript was co-written by Eleonora Petryayeva and Dr. Algar.

Chapter 3 is an adaptation of published work, and is reproduced from Petryayeva, E.; Algar, W. R., Multiplexed Homogeneous Assays of Proteolytic Activity Using a Smartphone and Quantum Dots. *Analytical Chemistry* **2014**, *86*, 3195-3202, with permission from The American Chemical Society (Copyright 2014 The American Chemical Society). Eleonora Petryayeva and Dr. Algar conceived the research. Eleonora Petryayeva designed, completed, and analyzed the experiments and data presented. Eleonora Petryayeva wrote the manuscript with input and editing from Dr. Algar.

Chapter 4 contains currently unpublished data, with the exception of Section 4.2.4.1.1, which is an adaptation of published work, and is reproduced from Kim, H., Petryayeva, E., Algar, W. R., Enhancement of Quantum Dot Forster Resonance Energy Transfer within Paper Matrices and Application to Proteolytic Assays. *IEEE J. Sel. Top. Quantum Electron.* **2014**, *20* (3), 7300211, with permission from IEEE (Copyright 2014 IEEE). Eleonora Petryayeva and Dr. Algar conceived the research. H. Kim was an undergraduate summer student supervised by Dr. Algar and Eleonora Petryayeva, and, using methods and protocols developed by Eleonora Petryayeva, he prepared the samples used for fluorescence lifetime imaging (FLIM) that appear in this thesis. Olga Solodova was an undergraduate student supervised by Dr. Algar and Eleonora Petryayeva, and she contributed to experiments designed to determine the density of functional groups in cellulose paper samples. These results appear in this thesis in Section 4.2.2.1. Dr. Gethin Owen at the Centre for High-Throughput Phenogenomics, UBC, performed the SEM imaging reported in Section 4.2.3. Dr. Ken Wong at the Interfacial Analysis & Reactivity Laboratory, UBC, performed the XPS analysis of paper samples that appear in Section 4.2.2. For all the remaining sections in this chapter, Eleonora Petryayeva designed, completed, and analyzed the experiments and data presented.

Chapter 5 is an adaptation of published work, and is reproduced from Petryayeva, E.; Algar, W. R., Proteolytic Assays on Quantum Dot-Modified Paper Substrates Using Simple Optical Readout Platforms. *Anal. Chem.* **2013**, *85* (18), 8817-8825, with permission from the American Chemical Society (Copyright 2013 The American Chemical Society). Eleonora Petryayeva and Dr. Algar conceived the research. Eleonora Petryayeva designed, completed, and analyzed the experiments and data presented. The manuscript was written by Eleonora Petryayeva, with input and editing from Dr. Algar.

Chapter 6 is an adaptation of published work, and is reproduced from Petryayeva, E.; Algar, W. R., Single-step bioassays in serum and whole blood with a smartphone, quantum dots and paper-in-PDMS chips. *Analyst* **2015**, *140*, 4037-4045, with permission from The Royal Society of Chemistry (Copyright 2015 The Royal Society of Chemistry). Eleonora Petryayeva and Dr. Algar conceived the research. Eleonora Petryayeva designed, completed, and analyzed the experiments and data presented. Eleonora Petryayeva wrote the manuscript with input and editing from Dr. Algar.

Table of Contents

Abstract	ii
Preface	iv
Table of Contents	vi
List of Tables	xiii
List of Figures	xv
List of Schemes	xxxii
List of Abbreviations.....	xxxiii
Acknowledgements	xxxiv
Chapter 1 Introduction	1
1.1 Point-of-Care Diagnostics	2
1.1.1 Consumer electronic devices for POC	2
1.1.2 The need for point-of-care diagnostics	3
1.1.3 Clinical tests and biomarkers	5
1.1.4 Lateral flow assays	8
1.1.5 Utility of consumer electronic devices	10
1.1.6 Optical properties of nanoparticles	11
1.1.7 Bioassays with consumer electronics and nanoparticles	16
1.1.7.1 Light sources	16
1.1.7.2 CMOS image sensors: digital cameras to smartphones.....	18
1.1.7.2.1 Digital imaging technology.....	18
1.1.7.2.2 Growing analytical applications	20
1.2 Fluorescence	24
1.2.1 The Perrin–Jablonski diagram	24
1.2.2 Absorption–formation of the electronic excited state.....	26
1.2.2.1 Absorption spectrum: shape and intensity.....	28
1.2.3 The Franck-Condon electronic excited state.....	31
1.2.4 Quantum yield and fluorescence lifetime	33

1.2.5	Quenching processes	35
1.2.6	Factors affecting fluorescence	36
1.2.7	Fluorescence measurements	37
1.2.7.1	Fluorescence microscopy and imaging	39
1.2.8	Förster resonance energy transfer	39
1.2.8.1	Classical Förster formalism	41
1.2.8.2	Measurement of FRET efficiency	45
1.2.8.3	Assumptions underlying use of FRET	47
1.3	Semiconductor Quantum Dots.....	49
1.3.1	What is a quantum dot?.....	49
1.3.2	Absorption and photoluminescence	49
1.3.3	Quantum confinement and core/shell structures.....	51
1.3.3.1	Surface states and effects.....	53
1.3.4	Quantum dot materials.....	54
1.3.4.1	Synthesis of QDs	56
1.3.5	Functionalization of QDs	56
1.3.5.1	Interfacial chemistry	56
1.3.5.2	Bioconjugation of QDs.....	60
1.3.6	Quantum dots as FRET donors	62
1.3.6.1	Selection of QD-dye FRET pairs.....	69
1.4	Contributions of This Thesis.....	72
1.4.1	Background	72
1.4.2	Thesis overview	74
Chapter 2	Use of a Smartphone and 3-D Printed Accessory for All-in-One Excitation and Imaging of Photoluminescence.....	78
2.1	Introduction	78
2.2	Results.....	80
2.2.1	Design of the 3D-printed accessory	80
2.2.2	Substrates for all-in-one imaging	82
2.2.3	Photoluminescent materials	83
2.2.4	Detection of photoluminescence	86
2.2.5	Effect of smartphone imaging application parameters.....	89

2.2.6	Two-colour imaging.....	93
2.2.7	Model binding assay.....	96
2.2.8	Model FRET-based thrombin assay.....	97
2.2.8.1	FRET pairs.....	97
2.2.8.2	Thrombin assay.....	99
2.2.9	Tandem QD540a–A610 FRET conjugate.....	101
2.3	Discussion	102
2.3.1	Smartphone imaging platform	102
2.3.2	QDs are ideal for smartphone imaging	104
2.4	Conclusion.....	108
2.5	Experimental Section.....	109
2.5.1	Materials and reagents	109
2.5.2	Preparation of GSH-coated QDs.....	110
2.5.3	3D-printed apparatus.....	110
2.5.4	Binding assays	111
2.5.5	FRET experiments.....	111
2.5.6	Data analysis	112
2.5.6.1	Quantum yields.....	112
2.5.6.2	FRET calculations	112
 Chapter 3 Multiplexed Homogeneous Assays of Proteolytic Activity Using a Smartphone and Quantum Dots.....113		
3.1	Introduction	113
3.2	Results.....	116
3.2.1	RGB colour imaging of quantum dots	116
3.2.2	RGB colour imaging of mixtures of quantum dots	118
3.2.3	FRET pairs and their fidelity	119
3.2.3.1	Calibration curves	123
3.2.4	Validation of proteolytic assays with digital colour imaging.....	125
3.2.4.1	Temporal stability of UV lamp and smartphone camera	125
3.2.4.2	Red, green, and blue channel proteolytic assays.....	127
3.2.5	Multiplexed proteolytic assays with digital colour imaging	132
3.3	Discussion	136

3.4	Conclusions	137
3.5	Experimental Section.....	137
3.5.1	Materials and reagents	137
3.5.2	Peptide labeling.....	138
3.5.3	Instrumentation and data acquisition.....	139
3.5.4	Conjugation of peptides to QDs and enzyme assays.....	140
3.5.5	Data analysis	141
3.5.5.1	FRET parameters.....	141
3.5.5.2	RGB images analysis.....	141
3.5.5.2.1	Normalization of progress curves	141
3.5.5.2.2	Calculation of initial rates and specificity constants	142
Chapter 4	Characterization and Evaluation of Chemical Modification of Cellulose Paper	
	Substrates for Prospective Point-of-care Diagnostics with Immobilized Quantum Dots	143
4.1	Introduction	143
4.2	Results and Discussion.....	147
4.2.1	Selection of surface ligands.....	147
4.2.2	Characterization of surface chemistry	149
4.2.2.1	Quantification of accessible functional groups.....	153
4.2.3	Immobilization of quantum dots.....	158
4.2.3.1	Photobleaching	166
4.2.3.2	Long-term stability of QD-paper substrates	167
4.2.4	Immobilization of QD-peptide bioconjugates	168
4.2.4.1	FRET on paper substrates	168
4.2.4.1.1	Fluorescence lifetime imaging microscopy (FLIM).....	173
4.2.5	Effect of paper surface chemistry on proteolytic rates.....	174
4.3	Conclusions	175
4.4	Experimental Section.....	176
4.4.1	Materials and reagents	176
4.4.2	Preparation of paper substrates	177
4.4.2.1	Preparation of paper substrate (3)	177
4.4.2.2	Preparation of paper substrate (4b)	178
4.4.2.3	Synthesis of <i>N</i> -(2-aminoethyl)-5-(1,2-dithiolan-3-yl)pentanamide	180
4.4.2.4	Preparation of paper substrate (6b)	181

4.4.3	Quantification of functional groups	182
4.4.3.1	Aldehyde groups	182
4.4.3.1	Primary amine groups.....	183
4.4.3.2	Thiol groups	184
4.4.4	Characterization of paper substrates.....	184
4.4.5	Preparation of DHLA-coated QDs.....	184
4.4.5.1	Synthesis of DHLA	184
4.4.5.2	DHLA QD ligand exchange	185
4.4.6	Immobilization of QDs and QD-peptide conjugates.....	185
4.4.7	SEM imaging of immobilized QDs	186
4.4.8	Photobleaching experiments	186
4.4.9	Fluorescence lifetime imaging microscopy (FLIM)	186
4.4.10	Enzyme assays.....	187
4.4.11	Data analysis	187
Chapter 5	Proteolytic Assays on Quantum Dot-Modified Paper Substrates Using Consumer Digital Cameras for Optical Readout.....	189
5.1	Introduction	189
5.2	Results and Discussion.....	193
5.2.1	FRET pair and LED excitation.....	193
5.2.2	Assay design and characterization	193
5.2.3	Spectral validation of protease assays on paper substrates	195
5.2.4	Proteolytic assays with digital colour imaging	197
5.2.4.1	Trypsin and chymotrypsin paper-based assays	197
5.2.4.2	Aprotinin inhibition assays with digital colour imaging.....	202
5.2.4.3	Multiplexed proteolytic assays with digital colour imaging.....	202
5.2.4.4	Proteolytic activation assays with digital colour imaging	205
5.2.5	Assays with a webcam and smartphone camera	207
5.3	Conclusions	208
5.4	Experimental Section.....	209
5.4.1	Materials and reagents	209
5.4.2	Preparation of paper substrates	211
5.4.3	Enzyme assays.....	211

5.4.4	Instrumentation and data acquisition.....	211
5.4.5	Data analysis	214
5.4.5.1	FRET parameters.....	214
5.4.5.2	Analysis of spectral data	215
5.4.5.3	Analysis of RGB data	215
5.4.5.4	Normalization of progress curves	215
5.4.5.5	Calculation of normalized initial rates	216
Chapter 6 Single-Step Bioassays in Serum and Whole Blood with a Smartphone, Quantum		
Dots and Paper-in-PDMS Chips.....217		
6.1	Introduction	217
6.2	Results.....	220
6.2.1	Assay design: selection of QDs.....	220
6.2.1.1	The effect of QD emission wavelength range	221
6.2.1.2	The effect of QD excitation wavelength	221
6.2.1.3	Selection of FRET pair: QD630-A647 and QD650-A680	223
6.2.2	Assay design: immobilization, reference spot, and sample chip.....	225
6.2.3	Assay design: readout platform	228
6.2.3.1	LED brightness	229
6.2.3.1	LED crosstalk.....	231
6.2.3.2	LED emission attenuation by blood	232
6.2.4	Thrombin assays.....	232
6.2.4.1	Blind assay for thrombin activity in blood	234
6.2.5	Competitive binding assays.....	235
6.3	Discussion	237
6.4	Conclusions	240
6.5	Experimental Section.....	241
6.5.1	Materials and reagents	241
6.5.2	Peptide modifications	242
6.5.2.1	Dye-labeled peptides	242
6.5.2.2	Biotinylated peptide	242
6.5.3	Preparation of paper test strips	243
6.5.3.1	Sizing and chemical reduction of cellulose paper	243
6.5.3.2	Immobilization of QD-peptide conjugates.....	243

6.5.4	Fabrication of PDMS/glass chip.....	245
6.5.5	Assay procedures	246
6.5.5.1	Thrombin assays	246
6.5.5.2	Competitive binding streptavidin assay.....	247
6.5.6	Instrumentation and data acquisition.....	247
6.5.6.1	Characterization of LEDs	247
6.5.6.2	Absorbance, transmittance and fluorescence measurements	248
6.5.6.3	Sample matrix-dependent image acquisition parameters	250
6.5.7	Data analysis	251
6.5.7.1	FRET parameters.....	251
6.5.7.2	Image and RGB data analysis	252
Chapter 7	Conclusions and Future Work	253
7.1	Thesis Overview	253
7.2	Significance	254
7.3	Future Work	256
7.3.1	Improving sensitivity	256
7.3.2	Universal imaging platform for smartphones	259
7.3.3	Scope of analytes and assays	260
7.3.4	Interaction between nanoparticles and proteases	260
7.3.5	Interaction between nanoparticles, proteases, and solid substrates	264
7.4	Concluding Remarks	265
References	266
Appendix I	304
Appendix II	311
Appendix III	313
Copyright Acknowledgements	315

List of Tables

Table 1.1 NP materials for POC/PON diagnostics.....	13
Table 1.2 Properties of common fluorescent dyes used as acceptors in QD-FRET bioassays.....	70
Table 1.3 Summary of spectral overlap, Förster distance and crosstalk for QD-Alexa Fluor dyes.....	71
Table 2.1 Characteristics of QD materials, R-PE, and fluorescein.	85
Table 2.2 Peptides sequences.....	109
Table 2.3 First exciton wavelength and corresponding molar absorption coefficients for QDs.	110
Table 3.1 Properties of the QDs and FRET pairs used for RGB imaging.....	116
Table 3.2 Photophysical parameters of FRET pairs.	120
Table 3.3 Relative changes in RGB channel intensity after 1 h.....	122
Table 3.4 Comparison of the specificity constants, k_{cat}/K_m ($M^{-1} s^{-1}$), calculated for one-plex assays between the fluorescent plate reader and smartphone RGB imaging readout formats.	131
Table 3.5 Peptide substrate sequences.....	139
Table 3.6 Preparation of stock solutions of QD peptide conjugates.	140
Table 4.1 Apparent XPS surface composition characterizing surface modifications. ^a	150
Table 4.2 Summary of paper substrate (4b) pre-treatment procedures evaluated for QD immobilization.	164
Table 5.1 Peptide substrate sequences.....	210
Table 6.1 Photophysical parameters of QD630-A647 and QD650-A680 FRET pairs.	224
Table 6.2 Characterization of LEDs as excitation sources for QD630 and QD650.	230
Table 6.3 Results of blind assays for thrombin in whole blood.	235
Table 6.4 Peptide substrate sequences.....	242
Table 6.5 Spotted solutions of QD-peptide conjugates.....	245

Table 6.6 LEDs used for optimization experiments.	248
Table 6.7 Acquisition parameters for iPhone and Lapse It Pro application.	251
Table 6.8 Acquisition parameters for Thorlab CMOS camera and micro-Manager software.	251

List of Figures

Figure 1.1 An illustration of the convergence of consumer electronic devices and nanoparticles for POC/PON diagnostics..... 3

Figure 1.2 Basic design of a lateral flow immunochromatographic assay (LFIA). The device comprises a sample pad, conjugate pad, detection zone with test (T) and control (C) lines, and an absorbent pad. The sample containing analyte is added to the sample pad and drawn towards the absorbent pad by capillary action. NP-antibody conjugates bind to analyte (antigen) present in the sample and are captured on the test line, whereas NP-antibody conjugates that have not bound antigen are captured on the control line. . 9

Figure 1.3 (A) Size-dependent molar extinction coefficient of Au NPs as a function of wavelength. The inset photographs show solutions of 5, 10, 15 and 20 nm Au NPs at 1 nM concentration and with an optical density of 1 (ca. 90, 10, 3, and 1 nM concentrations for 5, 10, 15 and 20 nm Au NPs, respectively). **(B)** Size/composition-tunable absorbance and emission of CdSe/ZnS and CdSeS/ZnS QDs. The inset photograph shows samples of different sizes of CdSe/ZnS QDs under UVA (365 nm) illumination. Photograph reprinted with permission from ref. [126]. Copyright 2011 American Chemical Society. **(C)** Upconversion emission spectra of NaYF₄:Yb/Tm (20/0.2 mol %; blue line) and NaYF₄:Yb/Er (18/2 mol %; green line) nanoparticles. The inset photographs show samples of these nanoparticles under 980 nm excitation with a diode laser (600 mW). Adopted with permission from ref. [127]. Copyright 2008 American Chemical Society..... 15

Figure 1.4 Emission spectra of commercial light sources well-suited to POC/PON diagnostics: **(A)** various colour LEDs emitting in UV-visible region of the spectrum; **(B)** white-light LED; **(C)** five common wavelengths of laser diodes (the FWHM > 1 nm is a measurement artifact); and **(D)** and a UVA lamp or “black light.” 18

Figure 1.5 (A) Examples of consumer electronic devices equipped with CMOS cameras: (i) smartphones; (ii) digital cameras; and (iii) wearable devices. The image in (iii) is reproduced with permission from ref. [137]. Copyright 2014 American Chemical Society. **(B)** Simplified schematic of a CMOS image sensor. **(C)** Spectral sensitivity of a typical CMOS image sensor without (black) and with RGB colour filters (coloured lines). The typical blocking region of an IR filter is also shown. 19

Figure 1.6 (A) Cell phone-based fluorescence imaging of individual NPs and viruses: (i) Front view of the smartphone microscope and a schematic diagram of its components; (ii) Images of 100 nm fluorescent NPs acquired with the cell phone show excellent agreement with SEM images. Adapted with permission from ref. [157]. Copyright 2013 American Chemical Society. **(B)** Attachment that enables use of a smartphone as a spectrophotometer for fluorescence emission measurements. The key component is a

transmission diffraction grating. Reprinted with permission from ref. [158]. Copyright 2014 American Chemical Society.....21

Figure 1.7 Jablonski diagrams illustrating the processes of absorption and photoluminescence, as well as competing non-radiative relaxation processes. Singlet electronic states are labeled as S_n , and triplet electronic states are labeled as T_n . The electronic states are shown as potential energy wells with superimposed vibrational states, v_n . **(A)** An example of processes involved in a radiative pathway. (i) Absorption from S_0v_0 to S_1v_2 , followed by (ii) vibrational relaxation to S_1v_0 and (iii) radiative relaxation to the ground state—fluorescence. **(B)** Processes involved in non-radiative pathways. Absorption from S_0v_0 to S_1v_2 (i) or S_2v_4 (ii), followed by (iii) vibrational relaxation to S_2v_0 and (iv) internal conversion to S_1v_7 . This process is followed by vibrational relaxation to S_1v_0 and, from this state, an emission of photon can take place as shown in (A, iii) or by (v) internal conversion—a transition to S_0v_{20} , followed by (iii) vibrational relaxation to the S_0v_0 . **(C)** Other non-radiative relaxation pathways: (i) excitation to S_1v_2 , followed by (ii) vibrational relaxation to S_1v_0 , and then (iii) intersystem crossing to T_1v_1 . This process is followed by vibrational relaxation to T_1v_0 . From this state molecules return to the ground state either *via* non-radiative pathways or *via* radiative processes—delayed fluorescence or phosphorescence.25

Figure 1.8 Illustration of Franck-Condon principle for an electronic transition from the ground electronic state, S_0 to the excited state, S_1 . **(A)** The maximum transition probability is observed for transitions with maximum overlap between initial and final vibrational wavefunctions, based on Franck-Condon factors. The most probable excitation (blue line) is shown into the second vibrational state (v_2^*) of S_1 , and the corresponding most probable relaxation transition is shown to the second vibrational state (v_2) of S_0 (red line). The probability density function is shown in green. **(B)** A corresponding schematic for absorption and emission spectra. The spectral characteristics of individual transitions are typically only observed in a gas phase or at very low temperatures, broadening (shown as shaded region) is observed in solution at room temperature. As a result of the Franck-Condon principle, the absorption and emission spectra are approximately a mirror image of each other.....30

Figure 1.9 Jablonski diagram illustrating the FRET process. The donor is excited from the ground state S_0 to any of the vibrational levels of the first excited state S_1 , and then relaxes to the lowest vibrational level of S_1 *via* vibrational relaxation. During nonradiative resonance energy transfer, the donor relaxes to the ground state without emitting a photon, while an acceptor is simultaneously excited to a vibrational level of S_1 . Then acceptor undergoes the vibrational relaxation to the lowest vibrational level of S_1 , followed by either emission of a photon (*i.e.* fluorophore acceptor) as it relaxes to the ground state or nonradiative relaxation (*i.e.* dark quencher acceptor).40

Figure 1.10 Schematic representation of the spectral overlap integral, which is shown as the grey area, J , where the emission spectrum of the donor overlaps with absorption spectrum of acceptor.43

Figure 1.11 Representation of the donor and acceptor transition dipole moments and angles used to calculate the orientation factor, κ^244

Figure 1.12 (A) Size-tunable PL of CdSe QDs. The photograph was taken under UV illumination (365 nm). **(B)** TEM image of a CdSe/ZnS QD. A and B reprinted with permission from ref. [126]. Copyright 2011 American Chemical Society. **(C)** Size-dependent absorption and fluorescence spectra of CdSe QDs. Reprinted with permission from ref. [193]. Copyright 2010 American Chemical Society. **(D)** Absorption and PL spectra of $Zn_xCd_{1-x}Se$ QDs with Zn mole fractions of (a) $x = 0$, (b) 0.28, (c) 0.44, (d) 0.55, and (e) 0.67. Reprinted with permission from ref. [194]. Copyright 2003 American Chemical Society.50

Figure 1.13 Illustration of band gap engineering by selection of core and shell materials. The relative energy of conduction band and valence band edge states between the core and shell determine the localization of the electron and hole, and the nature of the transition associated with exciton recombination, offering an additional means of tuning the optical properties of QDs. **(A)** Type-I QD with localization of both carriers in the core; **(B)** Type-II QD with localization of the electron in the shell; **(C)** Type-II QD with localization of the hole in the shell; **(D)** Quasi-Type-II QD with localization of the electron in both and the core and shell; and **(E)** Inverse-Type-I QD with localization of both carriers in the shell. .52

Figure 1.14 Illustrative overview of the chemistry of core-shell QDs. Coatings for aqueous solubility: (i) amphiphilic polymer coating with carboxyl(ate) groups; (ii) amphiphilic polymer coating with PEG oligomers; (iii) dithiol ligand with a distal PEG oligomer; (iv) dithiol ligand with a distal zwitterionic functionality; (v) dithiol ligand with a distal carboxyl(ate) group. Common R groups include carboxyl, amine, and methoxy, although many others can be introduced (e.g. see vi, x, xi). Methods for conjugating biomolecules of interest (BOI): (vi) biotin-streptavidin binding; (vii) polyhistidine self-assembly to the inorganic shell of the QD; (viii) amide coupling using *N*-(3-dimethylaminopropyl)-*N'*-ethylcarbodiimide (EDC) and sulfo-*N*-hydroxysuccinimide (s-NHS) activation; (ix) heterobifunctional crosslinking using succinimidyl-4-(*N*-maleimidomethyl)cyclohexane-1-carboxylate (SMCC; structure not shown); (x) aniline-catalyzed hydrazone ligation; and (xi) strain-promoted azide-alkyne cycloaddition. The double arrows are intended to represent conjugation between the functional groups and, in principle, their interchangeability (not reaction mechanisms or reversibility). Not drawn to scale.58

Figure 1.15 (A) An illustration of the distance dependence of a QD-dye FRET pair with the corresponding FRET efficiency curve as a function of donor-acceptor separation in terms of r/R_0 . (drawn not to scale). **(B)** Absorption and emission spectra for a QD-dye FRET pair. The shaded area indicates qualitative spectral overlap.64

Figure 1.16 (A) Plot of FRET efficiency as a function of donor-acceptor separation in terms of r/R_0 for a fixed, a , the number of acceptors per QD donor. The effective enhancement from 50% to 91% with

increasing a from 1 to 10 is shown at the donor-acceptor separation equivalent to the Förster distance (dashed lines). **(B)** Plot of FRET efficiency as a function of the number of acceptors, a , per QD donor for a fixed r/R_o value.65

Figure 1.17 Poisson distribution of QD-MBP conjugates. Agarose gel electropherogram of CdSexS_{1-x}/ZnS QD-His₅-MBP conjugates assembled from different relative amounts of MBP per QD (indicated at top). The banding is characteristic of a distribution of conjugate valences (indicated at left).66

Figure 1.18 Overview of main design components and a flowchart of critical optimization parameters. ...77

Figure 2.1 Smartphone accessory for all-in-one excitation and imaging of PL. **(A)** 3D rendering of the accessory. The rendering is partially transparent. The two circular features are the filter positions (i, ii) and the light grey features are the reflector supports (iii, iv). Photographs of the 3D-printed accessory **(B)** without and **(C)** with the smartphone in position. **(D)** Schematic of the device, showing the excitation light path. The arrow in panel A indicates the orientation of this view.81

Figure 2.2 **(A)** Spectrum of light from the flash module of the smartphone with and without the blue band-pass excitation filter. **(B)** Transmission spectra of the band-pass excitation filter and long-pass emission filter. **(C)** False-colour image that characterizes the homogeneity of the combined excitation intensity and collection efficiency over the useful imaging area. The scale bar is 0.5 cm.82

Figure 2.3 **(A)** Smartphone PL images of PDMS-on-glass microfluidic chips filled with (i) QD525a (0.5 μ M), (ii) QD605 (0.2 μ M); and (iii) QD630 (0.2 μ M). The channel dimensions are \sim 300 μ m. **(B)** Smartphone PL images of QD525a immobilized on glass beads (0.5 mm dia.). **(C)** Smartphone PL image of paper substrates with immobilized QD520, QD525a, QD605, QD630. **(D)** Smartphone PL image of an agarose gel (1.0%) showing the difference in electrophoretic mobility between a QD605, QD605-[Pep(A488)]₂₀ conjugates, and an equivalent amount of Pep(A488).83

Figure 2.4 Absorption and emission spectra for the QDs, R-PE, and fluorescein. **(A)** Absorption spectra and **(B)** normalized PL emission spectra for the QD materials: (i) QD520, (ii) QD525a, (iii) QD540a, (iv) QD550, (v) QD565, (vi) QD585, (vii) QD605, (viii) QD630, (ix) QD650. **(C)** Absorption spectra (dotted lines) and emission spectra (solid lines) for R-PE and fluorescein.84

Figure 2.5 Smartphone PL imaging of QDs, fluorescein, and R-PE. **(A)** Images (i) of the PL from different concentrations of the nine different QD materials, and (ii) plots of G or R channel intensity measured from the smartphone images as a function of QD concentration. The QDs are grouped in the legend according to the imaging channel in which they appear brightest, and the corresponding channel is plotted. The limit of detection (LOD) for the R or G channel intensity is shown in the inset, which zooms in on the lower concentrations. **(B)** Analogous images (i) and plots (ii) for fluorescein (G channel) and R-PE (both

channels). Trend lines for selected QD materials are shown for comparison. All images were acquired with the following acquisition settings: shutter speed 1/4 s, ISO 2000, and white balance at 4500 Kelvin; these settings were optimized for sensitivity and not colour selectivity..... 87

Figure 2.6 R (red circles) and G (green circles) channel intensities from smartphone PL images for increasing concentrations of the nine QD materials from Figure 2.5. All images were acquired with the following acquisition settings: shutter speed 1/4 s, ISO 2000, and white balance at 4500 Kelvin; these settings were optimized for sensitivity and not colour selectivity..... 88

Figure 2.7 (A) Change in G (green circles) or R (red circles) channel intensity in smartphone images for samples of QD525a (G channel) and QD630 (R channel) as the ISO setting is changed. The inset shows the change in the crosstalk in the secondary image channel (as a percentage of the signal in the primary image channel) as the ISO setting is changed. **(B)** Crosstalk for fluorescein, R-PE, and QD605 as a function of ISO setting. 90

Figure 2.8 Change in G or R channel intensities in smartphone images for samples of QD525a, QD605, QD630 as the shutter speed is changed at **(A)** ISO 1000 and **(B)** ISO 2000. The main panel plots the channel intensities as a function of N, where 1/N is the shutter speed setting. The insets show the value of the exposure time (1/N) in units of seconds. QD525a were imaged in G channel and QD605 and QD630 were imaged in R channel in (A) and (B). 91

Figure 2.9 Effect of white balance/colour temperature (Kelvin) setting. **(A)** Images of solutions of QD525a, QD630, and a mixture of these two QDs (concentrations of each QD unchanged) at different white balance/colour temperature settings. **(B)** G or R channel intensities and crosstalk levels (secondary channel intensity as a percentage of the primary channel intensity) at ISO 2000, ISO 1000, and ISO 800. 92

Figure 2.10 R/G channel intensity ratio as a function of white balance/colour temperature (Kelvin) setting at ISO 2000, ISO 1000, ISO 800. 93

Figure 2.11 Changes in G or R channel intensity for mixtures of QD520 and QD630, where the concentration of only one QD varied and the concentration of the other was kept constant: **(A)** 0.1 μM QD630 with variable concentrations of QD520; and **(B)** 1.0 μM QD630 with variable concentrations of QD520. Control samples of only QD520 or only QD630 are shown for reference. The intensities are shown in panels (i), the corresponding G/R or R/G channels ratios are plotted in panels (ii), and the correlation between the spectrofluorimetric PL intensities for samples of QD520, QD630, and mixtures of QD520 and QD630 are shown in panels (iii). 95

Figure 2.12 Model binding assay with avidin as a target analyte. **(A)** Schematic of the avidin-binding assay. **(B)** Smartphone PL images (i) and G or R channel intensities (ii) as a function of avidin concentration. The G channel intensity was corrected for crosstalk from the QD630 signal. 97

Figure 2.13 Normalized absorption (dotted lines) and emission spectra (solid lines) for: **(A)** QD605 and A647, and **(B)** QD630 and A680. 98

Figure 2.14 (A) FRET between QD630 and A680: (i) PL emission spectra for QD630-[Sub_{THR}(A680)]_N conjugates with increasing *N*, the average number of A680 acceptors per QD; (ii) corresponding R channel intensity from smartphone images of the same samples. **(B)** FRET between QD605 and A647: (i) PL emission spectra for QD605-[Sub_{THR}(A647)]_N conjugates with increasing *N*, the average number of A647 acceptors per QD; (ii) corresponding R channel intensity from smartphone images of the same samples. The insets in (i) show the PL ratios (blue) and relative change in QD PL intensity (red) with increasing *N*, the average number of acceptors per QD. The PL ratios in the insets of (i) are in terms of peak heights (not areas)..... 99

Figure 2.15 FRET-based assay for proteolytic activity. **(A)** Schematic of the QD630-[Sub_{THR}(A680)]₁₆ conjugate and its mechanism of sensing thrombin activity *via* FRET. **(B)** R image channel intensity measured for QD630-[Sub_{THR}(A680)]₁₆ conjugates after incubation for 15 min with different concentrations of human thrombin spiked into 50% v/v serum (main panel) and buffer (inset). The QD PL intensity recovers as a result of thrombin activity. 100

Figure 2.16 Enhancement of dye PL emission intensity through FRET-sensitization from a QD donor. **(A)** Schematic of the conjugate. **(B)** Overlay of the absorption spectra of the QD and A610 with the spectrum of the excitation light. **(C)** Emission spectrum of the QD540a-[Pep(A610)]₈. **(D)** Graph showing the increase in A610 emission intensity (R channel) with smartphone PL imaging after conjugation to the QD540a, versus control samples of only QD540a and A610 alone. The inset shows representative smartphone images of the tandem conjugates and control samples. 101

Figure 2.17 Sizes of **(A)** fluorescein, **(B)** 3.5 nm diameter QD; **(C)** 6 nm diameter QD, and **(D)** R-PE. The R-PE structure was generated from PDB entry 1EYX. 105

Figure 2.18 TEM images of CdSe/CdS/ZnS core/shell/shell and alloyed CdSeS/ZnS core/shell QDs... 106

Figure 3.1 (A) Design of a homogeneous multiplexed assay to monitor protease activity *via* FRET with QD donors. Acceptor (QSY35, QSY9, or A647)-labeled peptide substrates containing a cleavage site for trypsin (TRP), chymotrypsin (ChT), or enterokinase (EK) were assembled on QDs with blue (QD450), green (QD540), and red (QD625) emission. The numbers in the abbreviations for the QDs indicate the approximate wavelength of their emission maximum. **(B)** Protease activity was measured through the

recovery of QD PL and the resulting increase in the corresponding RGB channel intensity in digital colour images acquired with a smartphone and a handheld UV lamp for excitation..... 115

Figure 3.2 False coloured, RGB split digital images of QD samples of various concentrations. Each row in the figure is an RGB channel from a digital colour image of a single microtiter plate row. 117

Figure 3.3 Colour images of various concentrations of QDs (inset) and the correlation between the measured RGB channel intensities and the integrated PL intensities for QD450 (blue), QD540 (green), and QD625 (red). 117

Figure 3.4 (A) QD PL spectra and **(B)** corresponding colour images for the (a) QD mixture, (b) QD450, (c) QD540, and (d) QD625. **(i)** QD450 (30 pmol), QD540 (5 pmol), and QD625 (5 pmol). **(ii)** QD450 (50 pmol), QD540 (10 pmol), and QD625 (10 pmol). **(iii)** QD450 (75 pmol), QD540 (20 pmol), and QD625 (20 pmol). RGB values shown in panel (B) were calculated by accounting for the crosstalk using eqns. 3.1-3.3 (Section 3.5.5.2, page 141). The dashed lines in panel (A) are spectra for mixtures, and the solid coloured lines are for the individual QDs..... 118

Figure 3.5 (A) Emission profile for the UV lamp excitation source; emission spectra of the QD450, QD520, QD625, and A647; and approximate cutoff wavelengths for the shortpass and longpass filters placed in front of the smartphone camera lens. Normalized absorption and emission spectra of **(B)** the QD450–QSY35 FRET pair, **(C)** the QD540–QSY9 FRET pair, and **(D)** the QD625–A647 FRET pair. ... 119

Figure 3.6 (A) Calibration curves showing the decrease in QD PL intensity as the number of acceptors per QD increases for QD450–[Sub_{TRP1}(QSY35)] (blue), QD540–[Sub_{ChT}(QSY9)] (green), and QD625–[Sub_{TRP2}(A647)] (red) conjugates. **(B)** Calibration curves for the same samples as in panel (A), showing decreases in RGB channel intensities as the number of acceptors per QD increases. **(C)** Photograph showing smartphone images of the samples in microtiter plate wells. The average number of acceptors per QD is shown at the top of the photograph..... 121

Figure 3.7 PL spectra for **(A)** QD450–[Sub_{TRP}(QSY35)] conjugates (blue channel), **(B)** QD540–[Sub_{ChT}(QSY9)] conjugates (green channel), and **(C)** QD625–[Sub_{EK}(A647)] conjugates (red channel). The insets show the corresponding FRET efficiency plots, raw data as open circles and Poisson corrected data as solid circles. 121

Figure 3.8 (A) Agarose gel electrophoresis (0.8%, 1×TBE, 100 V, 30 min) of QD450–[Sub_{TRP1}(QSY35)]₂₀, QD540, and QD625. The arrows at the left indicate the corresponding bands in the mixture (i). Reference samples of QD540 and QD625 were run in parallel, (ii) and (iii), respectively. The colour image was acquired with a smartphone camera with UV lamp excitation. Note the yellow colour from the overlap between the QD540 and QD625 in lane (i). A faint blue band can be observed above the QD540/QD625 band. **(B)** Intensity line profiles in the blue channel of gel image shown in panel (A). The QD540 and

QD625 have some crosstalk in the blue channel of the image, but there is distinct band for the QD450.
..... 123

Figure 3.9 Mixed digest/substrate calibration curves used for the analysis of progress curves in one-plex assays with **(A)** a fluorescence plate reader and **(B)** smartphone RGB imaging. The x-axis refers to the number of native peptide substrates per QD (with $N-x$ pre-digested peptide, where $N = 12$ or 16): (i) QD625–[Sub_{TRP2}(A647)]₁₂ conjugates, (ii) QD540–[Sub_{ChT}QSY9]₁₆ conjugates, (iii) QD450–[Sub_{TRP1}(QSY35)]₁₂ conjugates. The data points were fit with the simplest possible polynomial function (linear, quadratic, or cubic)..... 124

Figure 3.10 Relative decreases in QD625 PL intensity upon assembly of 4, 8, and 12 equivalents of peptide with various modifications of the C-terminal residue (A488 = Alexa Fluor 488, A555 = Alexa Fluor 555, Cys = cysteine). Note that neither A488 nor A555 is a FRET acceptor for QD625..... 125

Figure 3.11 Time trace of the relative output from UV lamp at 367 nm over 60 min. 126

Figure 3.12 Time traces for blue and green LED output measured with **(A)** a spectrometer and **(B)** a smartphone digital camera. **(C)** The blue and green LED emission spectrum and the corresponding colour image of the LEDs..... 126

Figure 3.13 Proteolytic digestion of QD625–[Sub_{TRP2}(A647)]₁₂ conjugates by TRP and comparison of data acquired with **(A)** a fluorescence plate reader and **(B)** a smartphone and RGB imaging: (i) raw PL data; (ii) normalized PL data; (iii) conversion of the normalized PL data to the average number of acceptors per QD and the bulk equivalent concentration of peptide substrate. **(C)** Comparison of initial proteolytic rates measured from the fluorescence plate reader data and smartphone RGB imaging data. 128

Figure 3.14 Proteolytic digestion of QD540–[Sub_{ChT}(QSY9)]₁₆ conjugates by ChT and comparison of data acquired with **(A)** a fluorescence plate reader and **(B)** a smartphone and RGB imaging: (i) raw PL data; (ii) normalized PL data; (iii) conversion of the normalized PL data to the average number of acceptors per QD and the bulk equivalent concentration of peptide substrate. **(C)** Comparison of initial proteolytic rates measured from the fluorescence plate reader data and smartphone RGB imaging data. 129

Figure 3.15 Proteolytic digestion of QD450–[Sub_{TRP1}(QSY35)]₁₂ conjugates by TRP and comparison of data acquired with **(A)** a fluorescence plate reader and **(B)** a smartphone and RGB imaging: (i) raw PL data; (ii) normalized PL data; (iii) conversion of the normalized PL data to the average number of acceptors per QD and the bulk equivalent concentration of peptide substrate. **(C)** Comparison of initial proteolytic rates measured from the fluorescence plate reader data and smartphone RGB imaging data.
..... 130

Figure 3.16 Progress curves for two-plex homogeneous assays of proteolytic activity. **(A)** RG two-plex assay with QD540–[Sub_{ChT}(QSY9)]₁₆ (20 pmol) and QD625–[Sub_{TRP2}(A647)]₁₂ (30 pmol). **(B)** GB two-plex assay with QD450–[Sub_{TRP1}(QSY35)]₁₂ (100 pmol) and QD540–[Sub_{ChT}(QSY9)]₁₆ (20 pmol). The conjugates were exposed to the indicated mixtures of TRP and ChT. The ordinate and abscissa scales are the same in each panel of (A) or (B). Corresponding raw data is shown in Figure 3.17. 132

Figure 3.17 Representative unprocessed RGB intensity time traces for two-plex assays with **(A)** QD540–[Sub_{ChT}(QSY9)]₁₆ and QD625–[Sub_{TRP2}(A647)]₁₂ conjugates upon exposure to various concentrations of TRP and ChT, and **(B)** QD540–[Sub_{ChT}(QSY9)]₁₆ and QD450–[Sub_{TRP1}(QSY35)]₁₂ conjugates upon exposure to various concentrations of TRP and ChT. Corresponding normalized data is shown in Figure 3.16. 133

Figure 3.18 Three-plex homogeneous proteolytic assays. **(A)** Representative colour images (brightness enhanced for clarity) for QD450–[Sub_{TRP1}(QSY35)]₁₂ (100 pmol), QD540–[Sub_{ChT}(QSY9)]₁₆ (20 pmol), and QD625–[Sub_{EK}(A647)]₁₂ (30 pmol) mixed with various concentrations of TRP, ChT, and EK: (i) reference sample (no proteases); (ii) 1 nM TRP, 1 nM ChT, and 4.5 nM EK; (iii) 8.6 nM TRP, 2 nM ChT, and 1.5 nM EK; (iv) 2.2 nM TRP, 16 nM ChT, and 0.5 nM EK. **(B)** Progress curves corresponding to (ii), (iii), and (iv). 135

Figure 4.1 Stepwise chemical modification of cellulose paper substrates to immobilize QDs *via* self-assembly. **(A)** cellulose oxidation was used to generate reactive aldehyde groups **(2)** that were subsequently reacted to prepare imidazole **(3)** and thiol **(4)** functionalized cellulose paper, **(B)** cellulose paper was modified with 3-aminopropyl triethoxysilane to give primary amine functionalized paper **(5)**, that was subsequently reacted with NHS-ester activated lipoic acid to yield thiol-modified cellulose paper **(6)**. Details of reagents and reaction conditions are given in Schemes 4.2–4.5 (p. 178–182). 148

Figure 4.2 XPS survey analysis for stepwise modification of cellulose paper with **(A)** imidazole and lipoic amine ligands; (i) full spectra, (ii) N 1s peak observed upon addition of imidazole ligands **(3)** and (iii) N 1s, S 2s, and S 2p peaks observed on lipoic amine modified paper **(4)**. **(B)** Chemical modification of paper *via* silanization with APTES; Full spectra are shown in (i) and a region of interest in (ii). The peaks corresponding to O 1s, C 1s, N 1s, S 2s, S 2p, Si 2s, and Si 2p orbitals are labeled. 151

Figure 4.3 ATR-FTIR spectra for each step of chemical modification of cellulose paper samples. **(1)** untreated cellulose, **(2)** oxidized cellulose, **(3)** imidazole ligand modified cellulose, **(4)** lipoic amine modified, **(5)** APTES modified and **(6)** cellulose modified with APTES and lipoic acid ligands. 152

Figure 4.4 **(A)** Absorption spectra for 1,3,5-triphenyl formazan (TTC formazane) in ethanol. **(B)** Calibration curve used to determine molar absorption coefficient for TTC formazane (slope = 8590 M⁻¹cm⁻¹, path length b = 0.5 cm) in ethanol. The inset shows the calibration curve fit at lower concentrations of TTC

formazan. (C) Experimental data for quantification of aldehyde functional groups in six replicate samples of paper substrate (2), the control sample corresponds to measurements made with untreated cellulose paper (1). All spectra were collected in > 97.5% ethanol. 155

Figure 4.5 (A) Representative absorption spectra for Ruhemann's purple collected to construct a calibration curve, shown in panel (B). (C) Digital photographs of paper samples with spotted Ruhemann's purple solution used for calibration curve and three replicate samples of (5) used for quantification of primary amines. 157

Figure 4.6 Representative absorption spectra showing formation of TNB²⁻ product as a result of the reaction of Ellman's reagent with thiol ligands (A) in paper substrate (4b), and (B) in paper substrate (6b). Control sample measured on untreated paper (1) (black dashed line) and blank sample containing no paper substrate (dashed blue line) are also shown for a reference. 157

Figure 4.7 Background corrected relative PL intensity of chemically modified paper substrates (according to ligands shown in Figure 4.1) after exposure to DHLA630 QDs. All data was normalized to the brightest sample functionalized with imidazole ligands (3). Paper substrates (3), (4b), and (6b) functionalized with surface ligands for specific QD immobilization. Paper substrate (2), (4a), (5), and (6a) retained QDs due to non-specific interactions. Error bars represent the standard deviation of three replicate measurements. The inset shows the corresponding QD PL emission spectra for selected modification steps. Dashed lines are used to show QD PL intensity from paper substrates (2), (4a), and (6a) that are not expected to have strong interactions with QDs (*i.e.* dithiolane groups in (4a, 6a) *versus* dithiol groups in (4b, 6b)) and signals are attributed to non-specific QD adsorption. 159

Figure 4.8 SEM images for cellulose paper modified with (A) imidazole, (B) lipoic amine, and (C) APTES and lipoic acid before (i) and after (ii) exposure to QDs. All scale bars are 200 μm for 100× magnification, 500 nm for 50 000× magnification, and 100 nm for 200 000× magnification. 161

Figure 4.9 Effect of buffer composition on optical properties of immobilized QDs in paper substrate (4b). (A) Absorption spectra of immobilized QDs deposited from different buffer solutions. (B) Relative QD PL intensity corresponding to (A) showing that increase in buffer pH and its buffering capacity is accompanied with higher brightness of immobilized QDs. 163

Figure 4.10 Effect of paper substrate (4b) pre-treatment with different buffers on the density of immobilized QDs and their relative brightness. (A) Absorption spectra collected for immobilized QDs on paper substrates washed with (i) ammonium acetate (pH 4.5), (ii) water, (iii) tris-borate buffer (pH 7.4), and borate buffer (pH 9.2), as noted in Table 4.2. (B) Relative QD absorption from (A) at 610 nm and corresponding PL intensity at 628 nm. Both QD absorption and emission are normalized to sample (i). 164

Figure 4.11 Two-photon imaging of immobilized QD630 **(A)** on paper substrate **(3)**, **(B)** on paper substrates **(4b)**, and **(C)** on paper substrates **(6b)**. 165

Figure 4.12 Photobleaching and photobrightening of QD630 capped with DHLA ligands in solution (black trace) and immobilized in paper substrates **(3)** (green trace), **(4b)** (blue trace), and **(6b)** (orange trace). 166

Figure 4.13 Comparison of storage stability of immobilized DHLA-QD630 on imidazole ligand modified paper **(3)** and lipolic amine modified paper **(4b)** in different media **(A)** buffer, **(B)** buffer:glycerol (1:1 v/v), and **(C)** dry samples as function of temperature (4°C and room temperature, RT). The PL intensity of QDs in solution is also shown for reference (dashed line). All data points are normalized to Day 0 and error bars represent the standard deviation of three replicate measurements. 168

Figure 4.14 FRET characterization. **(A)** Solution-phase FRET (i) Representative absorption spectra showing assembly of 0, 4, 8, 12, 16, and 20 A555-labeled peptides per QD, (ii) PL emission corresponding to samples in (i). The inset shows the FRET efficiency as a function of the number of A555 acceptors calculated from quenching of QD PL according to eqn. 1.24, (iii) The A555/QD PL ratio as a function of the number of A555 acceptors. **(B)** Representative paper-phase FRET on imidazole modified paper **(3)**. (i) Absorption spectra showing paper-phase assembly of QD bioconjugates prepared with 0, 4, 8, 12, 16, and 20 of A555-labeled peptides. (ii) PL spectra corresponding to (i) measured from fully hydrated paper samples, and (iii) PL spectra corresponding to (i) measured from air-dried samples. **(C)** Same as (B) on lipolic amine modified paper substrate **(4b)**. 171

Figure 4.15 Comparison of A555/QD PL ratio and FRET efficiency for QD bioconjugates immobilized in paper samples **(3)**, **(4b)**, and **(6b)** shown for hydrated samples **(A)** and dry samples **(B)**. FRET efficiency was calculated using eqn. 4.4. Corresponding PL spectra are shown in Figure 4.14. 172

Figure 4.16 **(A)** Fluorescence lifetime imaging of paper substrates functionalized with lipolic amine **(4b)** and modified with QD-A555 bioconjugates at ratios 0, 4, 8, 12, 16, and 20 A555 labeled peptides per QD. **(B)** Normalized average two-component fluorescence lifetime distributions for the six different conjugates in bulk solution: (i) 0, (ii) 4, (iii) 8, (iv) 12, (v) 16, and (vi) 20 A555 per QD. **(C)** Average two-component fluorescence lifetime distributions for the same conjugates subsequently immobilized on paper substrates. The data correspond to the images in (A). **(D)** Comparison of the FRET efficiency calculated from the decrease in QD PL lifetime between bulk solution in (B) and the paper substrates in (C). 174

Figure 4.17 Paper-based proteolytic activity assay with immobilized QDs in paper sample (i) imidazole-modified paper **(3)**; (ii) lipolic amine modified paper **(4b)**; and (iii) APTES-LA modified paper **(6b)**. 175

Figure 5.1 **(A)** Design of a paper-based assay to monitor protease activity via FRET with QD donors. Acceptor dye-labeled (A555) peptide substrates containing a cleavage site for trypsin (TRP),

chymotrypsin (ChT), and enterokinase (EK) were assembled on immobilized QDs. Protease activity was measured through changes in the intensity and colour of PL from the spots of immobilized QDs and peptides. **(B)** Synthetic steps used for modification of cellulose paper fibers with bidentate thiol surface ligands for immobilization of QDs. **(C)** Colour images of paper-immobilized QDs and A555-labeled QD-Sub(TRP) peptide conjugates under white light and their PL under UV illumination. 192

Figure 5.2 Normalized absorption and PL spectra for the QD and A555 FRET-pair. The emission profile for the LED excitation source is also shown..... 193

Figure 5.3 (A) Three-dimensional PL image of immobilized DHLA-coated QDs on cellulose paper fibers obtained using confocal microscopy. The image dimensions are $775 \times 775 \times 42 \mu\text{m}$. **(B)** Fluorescence lifetime images of paper substrates modified with green-emitting DHLA-coated QDs and QD-Sub_{TRP} conjugates (*i.e.* QD-A555). The scale bars in (A) and (B) are $100 \mu\text{m}$. **(C)** Fluorescence lifetime distributions for immobilized QDs and QD-Sub_{TRP} conjugates (*i.e.* QD-A555)..... 194

Figure 5.4 (A) Time-dependent PL spectra for paper-immobilized QD-Sub_{TRP} conjugates upon exposure to 430 nM TRP over 1 h. PL spectra were collected at 1 min intervals. Protease activity resulted in the simultaneous recovery of QD PL and loss of FRET-sensitized A555 PL. Residual A555 emission above the baseline is indicative of incomplete proteolysis or some limited adsorption of digested peptide fragments to the QDs. **(B)** Progress curves for the hydrolysis of QD-Sub_{TRP} conjugates catalyzed by different concentrations of TRP..... 196

Figure 5.5 (A) PL spectra of immobilized DHLA-QDs and QD-Sub_{TRP} conjugates (*i.e.* QD-A555). Dotted lines show the relative spectral response of the digital camera (Moticam 1 [484]) in the G and R channels. **(B)** Colour digital images of immobilized QD-Sub_{TRP} at various time points of protease activity acquired with a digital camera and corresponding pseudo-coloured images in the green and red channel upon R-G-B splitting. **(C)** The empirical relationship between R/G ratio and PL ratio. **(D)** R/G progress curves obtained from colour images of immobilized QD-Sub(TRP) spots upon exposure to different concentrations of TRP (see legend in panel E). **(E)** R/G progress curves in panel D converted to progress curves in terms of PL ratio using the data in panel C. **(F)** Calibration curve for measuring TRP activity based on the normalized initial rates of digestion. Normalized initial rates were reproducible within 10%. 198

Figure 5.6 (A) Examples of raw R/G ratio progress curves obtained from colour images of immobilized QD-Sub_{ChT} spots upon exposure to different concentrations of ChT. **(B)** Normalized R/G progress curves derived from the data in panel A and additional data. **(C)** PL ratio progress curves derived from the data in panel B and the power relationship between R/G and PL ratios, using relationship shown in Figure 5.5C. **(D)** Calibration curve for ChT activity based on normalized initial rates derived from the progress curves in

panel B. The curve was used to determine the apparent K_m . (E) Representative examples of changes in the mean intensity in the G and R channels for QD-Sub_{ChT} exposed to buffer (blank) and 20 nM ChT. . 201

Figure 5.7 Progress curves showing the inhibition of TRP (860 nM, 20 $\mu\text{g}/\text{mL}$) activity by different concentrations of aprotinin. 202

Figure 5.8 Two-plex assays of proteolytic activity. Progress curves and corresponding colour images acquired upon exposure of immobilized spots of QD-Sub_{TRP} and QD-Sub_{ChT} to protease mixtures containing (A) 215 nM (5 $\mu\text{g}/\text{mL}$) TRP and 8 nM (0.2 $\mu\text{g}/\text{mL}$) ChT, (B) 86 nM (2 $\mu\text{g}/\text{mL}$) TRP and 80 nM (2 $\mu\text{g}/\text{mL}$) ChT, and (C) 8.6 nM (0.2 $\mu\text{g}/\text{mL}$) TRP and 200 nM (5 $\mu\text{g}/\text{mL}$) ChT. Only the negative control spot with Sub_{TRP} is shown (blank). 203

Figure 5.9 Non-normalized R/G ratio progress curves for exposure of immobilized spots of QD-Sub_{TRP} and QD-Sub_{ChT} to protease mixtures containing (A) 215 nM (5 $\mu\text{g}/\text{mL}$) TRP and 8 nM (0.2 $\mu\text{g}/\text{mL}$) ChT, (B) 86 nM (2 $\mu\text{g}/\text{mL}$) TRP and 80 nM (2 $\mu\text{g}/\text{mL}$) ChT, and (C) 8.6 nM (0.2 $\mu\text{g}/\text{mL}$) TRP and 200 nM (5 $\mu\text{g}/\text{mL}$) ChT. Only the negative control spot with Sub_{TRP} is shown (blank). The corresponding normalized data is shown in Figure 5.8. 204

Figure 5.10 Progress curves and corresponding colour digital images for multiplexed protease assays. Spots of GSH-QDs functionalized with Sub_{TRP}, Sub_{ChT}, and Sub_{EK} were tested against a mixture containing TRP 8.6 nM (0.2 $\mu\text{g}/\text{mL}$), ChT 8.0 nM (0.2 $\mu\text{g}/\text{mL}$), and EK 7.6 nM (0.2 $\mu\text{g}/\text{mL}$). Only the negative control spot with Sub_{TRP} is shown. 205

Figure 5.11 (A) Schematic of cascaded pro-enzyme activation: EK activates pTRP to TRP (step I), which then activates pChT to ChT (step II). The formation of active TRP and ChT is monitored with Sub_{TRP} and Sub_{ChT}, respectively. (B) Progress curves and corresponding colour digital images for direct activation of 195 nM pChT (5 $\mu\text{g}/\text{mL}$) by 215 nM TRP (5 $\mu\text{g}/\text{mL}$). Open circles correspond to the control samples containing only pChT at 5 $\mu\text{g}/\text{mL}$. (C) Progress curves and corresponding colour digital images for cascaded activation of 210 nM pTRP (5 $\mu\text{g}/\text{mL}$) and 195 nM pChT (5 $\mu\text{g}/\text{mL}$) initiated with EK (5 units). Open circles correspond to the control samples containing a mixture of pTRP and pChT at 5 $\mu\text{g}/\text{mL}$ concentration each (no EK). 206

Figure 5.12 Comparison of R/G progress curves acquired with a digital camera, computer webcam, and iPhone (smartphone) upon exposure of spots of immobilized QD-Sub_{TRP} and QD-Sub_{ChT} to a mixture containing 215 nM TRP (5 $\mu\text{g}/\text{mL}$) and 160 nM ChT (4 $\mu\text{g}/\text{mL}$). The camera responses are almost indistinguishable. 208

Figure 5.13 Schematics of the instrumental setups used for (A) acquisition of PL spectra, (B) colour digital PL images with either a low-cost digital microscopy camera (Moticam 1) or consumer webcam, and

(C) colour digital PL images with a smartphone. For the smartphone imaging, the LED source was powered from three 1.5 V batteries (in series) instead of the USB connected DAQ module. Schematics are not to scale. In each case, a long-pass filter was used to block reflected LED light. The built-in colour filters of the cameras discriminated between QD and dye emission.....213

Figure 6.1 (A) Design of paper test strips to measure thrombin activity *via* FRET with immobilized QD donors and A647 acceptor dye-labeled peptide substrates containing a cleavage site recognized by thrombin. Protease activity was measured through the recovery QD PL with loss of FRET. (B) Paper test strips with sample and reference spots of immobilized QD-peptide conjugates were (i) enclosed within PDMS/glass sample cells that were then (ii) filled with a biological sample matrix such as serum, diluted blood or whole blood. Note the opacity of the whole blood. (C) Photograph of the setup used for smartphone readout of QD-FRET test strip assays with serum and blood samples. The inset shows the setup with the LED470 illuminating the PDMS/glass sample chip.219

Figure 6.2 Spectra showing the absorption of a blood sample, the absorption (dashed line) and emission (solid line) spectra associated with the QD630-A647 FRET pair, and the emission spectrum of the LED470 excitation source. The fluorescence spectra are normalized for easy comparison. The absorbance spectra were measured for the following solutions: 0.27 μM QD630, 4.0 μM A647, and 0.05% v/v blood (1 cm path length). The transmission spectrum of a 624/40 bandpass filter used to isolate QD emission prior to the smartphone camera is also shown.220

Figure 6.3 Normalized absorption and PL spectra for the (A) QD630 and (B) QD650. The transmission spectra of the bandpass filters are shown as solid black lines and the absorption spectrum of a 0.05% blood sample (path length = 1 cm) is shown as a shaded grey region.221

Figure 6.4 (A) Variation in the intensity of the QD630 and QD650 PL spectra as a function of sample matrix (excitation at 470 nm). (B) Excitation wavelength-dependent attenuation of the QD630 and QD650 PL in serum and whole blood (solid lines). The wavelength-dependent molar absorption coefficients of QD630 and QD650 are also shown (dashed lines). These measurements were done with a fluorescence plate reader.222

Figure 6.5 Normalized absorption and emission spectra for (A) the QD630-A647 FRET pair and (B) the QD650-A680 FRET pair. Absorption spectra are shown as dotted lines and emission spectra are shown as solid lines.223

Figure 6.6 TEM images of (A) QD630 and (B) QD650.223

Figure 6.7 Comparison of FRET efficiency between (A) the QD630-A647 and (B) the QD650-A680 FRET pairs in bulk solution, measured with a fluorescence plate reader. Insets in (A) and (B) show the FRET efficiencies calculated from quenching of QD PL according to eqn. 1.24 as a function of the number of

acceptors per QD (open circles, raw data; closed circles, Poisson corrected data). **(C)** PL spectra of paper-immobilized QD630-A647 peptide conjugates. The inset shows extent of QD PL quenching as a function of the number of acceptors, measured from spectra acquired with fluorescence plate reader (open circles) and digital images acquired with smartphone (closed circles).....225

Figure 6.8 (A) Experimental design to determine effect of the optical path length through blood on measured PL intensity of immobilized QDs. The paper substrates were placed between two glass slides and distance separation was controlled by placing cover slips ($n = 1-8$) between them. **(B)** Effect of the optical path length through blood on attenuation of QD630 PL intensity from paper substrates measured with iPhone and CMOS monochrome camera.227

Figure 6.9 Effect of thickness of the paper on the intensity of LED470 light transmitted through chemically modified Whatman chromatography paper No. 4 soaked in buffer.228

Figure 6.10 Normalized progress curves for thrombin activity in **(A, D)** buffer, **(B, E)** serum, and **(C, F)** whole blood samples, measured *via* smartphone imaging (A, B, C) and *via* a USB-CMOS camera (D, E, F). Representative smartphone images are shown for three points in the assays: prior to the addition of sample, immediately after adding sample, and after 30 min. In each image, the spiked thrombin concentrations were (i) 0, (ii) 15.1 NIH U mL⁻¹, (iii) 30.3 NIH U mL⁻¹, (iv) 121 NIH U mL⁻¹, (v) 242 NIH U mL⁻¹, and (vi) 484 NIH U mL⁻¹.233

Figure 6.11 Progress curves for the detection of thrombin activity in blind samples. Error bars describe standard deviation ($n = 5$).....234

Figure 6.12 (A) PL emission spectra corresponding to the increasing number of SA_v-A647 binding to immobilized QD630-Pep(biotin) conjugates. The number of SA_v per QD were 0, 0.5, 1, 1.5, 2, 2.5, 3, 3.5, 4, 4.5, 5, and 6. **(B)** QD PL intensity corresponding to (A); spectral data is plotted in terms of the QD peak PL intensity and smartphone data is plotted as the red channel intensity. The other panels show data from paper-based competitive SA_v assays in **(C)** buffer and **(D)** 50% blood. The data is the relative QD PL intensity as a function of time upon exposure to different concentrations of SA_v (analyte) and a fixed concentration of SA_v-A647 (competitor). For assays in buffer, the concentration of SA_v-A647 was 2.0 μM, whereas the concentration for assays in 50% blood was 1.0 μM.....236

Figure 6.13 Preparation of paper substrates with immobilized QD-peptide conjugates and assembly of glass/PDMS chip containing paper substrate within sample cell.244

Figure 6.14 Drawing of a positive-relief template used to mould PDMS to form 18 sample cells on a microscope slide-sized chip.246

Figure 6.15 Schematics of the instrumental setups used for (A) acquisition of LED spectra, (B) solution-phase QD PL with LED excitation, and (C) colour digital PL images with a smartphone. For the smartphone imaging, the pulsed LED source was powered from the USB connected DAQ module. Schematics are not to scale. A bandpass filter was used to isolate QD PL and reject reflected LED light and FRET-sensitized emission from dye-acceptor.....250

Figure 7.1 Representative data for proteolysis by (A) trypsin, (B) thrombin, and (C) plasmin on (i) GSH, (ii) DHLA, and (iii) PEG coated QDs as a function of additional peptide substrate assembled on QDs. A total number of peptides per QD is 10 (blue), 20 (green), 40 (orange), and (60) red on GSH (i) and DHLA (ii) capped QDs and 10 (blue), 20 (green), 30 (orange), and 40 (red) on PEG coated QDs. Maximum peptide loading on QD was determined using gel electrophoresis (data not shown): 60 peptides on GSH and DHLA capped QDs, and 40 peptides on PEG-coated QDs. Corresponding gel electrophoresis (0.7%, TB, pH 8.5) for QDs mixed with an increasing concentration of the protease are also shown; [QD] = 200 nM and protease concentration (from left to right on the image) 0, 0.1, 0.2, 0.4, 0.8, 1.6, 3.2, 6.4, 13, and 25 μ M.263

Figure A1 (A) Determining the quantum yields of green-emitting QD525 and QD540 relative to fluorescein, and (B) determining the quantum yields of red-emitting QD605 and QD625 relative to rhodamine B.312

Figure A2 Screenshot of the custom LabVIEW program used to control LEDs.313

Figure A3 Screenshot of the custom LabVIEW program used to acquire time-based spectra with Green-Wave spectrometer (StellarNet).314

List of Schemes

Scheme 4.1 Colorimetric tests used to estimate the surface densities of accessible functional groups. Aldehyde content was measured in sample (2) with TTC, primary amine content in sample (5) was measured with ninhydrin, and available thiol groups in samples (4b) and (6b) were determined with Ellman's reagent.....	154
Scheme 4.2 Chemical modification of cellulose paper fibers with imidazole-based ligands for immobilization of the QDs.	178
Scheme 4.3 Chemical modification of cellulose paper fibers with <i>N</i> -(2-aminoethyl)-5-(1,2-dithiolan-3-yl)pentanamide ligands for immobilization of the QDs.	179
Scheme 4.4 Synthesis of lipoic acid-NHS.	180
Scheme 4.5 Chemical modification of cellulose paper fibers with lipoic acid ligands for immobilization of the QDs.	182
Scheme A1 Synthesis of DHLA-PEG ligands.	304
Scheme A2 Synthesis of DHLA-zwitterionic (ZW) ligands.	308

List of Abbreviations

A488	Alexa Fluor 488
A555	Alexa Fluor 555
A610	Alexa Fluor 610
A647	Alexa Fluor 647
A680	Alexa Fluor 680
APTES	3-aminopropyltriethoxysilane
ATR-FTIR	Attenuated Total Reflectance FTIR
Au NP	Gold nanoparticle
BB	Borate buffer
BP	Bandpass (filter)
BSA	Bovine serum albumin
ChT	Chymotrypsin
CMOS	Complementary metal–oxide–semiconductor
Cys	Cysteine
DCC	Dicyclohexylcarbodiimide
DCM	Dichloromethane
DHLA	Dihydrolipoic acid
DHLA-PEG	Polyethylene glycol appended DHLA
DHLA-ZW	Zwitterion appended DHLA
DIC	Diisopropylcarbodiimide
DIPEA	<i>N,N</i> -diisopropylethylamine
DMF	Dimethylformamide
DMSO	Dimethylsulfoxide
DNA	Deoxyribonucleic acid
EK	Enterokinase
FLIM	Fluorescence lifetime imaging microscopy
FRET	Förster resonance energy transfer
FTIR	Fourier transform infrared
FWHM	Full-width-at-half-maximum
GSH	Glutathione
HEPES	<i>N</i> -2-hydroxyethylpiperazine- <i>N</i> -2-ethane sulfonic acid
HOMO	Highest occupied molecular orbital
ISO	International Organization for Standardization
LA	Lipoic acid
LA-NH2	<i>N</i> -(2-aminoethyl)-5-(1,2-dithiolan-3-yl)pentanamide

LED	Light emitting diode
LOD	Limit of detection
LUMO	Lowest unoccupied molecular orbital
MPA	Mercaptopropionic acid
MS	Mass spectrometry
NHS	<i>N</i> -hydroxysuccinimide
NP	Nanoparticle
PBS	Phosphate buffered saline
pChT	Chymotrypsinogen
PDMS	Polydimethylsiloxane
PEG	Polyethylene glycol
PL	Photoluminescence
POC	Point-of-care
PON	Point-of-need
pTRP	Trypsinogen
QD	Quantum Dot
QSY35	Quencher ($\lambda_{\max} = 476$)
QSY9	Quencher ($\lambda_{\max} = 561$)
R-PE	R-phycoerythrin
RGB	Red-Green-Blue
SAv	Streptavidin
SDS	Sodium dodecyl sulfate
SEM	Scanning electron microscopy
Sub	Substrate peptide
TB	Tris-borate
TEM	Transmission electron microscopy
THR	Thrombin
TMAH	Tetramethylammonium hydroxide
TTC	2,3,5-triphenyltetrazolium chloride
TRP	Trypsin
UV	Ultraviolet
UCNP	Upconversion nanoparticle
WB	White balance
XPS	X-ray photoelectron spectroscopy
ZW	Zwitterionic

Acknowledgements

I would like to thank my advisor Dr. Algar for the continuous support of my research and his guidance in writing this thesis. It has been a memorable and unique experience to be his first graduate student.

I would like to thank my PhD committee: Dr. Blades, Dr. Bizzotto, and Dr. Berlinguette, for their insightful comments and suggestions.

I want to extend my gratitude to Dr. Gethin Owen for assistance with SEM imaging, Dr. Saeid Kamal for assistance and training with microscopy imaging, Dr. Ken Wong for assistance with XPS analysis, Dr. Garnet Martens and Brad Ross for TEM training. Special thanks go to Pritesh Padhiar and Kenny Bach, and all the members of the Mechanical Engineering Shop. Special thanks are also extended to Brian Greene, who recently retired from Electronic Shop, Elena Polishchuk at Biological Services Laboratory, and Helen Wright. I also thank Yun Ling for assistance with mass spectrometry and Emily Seo at the Shared Instrument Facility.

I would like to thank all of my colleagues at the Algar lab and students I had the pleasure to mentor: Huyngki Kim and Olga Solodova. I also would like to thank all of my coauthors of my publications for the collaborations.

I am deeply grateful to the Natural Sciences and Engineering Research Council of Canada (NSERC) and the University of British Columbia for graduate scholarships, awards, and travel grants.

Last but not the least, I would like to thank my family: my parents, my husband, and his parents for continuous love, understanding and support throughout my PhD, writing this thesis and life in general.

Chapter 1 Introduction

This chapter is an adaptation of published work, and is reproduced in part from:

(1) Petryayeva, E.; Algar, W. R.; Medintz, I. L., Quantum Dots in Bioanalysis: A Review of Applications Across Various Platforms for Fluorescence Spectroscopy and Imaging. *Appl. Spectrosc.* **2013**, *67* (3), 215-252, with permission from The Society of Applied Spectroscopy (Copyright under Creative Commons Attribution - NonCommercial 4.0 International licence).

(2) Petryayeva, E.; Algar, W. R., Toward point-of-care diagnostics with consumer electronic devices: the expanding role of nanoparticles. *RSC Adv.* **2015**, *5* (28), 22256-22282, with permission from The Royal Society of Chemistry (Copyright 2015 The Royal Society of Chemistry).

This thesis presents original research towards the development of fluorescence-based point-of-care diagnostic platforms using smartphone and semiconductor quantum dots. Conceptually, this work represents: (1) the application of luminescent nanomaterials for smartphone imaging; (2) the development of new chemistries for the design of paper-based bioassays; and (3) capitalization on the unique optical properties of quantum dots to enable detection of biomarkers in biological fluids. These concepts are largely developed through model protease assays that rely on Förster resonance energy transfer (FRET). This introductory chapter reviews important background information, including an overview of progress in the field of point-of-care (POC) assays, the current role of smartphones and nanomaterials in the advancing POC devices, a physical description of fluorescence and FRET, and a review of the structure, chemistry and optical properties of semiconductor quantum dots.

1.1 Point-of-Care Diagnostics

1.1.1 Consumer electronic devices for POC

There is a critical need for point-of-care (POC) diagnostics in health care and a parallel need for similar point-of-need (PON) diagnostics in other sectors. Such technology could have a profoundly positive impact on health, wellness and quality-of-life in both the developed and developing worlds. Over the past decade, a rapidly growing trend has been the design of portable, low-cost bioassays that use consumer electronic devices such as smartphones, digital cameras, scanners, and CD/DVD/Blu-Ray disc players for quantitative readout of results. This trend is a new twist on an older concept embodied by many strip reader devices, which, although not a consumer product *per se*, can provide low-cost and portable readout of assays. The overarching objective of this research is to enable a full range of point-of-care (POC) diagnostic tests that can improve the efficiency and accessibility of health care globally, and eventually help realize personalized medicine [1, 2]. The technical strategies used to address POC applications are often transferable between health care and other sectors that stand to benefit from rapid on-site or field testing; for example, environment, agriculture/aquaculture, food and water quality assurance, and public safety and security, where such tests tend to be referred to as “point-of-need” (PON). Another important trend over the past decade has been the application of nanotechnology to problems of biomedical and analytical importance, where the unique properties of nanoparticles can increase the efficacy of therapies, improve analytical figures of merit in assays, and provide new opportunities for research and development [3-12]. Not surprisingly, the above trends are converging with exciting outcomes.

The general development and applications of POC/PON devices have been widely reviewed [13, 14] including assays for specific classes of analyte (*e.g.* microbes [15], cancer biomarkers [16], toxins [17]), specific analysis formats (*e.g.* paper-based assays and devices [18-22], lateral flow assays [23], lab-on-a-chip [24-26], and centrifugal microfluidic devices [24-26]), specific readout devices (*e.g.* scanners [27], CD/DVD [28], and Blu-Ray [29] drives, smartphones [1, 30-32]), and specialized areas of development (*e.g.* paper-based assays with nanoparticles [1, 30-32], immunoassays with nanoparticles [33], and microfluidic assays with gold nanoparticles [34]). The convergence of consumer electronic devices with nanoparticle materials for the development of assays and diagnostics that are amenable to POC/PON settings is illustrated

graphically in Figure 1.1. The devices of interest include the aforementioned smartphones, digital cameras, scanners, CD/DVD and Blu-Ray disc players, as well as strip readers and, to a limited extent, blood glucose meters. Nanoparticles of interest include gold nanoparticles, quantum dots, upconversion nanoparticles, silica and polymer nanoparticle composites, viral nanoparticles, and carbon nanoparticles—all of which lend themselves to optical readout. The extensive library of nanoparticles that are currently available offers remarkable choice in selecting materials that can maximize the analytical performance of assays with consumer electronic devices, providing exciting opportunities for current and long-term societal impact in the context of POC/PON assays and diagnostics.

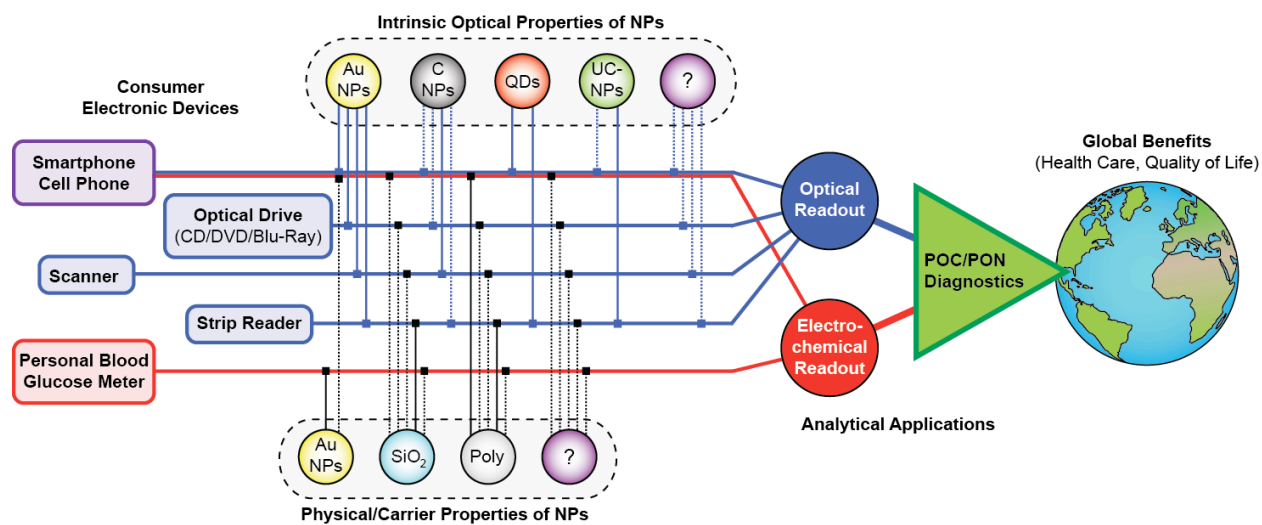


Figure 1.1 An illustration of the convergence of consumer electronic devices and nanoparticles for POC/PON diagnostics.

1.1.2 The need for point-of-care diagnostics

The aim of POC diagnostic technology is to provide robust, portable, reliable, rapid, inexpensive and simple testing of clinical biomarkers and other analytes. Minimization of the size, cost and operational complexity of the analysis method and instrumentation is integral to this goal, but achieving the best possible analytical figures of merit is not. Rather, it is sufficient to achieve figures of merit that satisfy clinically relevant thresholds and ranges of analyte. It should also be

possible to easily transport and store consumables and devices (if any) at points of care without loss of function. Both the U.S. Food and Drug Administration and the World Health Organization have recommended criteria for POC diagnostics [35-37].

POC diagnostic tests are needed in both developed and developing countries, where the current models of health care delivery are unsustainable, albeit for different reasons. In developed countries, advanced diagnostic technologies and services are readily available through centralized laboratories that can be accessed by the public, typically at the direction of physicians or during hospital stays. The demands on these services and their cost are such that the health care expenditures in developed countries are a growing fiscal burden, amounting to 7–9% of the gross domestic product (GDP) for G7 nations in 2012, with a projected increase to an average of 11% for advanced economies by 2050 [38, 39]. Moreover, rural areas and remote areas of developed countries tend to be underserved compared to urban centres. Travel to urban centres for medical testing creates extra stress for patients and adds further costs; for example, just in 2010-2011, the northern territory of Nunavut, Canada (pop. 33 000), had more than \$72M in health care costs that were associated with travel and out-of-territory services [40]. An array of POC diagnostic technologies that are sufficiently simple, rapid, reliable and economical to be deployed in a physician's office or in patient's homes would be a tremendous step toward increasing the efficiency of health care in developed countries.

In developing countries, the problem of accessibility to health care is greatly exacerbated, where large populations may have little or no access to even the basic health services of the developed world due to financial limitations, a shortage of skilled personnel, and a lack of infrastructure [35]. The lack of infrastructure is not only with respect to biomedical and clinical equipment, but may also include running water, refrigeration and electricity. In addition to basic medical tests and screening for chronic disease, affordable test kits for infectious diseases can be a life-saving intervention in many developing countries, where millions die every year due to inadequate diagnosis and these tests could help prevent epidemics from turning into pandemics [35]. Considering PON testing, rapid and low-cost methods of analysis for food safety and water quality, counterfeit medicine, and veterinary testing are also needed [19]. Foodborne illnesses are a direct result of ingestion of food contaminated with pathogens such as *Salmonella*, *E. coli O157:H7*, and cholera, the latter of which affects 3–5 million people and kills

more than 100 000 each year [41]. Non-existent protocols for water testing in rural areas also remains a major health issue associated with diarrheal diseases [42, 43]. Contamination of drinking water supplies with heavy metals (from industrial and mining production; *e.g.* mercury from gold mining), agricultural pesticides and fertilizers, sewage, and other wastewater contaminants poses both short-term and long-term health hazards. An estimated 50% of hospital patients worldwide suffer from illness associated with contaminated water [44]. PON diagnostic tests for food and water quality, and for early detection and screening of infectious disease, can improve life expectancy, shorten recovery times and reduce treatment costs [35, 45].

1.1.3 Clinical tests and biomarkers

To develop a comprehensive array of POC tests, it is necessary to detect a wide range of biomarkers and analytes with often disparate technical requirements. Ideally, these tests would use a common technology for quantitative readout, and would be able to directly analyze blood, urine, sputum, saliva, and sweat samples—all with little or no user intervention and straightforward readout of results. Most current clinical diagnostics do not meet these criteria.

Common classes of analytes in clinical diagnostics include blood gases (*e.g.* O₂, CO₂), pH, electrolytes (*e.g.* Ca²⁺, Mg²⁺, Na⁺, K⁺, Cl⁻), transport proteins (*e.g.* lipoproteins, ceruloplasmin, transferrin, haptoglobin, haemoglobin), metabolites (*e.g.* glucose, creatinine, urea, lactate), enzymes (*e.g.* creatine phosphokinase, alkaline phosphatase, aspartate/alanine aminotransferase), vitamins (*e.g.* beta-carotene; vitamins A, B12, C and 25-hydroxyvitamin D), hormones (*e.g.* thyroid stimulating, follicle stimulating, testosterone, estrogen), cytokines (*e.g.* interleukins; tumour necrosis factor), therapeutic drugs (*e.g.* digoxin, perhexiline, cyclosporine, tacrolimus), drugs of abuse (*e.g.* amphetamines, barbiturates, benzodiazepines, cannabinoids, opiates), cardiac and inflammatory markers (*e.g.* C-reactive protein, troponin I, myoglobin), genes (*e.g.* BRCA1, BRCA2), and infectious agents and pathogens (*e.g.* influenza, measles). Conventional laboratory procedures for assaying these analytes are often complex. Sample processing can be labourious and require specialized training, and the analyses often utilize instrumentation that is expensive, non-portable, and operated by skilled technicians; for example, spectrophotometric, electrochemical and chromatographic measurements, molecular biology techniques, cell culture and counting, among many other methods [46]. Notable exceptions to the above are lateral flow assays, which are much more amenable to POC applications, as described in Section 1.1.4.

The above classes of analyte can be reduced to three basic groups that can address most diagnostic needs: proteins, nucleic acids, and small molecules.

Proteins, whether enzymes, antibodies, certain hormones, cytokines, or otherwise, are frequent targets of POC diagnostics. The RCSB protein databank lists > 100 000 entries from various species [47], and more than 18 000 or 92% of gene-encoded human proteins have been catalogued, as well as many proteins from pseudogenes and non-coding RNA [48-51]. Depending on the target, protein biomarker concentrations typically range from picomolar to micromolar in bodily fluids. In the case of enzymes, their activity may also be of interest in addition to their concentration, in which case a product of that enzymatic activity is measured. When concentration is of interest, the biorecognition elements that are the basis for protein-targeting assays are usually antibodies, aptamers, or ligands that selectively bind to the target protein. Certainly, the standard format for protein detection is an immunoassay such as an enzyme-linked immunosorbent assay (ELISA), which has been one of the most prominent clinical laboratory tests over the past 20 years. As biorecognition elements, antibodies have remained indispensable because of their specificity and affinity but have several potential drawbacks, including limited stability, batch-to-batch variability, and high production costs. In many ways, aptamers are preferable biorecognition elements for POC/PON assays because they are more robust and more economically produced [52, 53]; however, aptamers that have affinity comparable to antibodies are not yet known for many target proteins.

Nucleic acid assays are increasingly important for the diagnosis of disease, identification of pathogens, and identification of genetic conditions and predispositions. Genes can be useful biomarkers for organisms and their physiology, and are sometimes preferable biomarkers over the proteins that they encode. Many thousands of genomes from eukaryotes, prokaryotes and viruses have been completely or partially sequenced [54], including the estimated 19 000 protein-coding human genes [55]. The analysis of DNA and RNA directly from bodily fluids is limited by its very small amount (*e.g.* 10^2 – 10^{11} copies per 1 mL of blood), necessitating multiple preparatory steps prior to analysis (*e.g.*, extraction, purification and amplification). Conventionally, polymerase chain reaction (PCR) is used for amplification of DNA. The thermocycling inherent to this process is not ideal for POC/PON applications, although computer-based thermocycling is possible [56]. Alternatively, there are now amplification

techniques that do not require thermocycling and may thus be more compatible with POC/PON applications. As reviewed recently [57], these isothermal techniques include loop-mediated amplification (LAMP), rolling circle amplification (RCA), nucleic acid sequence-based amplification (NASBA), signal mediated amplification of RNA technology (SMART), and nicking endonuclease signal amplification (NENNA). Synthetic oligonucleotides that are complementary to the sequence of target genes are typically used as biorecognition elements, and are robust and relatively inexpensive.

The most common small molecule targets for diagnostics are metabolites such as hormones, vitamins, amino acids, sugars, and other small organic molecules. The Human Metabolome Database lists *ca.* 42 000 entries [58, 59], and many of these can serve as indicators of disease. Similar to proteins, some metabolites are found at high concentrations (> 1 mM), at low concentrations (< 1 nM), and concentrations in between. The most common biorecognition element for metabolites are antibodies, although the small size and similar chemical structures of these analytes often yield limited sensitivity and specificity, including cross-reactivity, that makes immunoassay-based detection challenging. Aptamers are again promising alternatives to antibodies in these assays, but are still limited by the number of aptamers available and their affinity for their small molecule targets.

Another diagnostic test of interest is the detection of specific cell types and microorganisms; for example, pathogens that cause disease. Six common types of pathogens include viruses, bacteria, fungi, prions, protozoans and parasites. Infectious diseases contribute to more than 95% of all death in developing countries, and include human immunodeficiency virus (HIV), malaria (*Plasmodium* parasite), tuberculosis (*Mycobacterium tuberculosis*), and hepatitis A/B virus [60]. Moreover, at the time of writing, the worst recorded *Ebola* virus outbreak in history has infected >8 000 people and killed more than 5 000 people, mostly in West Africa [61]. Although pathogen outbreaks in the developed world are relatively rare and generally minor, there are nonetheless recurring instances of contamination of food with *Salmonella*, *Staphylococcus aureus*, *Listeria monocytogenes* and *E.coli* O157:H7 pathogens [62, 63]. The gold standard methods for detecting pathogens are culture-based assays that provide good sensitivity and selectivity, but require long incubation times that limit rapid responses to outbreaks [64]. An

alternative strategy for more rapid analysis is to target protein, nucleic acid, and small molecule biomarkers that are pathogen specific.

The above discussion on health-related targets for diagnostics is by no means comprehensive, and there is also significant demand for molecular diagnostic tests beyond health care. For example, public service employees are often tested for illegal recreational drugs, and elite athletes are tested for performance-enhancing substances. Many heavy metals and small molecules such as pesticides and other toxic pollutants are important targets in environmental analysis [65], while rapid monitoring and diagnostic tests are also valuable tools for biofuel production and other non-health areas of the biotechnology sector [66, 67]. Many of the approaches and challenges described for health-related diagnostics are equally applicable to these other sectors, and *vice versa*.

1.1.4 Lateral flow assays

Lateral flow assays have been one of the most successful and POC-amenable formats since the introduction of lateral flow immunochromatographic assays in 1988 by Unipath [68]. This format combines concepts from paper chromatography and immunosorbent assays. It frequently does not require the additional washing steps of the latter and typically needs only 0.1 mL of sample. LFA devices are suitable for the direct analysis of blood samples as plasma components are separated from blood cells within minutes, and are also suitable for the analysis of urine and other bodily fluids. Routinely used, commercially available POC immunochromatographic tests include those for pregnancy (human chorionic gonadotropin level) and ovulation; infectious diseases (*e.g.* malaria, influenza, HIV); drugs of abuse (*e.g.* NIDA-5 panel for cannabinoids, cocaine, amphetamines, opiates and phencyclidine); and cardiac biomarkers (*e.g.* troponin I, creatine kinase-MB, myoglobin).

Lateral flow immunochromatographic assay strips consist of a sample application pad, a conjugate pad, a membrane (*e.g.* nitrocellulose, cellulose), and an absorbent pad, as shown in Figure 1.2 [17, 19, 69]. Reporter antibodies conjugated with a contrast-providing reagent (dye-stained latex beads originally [70]) are deposited but not immobilized on the conjugate pad. A fluid sample is applied to the sample pad and wicks down the length of the test strip. As the sample passes through the conjugate pad, the contrast reagent-reporter antibody conjugates bind

to the target analyte. Further along the strip, the target analyte also binds to capture antibodies immobilized in the test zone, resulting in retention of the contrast label. Colour imparted to the test zone by the contrast label indicates the presence of target analyte in the sample. A control zone also tends to be included on the membrane, and this zone contains antibodies that bind to the reporter antibody. The absorbent pad ensures steady wicking of the sample fluid along the test strip. Many variations of this general assay design are possible; common variations include substitution of antibodies with other biorecognition elements, or the use of a competitive assay format rather than a sandwich assay format.

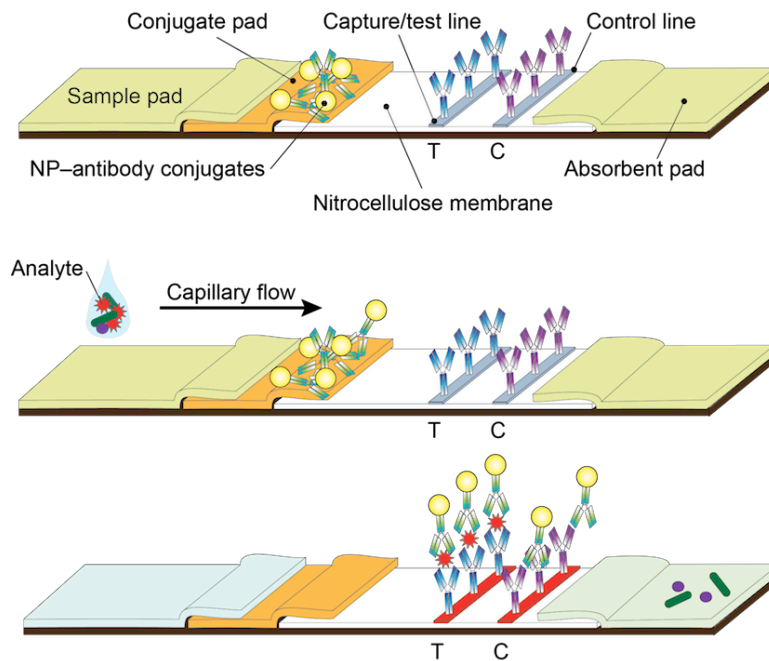


Figure 1.2 Basic design of a lateral flow immunochromatographic assay (LFIA). The device comprises a sample pad, conjugate pad, detection zone with test (T) and control (C) lines, and an absorbent pad. The sample containing analyte is added to the sample pad and drawn towards the absorbent pad by capillary action. NP-antibody conjugates bind to analyte (antigen) present in the sample and are captured on the test line, whereas NP-antibody conjugates that have not bound antigen are captured on the control line.

Although dye-stained latex beads are still used to generate contrast in lateral flow assays, many commercial assays now use gold nanoparticles, and additional nanoparticle materials have been investigated as contrast reagents in research toward new or improved diagnostics. There is also an increasing demand for quantitative rather than qualitative results from lateral flow assays, and this quantitation is often possible through analysis of digital images instead of simple visual inspection.

1.1.5 Utility of consumer electronic devices

Whether in the developed world or the developing world, modern consumer electronic devices can help address challenges in POC/PON testing in three principal ways: (i) lower equipment and infrastructure costs; (ii) miniaturization and portability; and (iii) data processing, storage and communication. The most common devices, which include scanners, CD/DVD and Blu-Ray players, web cams, cell phones and smartphones, offer the foregoing benefits to different degrees and have different suitability for the developed world *versus* the developing world.

In the developed world, all of the above devices share the benefit of low cost, which arises from their mass production and a highly competitive marketplace. Prices typically range from \$10–\$1000 depending on the device and much of the developed world already owns one or more of these devices. In the United States, for example, ownership statistics are 80% for DVD/Blu-Ray players, 64% for laptop computers, 57% for desktop computers, 45% for cell phones, and 62% for a smartphone (2013 data) [71]. In the developing world, one wishes to discuss cost in terms of cents rather than dollars; however, it must be recognized that the main role of consumer electronic devices in a POC/PON test will be quantitative readout and data handling, and these devices remain among the best candidates for establishing a frontline of health care infrastructure, particularly if the corresponding consumables for diagnostic tests cost pennies and also support qualitative assessment when these devices are not available. Moreover, these devices are not beyond the reach of the developing world as some people in these countries have easier access to mobile phone technology than they do to clean water [72].

From a technical perspective, scanners offer large-area colour imaging with reproducible positioning and illumination. Many current models of scanners are compact, support wireless communication, and can be fully operated *via* a USB connection to a laptop or notebook

computer. Disc players are common household items and optical drives are widely available as built-in or peripheral components of laptop/notebook computers. Discs also offer a substrate for arraying assay zones (*e.g.* microarray format) and integrating microfluidic channels, while disc players and drives offer optical readout and spinning motion that provides a centripetal force suitable for driving fluid flow. Cell phones, and later smartphones (the distinction being that smartphones have an operating system), have undergone remarkable technological growth over the last two decades. The first cell phone, the Motorola DynaTAC, became commercially available in 1984. It weighed 790 g and was 25 cm in length with a price of \$4 000 (*ca.* \$10 000 in 2016 dollars) [73]. The current generation of smartphones, such as the best-selling Samsung Galaxy and Apple iPhone models, offer immensely greater capabilities at a fraction of the price and a fraction of the size (\$600–\$1000, 130 g). These capabilities include high-quality built-in cameras, multiple modes of wireless communication (*e.g.* WiFi[®], Bluetooth, LTE), global positioning systems, security features, excellent data storage capacity, processing and graphics power to support software applications (apps), and many hours of battery life.

In the context of POC/PON diagnostics, smartphones are leading candidates to fulfill the role of computers in modern laboratory instrumentation, with lower cost and greater portability than notebook/laptop computers (which have built-in webcams and similar wireless connectivity). Furthermore, although a POC/PON test may be simple enough for a minimally skilled technician or unskilled person to conduct, determining a diagnosis or prognosis from test results may not always be as straightforward. Smartphone apps can potentially automate sample logging and data processing, and store or send results for subsequent interpretation by medical professionals or other highly-skilled personnel, whether locally or across the world. Importantly, these devices are also globally ubiquitous with 1.5 billion mobile telecommunications subscribers in the developed world and 5.4 billion in the developing world [74], albeit that the latter are primarily cell phone users rather than smartphone users.

1.1.6 Optical properties of nanoparticles

While consumer electronics can provide a means of assay readout, these devices cannot generate the readout signal or contrast themselves. These signals must come from selective recognition chemistry that is directly or indirectly coupled to a physical process that generates a measurable output. Nanoparticles (NPs) can be used for the generation of these signals and provide

enhancements or advantages over molecular reagents. By definition, NPs are particles that are less than 100 nm in their largest dimension [75], although here the definition is stretched to include particles with dimensions of hundreds of nanometers. The small size and molecule-like diffusion of NPs is complemented by large surface area-to-volume ratios, interfaces that can be further functionalized, and, in the case of many NP materials, size-dependent properties that are either not observed with their bulk analogues or are significantly enhanced. Table 1.1 briefly summarizes the key features of some NP materials that are currently used in POC/PON diagnostics or which are promising candidates for future use.

From the standpoint of optical diagnostics, there are many NP materials of interest. At present, the three most common materials are gold NPs (Au NPs), quantum dots (QDs), and lanthanide-based upconversion nanoparticles (UCNPs).

Au NPs have plasmon bands in their UV-visible absorption spectrum and exhibit strong light scattering that increases with increasing NP size (Figure 1.3A) [3, 5, 76]. These properties manifest as an intense red colour for assay readout with sensitivity that typically exceeds that of dyes and other materials. Although this red colouration can be seen by the naked eye and provide sufficient sensitivity for many assays, LODs can be improved by orders of magnitude with signal amplification strategies such as silver enhancement, which increase the optical contrast of the test zone. The silver enhancement strategy was popularized by Mirkin and coworkers [77] and relies on the reductive deposition of silver on Au NPs, thereby increasing the nanoparticle size and extinction coefficient, darkening their macroscopic appearance on a white background. The first and compelling demonstration of this strategy was the detection of 50 fM of target DNA with scanner readout [77]. Silver enhancement remains commonplace for POC diagnostic assays with scanners, as well as other consumer electronic devices. Alternatively, amorphous carbon NPs appear black and, like silver-enhanced Au NPs, provide high contrast under white-light illumination [78].

Table 1.1 NP materials for POC/PON diagnostics.

NP	Material ^a	Approx. Size (nm)	Optical Readout Features ^b	POC Usage	CMOS ^c	SCN	OD	SR
Au NPs	Gold	5–200	High optical density; intense red colour; silver amplification	High	✓[79-83]	✓[77, 84-90]	✓[91-98]	✓[99-102]
Polymer NPs	Polystyrene	10–1000	Properties of dopant/cargo molecule/NP (e.g., QDs, lanthanide complexes)	High ^d	✓[103]	◆	◆	✓[57, 104, 105]
Amorph. Carbon NPs	Carbon	< 1000 (irregular)	High optical density	Moderate	◆	✓[106-109]	◆	◆
QDs	CdSe/ZnS CdSeS/ZnS	3–10	Bright, tunable and spectrally narrow PL; spectrally broad light absorption	Moderate	✓[110]	--	--	✓[57, 105, 111-113]
UCNPs	NaYF ₄ :Yb doped with Eu ³⁺ , Tb ³⁺ , Ho ³⁺	20–50	Upconversion PL; spectrally narrow PL	Moderate	◆	--	--	✓[114-116]
Silica NPs	Silica	10–500	Properties of dopant/cargo molecule/NP (e.g., Au NPs, lanthanide complexes)	Low	◆	◆	◆	✓[99, 117]
Viral NPs	Protein	10–1000	Properties of dopant/cargo molecule/NP	Low	◆	✓[118]	◆	◆
Carbon dots	Carbon	2–6	Bright, spectrally broad PL	Future?	◆	--	--	◆
Pdots	π-conjugated polymers	5–50	Bright PL from very strong light absorption; composites with other optically-active materials	Future?	◆	--	--	◆

Legend: CMOS, device with CMOS image sensor; OD, optical drive for disc player for CDs/DVDs/BRDs; SCN, scanner; SR, strip reader; ✓, current use; ◆, possible or probable future use. Notes: ^a Typical materials listed. There are many possible materials for QDs and polymer NPs. ^b NPs may have properties beyond those listed here. ^c Includes cell phones, smartphones, digital cameras, wearable technology, etc. ^d There are many uncited examples of polymer NPs as carriers for dye molecules.

QDs exhibit bright, size-dependent photoluminescence (PL) that is easily excited and can be tuned across a wide spectral range (Figure 1.3B) [6, 7]. The optical properties of QDs, which are discussed in more detail in Section 1.3, are generally considered to be superior to those of fluorescent dyes: their light absorption is much stronger and more spectrally broad, and their emission is much more spectrally narrow and resistant to photobleaching. Lanthanide-based upconversion nanoparticles (UCNPs) convert near-infrared (NIR) excitation into visible emission, the colour of which depends on their composition (Figure 1.3C) [9-11]. Upconversion is not possible with fluorescent dyes. With both QDs and UCNPs, their light emission against a dark background provides contrast for assay readout. Further properties of QDs that make them advantageous for POC/PON assays with consumer electronics, and in comparison to fluorescent dyes and other materials, are described in detail in Section 1.3. More generally, the benefits of fluorescence detection in POC/PON assays include potentially greater sensitivity and lower LODs, potentially greater tolerance of sample colouration, and new possibilities for multiplexed analyses. The trade-off is that fluorescence measurements are somewhat more technically demanding, requiring an excitation light source and readout against a dark background (*i.e.* exclusion of ambient light). Fortunately, POC/PON-amenable light sources are widely available (see Section 1.1.7.1) and 3D printing provides a convenient means of producing ambient light-blocking enclosures or attachments for smartphones or other complementary-metal-oxide-semiconductor (CMOS) image sensor devices.

Other NP materials that are of interest in context of POC/PON diagnostics are silica NPs [119-121] and polymer NPs [122, 123]. However, in contrast to the foregoing materials, it is their physical properties that are of interest rather than their optical properties. These NPs, which can have dimensions of hundreds of nanometers, can serve as carriers of molecules or smaller NPs that provide contrast (*e.g.* Au NPs, QDs, UCNPs). Viral NPs and genome-free virus-like NPs (collectively, VNPs) can also serve as carriers of contrast reagents, with the benefit of being monodisperse, tailorable through genetic engineering and chemical functionalization, and producible at a large scale [124, 125]. Analogous to the original use of latex beads as a carrier for dye molecules, the concept is that many NP contrast reagents can be associated with a single binding event even though there will be no more than one carrier particle per binding event, resulting in greater sensitivity.

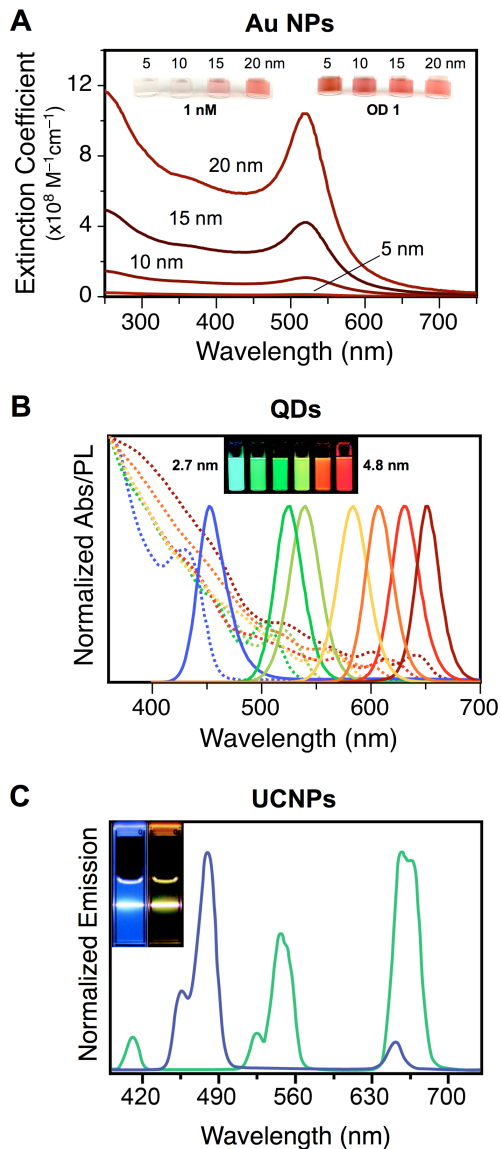


Figure 1.3 (A) Size-dependent molar extinction coefficient of Au NPs as a function of wavelength. The inset photographs show solutions of 5, 10, 15 and 20 nm Au NPs at 1 nM concentration and with an optical density of 1 (ca. 90, 10, 3, and 1 nM concentrations for 5, 10, 15 and 20 nm Au NPs, respectively). **(B)** Size/composition-tunable absorbance and emission of CdSe/ZnS and CdSeS/ZnS QDs. The inset photograph shows samples of different sizes of CdSe/ZnS QDs under UVA (365 nm) illumination. Photograph reprinted with permission from ref. [126]. Copyright 2011 American Chemical Society. **(C)** Upconversion emission spectra of NaYF₄:Yb/Tm (20/0.2 mol %; blue line) and NaYF₄:Yb/Er (18/2 mol %; green line) nanoparticles. The inset photographs show samples of these nanoparticles under 980 nm excitation with a diode laser (600 mW). Adopted with permission from ref. [127]. Copyright 2008 American Chemical Society.

Several other optically-active NP materials are known and, to the best of our knowledge, have yet to be utilized for POC/PON assays with consumer electronic devices. For example, carbon nanotubes [128, 129], graphene oxide [130, 131], carbon dots [132, 133], and nanodiamonds [134, 135] exhibit PL that can be useful for biological imaging and assays; however, it is not clear that the characteristics of this PL (*e.g.* brightness, spectral range of absorption and emission) is well-suited to readout with consumer electronic devices. On the other hand, semiconducting polymer nanoparticles (Pdots) [136] have exceptionally bright PL that is certainly promising for readout with consumer electronic devices, and the lack of examples to date is likely a product of the novelty of the materials. Beyond optical properties, many NP materials also have magnetic or electrochemical properties that are of interest.

1.1.7 Bioassays with consumer electronics and nanoparticles

This section describes consumer electronic components and devices that are being actively developed as platforms for readout of POC/PON diagnostics and assays. Light-emitting electronic components, which are common to all of the assays considered, are first reviewed, then, the basic design elements and functional principles underlying digital imaging utility as a readout platform are described, followed by examples of assays that use this device in combination with NPs for readout of results.

1.1.7.1 Light sources

Common light sources for POC/PON assays with NPs include white or coloured light-emitting diodes (LEDs), laser diodes and, to a lesser extent, hand-held ultraviolet (UV) lamps or “black lights.” These light sources permeate the developed world and are available at low price points. LEDs are ubiquitous as indicator lights and display backlights in electronic devices, in traffic signals and signage, and in both decorative and ambient lighting products. Laser diodes are critical components of optical drives/disc players, printers, barcode scanners, manufacturing technology, telecommunication systems, and are also used in medicine and dentistry. Hand-held UV lamps that emit long-wavelength UVA light have been traditionally used for forgery detection (*e.g.* monetary bills, documents) but are gradually being replaced by LEDs that emit in the same spectral range. All of these light sources can be battery-operated for extended periods, which is a critical consideration for use in POC/PON applications.

Of the above light sources, LEDs are the most economical (\$0.01–\$1.00 typical) and the most amenable to miniaturization (millimeter dimensions). LEDs usually have low operating voltages (3–5 V) and low power consumption ($\sim 10^{-3}$ – 10^{-2} W), although higher-power LEDs ($>10^{-1}$ W) are available at greater cost than noted above. Low-cost, low-power LEDs are the most relevant to POC/PON applications. The emission from an LED is incoherent and distributed over a relatively wide angular range. Its peak emission wavelength, which may be in the UV, visible or infrared region of the spectrum, is determined by the semiconductor composition of the diode. Spectral full-widths-at-half-maxima (FWHM) are typically in the range of *ca.* 15–50 nm. Representative examples of some low-cost LED spectra are shown in Figure 1.4A. Whereas colour LEDs (particularly blue and UV wavelengths) are well-suited to readout of photoluminescence, white-light LEDs are well-suited to colorimetric readout. Most white-light LEDs are actually blue LEDs with a phosphor coating that has broadband emission in the green-red region of the spectrum, as shown in Figure 1.4B. Colorimetric readout is also possible with a combination of red, green and blue LEDs.

Diode lasers provide more intense illumination than LEDs and have coherent, monochromatic emission (FWHM < 1 nm). From the perspective of POC/PON applications, laser diodes of the type found in laser pointers ($\sim 10^{-3}$ W) and optical disc drives and players ($\sim 10^{-1}$ W) are the most relevant. Figure 1.4C shows the emission from laser diodes that are commonly used for excitation of photoluminescence, including violet (405 nm), blue (447 nm), green (532 nm), red (650 nm) and infrared (980 nm) wavelengths. Note that many green laser diodes are actually infrared laser diodes that have been frequency doubled and fitted with an IR-blocking filter (DPSS lasers).

Hand-held, battery-operated UVA lights are another light source that is potentially suitable for POC/PON applications. These sources are low-pressure mercury discharge lamps where a phosphor converts the 254 nm emission from mercury to 365 nm emission from the lamp. A coating on the quartz tube absorbs any visible light. Power consumption is typically on the order of a few watts. The principal benefit of these sources is that relatively large areas can be illuminated with spectrally narrow light (FWHM ~ 15 nm, Figure 1.4D). Although “mini” or “pen” lamps are commercially available, UVA lights are less amenable to miniaturization than LEDs or diode lasers.

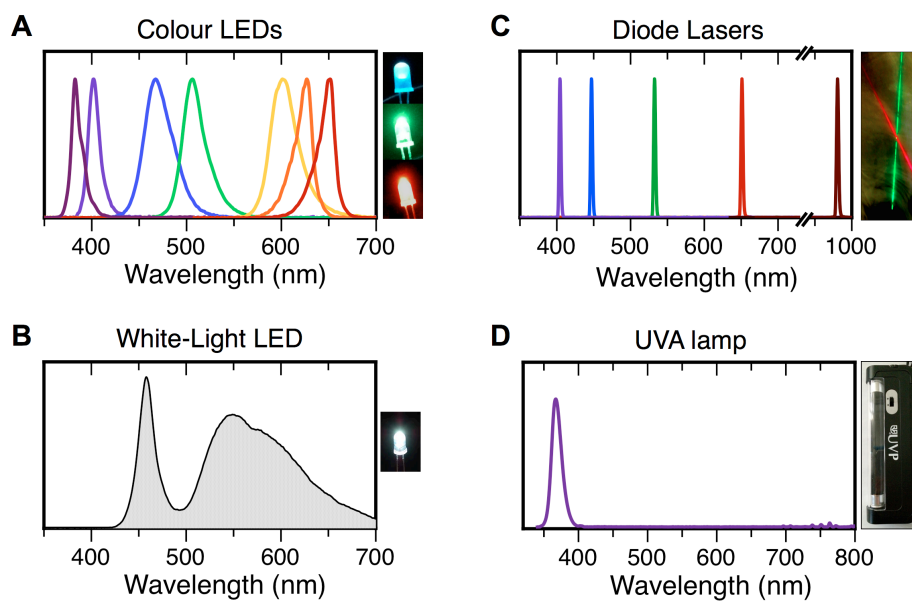


Figure 1.4 Emission spectra of commercial light sources well-suited to POC/PON diagnostics: **(A)** various colour LEDs emitting in UV-visible region of the spectrum; **(B)** white-light LED; **(C)** five common wavelengths of laser diodes (the FWHM > 1 nm is a measurement artifact); and **(D)** and a UVA lamp or “black light.”

1.1.7.2 CMOS image sensors: digital cameras to smartphones

1.1.7.2.1 Digital imaging technology

Modern CMOS image sensors are compact, provide high image quality, and are widely incorporated into consumer devices such as cell phone and smartphone cameras; webcams; wearable technology (*e.g.* Google Glass, Sony’s SmartEyeglass); and digital cameras for traditional photography, hobbies (*e.g.* Raspberry Pi), and recreational activities (*e.g.* GoPro). A selection of these devices is shown in Figure 1.5A. CMOS technology has also permeated scientific research in the form of microscopy cameras. The primary advantages of CMOS sensors over charge-coupled device (CCD) sensors are full integration of circuitry (which is more amenable to miniaturization), lower power consumption, and faster frame rates. Originally, these advantages were at the expense of image quality; however, improvements in fabrication technology and consumer demands for increased performance from their mobile devices have driven the advancement of CMOS technology to its current pinnacle.

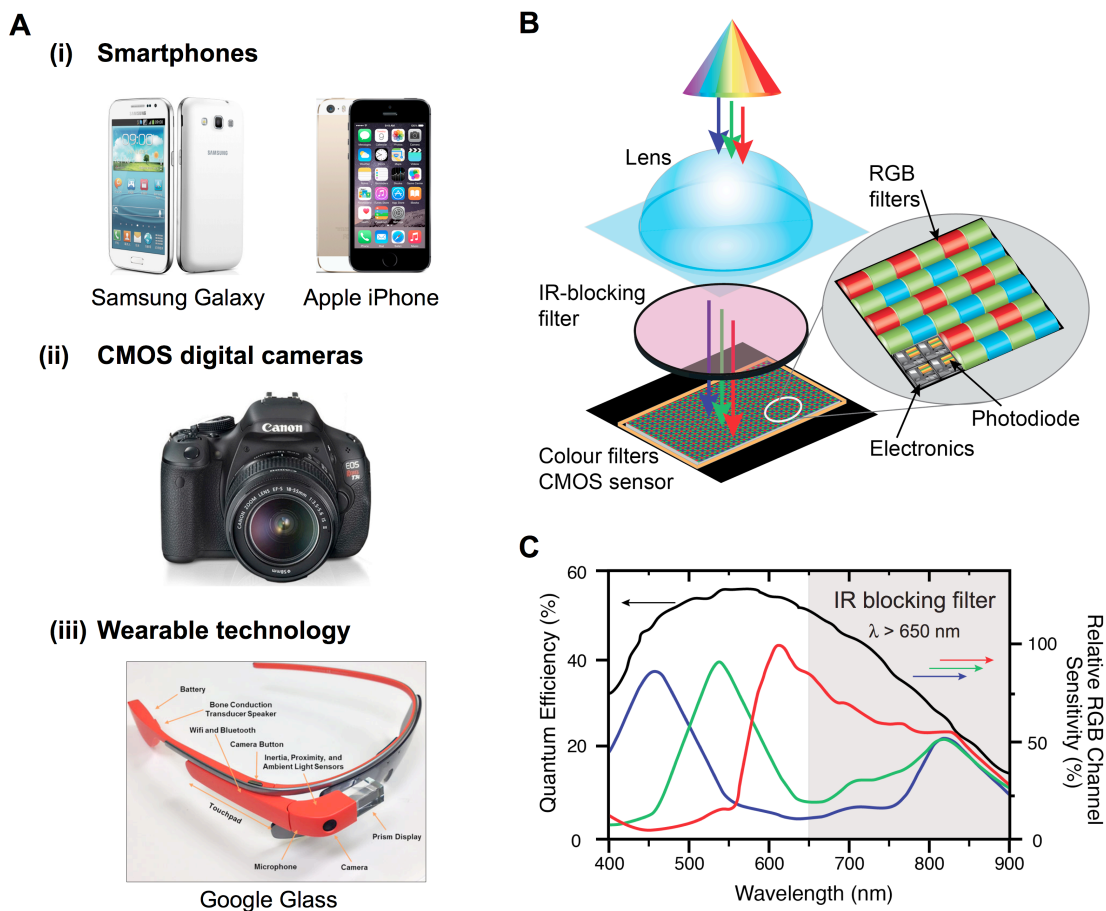


Figure 1.5 (A) Examples of consumer electronic devices equipped with CMOS cameras: (i) smartphones; (ii) digital cameras; and (iii) wearable devices. The image in (iii) is reproduced with permission from ref. [137]. Copyright 2014 American Chemical Society. **(B)** Simplified schematic of a CMOS image sensor. **(C)** Spectral sensitivity of a typical CMOS image sensor without (black) and with RGB colour filters (coloured lines). The typical blocking region of an IR filter is also shown.

As shown in Figure 1.5B, a CMOS image sensor has two main optical components: a pixel sensor array and optical filters for colour transmission (*e.g.* Bayer filter) and blocking UV and IR light. Millions of pixels capture light and convert that light into a voltage proportional to its intensity, where each pixel has its own amplification and digitization circuitry. CMOS sensors have wavelength-dependent sensitivity between *ca.* 380–1100 nm, as shown in Figure 1.5C. Colour information is obtained by superimposing an array of bandpass filters that transmit either blue, green or red light on the pixel array. The most common filter pattern is the “Bayer mosaic,”

which is a repetitive 2×2 grid with one red filter, two green filters, and one blue filter per four pixels. This ratio of filters was designed to mimic the human eye's greater sensitivity to green light [138]. IR and UV filters can be added to block unwanted wavelengths of light from outside the visible spectrum. Electronics and demosaicing algorithms convert the pixel signals into digital colour images.

1.1.7.2.2 Growing analytical applications

CMOS-based cameras, especially those in smartphones, have emerged as promising tools for health care and bioanalysis over the past few years. In particular, smartphones have been suggested to be amenable to POC diagnostics and telemedicine and Martinez *et al.* were among the first to suggest the use of a smartphone camera for quantitative analysis of colourimetric assays [139]. Numerous smartphone apps and accessories have become available to assist the general public with basic health monitoring; for example, heart rate [140, 141], blood pressure [140], body mass index [140], and detection of ear infections [142] and potential skin cancer [143, 144]. Initial evidence suggests that smartphone technology can support better health outcomes, as demonstrated with apps that promote physical activity and weight loss [145, 146]. Smartphone imaging has also been investigated as a POC/PON readout platform for molecular diagnostics such as immunoassays [147-149], nucleic acid hybridization assays [150], and colorimetric assays for cholesterol [151], food allergens [152], enzymes [153], and various urinary, salivary and sweat biomarkers [154, 155]. Digital images acquired with a smartphone camera can be analysed to extract quantitative information, most frequently in terms of the grayscale or RGB colour intensities for pixels of interest. These analyses can be done with computer-based image analysis software designed for either scientific research or consumer use (*e.g.* Adobe Photoshop), including freely available software (*e.g.* ImageJ), as well as smartphone apps.

Analytical and biological applications of cell phone and smartphone cameras also go beyond macroscopic digital photography. For example, when these cameras are combined with additional optics, they can be used for dark-field and bright-field microscopy of cells [156]. Imaging of a single fluorescent polystyrene NP (100 nm diameter) has also been demonstrated by the Ozcan Laboratory using a smartphone (Nokia PureView 808) [157]. The phone was equipped with a high-resolution CMOS sensor (41 MP) and utilized oversampling technology

(*i.e.* pixel binning) that enabled capture of five times more light than a typical zoom camera. A compact attachment to the phone was fabricated using 3D printing technology; it integrated a 405 nm laser diode excitation source (75 mW) powered by three 1.5V batteries (AAA size), a longpass filter to remove scattered excitation light, a 2× magnification lens, and optomechanics for focus adjustment (Figure 1.6A).

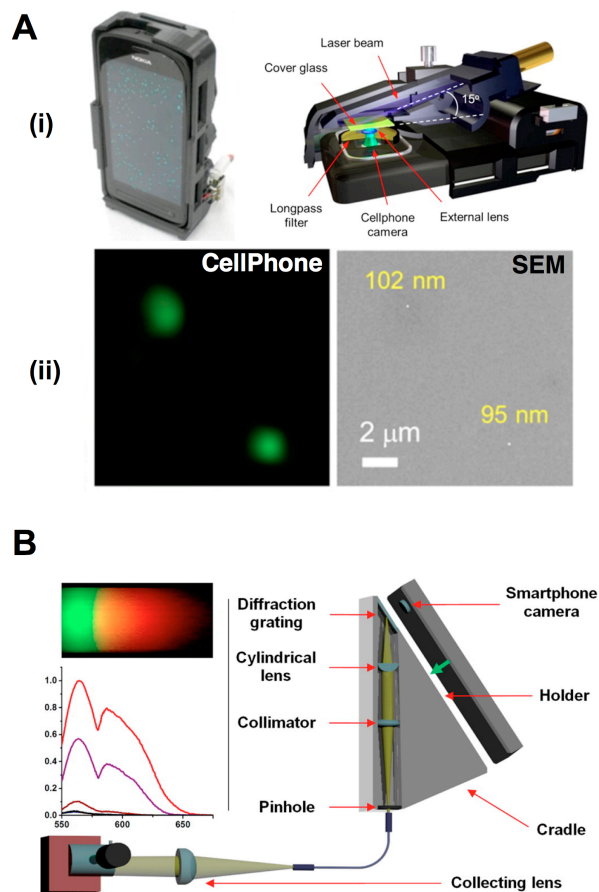


Figure 1.6 (A) Cell phone-based fluorescence imaging of individual NPs and viruses: (i) Front view of the smartphone microscope and a schematic diagram of its components; (ii) Images of 100 nm fluorescent NPs acquired with the cell phone show excellent agreement with SEM images. Adapted with permission from ref. [157]. Copyright 2013 American Chemical Society. **(B)** Attachment that enables use of a smartphone as a spectrophotometer for fluorescence emission measurements. The key component is a transmission diffraction grating. Reprinted with permission from ref. [158]. Copyright 2014 American Chemical Society.

Smartphone cameras can also be used as spectrographs [159]. As an example, the Cunningham Laboratory developed a simple transmission grating interface for a smartphone camera (iPhone 4) that enabled acquisition of full fluorescence emission spectra (Figure 1.6B) [158]. The diffraction grating (1200 lines/mm) dispersed fluorescence excited with a green diode laser pointer onto the camera. Due to the built-in UV and IR blocking filters, the smartphone camera-spectrophotometer was sensitive over the spectral range *ca.* 400–700 nm with a spectral dispersion of ~ 0.3 nm/pixel. Tests with a molecular beacon assay for microRNA demonstrated a limit of detection (LOD) of 1.3 pM, which was superior to a 3.6 nM LOD obtained with a conventional spectrofluorimeter. The observed enhancement was a combined effect of the greater quantum efficiency of the CMOS sensor in the smartphone *versus* the photomultiplier tube (PMT) in the spectrofluorimeter (40% *vs.* 12%, not accounting for PMT amplification), as well as a more than 30 000-fold increase in excitation efficiency. The latter was a result of the greater output power of the diode laser source (~ 300 mW) *versus* the xenon lamp in the spectrofluorimeter (10 μ W), and a more than 300-fold smaller illumination volume with laser excitation. The Dana Laboratory has demonstrated that a smartphone camera can also be integrated into a confocal Raman system for detection of the surface enhanced Raman scattering spectrum from ethanol [160]. Raman spectra were acquired with green laser excitation (532 nm, 10 mW) by placing a collimator and transmission grating in front of the camera sensor, which had overall sensitivity comparable to CCD and PMT detectors. Observation of blinking events from single molecules diffusing in and out of hot spots on a silver nano-island plasmonic substrate were observed with the smartphone at 30 fps video recording.

Smartphones can also serve as platforms for surface plasmon resonance (SPR)-based assays. Preechaburana *et al.* designed a disposable device that used a smartphone (iPhone 4) display screen as a light source and used its user-facing camera to measure reflectivity [161]. The SPR coupler was made from polydimethylsiloxane (PDMS) and epoxy to gently adhere to the phone's screen, which in turn displayed a guide for alignment with a red rectangle that provided illumination. Image acquisition was done using a custom app that allowed for control of exposure time and ISO number (*i.e.* sensitivity level to light). This platform was able to detect β_2 microglobulin (β_2 M), a biomarker for cancer, kidney disease and inflammatory disease, over a clinically relevant range of concentrations with an LOD of $0.1 \mu\text{g mL}^{-1}$ [161].

In addition to cell phones and smartphones, CMOS-based digital imaging assays run the gamut of technology from conventional digital cameras to new wearable devices. For example, Deiss *et al.* recently developed low-cost, portable paper-based culture devices for the analysis of antimicrobial susceptibility using a digital photography camera (Canon EOS Rebel T3i) for readout [162], whereas the Ozcan Laboratory demonstrated the use of Google Glass for readout of LFS immunoassay results, identification of sample codes, and transmission, analysis and storage of the results using hands-free voice operation [137].

Many of the CMOS-imaging assays that are being developed utilize a growing array of NP materials. To date, the most common materials include Au NPs for colourimetric detection, as was the case for the Google Glass example noted above, as well as QDs and UCNPs for fluorescence detection. Fluorescence-based assays offer a number of advantages in comparison to colorimetric assays, including improved selectivity and sensitivity. An overview of the fluorescence process and mechanism of resonance energy transfer are described in the following section.

1.2 Fluorescence

Luminescence is the emission of ultraviolet, visible or infrared radiation by any atom, molecule or lattice. If emission of light is a result of photon absorption, the process is termed *photoluminescence* (PL). Other types of luminescence include *chemiluminescence*, *bioluminescence*, and *electroluminescence*, as result from a chemical reaction, biochemical reaction, and passage of electrical current, respectively. A particular type of PL where emission of a photon is a result of an electronic transition from an excited state to a ground state without a change in spin multiplicity is termed *fluorescence*.

1.2.1 The Perrin–Jablonski diagram

Fluorescence is a photon emission process that takes place during molecular relaxation from electronic excited states to the ground state. This process involves transitions between both electronic and vibrational states of a polyatomic fluorescent molecule or *fluorophore*. The multi-step process of fluorescence is accompanied by a number of competing processes and is best described with introduction of a Jablonski diagram. As shown in Figure 1.7, the electronic states of a molecule are represented by potential energy wells. Within each electronic state, there are multiple vibrational energy states, each of which can be subdivided even further into rotational energy levels. For simplicity and clarity, only a few vibrational states (ν_n) are depicted in the diagram, and rotational levels are omitted entirely. Electronic states are typically separated by energies on the order of 1–10 eV (*ca.* 10 000–80 000 cm^{-1}) [163]. The separation between vibrational levels is typically on the order of 0.25 eV (*ca.* 2 000 cm^{-1}) [163]. Photons of light in the ultraviolet–visible region of the spectrum (200–800 nm, 6.2–1.6 eV) may trigger an electronic transition, as discussed in detail in Section 1.2.2.

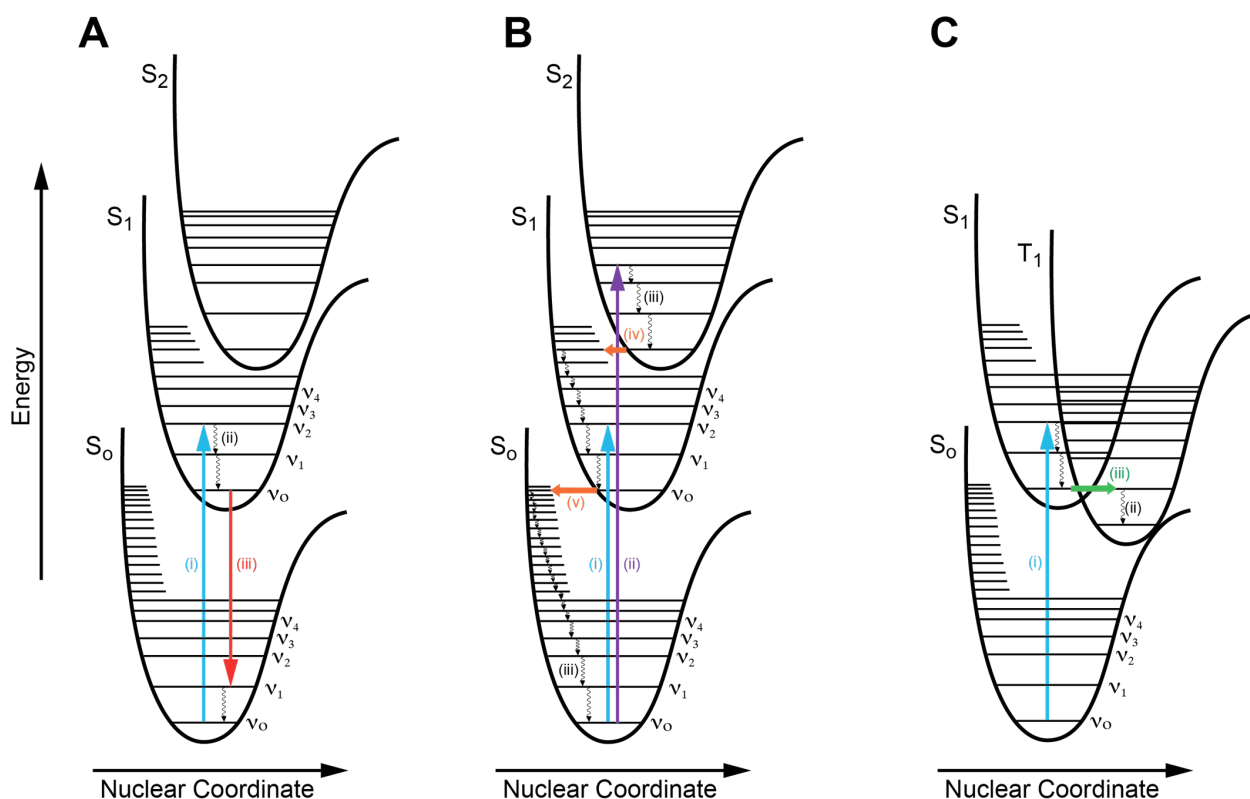


Figure 1.7 Jablonski diagrams illustrating the processes of absorption and photoluminescence, as well as competing non-radiative relaxation processes. Singlet electronic states are labeled as S_n , and triplet electronic states are labeled as T_n . The electronic states are shown as potential energy wells with superimposed vibrational states, v_n . **(A)** An example of processes involved in a radiative pathway. (i) Absorption from S_0v_0 to S_1v_2 , followed by (ii) vibrational relaxation to S_1v_0 and (iii) radiative relaxation to the ground state—fluorescence. **(B)** Processes involved in non-radiative pathways. Absorption from S_0v_0 to S_1v_2 (i) or S_2v_4 (ii), followed by (iii) vibrational relaxation to S_2v_0 and (iv) internal conversion to S_1v_7 . This process is followed by vibrational relaxation to S_1v_0 and, from this state, an emission of photon can take place as shown in (A, iii) or by (v) internal conversion—a transition to S_0v_0 , followed by (iii) vibrational relaxation to the S_0v_0 . **(C)** Other non-radiative relaxation pathways: (i) excitation to S_1v_2 , followed by (ii) vibrational relaxation to S_1v_0 , and then (iii) intersystem crossing to T_1v_1 . This process is followed by vibrational relaxation to T_1v_0 . From this state molecules return to the ground state either *via* non-radiative pathways or *via* radiative processes—delayed fluorescence or phosphorescence.

The simplest model used to describe a three-step fluorescence process is based on a system that comprises a singlet ground (S_0), and a singlet excited (S_1) states. First, a molecule absorbs a photon of appropriate wavelength and one of the electrons undergoes a transition from the

ground state, S_0 , associated with the highest occupied molecular orbital (HOMO) to an excited singlet state, S_1 , associated with lowest unoccupied molecular orbital (LUMO). This transition is very rapid and occurs on the femtosecond timescale. In the second step, the electron in the excited state undergoes rapid vibrational relaxation to the lowest vibrational state of S_1 . As a result, some of the energy deposited into the molecule by the photon is dissipated to the surroundings as heat. Vibrational relaxation takes place on a picosecond timescale. The third and final step is the return of electron from energetically unstable excited state, S_1 to any vibrational level of singlet ground state, S_0 , *via* emission of a photon (*i.e.* fluorescence). This process takes place on the sub-nano and nanosecond timescale. As a result of the differences in the timescales between fluorescence and vibrational relaxation processes, fluorescence almost always occurs from the lowest vibrational level of the first excited singlet state (S_1). This phenomenon, known as Kasha's rule [164], leads to an emission spectrum that is virtually identical irrespective of the excitation wavelength.

All of the processes introduced above, as well as other competing relaxation processes shown in Figure 1.7, are discussed in detail in following sub-sections.

1.2.2 Absorption–formation of the electronic excited state

Absorption of a photon by a molecule transforms light energy into electronic potential energy, thus promoting an electron from an occupied molecular orbital to an unoccupied molecular orbital of greater energy. Common types of electronic transitions include $n \rightarrow \pi^*$ and $\pi \rightarrow \pi^*$, where n , π , and π^* are non-bonding, pi bonding, and pi antibonding orbitals, respectively. These transitions are characteristic of conjugated pi electron systems, where the energy of the transition decreases as the extent of the conjugation increases [165]. The functional group of a molecule that absorbs light is known as a *chromophore*. The probability of light being absorbed by a chromophore is determined by a number of selection rules, as outlined below.

I. Resonance condition

Absorption occurs when the frequency of an incident photon matches the natural frequency of the transition from the lowest vibrational level (ν_0) of the ground state (S_0) to any of the

vibrational levels (ν_m) of the excited state (S_n), as given by eqn. 1.1, where f is the resonant frequency of photon, h is Planck's constant, and ΔE is the energy of transition.

$$E_{\text{photon}} = hf = \Delta E_{\text{transition}} = E(S_n \nu_m) - E(S_0 \nu_0) \quad (1.1)$$

II. Photoselection principle

An electronic transition from the HOMO to the LUMO alters the spatial electron distribution, often accompanied by a physical shift of the electron density, making the total electron density more diffuse. The transition moment is a vector that represents the transient dipole of charge displacement during this transition. Chromophores preferentially absorb polarized light with the electric field vector aligned along the transition moment. The probability of absorption is proportional to the square of the scalar product of the electric field vector of incident light, \bar{E} , and the transition dipole vector of the chromophore, $\bar{\mu}$, [165]:

$$P_{\text{Abs}} \propto (\bar{E} \cdot \bar{\mu})^2 = E^2 \mu^2 \cos^2 \alpha \quad (1.2)$$

where α is the angle between vectors \bar{E} and $\bar{\mu}$. According to eqn. 1.2, the maximum probability of light absorption occurs when light is polarized parallel to the transition dipole vector, and no absorption occurs when two vectors are perpendicular.

III. Electronic Selection rules

These selection rules are based on the conservation of angular momentum during a transition and determine whether transitions are observed (*i.e.* allowed transitions) or not (*i.e.* forbidden transitions). The following conditions must be satisfied for allowed transitions [166]:

1. Total orbital angular momentum quantum number, Λ , satisfies $\Delta\Lambda = 0, \pm 1$
2. Total spin angular momentum quantum number, Σ , satisfies $\Delta\Sigma = 0$
3. Total angular momentum quantum number, Ω , where $\Omega = \Lambda + \Sigma$, is the quantum number for the component of total angular momentum (orbital and spin), satisfies $\Delta\Omega = 0, \pm 1$.
4. Spin does not change: $\Delta S = 0$

The rule (4) states that electronic transitions between states of different multiplicities (*e.g.* between singlet and triplet states) are forbidden. However, these transitions do have a probability of occurring *via* spin-orbit coupling, a process that causes mixing of the singlet and triplet wavefunctions. Fundamentally, spin-orbit coupling is the result of the interactions of two magnetic moments arising from an electron spinning around a nucleus and about its own axis.

Other selection rules are based on changes in symmetry. The Laporte selection rule states that for centrosymmetric molecules, transitions can only occur if there is a change in parity—a parameter related to the orbital angular momentum summation over all electrons [167]. In practice, molecular vibrations can distort symmetry and Laporte forbidden transitions become partially relaxed [167].

1.2.2.1 Absorption spectrum: shape and intensity

The light-induced transitions of chromophores to their excited states involve simultaneous electronic and vibrational transitions. The electronic levels determine the position of the absorption bands (energy or wavelength) and the vibrational and rotational levels define the band shape. Therefore, the magnitude and the shape of the absorption bands depend on the probability of each separate transition between the ground state and vibrational levels of the excited states. At room temperature, the initial position of an electron in the ground electronic state is assumed to be the lowest vibrational level ($v_n = 0$). The Boltzmann distribution function, eqn. 1.3, describes the occupancy of the vibrational states in a molecule:

$$\frac{N_{v=n+1}}{N_{v=n}} = e^{(-\Delta E_{vib}/k_B T)} \quad (1.3)$$

where N is the number of molecules in the corresponding vibrational state ($v_n = 0, 1$), ΔE_{vib} is the energy difference between two vibrational states, k_B is the Boltzmann constant, and T is the absolute temperature. The thermal energy, $k_B T$, is only about 0.025 eV (200 cm^{-1}) at room temperature in comparison to the vibrational energy of 0.12–0.37 eV ($1000\text{--}3000 \text{ cm}^{-1}$), implying that the population of higher vibrational levels of the ground state is negligible [168].

The Franck-Condon principle states that all transitions from the ground state to the excited state are vertical transitions, as shown in the Perrin-Jablonski diagram (Figure 1.7), occurring without

any change in the position of nuclei. This principle is the result of differences in the timescale of the processes: the absorption of light is extremely rapid (10^{-15} s) in comparison to nuclear motions, which occur 10^2 – 10^3 times slower [165]. The quantum mechanical formulation of this principle is that the intensity of a vibrational transition is proportional to the square of the overlap integral between the vibrational wavefunctions, ψ , of the initial and final state (eqn. 1.4). This squared integral is known as the Franck-Condon Factor (FCF) and the total optical strength is the product of FCF and the constant electronic interaction term.

$$FCF = \left[\int \psi_{final}^* \cdot \psi_{initial} d\tau \right]_{vib}^2 \quad (1.4)$$

The vibrational overlap integral depends on the offset between the equilibrium bond lengths for the ground state and the excited state potential energy wells [168]. As shown in Figure 1.8, as a molecule moves to a vibrational level of the excited state during an electronic transition, this level must be instantaneously compatible with the nuclear position of the initial state. The excitation process is much faster than motions of nuclei, such that absorption is a vertical transition. Once molecule is in the excited state, its electronic configuration changes and the nuclei must move to reorganize to the new electronic configuration *via* molecular vibration [165]. As a result, there is an offset along the nuclear coordinate axis in the ground state and the excited state potential energy wells. The absorption of light results in the transition of a molecule to a nonequilibrium excited state, known as a *Franck-Condon state*. The multiple pathways available for a molecule to return to the ground state are discussed in Section 1.2.3.

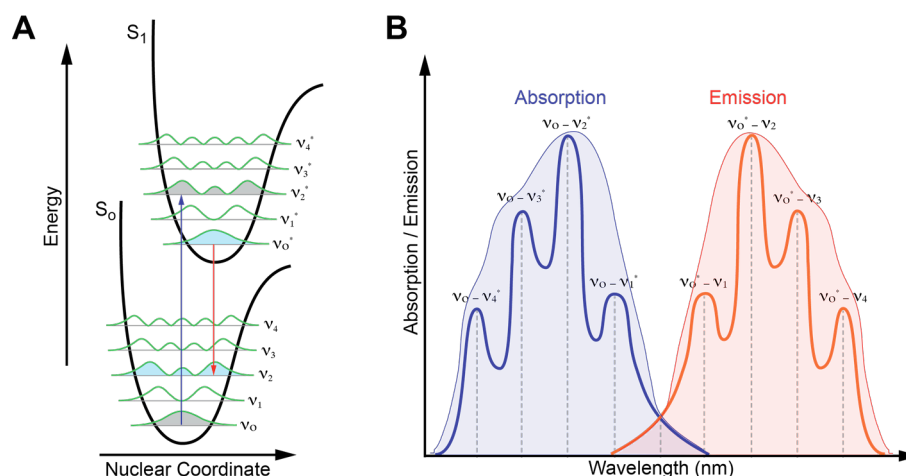


Figure 1.8 Illustration of Franck-Condon principle for an electronic transition from the ground electronic state, S_0 to the excited state, S_1 . **(A)** The maximum transition probability is observed for transitions with maximum overlap between initial and final vibrational wavefunctions, based on Franck-Condon factors. The most probable excitation (blue line) is shown into the second vibrational state (v_2^*) of S_1 , and the corresponding most probable relaxation transition is shown to the second vibrational state (v_2) of S_0 (red line). The probability density function is shown in green. **(B)** A corresponding schematic for absorption and emission spectra. The spectral characteristics of individual transitions are typically only observed in a gas phase or at very low temperatures, broadening (shown as shaded region) is observed in solution at room temperature. As a result of the Franck-Condon principle, the absorption and emission spectra are approximately a mirror image of each other.

The probability of a given transition between the ground state and an excited state is measured with either the molar absorption coefficient (ϵ , $\text{L mol}^{-1}\text{cm}^{-1}$) or the oscillator strength (f) [165]. The oscillator strength is a dimensionless parameter that compares a quantum mechanical transition to the expected fully allowed one. A strong transition is associated with $f=1$, whereas quantum-mechanically forbidden transitions can have f values of 10^{-3} or less [165].

The molar absorption coefficient is linearly proportional to the absorption cross-section, σ (in the units of cm^2) of a chromophore, according to eqn. 1.5:

$$\sigma = 2.303 \frac{\epsilon C}{n} = 2.303 \frac{\epsilon C}{(Nc/10^3)} = 3.82 \times 10^{-21} \epsilon \quad (1.5)$$

where c is concentration of chromophore, n is the number of molecules per cm^3 , and N is the Avogadro's number. A larger molar absorption coefficient and absorption cross-section indicates a greater probability of an electronic transition. For “fully allowed” transitions (*i.e.* spin rule and Laporte rule), molar absorption coefficients are greater than 10^5 . In cases where transitions are spin allowed but symmetry forbidden, the values fall in the range 10^2 – 10^4 due to the symmetry distortion described above [169]. The relationship between the molar absorption coefficient and oscillator strength, f , is described by eqn. 1.6:

$$f = 4.3 \times 10^{-5} \int \varepsilon(\bar{\nu}) d\bar{\nu} \quad (1.6)$$

where $\bar{\nu}$ is the frequency in units μm^{-1} .

The Beer-Lambert law characterizes the absorption process of a chromophore according to eqn. 1.7, where A is the absorbance, T is the transmittance, λ is the wavelength, $I_0(\lambda)$ is the incident light intensity, and $I(\lambda)$ is the remaining light intensity after passing through the sample with chromophore concentration, c , and sample path length, b .

$$A(\lambda) = -\log T(\lambda) = \log \left(\frac{I_0(\lambda)}{I(\lambda)} \right) = \varepsilon(\lambda) b c \quad (1.7)$$

1.2.3 The Franck-Condon electronic excited state

Upon excitation of a chromophore with light, it reaches one of the vibrational levels of the excited state ($S_m v_n$), as shown on the Perrin-Jablonski diagram in Figure 1.7. Subsequently, a chromophore will undergo several relaxation processes to return to its ground state. These include non-radiative (vibrational relaxation, internal conversion, intersystem crossing) and radiative (fluorescence, phosphorescence) processes.

An electronic excited state is energetically unstable as the chromophore is not in thermal equilibrium with the surrounding medium. As a result, rapid *vibrational relaxation* on the timescale of 10^{-13} – 10^{-11} s brings a molecule from the higher vibrational levels ($n > 0$) to the lowest vibrational level ($n = 0$) of S_1 [165]. During this process, chromophores collide with other

molecules (*i.e.* solvent) and transfer some of the energy imparted by the absorption of the photon to the surroundings as heat. Vibrational relaxation is the most efficient process, with a timescale shorter than any other relaxation process, so that a molecule always relaxes to $S_m\nu_0$ state before any other process will take place.

Internal conversion is a non-radiative process that allows for transitions between different electronic states with the same multiplicity, such as from the $S_m\nu_0$ state to the $S_{(m-1)}\nu_n$ state. The internal conversion process is typically described by either direct vibrational coupling (vibronic level overlap) or quantum mechanical tunneling (no direct vibronic overlap but small energy gap). The energy gap between electronic excited states ($S_{n,n-2}$) is small compared to that between the first excited state, S_1 , and ground state, S_0 . Furthermore, the numerous vibrational states with a typical energy gap of *ca.* 0.1 eV, along with superimposed rotational levels (10^{-3} - 10^{-2} eV) can generate approximately isoenergetic levels between two electronic states. Since internal conversion takes place between two isoenergetic levels without energy loss, it is a horizontal transition on the Perrin-Jablonski diagram. Quantitatively, the rate constant for non-radiative transition is described by *Fermi's golden rule*, which states that the rate is proportional to the product of two parameters: (1) the density of energetically matching vibrational levels between the initial and final states, and (2) the square of the vibronic coupling term [170]. Empirically, rate constants decrease exponentially as the energy difference between two electronic states increases [170]. This trend is known as the *energy gap law*. In general, as the energy gap between two electronic states decreases, the density of the vibrational states increases, and the Franck-Condon factors between two states increase, as well as the efficiency of internal conversion. Importantly, because there is a large energy gap between the first excited state, S_1 , and the ground state, S_0 , the rate of internal conversion is much slower, and fluorescence becomes a significant competitive relaxation process. The timescale of internal conversion between two excited states is comparable to the timescale of vibrational relaxation (10^{-13} - 10^{-11} s), while internal conversion to the ground state can be on the order 10^{-9} - 10^{-7} s.

A direct consequence of the rates of vibrational relaxation and internal conversion is the empirical *Kasha's rule*. It states that for polyatomic molecules, irrespective of the electronic excitation, the luminescence is only observed from the lowest vibrational level of the first excited electronic state of a given multiplicity. Exceptions to Kasha's rule have been observed.

For example, for molecules with large energy gaps between S_1 and S_2 , fluorescence corresponding to the $S_2 \rightarrow S_1$ transition is observed (e.g. azulene, cycl[3.3.3]azine) [170]. Alternatively, for molecules in which the oscillator strength of the $S_0 \rightarrow S_1$ transition is very small in comparison to $S_0 \rightarrow S_2$, a two-level $S_2 \rightarrow S_0$ fluorescence transition can be observed (e.g. ovalene) [170].

Fluorescence is the spontaneous emission of radiation by the excited molecule as it transitions from S_1v_0 to S_0v_n . The energy of the emitted photon is equal to the energy difference of the corresponding transition. The timescale of the fluorescence process is 10^{-10} – 10^{-7} s, which corresponds to the duration an excited state molecule remains in the first excited state before emitting photon [165]. The emission of a photon is as fast as the absorption of a photon (10^{-15} s). Similar to the absorption transition, the emission transition is governed by the Franck-Condon principle, which is represented by an approximate mirror-image relationship between the fluorescence spectra and first absorption band of a fluorophore, as illustrated in Figure 1.8. As a consequence of Kasha's rule, the Franck-Condon principle, and solvent effects (see page 36), the fluorescence emission spectrum is shifted to longer wavelengths in comparison to the absorption spectrum. The difference between absorption and emission maxima is known as *Stokes shift*.

Another de-excitation process from the S_1v_0 state that competes with fluorescence is *intersystem crossing* to the excited triplet state, T_1v_n . This process occurs between two isoenergetic vibrational levels of two electronic states with different multiplicity. Although such transitions are forbidden, spin-orbit coupling (i.e. coupling between spin magnetic moment and orbital magnetic moment) can be sufficiently large for efficient intersystem crossing. *Phosphorescence* is a radiative transition from the T_1v_n state to the S_0v_n state. This transition is forbidden but, similar to the intersystem crossing process, can be observed as a result of spin-orbit coupling. The radiative rates for phosphorescence are very low with a timescale on the order of 10^{-6} – 10^{-3} s. With such a slow process, the high probability of collisions with solvent molecules favors non-radiative relaxation to the ground state *via* intersystem crossing and vibrational relaxation.

1.2.4 Quantum yield and fluorescence lifetime

The fluorescence intensity and fluorescence lifetime of a fluorophore depend on the relative magnitudes of the rates for the radiative and non-radiative processes described in Section 1.2.3.

The quantum yield represents the fraction of excited molecules that decay to the ground state, S_0 , with the emission of photon. The fluorescence quantum yield, Φ_f , is defined in terms of all rate constants involved in depopulation of the excited state according to eqn. 1.8.

$$\Phi_f = \frac{k_f}{k_f + \sum k_{nr}} \quad (1.8)$$

$$\sum k_{nr} = k_{ic} + k_{isc} + k_q + k_{et} + k_{pd} + \dots \quad (1.9)$$

where k_f is the fluorescence decay rate, k_{nr} is the total non-radiative decay rate grouped according to eqn. 1.9, k_{ic} is the rate of internal conversion, k_{isc} is the rate of intersystem crossing, k_q is the rate of any fluorescence quenching process, k_{et} is the rate of energy transfer, and k_{pd} is the rate of photodegradation of the fluorophore. Since the quantum yield represents a fraction of fluorophores that relax to the ground state *via* emission of photon, its value always varies within $0 \leq \Phi_f < 1$. Although quantum yield can be very close to unity, some non-radiative losses occur, as k_{nr} is almost never zero [164].

The fluorescence lifetime is the average time a molecule spends in the excited state prior to relaxation to the ground state, and defined as a reciprocal rate constant for the decay of the excited state:

$$\tau = \frac{1}{k_f + \sum k_{nr}} = \frac{\Phi_f}{k_f} \quad (1.10)$$

The rate equation for depopulation of the excited state, S_1 , at time, t , following excitation is a first-order process given by eqn. 1.11.

$$-\frac{d[S_1(t)]}{dt} = (k_r + \sum k_{nr}) [S_1(t)] \quad (1.11)$$

Emission is a random event and the response that follows a pulsed excitation (used to instantaneously generate an excited state population) is an exponential decay:

$$I(t) = I_0 \exp(-t/\tau) \quad (1.12)$$

where $I(t)$ is the fluorescence intensity measured at time t , and I_0 is the intensity at time, $t = 0$. The fluorescence lifetime is a statistical average and fluorophores emit randomly throughout the decay. According to eqn. 1.12, the excited state lifetime is the time at which 63% of the fluorophores have relaxed to their ground state.

1.2.5 Quenching processes

Fluorescence is strongly dependent on the local environment and a variety of processes may decrease or quench fluorescence intensity. A wide range of molecules and ions can act as quenchers. The major mechanisms of the interaction between a fluorophore and a quencher include *static quenching*, *dynamic quenching*, and *combined quenching* [164]. Static quenching occurs when a nonfluorescent ground state complex is formed between a fluorophore and a quencher. Static quenching is a concentration-dependent process. Dynamic quenching describes any quenching process that affects the excited state, leading to a change in the excited state lifetime of a fluorophore. Dynamic quenching processes are distance-dependent and are based on collisional quenching, a process of depopulation of the excited state *via* intermolecular collisions with quencher. Charge transfer, electron transfer, and through space quenching—Förster resonance energy transfer (see Section 1.2.8) are all examples of dynamic quenching. Cases where fluorophore can be quenched by both collisions and complex formation with the same quencher are classified as combined quenching. All three quenching mechanisms described above are often analyzed using the Stern-Volmer equation. The relative changes in fluorescence intensity and lifetime as a function of quencher concentration, the effect of temperature, and changes in absorption and emission spectra can be used to identify the mechanism of quenching [164].

Photobleaching or dye photolysis results in an irreversible loss of dye fluorescence as a result of photochemical modification. Although photobleaching is not a quenching process *per se*, it can contribute strongly to decreases of fluorescence intensity. During this process, a molecule in the excited state undergoes a permanent structural change and ground state fluorophore is never recovered. Many factors, including local environment and the power of the excitation light may affect the mechanism of photobleaching, and therefore reaction rates [171]. In contrast to the quenching mechanisms discussed above that are reasonably well understood, photodegradation is still poorly understood phenomenon. Among several theories used to explain photobleaching, the

main mechanism is attributed to the interactions of excited state fluorophore and molecular oxygen in its triplet state ($^3\text{O}_2$) generating singlet oxygen [171]. The long-lived triplet state permits excited state molecules to interact with their surrounding for longer time (10^{-6} – 10^{-3} s). The photoionization of fluorophores in the triplet excited state generates highly reactive dye radicals towards solvent and other solutes. Susceptibility to photobleaching varies from dye to dye. Some dyes have shorter lifespans and degrade after emitting a few hundred photons, while other dyes may emit millions of photons before being bleached [171]. Importantly, the intensity of excitation light plays a non-trivial role in all photobleaching mechanisms.

1.2.6 Factors affecting fluorescence

The fluorescence intensity, quantum yield, and excited state lifetime in most molecules are extremely sensitive to their local microenvironment. The effects of the temperature, solvent polarity, viscosity, acidity, hydrogen bonding, and presence of quenchers are often the basis for analysis, as they modulate the rate of non-radiative processes [165]. In contrast, the radiative decay rate and natural lifetime are typically intrinsic properties of a fluorophore, and show little to no dependence on the microenvironment [172], with the exception of the environment of plasmonic metal structures [173, 174]. An increase in temperature is always accompanied by a decrease in the quantum yield and the lifetime because of the increase in non-radiative decay rates. Higher temperatures result in greater diffusion, increased collisions with solvent molecules, more efficient intramolecular vibrations and rotation—all of which promote non-radiative relaxation pathways. High viscosity solvents, as well as low temperatures reduce the number of collisions with excited state molecules, thereby slowing down non-radiative deactivation process and increasing quantum yield.

The role of the solvent and its polarity becomes important not just in its influence on the quantum yield of a fluorophore, but also on the broadening, shape and position of its fluorescence spectra. The latter effects are referred to as *solvatochromism*, where interactions of solvent molecules with fluorophore can cause bathochromic shifts (*i.e.* shifts to longer wavelength). Therefore, Stokes shifts are a result of vibrational relaxation to $S_1\nu_0$, the Franck-Condon factors, and solvent polarity [168]. Solvent molecules surround a ground state fluorophore based on the interactions of their dipole moments. Upon excitation of a fluorophore, the energy difference between the ground state and the excited state produces an increase in its

electric dipole moment. The surrounding solvent molecules respond to stabilize an excited state fluorophore. First, an instantaneous electronic polarization of the surrounding solvent molecules, and second, by absorbing excess vibrational energy released as fluorophore relaxes to the lowest vibrational level of the first excited state. Finally, solvent molecules stabilize and lower the energy of the excited state by rearranging around the fluorophore. This process, known as *solvent relaxation*, reduces the energy difference between excited state and ground state which induces the red-shift of fluorescence emission spectrum [164, 168]. Increased solvent polarity generally leads to a larger stabilization effect, while the polarity of the fluorophore determines its sensitivity to solvent effects.

Another parameter that affects the fluorescence of molecules with basic or acidic substituents is pH. The fluorescence intensity, shape and spectral position of absorption and emission bands may be different for protonated and deprotonated forms of a fluorophore. For example, fluorescein can exist as a cation, neutral molecule, anion, and dianion with pKa's of 2.08, 4.31, and 6.43, respectively [175]. All these forms have different absorption spectra and molar absorption coefficients ($\epsilon_{437,\text{cation}} = 53\ 000$, $\epsilon_{434,\text{neutral}} = 11\ 000$, $\epsilon_{453,\text{anion}} = 29\ 000$, $\epsilon_{490,\text{dianion}} = 76\ 900\ \text{M}^{-1}\text{cm}^{-1}$). Furthermore, the most intense quantum yield is observed for dianion (0.93), whereas the anion and cation have quantum yields of 0.37 and 0.18, respectively [175].

In addition to the parameters discussed above that affect fluorescence, and the quenching processes introduced in Section 1.2.5, a variety of other photophysical processes may also affect fluorescence, including collisions with heavy atoms (*e.g.* halogens) or paramagnetic species (*e.g.* dissolved oxygen), excimer or exciplex formation, electron transfer, and proton transfer [164].

1.2.7 Fluorescence measurements

Steady-state and time-resolved fluorescence spectroscopy are among the primary tools used to investigate physical, chemical, and biological systems. Some of the common parameters used to gain a physical insight or analytical information include changes in quantum yield, excited state lifetime, number of emitters, emission wavelength, and anisotropy.

Steady-state fluorescence measurements are based on constant illumination of the sample with a continuous beam of excitation light. This measurement represents equilibrium conditions, such

that the concentration of excited state fluorophores is constant under constant illumination. Typically, steady-state fluorescence measurements are done by (i) measurement of fluorescence intensity integrated over a fixed bandwidth of emission wavelengths, (ii) measurement of fluorescence intensity as a function of emission wavelength with a fixed excitation wavelength (an *emission spectrum*), and (iii) measurement of fluorescence intensity at a fixed emission wavelength as a function of excitation wavelength (an *excitation spectrum*).

The fluorescence intensity, F , measured by a given spectrofluorimeter for sufficiently dilute samples ($\epsilon bc < 0.05$) is given by eqn. 1.13, where Φ_f is the quantum yield of a fluorophore, b is the path length of the excitation light through the sample, c is the concentration of the fluorophore in the sample, $\epsilon(\lambda)$ is the molar absorption coefficient of the fluorophore, $P_o(\lambda)$ is the spectral power density of the excitation light, $K(\lambda')$ is the combined collection and detection efficiency of spectrofluorimeter, and $L(\lambda')$ is the band shape function of the fluorophore emission [176].

$$F(\lambda') = 2.303\Phi_f bc \iint P_o(\lambda) \epsilon(\lambda) K(\lambda') L(\lambda') d\lambda d\lambda' \quad (1.13)$$

Fluorescence measurements are typically performed on the same instrument and under the same excitation conditions as relative changes in intensity. From eqn. 1.13, it can be seen that fluorescence intensity is proportional to the concentration and quantum yield of a fluorophore, while all other terms can be approximated as constant for a given instrument under a specified set of conditions (*i.e.* excitation wavelength, sample path length).

In time-resolved measurements, the decay in fluorescence intensity is measured as a function of time on a timescale of the excited state lifetime after excitation with a pulsed light source. In contrast to steady-state measurements, time-resolved experiments are not at equilibrium conditions and rather provide information about dynamic changes in the excited state population.

Two methods for measuring time-resolved fluorescence are time-domain and frequency-domain spectroscopy. In the time-domain method, the sample is excited with a short pulse of light and the decay in fluorescence intensity is recorded as a function of time. Time correlated single photon counting (TCSPC) is a common approach for time-domain measurements being used for routine lifetime measurements, fluorescence lifetime imaging microscopy (FLIM), and various

single molecule studies [164, 177]. In the frequency-domain method, the sample is excited by sinusoidally modulated light at high frequency. The fluorescence response has a similar waveform, but is modulated and phase-shifted from the excitation curve based on the lifetime of the sample emission [164].

1.2.7.1 Fluorescence microscopy and imaging

Fluorescence microscopy provides spatial and intensity information about a fluorescent sample. Similar to the steady-state measurements described above, the sample is illuminated with a fixed bandwidth of excitation light and emission over a fixed bandwidth is acquired. The difference is the method and the detector used to record fluorescence emission—a digital image is created when an optical image formed by the microscope is recorded by a detector. Common imaging detectors include charge-coupled devices (CCDs) and scientific CMOS. When digital image of the sample is reconstructed from individual measurements across the sample (*i.e.* scanning), photomultiplier tubes (PMTs) are often used as detectors. A digital image is a two-dimensional grid of equally sized pixels, where each pixel represents a defined finite sized area in a specific location of the sample. The number of photons detected at each pixel during image acquisition is converted to the intensity value that can be correlated to the concentration of fluorophore depending on the nature of the sample [178]. Fluorescence microscopy is used for relative intensity measurements (*e.g.* fluorescent staining), co-localization studies, as well as Förster resonance energy transfer (FRET) and fluorescence recovery after photobleaching (FRAP) experiments [178].

1.2.8 Förster resonance energy transfer

Förster resonance energy transfer (FRET) is a mechanism of energy transfer *via* non-radiative through-space dipole-dipole interactions between a donor molecule its excited state (D^*) and an acceptor molecule its ground state (A). The acceptor can be a chromophore that is non-fluorescent (quencher), another fluorophore, or the same type of fluorophore as the donor (homoFRET) [164]. The dipole-dipole interaction (*i.e.* donor relaxation and acceptor excitation transition moments) does not require molecular contact between the donor and the acceptor; however, close proximity (< 10 nm) is necessary for efficient energy transfer. FRET is a resonant process, indicating that the energy difference between the excited and ground state of the

acceptor must be equal to the energy difference between the excited and ground state of the donor. This energetic resonance is expressed by the spectral overlap between the absorption spectrum of the acceptor and the emission spectrum of the donor. In this energy transfer process, there is no net change in the energy of the system and any excess energy is dissipated into vibrational modes in accordance with conservation of energy. The process of FRET is conceptually summarized in eqn. 1.14 and illustrated in Jablonski diagram in Figure 1.9.

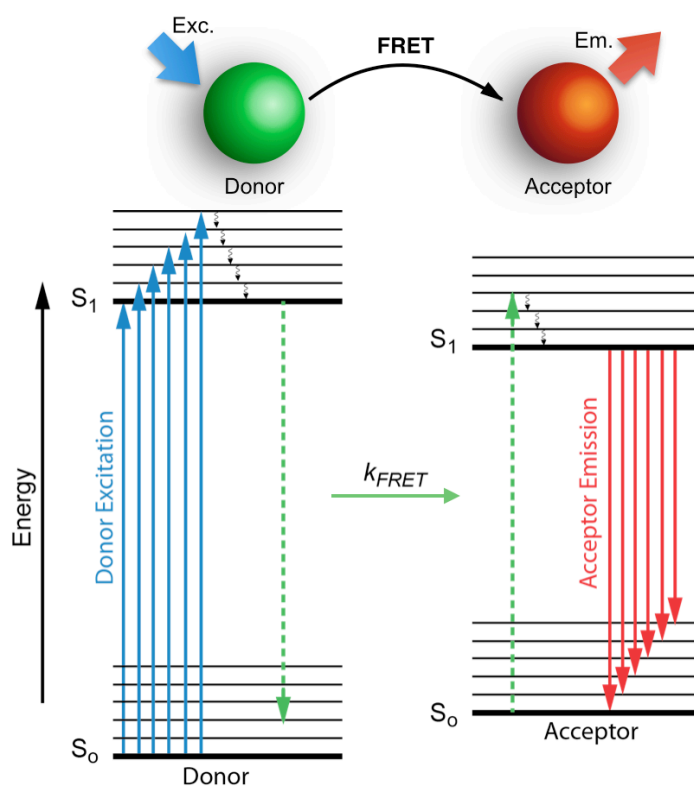


Figure 1.9 Jablonski diagram illustrating the FRET process. The donor is excited from the ground state S_0 to any of the vibrational levels of the first excited state S_1 , and then relaxes to the lowest vibrational level of S_1 via vibrational relaxation. During nonradiative resonance energy transfer, the donor relaxes to the ground state without emitting a photon, while an acceptor is simultaneously excited to a vibrational level of S_1 . Then acceptor undergoes the vibrational relaxation to the lowest vibrational level of S_1 , followed by either emission of a photon (*i.e.* fluorophore acceptor) as it relaxes to the ground state or nonradiative relaxation (*i.e.* dark quencher acceptor).

1.2.8.1 Classical Förster formalism

The quantum mechanical treatment of nonradiative energy transfer is based on Fermi's golden rule [170]:

$$k = \frac{2\pi}{\hbar} |V_{D^*A-DA^*}|^2 \rho \quad (1.15)$$

where k is the rate constant for the radiationless transition, \hbar is the reduced Planck constant, ρ is the density of final states relevant for the transition (*i.e.* the density of isoenergetic donor-acceptor states), and V represents an interaction term coupling the wavefunctions of the initial and final states. When the intermolecular distance between donor and acceptor is much larger than the size of the molecules, the dipole-dipole interaction between the transition moments of the donor (D^*) and the acceptor (A) can be represented by a dominant Coulombic coupling term, V_{Coul} [179]. The orbital overlap term is negligible and only becomes significant at very short distances (Dexter energy transfer). Therefore, eqn 1.15 can be modified for a FRET process as follows:

$$k_{FRET} = \frac{2\pi}{\hbar} |V_{Coul}|^2 \rho = \frac{2\pi}{\hbar} \left| \frac{\kappa |\vec{\mu}_D| |\vec{\mu}_A|}{4\pi\epsilon_0 n^2 r^3} \right|^2 \rho \quad (1.16)$$

where μ_D and μ_A are the transition dipole moments associated with donor relaxation and acceptor excitation, κ is the orientation factor between these two dipole moments, ϵ_0 is the vacuum permittivity, n is the refractive index, and r is the intermolecular distance between donor and acceptor. Since the interaction between the two dipoles decreases with the third power of distance, the FRET rate constant, k_{FRET} , exhibits an inverse sixth power dependence on the distance between donor and acceptor. In addition, eqn. 1.16 shows the origin of the n^{-4} and κ^2 dependences of energy transfer rate. The expression given in 1.16 can be further represented by experimentally measurable spectral quantities according to eqn. 1.17, known as the Förster equation. The square of the transition dipole moments is proportional to the oscillator strength, which can be represented by either a radiative lifetime for the donor, τ_D or molar absorption

coefficient for the acceptor, ϵ_A , according to eqn. 1.6. The density of states, ρ , combined with ϵ_A is substituted by the normalized spectral overlap integral, J .

$$k_{FRET} = \frac{9(\ln 10) \kappa^2 \Phi_D}{128 \pi^5 N_{Av} n^4 \tau_D} J \quad (1.17)$$

where Φ_D is the quantum yield of the donor, N_{Av} is Avogadro's number, and τ_D is the excited state lifetime of the donor in the absence of acceptor. When rate constants for energy transfer and spontaneous decay are equal ($k_{FRET} = k_r + k_{nr} = \tau_D^{-1}$), the donor-acceptor distance is known as critical transfer distance (or Förster distance), R_0 :

$$R_0^6 = \frac{9(\ln 10) \Phi_D \kappa^2 J(\lambda)}{128 \pi^5 N_{Av} n^4} = (8.79 \times 10^{-28} \text{ mol}) n^{-4} \Phi_D \kappa^2 J(\lambda) \quad (\text{cm}^6) \quad (1.18)$$

The typical range of a Förster distance for a donor-acceptor pair is 20–60 Å [164, 165]. A larger Förster distance implies higher FRET efficiency for a given donor-acceptor separation; however, there is always an upper limit at which the transition dipoles of the donor and the acceptor can no longer interact.

Combining eqn. 1.17 and 1.18, the rate of energy transfer is given by eqn. 1.19. FRET is the relaxation process that competes with all other processes including fluorescence, as was seen in eqn. 1.9. In the absence of an acceptor, k_{FRET} is zero.

$$k_{FRET} = \frac{1}{\tau_D} \left(\frac{R_0}{r} \right)^6 \quad (1.19)$$

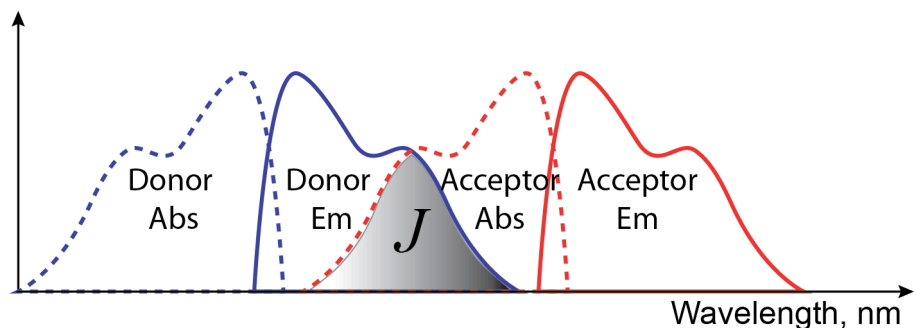


Figure 1.10 Schematic representation of the spectral overlap integral, which is shown as the grey area, J , where the emission spectrum of the donor overlaps with absorption spectrum of acceptor.

The spectral overlap integral is derived from the spectral overlap between the donor emission and acceptor absorption and provides a quantitative measure of the possible resonant transitions. The conceptual representation of spectral overlap is illustrated in Figure 1.10. Mathematically, the spectral overlap is defined by eqn. 1.20, where I_D is the normalized donor fluorescence intensity (eqn. 1.21) as a function of wavelength, λ and $\epsilon_A(\lambda)$ is the wavelength-dependent molar absorption coefficient of acceptor ($M^{-1}cm^{-1} = 10^3 mol^{-1}cm^2$) [164].

$$J(\lambda) = \int \overline{I_D} \epsilon_A(\lambda) \lambda^4 d\lambda \quad (1.20)$$

$$\int \overline{I_D} d\lambda \equiv 1 \quad (1.21)$$

FRET occurs as a result of the interaction between the transition dipoles of a donor and acceptor; the magnitude of this interaction, as was noted above, depends on the relative orientation and separation of these two transition dipole moments. The strongest interaction is observed for the parallel orientation ($\kappa^2 = 4$) and no interaction occurs when two vectors are perpendicular ($\kappa^2 = 0$) [164]. The magnitude of the orientation factor is determined according to eqn. 1.22, where θ_T is the angle between the donor and acceptor transition dipoles, and θ_A and θ_D are the angles the donor and acceptor dipoles make to the line connecting them, as illustrated in Figure 1.11 [164]. Experimentally, it can be challenging to determine the actual orientation of dipoles for molecules

that are free to move or rotate, although fluorescence anisotropy experiments are useful in determining this parameter [164, 180]. For instance, the polarization of two randomly oriented dipoles for donor and acceptor can be measured and correlated to the range of possible orientation factors [180]. Typically, it is assumed that for a dynamic isotropic distribution (random rotation), the orientation factor, κ^2 , is $2/3$, and, for a static isotropic distribution (orientations do not change during timespan of energy transfer), κ^2 is 0.476 [164]. In general, variation in κ^2 does not result in significant errors for calculated distances [164, 181].

$$\kappa^2 = (\cos\theta_T - 3\cos\theta_A \cos\theta_D)^2 \quad (1.22)$$

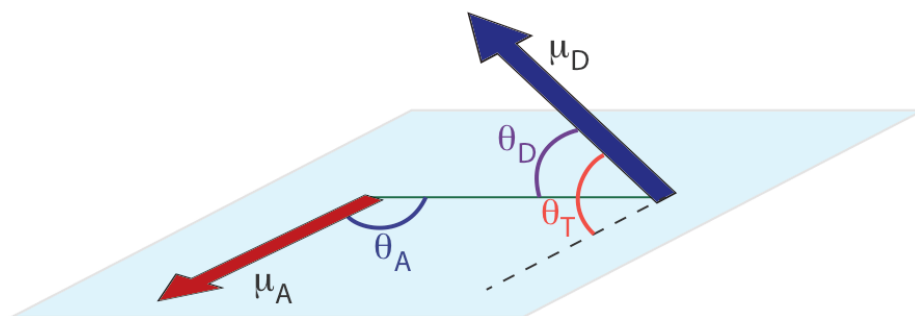


Figure 1.11 Representation of the donor and acceptor transition dipole moments and angles used to calculate the orientation factor, κ^2 .

The FRET efficiency (*i.e.* quantum yield of energy transfer), E , is strongly dependent on the donor-acceptor separation and the Förster distance, as shown by eqn. 1.23. This relationship applies to an isolated donor-acceptor pair, where a single donor interacts with a single acceptor. For a case where a single donor can interact with multiple acceptors and *vice versa*, this expression may not necessarily be applicable (see Section 1.3.6 for details).

$$E = \frac{k_{FRET}}{k_{FRET} + k_r + \sum k_{nr}} = \frac{R_0^6}{r^6 + R_0^6} \quad (1.23)$$

The FRET efficiency approaches 100% at distances $r < 0.5R_0$ and approaches 0% when $r > 2R_0$. The separation range $0.5R_0 < r < 1.5R_0$ provides the most sensitive transduction in FRET efficiency and allows FRET to operate as a “molecular ruler” [164]. The transduction is commonly achieved over separation distances 1–10 nm.

1.2.8.2 Measurement of FRET efficiency

The characteristic parameters used to quantify FRET include a decrease in donor fluorescence intensity, an increase in FRET-sensitized acceptor fluorescence intensity, a decrease in donor lifetime, a decrease in donor emission anisotropy, and depolarization of the acceptor emission [164].

Experimentally, the FRET efficiency is often determined from measurable changes in fluorescence intensity (F), quantum yield (Φ), or lifetime (τ) between an isolated donor (denoted with a subscript D) and a donor in the presence of acceptor (denoted with a subscript DA), as described by the relationships given by eqn. 1.24 [164]. These approaches rely on a relative measurement by comparing two systems with and without introduction of resonance energy transfer pathway. Therefore, identical excitation conditions must be used when FRET efficiency is determined from the changes in intensity or quantum yield.

$$E = 1 - \frac{F_{DA}}{F_D} = 1 - \frac{\Phi_{DA}}{\Phi_D} = 1 - \frac{\tau_{DA}}{\tau_D} \quad (1.24)$$

Calculation of FRET efficiencies from time-resolved experiments through the changes in excited state lifetime of the donor assumes that both lifetimes, τ_D and τ_{DA} , are monoexponential or amplitude weighted average lifetimes [164]. From a practical perspective, the advantage of eqn. 1.24 in comparison to eqn. 1.23 is that it is applicable to FRET pairs where the donor–acceptor ratio is not just 1:1, but a general case 1: a , where $a > 0$. A modified form of eqn. 1.23 for a number of acceptors ($a > 0$) is introduced in Section 1.3.6.

The FRET efficiency can also be determined from changes in the FRET-sensitized acceptor emission accounting for contributions of direct excitation (*i.e.* acceptor only system). This approach requires a correction factor to account for differences in the molar absorption coefficients of the donor and the acceptor. Two common approaches are based on either (i) an

internal reference acquired at an excitation wavelength where donor does not absorb, or (ii) an external reference with a sample containing only acceptor. For a sample with an internal reference, the FRET efficiency is given by:

$$E = \frac{F_{AD}A_{AA} - F_{AA}A_{AD}}{F_{AA}A_{DD}} \quad (1.25)$$

where F_{AD} is the FRET sensitized acceptor intensity with donor excitation, F_{AA} is the acceptor intensity following acceptor excitation, A_{AA} is the acceptor absorbance at acceptor excitation wavelength, and A_{AD} and A_{DD} are the acceptor and donor absorbance, respectively, at the donor excitation wavelength.

The expressions given in eqn. 1.24 and 1.25 are often used for characterization of a FRET system by determining the donor-acceptor separation, r . The Förster distance, R_0 , for a given FRET pair is constant, and therefore measurements of the FRET efficiency can permit measurements of r . Consequently, FRET has been used to quantitatively determine molecular distances in biochemical and molecular biological systems (*e.g.* to study conformational changes during protein folding or protein interactions in living cells) [182-184]. In contrast, FRET-based bioassays do not generally rely on measuring the donor-acceptor separation, but rather the quantification of the relative concentrations of donor-acceptor pairs is used [185]. The processes of association (*e.g.* DNA hybridization) or dissociation (*e.g.* proteolysis) of biomolecules result in either increases or decreases in the number of FRET pairs. These changes are often measured using a FRET ratio, where the donor emission in the absence of acceptor is not required, provided that the quantum yields of the donor and the acceptor are known. The expression given by Eq. 1.26 is valid assuming direct excitation of the acceptor is negligible:

$$\frac{F_{AD}}{F_{DA}} = \frac{\Phi_A E}{\Phi_D (1 - E)} \quad (1.26)$$

where F_{AD} is FRET-sensitized acceptor emission and F_{DA} is donor emission.

1.2.8.3 Assumptions underlying use of FRET

There are several assumptions routinely applied in the analysis of FRET systems, including the ideal dipole approximation, the magnitude of the orientation factor, the refractive index of the media and the effect of spectral broadening on the calculated spectral overlap. The conditions under which these assumptions are valid, and the consequences of their breakdown on the interpretation of the FRET data are introduced in this section.

The derivation of the simple relationship between the energy transfer rate and the relative separation and orientation of donor and acceptor is given by eqn. 1.17, which is based on the assumption that transition densities can be approximated as point dipoles. The representation of the electronic coupling term, V , in Fermi's golden rule (eqn. 1.15) by the transition dipole-transition dipole interaction energy is a special case of the multipole expansion used by T. Förster [179]. The space around the donor is visualized as a group of electrical oscillators producing an electric field is divided into four zones. These are the contact or Dexter zone (< 1 nm), the near-field zone (1-10 nm), the intermediate zone (10-1000 nm), and the radiation zone (> 1000 nm) [186]. The Förster formalism is only valid within the near-field zone, as the total electronic coupling can be represented adequately by the Coulombic interactions, $V \approx V_{Coul}$. The expansion of the interaction energy into power series (*i.e.* multipole expansion) results in the main dipole-dipole interaction term for uncharged molecules [187]. The contributions from multipole terms are generally negligible [187]. Therefore, within the ideal dipole approximation, the interactions between molecules can be described by $V \approx V_{Coul} \approx V_{dip-dip}$. This approximation is valid at donor-acceptor separation down to 20 Å [179]. Within the Dexter zone, the exchange interactions caused by the overlap of molecular orbitals of the donor and the acceptor require an additional coupling term: $V = V_{Coul} + V_{overlap}$. Therefore, as molecular separation becomes comparable to the size (*i.e.* a spatial extent of transition density) of the molecules, $V_{overlap}$ term becomes significant and the validity of ideal dipole approximation becomes questionable [179].

The orientation factor, which depends on the mutual orientation of the donor and acceptor, represents another facet of Förster formalism. In biological samples, there may be fluctuations in the positions and relative orientations of donors and acceptors, allowing for assumption of a dynamic isotropic distribution of transition moments [164]. Therefore, the value of κ^2 is taken as 2/3, an average value over time, which corresponds to the dynamic isotropic limit, where

rotations of donor and acceptor are fast in comparison to the excited state lifetime [188]. This assumption can lead to large errors in single molecule measurements, where averaging over many FRET-pairs or over longer times would be unpractical [185]. In ensemble measurements, this assumption may not be strictly valid for all the cases; however, the corresponding error may not be significant enough. While the rate of energy transfer, k_{FRET} , has a linear relationship with orientation factor, κ^2 , the Förster distance, R_0 , and the experimentally calculated donor-acceptor separation, r have an inverse sixth power dependence. Given that for a static isotropic distribution found in rigid systems, the orientation factor is assumed to be 0.475, the discrepancy in the R_0 or r between static and dynamic distributions is estimated to be 5%. Different donor-acceptor conformations can lead to the orientation factor values in the range $0 \leq \kappa^2 \leq 4$. In unfavorable cases ($0 \leq \kappa^2 \leq 2/3$) often found in anisotropic systems or systems with reduced fluidity, a two-fold discrepancy can be observed if the assumption is used [188]. In contrast, favorable systems ($2/3 \leq \kappa^2 \leq 4$) produce a maximum error of 35% in the calculation of the distance between donor and acceptor [164]. Fluorescence anisotropy measurements can be used to confirm fast isotropic rotation that lead to unpolarized emission and can be used to estimate limits on orientation factor [180, 189].

Another parameter that often requires an approximation during FRET analysis is the refractive index, n , of the microenvironment surrounding the donor and the acceptor. The extent of the dielectric screening of the Coulomb interaction between the donor and the acceptor exhibits a $V_{Coul} \propto n^{-2}$ dependence. In many bioassays the fluorophores are attached to larger biomolecules (*e.g.* proteins) that may have a different refractive index in comparison to the solvent. For convenience, it was proposed that, in applying the Förster formalism to fluorophores in proteins, the refractive index of the solvent may be used instead of the one corresponding to the dielectric screening of the protein [190]. This approach continues to be widely adopted, although there are examples of using a local refractive index (*e.g.* protein, membrane) rather than the solvent refractive index [191]. The typical range of refractive indices associated with biological media fall within a very narrow range. For example, water has a refractive index of 1.33, lipid membranes a refractive index of 1.46, proteins a refractive index of 1.5 [192], corresponding to less than 10% variation in the Förster distance based on $R_0^6 \propto n^{-4}$.

1.3 Semiconductor Quantum Dots

1.3.1 What is a quantum dot?

QDs are colloidal semiconductor nanocrystals with dimensions between *ca.* 1-10 nm. Excitons are generated in the nanocrystals upon the absorption of light, and electron-hole recombination leads to luminescence. Although depicted as spheres in most illustrations, QDs are crystalline materials with facets and a lattice structure analogous to the bulk semiconductor material. Depending on its size, each nanocrystal can comprise hundreds to thousands of atoms, a large fraction (>10%) of which are located at the nanocrystal surface (*i.e.* a high surface area-to-volume ratio). As described in more detail below, most of the QDs used in analytical applications are synthesized as core/shell structures, where the core nanocrystal is overcoated with another semiconductor material to protect and improve its optical properties. The “flagship” QD material is undoubtedly core/shell CdSe/ZnS.

1.3.2 Absorption and photoluminescence

It was the unique photophysical properties of QDs that first generated excitement for biological imaging and analysis. QDs have become renowned for eye-catching photographs (Figure 1.12A) of differentially sized QDs under ultraviolet (UV) illumination that show a bright rainbow of photoluminescence (PL). The bright PL is the result of high quantum yields ($\Phi = 0.1\text{--}0.9$) combined with large molar extinction coefficients ($10^5\text{--}10^7 \text{ M}^{-1} \text{ cm}^{-1}$). As shown in Figure 1.12B-C, QDs have broad absorption spectra that continuously increase in magnitude from their first exciton peak to shorter wavelengths in the near-UV. QD PL spectra are shifted to slightly longer wavelengths than the first exciton absorption peak, such that an *effective* Stokes shift >100 nm can be achieved. The PL is also spectrally narrow with an approximately Gaussian profile (FWHM 25–35 nm). The stunning rainbow of QD PL arises from the fact that the peak emission wavelength shifts as a function of nanocrystal size and material. The QD size and PL colour can be selected by controlling the temperature and duration of crystal growth during synthesis. Photographs of the type in Figure 1.12A exemplify the utility of QDs for multiplexed analyses and multicolour imaging: a single light source can excite many colours of QD simultaneously (broad absorption) and each PL contribution can be readily resolved or deconvolved (narrow emission).

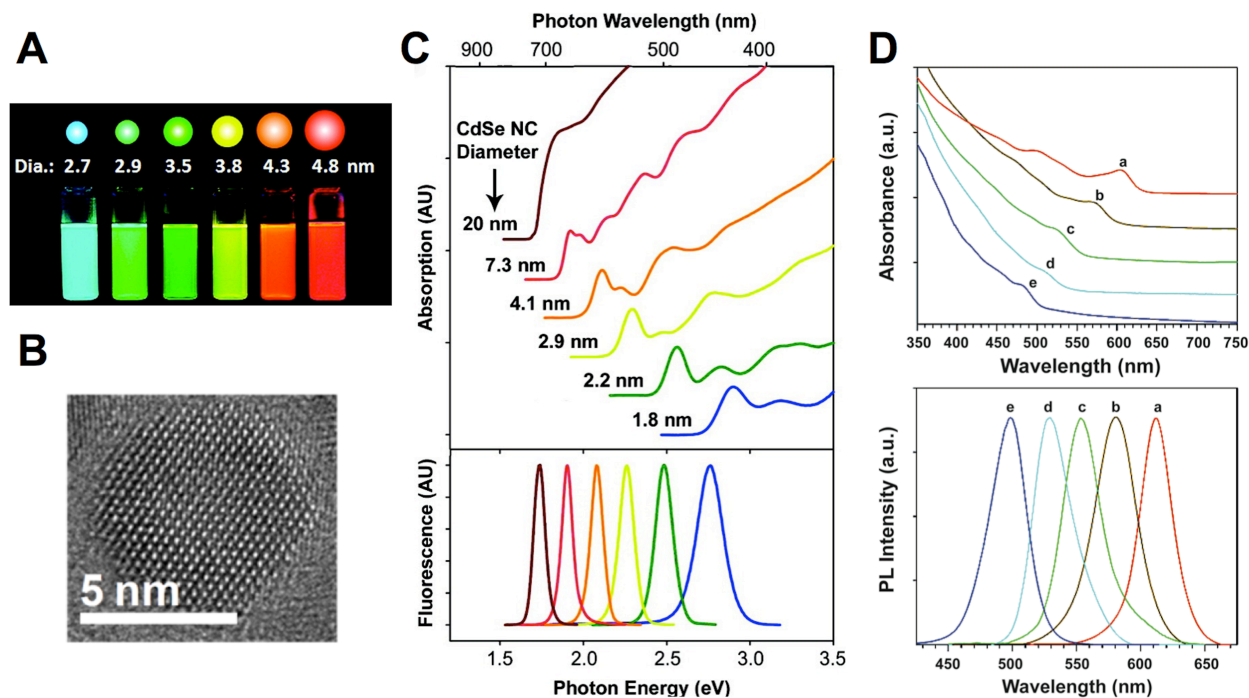


Figure 1.12 (A) Size-tunable PL of CdSe QDs. The photograph was taken under UV illumination (365 nm). **(B)** TEM image of a CdSe/ZnS QD. A and B reprinted with permission from ref. [126]. Copyright 2011 American Chemical Society. **(C)** Size-dependent absorption and fluorescence spectra of CdSe QDs. Reprinted with permission from ref. [193]. Copyright 2010 American Chemical Society. **(D)** Absorption and PL spectra of Zn_xCd_{1-x}Se QDs with Zn mole fractions of (a) $x = 0$, (b) 0.28, (c) 0.44, (d) 0.55, and (e) 0.67. Reprinted with permission from ref. [194]. Copyright 2003 American Chemical Society.

Other advantageous optical properties of QDs include excited state lifetimes that tend to be longer than those of fluorescent dyes (> 10 ns), superior resistance to photobleaching and chemical degradation (due to the inorganic composition and confinement of the exciton), and two-photon absorption cross sections (10^3 – 10^4 GM) that are orders of magnitude larger than those of fluorescent dyes [195]. QDs are thus excellent probes for tracking dynamic processes over time, and for two-photon imaging of tissues or other complex biological specimens where near-infrared (NIR) excitation mitigates challenges associated with autofluorescence and attenuation of excitation light by strong protein absorbance (*e.g.* hemoglobin) in the visible region [196, 197].

1.3.3 Quantum confinement and core/shell structures

The size-dependence of QD PL is the result of *quantum confinement*. As a bulk material is reduced to nanoscale dimensions, the density of states decreases near the conduction band and valence band edges, resulting in the emergence of discrete excitonic states. The band gap energy further increases with decreasing nanocrystal size as the exciton is confined to smaller dimensions than its Bohr radius (*i.e.* the preferred distance between the electron and hole). The PL emission wavelength shifts since exciton recombination occurs between the band edge states. For example, bulk CdSe has a bandgap energy of 1.76 eV and a Bohr exciton diameter of 9.6 nm [193], whereas the band gap energy of 2–7 nm CdSe nanocrystals decreases from 2.8 eV to 1.9 eV with PL shifting between 450–650 nm. The range over which the band gap energy and PL wavelength can be tuned by quantum confinement depends on the material of the nanocrystal (*vide infra*) and its bulk band gap energy. PL emission centered at wavelengths between 380–2000 nm can be obtained with appropriate selection of the semiconductor material and nanocrystal size [198].

While a QD is approximately a physical representation of the particle-in-a-box concept, an important difference is that the core nanocrystal does not provide an infinite potential barrier for confinement of the exciton. Furthermore, the lattice structure of the nanocrystal abruptly terminates at its surface, which can lead to localized “trap” states within the quantum confined band gap. Trap states can sometimes be observed as band gap emission, which appears as a broad peak on the bathochromic side of the expected band edge emission. These states, as well as leakage of the excitonic wavefunction outside the core nanocrystal, promote non-radiative pathways for recombination of the exciton [193]. To improve PL efficiency, the core nanocrystal can be coated with a few layers of a structurally similar semiconductor with a higher band-gap energy, as is the case with widely utilized CdSe/ZnS and CdTe/ZnS QDs. Such an arrangement, where the core band edge states are both intermediate in energy to those of the shell, is referred to as a Type-I heterostructure. This configuration is the most common in bioanalytical applications since it offers the best confinement of the exciton (Figure 1.13A) and the highest rates of radiative recombination (*i.e.* brighter PL). Confinement is not complete, however, as shell growth is typically accompanied by a 5–10 nm bathochromic shift in the QD PL spectrum.

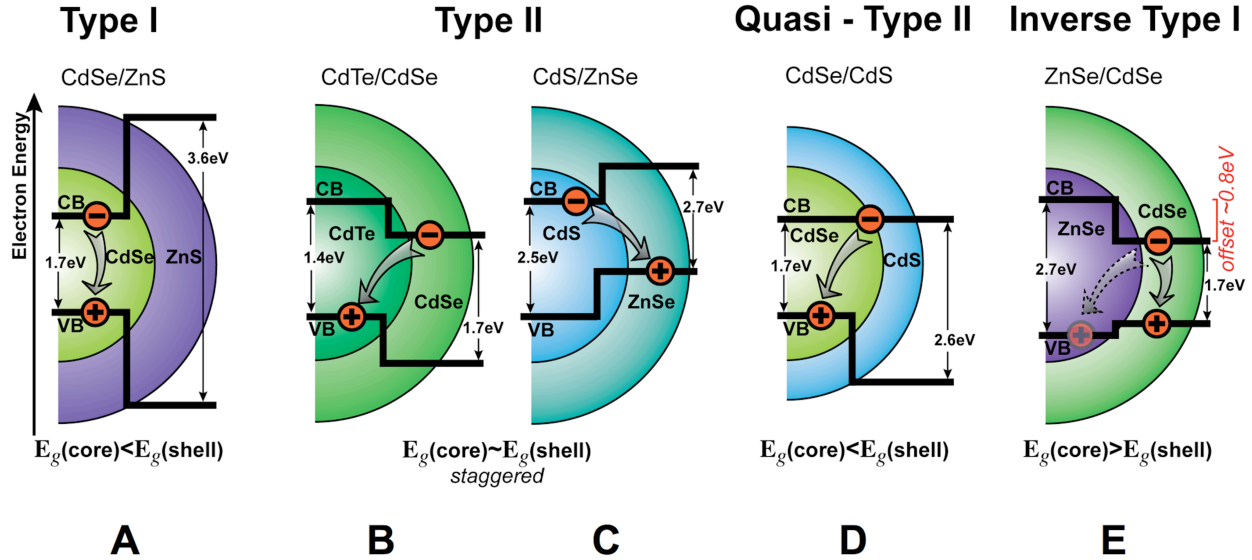


Figure 1.13 Illustration of band gap engineering by selection of core and shell materials. The relative energy of conduction band and valence band edge states between the core and shell determine the localization of the electron and hole, and the nature of the transition associated with exciton recombination, offering an additional means of tuning the optical properties of QDs. **(A)** Type-I QD with localization of both carriers in the core; **(B)** Type-II QD with localization of the electron in the shell; **(C)** Type-II QD with localization of the hole in the shell; **(D)** Quasi-Type-II QD with localization of the electron in both and the core and shell; and **(E)** Inverse-Type-I QD with localization of both carriers in the shell.

Other heterostructure configurations are designed to localize the electron and/or hole outside of the core nanocrystal. For example, in Type-II heterostructures (e.g. CdTe/CdSe, CdSe/ZnTe), [199] the electron and hole are localized in the shell and core, respectively, or *vice versa*. This behaviour arises from an offset between the band edge states of the core and shell (Figure 1.13B). The exciton recombines across the core/shell interface and, consequently, the emission wavelength corresponds to an energy less than the band gap of either the core or shell material. The decreased overlap between the electron and hole wavefunctions also results in lower absorption coefficients and longer PL decay times. Type-II QDs are potential NIR emitters and growth of a second Type-I shell (e.g. CdSe/CdTe/ZnSe) [200] can enhance quantum yields; however, other Type-I and alloyed NIR emitting QDs (e.g. InAs/ZnSe, InAs/CdSe, InAs/InP, Cu:InP/ZnSe and InAs_xP_{1-x}/InP/ZnSe) are also being actively developed [201-203]. Quasi Type-II QDs have only a small offset between, for example, the conduction band edge states of the

core and shell, such that the electron is delocalized over the whole nanocrystal while the hole is confined to the core (Figure 1.13C) [204]. Inverse (or reverse) Type-I QDs (*e.g.* CdS/CdSe, ZnSe/CdSe) [205] are designed to localize both the electron and hole into the shell. The band edge states for the shell are both intermediate to those of the core (Figure 1.13D). These configurations also require a secondary Type-I shell (*e.g.* ZnSe/InP/ZnS) [206] to enhance PL emission. Finally, lattice strain between the core and shell can be used to tune the optical properties of certain QDs. For example, growth of epitaxial shells on ZnS, ZnSe, CdS, or CdSe on small, soft CdTe cores can be used to shift band energies and thus PL emission. Compressive strain in the core increases the energy of its band edge states while synergistic tensile strain in the shell decreases the energy of its band edge states [207]. The effect of growing thicker shells can be large enough to induce Type-II band alignment in a Type-I heterostructure such as CdTe/ZnSe [207]. To date, Type-II QDs have not found widespread use in bioanalytical applications.

1.3.3.1 Surface states and effects

The energies of band edge states are not the only determinants of QD PL. Even with growth of a Type-I shell, surface states can still affect the PL of real QDs (*i.e.* imperfect structures). For example, the “blinking” or fluorescence intermittency of QDs, which is perhaps the second most renowned property after their size-tunable emission, is associated with surface states. Blinking can be observed at the single particle level, has a power law probability distribution, and is a consequence of either (i) charging and discharging of the core nanocrystal, or (ii) trapping of carriers at surface states before they can relax to emissive band edge core states [208]. Auger recombination is the predominant relaxation mechanism in charged QDs, resulting in very efficient PL quenching until the QD core is neutralized. While detrimental in some applications of QDs, the observation of blinking is useful to confirm tracking of a single QD [209, 210] and has enabled super-resolution imaging [211].

In addition to blinking, QDs sometimes exhibit other interesting optical phenomena under high intensity excitation. These phenomena include bluing, photobrightening, and photodarkening, which are observable in the ensemble [212]. Bluing corresponds to an irreversible hypsochromic shift in the band edge emission, and is the manifestation of photooxidative etching of the average nanocrystal size [213]. Brightening, or photoactivation, is an increase in the QD PL intensity

under irradiation and is associated with changes in the properties of the QD surface. These changes have been suggested to include the passivation of defect states and dangling bonds [212], or displacement of trapped charges [214, 215], each leading to a decrease in a “dark fraction” of non-luminescent QDs in the ensemble. The extent of photobrightening, as well as the opposite effect, photodarkening, depends on the duration and intensity of irradiation, although the latter seems to be induced at higher irradiation intensities, above-gap excitation energies, and longer irradiation times. The competitive kinetics of photobrightening and photodarkening have been investigated and found to yield different steady state QD PL intensities for different irradiation intensities [215].

The aforementioned dark fraction, which has been observed experimentally *via* fluorescence coincidence analysis (FCA), is inversely correlated to the ensemble quantum yield [216, 217]. It has been suggested that the mechanism for formation of the dark fraction is analogous to that for blinking behavior [218], albeit that the dark fraction is not a byproduct of blinking over extended timescales [216, 217]. Interestingly, a decrease in the size of the dark fraction is responsible for the apparent increase in the ensemble QD quantum yield that is frequently observed upon “passivation” with adsorbed macromolecules such as proteins [219].

The importance of the above effects in analytical applications of QDs is variable, depending on both the characteristics of the batch of QDs utilized and the spectroscopic parameters of the experiment (*e.g.* laser power). Ensemble assay methodologies based on one-time measurements at low power excitation tend to be relatively immune, whereas single molecule tracking experiments with high intensity excitation are the most susceptible to these effects. In either case, good or poor quality QDs can make a tremendous difference in the outcome of an experiment. Maintaining continuity in the properties of QD materials is thus an ongoing challenge in the field.

1.3.4 Quantum dot materials

As alluded to above, QDs have been synthesized from a broad range of semiconductor materials. The most popular materials have been CdSe, CdTe and their core/shell analogs, CdSe/ZnS and CdTe/ZnS. This popularity can be attributed to well-established synthetic protocols, emission that can be size-tuned over the visible/NIR region, and, not least of all, commercial availability.

Traditionally, emission has been tuned on the basis of core nanocrystal size with these materials, and the role of the Type-I shell has been to passivate dangling bonds on the surface of the core, better confine the exciton (*vide supra*), and enhance the QD's optical properties (*e.g.* the quantum yield can increase by 20–35%) [220, 221]. For this purpose, the growth of a thin shell is important. For example, with CdSe/ZnS QDs, the 12% lattice mismatch between CdSe and ZnS necessitates that growth of the ZnS shell be limited to a few atomic layers before lattice strain detrimentally affects the PL properties [222]. Thicker shells have been desirable to render QDs more robust or prevent blinking [223]. Effective approaches for growing thicker shells and relaxing lattice mismatch have included incorporating a small amount of Cd into the shell material [224], and synthesis of gradient or multi-shell structures (*e.g.* CdSe/CdS/ZnS) [223, 225, 226]. As an alternative to size-tuning of PL, QD core materials can also be alloyed. The PL emission of ternary alloyed QDs (*e.g.* CdSe_xTe_{1-x}, CdS_xSe_{1-x}, Cd_xZn_{1-x}S, Cd_{1-x}Zn_xSe) can be varied while maintaining a constant size (Figure 1.12C) [194, 227-231], and these materials are also commercially available.

In addition to II-VI semiconductors, other materials used for QD synthesis include III-V (*e.g.* InP) [232, 233] or group IV (*e.g.* Si) [234, 235] semiconductors. To some degree, the investigation of alternative materials to CdSe and CdTe has been driven by the perceived toxicity of Cd-based QDs (see refs. [236-238] for a discussion of the complex issue of toxicity; QDs can be used in both toxic and non-toxic capacities). Although synthesis protocols for alternative materials are still being optimized to yield optical properties that match those of CdSe/ZnS and CdTe/ZnS QDs, there has been considerable progress. For example, InP/ZnS QDs [239] (with emission in the 480–750 nm range) and InP/ZnSe/ZnS QDs [240] have been reported with $\Phi = 0.4$ – 0.6 and a FWHM of 50–60 nm. In addition to the benefits of NIR emission for *in vivo* applications, QD size plays an important role in determining their fate *in vivo*. Renal clearance and minimal accumulation in organs (*e.g.* spleen, kidney, liver, *etc.*) is observed with nanoparticles < 5.5 nm in hydrodynamic diameter [241]. Recently, Park *et al.* reported synthesis of highly luminescent CuIn_xSe_y/ZnS core/shell QDs ($\Phi = 0.6$) with emission within the NIR biological window at 741 nm, a FWHM of 175 nm, and an average diameter of 5 nm [242]. With the exception of the large FWHM, these QDs are almost ideal for prospective *in vivo* applications. Some non-Cd QD materials (*e.g.* InP/ZnS and InGaP/ZnS) are currently available commercially.

1.3.4.1 Synthesis of QDs

Unfortunately, the laboratory synthesis of high-quality colloidal QDs is still largely restricted to experienced chemists. Despite numerous attempts in the literature to synthesize QDs in aqueous media using convenient air-stable precursors, QDs with narrow FWHM (a function of the distribution of particle size, *i.e.* monodispersity) and high quantum yields have been almost exclusively obtained through solvothermal methods that use organometallic precursors and non-polar organic solvents at high temperature and under inert atmosphere (*i.e.* pyrolysis of inorganic precursors) [243-245]. The possible exception is the aqueous synthesis of CdTe QDs, where quantum yields have been reported to reach 82%, but are typically closer to *ca.* 40% [246-248]. These QDs can also be relatively monodisperse, with FWHM typically in the range of 30–60 nm.

1.3.5 Functionalization of QDs

While the optical properties of QD attract the lion's share of excitement, experts have now come to realize that the surface area of the QD is almost as valuable: A QD can serve as a nanoscale scaffold with physicochemical properties and biological activity that can be tailored through interfacial chemistry and bioconjugation. Functionalization is done in multiple steps, and the design and execution at each step is critical to the efficacy of the QD in its intended application [126, 249-253].

1.3.5.1 Interfacial chemistry

Since most biological applications use core/shell QDs, the inorganic shell is generally the first site for modification. In particular, high quality QDs prepared by solvothermal methods are coated with hydrophobic surfactants and require modification to render them water-soluble for biological applications. As shown in Figure 1.14i-v, there are two well established routes to water soluble QDs: (i) ligand exchange (*i.e.* replacement of the native surfactants), which yields more compact QDs; and (ii) encapsulation with an amphiphilic polymer (building around the native surfactants), which typically yields brighter QDs. Ideally, the core/shell QD PL properties are insensitive to interfacial chemistry; however, the typical few-atom thick Type-I shells do not fully isolate the nanocrystal core, and the optical properties of QDs are still somewhat affected by adsorbed molecules, pH, temperature, and other properties of the local environment [254]. This sensitivity is a consequence of imperfect confinement of the exciton and/or non-uniform

coverage of the shell material on the core [224]. Other important considerations for the hydrophilic modification of QDs include the net charge, colloidal stability (*i.e.* resistance to aggregation), long-term coating stability (*i.e.* stable association between the organic coating and inorganic QD), compatibility with bioconjugate chemistries (*i.e.* for attaching biomolecules of interest), and resistance to the non-specific adsorption of proteins and other biomolecules in a sample matrix (*i.e.* non-fouling). In the following paragraphs, the chemistry of coating QDs for aqueous dispersion is discussed in more detail, focusing first on the interface exposed to bulk solution, then discussing the interface between the organic coating and the inorganic QD.

One of the most widely used methods for dispersing QDs in aqueous solution is to modify their outer surface with anionic carboxylate groups. At sufficiently basic pH and low ionic strength, electrostatic repulsion between QDs affords a stable colloidal suspension; however, efficient charge screening at high ionic strength and/or neutralization of the carboxylates at acidic pH yields insoluble aggregates of QDs [255, 256]. Carboxylate coatings (Figure 1.14i, v) also tend to be prone to the non-specific adsorption of proteins due to their charge. Popular alternatives to carboxylate coatings are those featuring poly(ethylene glycol) (PEG; Figure 1.14ii, iii) oligomers or zwitterionic moieties (Figure 1.14iv). Both PEGylated and zwitterionic coatings offer colloidal stability over broad ranges of pH and ionic strength, and minimal non-specific adsorption for improved biocompatibility [257, 258]. The advantage of zwitterionic coatings over those based on PEG is more compact size [259, 260]; however, PEG oligomers can be modified with a variety of terminal functional groups (*e.g.* carboxylic acids, amines, hydroxyl, PEG, biotin) with minimal impact on the overall colloidal stability of the QDs [261]. Albeit that numerous well-established protocols for QD ligand exchange (*i.e.* replacement of native hydrophobic ligands with hydrophilic ligands) have been reported, it remains a challenge to characterize this process, including the number of hydrophobic ligands remaining, the density or number of hydrophilic ligands per QD, and the homogeneity of ligand distribution on QD interface. Batch-to-batch variation in these parameters can have a significant impact on the reproducibility of assays, and the interactions observed between QDs and biomolecules (*e.g.* non-specific adsorption).

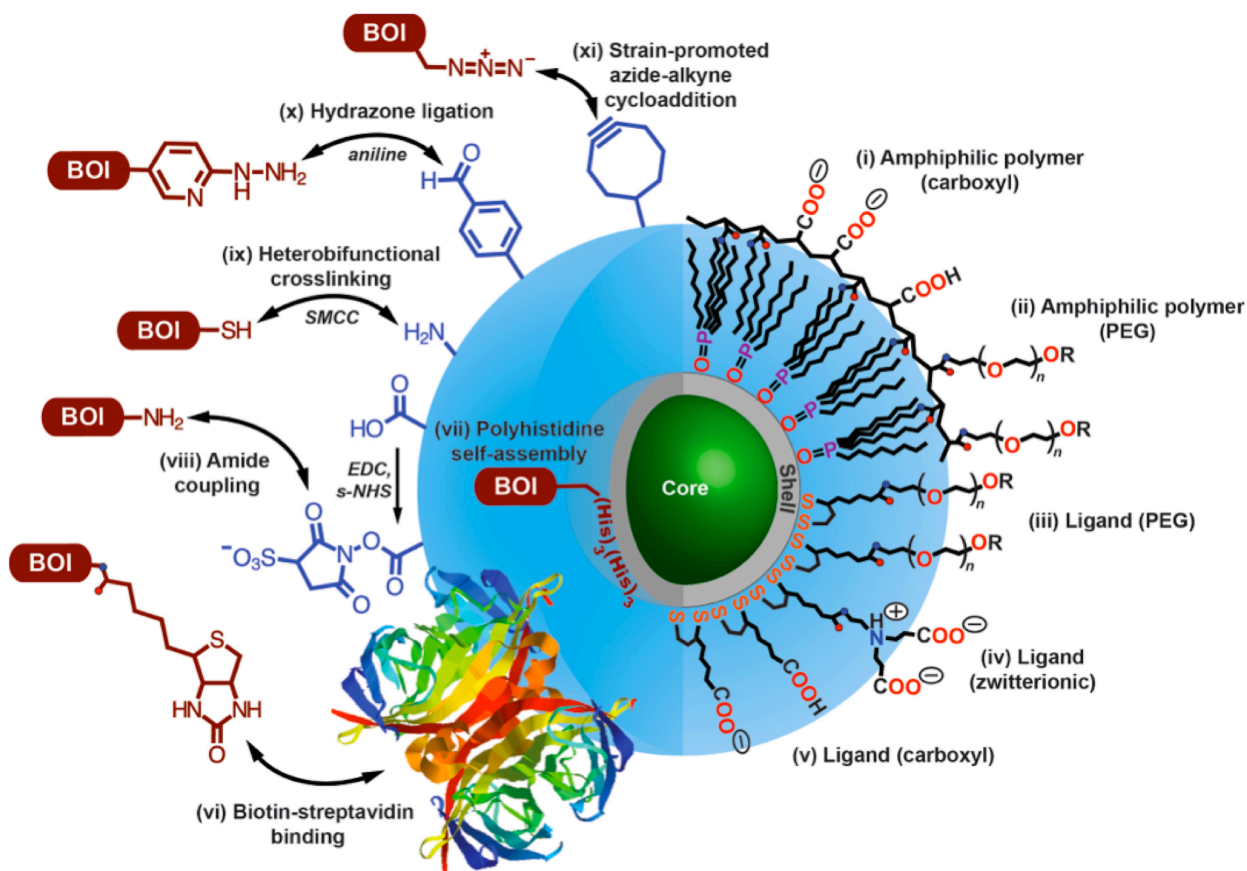


Figure 1.14 Illustrative overview of the chemistry of core-shell QDs. Coatings for aqueous solubility: (i) amphiphilic polymer coating with carboxyl(ate) groups; (ii) amphiphilic polymer coating with PEG oligomers; (iii) dithiol ligand with a distal PEG oligomer; (iv) dithiol ligand with a distal zwitterionic functionality; (v) dithiol ligand with a distal carboxyl(ate) group. Common R groups include carboxyl, amine, and methoxy, although many others can be introduced (e.g. see vi, x, xi). Methods for conjugating biomolecules of interest (BOI): (vi) biotin-streptavidin binding; (vii) polyhistidine self-assembly to the inorganic shell of the QD; (viii) amide coupling using *N*-(3-dimethylaminopropyl)-*N'*-ethylcarbodiimide (EDC) and sulfo-*N*-hydroxysuccinimide (*s*-NHS) activation; (ix) heterobifunctional crosslinking using succinimidyl-4-(*N*-maleimidomethyl)cyclohexane-1-carboxylate (SMCC; structure not shown); (x) aniline-catalyzed hydrazone ligation; and (xi) strain-promoted azide-alkyne cycloaddition. The double arrows are intended to represent conjugation between the functional groups and, in principle, their interchangeability (not reaction mechanisms or reversibility). Not drawn to scale.

As noted above, there are two main methods for modifying QDs with functional groups such as carboxylic acids and PEG oligomers. The first of these methods is ligand exchange, which

involves the replacement of hydrophobic surfactants from QD synthesis with higher-affinity hydrophilic ligands *via* mass-action. The most common ligands are bifunctional molecules with thiol groups that coordinate to Zn^{2+} sites on the surface of the QD at one end, and display carboxylate or PEG groups at the other (Figure 1.14iii-v). While thiols will also coordinate to the Cd^{2+} at the surface of a bare CdSe core, the ZnS shell is less prone to oxidation and Zn^{2+} has higher binding affinity with basic ligands, improving the coating stability of the final aqueous QDs [226]. Coating stability is also improved by using bidentate ligands with two coordinating thiol groups. For example, an extensive library of bidentate ligands derived from dihydrolipoic acid (DHLLA) have been reported, including those appended with functional group-terminated PEG oligomers [256] or compact zwitterionic moieties [260]. The major challenge of ligand exchange with thiols is a reduction in the quantum yield of the QD. Considerable efforts have been made to refine ligand exchange procedures to minimize such effects [262-264]. Commercially available QDs with hydrophobic surfactants are often made water-soluble by ligand exchange with commercially available thiol ligands (*e.g.* 3-mercaptopropionic acid) [72].

Amphiphilic polymers are a second type of coating that can be applied to QDs, and are designed to have a mixture of hydrophilic groups and hydrophobic alkyl side-chains. The alkyl side-chains interdigitate with alkyl-bearing surfactants from QD synthesis (*e.g.* trioctylphosphine oxide, TOPO), leaving the hydrophilic groups at the surface of the now water-soluble QDs (Figure 1.14 i, ii). Common chemical strategies for preparing amphiphilic polymers include partial grafting of polyacrylic acid or poly(maleic anhydride) backbones with alkyl amines, where the remaining sites on the backbone are left as carboxylic acids or appended with PEG chains [265-269]. These polymer coatings better retain the original brightness of synthesized QDs since they build an additional layer onto the surface of the QD without altering coordination to the inorganic interface (*i.e.* less opportunity for forming surface traps). Polymer coatings also provide good long-term coating stability, but typically larger hydrodynamic radii than QDs coated with bifunctional ligands [198]. Water-soluble QDs with amphiphilic polymer coatings are available commercially, as are QDs coated with phospholipids, which interact with the as-synthesized QDs in an analogous fashion. Further details on the diversity of possible coatings for QDs, including those that are less widely utilized or still emerging (*e.g.* coordinating polymers [270, 271]) can be found in recent reviews [6, 126, 261, 272].

1.3.5.2 Bioconjugation of QDs

Bioconjugation strategies of QDs can be broadly classified into (i) covalent coupling and (ii) self-assembly/specific recognition; both strategies have been used to couple enzymes, proteins, peptides, antibodies, and oligonucleotides to QDs [6, 250]. It is critical to note that, without suitable bioconjugation, the utility of QDs in bioimaging and bioanalysis will be greatly hindered, regardless of their highly favorable optical properties. Further, irreproducibility in bioconjugation also tends to translate into irreproducibility in experimental results. A key conceptual difference between QDs and fluorescent dyes is that QDs are effectively surfaces that can be modified with many biomolecules at many different sites, whereas fluorescent dyes typically have one reactive group that labels one of many sites on a biomolecule. This difference creates unique challenges for QDs and other nanoparticles, which have been thoroughly reviewed elsewhere [250]. Some of the most general and pragmatic strategies for the bioconjugation of QDs are summarized below and a few these strategies are illustrated in Figure 1.14vi-xi.

Covalent conjugation methods provide a new chemical bond between a biomolecule of interest and the ligand or polymer coating of a QD. The robustness of the linkage is a function of both the bond stability and coating stability. The most common chemistry is to couple amine-bearing biomolecules to carboxylated QDs (or the opposite configuration) using amide-bond forming, water-soluble activating reagents such as *N*-(3-dimethylaminopropyl)-*N'*-ethylcarbodiimide (EDC) and sulfo-*N*-hydroxysuccinimide (s-NHS) (Figure 1.14viii) [273]. This approach is an effective “shotgun” method that works well in some applications and poorly in others. With many proteins, this chemistry neither provides good control over the number of proteins conjugated per QD nor their orientation (potentially affecting biological activity). Another common outcome is a fraction of crosslinked aggregates, which tend to result from coupling between the large number of amine and carboxyl groups present on the surface of a protein. EDC chemistry is often most effective with mono-reactive biomolecules, which is the case for many synthetic oligonucleotides and peptides. As an alternative to EDC, some commercial QD suppliers offer bioconjugation kits that target either amine or sulfhydryl groups on biomolecules, and couple *via* hydrazone ligation (Figure 1.14x) and heterobifunctional crosslinkers with maleimide groups (Figure 1.14ix), respectively [274]. These reactions tend to offer somewhat

better control over the final bioconjugates. The liabilities of conventional covalent conjugation methods have generated strong interest in developing highly chemoselective ligation reactions that provide excellent control over nanoparticle bioconjugation [250]. The aforementioned hydrazone ligation [275] is one such example, as is copper-free strain-promoted azide-alkyne cycloaddition (Figure 1.14xi; often called “click chemistry”) [276, 277]. Both of these chemistries have commercially available ‘chemical handles’ that can be used to modify amine-bearing QDs and biomolecules for subsequent ligation [278].

Alternative bioconjugation strategies based on self-assembly and specific recognition take advantage of high-affinity non-covalent interactions to assemble biomolecules of interest to QDs. The best-known example of specific recognition is the tight-binding (femtomolar dissociation constants) between biotin and the avidin family of tetravalent proteins (Figure 1.14vi). Almost any biomolecule can be biotinylated using commercially available kits and reagents, assuming that it is not already sold with a biotin modification. Streptavidin-modified QDs are also available commercially, permitting widespread access to a diverse array of QD bioconjugates. This strategy permits a moderate level of control over the number of biomolecules assembled per QD (conjugate valence) and their orientations; however, there are limitations associated with the heterogeneous attachment of the streptavidin to the underlying QD coating [279]. To date, the bioconjugate method that has provided the best overall control is self-assembly between polyhistidine-appended biomolecules and the ZnS shell of ligand-coated QDs (Figure 1.14vii; nanomolar dissociation constants), which provides excellent control over conjugate valence and orientation [280]. Both expressed proteins and commercially synthesized peptides can be readily obtained with polyhistidine tags. Relatively facile methods have also been developed for chemically ligating these tags to synthetic oligonucleotides [281]. Polyhistidine assembly has also been extended to commercial carboxylate polymer-coated QDs [280]. The primary advantage of polyhistidine self-assembly and biotin-streptavidin is that bioconjugations proceeds almost quantitatively without need for excess reagents and purification. A variety of other self-assembly/recognition methods have been developed, but do not yet enjoy the same widespread use and accessibility; these methods have been reviewed elsewhere [250].

1.3.6 Quantum dots as FRET donors

A majority of FRET-based bioanalyses utilize QDs as donors for organic dye acceptors, and these configurations have several advantages over more traditional dye-dye FRET pairs. From the Förster formalism, FRET efficiencies for QD-dye FRET pairs scale according to the inverse sixth power relationship with donor-acceptor separation distance, as described in eqn. 1.23. As shown in Figure 1.15A, the sensitivity of the FRET efficiency to donor-acceptor separation is most optimum in a region between $0.5R_0 < r < 1.5R_0$. Some of the important optical and physical properties of QDs and their impact on QD-dye FRET systems are listed below:

- Strong and broad absorption with high molar absorption coefficients in the UV region of the spectrum ($\epsilon = 10^6\text{--}10^7 \text{ M}^{-1}\text{ cm}^{-1}$)
 - Strong QD absorption in the UV–blue region allows selection of an excitation wavelength that minimizes direct excitation of the acceptor dye (see Figure 1.15B)
 - When this attribute is paired with high QD quantum yields, it becomes possible to use lower intensities of excitation radiation without sacrificing signal-to-noise [282, 283]
 - Low power excitation minimizes direct excitation of acceptor, and also minimizes the effect of photobleaching of organic dyes [185]
- Narrow, symmetric and size-tunable QD PL with the full-width-half-maximum (FWHM) *ca.* 25–35 nm
 - It permits optimization of the spectral overlap integral with only limited crosstalk between donor and acceptor emission
- High quantum yield (10–60%)
 - Higher quantum yields lead to larger Förster distance (see eqn. 1.18) and observed FRET efficiency
- Large surface area
 - Supports modification with multiple acceptor dyes, thus enhancing the rate and efficiency of energy transfer compared to a discrete donor-acceptor pair

A priori, the strong and broad light absorption by QDs also suggests that they would be ideal acceptors; however, efficient and unavoidable direct excitation of the QDs, coupled with their

relatively long excited state lifetime, largely negates this advantage when paired with putative fluorescent dye donors (an excited state QD is not a good acceptor). The solution to this challenge has been to pair QDs as FRET acceptors with luminescent lanthanide complexes as donors [284, 285]. Lanthanide ions (*e.g.* Tb^{3+} , Eu^{3+}) typically have excited state lifetimes on the order of 10^{-4} – 10^{-3} s (*cf.* 10^{-9} – 10^{-8} s for dyes and 10^{-8} – 10^{-7} s for QDs). As such, directly excited QDs return to their ground state and become good acceptors following a microsecond delay after flash/pulsed excitation, while lanthanide ions remain in their excited state as good donors [281, 284]. Förster distances can reach ~ 10 nm with lanthanide-QD FRET pairs and >7 nm with QD-dye pairs [281], compared to < 6 nm with conventional dye-dye pairs.

In bioanalytical applications, the great advantage of FRET is the ability to turn QD PL ‘on’ or ‘off’ in response to biorecognition events (*e.g.* ligand-receptor binding, enzyme activity, DNA hybridization) or other physicochemical stimuli (*e.g.* pH). Since measured signals are not strictly based on the accumulation of QDs, FRET methods can be applied in the ensemble and down to the level of single particles. Numerous configurations using QDs and FRET have been reported for the detection of metal ions [278, 286], small molecules [219, 287, 288], toxins [289], drugs [290], protease [291, 292] and nuclease [293, 294] activity, hybridization assays [295, 296], immunoassays [297], and pH [298, 299]. In each case, the underlying idea is that a donor/acceptor is added or removed from the vicinity of a FRET-paired QD, either physically (*e.g.* association or dissociation) or through a change in its resonance (*i.e.* a large spectral shift).

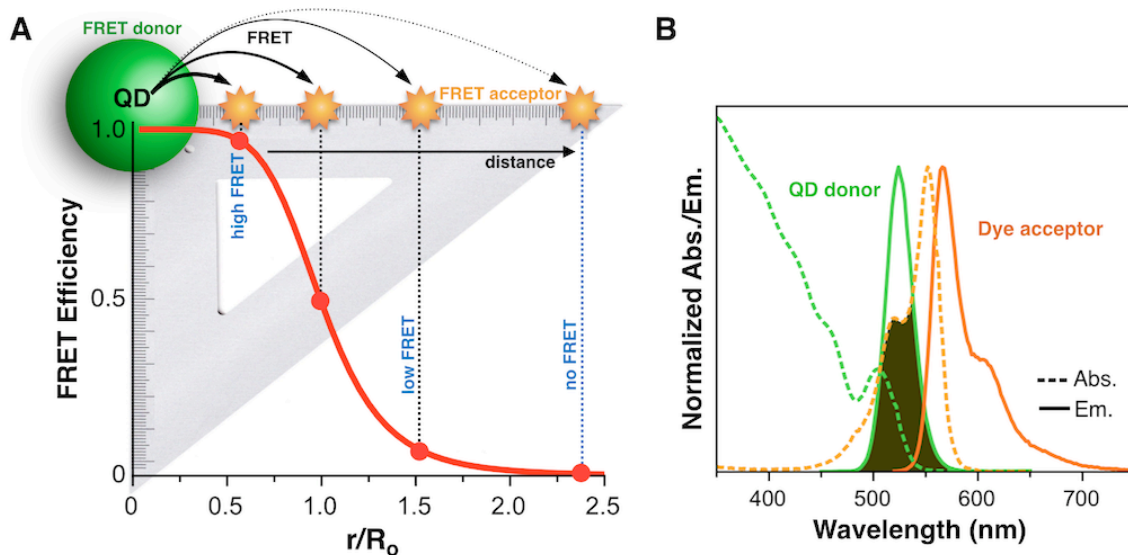


Figure 1.15 (A) An illustration of the distance dependence of a QD-dye FRET pair with the corresponding FRET efficiency curve as a function of donor-acceptor separation in terms of r/R_0 . (drawn not to scale). **(B)** Absorption and emission spectra for a QD-dye FRET pair. The shaded area indicates qualitative spectral overlap.

From the standpoint of the design of QD-FRET bioassays, the ability to exploit the non-trivial surface area of QDs and their numerous sites for bioconjugation offers significant advantages. First, QDs can be assembled with various biomolecules to achieve different functionality (*e.g.* sensing, targeting, *etc.*). Second, QDs can be assembled with an increasing number of acceptors tuning the FRET efficiency without changing the donor-acceptor separation distance. The effect of additional acceptors surrounding QDs on the FRET efficiency is described by introducing a modification of eqn. 1.23, where a is the total number of acceptors.

$$E = \frac{\sum_i^n (R_0 / r)^6}{1 + \sum_i^n (R_0 / r)^6} \approx \frac{aR_0^6}{r^6 + aR_0^6} \quad (1.27)$$

QDs act as scaffolds, providing the opportunity for a single QD to interact with multiple acceptors. Although, each acceptor may be located at a slightly different relative separation, these variations are commonly neglected and it is assumed that acceptors are located centrosymmetrically around a QD core [282]. A sequential increase in the number of acceptors leads to

a non-linear increase in FRET efficiency. The dependence of the FRET efficiency on the acceptor stoichiometry is best illustrated with a FRET efficiency plot as shown in Figure 1.16, where additional interactions between donor and acceptor transition dipoles generates a new scaling relationship (eqn. 1.27).

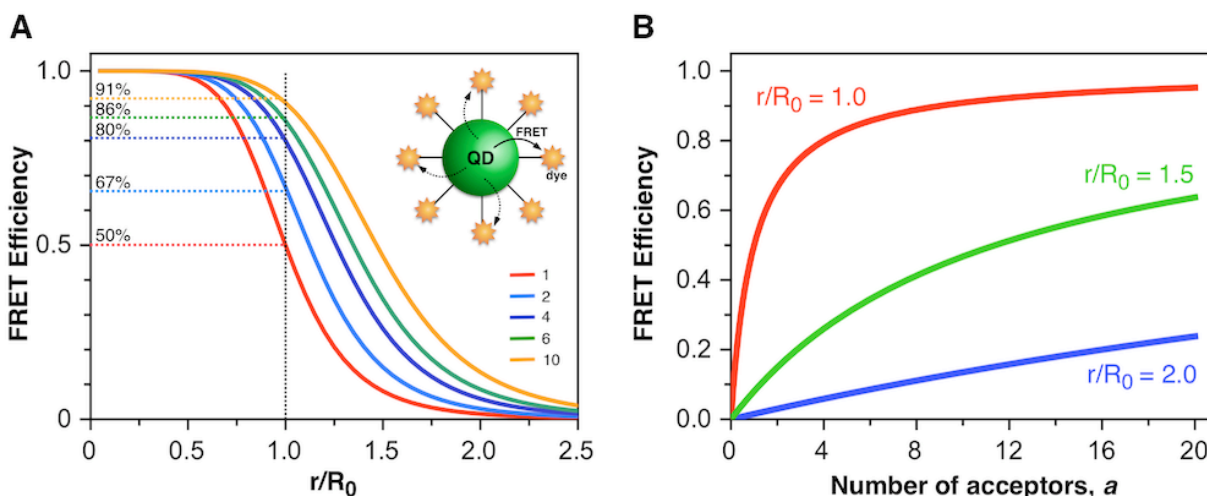


Figure 1.16 (A) Plot of FRET efficiency as a function of donor-acceptor separation in terms of r/R_0 for a fixed, a , the number of acceptors per QD donor. The effective enhancement from 50% to 91% with increasing a from 1 to 10 is shown at the donor-acceptor separation equivalent to the Förster distance (dashed lines). (B) Plot of FRET efficiency as a function of the number of acceptors, a , per QD donor for a fixed r/R_0 value.

Quantification of the strong dependence of the FRET efficiency on the number of acceptors requires a precise knowledge of the conjugate valence. Most bioconjugates exhibit a heterogeneous distribution of valencies in accordance with Poisson statistics, as given by eqn. 1.28, where P is the probability of forming a QD conjugate with precisely n acceptors with an ensemble average of N acceptors [300]. With sufficient resolution, a distribution of conjugate valences can be observed using gel electrophoresis, as shown in Figure 1.17.

$$P(N, n) = \frac{e^{-N} N^n}{n!} \quad (1.28)$$

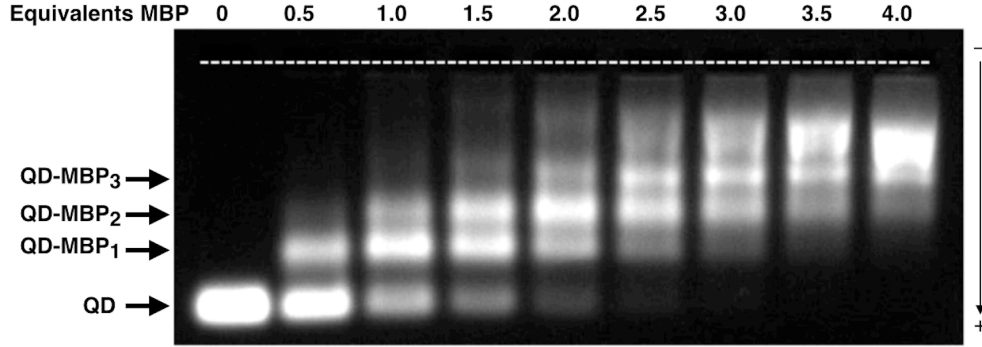


Figure 1.17 Poisson distribution of QD-MBP conjugates. Agarose gel electropherogram of CdSexS_{1-x}/ZnS QD-His₅-MBP conjugates assembled from different relative amounts of MBP per QD (indicated at top). The banding is characteristic of a distribution of conjugate valences (indicated at left).

The effect of this distribution on FRET efficiency is estimated by taking into account the existence of all of the subpopulations ($n = 0, 1, 2, 3, 4, \text{etc.}$) and summing up the individual contributions to the FRET efficiency over the entire sample [291]:

$$E(N) = \sum_{n=1}^{\infty} P(N, n) \frac{nR_0^6}{r^6 + nR_0^6} \quad (1.29)$$

This equation provides a Poisson distribution weighting of the FRET efficiency. The errors in FRET efficiency introduced by assuming a single population model for $N < 4$ can be very significant, but such errors decrease with increasing number N . The maximum error for $N \geq 4$ is *ca.* 5.6 % irrespective of r/R_0 ratio [291]. However, for a case of $N = 1$ and $r/R_0 = 1$, the single population model overestimates FRET efficiency by *ca.* 36 %. A further decrease in the r/R_0 ratio will produce even larger discrepancies [291]. Although a single population can be sufficiently accurate to describe bioconjugate systems with four or more acceptors, eqn. 1.29 should be applied for systems with small N to minimize potential errors in calculated FRET efficiencies.

It was noted in Section 1.2.8.3 that the Förster formalism is only applicable in the systems that can be approximated as point dipoles, and that these dipoles are not in close contact. For spherical QDs, the charge carrier wave functions are symmetric and their maxima are located at the center of QD. Therefore, an approximation that the point dipole of the QD is located at its

center is generally valid. Theoretical calculations by Allan and Delerue, and Curutcher *et al.*, have determined that the Förster formalism is valid for all direct bandgap semiconductor nanocrystals such as CdSe/ZnS QDs [301, 302]. This model also provides a good approximation even when an acceptor is in a direct contact with the QD surface, contrary to the case of organic fluorophores. Since the QD point dipole is located at the centre of the nanocrystal, the radius of QD defines the minimum possible donor-acceptor separation (*i.e.* 1–4 nm depending on the QD size, see Section 1.3.2). It is known that the dipole-dipole approximation fails with dyes at length scales on the order of their dimension [179]; however, FRET involving QDs is typically over distances comparable to the size of QDs, such that the approximation does not become invalid in real systems. The transition density of the QD is built up from two quasi-spherical clouds of opposite sign, while the potential it generates can be approximated as a sum of the two potentials created by the point charge located at the centers of these oppositely charged clouds [302]. In CdSe QDs, the positive and negative charges are located at the centre of the nanocrystal and separated by a dipole of *ca.* 7 Å [302]. As a consequence of the localized dipole at the centre of the QD, the total volume of the QD and its radius are taken into account in estimating donor-acceptor separation distances. In other words, the radius of a nanocrystal imposes a minimum separation distance for any acceptor located above the QD surface. This implication is often taken into consideration upon selection of surface ligands that are sufficiently small in size or length so as to not contribute extensively to donor-acceptor separation. This factor is often a limitation for amphiphilic coatings that offer a higher quantum yield, and protein (streptavidin) coated QDs that allow for easy bioconjugation as noted in Section 1.3.5.

The validity of the Förster formalism with QD donors has also been confirmed by a number of experimental studies. One early study used a dye labeled maltose binding protein conjugated to a QD, which allowed the separation of the dye and core to be smaller than 100 Å [300]. The authors found a good agreement between theoretical and experimental data for the FRET efficiency and spectral overlap. The apparent donor-acceptor distances calculated from efficiency and Förster distances correlated well with the bioconjugate dimensions based on structural data. Two separate studies have observed agreement between measured and predicted FRET efficiencies as a function of variation of donor-acceptor separation using a rigid polypeptide as a variable length linker [303, 304]. The FRET efficiencies determined from steady-state and lifetime measurements followed the Förster formalism and exhibited inverse

sixth power dependence (r^{-6}), as indicated by eqn. 1.22 and 1.23. Pons *et al.* characterized FRET with single molecule spectroscopy and found a good agreement with ensemble measurements by observing a systematic increase in energy transfer efficiency with an increasing number of acceptors [305].

As was mentioned in Section 1.2.8.3, the orientation factor (κ^2) is often assumed to be 2/3 for isotropic systems where the donor and acceptor transition dipoles sample a random orientation during the donor excited state lifetime. However, the QD dipole transition has significantly different angular distribution in contrast to organic fluorophores [306]. Organic fluorophores have a fixed emission dipole orientation (nondegenerate or linear emitters), whereas CdSe nanocrystals have been shown to have a degenerate transition dipole oriented isotropically in two dimensions (circular emitter), giving rise to a dark axis (*c*-axis) in the orthogonal plane that does not couple to the light field [306-308]. The two dimensional degenerate dipole (2D-DD) is a result of equal contributions of two transitions from two different electron-hole fine structure states driven by right- and left-circularly polarized light [308]. This phenomenon suggests that the assumption $\kappa^2=2/3$ is not necessarily valid and depends on the relative orientation of acceptors to the dark axis. However, it was suggested that errors introduced by this assumption are small and the value 2/3 is a good first approximation for a system with partially random orientation of the QD transition dipole and random and dynamic orientation of an acceptor transition dipole [282].

Another advantage of using QDs as FRET donors is their typically longer lifetimes (>10 ns) in comparison to organic fluorophores. As a consequence, QDs may remain in the excited state, when many acceptors have already returned to their ground state. The result is the formation of a population of available acceptors (even when direct excitation of the acceptor is non-zero). A large majority of fluorescent dyes have lifetimes in the range of 0.5–5 ns, and decay kinetics that are described by mono-exponential decay functions [283]. The PL decay dynamics of QDs are typically more complex in comparison to organic fluorophores and appropriate data analysis is required. QDs exhibit multi-exponential behaviour that can continuously change over the course of measurements [309, 310]. The correlation of decay rates to the emission intensities revealed that at high intensities (longer lifetimes), the decay rate is mono-exponential, while at low intensities (shorter lifetimes) it is multi-exponential. This observation implies that fluctuations in

emission intensities are dominated by the dynamics of the non-radiative rate component, k_{nr} . Maximum-intensity single exponential decays (radiative, k_r) are consistent among different batches of QDs of the same size, as it is an intrinsic parameter of the QD core, while non-radiative decay rates (quality of surface, trap sites, shell coating, ligands) contribute to multi-exponential decay dynamics [309]. In comparison, multi-exponential decays with dyes are observed when attached to organic and biological molecules upon conformational changes or when they sample two different environments (*e.g.* exposed and shielded from water) [309]. In order to calculate the FRET efficiency from the changes in the excited state lifetime (*i.e.* according to eqn. 1.24) for a QD FRET donor with a biexponential lifetime, an amplitude-weighted average lifetime is calculated according to eqn. 1.30:

$$\tau_{av} = \frac{A_1 \tau_1 + A_2 \tau_2}{A_1 + A_2} \quad (1.30)$$

where A_i denotes the amplitude and τ_i the lifetime of the i th component.

Despite the numerous advantages that QDs offer as FRET donors in comparison to organic fluorophores, the complex photophysical properties give rise to some drawbacks, which include photoactivation, emission enhancement, intermittency and bluing (these phenomena are described in detail in Section 1.3.3.1). All these process, with the exception of intermittency, introduce a systematic error in determining the FRET efficiency of the system.

1.3.6.1 Selection of QD-dye FRET pairs

There are a number of factors that need to be taken into consideration when selecting QD-dye FRET pairs for bioanalytical applications. Three important considerations are (i) direct excitation of FRET acceptor dye, (ii) spectral overlap between the QD donor and the dye acceptor, and (iii) emission crosstalk between the QD donor PL in the dye acceptor PL. Since FRET can only take place between the donor in its excited state and the acceptor in its ground state, selecting an excitation wavelength that preferentially excites the donor with minimal direct excitation of acceptor is crucial. Fortunately, QD donors exhibit broad absorption and can be efficiently excited with any wavelength in the UV-visible region of the spectrum. Over this region, it is also possible to select a wavelength that provides minimal excitation of the dye acceptor. Although

this selection criterion is rarely discussed in the literature, it is important to consider, particularly in the designs where the excitation wavelength is restricted by the instrumentation used (*i.e.* laser, LED).

It is apparent at this point that spectral overlap is an essential condition for FRET to take place. However, there needs to be a careful balance as to how closely QD emission is located to dye emission. Most dyes have small Stokes shifts, such that the greater spectral overlap desired for greater FRET efficiency (*i.e.* QD PL superimposed with dye absorption) leads to a larger spectral crosstalk, γ from QD PL in dye emission:

$$\gamma = \frac{F_{QD, \lambda=Dye\ Max}}{F_{QD, \lambda=QD\ Max}} \times 100\% \quad (1.31)$$

Table 1.2 lists some optical properties of selected Alexa Fluor dyes commonly used as FRET acceptors with QDs [311]. Table 1.3 provides information on the calculated spectral overlap (eqn. 1.20) between QD donors (FWHM 30 nm) denoted as QDX, where X corresponds to the wavelength of emission maxima, and these dye acceptors. The Förster distances, calculated according to eqn. 1.18, depend on the quantum yield of QDs, such that for all QD-dye FRET pairs, an increase in QD quantum yield from 0.1 to 0.5 results in *ca.* 1–2 nm increase in Förster distance.

Table 1.2 Properties of common fluorescent dyes used as acceptors in QD-FRET bioassays.

Dye	λ_{Abs} (nm)	$\epsilon(\lambda_{max})$ ($M^{-1}cm^{-1}$)	λ_{Em} (nm)	Quantum Yield
A488	496	73 000	519	0.92
A546	556	112 000	573	0.79
A555	555	155 000	565	0.10
A568	578	88 000	603	0.69
A594	590	92 000	617	0.66
A610	612	144 000	628	N/A ^a
A633	632	159 000	647	N/A ^a
A647	650	270 000	668	0.33
A660	663	132 000	690	0.37
A680	679	184 000	702	0.36

^aN/A = not available. All reported values are obtained from ref. [309].

Table 1.3 Summary of spectral overlap, Förster distance and crosstalk for QD-Alexa Fluor dyes.

		QD490	QD520	QD540	QD565	QD585	QD605	QD630	QD650
A488	J ($\times 10^{-9}$) ^a	3.02							
	R ₀ ($\Phi_{QD}=0.1$) ^b	4.21							
	R ₀ ($\Phi_{QD}=0.5$) ^b	5.51							
	γ^c	14.2%							
A546	J ($\times 10^{-9}$) ^a	0.746	3.06	4.98					
	R ₀ ($\Phi_{QD}=0.1$) ^b	3.34	4.22	4.58					
	R ₀ ($\Phi_{QD}=0.5$) ^b	4.36	5.52	5.98					
	γ^c	0.06%	1.6%	9.0%					
A555	J ($\times 10^{-9}$) ^a	1.87	6.38	8.73					
	R ₀ ($\Phi_{QD}=0.1$) ^b	3.89	4.77	5.03					
	R ₀ ($\Phi_{QD}=0.5$) ^b	5.08	6.24	6.57					
	γ^c	0.10%	4.1%	21.7%					
A568	J ($\times 10^{-9}$) ^a	0.453	2.35	3.80	6.68	7.18			
	R ₀ ($\Phi_{QD}=0.1$) ^b	3.07	4.04	4.37	4.81	4.86			
	R ₀ ($\Phi_{QD}=0.5$) ^b	4.01	5.28	5.72	6.28	6.36			
	γ^c	0.04%	0.07%	0.3%	5.2%	41.4%			
A594	J ($\times 10^{-9}$) ^a	0.369	1.67	2.90	5.71	8.48	6.83		
	R ₀ ($\Phi_{QD}=0.1$) ^b	2.98	3.81	4.18	4.68	5.00	4.82		
	R ₀ ($\Phi_{QD}=0.5$) ^b	3.88	4.99	5.47	6.12	6.54	6.31		
	γ^c	0.03%	0.05%	0.09%	1.0%	10.0%	66.0%		
A610	J ($\times 10^{-9}$) ^a	0.193	1.12	2.19	4.94	8.46	13.9		
	R ₀ ($\Phi_{QD}=0.1$) ^b	2.66	3.57	3.99	4.57	5.00	5.43		
	R ₀ ($\Phi_{QD}=0.5$) ^b	3.48	4.67	5.22	5.98	6.54	7.11		
	γ^c	0.03%	0.03%	0.05%	0.3%	2.8%	26.0%		
A633	J ($\times 10^{-9}$) ^a	0.0856	0.752	1.42	3.90	6.53	10.7	18.6	
	R ₀ ($\Phi_{QD}=0.1$) ^b	2.33	3.34	3.71	4.39	4.79	5.20	5.70	
	R ₀ ($\Phi_{QD}=0.5$) ^b	3.04	4.37	4.86	5.75	6.26	6.80	7.45	
	γ^c	0.03%	0.03%	0.03%	0.06%	0.3%	0.3%	45.0%	
A647	J ($\times 10^{-9}$) ^a	0.0889	0.607	1.16	3.27	7.08	12.7	26.4	36.0
	R ₀ ($\Phi_{QD}=0.1$) ^b	2.34	3.22	3.59	4.27	4.85	5.35	6.04	6.36
	R ₀ ($\Phi_{QD}=0.5$) ^b	3.06	4.21	4.69	5.58	6.35	6.99	7.90	8.32
	γ^c	N/D	N/D	N/D	N/D	0.06%	0.3%	5.2%	41.0%
A660	J ($\times 10^{-9}$) ^a	0.572	1.75	2.69	5.05	7.89	11.2	15.6	20.6
	R ₀ ($\Phi_{QD}=0.1$) ^b	3.19	3.85	4.13	4.59	4.94	5.24	5.54	5.80
	R ₀ ($\Phi_{QD}=0.5$) ^b	4.17	5.03	5.40	6.00	6.46	6.85	7.24	7.59
	γ^c	N/D	N/D	N/D	N/D	N/D	0.06%	0.4%	4.1%
A680	J ($\times 10^{-9}$) ^a	0.115	0.760	1.25	2.63	4.50	7.38	12.7	20.9
	R ₀ ($\Phi_{QD}=0.1$) ^b	2.44	3.35	3.64	4.12	4.50	4.89	5.35	5.81
	R ₀ ($\Phi_{QD}=0.5$) ^b	3.20	4.37	4.75	5.38	5.88	6.39	6.99	7.60
	γ^c	N/D	N/D	N/D	N/D	N/D	N/D	0.1%	1.0%

^aSpectral overlap, J in units $\text{cm}^6\text{mol}^{-1}$; ^bFörster distance in nm; ^cQD crosstalk calculated using eqn. 1.31.

1.4 Contributions of This Thesis

This thesis describes original research toward development of smartphone-based POC platforms for “one-step” multiplexed assays. “One-step” implies that no additional pre-treatment and post-washing would be required, and this goal was achieved by using the highly distance-dependent FRET assay format with QDs as donors. The author’s work began in September 2012—mere months after publication of the work by the Ozcan Laboratory demonstrating QD-based detection of *E.coli* [110]. Design of a smartphone-based platform using combination of QDs and FRET was an original idea of the author, and later served as inspiration for the work published by Noor *et al.* [312, 313]. The overall objective of this thesis was to develop a proof-of-principle diagnostic platform that exploited the unique properties of QDs and the imaging capability of smartphones. In particular, the research in this thesis emphasizes the *multiplexing* capabilities of QDs and FRET for protease activity assays and research towards *paper-based* on-chip assays amenable for direct detection in *biological matrices* (serum and whole blood) *via* QD *immobilization*.

1.4.1 Background

In the past five years, there has been a surge in the number of publications that have used smartphones or cellphones in bioassay development. On one hand, this interest was driven by the need to develop POC diagnostics that can enable personalized medicine and increase the efficiency and accessibility of health care, particularly in resource-limited settings such as developing countries. On the other hand, today there are nearly 7 billion mobile subscriptions worldwide, equivalent to 95.5% of the world population. Smartphones have become an essential tool in people’s daily lives. Mass produced, portable and relatively low-cost, these devices provide an ever-expanding set of features including data storage, spatial mapping, temporal tracking, and wireless transmission of information. The role of smartphones for POC diagnostics falls in two main categories: (1) control modules, power sources, and data handling hubs, and (2) optical detectors utilizing their built-in cameras. The latter case was primarily developed for direct imaging applications. In one of the earliest studies, the Fletcher laboratory demonstrated brightfield imaging of sickle red blood cells and fluorescence imaging with LED excitation of Auramine O stained *M. tuberculosis*-infected sputum samples [314]. In 2011, the Ozcan laboratory demonstrated platform for cell counting [315, 316] that was ultimately suitable to

count white blood cells in brightfield mode, red blood cells in fluorescent mode, and hemoglobins in transmission/absorbance mode [317]. Numerous assays based on colorimetric detection have been developed to date [147, 152, 318-321]. For example, on-chip ELISA-based detection of an ovarian cancer biomarker, HE4, in urine was demonstrated by correlating the red pixel intensity of colour images with 3,3',5,5'-tetramethylbenzidine (TMB) substrate concentration [147]. More recently, the Ozcan laboratory developed a 96-well ELISA using transmission mode smartphone imaging with blue LEDs as an excitation source [320]. This LED light was passed through each well, and then was collected *via* 96 individual optical fibers, quantifying mumps, measles and herpes simplex virus IgGs.

The recent advances in the area of POC diagnostics cannot be fully appreciated without acknowledging progress in the areas of nanomaterials and nanotechnology. Gold nanoparticles became a preferred choice among colour reagents in lateral flow assays. They have large, size-dependent molar absorption coefficient, and are observed as an intense dark red colour, and exhibit pronounced colour changes (from red to blue) upon aggregation. Many Au NP-based assay formats developed previously for qualitative lateral flow assays and solution-based assays were translated into smartphone-enabled quantitative formats [79, 80, 322-324]. The second most popular nanomaterial explored for bioassay development is QDs. The unique optical and physical properties of semiconductor QDs attracted the attention of numerous research groups that develop fluorescence-based assays. From the standpoint of smartphone-based assay development, the main advantages of QDs include (i) their brightness, which permits use of low-power excitation sources; (ii) their narrow emission, which can be matched with the RGB channels of the built-in colour filters of smartphones; (iii) their broad absorption spectra, which permit use of relatively broad-band excitation sources without increasing background in detection channel; and (iv) their amenability to multiplexing. In 2012, the Ozcan Laboratory exploited the brightness of QDs to demonstrate detection of *Escherichia coli* O157:7 (*E. coli*) using cell phone imaging [110]. The inner surface of glass capillaries was used as a solid support for the immobilization of anti-*E. coli* antibodies. The capillaries were placed in a custom-built cell phone attachment that accommodated two sets of UV LEDs for excitation of the red-emitting QDs and a suitable longpass filter to isolate QD emission. *E. coli* were detected in a sandwich immunoassay with biotinylated secondary antibody and streptavidin-coated QDs. The LOD in buffer and milk samples was *ca.* 5–10 CFU mL⁻¹ with good specificity. In 2015, the

Chan Laboratory demonstrated multiplexed detection using QD barcodes of pathogen DNA, extracted from patient samples, following an amplification step [325].

In addition to approaches that utilize QDs as fluorescent labels, QDs have been shown to be excellent FRET donors. Since the seminal work by Medintz *et al.* in 2003, QD-FRET assays have been developed for the detection of various analytes [185]. However, until recently, all of these assays required sophisticated laboratory instrumentation for measurements. In 2014, Noor *et al.* reported digital image (iPad) based detection of paper-based QD-FRET nucleic acid hybridization assay [312]. Amplification of the signals observed by drying paper substrates permitted 450 pmol detection limit with UV lamp excitation. In subsequent work, Noor *et al.* integrated thermophilic helicase-dependent amplification step to achieve a 37 zmol detection limit with digital imaging [313].

Despite many advances to the field of smartphone diagnostics, as demonstrated by the studies highlighted above, there remains many limitations to translating these technologies in to molecular diagnostics of wider utility. To date, the vast majority of these assays were based on direct imaging of the sample (*e.g.* cells, bacteria) or commercially available kits. Other challenges associated with POC devices often include poor analytical sensitivity, reproducibility, and lack of multiplexing.

1.4.2 Thesis overview

This thesis is divided into seven chapters, including this introductory chapter, and is complemented by the appendices that contain additional experimental methods and details. Published results are noted at the beginning of each chapter.

Chapter 2 describes a simple, 3D-printed prototype accessory that enables all-in-one smartphone excitation and imaging of PL. The requirement of an external excitation source for smartphone imaging of fluorescence assays is eliminated by demonstrating that the built-in LED photographic flash of the smartphone can be used for this purpose. Moreover, this chapter shows that the sensitivity of smartphone fluorescence imaging with built-in flash excitation is competitive with imaging using an external UV lamp, and that QDs are superior for smartphone imaging assays over traditional dyes and fluorescent proteins. A proof-of-concept protein

binding assay and FRET-based protease activity assay were demonstrated, and the use of QDs as FRET donors can permit imaging of fluorescent dyes that would otherwise not be bright enough to detect using all-in-one smartphone PL excitation and imaging. This work provides a foundation for smartphone-based PL bioassays without external optoelectronic devices, helping to maximize simplicity and robustness while minimizing cost, which are important features for prospective POC diagnostic technologies.

Chapter 3 demonstrates a first step towards the development of multiplexed assay of proteolytic activity with QD peptide conjugates. The spectrally narrow PL emission and strong, broad light absorption of QDs was combined with red-green-blue (RGB) digital color imaging for quantitative, multiplexed homogeneous assays. Alloyed CdSeS/ZnS QDs with emission in the blue, green, and red region of the spectrum were carefully paired with FRET acceptors, such that the changes in QD PL as a result of proteolysis were measured from RGB channel intensities in digital colour images. Importantly, this work shows that quantification of proteolytic rates is identical for smartphone based detection and a sophisticated fluorescence plate reader. This work was recently highlighted by Stevens as an important contribution to nanoparticle based POC diagnostics [326], and, to date, remains the only report of smartphone digital imaging as a readout for multiplexed FRET-based assay with QD donors.

Chapter 4 evaluates three surface chemistries for the immobilization of water-soluble QDs on cellulose paper fibers *via* self-assembly. These chemistries included:

- i. modification of oxidized cellulose with 1-(3-aminopropyl)imidazole to afford substrates modified with imidazole ligands;
- ii. modification of oxidized cellulose with *N*-(2-aminoethyl)-5-(1,2-dithiolan-3-yl)pentanamide, a derivative of lipoic acid, to afford substrates with thiol ligands;
- iii. modification with lipoic acid *via* silanization step with 3-aminopropyltriethoxysilane (APTES) to afford substrates modified with thiol ligands.

These methods yielded a high density of ligands that were successful in immobilizing QDs at high density. It was possible to immobilize QDs coated with a variety of ligands, as well as pre-assembled QD-peptide conjugates. Furthermore, each of the three evaluated chemistries had a different effect on the photobleaching behaviour of QDs, their long-term stability, the density of

immobilized QDs, and the enhancement in the rate and efficiency of FRET between immobilized QDs and dye acceptors within paper matrix in comparison to solution-phase FRET. Overall, development of underlying chemistry of cellulose fibers used for immobilization of QDs offers a promising platform for the design of new methods of bioanalysis. Furthermore, it acts as an important component of assay development providing opportunities and challenges in controlling the properties of immobilized QDs and the extent of the interactions between biomolecules and cellulose interface. Understanding the effects of the underlying surface chemistry was a crucial component for development of the solid-phase assays described in Chapter 5 and Chapter 6.

Chapter 5 evaluates the suitability of using paper immobilized QDs for FRET-based transduction of protease activity. This chapter represents one of the most significant contributions of this thesis, as it merges many ideas developed to combine smartphone imaging with a “one-step” assay format *via* QD-FRET. The PL response was acquired with a smartphone and compared with other devices such as a miniature fiber-optic spectrometer (\$2000), an educational-grade digital microscopy camera (\$250), and a consumer webcam (\$40). The diagnostic utility of QD-modified paper substrates with each of the foregoing detection systems was demonstrated through a series of solid-phase proteolytic assays based on FRET for simultaneous detection of three proteases that belong to pancreatic family of enzymes—enterokinase, trypsin, and chymotrypsin. Overall, this chapter makes the idea of smartphone-based QD-FRET assay in complex biological matrix developed in Chapter 6 more feasible.

Chapter 6 outlines design criteria and demonstrates proof-of-concept for an assay format that utilizes smartphone readout for the single-step, FRET-based detection of hydrolase activity in serum and whole blood, using thrombin as a model analyte. This study builds on the work described in Chapter 2-5, which highlights the design components necessary for an assay format that permits direct measurements in whole blood. Essentially, every component was carefully optimized to circumvent challenges of whole blood as a matrix including: the LED illumination, the QD-dye FRET pair, the reference signal, the paper test strips, and the PDMS-on-glass sample chip. Overall, this chapter shows how smartphones and QDs can be integrated to permit assays in serum and whole blood in a format that will ultimately be suitable for many point-of-care diagnostic applications. An overview of the main design components and a summary of

guidelines that can be used to “*build your own smartphone-based QD-FRET assay platform*” are shown in Figure 1.17.

Chapter 7 provides a brief summary of the achievements presented in the preceding chapters, as well as an outline for future work.

In summary, this thesis presents unique contributions to the areas of nanotechnology, bioanalytical chemistry, and the development of point-of-care diagnostics with consumer electronic devices. Smartphone imaging combined with QDs, FRET and paper substrates was successfully demonstrated for multiplexed bioanalysis, as well as addressing challenges of performing assays in whole blood.

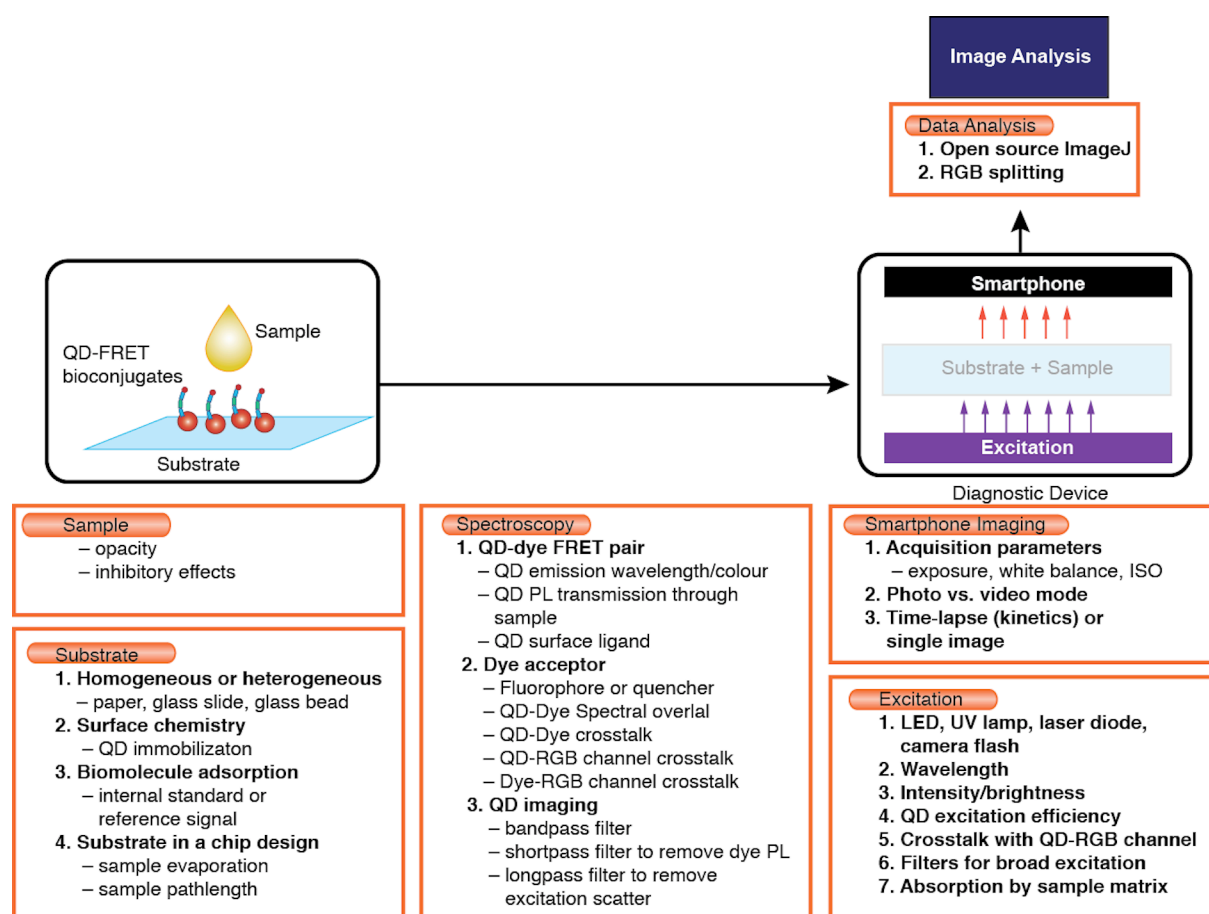


Figure 1.18 Overview of main design components and a flowchart of critical optimization parameters.

Chapter 2 Use of a Smartphone and 3-D Printed Accessory for All-in-One Excitation and Imaging of Photoluminescence

This chapter is an adaptation of published work, and is reproduced from Petryayeva, E.; Algar, W. R., A Job for Quantum Dots: Use of a Smartphone and 3D-Printed Accessory for All-In-One Excitation and Imaging of Photoluminescence. *Anal. Bioanal. Chem.* **2016**, *408* (11), 2913-2925, with permission of Springer (Copyright 2016 Springer).

2.1 Introduction

The cost and efficiency of health care is a global concern. Health care systems in many developed countries are overburdened, increasingly expensive and/or poorly sustainable [327, 328], whereas many developing countries suffer from poor access to facilities, inadequate resources, and barriers to implementing the basic health care solutions currently used in developed countries [35, 36]. Point-of-care (POC) diagnostics are potential solutions to many of these challenges, as these technologies and methods aim to translate laboratory-based bioanalytical assays to robust, rapid, portable, and low-cost formats [35, 36]. As recently reviewed, mobile phones have emerged as a potentially powerful platform for bioanalysis in this context [1, 329]. These mass-produced consumer devices are already globally ubiquitous, and their ever-growing range of features and capabilities can be increasingly leveraged for POC diagnostics. One role proposed for smartphones and cell phones is as control modules, power sources, and data handling hubs that connect to peripheral devices or dongles that are custom designed for particular bioassays. Recent examples of such devices include microfluidic platforms for immunoassays [21, 330] and DNA detection [331], and an electrochemical platform for detection of glucose in blood, heavy metals in water, sodium in blood, and pathogens *via* immunoassays [332].

An alternative strategy for utilizing smartphones as platforms for POC diagnostics is to exploit their built-in cameras as optical detectors for the readout of bioassays. Most smartphone cameras are complementary metal-oxide-semiconductor (CMOS) photosensor arrays with overlaid red-green-blue (RGB) colour filters, an infrared (IR) filter, and optics. Analysis of RGB or grayscale pixel intensities in smartphone-acquired digital images can provide quantitative information useful for assay readout. To date, most bioassays with smartphone readout have utilized colourimetric detection. Representative examples include enzyme-linked immunosorbent assays (ELISAs) with turnover of a chromogen for detection of human Interleukin-6 [333] and screening for disease susceptibility [320], chromogen assays for detection of uracil-DNA glycosylase [334] and methyl parathion [335], colourimetric gold nanoparticle aggregation assays for DNA detection [336], and barcode-style immunoassays [337] and competitive binding vitamin D assays [79] with silver-enhanced gold nanoparticles. Other less common optical formats have included smartphone readout of photonic crystal biosensors [338] and analysis of diffraction patterns from microbead labels [339]. There is also a growing number of bioassays that utilize smartphone readout with fluorescence detection, including immunoassays for bacteria detection [110, 340]; paper-based [150, 312, 313], chip-based [341] and microreactor-based [342] assays for nucleic acids; and fluorescence imaging of a photosensitizer in cell aggregates [343], *Giardia lamblia* cysts [344], and stretched DNA molecules [345]. A requirement of all of these assays with smartphone readout of fluorescence has been the use of excitation light sources that are separate from the smartphone, including light-emitting diodes (LEDs) [110, 150, 340-344, 346, 347], diode lasers [158, 345], and UV lamps [312, 313]. These sources are sometimes integrated with the smartphone using dichroic mirrors, objective lenses, non-trivial optomechanics and component housings that are designed for specific assay formats. Such complexity can increase cost, operational and training requirements, and limit the applications and robustness of the hardware, reducing their appeal and practicality for POC diagnostics and other settings with limited resources.

This chapter describes an approach that eliminates the requirement of an external excitation source for smartphone imaging of fluorescence assays by demonstrating that the built-in LED photographic flash of the smartphone can be used for this purpose. A simple, broadly useful, and robust 3D-printed accessory is used to provide a dark environment for fluorescence measurements under ambient light conditions, and to support the smartphone in proper alignment

with reflectors and filters for excitation and imaging of emission. In contrast to many devices with excitation sources external to the smartphone, this smartphone accessory does not require the use of dichroic mirrors, additional lenses, or optomechanics. Moreover, this chapter shows that the sensitivity of smartphone fluorescence imaging with built-in flash excitation is competitive with imaging using an external UV lamp, and that QDs are ideal for smartphone imaging assays. For comparison, fluorescein, a molecular dye, and *R*-phycoerythrin, a phycobiliprotein were selected as organic fluorescent materials that are known for their high brightness, routinely used in bioanalysis, and compatible with the excitation light from the smartphone flash were evaluated. To demonstrate proof-of-concept for bioanalysis with all-in-one smartphone imaging of QDs, a model protein binding assay with avidin and a FRET-based assay for the proteolytic activity of thrombin were carried out, including imaging of QD PL in serum. In addition, tandem QD-dye conjugates were shown to enable all-in-one imaging of dye fluorescence that was otherwise unobservable. This work provides an important foundation for developing low-cost and portable accessories for smartphone-based PL bioassays without external optoelectronic devices. Such devices have great potential for future POC diagnostic applications and, by extension, as readily accessible tools for research laboratories.

2.2 Results

2.2.1 Design of the 3D-printed accessory

Figure 2.1 illustrates the design of the 3D-printed accessory for smartphone excitation and imaging of PL. There are three key components in the design of the accessory, each of which is highlighted in Figure 2.1A-D. The first component is a blackout box that sits on a non-reflective surface or sample stage. This box functions to prevent ambient light from interfering with PL imaging. The second component is the box lid, which has a recess with two circular apertures. The recess fits the dimensions of the smartphone, which is fitted in the lid such that one aperture is positioned below the smartphone camera module and the other is positioned below the smartphone flash module. Each aperture is large enough to hold a 12.5 mm diameter optical filter. The third component is a pair of low-cost plastic reflectors attached to the underside of the lid that directs the excitation light from the flash module onto the sample, which is positioned in the field of view of the smartphone camera. Photographs of the prototype accessory are shown in Figure 2.1B-C.

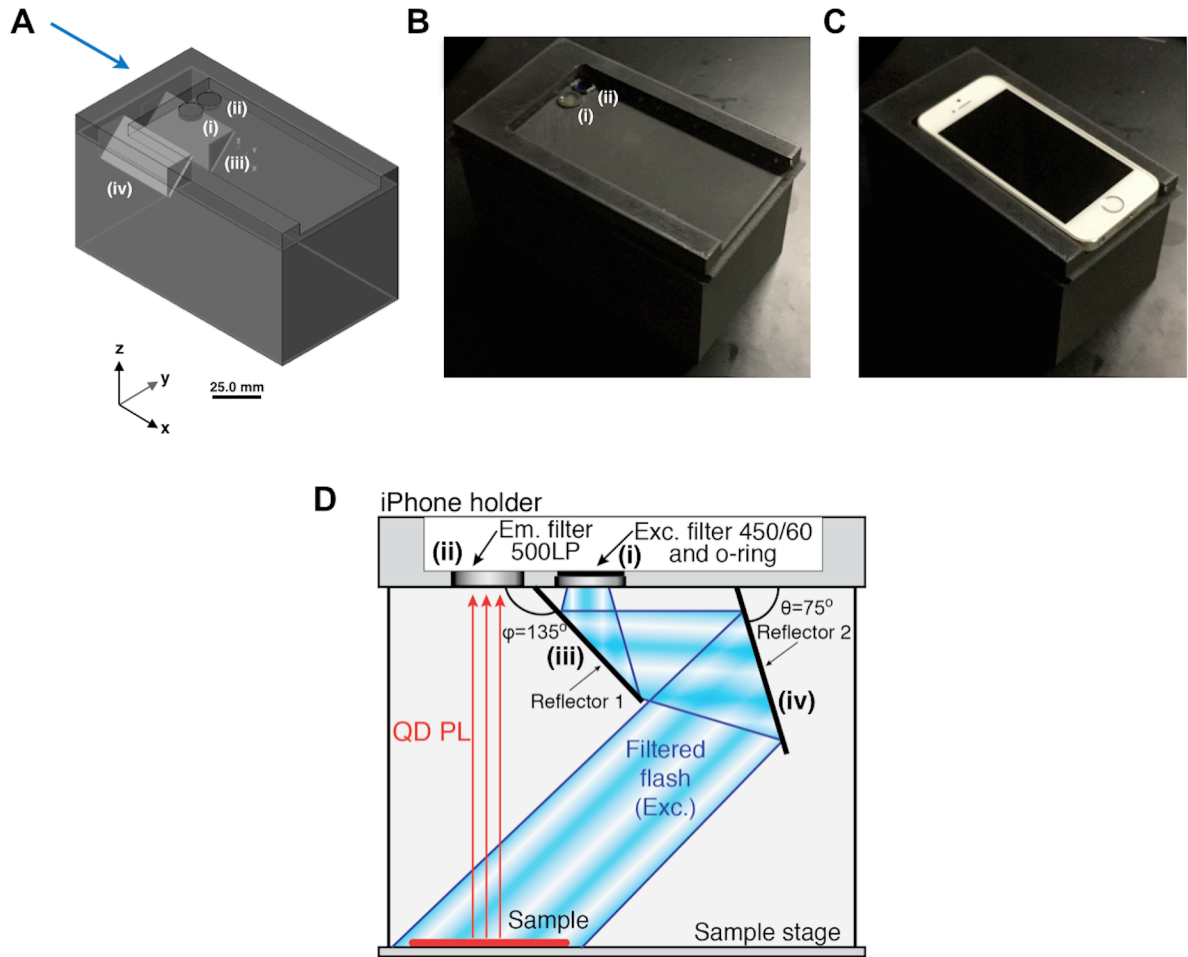


Figure 2.1 Smartphone accessory for all-in-one excitation and imaging of PL. **(A)** 3D rendering of the accessory. The rendering is partially transparent. The two circular features are the filter positions (i, ii) and the light grey features are the reflector supports (iii, iv). Photographs of the 3D-printed accessory **(B)** without and **(C)** with the smartphone in position. **(D)** Schematic of the device, showing the excitation light path. The arrow in panel A indicates the orientation of this view.

The optical filter inline with the flash module is a band-pass filter that limits the excitation light to the blue region of the spectrum and blocks longer wavelengths, as shown Figure 2.2A. The optical filter inline with the camera module is a long-pass filter that rejects blue light and transmits green through near-infrared light. The transmission spectra of both filters are shown in Figure 2.2A-B. Even with this relatively simple configuration, a working imaging area of approximately 25 mm × 45 mm is obtained, with an estimated power of ~0.14 mW at the

imaging plane. Figure 2.2C shows that the relative standard deviation is less than 5% over the useful imaging area for the combined excitation intensity and emission collection efficiency.

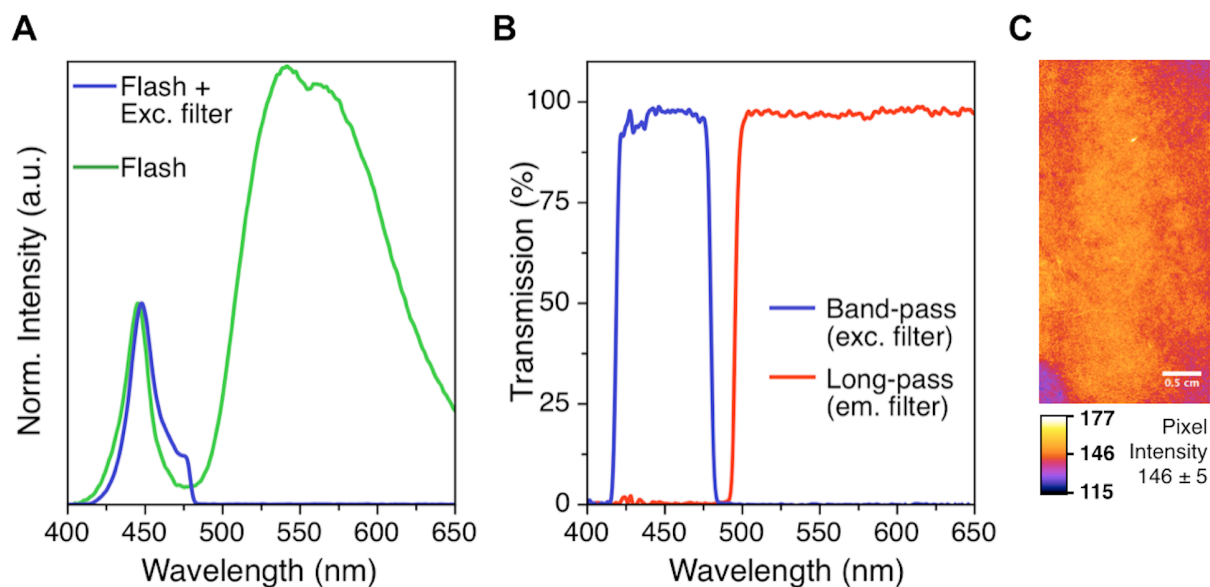


Figure 2.2 (A) Spectrum of light from the flash module of the smartphone with and without the blue band-pass excitation filter. (B) Transmission spectra of the band-pass excitation filter and long-pass emission filter. (C) False-colour image that characterizes the homogeneity of the combined excitation intensity and collection efficiency over the useful imaging area. The scale bar is 0.5 cm.

2.2.2 Substrates for all-in-one imaging

The imaging apparatus can accommodate a variety of sample cells or holders, with the provision of a low height profile to avoid obstruction or strong reflection of the excitation light. This apparatus was successfully used for imaging of droplets (6 μL) of photoluminescent sample solutions spotted on glass slides patterned with an array of microwells, injected into PDMS-on-glass microchannels, and as bands in an agarose slab gel. Photoluminescent materials immobilized on glass beads and paper substrates were also imaged (see Figure 2.3).

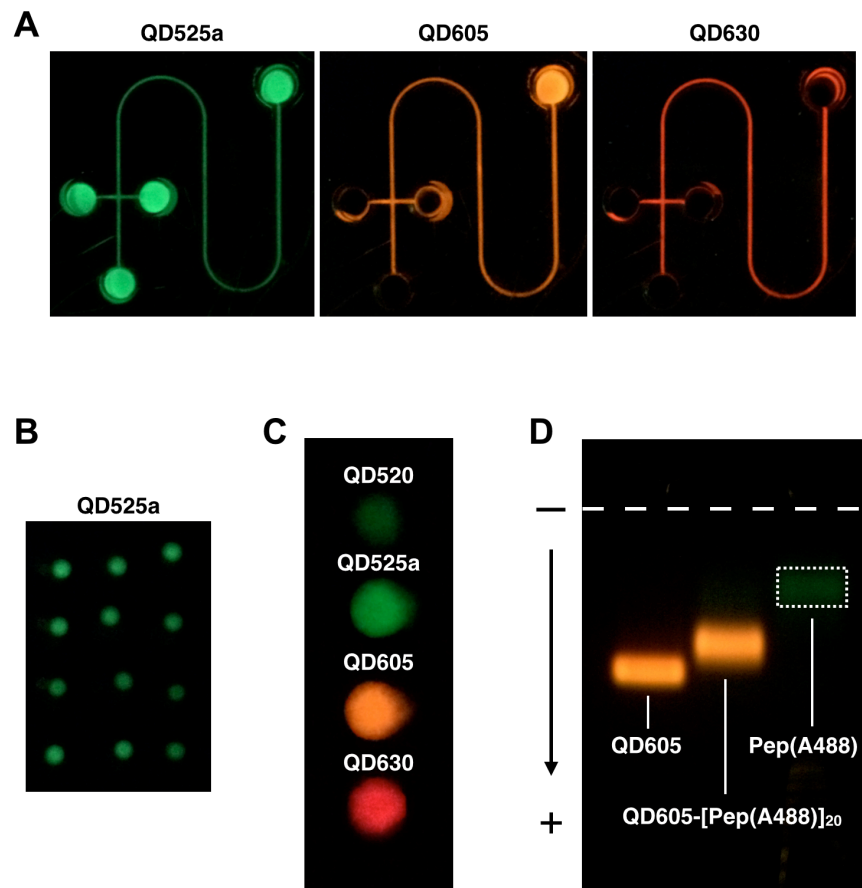


Figure 2.3 (A) Smartphone PL images of PDMS-on-glass microfluidic chips filled with (i) QD525a (0.5 μM), (ii) QD605 (0.2 μM); and (iii) QD630 (0.2 μM). The channel dimensions are $\sim 300 \mu\text{m}$. (B) Smartphone PL images of QD525a immobilized on glass beads (0.5 mm dia.). (C) Smartphone PL image of paper substrates with immobilized QD520, QD525a, QD605, QD630. (D) Smartphone PL image of an agarose gel (1.0%) showing the difference in electrophoretic mobility between a QD605, QD605-[Pep(A488)]₂₀ conjugates, and an equivalent amount of Pep(A488).

2.2.3 Photoluminescent materials

Figure 2.4 summarizes the key absorbance and emission properties of the photoluminescent materials evaluated for all-in-one smartphone PL imaging. These materials included nine different QD materials, shown in Figure 2.4A-B, which varied primarily in their wavelength of

emission, indicated by $QD\lambda$ (where λ is the wavelength of peak PL; *i.e.* QD605 had its peak PL at 605 nm). Although most of the QDs were CdSe/CdS/ZnS core/shell/shell nanocrystals, two QD materials were alloyed CdSeS/ZnS core/shell nanocrystals (indicated by a lowercase ‘a’ after the PL wavelength; *e.g.* QD525a). The primary optical difference between the CdSeS/ZnS QDs (QD525a, QD540a) and their similarly emitting CdSe/CdS/ZnS counterparts (QD520, QD550) was that the former had larger molar absorption coefficients (see Table 2.1).

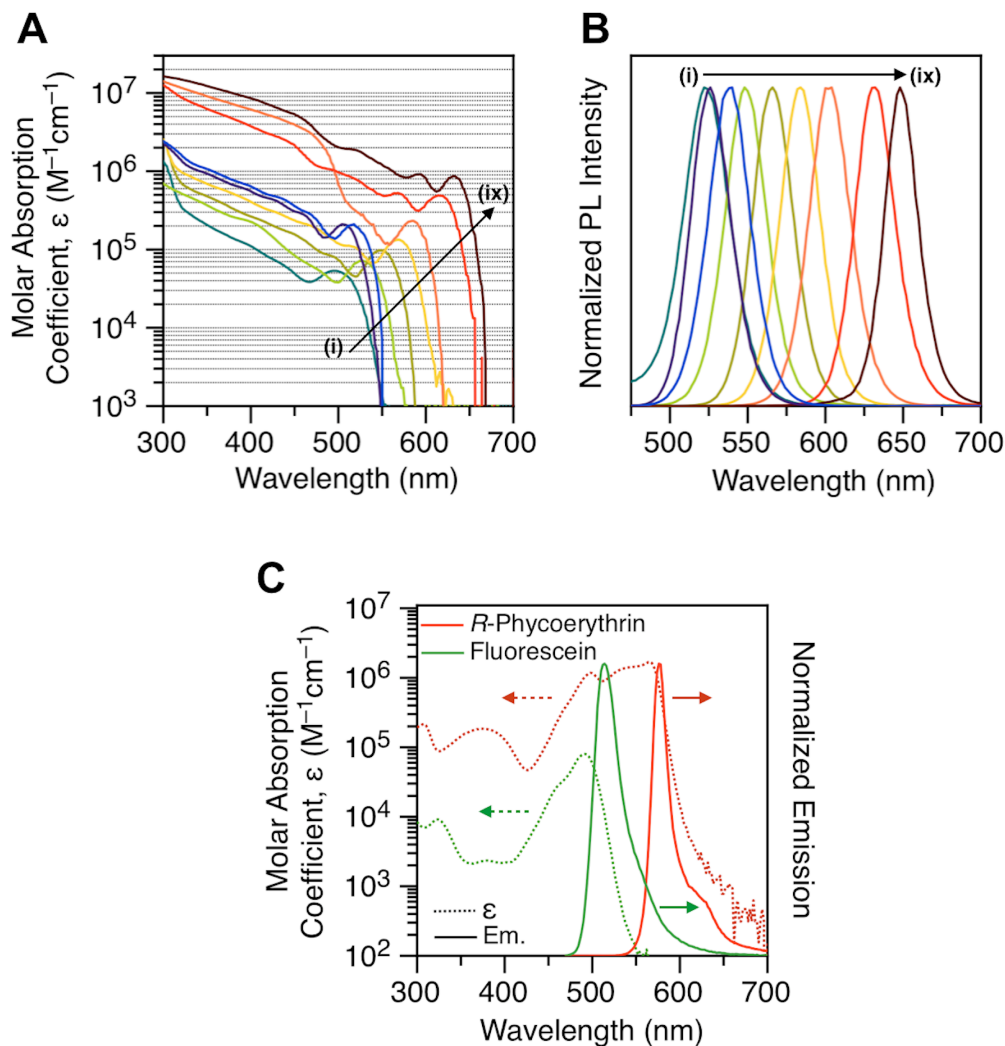


Figure 2.4 Absorption and emission spectra for the QDs, R-PE, and fluorescein. **(A)** Absorption spectra and **(B)** normalized PL emission spectra for the QD materials: (i) QD520, (ii) QD525a, (iii) QD540a, (iv) QD550, (v) QD565, (vi) QD585, (vii) QD605, (viii) QD630, (ix) QD650. **(C)** Absorption spectra (dotted lines) and emission spectra (solid lines) for R-PE and fluorescein.

Shown in Figure 2.4C are the spectra for fluorescein and R-phycoerythrin (R-PE). The fluorescein had the most spectrally narrow absorption spectrum (full-width-at-half-maximum, FWHM ~33 nm) and the most spectrally broad emission spectrum (FWHM ~36 nm). The R-PE had a broader absorption spectrum (FWHM ~89 nm) and narrower emission spectrum (FWHM ~24 nm). Note that the FWHM values for fluorescein and R-PE do not account for the asymmetry of their spectra. Both the fluorescein and R-PE had absorption shoulders that overlapped with the filtered excitation light (~450 nm) from the flash module. In contrast, the absorption of the QDs was too broad to define a FWHM, and the emission spectra were symmetric with FWHM values between 27–35 nm (the average, median, and mode FWHM were all ~31 nm). The reported quantum yields for fluorescein and R-PE are both ~0.8 [348, 349], and the quantum yields of the QDs were measured to be between 0.36–0.75 (average quantum yield $\sim 0.5 \pm 0.1$), as summarized in Table 2.1.

Table 2.1 Characteristics of QD materials, R-PE, and fluorescein.

Material	Em. Max.	Em. FWHM	$\epsilon(\text{peak})$	$\epsilon(450 \text{ nm})$	Φ	Rel. Int.
QD520	522 nm	35 nm	53 500 M ⁻¹ cm ⁻¹	49 500 M ⁻¹ cm ⁻¹	0.52	0.04
QD525a	526 nm	29 nm	210 000 M ⁻¹ cm ⁻¹	307 000 M ⁻¹ cm ⁻¹	0.44	0.27
QD540a	540 nm	32 nm	210 000 M ⁻¹ cm ⁻¹	358 000 M ⁻¹ cm ⁻¹	0.42	0.28
QD550	547 nm	31 nm	71 600 M ⁻¹ cm ⁻¹	84 400 M ⁻¹ cm ⁻¹	0.36	0.06
QD565	566 nm	31 nm	97 600 M ⁻¹ cm ⁻¹	157 000 M ⁻¹ cm ⁻¹	0.55	0.16
QD585	582 nm	31 nm	133 000 M ⁻¹ cm ⁻¹	236 000 M ⁻¹ cm ⁻¹	0.59	0.23
QD605	604 nm	30 nm	232 000 M ⁻¹ cm ⁻¹	2 530 000 M ⁻¹ cm ⁻¹	0.53	0.81
QD630	632 nm	32 nm	492 000 M ⁻¹ cm ⁻¹	1 900 000 M ⁻¹ cm ⁻¹	0.75	0.94
QD650	648 nm	27 nm	870 000 M ⁻¹ cm ⁻¹	2 150 000 M ⁻¹ cm ⁻¹	0.41	1.00
R-PE	578 nm	24 nm	198 000 M ⁻¹ cm ⁻¹	125 000 M ⁻¹ cm ⁻¹	0.8	0.07
Fluorescein	514 nm	36 nm	80 000 M ⁻¹ cm ⁻¹	16 800 M ⁻¹ cm ⁻¹	0.8	0.02

Notes: Em. Max., wavelength of maximum emission; Em. FWHM, full-width-at-half-maximum of the emission spectrum; $\epsilon(\text{peak})$, molar absorption coefficient of the QDs and their exciton peak or at the absorption maximum for the fluorescein and R-PE; $\epsilon(450 \text{ nm})$, molar absorption coefficient at 450 nm; Φ , quantum yield; Rel. Int., relative intensity for equal concentrations of the materials, measured from PL emission spectra with 450 nm excitation and normalized to the brightest QD.

2.2.4 Detection of photoluminescence

Figure 2.5A(i) shows smartphone images of solutions of the QD materials. The green (G) or red (R) channel intensities from these images are plotted as a function of QD concentration in Figure 2.5A(ii). Two general trends should be noted: first, the R or G channel intensity tended to increase as the emission wavelength of the QDs increased; and second, the green-emitting alloyed core CdSeS/ZnS QDs exhibited more intense PL than the same concentration of similar green-emitting binary core CdSe/CdS/ZnS QDs. These trends largely correlated with the brightness of the QD materials as measured from PL emission spectra (see Table 2.1). For each QD, the channel (R or G) plotted in Figure 2.5A(ii) represents the brightest or “primary” channel for that particular QD. Although the green-emitting QDs (QD520, QD550, QD525a, QD540a) and red-emitting QDs (QD630, QD650) had a clearly dominant detection channel in smartphone images, the yellow- and orange-emitting QDs (QD565, QD585, QD605) produced significant intensity in both the R and G channel of smartphone images (see Figure 2.6). The images acquired in Figure 2.5 were obtained with the following acquisition settings: shutter speed 1/4 s, ISO 2000, and white balance at 4500 Kelvin. The shutter speed functioned analogously to the integration time/exposure time for a conventional scientific camera or detector, the white balance (Kelvin) makes digital colour adjustments to digital photographs so that white objects appear white in the final images, and the ISO setting (or ISO number) sets the image sensor sensitivity by adjusting the gain on the analog amplifiers for each pixel prior to analog-to-digital conversion. All three acquisition parameters are described and characterized in more detail in Section 2.2.5. The shutter speed and ISO setting were optimized for maximum sensitivity. Although the trends in the R or G channel intensities can be approximated as linear over segments of the curves in Figure 2.5, the overall trends are non-linear with a sigmoid-like shape. The relative response of the camera per unit concentration of QD decreased at both high and low intensities. As expected for 8-bit images, the camera response saturated at intensity values approaching 255.

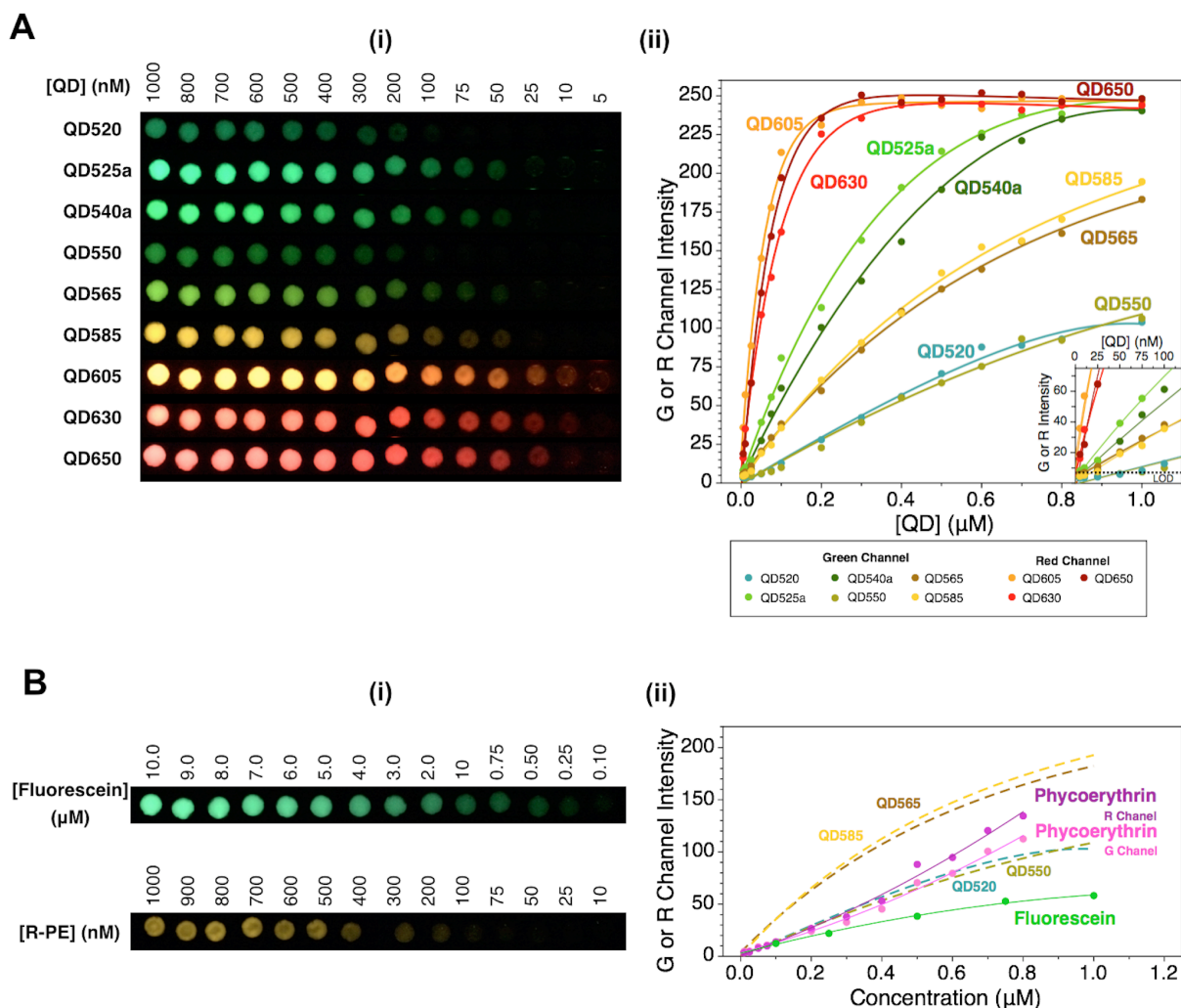


Figure 2.5 Smartphone PL imaging of QDs, fluorescein, and R-PE. **(A)** Images (i) of the PL from different concentrations of the nine different QD materials, and (ii) plots of G or R channel intensity measured from the smartphone images as a function of QD concentration. The QDs are grouped in the legend according to the imaging channel in which they appear brightest, and the corresponding channel is plotted. The limit of detection (LOD) for the R or G channel intensity is shown in the inset, which zooms in on the lower concentrations. **(B)** Analogous images (i) and plots (ii) for fluorescein (G channel) and R-PE (both channels). Trend lines for selected QD materials are shown for comparison. All images were acquired with the following acquisition settings: shutter speed 1/4 s, ISO 2000, and white balance at 4500 Kelvin; these settings were optimized for sensitivity and not colour selectivity.

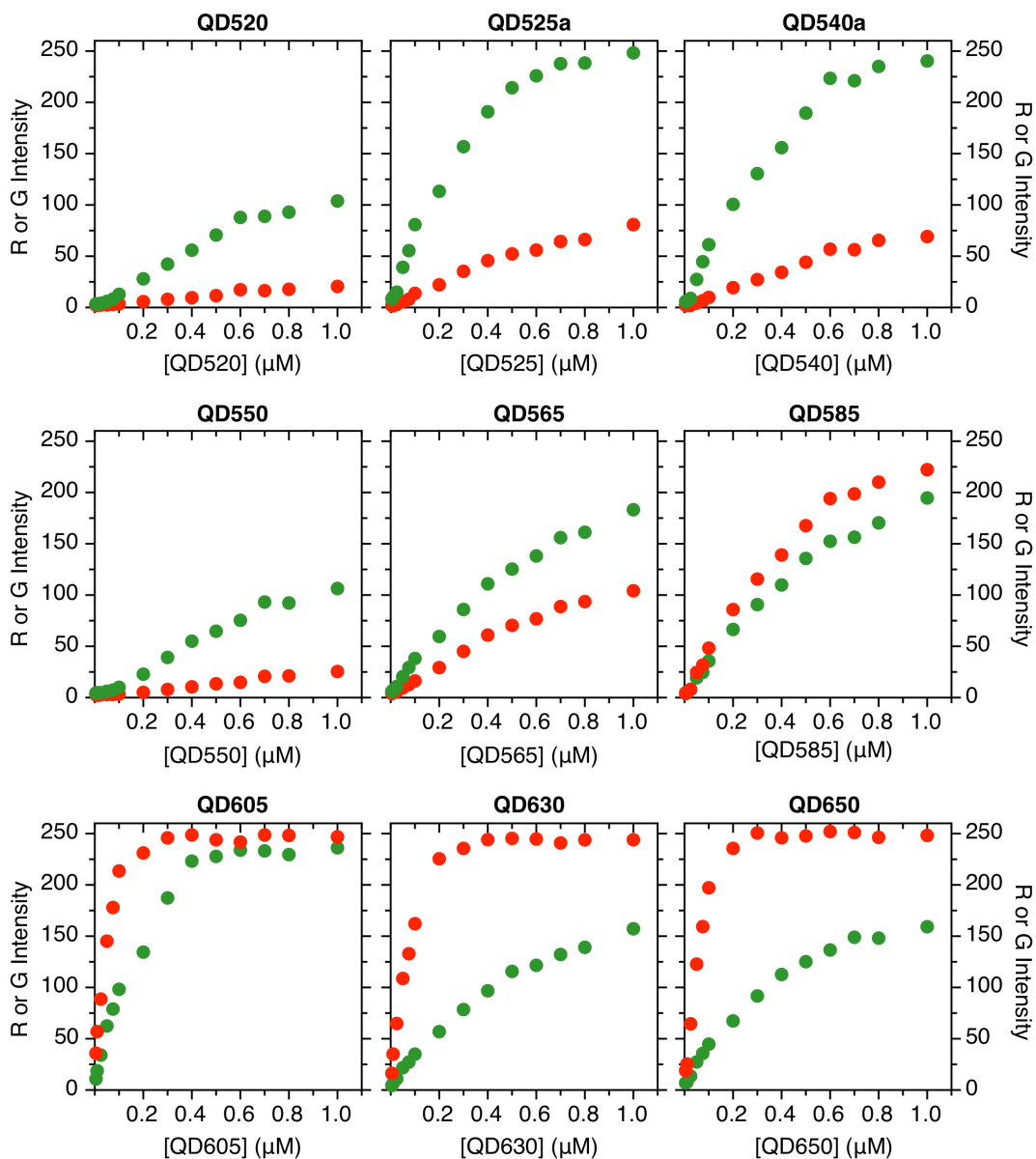


Figure 2.6 R (red circles) and G (green circles) channel intensities from smartphone PL images for increasing concentrations of the nine QD materials from Figure 2.5. All images were acquired with the following acquisition settings: shutter speed 1/4 s, ISO 2000, and white balance at 4500 Kelvin; these settings were optimized for sensitivity and not colour selectivity.

The PL intensities obtained from smartphone images of fluorescein and R-PE are compared with those of the QDs in Figure 2.5B(ii). The R-PE has very similar emission intensities in both the R and G channels of smartphone images, and is comparable in its intensity per unit concentration to

the QD520 and QD550, but is considerably less intense than all other QD materials. Fluorescein is less bright than R-PE, and is thus much less bright than all of the QDs. Overall, the QD525a and QD540a were *ca.* 6-fold brighter than R-PE and 18-fold brighter than fluorescein under these smartphone PL imaging conditions (estimated from the slopes of the approximately linear regions of the curves in Figure 2.5A(ii)). The QD605, QD630, and QD650 were *ca.* 19-fold and 58-fold brighter than R-PE and fluorescein, respectively. In the imaging configuration with the glass slide-supported wells, the estimated limits of detection (LODs) for the foregoing QDs were between 2–10 nM (average LOD 5 ± 3 nM), whereas the LODs for R-PE and fluorescein were *ca.* 40 nM and 80 nM, respectively. The brightness of the QDs with smartphone excitation was between 45–70% of that observed with excitation using a long-wave UV lamp (~365 nm; 6 W bulb) that plugged into an electrical outlet. This difference was attributed to a combination of the larger molar absorption coefficient of the QDs at 365 nm *versus* 450 nm (see Figure 2.4A; coefficients were between 2–4-fold larger), and the lower excitation power at the sample (~0.08 mW) with the UV lamp, which was necessarily offset from the axis connecting the camera and sample.

2.2.5 Effect of smartphone imaging application parameters

Figures 2.7-2.10 summarize the effect of different smartphone image acquisition parameters that were available through the Camera⁺ app on imaging sensitivity and colour selectivity. There were three variable acquisition parameters. First, the shutter speed, which functioned analogously to the integration time/exposure time for a conventional scientific camera or detector. Second, the white balance (Kelvin), which makes colour adjustments to digital photographs so that white objects appear white in the final images. The Kelvin scale is an analogy to the output spectrum of a blackbody radiator at a certain temperature and is intended to account for the relative colour intensities of the light in the photographic scene. White balance is a digital correction applied to the image data acquired by the camera. The third setting is the ISO setting (or ISO number), which sets the image sensor sensitivity by adjusting the gain on the analog amplifiers for each pixel prior to analog-to-digital conversion. The camera sensor sensitivity decreases upon lowering the ISO setting. Therefore, more accurate colours tend to be obtained at lower ISO settings.

Figure 2.7A shows the effect of the ISO setting for samples of QD525a and QD630. In both cases, G and R channel intensities (respectively) increased as the ISO number increased. It was also observed that the colour selectivity decreased suddenly at ISO settings greater than 1000. This result was measured as the crosstalk of the QD PL in the non-optimal colour imaging channel. Figure 2.7B shows the change in crosstalk with ISO number for fluorescein, R-PE, and QD605. The data for fluorescein was similar to that of the QD525a, exhibiting a step increase in crosstalk at higher ISO numbers. In contrast, the ISO setting had a much smaller effect on the crosstalk observed with QD605, and almost no effect on the R-PE crosstalk, because the emission spectra of these two materials more equitably straddled the transmission spectra of the optical filters for the R and G smartphone image channels.

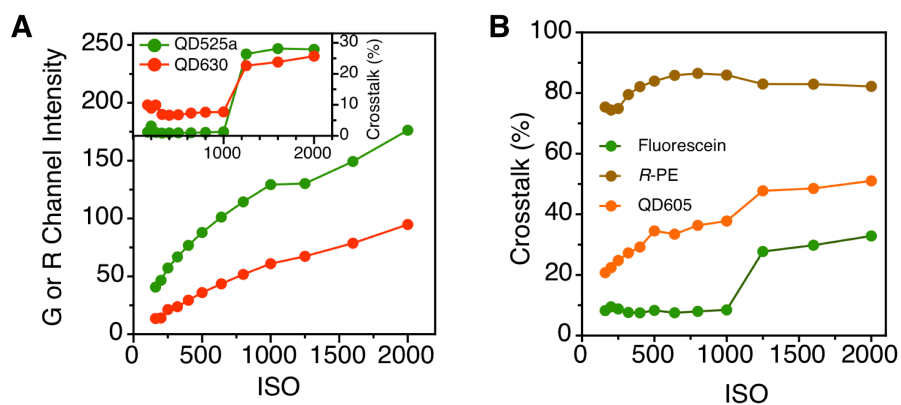


Figure 2.7 (A) Change in G (green circles) or R (red circles) channel intensity in smartphone images for samples of QD525a (G channel) and QD630 (R channel) as the ISO setting is changed. The inset shows the change in the crosstalk in the secondary image channel (as a percentage of the signal in the primary image channel) as the ISO setting is changed. **(B)** Crosstalk for fluorescein, R-PE, and QD605 as a function of ISO setting.

Figure 2.8 shows the effect of shutter speed on the measured G or R channel intensities for samples of QD525a, QD605, and QD630 at two different ISO settings. The channel intensities increase as the shutter speed decreases (equivalent to integration/exposure time increasing). A plateau was observed at longer exposure times with ISO2000, while a steady increase was measured with ISO1000.

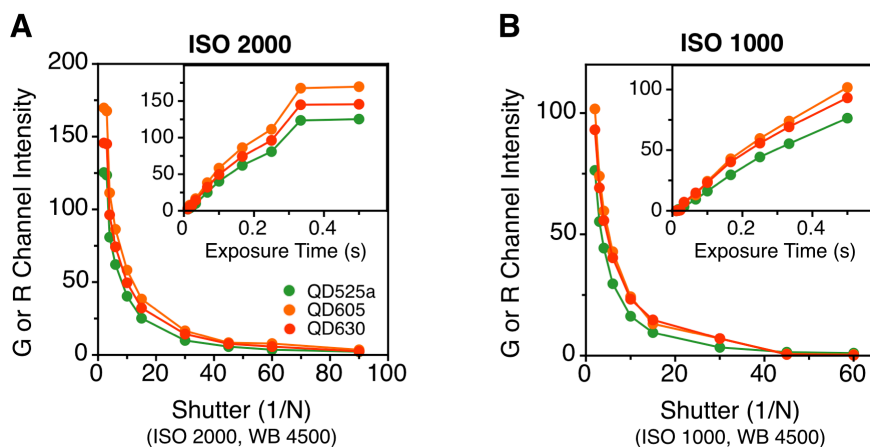


Figure 2.8 Change in G or R channel intensities in smartphone images for samples of QD525a, QD605, QD630 as the shutter speed is changed at (A) ISO 1000 and (B) ISO 2000. The main panel plots the channel intensities as a function of N , where $1/N$ is the shutter speed setting. The insets show the value of the exposure time ($1/N$) in units of seconds. QD525a were imaged in G channel and QD605 and QD630 were imaged in R channel in (A) and (B).

Figure 2.9 shows the effect of the white balance setting on the G or R channel intensities and crosstalk for samples of QD525a, QD630, and a mixture of these two QDs at three different ISO settings. The G channel intensity decreased as the ISO initially increased, but then leveled out to an approximately constant value at a white balance/colour temperature setting of 3000 K. In contrast, the R channel intensity gradually increased throughout the range of colour temperature settings. The QD630 crosstalk decreased and the QD525a crosstalk increased as the colour temperature increased. Interestingly, the crosstalk values converged to a common value of *ca.* 25–30% at settings of 5000 Kelvin and higher.

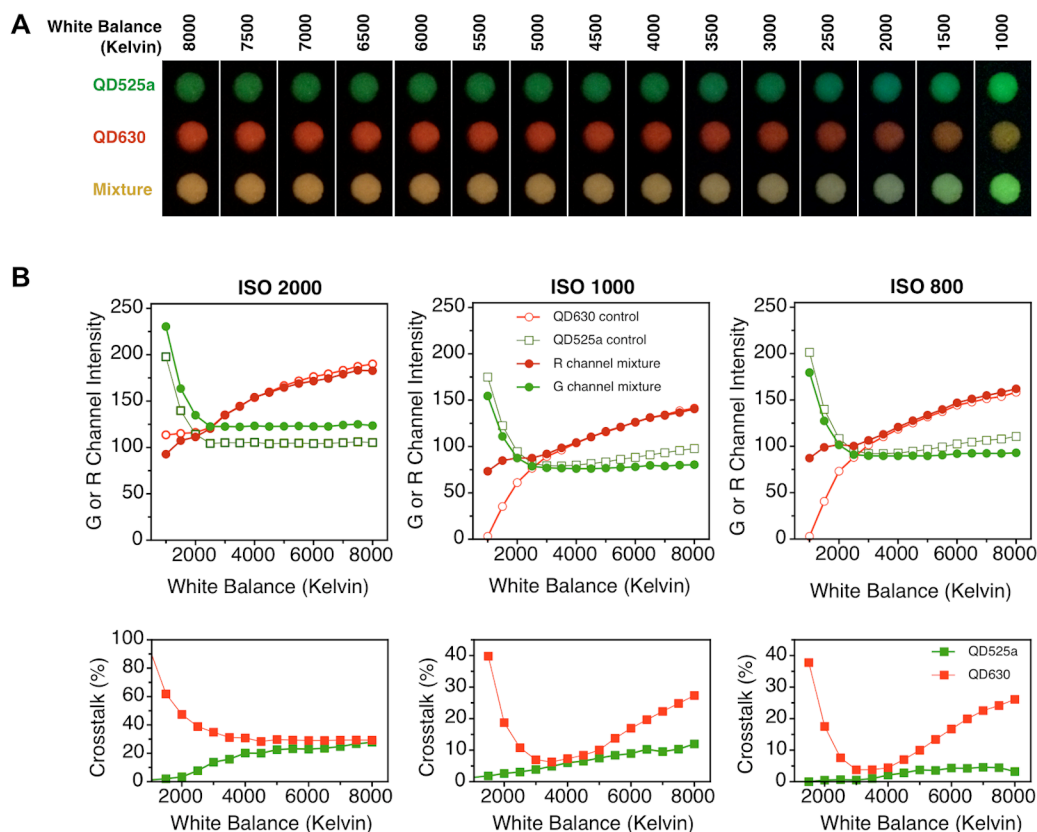


Figure 2.9 Effect of white balance/colour temperature (Kelvin) setting. **(A)** Images of solutions of QD525a, QD630, and a mixture of these two QDs (concentrations of each QD unchanged) at different white balance/colour temperature settings. **(B)** G or R channel intensities and crosstalk levels (secondary channel intensity as a percentage of the primary channel intensity) at ISO 2000, ISO 1000, and ISO 800.

Figure 2.10 shows the R/G intensity ratios obtained from smartphone images for a mixture of QD525a and QD630, and between the corresponding control samples. The R/G ratio increased as the colour temperature increased. For the ratio between control samples of QD525a and QD630 (imaged simultaneously in separate wells), the ISO setting had only a small effect on the measured R/G ratio, whereas for the mixture of QD525a and QD630, ratios measured at ISO 2000 diverged from those measured at ISO 800 as colour temperature setting decreased (less than 2500 Kelvin). Moreover, the mixtures generally yielded lower R/G ratios than the control samples, particularly at low colour temperatures (less than 3000 Kelvin) and high colour temperatures (more than 4500 Kelvin). The origin of these offsets is unclear and is presumed to be due to an inaccessible layer of image processing and/or the white balance algorithm itself. The

offsets are not consistent with inner filter effects or energy transfer. A colour temperature of 4500 Kelvin was chosen for all subsequent work, as well as two-colour QD imaging (see Section 2.2.6), which gave an R/G ratio that corresponded to the ratio between peak emission intensities of the QD525a and QD630 in spectrofluorimetric measurements. This setting also had a relatively small difference in the R/G ratio between the mixture and control samples.

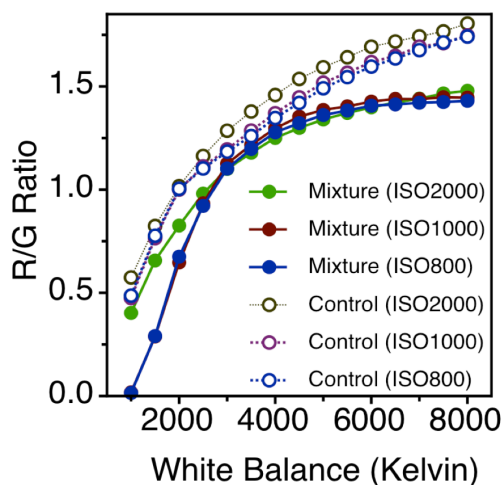


Figure 2.10 R/G channel intensity ratio as a function of white balance/colour temperature (Kelvin) setting at ISO 2000, ISO 1000, ISO 800.

2.2.6 Two-colour imaging

As noted above, the majority of the emission from the green-emitting (QD520, QD550, QD525a, QD540a) and red-emitting (QD630, QD650) QDs is detected in the G and R channel of smartphone images, respectively. Under the imaging settings optimized for sensitivity (ISO 2000), the R-PE had >80% crosstalk in the G channel (a 1:0.8 ratio between the R and G channels). In the case of fluorescein, the crosstalk in the R channel was ~30%. For comparison, the green- and red-emitting QDs had ~20% crosstalk in their secondary channel. A different ISO setting, ISO 800, was optimal for two-colour detection. Under this setting (with a shutter speed

of 1/4 s and a white balance of 4500 Kelvin), the green-emitting QD520 crosstalk decreased to <2% and the red-emitting QD630 crosstalk decreased to ~8%. Although the fluorescein crosstalk decreased to a respectable level of ~8% at these settings, the crosstalk was still more than four-fold higher than for QD520. The R-PE crosstalk remained >80%.

The green- and red-emitting QDs, by virtue of their lower crosstalk values and the ability to excite both colours simultaneously with blue light, were thus well suited to two-colour detection with smartphone excitation and imaging of PL. Figure 2.11A(i) shows G and R channel intensities measured when the QD630 concentration was constant (0.1 μM) and the QD520 concentration was varied. Control samples of only QD520 and QD630 at the same concentrations were imaged in parallel as control samples. Figure 2.11B shows analogous data for samples where the concentration of QD520 was kept constant (1.0 μM) and the concentration of QD630 was varied. In both experiments, the intensities in the primary channel of smartphone images for the QDs at fixed concentration were approximately constant, and the intensities for the QDs at variable concentration increased linearly, resulting in consistent change in R/G channels ratio shown in panels (ii) of Figure 2.11. Although small offsets between the channel intensities measured for the mixtures and control samples were consistently observed, the most important result was that the slopes of the trend lines were equal. This result indicated that two-colour assays are possible with green- and red-emitting QDs. The offsets are an artifact of the image processing of the smartphone, as they were not observed in PL emission spectra, resulting in a nearly horizontal translation between the spectrofluorimetric data point and the smartphone data point as seen in panels (iii) of Figure 2.11.

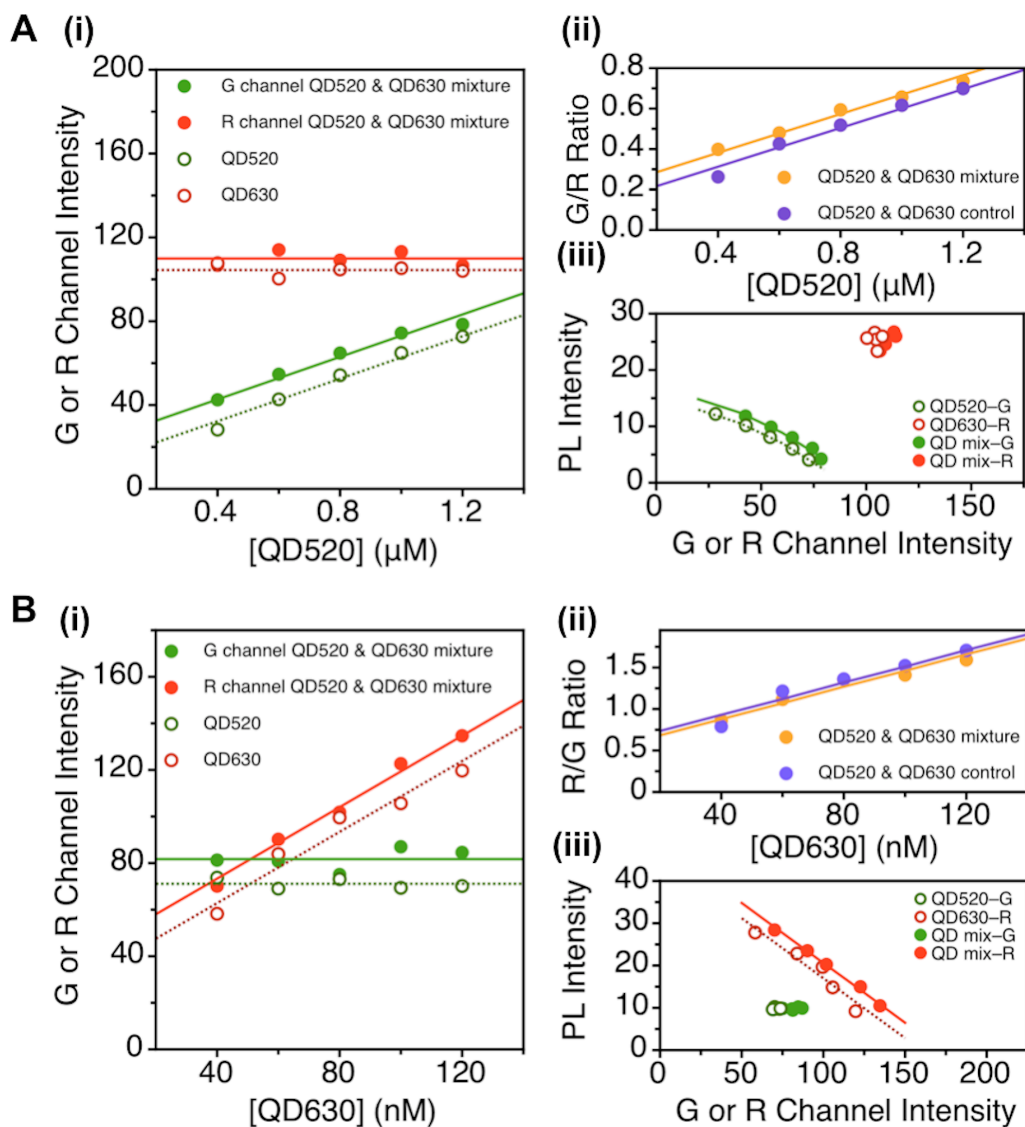


Figure 2.11 Changes in G or R channel intensity for mixtures of QD520 and QD630, where the concentration of only one QD varied and the concentration of the other was kept constant: **(A)** 0.1 μM QD630 with variable concentrations of QD520; and **(B)** 1.0 μM QD630 with variable concentrations of QD520. Control samples of only QD520 or only QD630 are shown for reference. The intensities are shown in panels (i), the corresponding G/R or R/G channels ratios are plotted in panels (ii), and the correlation between the spectrofluorimetric PL intensities for samples of QD520, QD630, and mixtures of QD520 and QD630 are shown in panels (iii).

2.2.7 Model binding assay

To further evaluate the bioanalytical potential for all-in-one smartphone PL imaging, a binding assay was carried out using avidin as a model analyte. Avidin was selected as a model analyte because its high-affinity binding, robustness, and well-characterized properties permitted evaluation of smartphone PL imaging capabilities while minimizing influence from assay chemistry. The green-emitting QDs (QD490a) were immobilized on paper substrates and functionalized with biotin-modified short His-tag appended peptides, Pep(biotin), as illustrated in Figure 2.12A. The peptide amino acid sequence is given in Table 2.2 (see Section 2.4.1, page 109) The details of immobilization chemistry are discussed in detail in Chapter 4. Solutions with different concentrations of avidin were spotted on the paper substrates, which were then washed with buffer, incubated with QD630-[Pep(biotin)]₄ conjugates, where QDs had emission maxima at 630 nm (*i.e.* QD630) and where assembled with four equivalents of His-tag peptide modified with biotin (*i.e.* [Pep(biotin)]₄). Then paper substrates modified with QD630 reporters were washed again with buffer prior to imaging. This procedure mirrors that of many sandwich binding assays. Red-emitting QD630 were selected as reporter QDs because of their high brightness and compatibility with two-colour measurements. The immobilized green-emitting QDs functioned as a reference PL signal, provided a convenient scaffold for immobilization of biotin on the paper substrates, and acted as barrier against the non-specific adsorption of proteins on the cellulose paper fibers. Initially, QD520 were used as the immobilized green-emitting QDs; however, the intense green emission from the large number of QDs immobilized, even with the low levels of crosstalk at ISO 800, made it challenging to detect low levels of red emission. Consequently, blue-green-emitting QD490a, which were much less bright in the G channel of smartphone images, were adopted as the immobilized QDs. Results of the model assay are shown in Figure 2.12B. Smartphone PL images show weak green PL from the immobilized QD490a with progressively more red PL from the QD630 reporters as the concentration of avidin increased. Visual detection of as little as 5–10 µg/mL of avidin was possible, and detection of 50–100 ng/mL was possible with quantitative image analysis.

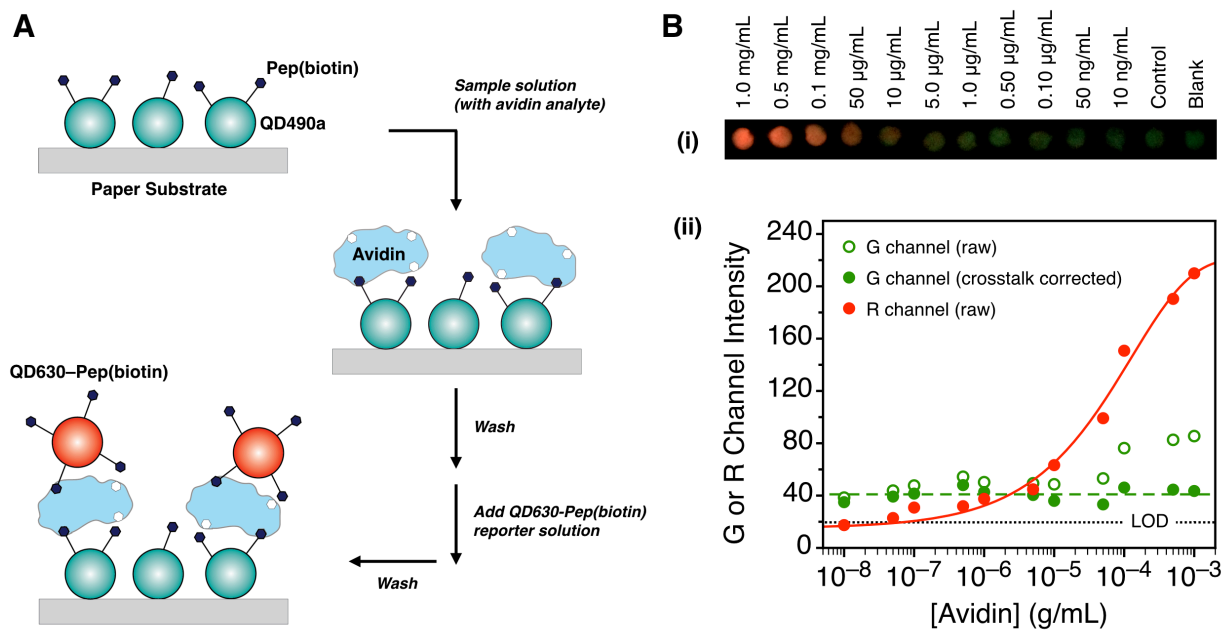


Figure 2.12 Model binding assay with avidin as a target analyte. **(A)** Schematic of the avidin-binding assay. **(B)** Smartphone PL images (i) and G or R channel intensities (ii) as a function of avidin concentration. The G channel intensity was corrected for crosstalk from the QD630 signal.

2.2.8 Model FRET-based thrombin assay

2.2.8.1 FRET pairs

The all-in-one smartphone PL imaging apparatus was also evaluated in a model homogeneous protease assay. In order to be able to image QD PL in buffer and a biological matrix (*i.e.* serum), QDs with emission in orange-red region were selected due to their brightness and minimal sample background over this region of the spectrum. Figure 2.13 shows the normalized absorption and PL emission spectra for two donor-acceptor pairs considered for detection of the proteolytic activity of thrombin: QD605-A647 and QD630-A680 FRET pairs. The Förster distances were 6.3 nm for QD605-A647 and 7.0 nm for QD630-A680.

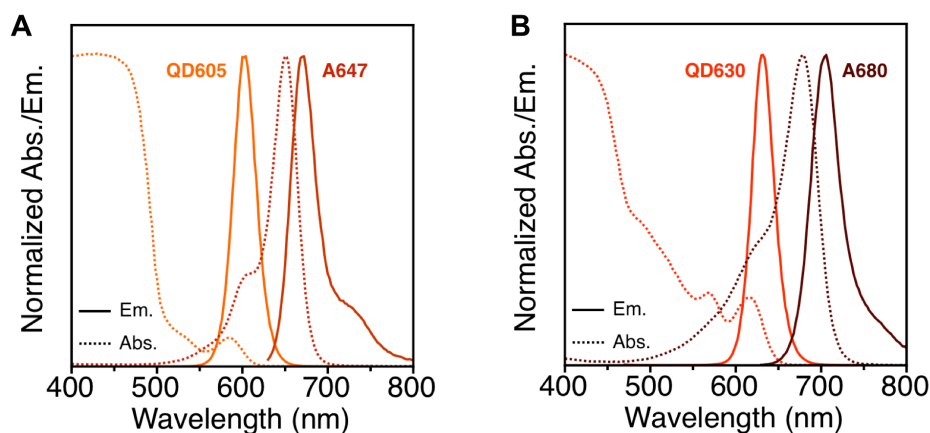


Figure 2.13 Normalized absorption (dotted lines) and emission spectra (solid lines) for: (A) QD605 and A647, and (B) QD630 and A680.

QD605 and QD630 donors were self-assembled with different numbers of equivalents of peptide containing recognition site for thrombin (*i.e.* Sub_{THR}) and labeled with Alexa Fluor 647 (A647) or Alexa Fluor 680 (A680) acceptor dyes, respectively. The amino acid peptide sequence for Sub_{THR} is given in Table 2.2 (see Section 2.4.1, page 109). The conjugates (100 nM, 60 μ L) were prepared in borate buffer and the PL emission spectra of aliquots (45 μ L) were measured in parallel with smartphone imaging (6 μ L aliquots). Measurements of PL emission spectra (Figure 2.14) showed that, for both FRET pairs, the QD PL was progressively quenched with the assembly of increasing amounts of dye-labeled peptide per QD. Smartphone R channel intensities also decreased with increasing peptides per QD, albeit at a slower rate than measured from PL emission spectra. This result was attributed to the response of the smartphone as a function of intensity, which was not strictly linear. For the QD630-A680 FRET pair, the FRET-sensitized A680 emission was largely undetected, and a smooth decrease in QD PL was observed in smartphone images with increasing A680 acceptors per QD. For the QD605-A647 FRET pair with increasing amounts of A647 per QD, it is hypothesized that smartphone detection of the FRET-sensitized A647 emission was at least partly the cause of the abrupt change in the trend of decreasing R channel intensity in smartphone images.

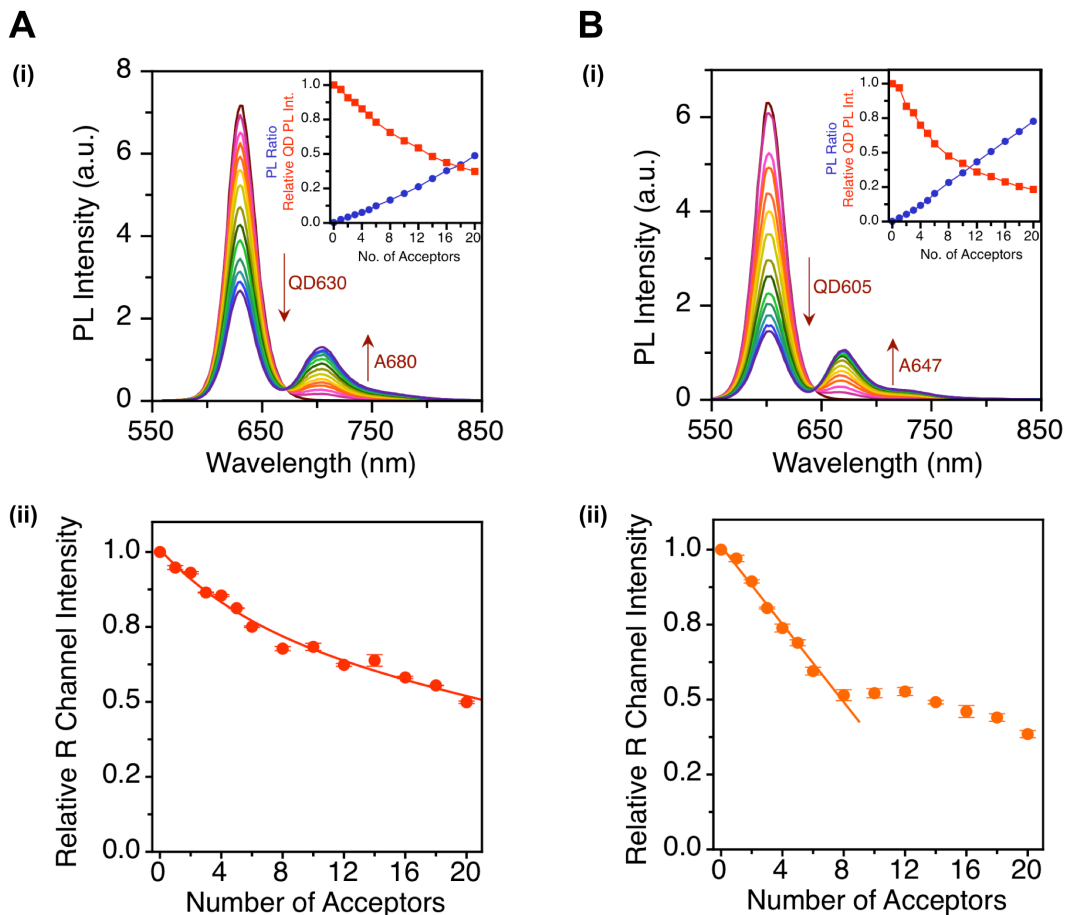


Figure 2.14 (A) FRET between QD630 and A680: (i) PL emission spectra for QD630- $[\text{Sub}_{\text{THR}}(\text{A680})]_N$ conjugates with increasing N , the average number of A680 acceptors per QD; (ii) corresponding R channel intensity from smartphone images of the same samples. **(B)** FRET between QD605 and A647: (i) PL emission spectra for QD605- $[\text{Sub}_{\text{THR}}(\text{A647})]_N$ conjugates with increasing N , the average number of A647 acceptors per QD; (ii) corresponding R channel intensity from smartphone images of the same samples. The insets in (i) show the PL ratios (blue) and relative change in QD PL intensity (red) with increasing N , the average number of acceptors per QD. The PL ratios in the insets of (i) are in terms of peak heights (not areas).

2.2.8.2 Thrombin assay

As a next step, a FRET-based assay for protease activity was tested with the smartphone imaging platform. QD630 were assembled with 16 equivalents of A680-labeled peptide substrates for thrombin, $\text{Sub}_{\text{THR}}(\text{A680})$, resulting in efficient quenching of QD PL. This FRET pair was

selected (as described in Section 2.2.8.1) because the smartphone camera appeared to be largely insensitive to FRET-sensitized A680 emission, whereas the camera appeared to have some sensitivity to A647 emission from the QD605-A647 FRET pair. The proteolytic activity of thrombin cleaved the assembled peptides, resulting in loss of FRET and recovery of QD PL, as illustrated in Figure 2.15A. The relative increase in QD PL intensity, measured by the smartphone after 15 min of incubation of the QD630-[Sub_{THR}(A680)]₁₆ conjugates with different concentrations of thrombin, is shown in Figure 2.15B. The inset shows the assay results with thrombin spiked in buffer, where the activity of < 1 nM thrombin was detected. The main panel shows assay results with thrombin in 50% v/v serum. The activity of < 0.1 μM of thrombin was detectable; however, it must be noted that serum contains inhibitors for thrombin. The most important result with serum was not the sensitivity to thrombin, but rather that optical detection was nearly unaffected by the biological sample matrix. In both buffer and serum, the relative QD PL intensity increased by about 80% at full response.

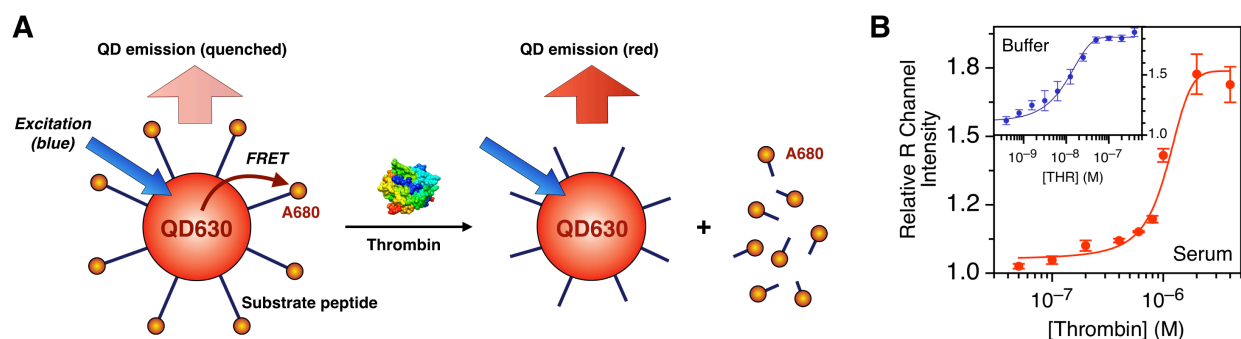


Figure 2.15 FRET-based assay for proteolytic activity. **(A)** Schematic of the QD630-[Sub_{THR}(A680)]₁₆ conjugate and its mechanism of sensing thrombin activity *via* FRET. **(B)** R image channel intensity measured for QD630-[Sub_{THR}(A680)]₁₆ conjugates after incubation for 15 min with different concentrations of human thrombin spiked into 50% v/v serum (main panel) and buffer (inset). The QD PL intensity recovers as a result of thrombin activity.

2.2.9 Tandem QD540a–A610 FRET conjugate

The potential of FRET from a green-emitting QD donor to enhance emission from a fluorescent dye toward which the smartphone excitation and imaging platform is otherwise insensitive was investigated. One such dye is Alexa Fluor 610 (A610), which has red fluorescence. Given its brightness in Figure 2.5, Q540a was selected as the green-emitting FRET donor for the A610 with a Förster distance of 5.1 nm. Figure 2.16A is a schematic of a QD540a-[Pep(A610)]₈ conjugate, and Figure 2.16B shows that the A610 had an absorption minimum at 450 nm ($\sim 3000 \text{ M}^{-1} \text{ cm}^{-1}$), the approximate excitation wavelength from the filtered smartphone flash, whereas the QD540a was strongly absorbing ($\sim 358\,000 \text{ M}^{-1} \text{ cm}^{-1}$).

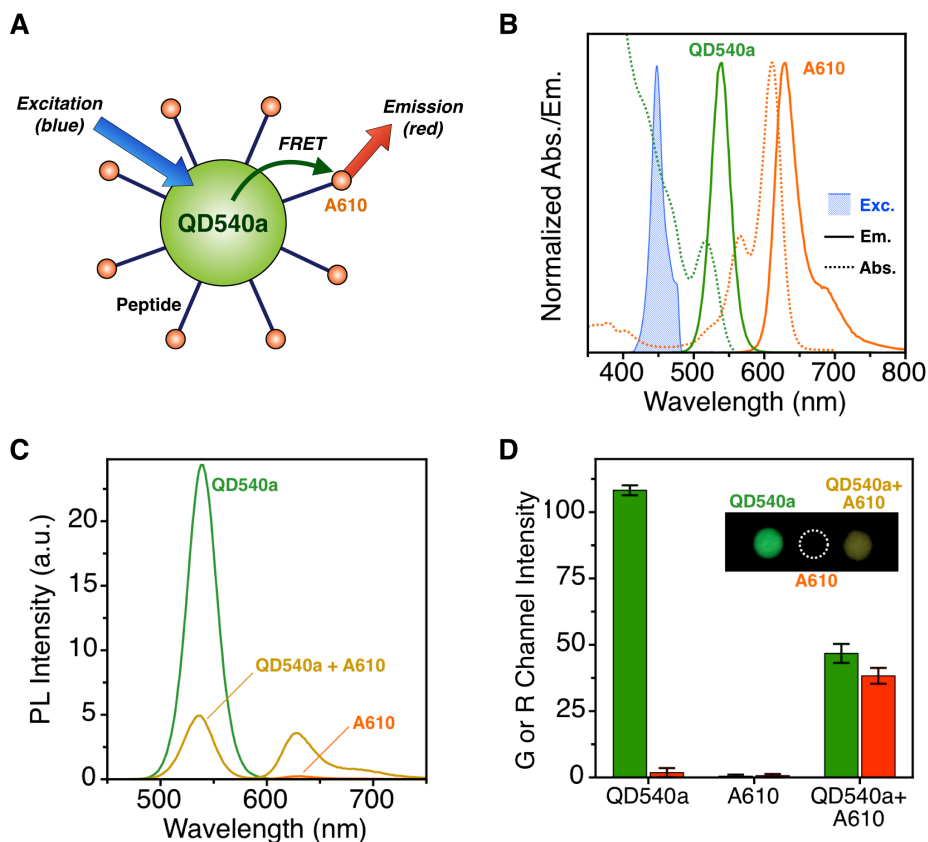


Figure 2.16 Enhancement of dye PL emission intensity through FRET-sensitization from a QD donor. (A) Schematic of the conjugate. (B) Overlay of the absorption spectra of the QD and A610 with the spectrum of the excitation light. (C) Emission spectrum of the QD540a-[Pep(A610)]₈. (D) Graph showing the increase in A610 emission intensity (R channel) with smartphone PL imaging after conjugation to the QD540a, versus control samples of only QD540a and A610 alone. The inset shows representative smartphone images of the tandem conjugates and control samples.

Figure 2.16C shows PL emission spectra for the QD540a-[Pep(A610)]₈ conjugate compared to equivalent amounts of only QD540a or Pep(A610). The FRET efficiency was ~80% with an A610/QD540a emission ratio of ~1.02 (measured from peak areas). As shown in Figure 2.16D, A610-labeled peptide alone was undetectable in smartphone imaging; however, when assembled with QD540a, a bright signal in the R channel was observed. Control samples of only QD540a confirmed that the R channel signal was not crosstalk from the QD540a PL. The overall enhancement of the A610 emission was ~16-fold when measured from PL emission spectra, but could not be determined from smartphone images because the signal from A610 alone was below background levels.

2.3 Discussion

2.3.1 Smartphone imaging platform

The main advantages of smartphone imaging are the portability of the smartphone and its already extensive and growing availability worldwide [1, 329]. These advantages have been widely recognized in the context of colorimetric assays, where the smartphone represents a truly standalone platform for acquisition, processing, logging and communication of data. In the case of fluorescence assays, the smartphone has frequently not been a standalone device because of the requirement of an external excitation light source, which is either separate from the smartphone [150, 158, 312, 313, 341, 346] or part of a sophisticated device that integrates with the smartphone [110, 340, 342, 344, 345, 347]. This chapter describes a simple 3D-printed accessory that allows the smartphone to be used as both an excitation source and an imaging camera. The accessory has a small footprint, is lightweight, and economically produced. It is potentially suitable for use in the laboratory, in the field, and in prospective POC settings. With recent advances in 3D-printing, a foldable box can likely be designed in the near future, further enhancing the portability of the system. When combined with QDs, the sensitivity of the smartphone platform with combined excitation and imaging of emission is viable for many prospective bioassays, and is also competitive with the use of external light sources such as a plug-in UV lamp. Importantly, the system is also suitable for imaging QD PL in serum, demonstrating its future potential for analyzing clinical samples.

The primary disadvantage of the smartphone imaging platform, which is to be expected, is that it is outperformed by laboratory fluorescence instrumentation. Three main limitations are the lesser sensitivity and dynamic range of the camera module as a detector, and the lower power of the flash module as an excitation source. The brightness of QDs was an important feature that helped compensate for these limitations. Significant improvements may be possible in subsequent designs, as ~ 2.3 mW of blue excitation light were produced at the flash module, but the efficiency of delivering that light to the sample was only $\sim 6\%$ (due to both the divergence of the light and reflector efficiency). In addition to delivering more light to the sample, the emission collection efficiency could be improved with a shorter distance between the sample and camera module. Despite the limitations of the current design, it was still possible to detect sub- $\mu\text{g}/\text{mL}$ levels of target protein, which is suitable for many (although not all) serum-borne protein biomarkers of clinical interest (see, for example, ref. [350]). FRET assays with QDs, such as the thrombin assay demonstrated here, will often be a good match for smartphone imaging assays because the initial signal level can be set by the chosen concentration of QDs and changes in PL generally only span 1–2 orders of magnitude [282]. A drawback of using blue light filtered from the flash module for excitation is that the blue (B) imaging channel of the smartphone camera is rendered unavailable. For comparison, use of an external long-wave UV lamp permits the use of red-, green-, and blue-emitting QDs matched to the RGB image channels as described in Chapter 3 of this thesis. The loss of the B imaging channel is, however, a minor inconvenience. Green and especially red PL is better suited for biological imaging and assays [351], and blue-emitting QDs tend to be much less bright than other colours.

A technical challenge for smartphone imaging is the optimization of these consumer devices for analytical usage. Many smartphone applications for image capture have layers of image processing intended for photography, which can potentially interfere with analytical PL measurements. It was found that this interference was especially prominent for two-colour imaging, where camera settings such as the ISO number and white balance were important for imaging measurements and somewhat non-intuitive. As noted in Section 2.2.6, the crosstalk levels exhibited a large step increase with increasing ISO number, and the white balance setting had a non-monotonic effect on the red-emitting QD crosstalk but a monotonic effect on green-emitting QD crosstalk. As a consequence of this image processing, the settings could be optimized for sensitivity (ISO 2000, adjustment of WB to favor the colour of QD PL) or for two-

colour measurements (ISO 800, intermediate WB), but not for both simultaneously. Fortunately, the white balance setting that best reproduced the spectral intensities of mixtures of red- and green-emitting QDs also offered favorably low crosstalk for two-colour measurements. The most intuitive parameter was the shutter speed, which reliably increased the measured intensity until a maximum was reached. Aside from optimizing the effects of these different settings, it was a challenge to find a smartphone app that provided control over these parameters along with control of the flash module. The ideal smartphone application for fluorescence imaging would not only provide these features, but would also provide access to the raw, unprocessed image. The latter is likely to be forthcoming in the future (if not already available on other smartphone operating systems) as raw image files are easily accessible with consumer digital cameras.

2.3.2 QDs are ideal for smartphone imaging

The results in this chapter have shown that QDs are exceptional in their suitability for smartphone fluorescence imaging, where their brightness compensates for the limited sensitivity of the smartphone system compared to laboratory instrumentation. QDs outperformed both fluorescein and R-PE, which were carefully chosen as materials for comparison. Fluorescein, a xanthene dye, is widely used as a bright, water-soluble label for fluorescence microscopy, flow cytometry, and FRET applications [175, 352, 353]. Although its excitation is optimal between 480–490 nm (nominally a 488 laser line), it is nonetheless efficiently excited at 450 nm, and it has one of the highest quantum yields available for a dye in aqueous solution (as high as ~0.9 at basic pH) [175]. R-PE, a water-soluble phycobiliprotein, is also used as a bright label for fluorescence microscopy, flow cytometry, and FRET [349, 353, 354]. Its advantages compared to most fluorescent dyes include a high quantum yield (~0.8), a more than 10-fold larger peak molar absorption coefficient ($1\ 960\ 000\ \text{M}^{-1}\ \text{cm}^{-1}$), and larger spectral separation between excitation and emission wavelengths (up to ~100 nm or more) [349]. In this context, R-PE is arguably similar to a QD, and is indeed competitive with QD520 and QD550 for smartphone imaging. However, the R-PE exhibits overall yellow-orange emission with a peak at ~580 nm but is less bright than the QD585 and much less bright than the orange-emitting QD605. Moreover, as shown in Figure 2.17, the R-PE predominantly exists as a hexamer (240 kDa) in aqueous solution, with the result being a larger physical size than the QDs. TEM images of QDs

are shown for comparison in Figure 2.18. R-PE is also more readily photobleached than QDs [355] and, as a protein, more susceptible to degradation.

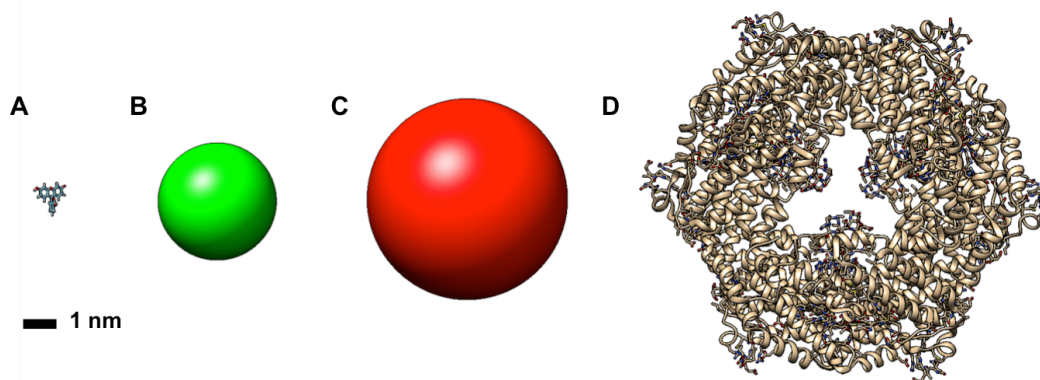


Figure 2.17 Sizes of (A) fluorescein, (B) 3.5 nm diameter QD; (C) 6 nm diameter QD, and (D) R-PE. The R-PE structure was generated from PDB entry 1EYX.

Arguably, the advantages of the fluorescein are its small size and lowest cost per mole, but at the expense of poor brightness in smartphone imaging, intrinsic sensitivity to pH, quenching upon bioconjugation, and susceptibility to photobleaching [175, 356, 357]. While the susceptibility to photobleaching can be partially mitigated through the use of superior fluorescein derivatives, such as Alexa Fluor 488 and Atto 488, the low brightness cannot be mitigated. Many other fluorescent dyes will fare worse in their brightness than fluorescein for two reasons: their quantum yields are lower, and their absorption bands will align less favorably with the blue excitation light from the smartphone flash. Given the small Stokes shifts of most fluorescent dyes (< 20 nm), only green emitters will be efficiently excited by the blue light, and the majority of orange- and red-emitting dyes (*e.g.* A610) will not be efficiently excited. A Stokes shift of ~50 nm is needed to match a dye absorption peak to the ~450 nm excitation wavelength in the smartphone system and have the majority of the dye emission band fall within the G channel of smartphone images. Although some long Stokes shift dyes meet this criterion (*e.g.* DyLight 510-LS, Chromeo 494), their brightness is still limited by their absorption coefficients and quantum yields. In addition to brightness, green dyes similar to fluorescein are also frequently limited by an emission tail that yields more crosstalk in the R channel than the emission from a green-

emitting QD, making fluorescein and other green fluorescent dyes less favorable for two-colour applications.

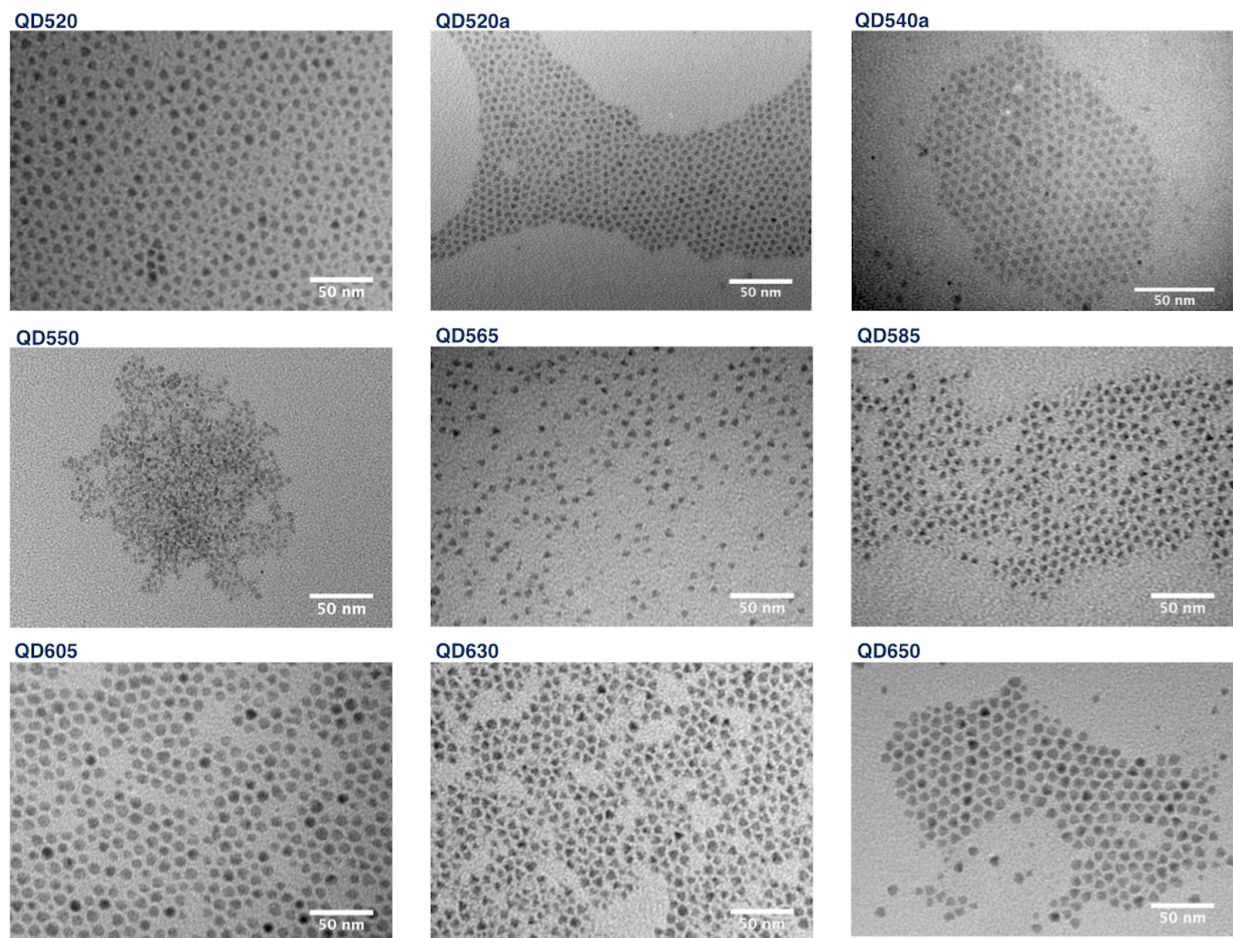


Figure 2.18 TEM images of CdSe/CdS/ZnS core/shell/shell and alloyed CdSeS/ZnS core/shell QDs.

As discussed above, the brightness of R-PE was more competitive with QDs than fluorescent dyes. Tandem R-PE/fluorescent dye conjugates are available commercially (*e.g.* R-PE/A610, R-PE/Cy7), where the R-PE acts as a light absorber and almost quantitatively transfers its excitation energy to conjugated dye molecules, resulting in predominantly dye emission. The

main application of these tandem conjugates is multicolour flow cytometry with a common excitation wavelength (typically a 488 nm laser line). As was shown in Section 6.2.8, a similar tandem conjugate concept can be applied with QDs for smartphone imaging. QD540a acted as an effective light absorber and FRET donor for A610, permitting detection of the sensitized dye emission when the equivalent amount of A610 by itself could not be detected. The excellent properties of QDs as FRET donors can thus enable effective smartphone imaging of fluorescent dyes, which will be advantageous when an environmentally sensitive dye is of interest for sensing applications with a smartphone readout platform. The enhancement of dye emission intensity is expected to be approximated by eqn. 2.1, where $I_{\text{dye, QD-FRET}}$ is the intensity of the dye emission from a QD conjugate, $I_{\text{dye, 0}}$ is the emission intensity of the dye alone, a is the number of dye acceptors per QD, and $\epsilon_X(\lambda_{\text{exc}})$ ($X = \text{QD}$ or dye) is a molar absorption coefficient at the excitation wavelength. The FRET efficiency, E , is determined according to eqn. 1.27. For the QD540a-A610 conjugate, an enhancement factor of ~ 12 would be expected from eqn. 2.1, which is close to the factor of ~ 16 measured from PL emission spectra.

$$\frac{I_{\text{dye, QD-FRET}}}{I_{\text{dye, 0}}} \approx \frac{\epsilon_{\text{QD}}(\lambda_{\text{exc}})E + a\epsilon_{\text{dye}}(\lambda_{\text{exc}})}{a\epsilon_{\text{dye}}(\lambda_{\text{exc}})} \quad (2.1)$$

Through comparison of the various QDs with fluorescein, A610 and R-PE, the key factors to be considered for smartphone excitation and imaging of PL were determined, and comparisons to other materials can therefore be extrapolated. The most important factor is brightness, which is the product of molar absorption coefficient and quantum yield. The absorption coefficients of the materials that were compared in this work varied by two orders of magnitude, whereas the quantum yields varied by less than a factor of two. As the brightness of the materials tested with smartphone excitation and imaging of PL varied by close to two orders of magnitude, it is clear that strong absorption of blue excitation light is critical. While many fluorescent dyes will be competitive in terms of quantum yield, the absorption coefficients of these materials will generally be too small to be competitive with QDs in terms of overall brightness. In addition to R-PE, two other common phycobiliproteins for fluorescence applications are B-phycoerythrin (B-PE) and allophycocyanin (APC), which have less favorable quantum yields, absorption spectra and absorption coefficients than R-PE, and thus will also be unable to match the brightness of QDs.

Many other materials are also expected to fall short of the bar set by QDs. For example, lanthanide complexes [358] and upconversion nanoparticles [359, 360] have spectrally narrow emission lines that would be promising for two-colour applications (*e.g.* Tb³⁺ and Eu³⁺ emission) if not for the requirement of UV and NIR excitation, respectively, which cannot be produced with the smartphone flash module. If sufficiently narrow emission spectra for two-colour applications are not a requirement and brightness is the main consideration, then several other nanoparticle materials are interesting to consider. Fluorescent metal nanoclusters [361, 362] have estimated molar absorption coefficients on the order of 10⁵ M⁻¹ cm⁻¹ and typical quantum yields of ≤ 10%, and are therefore unlikely to be as bright as QDs. Although carbon dots [363] have competitive quantum yields, their quantitative absorption properties remain nebulous and their excitation maxima are typically at wavelengths < 450 nm, suggesting that these materials will also be less favorable than QDs. The most promising alternatives to QDs are fluorescent dye-doped silica nanoparticles [121, 364] and semiconducting polymer dots (Pdots) [365, 366], which host a large number of chromophore units and can have very large molar absorption coefficients near 450 nm. Pdots have been reported to be brighter than QDs [366]; however, both Pdots and dye-doped silica nanoparticles can be an order of magnitude larger in size than QDs, where particle size may be a factor in assay design and performance. In general, the comparatively broad emission spectra (FWHM 50–100 nm) of both materials will also be less favorable for multicolour applications. QDs thus appear to have the best overall balance of properties for assays with smartphone excitation and imaging of PL.

2.4 Conclusion

This chapter introduced a simple, 3D-printed prototype accessory that enables all-in-one smartphone excitation and imaging of PL. The brightness, spectrally broad absorption and narrow emission of QDs make them optimal photoluminescent materials for bioanalysis with a smartphone and this accessory. A proof-of-concept protein binding assay and FRET-based activity assay were demonstrated, and the use of QDs as FRET donors can permit imaging of fluorescent dyes that would otherwise not be bright enough to detect using all-in-one smartphone PL excitation and imaging. This work provides a foundation for smartphone-based PL bioassays without external optoelectronic devices, helping to maximize simplicity and robustness while minimizing cost, which are important features for prospective POC diagnostic technologies.

2.5 Experimental Section

2.5.1 Materials and reagents

CdSe_{1-x}S_x/ZnS QDs were obtained from Cytodiagnostics (Burlington, ON, Canada) and CdSe/CdS/ZnS QDs were synthesized using established methods [245, 367]. These hydrophobic QDs were coated with hydrophilic glutathione ligands as described in Section 2.5.2. Alexa Fluor 488 C5 maleimide, Alexa Fluor 610-X NHS ester, Alexa Fluor 647 C2 maleimide, Alexa Fluor 680 C2 maleimide, and EZ-Link amine-PEG₃-biotin (biotinyl-3,6,9-trioxaundecanediamine) were from Thermo-Fisher Scientific (Carlsbad, CA, USA). Peptides were from Bio-Synthesis, Inc. (Lewisville, TX, USA) and the full sequences can be found in Table 2.2. The peptides are denoted by Pep(X), where X is a terminal label such as a fluorescent dye or biotin, and as Sub_{THR}(X), which is a substrate for thrombin. The peptides were labeled and purified using published protocols [368]. Each peptide had a hexahistidine segment to enable self-assembly to QDs [369, 370]. Human alpha-thrombin was from Haematologic Technologies (Essex Junction, VT, USA). Avidin, biotin, bovine serum (adult), bovine serum albumin (BSA), R-phycoerythrin (R-PE), and fluorescein were from Sigma-Aldrich (Oakville, ON, Canada). QDs were imaged in borate buffer (50 mM, pH 8.5) unless otherwise noted. Fluorescein was imaged in 0.1 M NaOH (aq) and R-PE was imaged in phosphate buffered saline (PBS; 10 mM, pH 7.4, 137 mM NaCl, 2.7 mM KCl, 0.1% w/v BSA). Absorption and emission spectra for the QD, R-PE, and fluorescent dyes were measured with an Infinite M1000 Pro multifunction plate reader (Tecan Ltd., Morrisville, NC, USA).

Table 2.2 Peptides sequences.

Abbreviation	Sequence (N-terminal to C-terminal)	Modification Site
Sub _{THR} (A647)	Ace-H ₆ SP ₆ GSDGNESGLVPRGSGC-A647	C-terminal Cys
Sub _{THR} (A680)	Ace-H ₆ SP ₆ GSDGNESGLVPRGSGC-A680	C-terminal Cys
Pep(A488)	Ace-H ₆ SP ₆ SGQGEGERNSGRGGSGNGC-A488	C-terminal Cys
Pep(biotin)	GSGP ₄ GSGH ₆ -Am	N-terminus
Pep(A610)	GGNGNGGNNGGP ₅ GGH ₆ -Am	N-terminus

Notes: Ace, acetylated; Am, amidated.

2.5.2 Preparation of GSH-coated QDs

GSH-QDs were prepared by mixing 1000 μL of 1-2 μM QDs in chloroform with a solution of GSH (100 mg) prepared in 300 μL of 25% TMAH in methanol. This mixture was vortexed and allowed to stand for 12 h. GSH-coated QDs were then extracted into 200 μL of borate buffer (pH 9.2, 50 mM, 250 mM NaCl), the organic layer discarded, and the QDs were washed by precipitation with ethanol and centrifugation (4800 rcf, 4 min). QDs were redispersed in 200 μL of buffer and washed twice more with ethanol. After the final wash, QDs were dissolved in borate buffer (pH 8.5, 50 mM) and stored at 4 $^{\circ}\text{C}$. QDs were quantified using UV-visible spectroscopy using molar absorption coefficient at first exciton, as listed in Table 2.3 [371, 372].

Table 2.3 First exciton wavelength and corresponding molar absorption coefficients for QDs.

QD sample	$\lambda_{\text{first exciton}}$, (nm)	$\epsilon(\lambda)$, ($\text{M}^{-1}\text{cm}^{-1}$)
QD520	494	53 500
QD525a	504	210 000
QD540a	518	210 000
QD550	526	71 642
QD565	548	97 556
QD585	568	133 580
QD605	582	232 268
QD630	616	492 411
QD650	638	870 000

2.5.3 3D-printed apparatus

The smartphone accessory was printed using a CubePro (3D Systems, Rock Hill, SC, USA) with acrylonitrile butadiene styrene (ABS) filament and painted black. A blue band-pass excitation filter (447 nm center wavelength; 60 nm bandwidth; OD 6; 12.5 mm dia.) and a long-pass

emission filter (500 nm cut-on; OD 4; 12.5 mm dia.) were from Edmund Optics (Barrington, NJ, USA). Filter transmission spectra were measured using a UV4 spectrophotometer (Pye Unicam). The spectral profile for the filtered and unfiltered excitation light from the smartphone flash module was measured using a Green-Wave portable USB fiber-optic spectrometer (Stellar Net, Inc., Tampa, FL, USA). Reflective Mylar plastic sheeting (Nielsen Enterprises, Kent, WA, USA) was used as a mirrored surface/reflector. The smartphone was an iPhone 5S (Apple, Cupertino, CA, USA) and the app used to acquire images was Camera+ (ver. 7.1.1, tap tap tap, USA). Unless otherwise noted, solutions to be imaged were spotted onto a glass slide modified with a black plastic mask with a 4×7 array of wells (3 mm well dia.) that held 6 μL . To determine the homogeneity of the excitation light, a solution of QD630 (15 nM) was added to a clear plastic container (larger than the useful imaging area) and imaged. All images were analyzed using ImageJ (National Institutes of Health, Bethesda, MD, USA).

2.5.4 Binding assays

Cellulose paper substrates were modified with *N*-(2-aminoethyl)-5-(1,2-dithiolan-3-yl)pentanamide, a lipoic acid derivative, as described in detail in Chapter 4 (Scheme 4.3, page 179). QD490a were immobilized by spotting a solution (1 μL , 0.25 mg/mL) in borate buffer (pH 9.2, 50 mM) onto 3 mm diameter punched paper substrates. Samples were incubated for 20 min in a humid chamber, then a solution of Pep(biotin) (2 μL , 100 μM) was spotted onto each paper substrate and incubated for 40 min. The modified paper substrates were washed three times in borate buffer (pH 8.5, 5 mM) and excess buffer drained. Avidin solutions (3 μL , 10 ng/mL–1.0 mg/mL) prepared in borate buffer (pH 8.5, 50 mM, 100 mM NaCl, 0.25 mg/mL BSA) were spotted on each paper substrate and incubated for 30 min in a humid chamber. Samples were washed once in borate buffer before a solution of QD630-[Pep(biotin)]₄ conjugates were spotted (1 μL , 1 μM) and incubated for 20 min. Paper substrates were washed once in borate buffer with 0.25 mg/mL BSA added, washed once in borate buffer without BSA, then placed on a glass slide for smartphone imaging.

2.5.5 FRET experiments

To prepare QD-peptide conjugates, QDs were mixed with *N* equivalents of dye-labeled peptide and let stand at room temperature for 60 min. The polyhistidine portion of the peptides is well

known to spontaneously assemble to the surface of QDs [369, 370]. Binding is nearly quantitative and no purification was required. For thrombin assays, stock solutions of QD630-[Sub_{THR}(A680)]₁₆ conjugates (1.0 μM, 20 μL) were prepared in borate buffer, diluted (200 μL), and an aliquot (10 μL) mixed with an equal volume of buffer or serum spiked with thrombin (the final concentration of conjugate was 50 nM). PL images of 6 μL samples were obtained after 15 min. For measurement of the FRET enhancement of A610 emission in tandem QD-A610 conjugates, QD540a-[Pep(A610)]₈ conjugates (0.2 μM, 60 μL) were prepared in borate buffer, as were control samples with an equal amount of Pep(A610) only, and 6 μL aliquots were imaged.

2.5.6 Data analysis

2.5.6.1 Quantum yields

Quantum yields were calculated relative to standard dyes according to eqn. 2.2, where $A(\lambda_{exc})$ is a measured absorbance at the excitation wavelength, $\int I(\lambda_{em})d\lambda$ is an integrated emission intensity across all emission wavelengths, η is the solvent refractive index, Φ is a quantum yield, and the subscripts x and std refer to an unknown and a reference standard, respectively. A series of concentrations was measured for each emitter and the slopes of plots of PL *versus* absorbance were used for calculations (see Appendix II for details). Standard dyes were fluorescein in 0.1 M NaOH ($\Phi = 0.79$) and rhodamine B in water ($\Phi = 0.31$) [348, 373].

$$\frac{\int I_x(\lambda_{em})d\lambda}{\int I_{std}(\lambda_{em})d\lambda} = \frac{A_x(\lambda_{exc})}{A_{std}(\lambda_{exc})} \left(\frac{\Phi_x}{\Phi_{std}} \right) \left(\frac{\eta_{std}^2}{\eta_x^2} \right) \quad (2.2)$$

2.5.6.2 FRET calculations

FRET efficiencies were calculated using eqn. 1.24 and the spectral overlap integral for a FRET pair was calculated according to eqn. 1.19. The corresponding Förster distance was calculated using eqn. 1.18, where the refractive index, n was assumed to be 1.34 and the orientation factor, κ^2 , was assumed to be 2/3.

Chapter 3 Multiplexed Homogeneous Assays of Proteolytic Activity Using a Smartphone and Quantum Dots

This chapter is an adaptation of published work, and is reproduced from Petryayeva, E.; Algar, W. R., Multiplexed Homogeneous Assays of Proteolytic Activity Using a Smartphone and Quantum Dots. *Analytical Chemistry* **2014**, *86*, 3195-3202, with permission from The American Chemical Society (Copyright 2014 American Chemical Society).

3.1 Introduction

Semiconductor quantum dots (QDs) are one of many promising nanomaterials for bioanalytical applications [6, 374, 375]. Their cumulatively unique properties include, but are not limited to, size- and composition-tunable photoluminescence (PL), broad absorption spectra with large molar absorption coefficients, and an inorganic interface that can be chemically derivatized and conjugated with biomolecules [6, 374]. QDs can therefore act as scaffolds for the assembly of bioprobes and biosensors, and have been widely utilized for multiplexed assays and multicolour imaging, where their spectrally narrow PL and the ability to excite many colours of QD at a common wavelength are highly advantageous [375]. Many of these applications utilize Förster resonance energy transfer (FRET) for the detection of biological targets such as nucleic acids [376], metal ions [286], drugs [377], nitric oxide [378], and antigens [379], as well as the activity of proteases [291], kinases [380], and nucleases [293]. The optical properties of QDs are ideal for FRET, permitting optimization of spectral overlap integrals and FRET efficiencies while minimizing crosstalk and background signals. Increases and decreases in FRET efficiency can be coupled to biorecognition events to generate “turn off” and “turn on” sensing depending on the design. Such configurations have been the topic of several detailed reviews [282, 381].

Despite the capabilities and growing popularity of QDs, there are still impediments to their broader utilization in laboratories that do not specialize in nanomaterials. That is, laboratories in which researchers want to use QDs in a “kit”-like fashion for bioanalyses, but the QD itself is not

a focus of the research. One impediment is the availability of biofunctional QD materials, which is being addressed through growing commercial availability, as well as refined synthetic, derivatization, and bioconjugation methods that are both simpler and greener [274, 382, 383]. Another impediment to the broader utilization of QDs is the availability of instrumentation that can fully access the advantages of QDs, such as in optical multiplexing. For example, many laboratories may not have convenient access to fluorimetric equipment that can operate with excitation at ultraviolet/blue wavelengths and offer spectral acquisition or suitable filter-based colour channels across the visible spectrum, particularly when real-time detection is desired. In such cases, there is no reason to switch from assay methods that are compatible with existing equipment, even if a multiplexed assay with QDs would be advantageous in principle. There is a clear need for analytical methods that can take full advantage of the optical properties of QDs, and which have a minimal barrier for adoption in laboratories that have little or no prior experience with QDs, or limited instrumentation available. Importantly, methods that can achieve this goal are also a critical step toward adapting QD-based bioanalyses for point-of-care (POC) diagnostics.

To address the above challenges, the spectrally narrow PL emission and strong, broad light absorption of QDs was combined with red-green-blue (RGB) digital colour imaging for quantitative, multiplexed homogeneous assays. A smartphone camera, which is ubiquitous in modern society, was used as the imaging platform, and multiplexed homogeneous assays of proteolytic activity were demonstrated as proof-of-concept. As shown in Figure 3.1, alloyed CdSeS/ZnS QDs with emission in the blue, green, and red region of the spectrum were each conjugated with a dye-labeled peptide substrate containing a recognition site that was hydrolyzed by one of three proteases (trypsin, chymotrypsin, or enterokinase). The dye labels were selected to be acceptors for the QDs, quenching their PL *via* FRET. In the absence of protease activity, the FRET acceptors remained in close proximity to their QDs, leading to efficient energy transfer. Proteolysis of the peptide substrates released the acceptor dyes from the QD and restored QD PL. Analogous FRET-based probes for sensing proteolytic activity have been reported previously [5, 291, 384, 385], but have required spectrofluorimeters, fluorescence plate readers, or fluorescence microscopes for readout. Most of these proteolytic assays have also been non-multiplexed. This chapter shows that quantitative, real-time detection of proteolytic activity was possible using a readout platform as simple and as accessible as a smartphone camera and a

handheld UV lamp (*i.e.* black light), where changes in QD PL were measured from RGB channel intensities in digital colour images. The smartphone readout was first validated by comparison to assays done with a fluorescence plate reader, then multiplexed smartphone assays were demonstrated, including a homogeneous three-plex assay of proteolytic activity with QDs. The results show that the unique optical properties of QDs can be combined with FRET and signal readout from smartphone camera images for multiplexed, quantitative bioanalyses that are feasible in almost any laboratory.

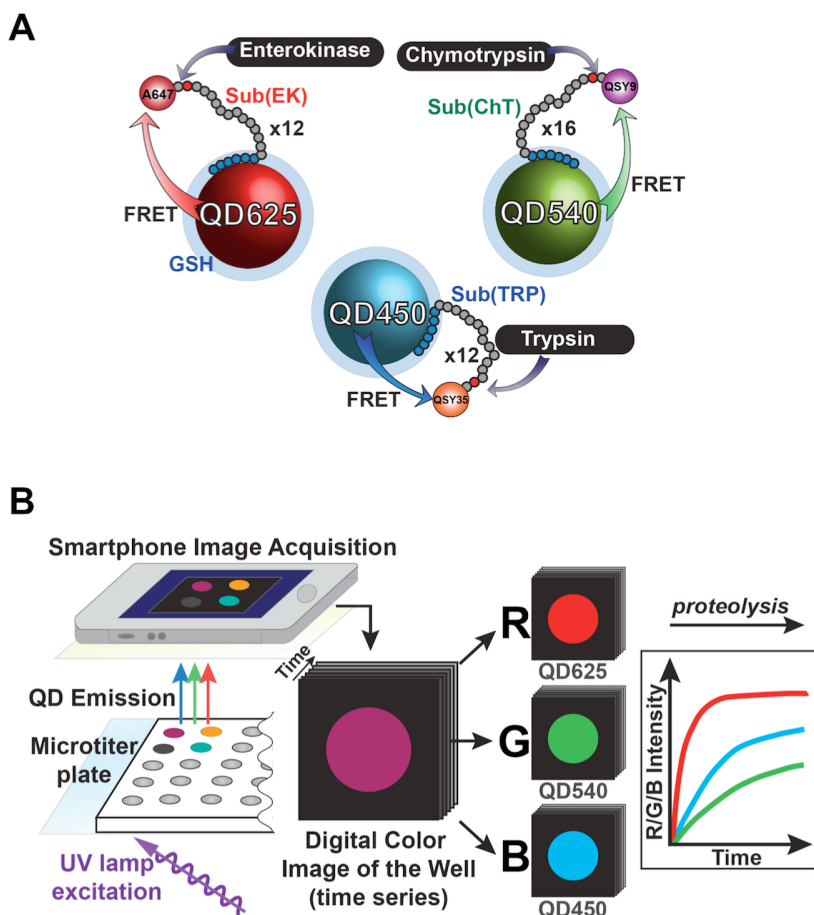


Figure 3.1 (A) Design of a homogeneous multiplexed assay to monitor protease activity *via* FRET with QD donors. Acceptor (QSY35, QSY9, or A647)-labeled peptide substrates containing a cleavage site for trypsin (TRP), chymotrypsin (ChT), or enterokinase (EK) were assembled on QDs with blue (QD450), green (QD540), and red (QD625) emission. The numbers in the abbreviations for the QDs indicate the approximate wavelength of their emission maximum. (B) Protease activity was measured through the recovery of QD PL and the resulting increase in the corresponding RGB channel intensity in digital colour images acquired with a smartphone and a handheld UV lamp for excitation.

3.2 Results

3.2.1 RGB colour imaging of quantum dots

Digital cameras produce colour images using a built-in Bayer mosaic or similar filter placed over CCD or CMOS detectors, where colour images are interpolated from 2×2 arrays of physical pixel elements with overlaid red, green, and blue (RGB) filters [386]. The wavelength ranges are estimated to be 360–510 nm, 500–600 nm, and 560–700 nm for the blue, green, and red channels, respectively. To test the suitability of the Bayer filter pattern for imaging multiple colours of QDs, samples of QDs with emission maxima within the transmission range of each RGB channel (QD625, QD525 or QD540, and QD450) were added to the clear-bottomed wells of a microtiter plate, obliquely trans-illuminated with a handheld UV lamp, and RGB colour images acquired using a smartphone camera. These are CdSeS/ZnS alloyed QDs; however, for simplicity the notation QDXa used in Chapter 2 to distinguish alloyed QDs from binary QDs will be dropped (*i.e.* QDX). The relative crosstalk between the RGB channels for QD450, QD540, and QD625 is summarized in Table 3.1, and the corresponding images are shown in Figure 3.2. Compared to the QD540, the QD525 had more than triple the crosstalk in the blue channel, making the QD540 the better choice as the green emitter.

Table 3.1 Properties of the QDs and FRET pairs used for RGB imaging.

Channel	QD PL (nm)	QY	BX	GX	RX	Acceptor	R_0 (nm)
Blue (B)	450	0.03	–	< 0.1%	< 1%	QSY35	3.5
Green (G)	540	0.16	9%	–	< 0.1%	QSY9	4.7
Red (R)	625	0.10	7%	6%	–	A647	5.3

QY = QD donor quantum yield; X = crosstalk; B = blue channel; G = green channel; R = red channel; R_0 = Förster distance.

The relationship between the colour channel intensity (measured with the smartphone camera) and the integrated QD PL intensity (measured with a fluorescence plate reader) is shown in Figure 3.3 for increasing concentrations of QD450, QD540, and QD625. The observed trends

were approximately linear over short intervals but exhibited some curvature as the upper limit of the RGB channel intensity was approached (R, G, B = 255). The red channel was the most sensitive and retained good linearity at low PL intensities. In contrast, the green and blue channels exhibited sharp decreases in sensitivity at low PL intensities. These observations defined the working range for assays.

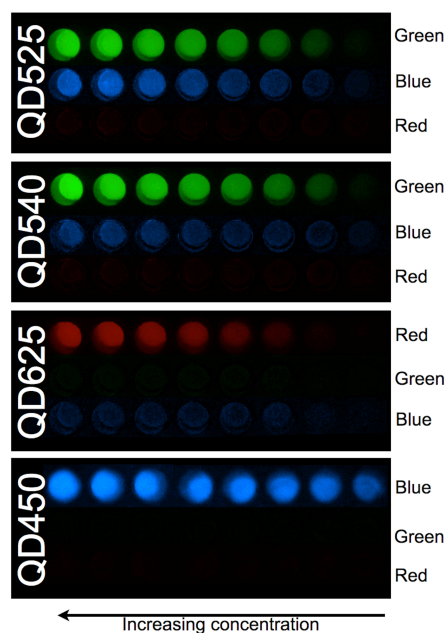


Figure 3.2 False coloured, RGB split digital images of QD samples of various concentrations. Each row in the figure is an RGB channel from a digital colour image of a single microtiter plate row.

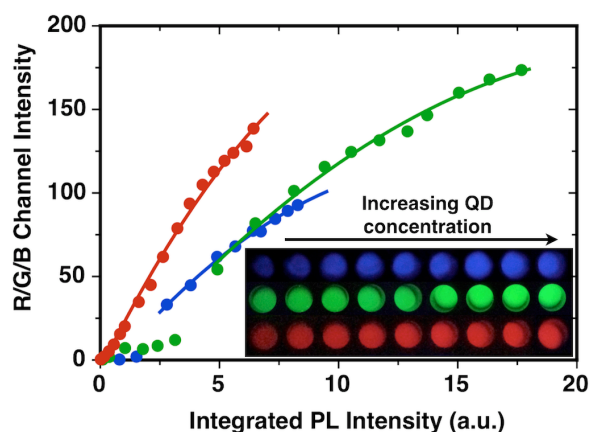


Figure 3.3 Colour images of various concentrations of QDs (inset) and the correlation between the measured RGB channel intensities and the integrated PL intensities for QD450 (blue), QD540 (green), and QD625 (red).

3.2.2 RGB colour imaging of mixtures of quantum dots

To assess QD mixtures, a range of samples with various concentrations of QD450, QD540, and QD625 were prepared. Concurrent analysis of PL spectra and RGB channel intensities for QD450, QD540, QD625, and their mixtures were well correlated, where increases in QD concentration resulted in increases in observed PL intensities, as shown in Figure 3.4. However, a direct comparison of the PL intensities between equal concentrations of a colour of QD in a mixtures *versus* alone indicated an overall decrease in the observed PL intensity and RGB channel intensity at higher concentrations, presumably due to the increased optical density of the samples and decreased excitation efficiency (*i.e.* inner filter effects).

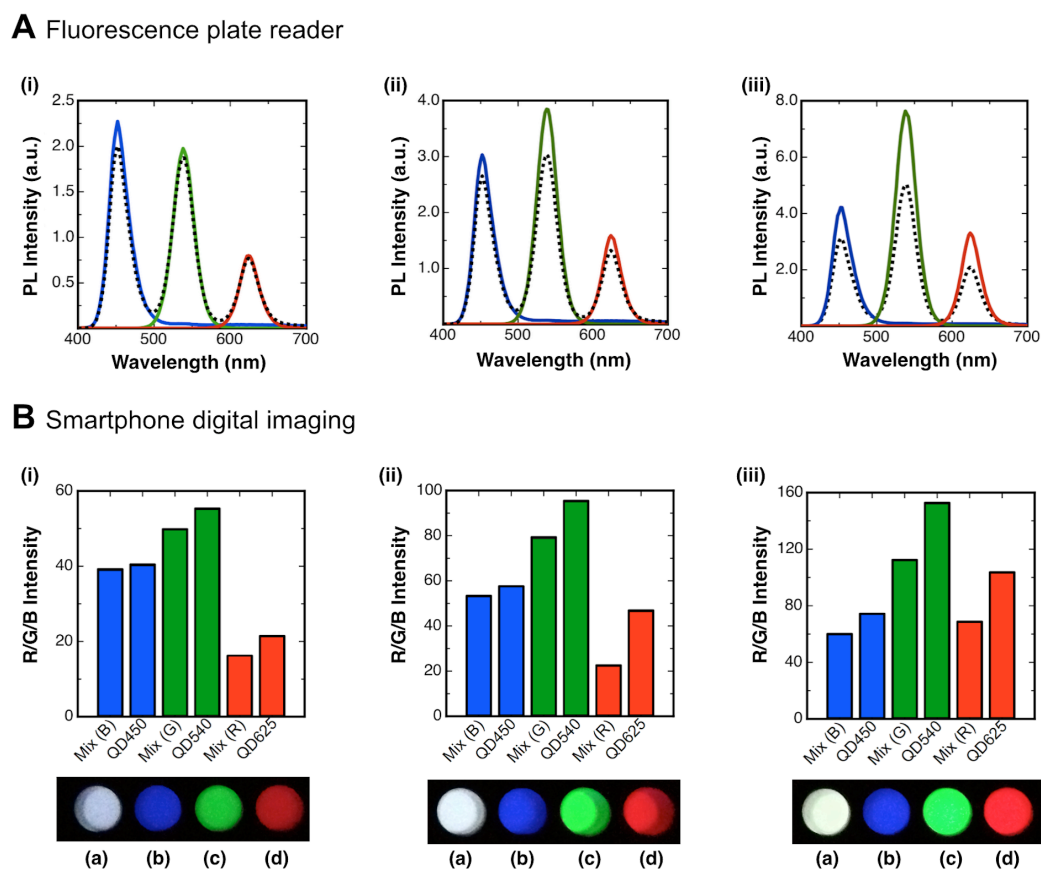


Figure 3.4 (A) QD PL spectra and (B) corresponding colour images for the (a) QD mixture, (b) QD450, (c) QD540, and (d) QD625. (i) QD450 (30 pmol), QD540 (5 pmol), and QD625 (5 pmol). (ii) QD450 (50 pmol), QD540 (10 pmol), and QD625 (10 pmol). (iii) QD450 (75 pmol), QD540 (20 pmol), and QD625 (20 pmol). RGB values shown in panel (B) were calculated by accounting for the crosstalk using eqns. 3.1-3.3 (Section 3.5.5.2, page 141). The dashed lines in panel (A) are spectra for mixtures, and the solid coloured lines are for the individual QDs.

3.2.3 FRET pairs and their fidelity

The three FRET pairs used in this work were QD450-QSY35, QD540-QSY9, and QD625-A647 (written as donor-acceptor). The absorption and emission spectra for each QD and each dye are shown in Figure 3.5. The dark quenchers, QSY35 and QSY9, were paired with QD450 and QD540 to maximize the multiplexing capacity of the homogeneous assay within the visible spectrum. Use of a fluorescent dye acceptor would have introduced broad FRET-sensitized dye emission, causing significant crosstalk in other colour channels (*e.g.* a fluorescent acceptor for the QD540 would have had emission in the red channel, which was used to measure QD625 PL). A647 was used as the acceptor for the QD625 because it provided a large Förster distance and because its FRET-sensitized emission was easily blocked with a short-pass filter. The Förster distances for the FRET pairs, the spectral overlap integrals and other pertinent photophysical parameters are given in Table 3.2.

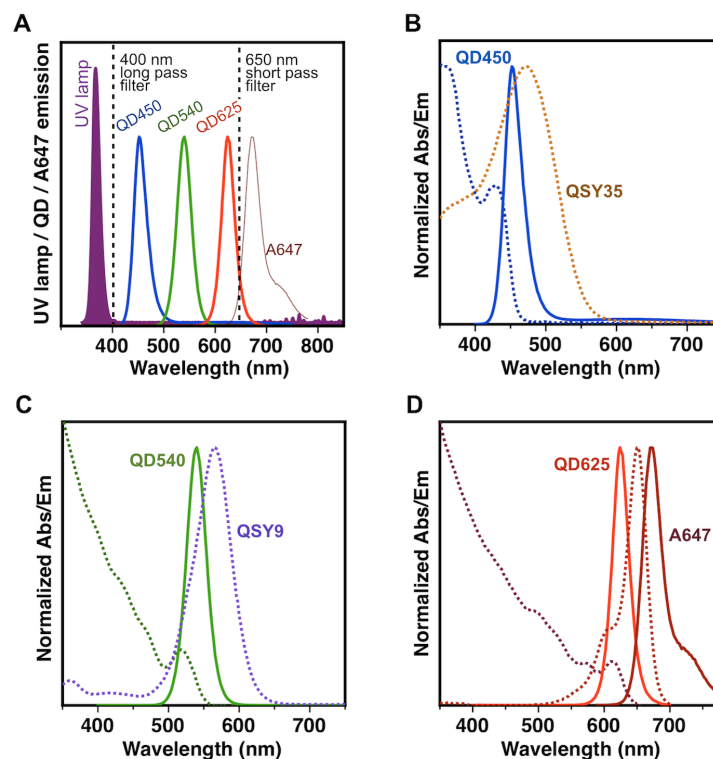


Figure 3.5 (A) Emission profile for the UV lamp excitation source; emission spectra of the QD450, QD520, QD625, and A647; and approximate cutoff wavelengths for the shortpass and longpass filters placed in front of the smartphone camera lens. Normalized absorption and emission spectra of (B) the QD450–QSY35 FRET pair, (C) the QD540–QSY9 FRET pair, and (D) the QD625–A647 FRET pair.

Table 3.2 Photophysical parameters of FRET pairs.

$\lambda_{\text{em, QD}}^a$ (nm)	Φ_D	Acceptor	$\lambda_{\text{Abs, A}}^b$ (nm)	$\epsilon_{\text{max, A}}^c$ ($\text{cm}^{-1} \text{M}^{-1}$)	J^d ($\text{mol}^{-1} \text{cm}^6$)	R_0 (nm)	r^e (nm)
450	0.03	QSY35	476	25 400	8.6×10^{-11}	3.5	5.1
540	0.16	QSY9	561	98 000	5.5×10^{-10}	4.7	5.1
625	0.10	A647	651	250 000	1.9×10^{-9}	5.3	4.5

^a Wavelength of maximum donor PL; ^b wavelength of maximum acceptor absorption; ^c molar absorption coefficient at absorption maximum of the acceptor; ^d spectral overlap integral; ^e experimentally calculated donor-acceptor separation distance.

One of the advantages of using QDs as FRET donors is that energy transfer efficiencies can be incrementally improved by the progressive assembly of more acceptor-labeled peptides per QD. Figure 3.6A shows changes in QD PL intensity, measured with a fluorescence plate reader, as a function of the number of acceptor-labeled peptides per QD. Figure 3.6B shows the same calibration curves but instead plots the RGB colour channel intensities measured from smartphone camera images. The QD PL and RGB channel intensities decreased as the number of acceptors increased. FRET efficiencies (see Figure 3.7) were calculated from QD PL quenching and reached 77% for QD450–QSY35 (20 peptides), 73% for QD540–QSY9 (20 peptides), and 74% for QD625–A647 (12 peptides).

To demonstrate multiplexed protease detection with QDs, three peptide substrates were designed for subsequent assays with trypsin (TRP), chymotrypsin (ChT), and enterokinase (EK). These peptides contain four modules along their sequence: (i) a hexahistidine tag for self-assembly with QDs ($K_d \approx 1 \text{ nM}$); (ii) a polyproline helix, a rigid component, used to extend peptide away from the surface of QDs; (iii) a protease recognition site (*i.e.* arginine for TRP, tyrosine for ChT, and four aspartic acids and lysine for EK); (iv) a terminal cysteine residue used for labeling with quencher (*i.e.* QSY35, QSY9) or A647 dye. The peptide sequences were chosen to minimize cross-reactivity with non-target protease and their full sequences are given in Table 3.5 (Section 3.5.3, page 139). Throughout this chapter, each peptide is denoted as a substrate for a specific protease (*i.e.* Sub_{TRP}), where the identity of protease is written as the subscript and the FRET acceptor used to label that peptide is indicated in brackets. For example, Sub_{TRP}(QSY35) is a substrate for trypsin and labeled with QSY35 dark quencher acceptor.

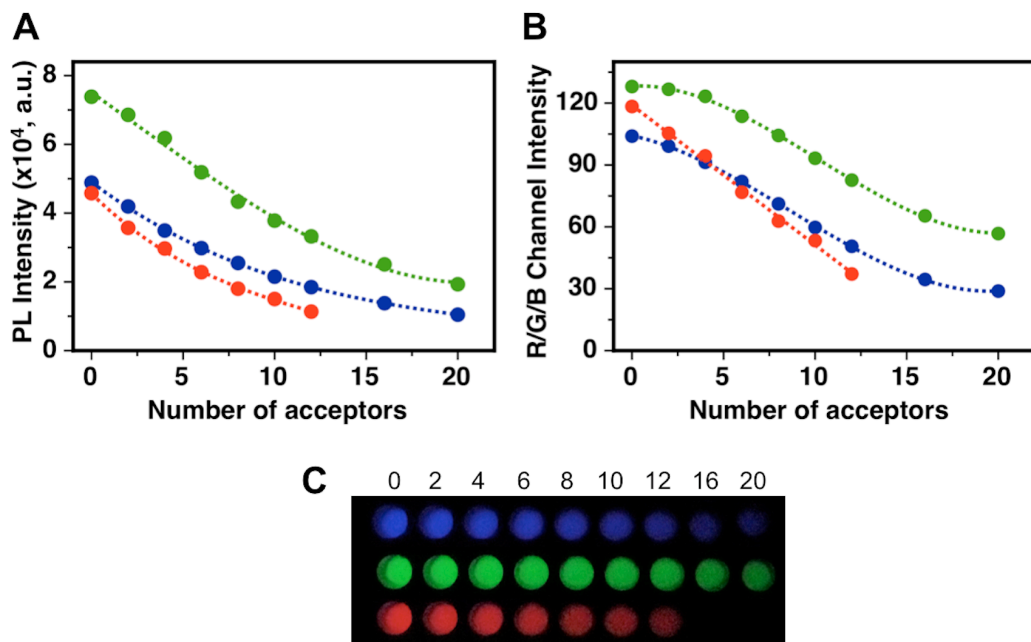


Figure 3.6 (A) Calibration curves showing the decrease in QD PL intensity as the number of acceptors per QD increases for QD450–[Sub_{TRP1}(QSY35)] (blue), QD540–[Sub_{ChT}(QSY9)] (green), and QD625–[Sub_{TRP2}(A647)] (red) conjugates. (B) Calibration curves for the same samples as in panel (A), showing decreases in RGB channel intensities as the number of acceptors per QD increases. (C) Photograph showing smartphone images of the samples in microtiter plate wells. The average number of acceptors per QD is shown at the top of the photograph.

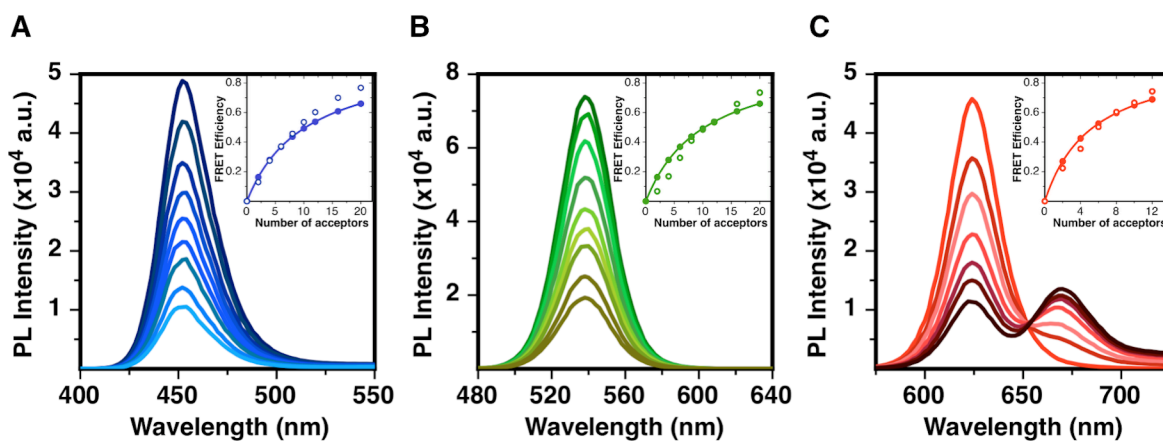


Figure 3.7 PL spectra for (A) QD450–[Sub_{TRP}(QSY35)] conjugates (blue channel), (B) QD540–[Sub_{ChT}(QSY9)] conjugates (green channel), and (C) QD625–[Sub_{EK}(A647)] conjugates (red channel). The insets show the corresponding FRET efficiency plots, raw data as open circles and Poisson corrected data as solid circles.

It should be noted that the final concentration of QD450 was 1.00 μM in all experiments (*cf.* 0.20 μM for QD540 and 0.30 μM for QD625) to achieve signal intensities in the blue channel that were comparable to those in the green and red channels of colour images. This concentration was necessitated by the lower quantum yield of the QD450 (see Table 3.2). Although it was possible to acquire smartphone images of QDs down to concentrations as low as 10–50 nM by adjusting the excitation intensity from the UV lamp (*i.e.* proximity to the microtiter plate), a minimum QD concentration of 0.20 μM was used to ensure complete assembly with the labeled peptides. The coordination of the hexahistidine-terminated peptides to QDs is an equilibrium process governed by $K_d \approx 10^{-9}$ M and the overall concentrations of peptide and QD [369, 370]. The fidelity of the unique QD-FRET-pair probes prepared for multiplexed assays depended on the off-rate (k_{off}) for the assembled peptides being slow relative to the duration of the assay. To confirm the stability of the prepared QD-peptide conjugates, RGB channel intensities were tracked over 1 h in the presence and absence of other QDs. Less than 4% increases in RGB channel intensities (see Table 3.3) were observed for QD donors in mixtures with unconjugated QDs (*cf.* >150% change during proteolysis), suggesting that there was minimal dissociation of peptides from QDs.

Table 3.3 Relative changes in RGB channel intensity after 1 h.

Sample ^a	ΔB^b	ΔG^b	ΔR^b
QD625–A647	N/A	N/A	–13
QD450 + QD540	–0.2	–3.1	N/A
(QD625–A647) + QD450 + QD540	–2.3	–3.8	–13
QD540–QSY9	N/A	0.3	N/A
QD450 + QD625	1.4	N/A	–11
(QD540–QSY9) + QD450 + QD625	–3.9	2.3	–18
QD450–QSY35	–1.5	N/A	N/A
QD540 + QD625	N/A	–0.8	–10
(QD450–QSY35) + QD540 + QD625	–0.4	–22	–35
QD450	2.0		
QD540		–3	
QD625			–12

^a QD625–A647 conjugates were prepared at a ratio 1:8; QD540–QSY9 and QD450–QSY35 conjugates were prepared at a ratio 1:10. ^b Change in the signal of the corresponding colour channel: B = blue, G = green, and R = red. N/A = not applicable.

The fidelity of the initial peptide assembly was further confirmed by tracking mobility shifts between QDs and QD-peptide conjugates on an agarose gel using gel electrophoresis, where a QD-peptide conjugate in a mixture retained an electrophoretic mobility that was lower than the non-conjugated QDs and consistent with that measured for the conjugate alone (see Figure 3.8).

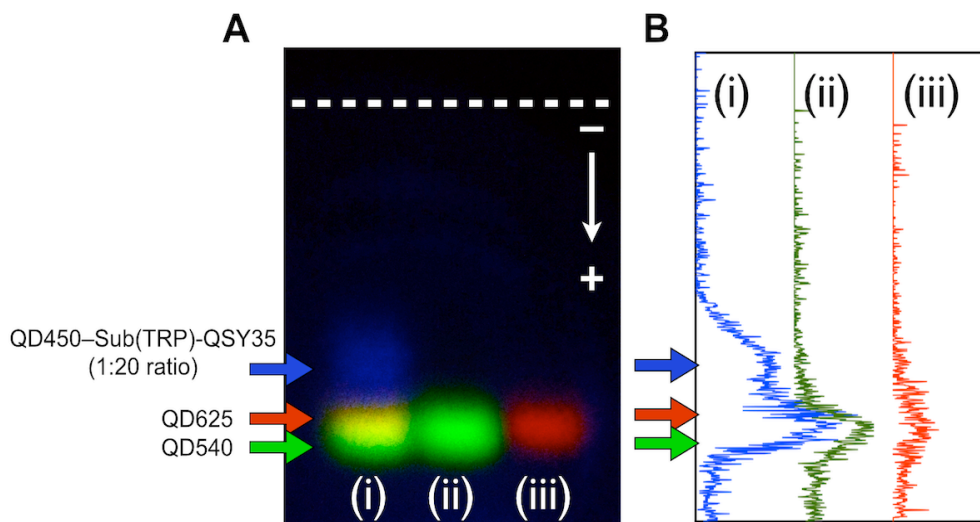


Figure 3.8 (A) Agarose gel electrophoresis (0.8%, 1×TBE, 100 V, 30 min) of QD450–[Sub_{TRP1}(QSY35)]₂₀, QD540, and QD625. The arrows at the left indicate the corresponding bands in the mixture (i). Reference samples of QD540 and QD625 were run in parallel, (ii) and (iii), respectively. The colour image was acquired with a smartphone camera with UV lamp excitation. Note the yellow colour from the overlap between the QD540 and QD625 in lane (i). A faint blue band can be observed above the QD540/QD625 band. **(B)** Intensity line profiles in the blue channel of gel image shown in panel (A). The QD540 and QD625 have some crosstalk in the blue channel of the image, but there is distinct band for the QD450.

3.2.3.1 Calibration curves

Given the difference in the response between smartphone imaging and spectrofluorimeter measurements, as was shown in Figure 3.6, it was important to measure calibration curves suitable for analysis of proteolytic rates. For quantitative analysis of proteolysis kinetics, the relative QD PL signals were converted into the number of substrate peptides per QD at each time point in an assay by comparison to calibration curves (see Figure 3.6B). These calibration curves needed to account for the non-specific adsorption of digested peptide on the QDs, and therefore, mixed digest/substrate calibration curves were prepared as described previously [387, 388].

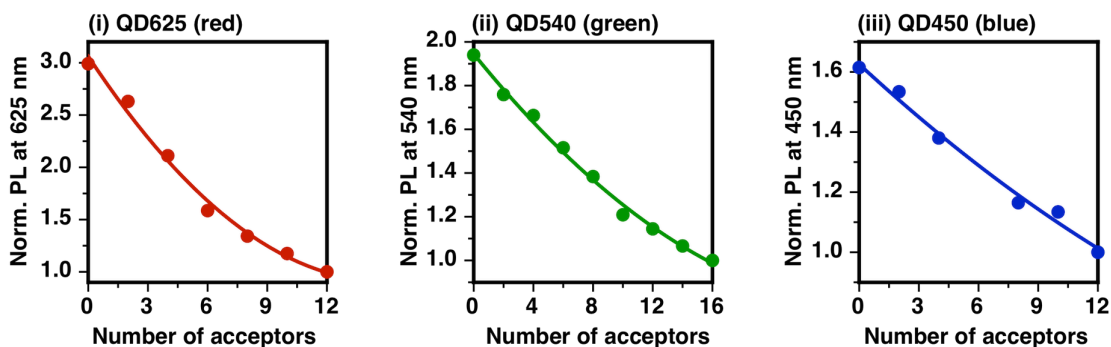
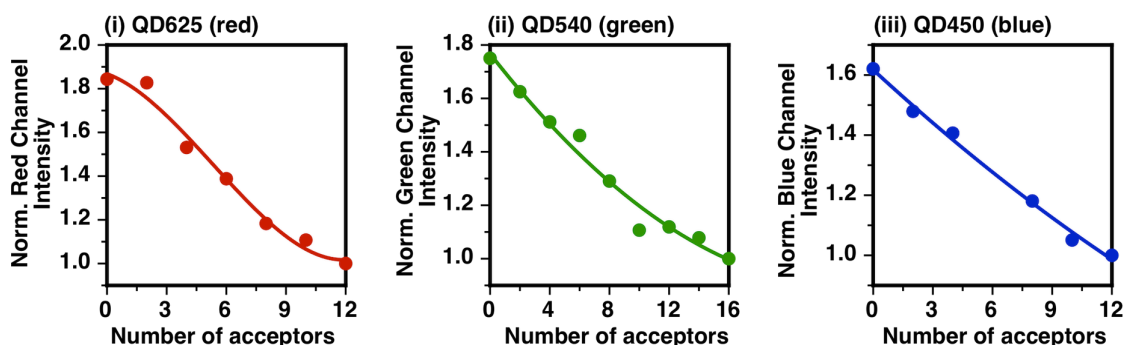
A Fluorescence plate reader**B** Smartphone digital imaging

Figure 3.9 Mixed digest/substrate calibration curves used for the analysis of progress curves in one-plex assays with **(A)** a fluorescence plate reader and **(B)** smartphone RGB imaging. The x-axis refers to the number of native peptide substrates per QD (with $N-x$ pre-digested peptide, where $N = 12$ or 16): (i) QD625–[Sub_{TRP2}(A647)]₁₂ conjugates, (ii) QD540–[Sub_{ChT}QSY9]₁₆ conjugates, (iii) QD450–[Sub_{TRP1}(QSY35)]₁₂ conjugates. The data points were fit with the simplest possible polynomial function (linear, quadratic, or cubic).

Importantly, this calibration was also able to account for other mechanisms of QD PL quenching. Three mechanisms were identified through which dye-labeled peptides quenched QD PL: (1) energy transfer from the QD to acceptor-labeled peptide assembled through its terminal hexahistidine tag (important with native substrate); (2) energy transfer from the QD to acceptor-labeled peptide that was non-specifically adsorbed (important with protease-digested substrate); and (3) changes in the quantum yield of the QD as a result of binding of the hexahistidine tag to its surface (important with both native and digested substrate). Point (3) is not common to all QDs, but was found to be important for these commercial QDs. Figure 3.10 shows the relative

decrease in QD625 PL intensity upon the assembly of 4, 8, or 12 peptides per QD. Peptides with different amino acid sequences and modified with Alexa Fluor 488 (A488), Alexa Fluor 555 (A555), or a capped cysteine residue were used for these experiments. Neither A488 nor A555 is a FRET acceptor for the QD625. As a general trend, the magnitude of QD PL quenching, as a result of point (3), increased with increasing number of peptides, whereas the extent of this quenching depended on the peptide.

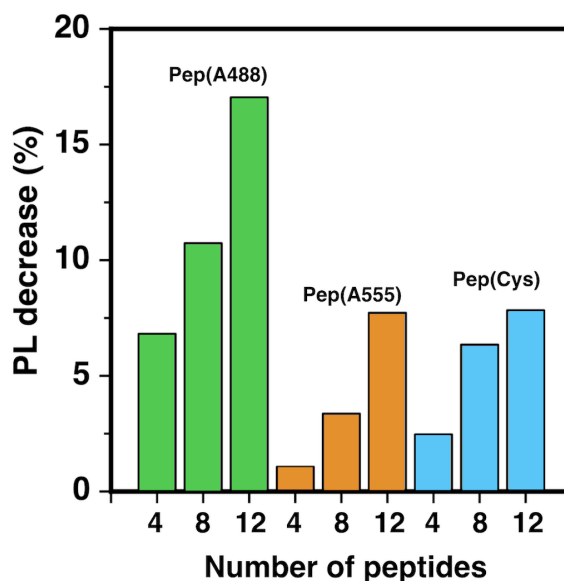


Figure 3.10 Relative decreases in QD625 PL intensity upon assembly of 4, 8, and 12 equivalents of peptide with various modifications of the C-terminal residue (A488 = Alexa Fluor 488, A555 = Alexa Fluor 555, Cys = cysteine). Note that neither A488 nor A555 is a FRET acceptor for QD625.

3.2.4 Validation of proteolytic assays with digital colour imaging

3.2.4.1 Temporal stability of UV lamp and smartphone camera

In order to conduct time-based kinetic measurements with a smartphone, the temporal stability of the excitation source and the consistency of smartphone images had to be evaluated. The UV lamp output was measured over 1 h using a portable USB spectrometer. The time trace of the intensity measured at 367 nm is shown in Figure 3.11. There is an initial decrease of *ca.* 20% in the intensity of the UV lamp output that stabilizes after 30 min. Therefore, to account for variation in UV lamp output, a control sample must be measured in parallel.

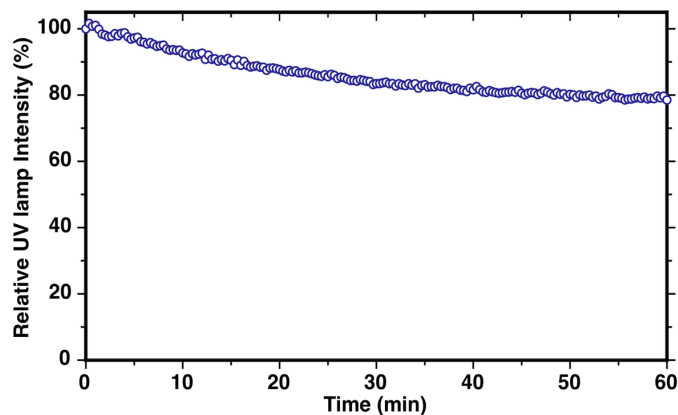


Figure 3.11 Time trace of the relative output from UV lamp at 367 nm over 60 min.

The potential for temporal variation in RGB channel intensities from a time series of smartphone images was investigated using LEDs with blue and green emission (470 nm and 530 nm peak wavelength; Visual Communications Company, CA, USA). The LEDs were powered using data acquisition module (DAQ USB-6008, National Instruments, Austin, TX, USA). Following a 6 h warm-up period with operation at the manufacturer-specified voltage, LED emission spectra were collected every 20 s using a fiber-optic spectrometer (Greenwave16 VIS-50, StellarNet, Tampa, FL, USA) and a custom data acquisition program written in LabVIEW (National Instruments).

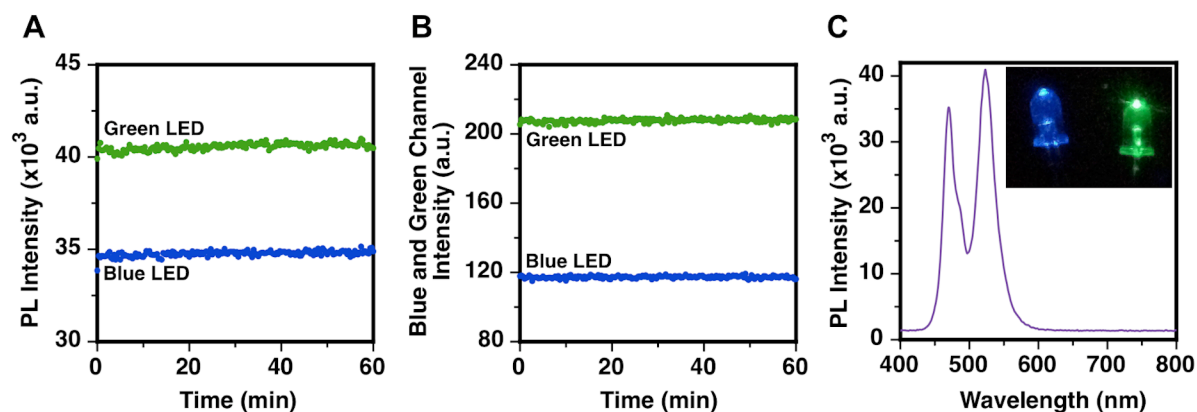


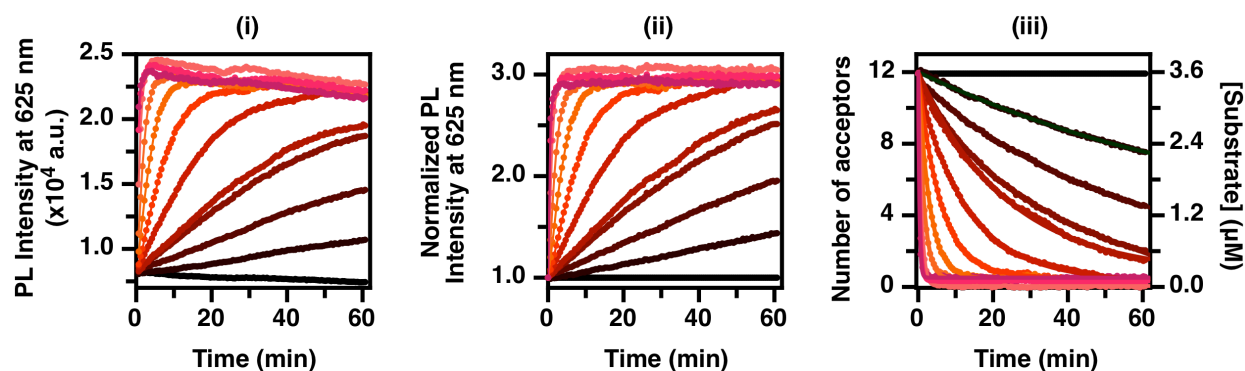
Figure 3.12 Time traces for blue and green LED output measured with (A) a spectrometer and (B) a smartphone digital camera. (C) The blue and green LED emission spectrum and the corresponding colour image of the LEDs.

The maximum emission intensity output by LEDs was measured at 468 nm for the blue LED and 523 nm for the green LED. The time traces are shown in Figure 3.12A, where the relative variation was *ca.* $\pm 0.45\%$ for both LEDs. In parallel, colour images were acquired with the iPhone using iLapse software and were split into RGB channels using Image J. Emission intensities from the blue and green LEDs were measured from the blue channel and green channel of the RGB images, respectively. These time courses are shown in Figure 3.12B. The saturated pixels observed at the tip of the LEDs (inset, Figure 3.12C) were omitted from the calculations. The relative variation associated with the RGB images was $< 0.6\%$, indicating that the precision of the RGB image analysis was comparable to that of a research grade spectrometer.

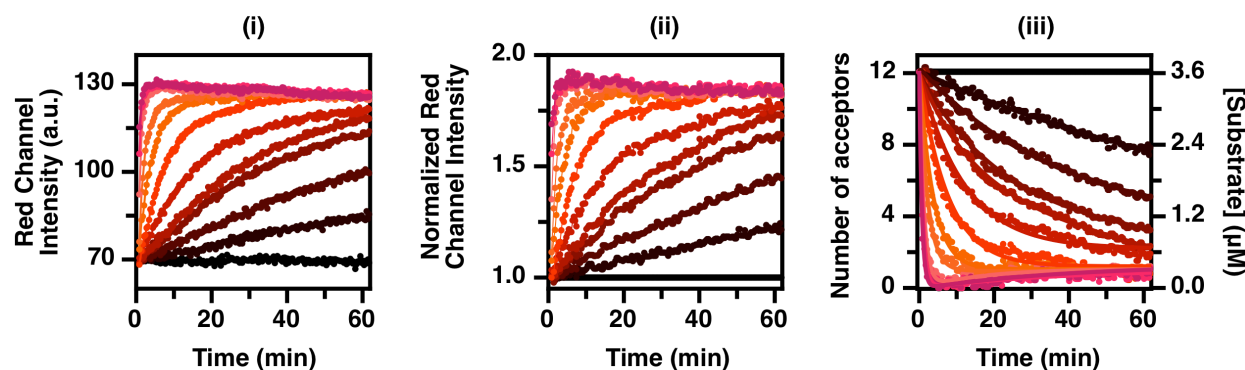
3.2.4.2 Red, green, and blue channel proteolytic assays

The ability to track protease activity using RGB digital images was first tested in a one-colour format. QD450-[Sub_{TRP1}(QSY35)]₁₂, QD540-[Sub_{ChT}(QSY9)]₁₆, and QD625-[Sub_{TRP2}(A647)]₁₂ conjugates were exposed to various concentrations of either TRP or ChT, as shown in Figures 3.13-3.15. In each case, the number of peptides per QD was chosen so that there would be an approximately linear increase in the corresponding RGB channel intensity as the number of acceptors per QD decreased with proteolysis (see Figure 3.6B). Samples dispensed into the wells of a microtiter plate were illuminated with a UV lamp and digital colour images were acquired with a smartphone. A blank sample (*i.e.* no enzyme) was measured in parallel and used as a reference to account for drift in the UV lamp intensity, as shown in Figure 3.11, and potential photobrightening or photobleaching of the QDs [212]. Figure 3.13 shows representative data for the activity of TRP with QD625-[Sub_{TRP2}(A647)]₁₂ conjugates, where changes in QD625 PL were monitored in the red channel of digital images. Increases in protease concentration increased the rate of peptide digestion, resulting in faster increases in the red channel intensity. For data analysis, the measured red channel intensities of the acquired images were normalized to unity at the initial time point, thereby accounting for small variations in excitation intensity between different wells of the microtiter plate and between different experiments. The validity of the smartphone imaging readout was confirmed by measuring proteolytic activity in replicate samples with a fluorescence plate reader in parallel.

(A) Fluorescence plate reader data



(B) Smartphone RGB imaging data



(C)

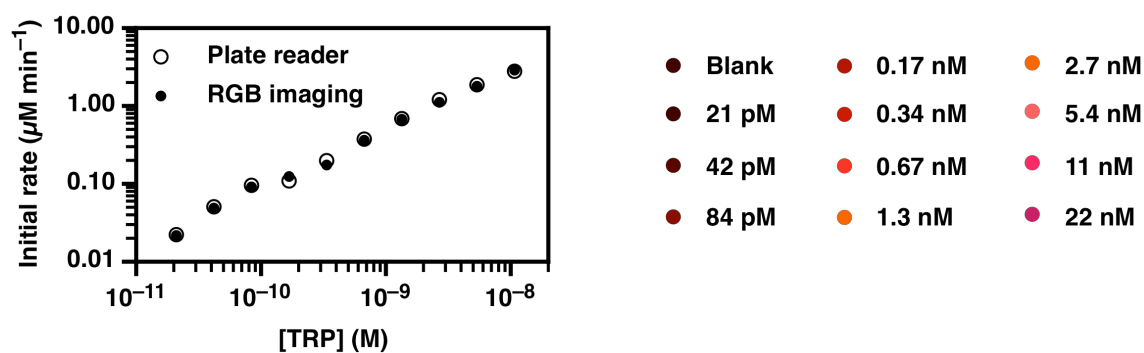
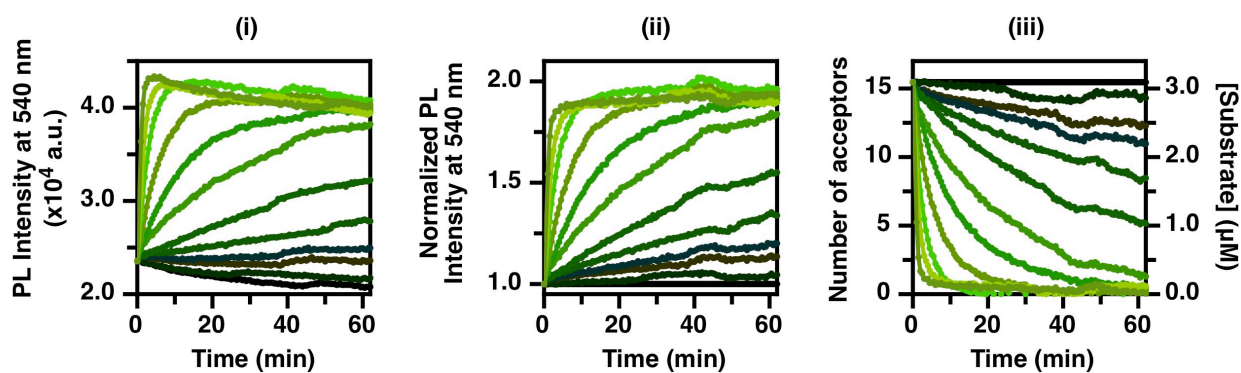
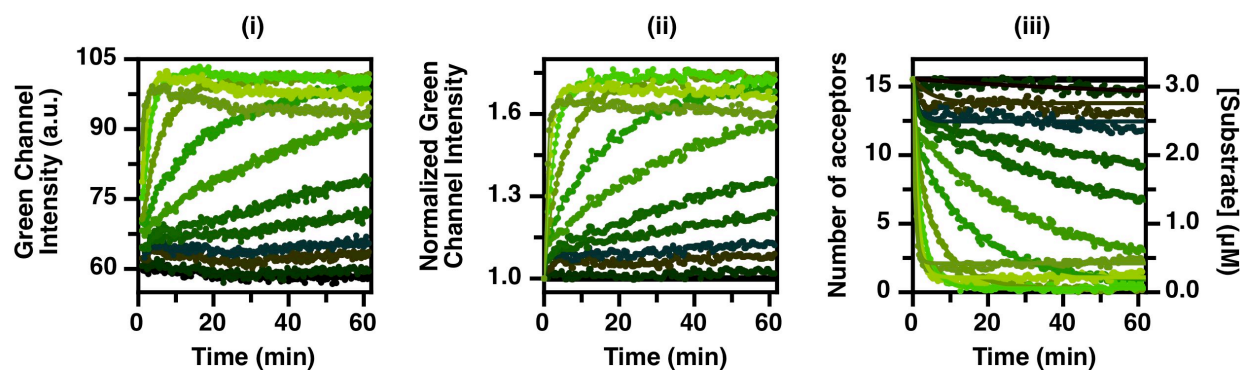


Figure 3.13 Proteolytic digestion of QD625-[Sub_{TRP2}(A647)]₁₂ conjugates by TRP and comparison of data acquired with (A) a fluorescence plate reader and (B) a smartphone and RGB imaging: (i) raw PL data; (ii) normalized PL data; (iii) conversion of the normalized PL data to the average number of acceptors per QD and the bulk equivalent concentration of peptide substrate. (C) Comparison of initial proteolytic rates measured from the fluorescence plate reader data and smartphone RGB imaging data.

(A) Fluorescence plate reader data



(B) Smartphone RGB imaging data



(C)

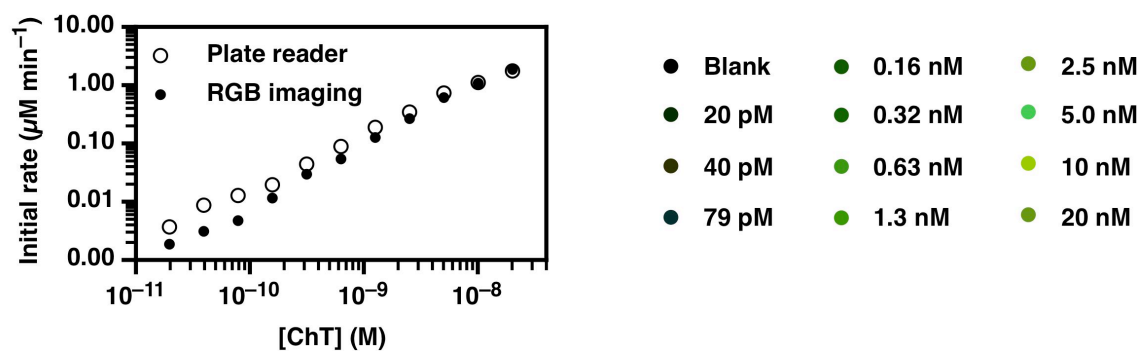
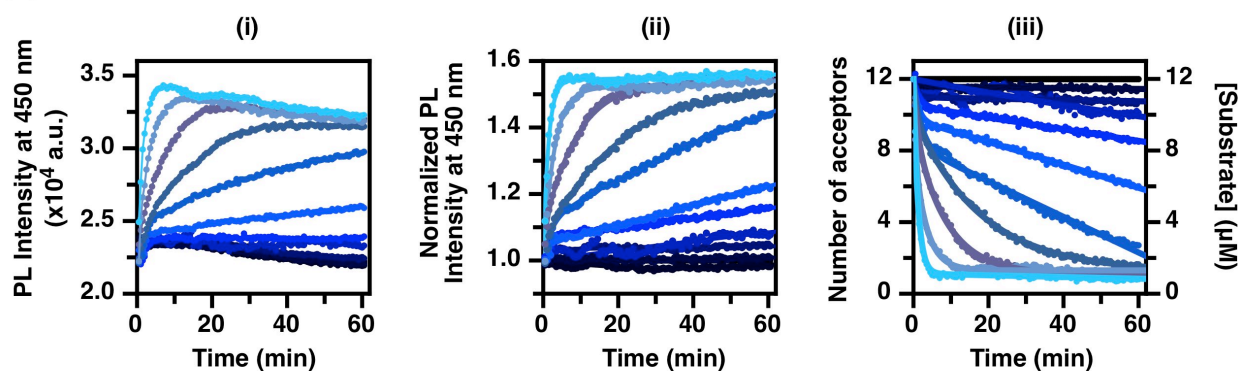
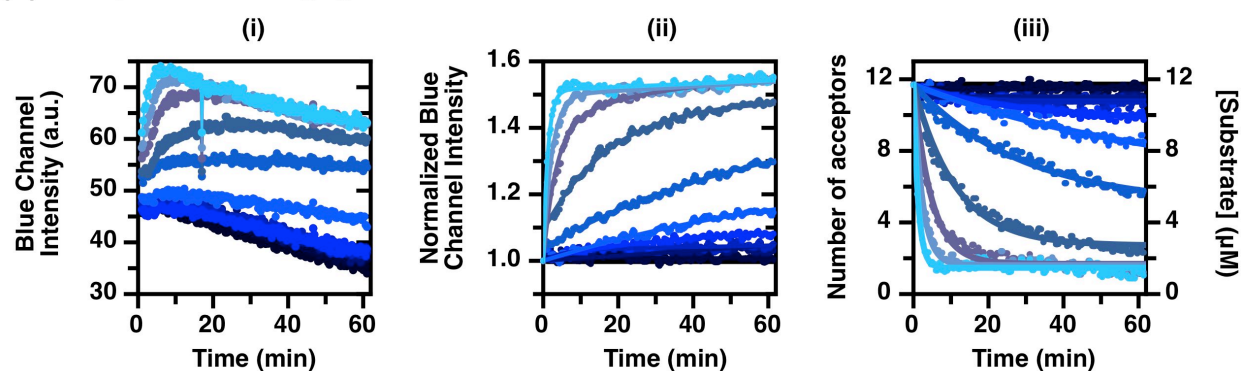


Figure 3.14 Proteolytic digestion of QD540-[Sub_{ChT}(QSY9)]₁₆ conjugates by ChT and comparison of data acquired with **(A)** a fluorescence plate reader and **(B)** a smartphone and RGB imaging: (i) raw PL data; (ii) normalized PL data; (iii) conversion of the normalized PL data to the average number of acceptors per QD and the bulk equivalent concentration of peptide substrate. **(C)** Comparison of initial proteolytic rates measured from the fluorescence plate reader data and smartphone RGB imaging data.

(A) Fluorescence plate reader data



(B) Smartphone RGB imaging data



(C)

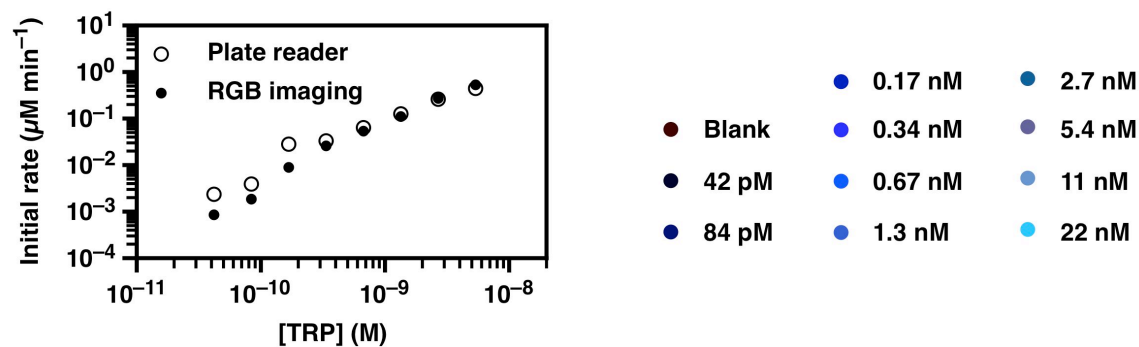


Figure 3.15 Proteolytic digestion of QD450-[Sub_{TRP1}(QSY35)]₁₂ conjugates by TRP and comparison of data acquired with **(A)** a fluorescence plate reader and **(B)** a smartphone and RGB imaging: (i) raw PL data; (ii) normalized PL data; (iii) conversion of the normalized PL data to the average number of acceptors per QD and the bulk equivalent concentration of peptide substrate. **(C)** Comparison of initial proteolytic rates measured from the fluorescence plate reader data and smartphone RGB imaging data.

Initial rates of digestion were determined from the initial slope of the progress curves as described in Section 3.5.6 and plotted as a function of protease concentration to determine the apparent specificity constant, k_{cat}/K_m . Although proteolysis at the interface of nanoparticles does not necessarily follow standard Michaelis-Menten kinetics [387], this parameter was useful for comparing the data between the smartphone and fluorescence plate reader detection formats. As listed in Table 3.4, similar values of k_{cat}/K_m were obtained from both the smartphone and plate reader formats, indicating good quantitative agreement between the two methods. A paired t-test comparison of the initial rates measured with the smartphone and plate reader readout formats indicated that the null hypothesis could not be rejected at any reasonable level of confidence ($p = 0.47$ across all TRP concentrations, where p is the probability that the observed variation will occur if the null hypothesis is true).

Similar analysis of proteolytic assays were done with QD540–[Sub_{ChT}(QSY9)]₁₆ and QD450–[Sub_{TRP1}(QSY35)]₁₂ conjugates using both smartphone digital imaging and the fluorescence plate reader (see Figure 3.14 and Figure 3.15). Again, the progress curves generated from the smartphone imaging and plate reader measurements were qualitatively similar and, in a statistical comparison of the initial rates, the null hypothesis could not be rejected at a reasonable level of confidence ($p = 0.21$ or 0.30 for QD540 across all ChT concentrations or [ChT] > 0.6 nM, respectively; $p = 0.68$ for QD450 across all TRP concentrations). As shown in Table 3.4, there was also good agreement between the calculated specificity constants. Overall, the utility of the smartphone readout format for quantitative measurements of protease activity was confirmed by the close correlation between the data generated with a fluorescence plate reader and the data generated *via* RGB imaging.

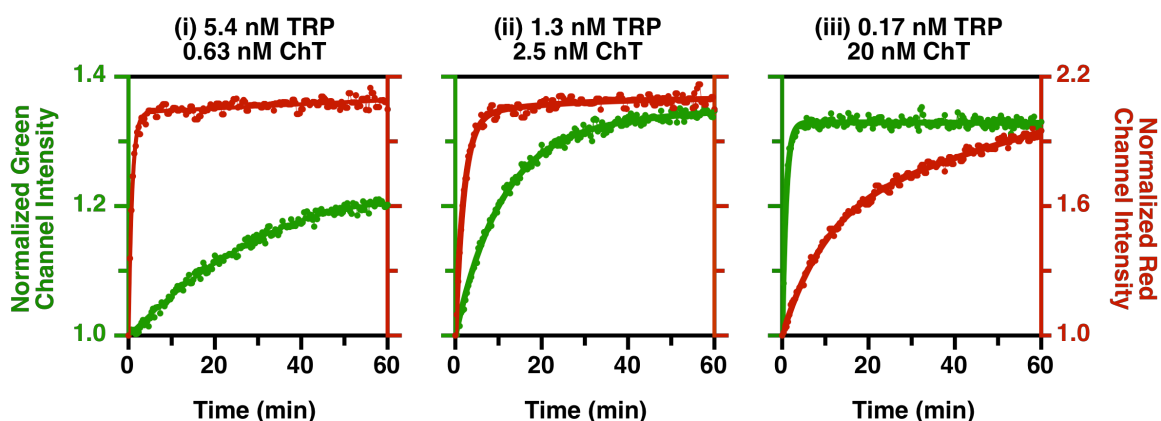
Table 3.4 Comparison of the specificity constants, k_{cat}/K_m ($M^{-1} s^{-1}$), calculated for one-plex assays between the fluorescent plate reader and smartphone RGB imaging readout formats.

Readout format	QD450/TRP	QD540/ChT	QD625/TRP
Plate reader	1.2×10^5	4.9×10^5	2.2×10^6
Smartphone	1.4×10^5	5.0×10^5	2.0×10^6

3.2.5 Multiplexed proteolytic assays with digital colour imaging

The two-plex detection of TRP and ChT using the smartphone imaging readout was evaluated next. Mixtures of QD450–[Sub_{TRP}(QSY35)]₁₂ and QD540–[Sub_{ChT}(QSY9)]₁₆, or QD625–[Sub_{TRP2}(A647)]₁₂ and QD540–[Sub_{ChT}(QSY9)]₁₆, were exposed to different concentrations of TRP and ChT. Progress curves for three different combinations of ChT and TRP are shown in Figure 3.16. Representative raw data is shown in Figure 3.17.

(A) RG two-plex assay



(B) GB two-plex assay

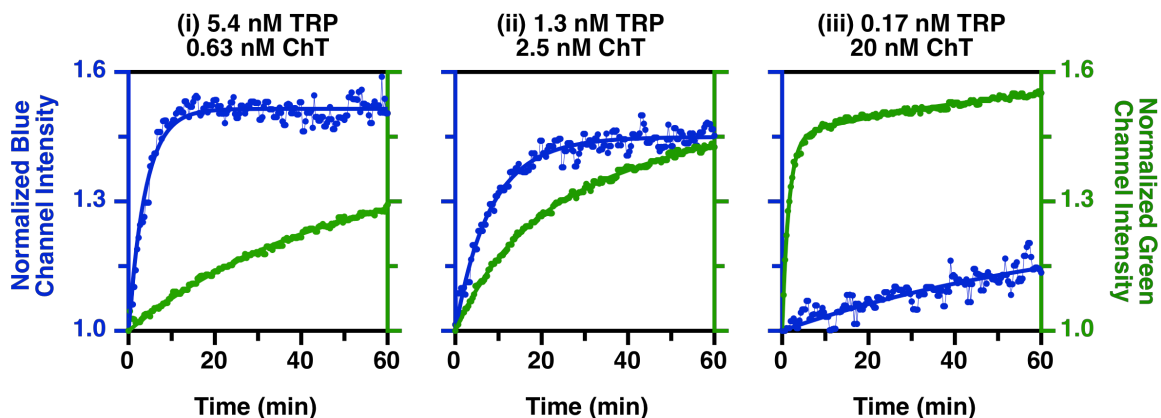


Figure 3.16 Progress curves for two-plex homogeneous assays of proteolytic activity. **(A)** RG two-plex assay with QD540–[Sub_{ChT}(QSY9)]₁₆ (20 pmol) and QD625–[Sub_{TRP2}(A647)]₁₂ (30 pmol). **(B)** GB two-plex assay with QD450–[Sub_{TRP1}(QSY35)]₁₂ (100 pmol) and QD540–[Sub_{ChT}(QSY9)]₁₆ (20 pmol). The conjugates were exposed to the indicated mixtures of TRP and ChT. The ordinate and abscissa scales are the same in each panel of (A) or (B). Corresponding raw data is shown in Figure 3.17.

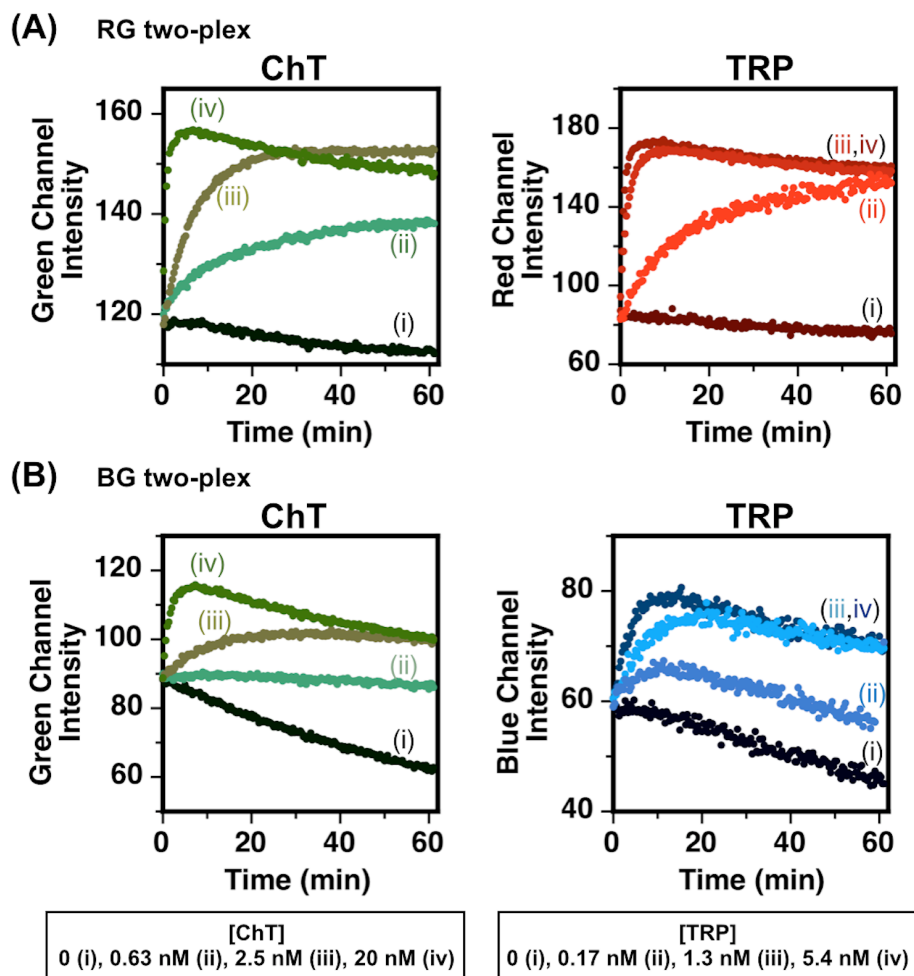


Figure 3.17 Representative unprocessed RGB intensity time traces for two-plex assays with **(A)** QD540–[Sub_{ChT}(QSY9)]₁₆ and QD625–[Sub_{TRP2}(A647)]₁₂ conjugates upon exposure to various concentrations of TRP and ChT, and **(B)** QD540–[Sub_{ChT}(QSY9)]₁₆ and QD450–[Sub_{TRP1}(QSY35)]₁₂ conjugates upon exposure to various concentrations of TRP and ChT. Corresponding normalized data is shown in Figure 3.16.

Analogous to the one-plex assays, the rates of change in the RGB channel intensities were proportional to the concentrations of the corresponding proteases. Interestingly, small decreases in the initial rates of digestion were observed in two-plex assays relative to one-plex assays with QD625–[Sub_{TRP2}(A647)]₁₂ (30 pmol) and QD540–[Sub_{ChT}(QSY9)]₁₆ (20 pmol), and a significant decrease was observed for ChT activity in the system containing the QD450–[Sub_{TRP1}(QSY35)]₁₂ (100 pmol) and QD540–[Sub_{ChT}(QSY9)]₁₆ (20 pmol) conjugates. This

effect was observed with both the smartphone imaging and the fluorescence plate reader detection formats. Non-trivial interactions between proteases (or other proteins) and nanoparticle interfaces have been reported previously [387, 389-391]. These results suggest that protease activity can be influenced by the total concentration of QDs in a sample, and not just the concentration of the QDs carrying the substrate of interest. Similar observations of such interactions between QDs and proteases have been reported recently [391]. Another interesting observation in two-plex assays was that the increased optical density of QD mixtures decreased the overall signal intensities relative to samples with only one colour of QD, in both the RGB imaging and plate reader formats, as shown in Figure 3.4. Quantitative multiplexed assays should therefore be calibrated as mixtures.

To demonstrate three-plex assays, a series of samples containing QD450-[Sub_{TRP1}(QSY35)]₁₂ (100 pmol), QD540-[Sub_{ChT}(QSY9)]₁₆ (20 pmol), and QD625-[Sub_{EK}(A647)]₁₂ (30 pmol) were exposed to various concentrations of TRP, ChT, and EK. Mixtures were interrogated in microtiter plates using UV lamp illumination and smartphone digital imaging. Figure 3.18 shows progress curves and a time series of RGB colour images obtained with three different mixtures of TRP, ChT, and EK. Consistent with the expectations, increases in the concentration of one of the proteases in the mixture correlated with more rapid changes in the RGB channel intensity for the corresponding colour of QD. The normalized initial rates of digestion of QD450-[Sub_{TRP1}(QSY35)]₁₂ conjugates by TRP were in relatively good agreement with those in the one-plex assay; however, ChT activity in the three-plex assays decreased by *ca.* 50% in comparison to the one-plex assay, suggesting that there may be stronger non-proteolytic interactions between QDs and ChT than between QDs and TRP. Nonetheless, the rates of change in the RGB channel intensities in each three-plex assay were proportional to the concentration of the corresponding target protease.

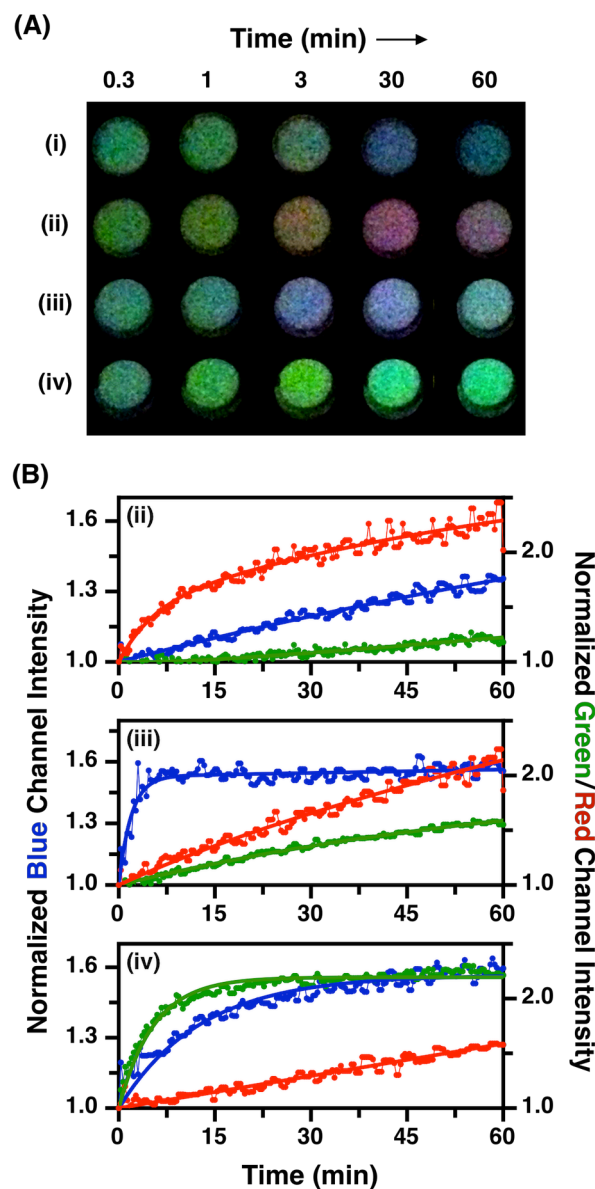


Figure 3.18 Three-plex homogeneous proteolytic assays. (A) Representative colour images (brightness enhanced for clarity) for QD450–[Sub_{TRP1}(QSY35)]₁₂ (100 pmol), QD540–[Sub_{ChT}(QSY9)]₁₆ (20 pmol), and QD625–[Sub_{EK}(A647)]₁₂ (30 pmol) mixed with various concentrations of TRP, ChT, and EK: (i) reference sample (no proteases); (ii) 1 nM TRP, 1 nM ChT, and 4.5 nM EK; (iii) 8.6 nM TRP, 2 nM ChT, and 1.5 nM EK; (iv) 2.2 nM TRP, 16 nM ChT, and 0.5 nM EK. (B) Progress curves corresponding to (ii), (iii), and (iv).

3.3 Discussion

The foregoing experiments have clearly demonstrated that RGB imaging of QD PL with a smartphone camera is suitable for quantitative, real-time, *in vitro* bioanalysis. Although a kinetic assay format was used to demonstrate the full capability of the method, single-point measurements are also possible. Suitable assay times may range from 10 min to upwards of 1 h with longer times providing lower limits of detection. A kinetic analysis using initial rates offers a larger dynamic range. Proteolytic assays were an excellent model system because QD-FRET probes for protease activity are well known [5, 392], and because assays of proteolytic activity have diagnostic and therapeutic value. Abnormal protease activity is associated with various diseases, including cancer [393], neurodegenerative diseases [394], and arthritis [395], among many others. Protease inhibitors are also an important class of drugs [396]. The apparent effect of QD concentration on proteolytic rates is a biophysical phenomenon that was associated with an inhibitory effect of QDs with strong dependence on the QD ligand used to prepare water-soluble QDs [391], but this effect is independent of the analytical readout platform, and assays of activity and inhibition remain possible. This smartphone readout methodology is expected to be compatible with many other QD-FRET assays reported in the literature, including hybridization assays [376], carbohydrate assays [397], and immunoassays [297, 398]. The methodology should also be compatible with charge transfer-based quenching assays with QDs [399, 400].

There is a growing body of literature on the use of smartphones as detectors in various analytical methods, as was described in Chapter 1. This Chapter presented work that adds to this literature, introducing for the first time the possibility of a homogenous multiplexed analysis of a single sample volume through the unique PL properties of QDs and the colour channels of a smartphone camera. In parallel, this method also provides for the simultaneous analysis of many samples in an array format through imaging. These capabilities are achieved with minimal expense, without custom or complex instrumentation, and would not have been feasible without QDs. Tunable, spectrally narrow PL was needed to match the Bayer colour filter channels of the smartphone camera, and a large effective Stokes shift was necessary to permit rejection of excitation light with simple optical filters. Moreover, the bright QD PL was needed to provide sufficient sensitivity as was described in Chapter 2. Overall, this work makes QDs a more accessible research tool for homogenous format with spectral multiplexing for all laboratories,

and further suggests that smartphone imaging—particularly with QD probes—has long-term potential for POC diagnostics.

3.4 Conclusions

The combination of QDs, FRET, and imaging with a smartphone is a viable, easily accessible platform for quantitative, real-time bioanalyses. The optical properties of QDs also enhance the general utility of smartphone cameras as detectors in analytical methods, particularly in terms of multiplexing. Homogeneous assays of proteolytic activity were used as model systems for proof-of-concept, where a deep-red fluorescent dye and dark quencher labels on peptides were FRET acceptors for red-, green-, and blue-emitting QD donors. Changes in the PL emission from these QDs were detected in the RGB colour channels of digital colour images and could be correlated to the activity of picomolar to nanomolar concentrations of protease. Importantly, RGB imaging with a smartphone yielded the same quantitative results as replicate assays done with a sophisticated fluorescence plate reader. In addition to assays with a single colour of QD, homogeneous two-plex and three-plex assays for the activity of TRP, ChT, and EK were also demonstrated. It is expected that the methods and data analysis presented in this chapter can be extended to a wide range of established QD-FRET bioanalyses for targets other than proteases. Given the ubiquity of smartphones, this work largely removes any instrumental impediments to the adoption of QDs as routine bioanalytical tools in laboratories that do not specialize in luminescent nanomaterials. Additionally, this work represents an important preliminary step toward POC diagnostics based on QDs.

3.5 Experimental Section

3.5.1 Materials and reagents

Glutathione (GSH) and tetramethylammonium hydroxide (TMAH) in methanol (25% w/v) were from Sigma-Aldrich (Oakville, ON, Canada). All buffer salts were from Fisher Scientific (Ottawa, ON, Canada).

Trypsin (TRP) from bovine pancreas (#T1426, TPCK treated, $\geq 10,000$ BAEE units/mg protein) and α -chymotrypsin (ChT) from bovine pancreas (#C3412, TLCK treated, Type VII, ≥ 40

units/mg protein) were from Sigma-Aldrich. Recombinant light chain bovine enterokinase (EK, P8070S) was from New England Biolabs (Whitby, ON, Canada).

CdSe_{1-x}S_x/ZnS core/shell nanocrystals (dispersed in toluene) with emission maxima at 450 nm (Blue), 525 nm and 540 nm (Green), and 625 nm (Red) were from CytoDiagnostics (Burlington, ON, Canada). Water soluble GSH coated QDs were prepared as described in Section 2.5.2. Peptides were from Bio-Synthesis Inc. (Lewisville, TX, USA) and the peptide sequences are shown in Table 3.5. Alexa Fluor 647 (A647) C2 maleimide dye, QSY35 iodoacetamide, and QSY9 C5 maleimide were purchased from Life Technologies (Carlsbad, CA, USA). Buffers were prepared with water purified by a Barnstead Nanopure water purification system (Thermo Scientific, Ottawa, ON, Canada) and sterilized by autoclaving prior to use. Buffers included borate buffer (50 mM, pH 9.2), borate buffered saline (BBS, 10 mM, 50 mM NaCl, pH 8.5), and phosphate buffered saline (PBS, 137 mM NaCl, 10 mM phosphate, 2.7 mM KCl, pH 7.4).

3.5.2 Peptide labeling

Peptides with a terminal cysteine residue (see Table 3.5) were labeled with Alexa Fluor 647 C2 maleimide (A647) and QSY9 C5 maleimide dye according to previously published protocols with slight modifications [368, 401]. Briefly, 0.75 mg (0.22–0.27 μ mol) of peptide was dissolved in 50 μ L of 50% v/v MeCN (aq), diluted with 550 μ L of HEPES buffer (pH 7.0, 100 mM, 50 mM NaCl), and mixed with 0.5 mg (0.4 μ mol) of the A647 dye dissolved in 25 μ L of DMSO. The reaction was placed on a mixer for 24 h at room temperature in the dark. The QSY35 iodoacetamide labeling reaction was done in anhydrous DMF over 24 h at room temperature using 5–10 equivalents of dye per peptide and subsequently diluted with borate buffer. All labeled peptides were purified using a nickel(II)-nitrilotriacetic acid (Ni-NTA) agarose resin (Qiagen Valencia, CA). Excess dye was removed by washing with 50% DMSO/BBS (10 mL), PBS (10 mL), 50% EtOH/PBS (10 mL), and PBS (3 \times 10 mL). The labeled peptide was eluted with 1.5 mL of 300 mM imidazole in PBS (filtered through decolorizing carbon) per cartridge and desalted using an oligonucleotide purification cartridge (OPC, Life Technologies, Carlsbad, CA, USA). Labeled peptide was eluted using 70% acetonitrile in water and quantitated using UV-visible spectrophotometry (see Table 3.2 for molar extinction coefficients). The peptide was aliquoted into 20 nmol fractions, dried under vacuum, and stored at –20 °C until needed.

Table 3.5 Peptide substrate sequences.

Amino acid sequence (written N-terminal to C-terminal) ^a	Abbreviation
HHHHHH SPPPPPPS GQGE GEGNSGR↓GGSGNG C(QSY35)	Sub _{TRP1} (QSY35)
HHHHHH SPPPPPPG SDGNESGLVPR↓GSGC(A647)	Sub _{TRP2} (A647)
HHHHHH SPPPPPPS GQGE GEGNSAAY↓ASGNG C(QSY9)	Sub _{ChT} (QSY9)
HHHHHH SPPPPPPS GQGE GGN DDDDK ↓SGNG C(A647)	Sub _{EK} (A647)

^a Protease recognition sites are indicated in bold and the cut position is indicated by the downwards arrow.

3.5.3 Instrumentation and data acquisition

Sample solutions were added to the wells of a 96-well microtiter plate (#3615; special optics, flat, clear bottom, black walls; Corning, Corning, NY, USA) and illuminated obliquely (40–50° angle of incidence) from underneath with a UV lamp. The UV excitation source was either a handheld (6 W, UVGL-58) or portable, AA battery-powered (4 W, UVL-4) UV lamp with emission at 365 nm (UVP, Upland, CA, USA). The microtiter plate was placed on top of an elevated glass pane with the UV lamp underneath. The distance between the lamp and the glass pane was adjusted to obtain QD PL intensities within the dynamic range of the smartphone camera. A longer distance was used with a more powerful lamp. The smartphone (iPhone) digital camera was placed above the microtiter plate at a distance of *ca.* 16 cm. The camera was set on a UV-blocking plastic plate (UVP 38-0013-01) with a long-pass filter (400 nm cut-off; FEL0400, Thorlabs, Newton, NJ, USA) and a short-pass filter (650 nm cut-off; FES0650, Thorlabs) placed prior to the camera lens on the other side of the plastic plate. Images were acquired using the TimeLapse software available for the iPhone. All image analysis was done using ImageJ software (National Institutes of Health, Bethesda, MD, USA). Solution-phase PL spectra and absorbance spectra were acquired with an Infinite M1000 fluorescence plate reader (Tecan, Morrisville, NC, USA).

Note: The off-axis alignment of the UV light source was observed as a shadow at the edge of some wells. This artifact did not interfere with data analysis. In Figure 3.3, the change in the

position of the shadow for the QD540 images is a result of stitching together two separate fields of view to form a single image.

3.5.4 Conjugation of peptides to QDs and enzyme assays

Stock solutions of QD-peptide conjugates were prepared by mixing QD450, QD540, and QD625 with 12, 16, and 12 equivalents of peptide, respectively, in BBS for 1 h in the dark. For multiplexed assays, the different QD-peptide conjugates were mixed together in the same final volume. The concentrations of the QD-peptide conjugates in the solutions were twice the desired concentration in the assays. Table 3.6 summarizes the stock solution recipes. Stock solutions of TRP, ChT, and EK were prepared in BBS and diluted to twice the concentrations desired for assays. For multiplexed assays, TRP/ChT/EK were mixed together in the same final volume. Proteolytic assays were started by adding 50 μ L of enzyme solution to 50 μ L of QD-peptide conjugates in microtiter plate wells. Images were acquired every 20 s for 1 h under UV illumination.

Table 3.6 Preparation of stock solutions of QD peptide conjugates.

Assay	QD Colour	QD (nmol)	Peptide Substrate	Substrate (nmol)	[QD] (μ M)	[Peptide Substrate] (μ M)	Final volume (μ L)
1-plex	QD625	0.49	Sub _{TRP2} (A647)	5.9	0.60	7.2	820
1-plex	QD540	0.33	Sub _{ChT} (QSY9)	5.25	0.40	6.4	820
1-plex	QD450	1.04	Sub _{TRP1} (QSY35)	12.5	2.00	15.2	820
2-plex	QD625	0.30	Sub _{TRP2} (A647)	3.6	3.00	36.0	100
3-plex	QD625	0.30	Sub _{EK} (A647)	3.6	3.00	36.0	100
2- or 3-plex	QD540	0.28	Sub _{ChT} (QSY9)	4.48	2.00	32.0	140
2- or 3-plex	QD450	0.83	Sub _{TRP1} (QSY35)	9.9	3.33	39.6	250

3.5.5 Data analysis

3.5.5.1 FRET parameters

The FRET pairs were characterized using the Förster formalism as described in Chapter 1 (Section . The Förster distance, R_0 , was calculated using Eqn. 1.18, where the refractive index of surrounding media, n , was taken to be 1.335, and the orientation factor, κ^2 , was assumed to be 2/3. The quantum yield of QDs was measured experimentally as described in Appendix II. The spectral overlap integral was calculated according to Eqn. 1.19. The FRET efficiency, E , was calculated from spectra measurements of QD PL using Eqn. 1.24.

3.5.5.2 RGB images analysis

The RGB channel intensities in digital colour images were calculated by splitting the images into corresponding RGB channels and determining the mean intensity (I) of a well of interest in blue (B), green (G), and red (R) channels. All of these operations were done in ImageJ. Next, eqns. 3.1-3.3 were applied to account from crosstalk in the analysis of mixtures for multiplexed assays. The terms I_R , I_G , and I_B denote measured, background-corrected intensities in the corresponding RGB channels of colour images. The correction factors were determined experimentally (see Section 3.2.1).

$$I_{\text{QD625}} = I_R \quad (3.1)$$

$$I_{\text{QD540}} = I_G - (0.06)I_{\text{QD625}} \quad (3.2)$$

$$I_{\text{QD450}} = I_B - (0.09)I_{\text{QD540}} - (0.07)I_{\text{QD625}} \quad (3.3)$$

3.5.5.2.1 Normalization of progress curves

All experiments were done in parallel with at least one control sample with no added protease (*i.e.* blank) to account for any drift in the UV lamp intensity (see Figure 3.11) or other non-proteolytic sources of temporal variation, including potential photobrightening or photobleaching of the QDs. At each time point, t , the RGB channel intensity, $I_{t, [E]}$, was calculated. As shown in eqn. 3.4, each of these values for a given enzyme concentration, $[E]$, were normalized to an

initial value of unity by dividing by the intensity value at $t = 0$. All subsequent time points were then scaled to the control sample as a reference point.

$$(I_t)_{\text{normalized}} = \frac{(I_{t,[E]}/I_{t=0,[E]})}{I_{t,[E]=0}} \quad (3.4)$$

3.5.5.2.2 Calculation of initial rates and specificity constants

Initial rates of proteolysis were determined from the slope of the initial linear region of progress curves using a regression analysis in ProFit software (QuantumSoft, Uetikon am See, Switzerland). The progress curves with very fast digestion (the first data point corresponded to >50% digestion) were omitted from the initial rate analysis. Plots of initial proteolytic rate *versus* protease concentration were analyzed using a simplification of the Michaelis-Menten equation, eqn. 3.5 [402], where v_0 is the initial reaction rate, $[S]$ is the substrate concentration, K_m is the Michaelis constant, $V_{\max} = k_{\text{cat}}[E]_0$, is the limiting reaction rate, $[E]_0$ is the protease concentration, and k_{cat} is the turnover number. Eqn. 3.6 is a good approximation of eqn. 3.5 when $[S] \ll K_m$. Initial rates measured for high protease concentrations were omitted from the regression analysis if they deviated from a linear trend (*i.e.* the rates began to slow as the limiting velocity started to be approached).

$$v_0 = \frac{d[P]}{dt} = \frac{V_{\max} [S]}{K_m + [S]} \quad (3.5)$$

$$v_0 \approx \frac{k_{\text{cat}}}{K_m} [E]_0 [S]_0 \quad (3.6)$$

Only the specificity constant, k_{cat}/K_m , was calculated because the protease concentrations used in experiments did not approach V_{\max} , and thus the data did not permit reliable determination of both k_{cat} and K_m . It is important to note that the specificity constant was calculated for the purpose of comparison between the two readout formats (fluorescence plate reader *versus* smartphone imaging), and not to characterize the enzymes and their mechanism of action.

Chapter 4 Characterization and Evaluation of Chemical Modification of Cellulose Paper Substrates for Prospective Point-of-care Diagnostics with Immobilized Quantum Dots

A part of this Chapter (Section 4.2.4.1.1) is an adaptation of published work, and is reproduced from Kim, H., Petryayeva, E., Algar, W. R., Enhancement of Quantum Dot Forster Resonance Energy Transfer within Paper Matrices and Application to Proteolytic Assays. *IEEE J. Sel. Top. Quantum Electron.* **2014**, 20 (3), 7300211, with permission from IEEE (Copyright 2014 IEEE).

4.1 Introduction

Paper-based analytical devices continue to be a subject of great interest for the development of low-cost point-of-care (POC) diagnostics. In the past few decades, paper-based assays have attracted particularly strong interest in the design of lateral flow assays (LFA), a few of which are now available commercially (*e.g.* pregnancy tests and other urine test strips). These devices are also good examples of POC assays performed outside of the laboratory. Most LFA devices are based on nitrocellulose paper that facilitates immobilization of proteins and antibodies *via* physical adsorption driven by hydrophobic interactions, as was described in Section 1.1.4. Cellulose, a cheaper and non-hazardous alternative to nitrocellulose, offers low production costs, portability, durability and excellent wicking ability of aqueous solution *via* capillary action [18, 36, 403]. The latter property is one of the major advantages of paper substrates as it eliminates the need for external power sources necessary to drive the fluid flow. Furthermore, cellulose is a readily available biopolymer with excellent biocompatibility and biodegradation properties [403, 404]. To date, paper-based materials have been applied in clinical diagnosis [36, 405], food quality control, environmental control, and cell culture devices [162, 406]. Some of the prominent developments in the area of paper-based technology include microfluidic paper analytical devices (μ PADs), LFA strips, dipstick assays, and thread-based networks [36, 81, 407-413]. Multiplexing in these assays remains a challenge and is generally demonstrated with

branched multiple channels on μ PAD, where a drop of sample is transported to multiple test zones *via* capillary action.

Bioassay development on paper substrates requires long-term and stable immobilization of biomolecules or nanoparticles (NPs). Cellulose is a biopolymer that represents one of the simplest polysaccharides composed of glucose units. As a result, cellulose contains a large amount of free hydroxyl groups located at the C2, C3, and C6 positions of glucose. These hydroxyl groups contribute to the extensive intra- and intermolecular hydrogen bonding network that is responsible for the integrity of polymer chains and supramolecular arrangements [404]. Given its chemical composition, cellulose does not promote biomolecule immobilization *via* physical adsorption, in contrast to nitrocellulose and polyvinylidene difluoride (PVDF) membranes. As a result, numerous approaches for chemical modification of cellulose for bioconjugation purposes have been successfully demonstrated. These methods include oxidation to form carbonyl groups, amination, esterification, and radical copolymerization [404, 414]. Although these chemical approaches were developed for immobilization of biomolecules (particularly antibodies), they can be expanded to achieve suitable functionalization for immobilization of NPs.

Many recent efforts have sought to integrate NPs and their advantages into the development of paper based POC diagnostics [34, 415]. Depending on the assay format and transduction mechanism, NPs may or may not require direct immobilization on a paper substrate. For instance, assays that rely on a NP as a label for a biorecognition binding event are incorporated in a flow solution. This assay format relies heavily on Au NPs due to their facile synthesis, intense red colour, distinct red to blue colour change upon aggregation, and silver enhancement method making them a hallmark in LFA and dipstick assays [34, 416]. A few examples have demonstrated fluorescence based detection in immunoassays with quantum dots (QDs) as labels [111, 112, 417]. In addition to using NPs as reporters in flow solution, there is a strong interest to develop assays where NPs serve as anchoring point to the surface. In order to achieve stable and reliable immobilization of NPs within paper matrix, chemical modification of the surface functional groups of the paper and NP are often necessary. A few studies attempted to mitigate the need for chemical modification of the paper by impregnating it with hydrophobic NPs from organic solvents. For example, oleylamine capped palladium NPs were loaded into cellulose

paper for the development of reusable catalytic system for organic synthesis [418]. In a separate study, paper substrates were doped with hydrophobic nickel NP, that served as “docking sites” for immobilization of polyhistidine tag containing protein G, which, in turn, was used for antibody immobilization [419]. Direct paper impregnation with hydrophobic QDs for sensing applications has also been demonstrated. Recently, hydrophobic QD-loaded paper substrates were modified with glucose oxidase enzyme *via* physical adsorption and subsequently used for detection of glucose [420]. The product of this enzymatic reaction is hydrogen peroxide that etches the QD surface, resulting in concentration dependent QD PL quenching. Arguably, this approach simplifies preparation steps by eliminating the need for chemical modification of paper and preparation of water-soluble QDs. However, this approach is not easily applicable to the detection of other analytes (*i.e.* bioreactions that do not generate QD PL quenching species, such as H₂O₂), is not suitable for multiplexing, and does not permit detection of enzyme activity (*e.g.* proteases, kinases, and nucleases).

Development of QD immobilization strategies applicable to a larger scope of bioassays is crucial. One such strategy is developing immobilization chemistry suitable for a QD-FRET transduction approach, which opens up possibilities for translation of a multitude of already developed homogeneous bioassays [185] to paper-based formats amenable to POC diagnostics. Over the last decade, it was demonstrated that much of the versatility of QDs stems from their ability to participate in Förster resonance energy transfer (FRET) [421], which is one of the most widely used techniques for fluorescence-based measurements of biological molecules and systems [422]. QDs are most frequently used as FRET donors paired with fluorescent dyes, dark quenchers, or fluorescent proteins as acceptors [282, 381]. Advantages of QDs as donors were highlighted in Section 1.3.6 and include (i) the ability to excite the QD with minimal direct excitation of the acceptor, (ii) easily optimized spectral overlap between the QD and the acceptor, and (iii) the ability to further optimize FRET efficiency by arraying multiple acceptors per QD [185, 421]. QD-FRET probes have been developed for a variety of biological targets based on various mechanisms of detection, such as association (*e.g.* protein binding, DNA hybridization), dissociation, competitive binding, lysis (*e.g.* enzyme digestion), conformational changes, and by monitoring changes in donor-acceptor spectral overlap [185]. The versatility of QD-FRET is well established and has been demonstrated in the detection of metal ions [278, 286], small molecules [219, 287, 288], toxins [289], drugs [290], protease [291, 292] and

nuclease [293, 294] activity, hybridization assays [295, 296], immunoassays [297], and pH [298, 299]. The vast majority of these assays were done in a homogeneous format (*i.e.* solution phase) with only a few examples of heterogeneous (*i.e.* solid phase) formats. The latter examples include protease assays on glass chips [423], and nucleic acid hybridization assays on optical fibers [424], microfluidic chips [425], 96-well microtiter plates [426], and, more recently, paper substrates [312, 313, 427].

The approaches that are suitable for developing surface chemistry for QD immobilization are closely related to the approaches that exist for the preparation of QD bioconjugates described in Section 1.3.5. These methods can be classified into three main groups: (i) covalent coupling with QD ligands, (ii) self-assembly with the inorganic shell of the QD nanocrystal, and (iii) biomolecule driven binding (*e.g.* avidin-biotin binding, DNA hybridization) [428, 429]. The immobilization chemistries reported in this chapter were inspired by the well-established interactions used for QD self-assembly: (i) thiol-metal affinity interactions, which is the most common approach used to prepare water-soluble QDs, and (ii) imidazole-metal affinity, which is a reliable approach used to prepare QD bioconjugates modified with a hexahistidine tag (His-tag). Multidentate surface thiol ligand exchange has been shown to serve as a robust platform for QD immobilization on glass surfaces [430]. Imidazole-based ligands (the coordinating unit of histidine) have been successfully implemented on glass substrates [431] and 96-well microtiter plates [426]. Self-assembly methods offer numerous advantages in comparison to other strategies including rapid, spontaneous immobilization at room temperature without need for additional reagents. The extent of coupling reactions that proceed with high efficiency and selectivity in aqueous media at room temperature remains rather limited [428, 429]. Carbodiimide coupling requires reaction conditions that can promote QD aggregation and copper-free “click chemistries” can suffer from slow rates and poor coupling efficiency. Other QD immobilization strategies include use of oligonucleotides [432], proteins [433] and antibodies [434] as tethers, biotinylated surfaces for streptavidin-coated QDs [304, 435]. Surface coupling by means of oligonucleotide hybridization can offer a chemical “switch” for release of QDs upon carefully controlled dehybridization of double stranded DNA [432]. The stability of QDs immobilized using proteins or antibodies is limited to the structural integrity of the biomolecules, and any conditions that impose denaturation ultimately compromise QDs that are assembled at an interface.

It is possible that no single method for QD immobilization would be applicable to every bioassay format. Nevertheless, the primary focus of this chapter is to develop and evaluate QD immobilization approaches suitable for a larger scope of FRET-based assays. This chapter presents three different methods for QD immobilization within a cellulose paper matrix. The effects of surface chemistry on the density of immobilized QDs, long-term stability of immobilized QDs, enhancement of FRET efficiency (in comparison to bulk solution), and protease activity assays were investigated.

4.2 Results and Discussion

4.2.1 Selection of surface ligands

Three different chemistries were developed for modification of cellulose paper substrates and were evaluated for subsequent QD immobilization as shown in Figure 4.1. One of the methods was designed to functionalize cellulose paper with imidazole ligands, and the other two methods were designed to achieve thiol ligands; the primary difference between the two thiol-based chemistries was the approach used to generate reactive functional groups on cellulose (*i.e.* oxidation *versus* silanization). The first method for cellulose modification was based on the periodate oxidation of secondary alcohols in the glucose unit of cellulose (**1**) to aldehydes (**2**), and subsequent coupling with 1-(3-aminopropyl)imidazole *via* imine bond formation that was reduced to a secondary amine with sodium cyanoborohydride. The imidazole-functionalized paper (**3**) structurally resembles planar surfaces modified with polyhistidine-appended peptides suitable for QD immobilization [304] without the cost associated with peptide synthesis. The reaction duration and concentration of periodate in the oxidation step strongly influenced the structural integrity of cellulose composite. For example, a 3 h reaction resulted in disintegration of paper substrates. The final modification step, the reaction with 1-(3-aminopropyl)imidazole, required careful optimization of reaction conditions. The reagent, 1-(3-aminopropyl)imidazole, forms strongly basic aqueous solution and is capable of hydrogen bonding with glucose units of cellulose. As a result, the paper substrates were prone to lose their structural integrity when exposed to 1-(3-aminopropyl)imidazole, particularly under aqueous reaction conditions. Performing the reaction with 1-(3-aminopropyl)imidazole in organic solvent for shorter periods of time was found to preserve the paper integrity.

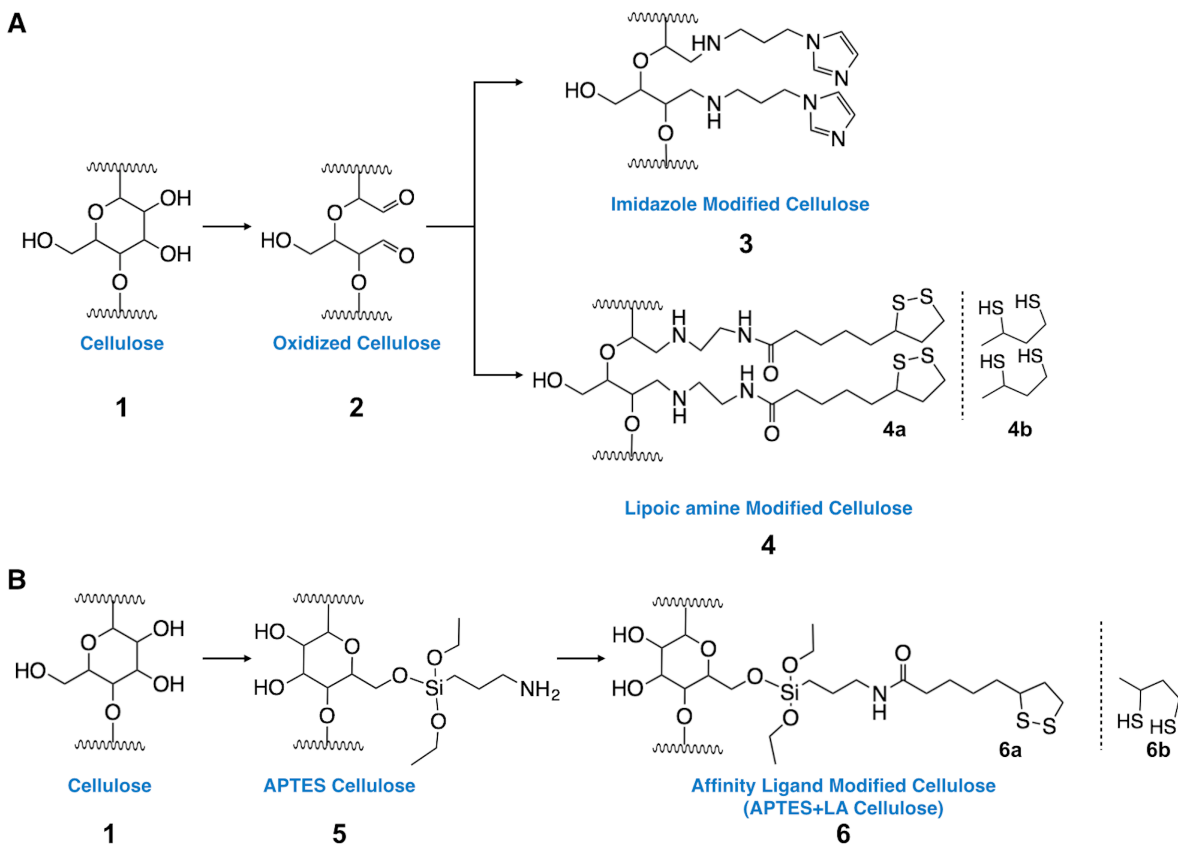


Figure 4.1 Stepwise chemical modification of cellulose paper substrates to immobilize QDs *via* self-assembly. **(A)** cellulose oxidation was used to generate reactive aldehyde groups (**2**) that were subsequently reacted to prepare imidazole (**3**) and thiol (**4**) functionalized cellulose paper, **(B)** cellulose paper was modified with 3-aminopropyl triethoxysilane to give primary amine functionalized paper (**5**), that was subsequently reacted with NHS-ester activated lipoic acid to yield thiol-modified cellulose paper (**6**). Details of reagents and reaction conditions are given in Schemes 4.2–4.5 (p. 178–182).

The second and the third approach shown in Figure 4.1 aimed to generate bidentate thiol ligands that exhibit high affinity for the ZnS shell of QDs. Bifunctional thiolate molecules, such as dihydrolipoic acid (DHLLA) [261] and its derivatives [256, 257, 260, 436] are widely used to modify the surface of QDs to provide aqueous stability. The primary difference between the second and the third approach was the initial step used to impart reactivity on cellulose fibers. In the second approach, cellulose was oxidized with periodate as described above and subsequently reacted with an amine-terminated derivative of lipoic acid, henceforth referred to as “lipoic

amine” to afford paper substrate (4). In the third approach, an attempt was made to increase the density of surface ligands by implementing a silanization step with 3-aminopropyltriethoxysilane (APTES) to afford paper substrate (5). Cellulose paper is hygroscopic and without special pre-treatment has water content proportional to air humidity [437]. The APTES is prone to rapid hydrolysis and condensation in the presence of water, potentially forming multilayered, resin-like coatings crosslinked with the hydroxyl groups of cellulose paper. Subsequently, the paper substrate (5) functionalized with primary amine groups was reacted with *N*-hydroxysuccinimide activated lipoic acid to generate paper substrate (6).

4.2.2 Characterization of surface chemistry

The outer surface layers of cellulose fibers were analysed at each step of modification with X-ray photoelectron spectroscopy (XPS). XPS allows identification of elements within ~10 nm deep subsurface layers [438]. Consistent with its chemical structure, the untreated cellulose paper (1) exhibited two signals corresponding to carbon and oxygen, as shown in Figure 4.2. The subsequent oxidation step to yield paper substrate (2) did not alter the relative amounts of oxygen and carbon, such that the relative C to O signal ratio remained almost unchanged (Table 4.1). The relative percent of nitrogen was increased following modification with 1-(3-aminopropyl)imidazole (3). The rise in the N 1s peak is shown in Figure 4.2A(ii). Similarly, nitrogen and sulphur content increased in paper substrates modified with lipoic amine (4). The XPS spectra shown in Figure 4.2A(iii) illustrates the appearance of N 1s, S 2s, and S 2p signals. Furthermore, the additional ten-carbon structure of lipoic amine resulted in slight increase in C along with a concurrent decrease in O content. The relative magnitude of the signals for nitrogen and sulphur is small, as modification occurs only on the outer layer, while XPS samples through multiple unmodified layers. In contrast, the silanization step to yield (5) introduced more significant changes in the relative elemental composition, indicating formation of multilayers with a thickness that was likely comparable to the analysis depth in XPS. As summarized in Table 4.1, the nitrogen content for sample (5) increased to 10.2% (*cf.* 1.0 % for imidazole and lipoic amine modified samples), and a strong Si signal appeared with a relative amount of 11.8%. Given the chemical structure of APTES, the relative ratio of ~1:1 for N:Si was expected. Successful modification of paper samples modified with NHS-ester activated lipoic acid (6) was confirmed by the appearance of a sulphur signal, as shown in Figure 4.2C. Based on the relative

percentages for nitrogen and sulphur signals (Table 4.1), it can be suggested that not all primary amine groups were available for coupling in sample (5) and only *ca.* 23% were functionalized with lipoic acid.

Table 4.1 Apparent XPS surface composition characterizing surface modifications.^a

Sample	Relative atomic percent, %				
	C (1s)	O (1s)	N (1s)	S (2s, 2p)	Si (2s, 2p)
1	59.8 (1)	40.2 (0.67)	–	–	–
2	58.8 (1)	41.2 (0.70)	–	–	–
3	58.0 (1)	41.0 (0.71)	1.0 (0.02)	–	–
4	60.3 (1)	38.0 (0.63)	1.0 (0.02)	1.0 (0.02)	–
5	56.0 (1)	21.7 (0.39)	10.2 (0.18)	–	11.8 (0.21)
6	60.5 (1)	22.3 (0.37)	7.7 (0.13)	1.9 (0.03)	7.4 (0.12)

^aNumbers in brackets indicate intensity relative to carbon signal

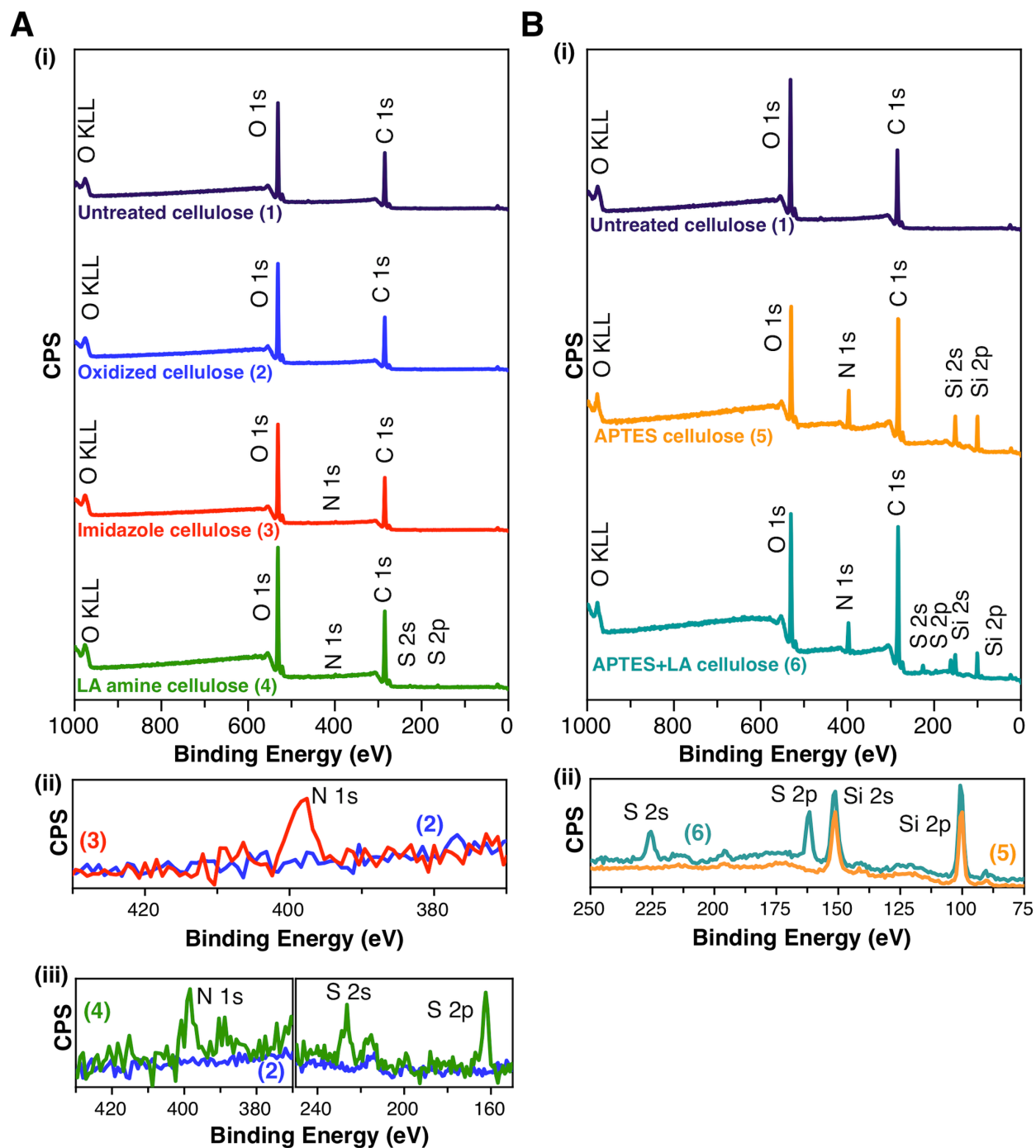


Figure 4.2 XPS survey analysis for stepwise modification of cellulose paper with **(A)** imidazole and lipoic amine ligands; (i) full spectra, (ii) N 1s peak observed upon addition of imidazole ligands **(3)** and (iii) N 1s, S 2s, and S 2p peaks observed on lipoic amine modified paper **(4)**. **(B)** Chemical modification of paper *via* silanization with APTES; Full spectra are shown in (i) and a region of interest in (ii). The peaks corresponding to O 1s, C 1s, N 1s, S 2s, S 2p, Si 2s, and Si 2p orbitals are labeled.

In addition to XPS analysis, ATR-FTIR analysis was performed at each step of the chemical modification of paper substrates, as shown in Figure 4.3. The broad peak observed between 3650 and 3300 cm^{-1} with all samples is from the hydroxyl groups of cellulose, as well as adsorbed water molecules. Another common peak observed in all analyzed samples is located in the region 2850-2950 cm^{-1} , a band that is associated with symmetric and asymmetric CH_2 stretching vibrations. Comparing the relative ratio between the hydroxyl and CH_2 signals between all samples indicates a relative decrease in the intensity of the hydroxyl peak in samples treated with APTES (5, 6). This observation is most likely attributed to a decrease in the water content within paper samples as a result of the reaction conditions used for silanization (*i.e.* reflux in toluene for 12 h).

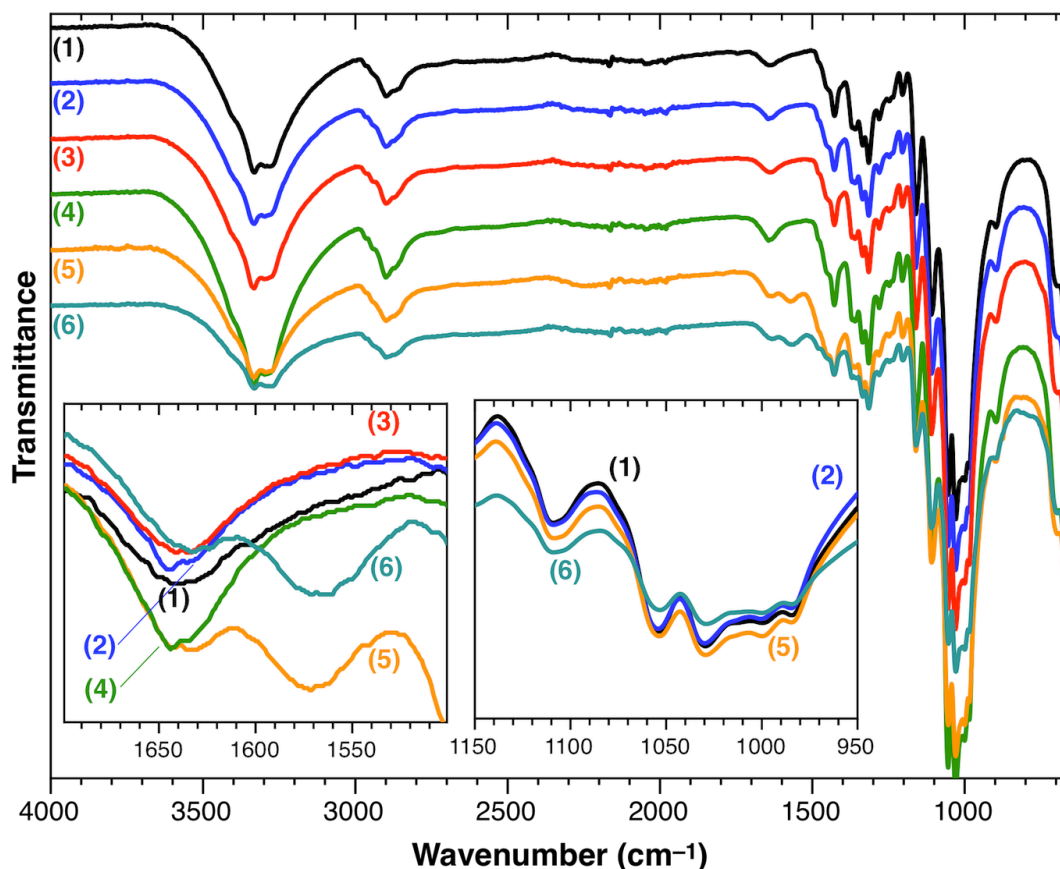


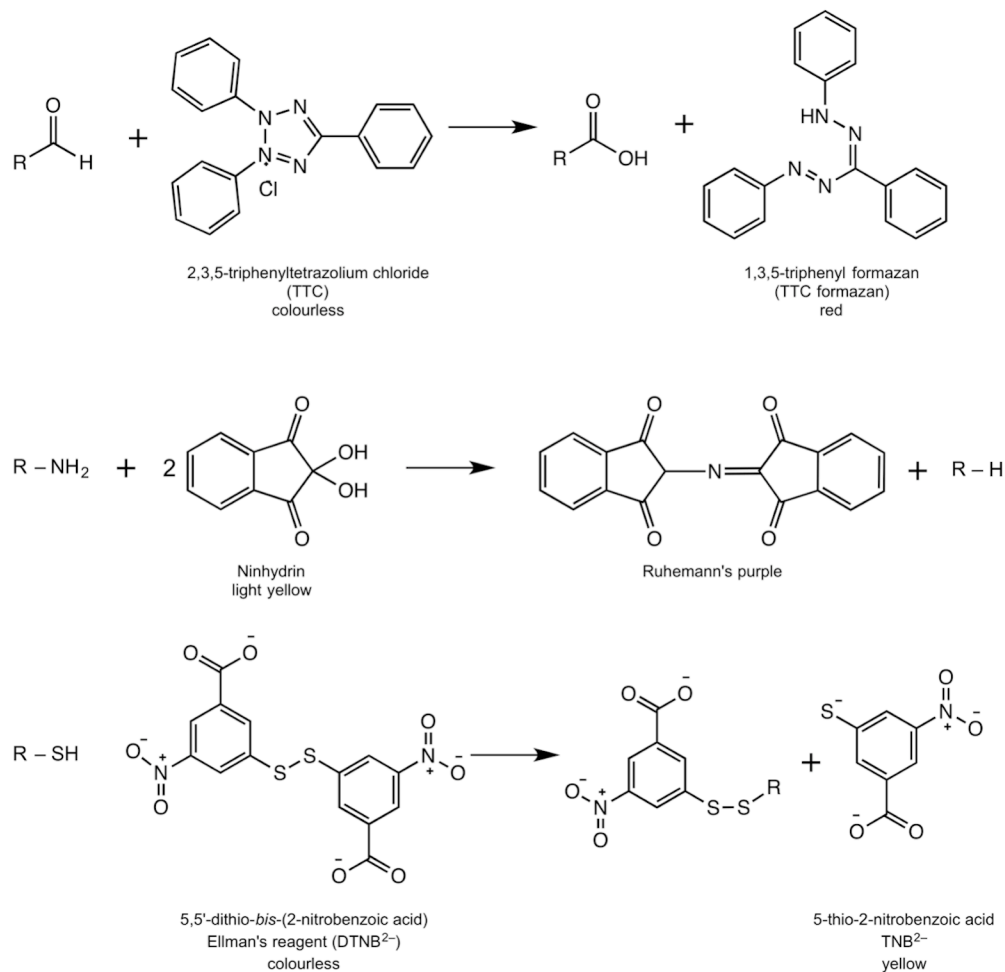
Figure 4.3 ATR-FTIR spectra for each step of chemical modification of cellulose paper samples. (1) untreated cellulose, (2) oxidized cellulose, (3) imidazole ligand modified cellulose, (4) lipolic amine modified, (5) APTES modified and (6) cellulose modified with APTES and lipolic acid ligands.

The ability to resolve the differences in spectral profile for each modification step was rather limited, given that the penetration depth of evanescent wave for ZnSe crystal is approximately 2 μm [439] and chemical modification likely occurs only at the surface of the cellulose fibers. Nevertheless, there is a clear difference between ATR-FTIR spectra of untreated (**1**) and APTES modified paper samples (**5**, **6**) in the region 1530–1600 cm^{-1} , as shown in Figure 4.3 (inset). These peaks are attributed to the presence of primary amines [440, 441], but the broad nature and poor signal-to-noise ratio may obstruct additional contributions from C=N stretch, observed in polymerized APTES sol-gels [441, 442]. The Si–O–Si and Si–O–C vibrations are known to appear in 1000–1100 cm^{-1} region [441]; however, due to the presence of dominant peaks from C–O–C bonds from the cellulose fiber, unequivocal assignment was not possible. Consistent with the XPS data described above, stronger signals for samples **5** and **6** (*cf.* **3** and **4**) indicated probable multilayer formation of APTES along the cellulose fiber. Small changes observed in XPS and ATR-FTIR for samples **2**, **3**, and **4** were, however, consistent with the literature [443–446]. Weak peaks at 1630–1660 cm^{-1} in samples (**2**) and (**4**) are consistent with carbonyl groups, while weak peaks in the fingerprint region at 615 cm^{-1} and 645 cm^{-1} in (**3**) are consistent with imidazole groups.

The chemical modifications of paper sample (**2**, **3**, and **4**) is based on direct modification of hydroxyl groups and is more likely restricted to partial grafting of the outer cellulose layer. Hydroxyl groups are involved in a wide ranging hydrogen bond network, which is responsible for the structure of cellulose fibers [404]. Therefore, a high degree of substitution is generally undesirable, a condition well noted in the literature [404] and observed in course of this work; whether from tearing of cellulose fibers or formation of cellulose particle suspension. Moreover, the accessibility of the reactive groups is determined by the crystallinity of cellulose fiber, and not all regions can be penetrated by chemical reagents [404].

4.2.2.1 Quantification of accessible functional groups

The densities of *accessible* functional groups in chemically modified paper were determined using colorimetric methods. The accessible aldehyde content in sample (**2**) was determined using a redox reaction with 2,3,5-triphenyltetrazolium chloride (TTC), primary amine content in (**5**) was estimated with ninhydrin, and thiol content in (**4**) and (**6**) was determined with Ellman's reagent. The summary of corresponding reactions is given in Scheme 4.1.



Scheme 4.1 Colorimetric tests used to estimate the surface densities of accessible functional groups. Aldehyde content was measured in sample (2) with TTC, primary amine content in sample (5) was measured with ninhydrin, and available thiol groups in samples (4b) and (6b) were determined with Ellman's reagent.

The density of accessible aldehyde functional groups in paper sample (2) was estimated to be 23 ± 3 nmol per mg paper with TTC reagent. The oxidation with TTC is a well established method for quantification of the reducing end groups in carbohydrates [447]. Upon oxidation of the aldehyde groups in basic medium to the corresponding carboxylic acid groups, a purple-coloured triphenyl formazan (TTC formazan) is formed, as shown in Scheme 4.1. Absorption spectra of TTC formazan is shown in Figure 4.4A. An improved method was developed by Strlic and Pihlar, where the reaction was done in a dimethylacetamide (DMAc)/LiCl solvent system in

the presence of *tert*-butylamine at 75°C for 10 min [448]. These conditions minimize cellulose hydrolysis often observed using KOH (*aq.*) solvent leading to the overestimation of aldehyde groups. Here, DMAc/LiCl reaction conditions were used and *tert*-butylamine base was substituted by diisopropylethylamine (DIPEA). Once the reaction was complete, it was diluted with ethanol, as TTC formazan had good solubility in alcohols. The colorimetric quantification was done in ethanol at 480 nm and an experimentally determined molar absorption coefficient for TTC formazan ($\epsilon_{480} = 17,180 \text{ M}^{-1}\text{cm}^{-1}$), as shown in Figure 4.4A-B. The product of the reaction was easily extracted into ethanol without signs of non-specific adsorption to paper. The variation between samples within the same batch was less than 8% and variation between different batches was less than 12%.

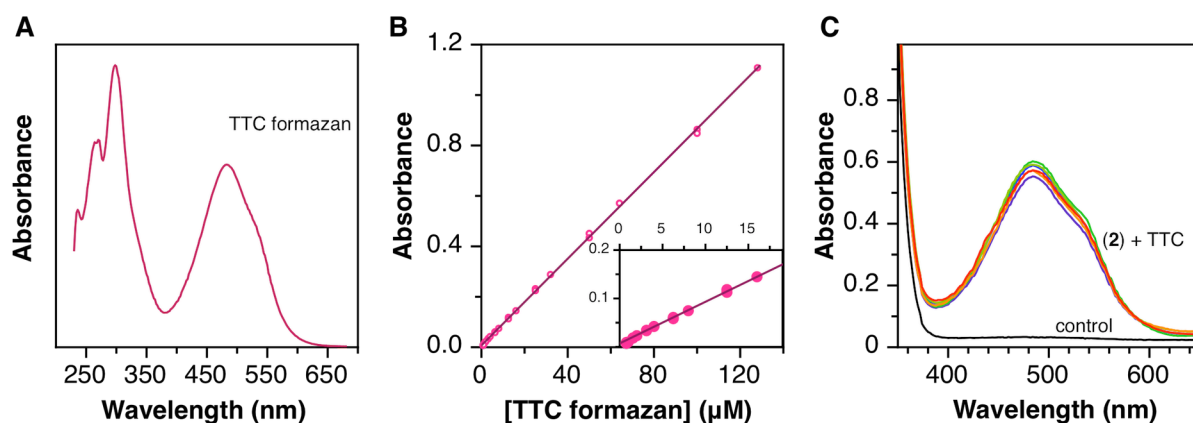


Figure 4.4 (A) Absorption spectra for 1,3,5-triphenyl formazan (TTC formazane) in ethanol. (B) Calibration curve used to determine molar absorption coefficient for TTC formazane (slope = $8590 \text{ M}^{-1}\text{cm}^{-1}$, path length $b = 0.5 \text{ cm}$) in ethanol. The inset shows the calibration curve fit at lower concentrations of TTC formazan. (C) Experimental data for quantification of aldehyde functional groups in six replicate samples of paper substrate (2), the control sample corresponds to measurements made with untreated cellulose paper (1). All spectra were collected in > 97.5% ethanol.

Quantification of primary amines introduced onto cellulose paper with APTES was done spectrophotometrically using ninhydrin, as shown in Scheme 4.1. Although ninhydrin is mostly intended for qualitative analysis [449], quantification is also possible [450-452]. In contrast to TTC formazan, Ruhemann's purple, a product of the reaction of ninhydrin with primary amine group, exhibited strong adsorption to paper substrate (5). The challenge of non-specific

adsorption of the products of ninhydrin reaction has been reported in the literature. Sarin *et al.* have proposed that ion-exchange mechanism is responsible for the formation of negatively charged coloured product strongly bound to quaternary amine resin [450]. All attempts in this work to fully recover purple coloured product from paper substrates either with base (*i.e.* triethylamine) or acid (*i.e.* acetic acid) were not successful. Therefore, quantification was done by combining measurements from the solution with those made directly on paper substrates by measuring absorbance at 560 nm, as shown in Figure 4.5A. The fraction of Ruhemann's purple recovered in the solution was typically in the range 1.5–3.0 nmol per mg paper. In order to quantify the amount of Ruhemann's purple retained on the paper, a calibration curve was prepared by adding known amounts of Ruhemann's purple to circular paper samples and absorbance was measured by sandwiching paper substrates between the windows of a NanoQuant plate. Representative data for such calibration is shown in Figure 4.5A-B. The Ruhemann's purple was synthesized using ethanolamine as a source of primary amine group and quantified using $\epsilon_{570} = 15,700 \text{ M}^{-1}\text{cm}^{-1}$ [450]. Based on this approach the estimated density of primary amine groups in sample (**5**) was calculated as sum of the number of moles determined from the solution and paper substrate, resulting in 1.8–4.1 nmol per mg paper. It should be noted again that this estimate corresponds to the number of accessible groups, whereas the actual number may be significantly higher.

The density of thiol groups in paper substrates (**4b**) and (**6b**) were estimated using Ellman's reagent as shown in Scheme 4.1. The product of the reaction, TNB^{2-} , is water-soluble and did not exhibit non-specific interactions with cellulose paper. Based on the strong absorption of TNB^{2-} at 412 nm in basic pH ($\epsilon_{412} = 14,150 \text{ M}^{-1}\text{cm}^{-1}$) [453], the number of thiol groups was estimated to be 16 ± 3 nmol per mg of paper substrate (**4b**) and 1.5 ± 0.2 nmol per mg of paper substrate (**6b**). Representative absorption spectra used in quantification of thiol groups are shown in Figure 4.6.

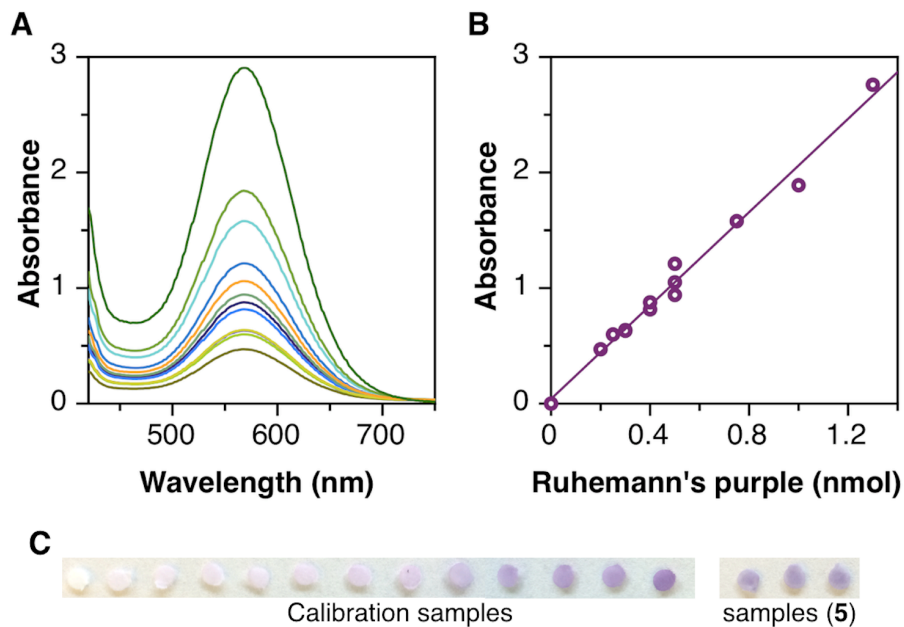


Figure 4.5 (A) Representative absorption spectra for Ruhemann's purple collected to construct a calibration curve, shown in panel (B). (C) Digital photographs of paper samples with spotted Ruhemann's purple solution used for calibration curve and three replicate samples of (5) used for quantification of primary amines.

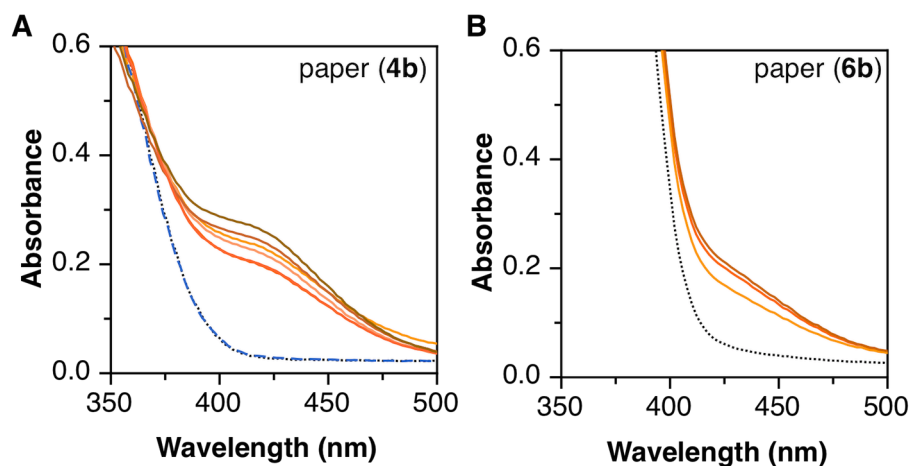


Figure 4.6 Representative absorption spectra showing formation of TNB²⁻ product as a result of the reaction of Ellman's reagent with thiol ligands (A) in paper substrate (4b), and (B) in paper substrate (6b). Control sample measured on untreated paper (1) (black dashed line) and blank sample containing no paper substrate (dashed blue line) are also shown for a reference.

4.2.3 Immobilization of quantum dots

Water-soluble QDs capped with GSH, MPA, cysteine, DHLA, DHLA-PEG, and zwitterionic ligands were readily immobilized on paper substrates modified with imidazole (**3**), lipoic amine (**4b**), and lipoic acid (**6b**). Immobilization was almost instantaneous and no difference in the density of immobilized QDs was observed at 5 min, 30 min, or 1 h. The immobilization efficiency was confirmed with absorbance measurements. QDs were not retained on unmodified paper (**1**). In the case of lipoic amine (**4**) and lipoic acid (**6**) substrates, the affinity for QDs was tested both with and without reduction of the dithiolane group (**4a**, **6a**) to a dithiol group (**4b**, **6b**). The dithiolane group does not exhibit strong affinity for inorganic ZnS shell of QDs, while dithiol groups exhibit high affinity (see Section 1.3.5.1). Therefore, QD PL intensity measured from substrates (**4a**) and (**6a**) is attributed to non-specific QD adsorption. With dithiol modified substrate (**4b**) the contrast was *ca.* 5-fold stronger QD PL intensity in comparison to its dithiolane form (**4a**). In contrast, APTES substrates (**5**) and APTES+LA substrates (**6a** and **6b**) showed no difference in measured QD PL intensities. Strong interaction between carboxylate functionalized QDs and amine terminated substrate (**5**) is attributed, in part, to electrostatic attractions and hydrogen bonding, while extensive QD adsorption on (**6a**) substrate may be attributed to various reasons. For example, multilayer formation of APTES may generate complex structures capable of physical entrapment of QDs, or remaining unreacted primary amine groups promote adsorption of negatively charged QDs *via* electrostatic interactions. Figure 4.7 shows representative data for immobilization of DHLA-capped red-emitting QDs (*i.e.* DHLA-QD630). The brightness of the spots was determined by two main factors: the efficiency of immobilization, and the effect of the immobilizing ligands on the quantum yield of the QDs. Retention of optical properties (*i.e.* quantum yield) of QDs is highly desirable, as it improves signal-to-noise ratio, improves sensitivity of the assay and leads to larger Förster distances in FRET-based assays. Samples (**4b**) and (**6b**) had *ca.* 50% and 62%, respectively, of the brightness of the samples prepared with imidazole ligands (**3**). No significant difference was observed in the peak emission wavelength or FWHM of QD PL between three immobilization chemistries.

The maximum loading capacity of QDs in paper samples modified with various ligands was estimated by titration. Addition of up to 2 pmol of QDs per circular sample (3 mm diameter, *ca.* 0.9–1.2 mg) resulted in nearly 100% immobilization efficiency. Beyond this point, increasing the amount of QDs spotted on the sample correlated with a slight but gradual increase in the amount of immobilized QDs, albeit with exponentially decreasing immobilization efficiency. Saturation of circular paper samples (3 mm diameter) with immobilized QDs was observed at 3.2 ± 0.6 pmol per samples (~ 1 mg) for **(3)** and **(4b)**, whereas *ca.* 4.5 pmol were immobilized on paper sample **(6b)**. Given that the estimated density of thiol groups on the surface was *ca.* 16 nmol per mg of paper sample **(4b)**, an average of up to 5000 ligands are available per QD, whereas ~ 360 thiol ligands were available per QD with paper samples **(6b)**. Given that QD nanocrystals exhibit curvature and are not expected to pack very closely on the surface, it is likely that not all available thiol ligands interacted with a QD shell.

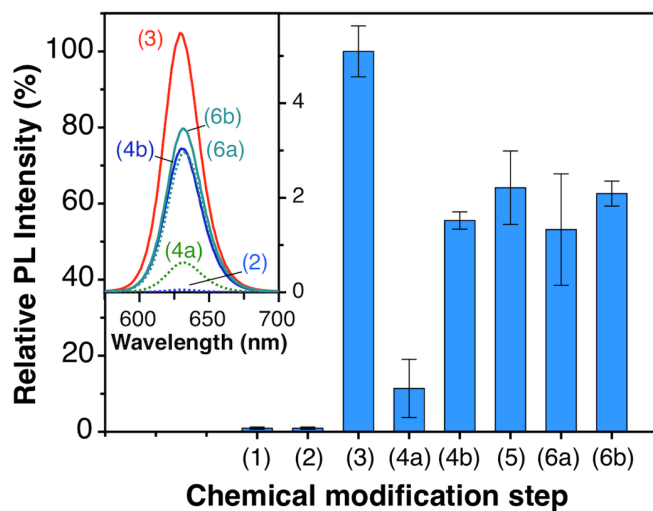


Figure 4.7 Background corrected relative PL intensity of chemically modified paper substrates (according to ligands shown in Figure 4.1) after exposure to DHLA630 QDs. All data was normalized to the brightest sample functionalized with imidazole ligands **(3)**. Paper substrates **(3)**, **(4b)**, and **(6b)** functionalized with surface ligands for specific QD immobilization. Paper substrate **(2)**, **(4a)**, **(5)**, and **(6a)** retained QDs due to non-specific interactions. Error bars represent the standard deviation of three replicate measurements. The inset shows the corresponding QD PL emission spectra for selected modification steps. Dashed lines are used to show QD PL intensity from paper substrates **(2)**, **(4a)**, and **(6a)** that are not expected to have strong interactions with QDs (*i.e.* dithiolane groups in **(4a, 6a)** versus dithiol groups in **(4b, 6b)**) and signals are attributed to non-specific QD adsorption.

The structural morphology of cellulose paper after chemical treatment and QD immobilization was evaluated using SEM imaging. As shown in Figure 4.8, the arrangement of cellulose fibers was unaffected and QDs were immobilized at high density. The morphology of QD-modified samples varies between samples **(3)**, **(4b)**, and **(6b)** with progressively greater immobilization density. Although, it appears in all samples that QDs are packed closely together, these images are not a true representation of common bioassay conditions. SEM images were acquired on dry, dehydrated samples, whereas under aqueous assay conditions, cellulose fibers swell and expand, which would increase the distance between QDs.

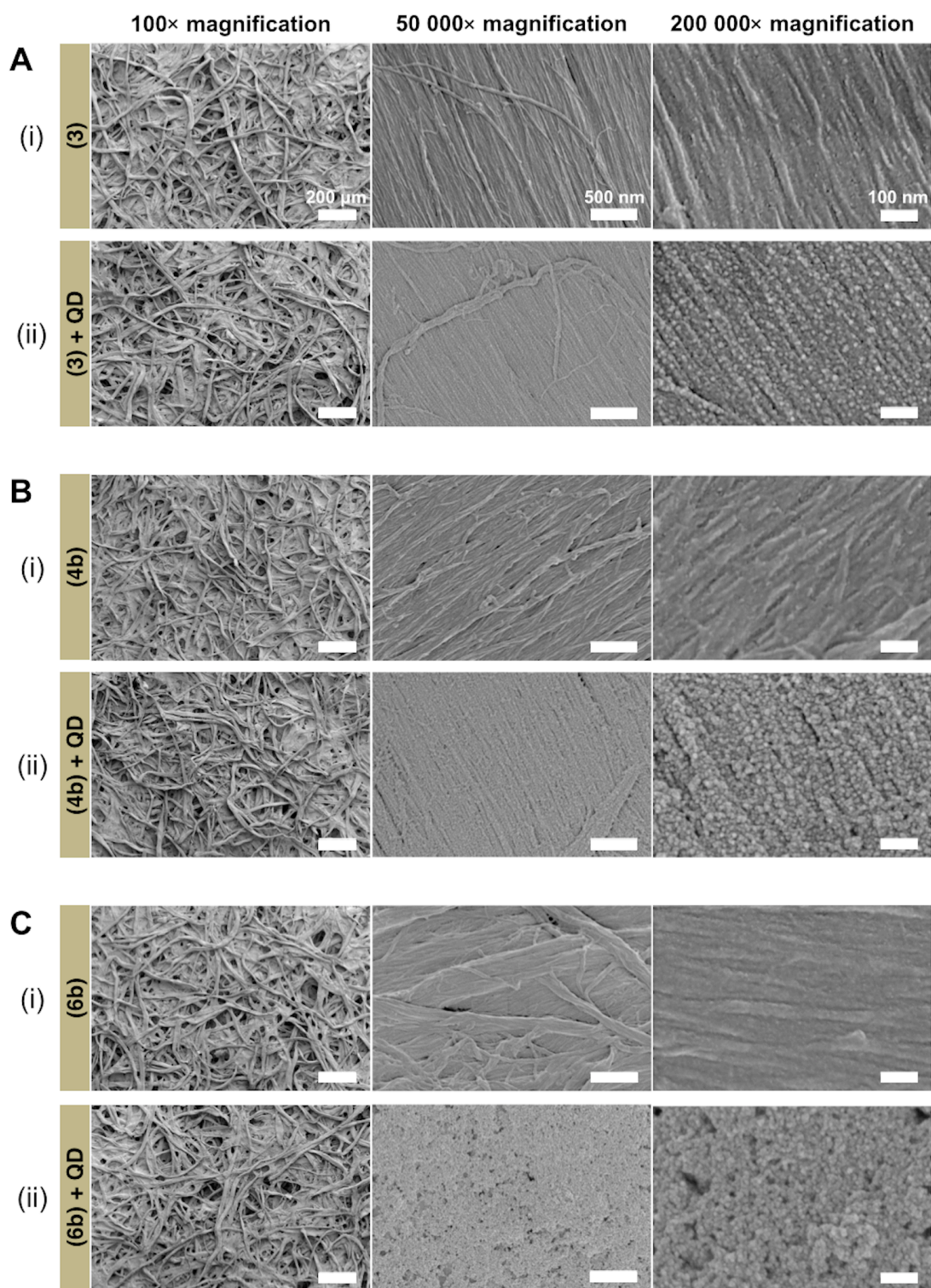


Figure 4.8 SEM images for cellulose paper modified with **(A)** imidazole, **(B)** lipoic amine, and **(C)** APTES and lipoic acid before (i) and after (ii) exposure to QDs. All scale bars are 200 μm for 100× magnification, 500 nm for 50 000× magnification, and 100 nm for 200 000× magnification.

Despite the higher density of immobilized QDs in thiol-modified paper samples, there was lower PL intensity (*cf.* imidazole) as shown in Figure 4.7. In the development of paper-based bioassays, it is desirable that QDs retain their optical properties upon immobilization. Any variability in the synthesis of QDs including the quality of the protective ZnS shell, is expected to affect the degree of change of their quantum yield upon immobilization. However, for a consistent batch of QDs, a question arises whether there are trends in optical changes between immobilization chemistries. Thiol ligands are known to decrease the quantum yield of QDs, as has been shown in literature for ligand exchange [454, 455] and immobilization methods [456]. The retention of higher quantum yield is typically associated with minimal damage to the ZnS shell, while harsh conditions can promote etching of Zn²⁺ ions generating trap states. Various attempts to modify ligand exchange protocols to retain high quantum yield have been reported, with the general trend of removing any thiolitic hydrogen which otherwise contribute to the formation of an acidic environment [262, 455, 457, 458].

Under typical immobilization conditions, the samples (**4b**) and (**6b**) were prepared by reducing the dithiolate ring with subsequent treatment with acidic buffer (pH 4.5) to quench any residual reducing agent and ensure protonation of thiols to minimize reoxidation. These conditions are expected to create a slightly acidic environment at the cellulose interface that affects QDs in two ways: (i) acid-driven etching and a decrease in the quantum yield of the QDs, and (ii) protonation of QD surface ligands (*e.g.* DHLA, GSH) altering their colloidal stability and stimulating immediate QD collapse to the interface. The latter can also contribute to the reduced inter-QD separation as a result of surface charge screening and a decrease in inter-QD electrostatic repulsion. This phenomenon typically contributes to QD aggregation in solution with a decrease in pH or an increase in ionic strength. In a typical immobilization procedure, 1.0 μ L of QD solution prepared in basic buffer is spotted on a 3 mm diameter circular paper substrate. Although it was expected that the buffering capacity of the QD buffer would be able to counteract any substantial changes in pH, a quick test with pH indicator dye Alizarin Red S, that changes colour from yellow to red over 4.6–6.0 pH range, indicated that the pH within the paper substrate was closer to 5-6. The effect of QD buffer composition (*i.e.* pH and its buffering capacity) on the brightness of QDs upon immobilization was evaluated. As shown in Figure 4.9A, the amount of QDs that was immobilized on the paper was not affected by changes in the

buffer composition and there are minimal changes in UV-visible absorption spectra of QDs immobilized on paper substrate. However, QD PL intensity measured for the same samples (Figure 4.9B) showed an increase of ~20% upon increasing pH from 8.5 to 9.2 and increasing ionic strength (*i.e.* buffering capacity) from 50 mM to 100 mM.

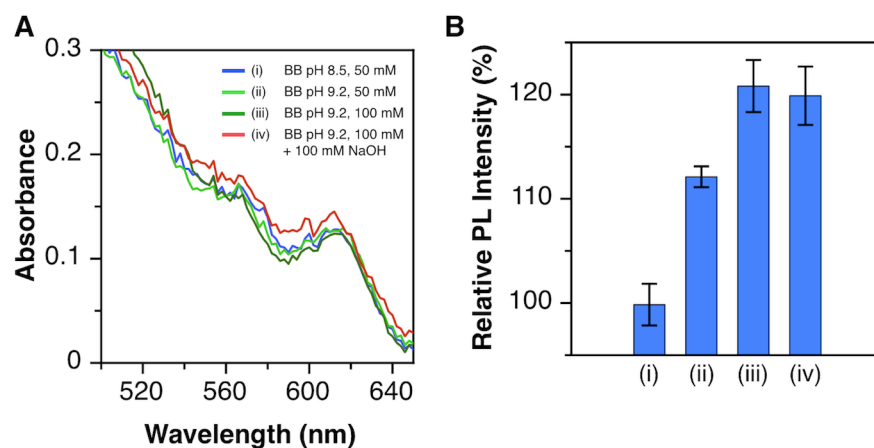


Figure 4.9 Effect of buffer composition on optical properties of immobilized QDs in paper substrate (**4b**). **(A)** Absorption spectra of immobilized QDs deposited from different buffer solutions. **(B)** Relative QD PL intensity corresponding to **(A)** showing that increase in buffer pH and its buffering capacity is accompanied with higher brightness of immobilized QDs.

Next, a set of the experiments was done with the goal of increasing the pH within the paper matrix prior to immobilization of QDs. Given the effect of pH on the brightness of immobilized QDs, the conditions summarized in Table 4.2 were evaluated to determine the effect of interfacial pH on QD immobilization. It was observed that the choice of reducing agent (NaBH_4 vs. Tris(2-carboxyethyl)phosphine hydrochloride, TCEP) did not have a pronounced effect; however, additional steps for washing paper substrates with water, tris-borate buffer (pH 7.4) or borate buffer (pH 9.2) prior to QD immobilization resulted in significant decrease in the amount of QDs captured on paper, as shown in Figure 4.10A. One of the possible reasons for the decrease in the number of QDs captured on the paper is the re-oxidation of dithiol groups to dithiolane. However, the rate of re-oxidation was not expected to be significant at neutral pH. Furthermore, it has been shown that pK_a 's of functional groups can be elevated by few units at the interface [459-461]. Despite the decrease in the number of QDs captured on paper substrate

(4b), the measurements of QD PL indicated that the pre-treatment step used to increase the pH within paper matrix correlated with better retention of the brightness of QDs upon immobilization (see Figure 4.10B).

Table 4.2 Summary of paper substrate (4b) pre-treatment procedures evaluated for QD immobilization.

	Wash 1	Wash 2	Relative Absorbance at 610 nm (%)	Relative QD PL at 628 nm (%)
(i)	Ammonium acetate buffer (pH 4.5)	Ammonium acetate buffer (pH 4.5)	100	100
(ii)	Ammonium acetate buffer (pH 4.5)	Water	20	71
(iii)	Ammonium acetate buffer (pH 4.5)	Tris-borate buffer (pH 7.4)	36	83
(iv)	Ammonium acetate buffer (pH 4.5)	Borate buffer (pH 9.2)	18	77
(v)	Ammonium acetate buffer (pH 4.5)	ZnCl (1 mM, pH 7)	60	89

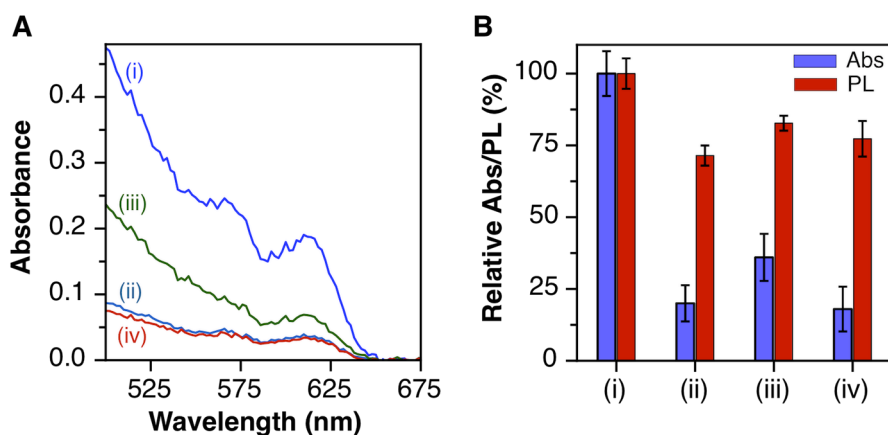


Figure 4.10 Effect of paper substrate (4b) pre-treatment with different buffers on the density of immobilized QDs and their relative brightness. **(A)** Absorption spectra collected for immobilized QDs on paper substrates washed with (i) ammonium acetate (pH 4.5), (ii) water, (iii) tris-borate buffer (pH 7.4), and borate buffer (pH 9.2), as noted in Table 4.2. **(B)** Relative QD absorption from (A) at 610 nm and corresponding PL intensity at 628 nm. Both QD absorption and emission are normalized to sample (i).

Inspired by the work of Liu and Snee [262], paper samples with reduced thiols (**4b**) and (**6b**) were also treated with ZnCl solution (pH 7) to remove thiolytic hydrogen (see Table 4.2), while retaining the thiols in their reduced form. In this approach, the amount of immobilized QDs estimated from the absorbance was still lower (*ca.* 60%) in comparison to the general protocol employed (*i.e.* paper sample (i)). However, QD PL intensity in this paper sample (v) was *ca.* 90% of acid pre-treated paper sample (i), indicating the extent of QD PL quenching can be reduced by pre-treatment of paper samples with aqueous zinc solution. This result is also consistent with the retention of higher quantum yield of QDs during ligand exchange with metalated ligands [262]. Given the results outlined above it can be summarized that acidic environment within thiol-modified samples is necessary to promote QD immobilization at high density with concomitant decrease in quantum yield of QDs.

In the evaluation of the methods for QD immobilization, another important parameter is the homogeneity of the distribution of QDs along cellulose fibers. Although SEM images (Figure 4.8) provided information about the relative density of QDs on the surface, two-photon 3D fluorescence imaging was used to investigate the microscopic distribution of QDs. Figure 4.11 shows representative images for immobilization of DHLA capped QD630 (*i.e.* DHLA-QD630) on paper samples (**3**), (**4b**), and (**6b**). A uniform distribution of QDs was observed in all cases based on qualitative image analysis, whereas samples modified with multilayered APTES+LA (**6b**) exhibited clusters of QD aggregates. Quantitative image analysis was not informative, presumable due to intrinsic heterogeneous structure of the cellulose fibers.

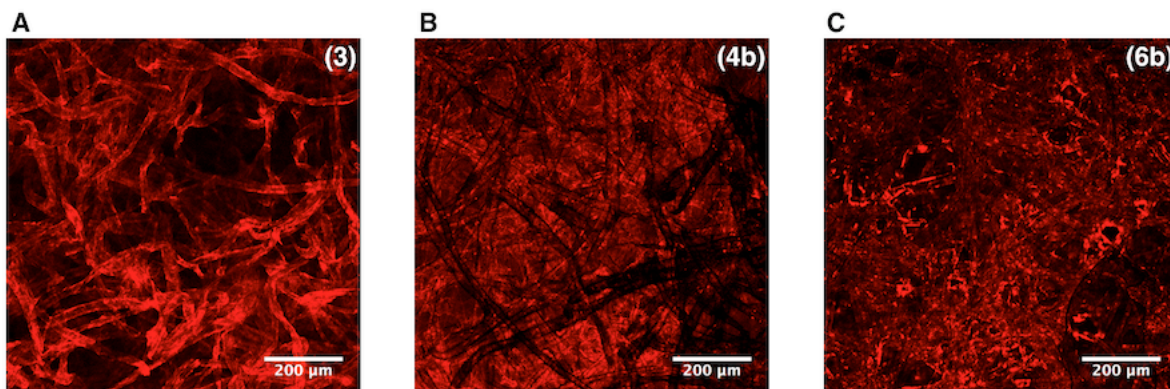


Figure 4.11 Two-photon imaging of immobilized QD630 (**A**) on paper substrate (**3**), (**B**) on paper substrates (**4b**), and (**C**) on paper substrates (**6b**).

4.2.3.1 Photobleaching

Bioassays aimed to evaluate response over time (*i.e.* kinetics) require continuous illumination of samples over longer periods of time. Although QDs are generally known to resist photobleaching, the effect of the underlying immobilization chemistry was evaluated. The photobleaching behavior of eight different samples was investigated: DHLA-QD525a and DHLA-QD630, immobilized on paper samples **(3)**, **(4b)**, **(6b)**, and in solution. Representative time-traces for DHLA-QD630 PL are shown in Figure 4.12. There was *ca.* 20% increase in QD PL over 4 h for QDs immobilized on imidazole ligand modified paper **(3)** and APTES+LA modified paper substrate **(6b)**. In contrast a 12–20% decrease in QD PL was observed for the QD samples in solution and those that used thiol ligands **(4b)** for QD immobilization. No sign of precipitation of aqueous QDs in solution was observed over the course of measurements. The excitation power (27 mW) used to evaluate photobleaching was substantially greater than what would be encountered in designs used for smartphone imaging applications. For instance, the maximum output from the blue filtered flash light of a smartphone is 2.3 mW (see Chapter 2), and output from a UV lamp is 0.9 mW and only about 0.08 mW reaches the sample (see Chapter 3).

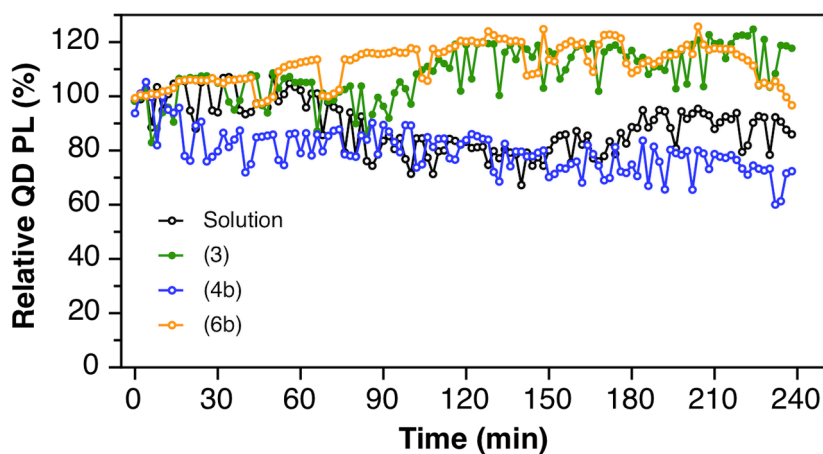


Figure 4.12 Photobleaching and photobrightening of QD630 capped with DHLA ligands in solution (black trace) and immobilized in paper substrates **(3)** (green trace), **(4b)** (blue trace), and **(6b)** (orange trace).

4.2.3.2 Long-term stability of QD-paper substrates

One of the main criteria for the development of test strips for POC diagnostics is their long-term stability. Fluorescence can be highly sensitive to its environment and various factors may contribute to the degradation of PL properties. The stability of QD PL is largely determined by the quality of the nanocrystal, its protective ZnS shell and ligands at its interface that can promote formation of surface states. As was noted above, thiol-modified paper samples induced a decrease in QD PL upon immobilization in comparison to imidazole ligands. The effect of these surface ligands on QD PL over 5 months was investigated using two types of QDs (DHHLA-QD525a and DHHLA-QD630), and two surface chemistries (imidazole sample **(3)** and lipoic amine sample **(4b)**). Parameters that were considered included (i) temperature, as either room temperature or 4°C; and (ii) media, as buffer, buffer/glycerol (1:1 v/v), or dry samples. Some samples were also stored in 60% glycerol at -20°C. Representative results for DHHLA630 QDs are shown in Figure 4.13. For all sets of conditions tested, QDs immobilized on paper samples **(3)** retained the most amount of their initial intensity over a 150-day period. One of the main causes of QD PL quenching is oxidation [462]. Therefore, re-oxidation of dithiols in paper sample **(4b)** can be a contributing factor to the loss of QD PL. Samples stored in buffer also exhibited much faster decay of the QD PL in comparison to the glycerol mixture. More than 95% of QD PL was lost after one day when paper samples **(4b)** were stored in buffer. As expected, the rate of the QD PL decrease was much faster at room temperature in comparison to samples stored at 4°C. Interestingly, samples stored dry showed the most resistance to the loss of QD PL, although no precaution was taken to seal samples from air. For instance, samples prepared on paper **(3)** and stored dry at 4°C have shown only *ca.* 8% loss in QD PL. Over 80% of QD PL signal was retained after 150 days on paper **(4b)** stored in 60% glycerol at -20°C (*cf.* 30% at 4°C and 0% at RT).

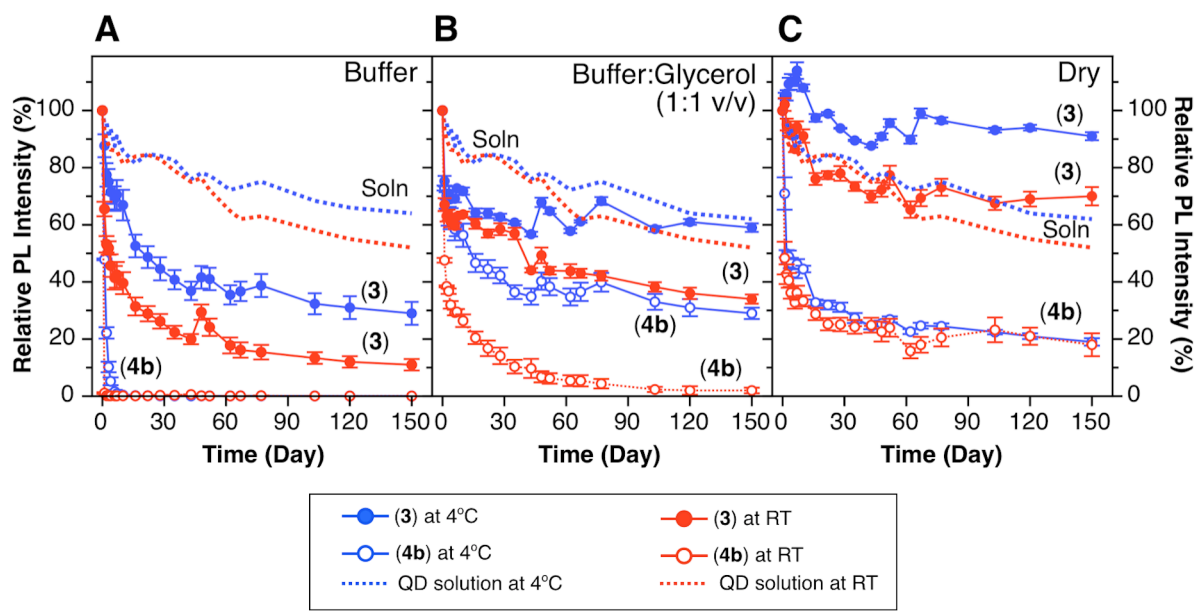


Figure 4.13 Comparison of storage stability of immobilized DHLA-QD630 on imidazole ligand modified paper (**3**) and lipionic amine modified paper (**4b**) in different media (**A**) buffer, (**B**) buffer:glycerol (1:1 v/v), and (**C**) dry samples as function of temperature (4°C and room temperature, RT). The PL intensity of QDs in solution is also shown for reference (dashed line). All data points are normalized to Day 0 and error bars represent the standard deviation of three replicate measurements.

4.2.4 Immobilization of QD-peptide bioconjugates

4.2.4.1 FRET on paper substrates

To investigate the immobilization of QD-bioconjugates in paper samples and compare FRET between bulk solution and a cellulose paper matrix, green-emitting GSH-capped QDs (GSH-QD525a) and Alexa Fluor 555 (A555) labeled peptides were chosen. As was noted in Section 1.3.6.1 QD525 donors and A555 acceptor have the necessary spectral overlap for FRET to take place, while there is a minimal crosstalk between QD PL and A555 emission, such that ratiometric (*i.e.* PL ratio) analysis can be easily applied. For the specific FRET pair used in this chapter, the spectral overlap was $5.93 \times 10^{-10} \text{ cm}^6 \text{ mol}^{-1}$ and the Förster distance was 5.9 nm ($\Phi_{\text{QD}} = 0.4$). The measured quantum yield of A555 conjugated to peptide was *ca.* 0.09. QD-peptide bioconjugates were prepared *via* self-assembly driven by high affinity between the inorganic ZnS shell of the QD and the hexahistidine (His-tag) end of the peptide [369].

Solution-phase samples were used as a reference point to evaluate FRET with immobilized bioconjugates. As shown in Figure 4.14A, the assembly of QDs with an increasing number of A555 labeled peptides resulted in a characteristic decrease in QD PL and increase in FRET-sensitized emission of A555 acceptor. The FRET efficiency calculated from QD PL quenching according to eqn. 1.23 indicated that the average donor-acceptor separation measured from the center of QD to A555 fluorophore was *ca.* 7.0 nm. The diameter of QDs estimated from TEM images (see Chapter 2, Figure 2.18, QD525a) was 4.6 ± 0.5 nm. Therefore, A555 is located approximately 3.6 nm from the surface of QD. The maximum peptide extension is expected to be 8.7 nm (using an estimate of 23 amino acids and a length of 0.38 nm per residue, with the assumption that the six histidine residues are bound to the QD surface and do not contribute to extension of the peptide), indicating that peptide is either tilted relative to QD surface or folds into a secondary or tertiary structure, thus bringing A555 dye closer to the surface. The trend in the PL ratio with an increasing number of A555 acceptors shown in Figure 4.14A (iii) was non-linear. Although, a linear trend is expected under ideal conditions [388], similar behaviour for QD-dye FRET pair was observed previously [463].

Immobilization of QD-peptide bioconjugates within paper samples modified with imidazole ligands (**3**) or thiol ligands (**4b**, **6b**) was possible either in a two step-procedure where QDs were immobilized first, followed by addition of peptide, or in a single step by preassembling QD-peptide conjugates prior to spotting on the paper substrate. The latter approach was convenient for FRET analysis, as the number of peptides assembled per QD could be controlled simply *via* stoichiometry of the solution. Therefore, this approach was used throughout this chapter and in Chapter 6, whereas two-step preparation of immobilized QD bioconjugates was adopted in Chapter 5.

QD-peptide conjugates prepared in solution (Figure 4.14A) were subsequently immobilized on paper samples (**3**), (**4b**), and (**6b**). Representative absorption and PL spectra for bioconjugates immobilized on paper (**3**) are shown in Figure 4.8B. The absorbance spectra remained essentially unchanged between bulk solution and paper matrix. However, PL spectra show more significant sensitization of A555 emission. It should be noted that PL spectra collected from paper samples was normalized to QD emission to account for the scattering by paper substrates, variation in the amount of sample (*e.g.* cellulose fiber and pore volume) present in measuring volume. It was

possible to determine relative PL ratio and FRET efficiency from normalized data according to eqn. 4.4 (see Section 4.4.11).

Another important observation was between fully hydrated, wet samples and dry samples, as shown in Figure 4.14B-C. Recently, it was reported that an enhancement in FRET efficiency within a paper matrix can be achieved for QD-oligonucleotide conjugates upon drying in the presence of high salt [312]. In contrast, enhancement in FRET with QD-peptide bioconjugates that was observed in this work did not require any additional reagents. Furthermore, there is a strong influence on the observed FRET efficiency between different paper substrates. These trends are also in good agreement with observed densities of immobilized QDs shown in Figure 4.8. The higher the density of immobilized QDs, the greater the magnitude of the observed enhancement in FRET efficiency. For instance, Figure 4.15 shows that paper samples modified with imidazole ligands (**3**) exhibited similar PL ratio slope as the one measured for QD bioconjugates in solution. FRET efficiency estimated from the relative QD and A555 intensities is shown in the inset of Figure 4.15 and was used to determine the effective donor-acceptor separation (eqn. 4.4 and eqn. 1.27). The effective QD-A555 separation distance for conjugates in the solution was calculated to be 7.0 nm (consistent with 7.0 nm calculated from QD PL quenching data). A progressive decrease in separation distance was observed for paper samples (**3**), (**4b**), and (**6b**) with calculated values of 6.8 nm, 5.9 nm, and 5.5 nm, respectively. Further decreases in the effective QD-A555 separation distance was observed in dry paper samples (Figure 4.8C – iii) with 5.5 nm, 4.8 nm, and 5.0 nm determined for paper samples (**3**), (**4b**), and (**6b**), respectively.

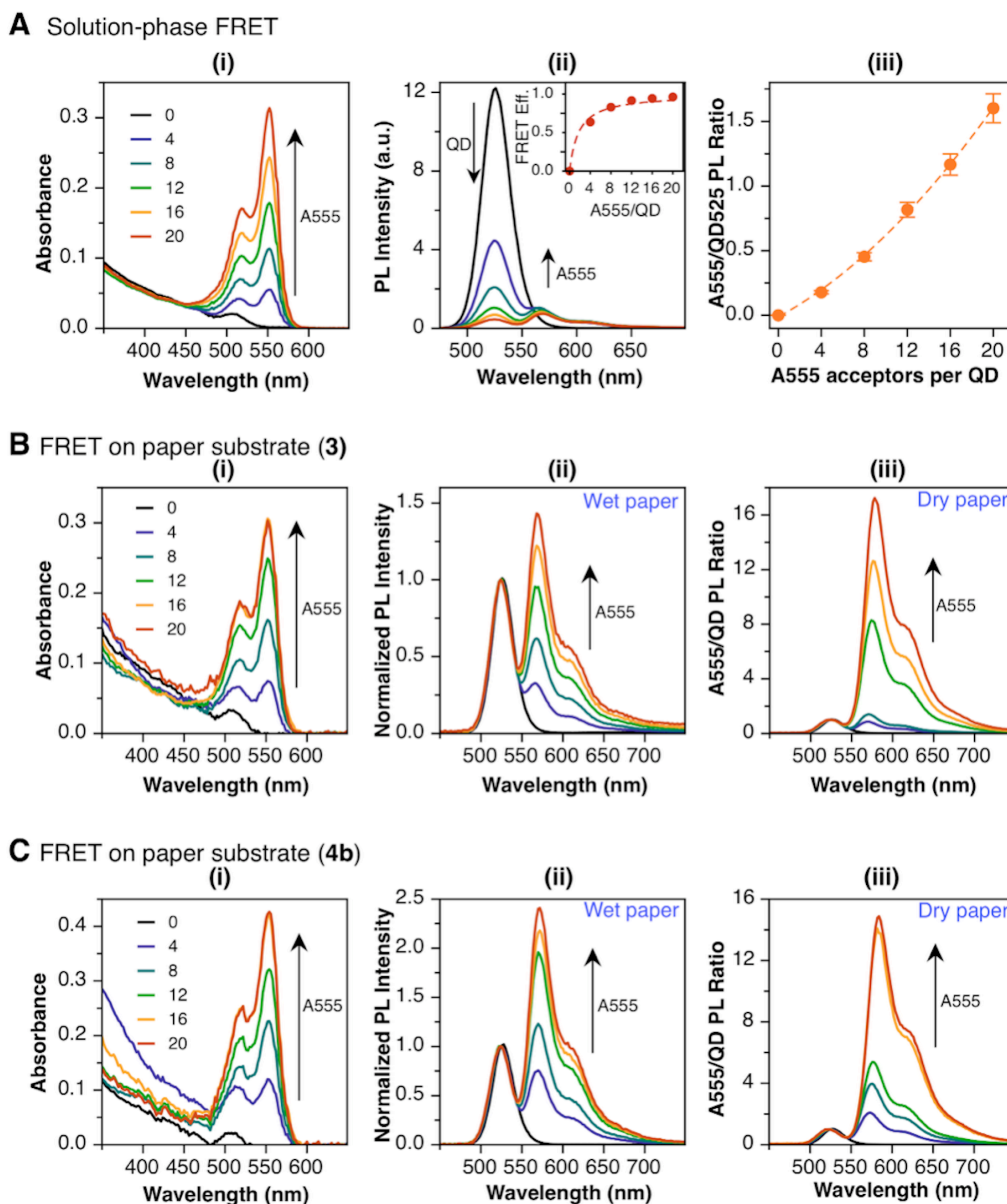


Figure 4.14 FRET characterization. **(A)** Solution-phase FRET (i) Representative absorption spectra showing assembly of 0, 4, 8, 12, 16, and 20 A555-labeled peptides per QD, (ii) PL emission corresponding to samples in (i). The inset shows the FRET efficiency as a function of the number of A555 acceptors calculated from quenching of QD PL according to eqn. 1.24, (iii) The A555/QD PL ratio as a function of the number of A555 acceptors. **(B)** Representative paper-phase FRET on imidazole modified paper **(3)**. (i) Absorption spectra showing paper-phase assembly of QD bioconjugates prepared with 0, 4, 8, 12, 16, and 20 of A555-labeled peptides. (ii) PL spectra corresponding to (i) measured from fully hydrated paper samples, and (iii) PL spectra corresponding to (i) measured from air-dried samples. **(C)** Same as (B) on lipoic amine modified paper substrate **(4b)**.

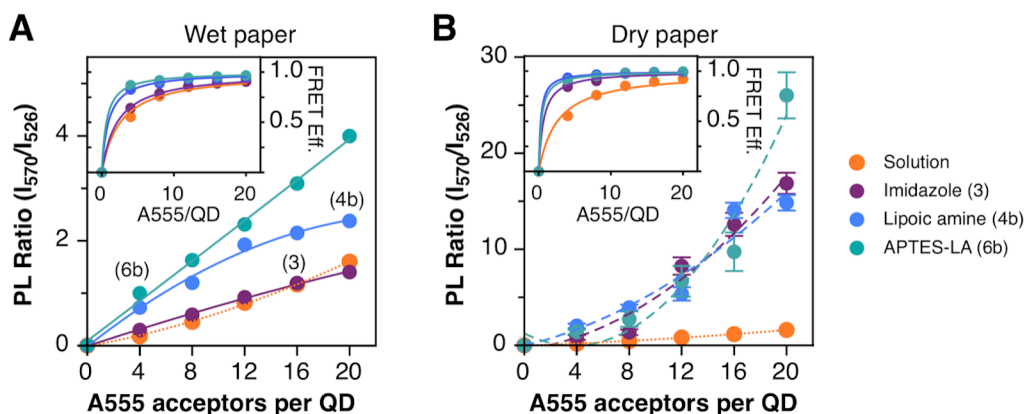


Figure 4.15 Comparison of A555/QD PL ratio and FRET efficiency for QD bioconjugates immobilized in paper samples (3), (4b), and (6b) shown for hydrated samples (A) and dry samples (B). FRET efficiency was calculated using eqn. 4.4. Corresponding PL spectra are shown in Figure 4.14.

Overall, the FRET behaviour of QD-bioconjugates immobilized on paper samples modified with imidazole ligands (3) were not strongly influenced by the underlying immobilization chemistry or potential interactions with neighboring QDs. The PL ratios and the FRET efficiencies determined for QD-A555 conjugates were in close agreement between solution-phase samples and those immobilized on paper substrate (3), as shown in Figure 4.14A-B and Figure 4.15A. In contrast, thiol ligand modified paper samples (4b and 6b) induced a significant enhancement in the observed FRET efficiency of immobilized QD525-A555 bioconjugates (see Figure 4.14C and Figure 4.15). Given that these surface chemistries also produced a higher density of immobilized QDs, a possible reason for the observed enhancement within the paper matrix is a physical decrease in the average separation between QDs and A555 acceptors. The overall *apparent* FRET efficiency of the system is the result of the probability of the acceptor to receive energy transfer *via* FRET (*effective* acceptor concentration dependence) and the probability of the donor to locate an acceptor in close proximity to transfer the energy (*effective* donor concentration dependence). As the inter-QD distance decreases upon immobilization, a simple spherical symmetry model for single QD donor–multiple acceptor system may be more appropriately described as a multiple donors–multiple acceptor system, where positioning of the dyes acceptors is not strictly spherically symmetric. As such, the effective donor-acceptor separation distance represents an average of the distribution of possible donor-acceptor distances.

These configurations can provide a greater overall number of donor-acceptor interactions, resulting in a greater probability of FRET. Although this model for FRET enhancement is plausible, there are limitations in quantitative analysis due to inherent assumptions of Förster formalism (*e.g.* orientation factor, refractive index) and assumptions that optical properties of QDs and dyes do not change upon immobilization (*e.g.* quantum yield). Furthermore, possible changes in peptide conformation at the QD interface can contribute to the observed enhancement in FRET efficiency. In fully hydrated paper samples, the conformation of peptide bound to QD is likely unaffected, since there was no difference between FRET efficiency measured in bulk solution and in wet samples (**3**). However, conformation of peptide in dry paper samples may be very different.

4.2.4.1.1 Fluorescence lifetime imaging microscopy (FLIM)

The enhancement of FRET efficiency observed for QD525a-A555 bioconjugates immobilized in paper samples (**4b**) was further analyzed with FLIM measurements. This technique is ideal for this purpose since the time-domain PL data is relatively immune to differences in absolute steady-state intensity and background levels between samples. Figure 4.16 shows fluorescence lifetime images for paper substrates modified with QD-A555 bioconjugates with nominal valences of 0, 4, 8, 16, and 20 labeled peptides per QD. The QDs in solution had an amplitude-weighted average lifetime of 5.5 ns, calculated from an experimental two-component lifetime (eqn. 1.30), whereas the immobilized QDs had an average two-component lifetime of 4.0 ns. The measured quantum yield for the batch of QD525 used for FLIM was 0.2 (*cf.* 0.4 for QDs used in steady-state analysis described above). In both bulk solution and paper formats, there is a clear decrease in the average lifetime of the QDs as the number of A555 acceptors per QD increases. Average lifetime distributions for the conjugates in bulk solution and immobilized in the paper matrix are shown in Figure 4.16 B-C. The FRET efficiencies for the two environments are calculated and compared in Figure 4.16D. Once again, there is a clear enhancement of FRET efficiency for the paper samples. Analysis indicates that the *effective* donor-acceptor distance decreased from 7.4 nm in bulk solution (*cf.* 7.1–8.2 from steady-state measurements) to 6.3 nm in the paper matrix (*cf.* 6.1 from relative steady-state PL measurements). A rate analysis indicated that the rate of FRET increased from $2.5 (\pm 0.9) \times 10^7 \text{ s}^{-1}$ in bulk solution to *ca.* $1.1 \times 10^8 \text{ s}^{-1}$ in the paper matrix.

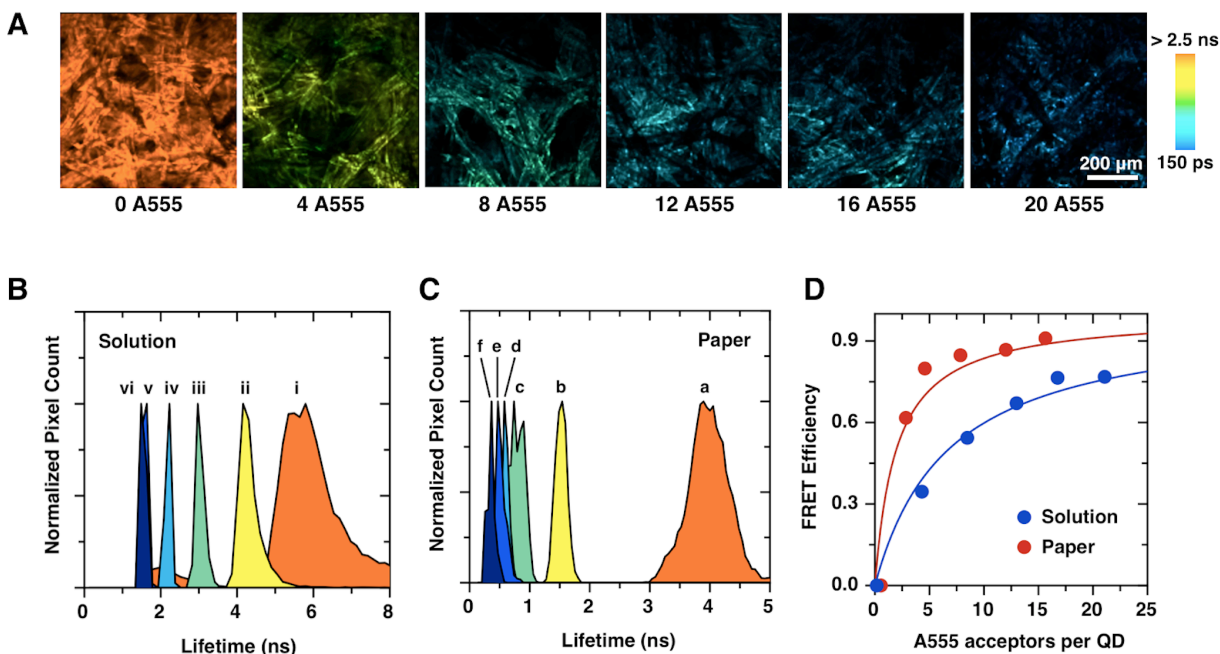


Figure 4.16 (A) Fluorescence lifetime imaging of paper substrates functionalized with lipoic amine (**4b**) and modified with QD-A555 bioconjugates at ratios 0, 4, 8, 12, 16, and 20 A555 labeled peptides per QD. (B) Normalized average two-component fluorescence lifetime distributions for the six different conjugates in bulk solution: (i) 0, (ii) 4, (iii) 8, (iv) 12, (v) 16, and (vi) 20 A555 per QD. (C) Average two-component fluorescence lifetime distributions for the same conjugates subsequently immobilized on paper substrates. The data correspond to the images in (A). (D) Comparison of the FRET efficiency calculated from the decrease in QD PL lifetime between bulk solution in (B) and the paper substrates in (C).

4.2.5 Effect of paper surface chemistry on proteolytic rates

Rates of proteolysis on nanoparticle bioconjugates have been shown to be strongly dependent on the interfacial QD surface chemistry based on the ligand used for preparation of water-soluble QDs [391]. One of the major factors affecting observed rates in bulk solution is non-specific adsorption of proteases to QDs. Given the heterogeneous, chemically-modified interface of paper substrates used for QD immobilization, it was crucial to investigate their effect on activity and inhibition of proteases. QD525 capped with GSH ligands were assembled with 16 equivalents of A555 labeled peptide that contained a recognition site for trypsin and immobilized on paper

samples **(3)**, **(4b)**, and **(6b)**. As a result of proteolysis, peptide is cleaved and FRET is lost. The relative increase in QD PL and decrease in FRET-sensitized emission of A555 acceptor was monitored over 90 min by measuring intensity at 525 nm and 570 nm. The corresponding changes in PL ratio as a result of proteolysis observed in three paper samples are shown in Figure 4.17.

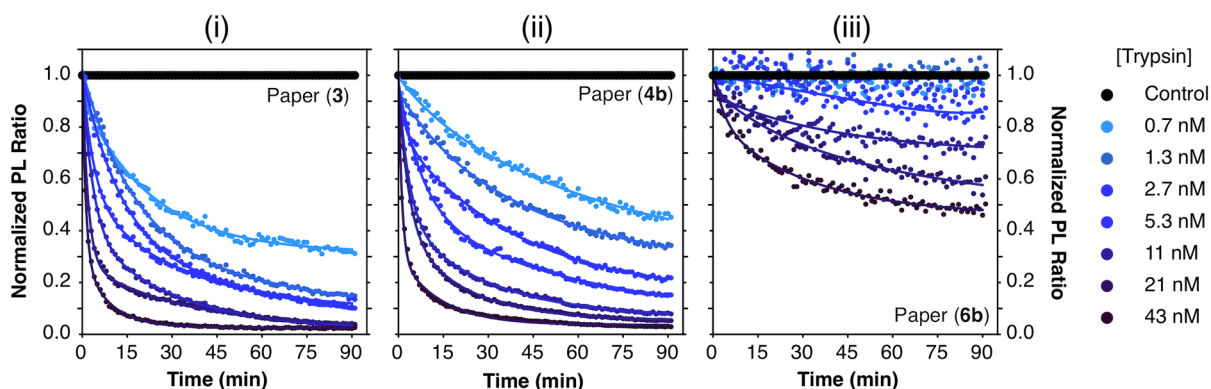


Figure 4.17 Paper-based proteolytic activity assay with immobilized QDs in paper sample (i) imidazole-modified paper **(3)**; (ii) lipioic amine modified paper **(4b)**; and (iii) APTES-LA modified paper **(6b)**.

Among the three paper surface chemistries evaluated, paper substrate **(3)** resulted in the least amount of non-specific inhibitory interaction with protease, as observed by the fastest rates in Figure 4.17(i). In contrast, APTES-LA surface chemistry, which was noted to provide the highest density of immobilized QDs and the highest enhancement in FRET efficiency, albeit significant non-specific adsorption of QDs, induced a strong inhibitory effect on trypsin activity.

4.3 Conclusions

Three methods were evaluated for the immobilization of water-soluble QDs on cellulose paper fibers *via* self-assembly. These methods yielded a high density of ligands that were successful in immobilizing QDs at high density. It was possible to immobilize QDs coated with a variety of ligands, including GSH, DHLA, DHLA-PEG, MPA, and DHLA-ZW, as well as pre-assembled QD-peptide conjugates. The immobilization of QDs using thiol-based chemistry was found to

affect the optical properties of QDs to a larger extent in comparison to imidazole-based ligands. The pre-treatment of paper samples, used to control pH within the paper matrix, was found to affect the density of immobilized QDs while mitigating the decrease in QD PL upon immobilization. Each of the three evaluated chemistries had an effect on the density of immobilized QDs, their photobleaching, and their long-term stability. Interestingly, an enhancement in the rate and efficiency of FRET between immobilized QDs and dye acceptors within the paper matrix was observed in comparison to solution-phase FRET. Once again, the extent of enhancement was found to be strongly influenced by the underlying ligands of cellulose fibers. Both steady-state and time-resolved fluorescence measurements performed on thiol-based chemistry indicated a decrease in the *effective* donor-acceptor distance, which lead to an approximately four-fold enhancement in the rate of FRET. Overall, paper substrates prepared *via* oxidation and subsequent coupling with lipoic amine offered a significant enhancement in FRET efficiency in comparison to paper modified with imidazole ligands, and they did not exhibit strong non-specific adsorption observed with silanized paper samples. Paper samples modified with imidazole ligands provided superior advantage in comparison to other chemistries for long-term stability of test strips. The silanization approach, albeit leading to more rigid and robust paper substrates, exhibited the aforementioned non-specific adsorption as well as very strong inhibition of protease activity. Overall, the selection of surface ligands for the immobilization of QDs within paper matrices is an important component of assay development providing opportunities to tune and control properties of QDs and the extent of interactions between biomolecules and cellulose interface.

4.4 Experimental Section

4.4.1 Materials and reagents

Lipoic acid (LA, $\geq 99\%$), *N,N'*-diisopropylcarbodiimide (DIC, $>98\%$), *N*-hydroxysuccinimide (NHS, 98%), ethylenediamine, tetramethylammonium hydroxide (TMAH) solution in methanol (25% w/v), sodium borohydride ($\geq 98\%$), sodium cyanoborohydride (95%), sodium (meta)periodate ($\geq 99\%$), 3-aminopropyltriethoxysilane, 1-(3-aminopropyl)imidazole, 2,3,5-triphenyltetrazolium chloride (TTC), ninhydrin, 5,5'-dithio-bis-(2-nitrobenzoic acid) (Ellman's reagent), glutathione (GSH), and trypsin from bovine pancreas were from Sigma-Aldrich

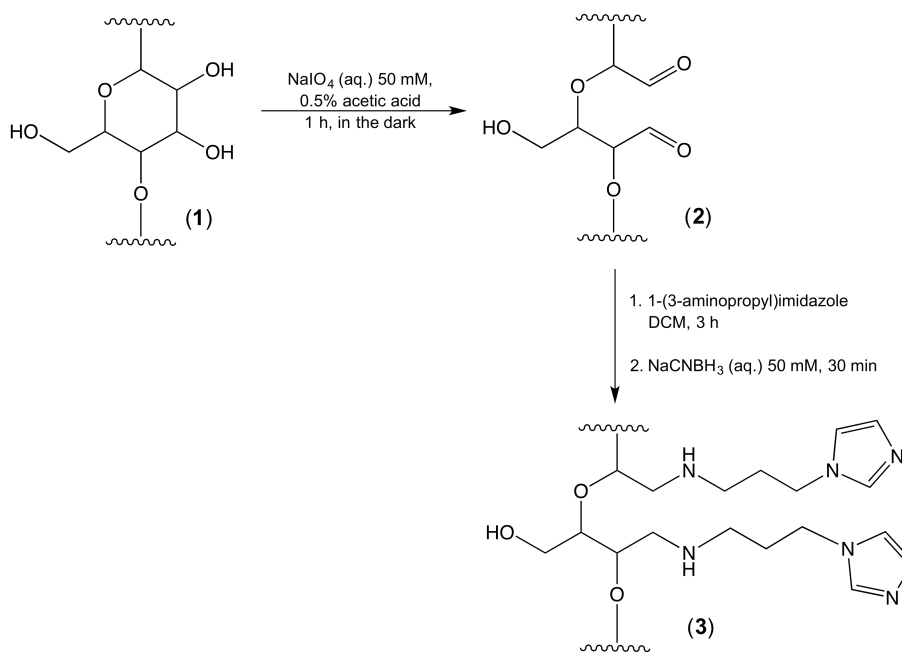
(Oakville, ON, Canada). Ammonium acetate, acetic acid, boric acid, Tris base and ammonium hydroxide (30% w/w) were from Fisher Scientific (Ottawa, ON, Canada).

CdSe_{1-x}S_x/ZnS core/shell nanocrystals (dispersed in toluene) with emission maxima at 525 nm (QD525) were from Cytodiagnosics (Burlington, ON, Canada). QDs were made water-soluble by coating with glutathione (GSH) (see Chapter 2, Section 2.5.2) or dihydrolipoic acid (DHLA) ligands. Additional water-soluble QDs included DHLA-PEG, MPA, cysteine, and DHLA-zwitterionic (ZW). Methods for ligand exchange and ligand synthesis can be found in Appendix I. Peptide with Ace-HHHHHHSPPPPPGSDGNESGLVPRGSGC sequence was from Biosynthesis Inc. (Lewisville, TX, USA) and was labeled with Alexa Fluor 555 (A555) C2 maleimide dye (Life Technologies, Carlsbad, CA) as described previously [368]. Buffers were prepared with water purified by a Barnstead Nanopure water purification system (Thermo Scientific, Ottawa, ON, Canada) and sterilized by autoclaving prior to use. Buffers included borate buffer (100 mM, pH 9.2), borate buffer (50 mM, pH 8.5), Tris-borate (50 mM, pH 7.4), and ammonium acetate (100 mM, pH 4.5; not autoclaved).

4.4.2 Preparation of paper substrates

4.4.2.1 Preparation of paper substrate (3)

Paper substrates (3) were prepared according to the steps summarized in Scheme 4.2. Chromatography paper (15–20 circular sheets, 42.5 mm, Whatman, grade 4) were oxidized in 50 mL of 50 mM sodium (meta)periodate prepared in 80 mM solution of acetic acid in the dark for 1 h. Each paper sheet was washed five times for 5 min with Nanopure water (Thermo Scientific, Waltham, MA, USA), three times with methanol, once with dichloromethane (DCM) and dried under vacuum for 4–6 h. Aldehyde-functionalized paper was immersed for 3 h in 100 mL of DCM containing *ca.* 4 mmol (477 μ L) of 1-(3-aminopropyl)imidazole. Paper sheets functionalized with this imidazole ligand were rinsed three times with DCM, briefly air-dried, and immediately immersed into aqueous solution of sodium cyanoborohydride (50 mM) for 30 min to reduce the imine bonds to secondary amines. Paper sheets were then rinsed three times with Nanopure water, three times with methanol, once with dichloromethane, dried under vacuum, and stored at 4°C until needed.

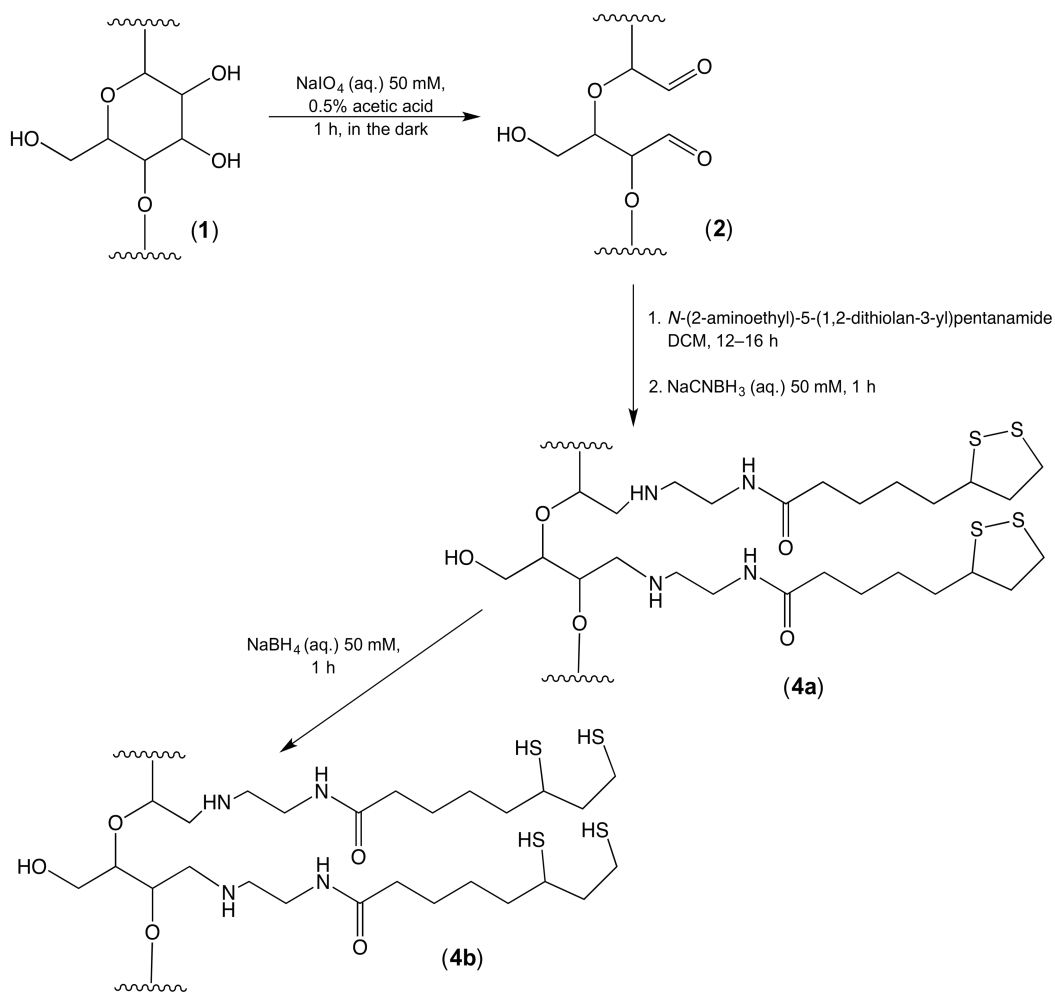


Scheme 4.2 Chemical modification of cellulose paper fibers with imidazole-based ligands for immobilization of the QDs.

4.4.2.2 Preparation of paper substrate (**4b**)

Paper substrates (**4b**) were prepared according to steps summarized in Scheme 4.3. Chromatography paper (15–20 circular sheets, 42.5 mm, Whatman, grade 4) were oxidized in 50 mL of 50 mM sodium (meta)periodate prepared in 80 mM solution of acetic acid (0.5% v/v) in the dark for 1 h. Each paper sheet was washed three times with Nanopure water (Thermo Scientific, Waltham, MA, USA), three times with methanol, once with DCM, and dried under vacuum for 4–6 h. Aldehyde-functionalized paper (**2**) was immersed for 12–16 h in 100 mL of DCM containing *ca.* 1 mmol of *N*-(2-aminoethyl)-5-(1,2-dithiolan-3-yl)pentanamide (see synthesis details in Section 4.4.2.2). Paper sheets functionalized with this lipoic acid derivative (*i.e.* “lipoic amine”) were rinsed three times with DCM, briefly air-dried, and immediately immersed into aqueous solution of sodium cyanoborohydride (50 mM) for 1 h to reduce the imine bonds to secondary amines. Paper sheets were then rinsed three times with Nanopure water, three times with methanol, once with dichloromethane, dried under vacuum, and stored at 4°C until needed. Prior to use, paper samples were cut to the desired size and the dithiolanes in

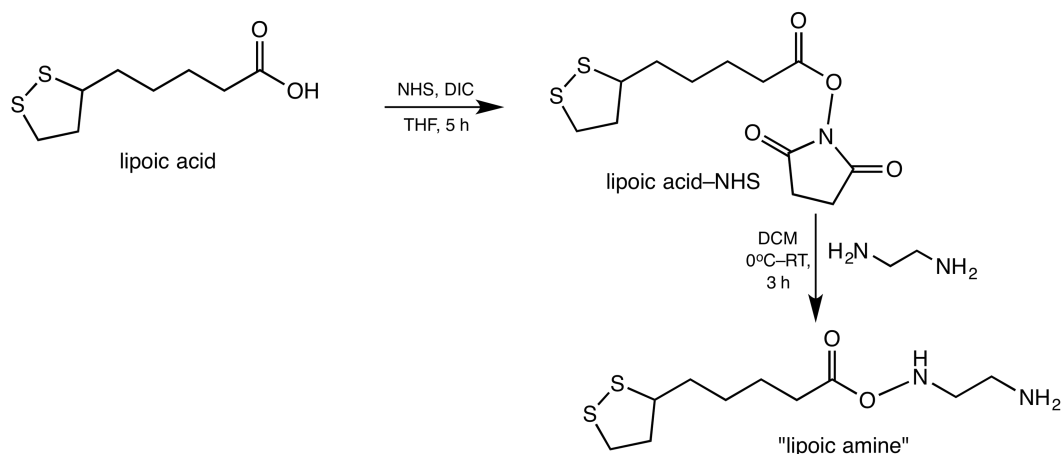
paper substrate (**4a**) were reduced in 50 mM aqueous sodium borohydride solution for *ca.* 1 h, rinsed once with water and once with ammonium acetate buffer (100 mM, pH 4.5), then dried on lint-free paper towels (Kimwipes).



Scheme 4.3 Chemical modification of cellulose paper fibers with *N*-(2-aminoethyl)-5-(1,2-dithiolan-3-yl)pentanamide ligands for immobilization of the QDs.

4.4.2.3 Synthesis of *N*-(2-aminoethyl)-5-(1,2-dithiolan-3-yl)pentanamide

This primary amine derivative of lipoic acid was synthesized in two steps as shown in Scheme 4.4.



Scheme 4.4 Synthesis of lipoic acid-NHS and *N*-(2-aminoethyl)-5-(1,2-dithiolan-3-yl)pentanamide.

Synthesis of lipoic acid-NHS. Lipoic acid (0.4 g, 2 mmol) and NHS (0.25 g, 2.2 mmol) were dissolved in 100 mL of anhydrous THF and cooled on ice. DIC (342 μ L, 2.2 mmol) was dissolved in 20 mL of THF and added dropwise to the reaction flask. The reaction was brought to room temperature and allowed to react an additional 5 h under argon. The reaction mixture was concentrated down to 5–10 mL and 2-propanol added until turbidity (typically 50–100 mL). The reaction flask was purged with argon and placed at -20 °C overnight. The product was collected by filtration, dried, and stored at -20 °C until needed. Typical yields were 60–80%.

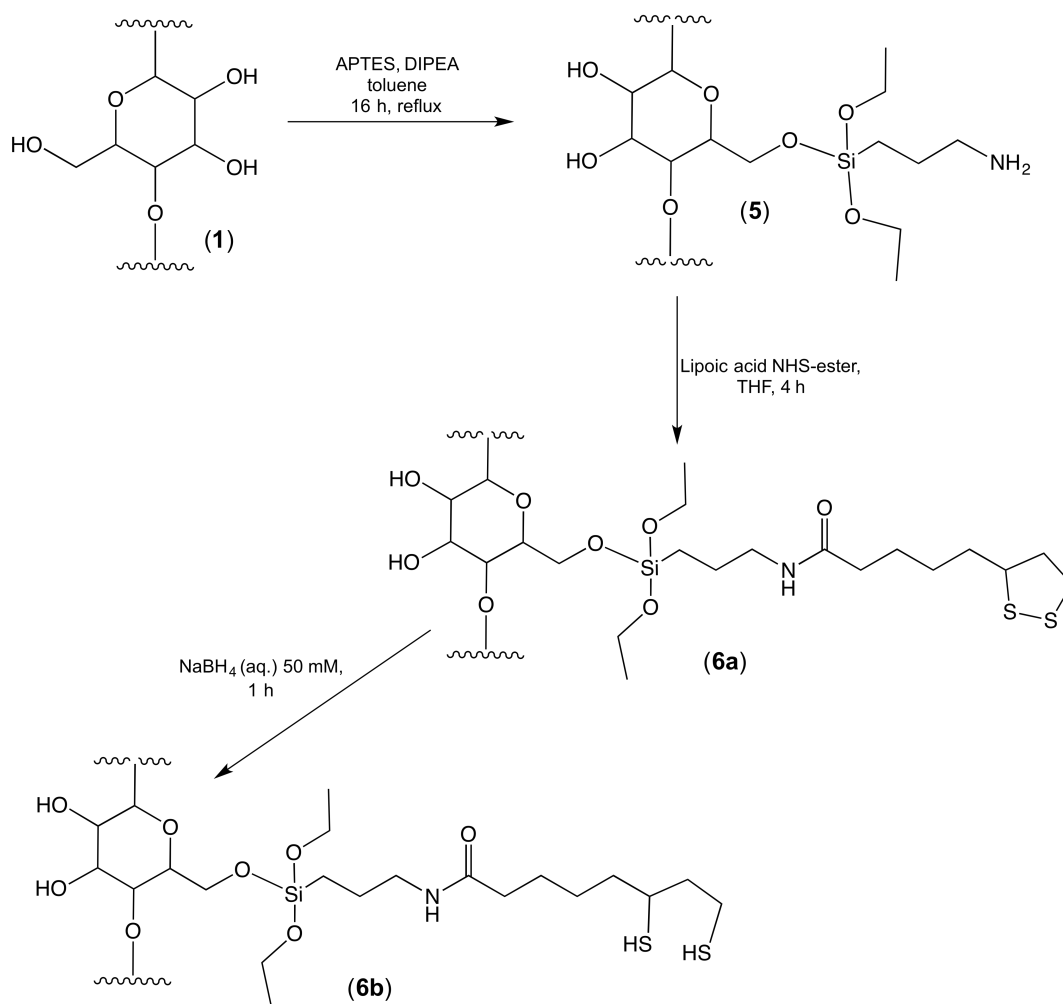
Synthesis of *N*-(2-aminoethyl)-5-(1,2-dithiolan-3-yl)pentanamide. Excess ethylenediamine (10 mL, 0.15 mol) was dissolved in 10 mL of DCM and cooled on ice. Lipoic acid-NHS (0.6 g, 2 mmol) was dissolved in 50 mL of DCM, placed in an addition funnel, and added dropwise over 2 h to ethylenediamine. The reaction was brought to room temperature and allowed to react for an additional 3 h. Next, the reaction mixture was transferred to a separation funnel and washed once with 75 mL water, three times with a solution made from 30 mL of 1 M NaOH and 20 mL of brine, and dried over sodium sulfate. The final product (LA-NH₂) is very prone to

polymerization (decyclization and crosslinking between dithiolane rings) upon drying and was therefore stored in DCM under argon at 4 °C. Thin layer chromatography: 9:1 (v/v) DCM:MeOH, R_f (LA-NH₂) = 0.02, R_f (LA-NHS) = 0.56. TLC plates were visualized under UV light, developed with permanganate stain, and the presence of a primary amine confirmed using ninhydrin stain. ESI⁺ MS (MeOH): m/z 249.4 (MH⁺), 271.4 (MNa⁺).

4.4.2.4 Preparation of paper substrate (**6b**)

Paper substrates (**6b**) were prepared according to the steps summarized in Scheme 4.5. Chromatography paper sheets (Whatman, grade 4) were cut into squares (4 × 4 cm²) and 16 of them were immersed in *ca.* 100 mL of anhydrous toluene, containing 4.68 mL (20 mmol) of 3-aminopropyltriethoxysilane (APTES) and 0.2 mL of diisopropylethylamine (DIPEA) as a catalyst in 1L round bottom flask. The solution was brought to reflux under argon and left to react 12–16 h. The solution was brought to room temperature, then decanted and paper substrates washed in succession with three portions of toluene, isopropanol, and DCM. Paper substrates modified with APTES (**5**) were functionalized with primary amines and used for subsequent reaction with NHS ester activated lipoic acid (see Section 4.4.2.3).

Ten APTES modified sheets (4 × 4 cm²) were immersed in 50 mL of anhydrous tetrahydrofuran (THF) containing approximately 120 mg (0.4 mmol) of lipoic acid-NHS ester. The reaction was left at room temperature for 4 h with occasional mixing. The solution was decanted and paper substrates (**6**) washed in succession with three portions of THF, methanol, and DCM. Paper sheets were then dried under vacuum (30 min) and stored at 4°C until needed. Prior to use, paper samples were cut to the desired size and the dithiolanes in paper substrate (**6a**) were reduced in 50 mM aqueous sodium borohydride solution prepared in 10% ethanol for 1–2 h, rinsed once with water and once with ammonium acetate buffer (100 mM, pH 4.5), then dried on lint-free paper towels (Kimwipes).



Scheme 4.5 Chemical modification of cellulose paper fibers with liponic acid ligands for immobilization of the QDs.

4.4.3 Quantification of functional groups

4.4.3.1 Aldehyde groups

Paper substrates (2) were pre-cut with a hole punch into 3 mm circular samples and 3–4 samples were pre-weighed into 1.7 mL eppendorf tube. To initiate the reaction with TTC, the reagents were added in the following order: (i) 20 μL of 100 mM TTC in dimethylacetamide (DMAc), (ii) 20 μL of 1 M LiCl in DMAc, (iii) 5 μL of DIPEA. Note: it is important to ensure that TTC

solution completely saturates paper samples prior to addition other reagents. Tubes were sealed, thoroughly vortexed, and placed on water bath at 75–80°C for 10 min in the dark. Immediately after, tubes were placed on ice for 2 min and diluted with 1 mL of ethanol. All tubes were vortexed to release red-coloured product, TTC formazan, in solution. Subsequent dilutions were made in ethanol as needed to acquired for absorbance measurements. Control sample was prepared in parallel using untreated cellulose paper (1). Absorption of solution samples was measured in 96-well UV transparent plate on Infinite M1000 Pro plate reader (Tecan Ltd.).

Calibration curve to determine TTC formazan molar absorption coefficient was prepared using commercially available reagent (product number T0175) from TCI (Portland, US).

4.4.3.1 Primary amine groups

Paper substrates (5) were pre-cut with a hole punch into 3 mm circular samples and 3–4 samples were pre-weighed into 1.7 mL eppendorf tube. To initiate the reaction, 100 μ L of 100 mM ninhydrin solution prepared in ethanol was added, the mixture was vortexed and placed in a water bath at 60°C for 20 min in the dark. The reaction was diluted with 400 μ L of ethanol, vortexed and supernatant transferred to a clean tube. The blue coloured paper sample was washed three times with 100 μ L portions of ethanol; all wash solutions were combined together and used to quantify the amount of Ruhemann's purple. The absorption of solution samples was measured in a 96-well UV transparent plate and the absorption of paper samples was measured by sandwiching them between windows of of a NanoQuant plate (Tecan Ltd.) on Infinite M1000 Pro plate reader (Tecan Ltd.).

Calibration curves on paper samples were prepared using synthesized Ruhemann's purple. Briefly, ethanolamine 0.5 mmol was added to 50 mL of ethanol containing 1 mmol ninhydrin. The reaction was left to stir for 4 h and used without further purification. The concentration of Ruhemann's purple was determined using absorption measurements at 570 nm. A series of samples were prepared with concentrations in the range 0.05–0.1 mM and 2 μ L volumes were spotted on 3 mm circular paper sample. Absorption was measured as described above.

4.4.3.2 Thiol groups

Paper substrates (**4a**) and (**6a**) were precut into rectangles (*ca.* $4 \times 8 \text{ mm}^2$), weighed, and placed in aqueous solution containing 200 mM sodium borohydride for 30 min. All paper samples (7 in total for each surface chemistry) were washed twice with dilute acetic acid, and dried on lint-free paper towels. Each paper sample was further cut into smaller pieces and placed into a 1.7 mL eppendorf tube. A volume of 100 μL of 0.5 mM Ellman's reagent prepared in ethanol was added to each tube, the reaction vortexed, and let stand for 5 min. This mixture was diluted with 400 μL of borate buffer (pH 8.5, 50 mM) and used for quantification from the absorbance at 412 nm. The reaction mixtures for paper samples (**4b**) were diluted another 10-fold prior to measurement. Control samples were measured in parallel using untreated paper (**1**).

4.4.4 Characterization of paper substrates

The X-ray photoelectron spectroscopy (XPS) analysis was done on a Leybold MAX200 XPS spectrometer at the Interfacial Analysis and Reactivity Laboratory (IARL), University of British Columbia. The X-ray source was Al K-alpha operated at 300 W (15 kV, 20 mA) and data was collected at a 90 degree take-off angle. Paper samples modified as described above were washed three additional times with DCM, placed in glass vials, and dried under vacuum for 4 h.

ATR-FTIR spectra were acquired on Perkin Elmer Frontier FT-IR spectrometer equipped with ZnSe ATR crystal. All measurements were acquired over a spectral range $4000\text{--}600 \text{ cm}^{-1}$.

4.4.5 Preparation of DHLA-coated QDs

4.4.5.1 Synthesis of DHLA

In a typical reaction, 2.06 g (10 mmol) of lipoic acid was dissolved in 200 mL water and placed on an ice bath. Sodium borohydride (2.0 g, *ca.* 54 mmol) was added in small portions over 30 min. The mixture was brought to room temperature and stirred for 4 h, then the reaction was diluted with 100 mL of water. The excess of sodium borohydride was quenched with 12 M HCl until the solution turned cloudy (pH 1–2) while keeping the reaction on ice. The product was extracted with three 50 mL portions of DCM. The organic fractions were combined, dried over sodium sulfate and the solvent was removed using a rotary evaporator to produce a clear to pale yellow oil. The product was transferred to a glass vial equipped with crimp seal and stored in the

freezer at -20°C .

4.4.5.2 DHLA QD ligand exchange

Neat dihydrolipoic acid (DHLA; 100 μL) was added to organic QDs (100 μL , 10 μM) in a culture tube. The tube was sealed, purged with argon and brought to 80°C for 4 h. The mixture was cooled briefly on ice and 200 μL of TMAH solution in methanol was added, followed by 200 μL of borate buffer (50 mM, 500 mM NaCl, pH 9.2). Approximately 1 mL of CHCl_3 was added to the culture tube to extract excess DHLA. The aqueous layer was transferred to 1.7 mL polypropylene centrifuge tubes in 200 μL fractions. The QDs were washed by precipitation with ethanol three times, redispersing in borate buffer (pH 9.2, 50 mM, 250 mM NaCl) between precipitation steps. After the final wash, QDs were redispersed in borate buffer (pH 8.5, 50 mM, no NaCl) and stored at 4°C . QDs were quantified using UV-visible spectroscopy as described in Chapter 2.

4.4.6 Immobilization of QDs and QD-peptide conjugates

Prior to QD or QD-peptide conjugates immobilization all paper samples were rinsed in buffer. Sample **(3)** was washed in borate buffer (pH 8.5, 5 mM), and samples **(4b)** and **(6b)** prepared by reduction with sodium borohydride as describe in Sections 4.4.2.2 and 4.4.2.4 were rinsed with ammonium acetate buffer (pH 4.5, 100 mM). Excess buffer was drained from paper samples by gently sandwiching them between lint-free paper towels (Kimwipes). QD solution was prepared at desired concentration (typically 2 μM) in borate buffer (pH 9.2, 50 mM) and 1 μL was spotted onto circular (3 mm diameter) paper substrate placed in humid chamber. The samples were let stand for 30 min (unless noted otherwise) before washing in borate buffer (pH 8.5, 5 mM). Noted above are the general procedures used for QD immobilization throughout this thesis, and any special modifications are highlighted in text.

The immobilization of QD-peptide conjugates was done similarly. The conjugates were prepared in borate buffer (pH 9.2, 50 mM) at the desired QD:peptide ratio and a final QD concentration of 2 μM . Conjugates were incubated for 30–60 min prior to spotting 1 μL onto circular (3 mm diameter) paper substrates placed in a humid chamber. The samples were allowed to stand for 30 min prior to washig with borate buffer (pH 8.5, 5 mM).

4.4.7 SEM imaging of immobilized QDs

Scanning electron microscopy (SEM) was done on a Helios NanoLab 650 Focused Ion beam SEM at the Centre for High-Throughput Phenogenomics, University of British Columbia. Paper substrates (**3**), (**4b**), and (**6b**) were functionalized with QDs as described above. In order to remove residual buffer salts and excess water, paper samples were washed in succession with three portions of Nanopure water, methanol, and DCM, and dried under vacuum in a glass container. Paper samples were adhered to SEM mount using adhesive carbon tabs. The loose edge of each paper sample was coated with silver solution to ensure contact with the carbon stage and the samples were left under vacuum for 24 h. Prior to imaging, samples were coated with an 8 nm thick iridium layer on Leica EM MED020 coating system. All images were acquired under 1.0 kV accelerating voltage and 25 pA current.

4.4.8 Photobleaching experiments

QDs were immobilized on paper substrates as described above. Photobleaching experiments were done on an IX83 inverted epifluorescence microscope (Olympus, Richmond Hill, ON, Canada) and PL spectra were obtained from paper samples using a Green-Wave spectrometer (StellarNet, Tampa, FL, USA) coupled with an optical fiber (1000 μm diameter; M37L01, Thorlabs, Newton NJ, USA). Spectra acquisition with a Green-Wave spectrometer was done using LabView software written in-house (see Appendix III for details). The microscope was equipped with an X-Cite 120XL metal-halide light source (Excelitas Technologies, Mississauga, ON, Canada), The excitation filter was always 405/20 and paired with a 470 nm cutoff dichroic mirror (Chroma). Paper samples or QD solution were added to wells in a UV transparent 96-well plate, and wells containing paper samples were filled with borate buffer (pH 8.5). Samples were continuously illuminated and spectra collected at 2 min intervals for 4 h. The total illumination power exiting the objective lens was ~ 27 mW.

4.4.9 Fluorescence lifetime imaging microscopy (FLIM)

FLIM was done with a Zeiss LSM510 scanning confocal microscope equipped with a time-correlated single-photon counting (TCSPC) fluorescence lifetime imaging module (Becker & Hickl GmbH, Berlin, Germany) and a tunable Chameleon XR femtosecond laser (Coherent, Santa Clara, CA) for two-photon excitation (840 nm). Data acquisition was done over 8

wavelength channels with an xy-resolution of 128×128 pixels and 256 time channels. QD fluorescence was detected in the 525 nm channel and the decay curves were fit with a biexponential function according to eqn. 1.30.

4.4.10 Enzyme assays

GSH-QD-peptide conjugates were pre-assembled by mixing QDs with the desired ratio of peptide in borate buffer (50 mM, pH 9.2) for 1 h. The final concentration of QDs was 2.0 μ M. The conjugates were then spotted on paper modified with (4b) in two 0.5 μ L increments, then let stand for 30 min before washing with borate buffer (pH 8.5, 5 mM). Trypsin protease solutions were prepared in borate buffer (50 mM, pH 8.5). Protease activity was monitored by adding 100 μ L of enzyme solution to paper substrates with immobilized QD-peptide conjugates in a well of a UV transparent 96-well plate. PL spectra were measured at 525 nm and 570 nm at 1 min intervals for 90 min on Infinity M1000 Pro (Tecan Ltd.).

4.4.11 Data analysis

A555/QD PL ratios were calculated using eqn. 4.1, where $F(\lambda)$ is the PL intensity at wavelength λ , and $\gamma_{D,\lambda}$ (= 0.02) is a correction factor accounting for the relative crosstalk of the QD emission at a wavelength with predominant A555 emission:

$$PL\ ratio = \frac{F(570nm) - \gamma_{D,570nm}F(525nm)}{F(525nm)} \quad (4.1)$$

FRET efficiencies, E , were measured from changes in QD PL intensity or lifetime relative to samples without any acceptor according to eqn. 1.24. The average lifetime used in eqn. 1.24 is the amplitude weighted lifetime (eqn. 4.2) derived from fitting PL decay curves with a biexponential function (eqn 4.3) [164].

$$\tau_{av} = \frac{A_1\tau_1 + A_2\tau_2}{A_1 + A_2} \quad (4.2)$$

$$F(t) = A_1e^{-t/\tau_1} + A_2e^{-t/\tau_2} \quad (4.3)$$

FRET efficiencies were also estimated from the relative QD donor and A555 acceptor emission using eqn. 4.4, where $F_A(\lambda)$ and $F_D(\lambda)$ are the acceptor and donor emission intensities as a function of wavelength, and Φ_A and Φ_D are the respective quantum yields:

$$E = \frac{\int F_A(\lambda) d\lambda}{(\Phi_A/\Phi_D) \int F_D(\lambda) d\lambda + \int F_A(\lambda) d\lambda} \quad (4.4)$$

Plots of FRET efficiency versus the number of acceptors per QD, a , were fit with eqn. 1.27 and FRET rates, k_{FRET} , were calculated from eqn. 1.21 after obtaining the value of $(R_0/r)^6$ from least-squares fitting of efficiency *versus* acceptors per QD curves and substituting $\tau_{0,\text{av}}$ from fluorescence lifetime measurements [164].

Chapter 5 Proteolytic Assays on Quantum Dot-Modified Paper Substrates Using Consumer Digital Cameras for Optical Readout

This chapter is an adaptation of published work, and is reproduced from Petryayeva, E.; Algar, W. R., Proteolytic Assays on Quantum Dot-Modified Paper Substrates Using Simple Optical Readout Platforms. *Anal. Chem.* **2013**, *85* (18), 8817-8825, with permission from The American Chemical Society (Copyright 2013 American Chemical Society).

5.1 Introduction

As was discussed in Chapter 1, diagnostic assays are a critical frontline for healthcare and should be sensitive, selective, and rapid in their response to target analytes. Improved benchmarks for these figures of merit continue to be reported across a myriad of different analyses, frequently with the aid of nanomaterials and nanotechnology [292, 464-469]. Unfortunately, many of these improvements require sophisticated instrumentation for readout. While such methods are potential healthcare solutions in some settings, it has been recognized that simple approaches are essential for developing diagnostics that are suitable for point-of-care applications, field deployment, or other low-resource settings [25, 36, 412]. In this context, other important criteria for assays include low cost, robustness, portable supporting instrumentation, few (if any) external reagents, and ease of use. Over the last decade, paper has become a preferred solid support for developing assays that can meet these additional criteria [36, 403, 470]. As was noted in Chapter 4, paper is inexpensive and ubiquitous, robust, easily patterned and chemically modified, biocompatible, and has intrinsic wicking action that can drive fluid flow [20, 36]. Dipstick assays, lateral flow assays, and microfluidic paper-based analytical devices (μ PADs) have been prominent developments in this area [81, 408-413].

Many researchers have sought to integrate nanomaterials with paper-based assay formats. The vast majority of these developments have utilized gold nanoparticles (Au NPs) [416], which

support visual detection with their strong red colour, pronounced colour change upon aggregation [464], and their ability to seed silver enhancement [77]. The latter has been the basis of highly sensitive “scanometric” assay formats requiring only benchtop scanners for readout [468, 471, 472]. Few paper-based assays, however, have been developed around other nanomaterials, including luminescent semiconductor quantum dots (QDs), which offer excellent brightness, size-tunable photoluminescence (PL), and superior resistance to photobleaching. QDs have emerged as outstanding probes for both cellular and *in vivo* imaging and, most pertinently, *in vitro* assays [6, 222, 374, 473]. To date, however, QD-based *in vitro* assays have largely relied on spectroscopic equipment that, although available in research laboratories, is not suitable for field work or point-of-care settings. In addition to lateral flow assays with QD-labeled antibodies on nitrocellulose membranes [112, 417, 474], some researchers have begun to explore the possibility of using QDs as part of paper-based assays to ameliorate these limitations. Noor *et al.* recently reported a quantitative DNA hybridization assay using spots of QDs immobilized on a paper substrate [427]; however, readout was done using a sophisticated fluorescence microscope equipped with a laser excitation source. While the assay chemistry was elegant, this readout system largely negated the advantages of the paper substrate. Yuan *et al.* deposited mixed films of QDs and glucose oxidase or tyrosinase on paper substrates for detecting glucose and phenol, respectively [475]. The byproducts of the enzyme catalyzed reactions quenched the QD PL. While this quenching could be visualized with a UV lamp, it was not quantitatively analyzed.

In this chapter, it is shown that QDs can be used to develop paper-based assays with quantitative readout methods that are relatively low-cost and suitable for point-of-care and field diagnostic applications. Expensive and electrical power-intensive laser and lamp sources are replaced with a violet light-emitting diode (LED; \$0.50) as the excitation source, while sophisticated instruments are replaced with three different detection systems that require no more than a universal serial bus (USB) connection to a computer. These detection systems are much less expensive than those commonly used in research labs (*e.g.* fluorimeters, plate readers, microscopes) and progressively scale-down in cost from a miniature fiber-optic spectrometer (\$2000) to an educational-grade digital microscopy camera (\$250) to a consumer webcam (\$40). Furthermore, a smartphone camera can be substituted for the webcam and the LED powered from batteries—a format amenable to the concept of telemedicine [139]. The diagnostic utility of QD-modified paper substrates with each of the foregoing detection systems is demonstrated through a series of

proteolytic assays based on Förster resonance energy transfer (FRET). As shown in Figure 5.1A, QDs are immobilized on paper and conjugated with fluorescent dye-labeled peptide substrates for protease targets of interest, where the dye is chosen to be a FRET acceptor for the QDs. Alexa Fluor 555 (A555) serves as an acceptor for alloyed CdSeS/ZnS QD donors with green PL emission. In the absence of proteolytic activity, the dye remains in close proximity to the QD such that FRET is “on” and very efficient, resulting in the observation of yellow/orange emission from the A555. Proteolysis cleaves the peptide allowing the dye to diffuse away from the QD, turning FRET “off” with recovery of green emission from the QD. These fluorescence colour changes, which are visible by eye, can be tracked with digital colour imaging for quantitative analysis. These optical readout modes are applied in various model assays of pancreatic protease activity, including multiplexed assays and pro-enzyme activation assays. Activity-based assays (*cf.* protease concentration) are crucial for evaluation of protease function [476]. This chapter demonstrates that QDs can be combined with low-cost and deployable readout platforms for paper-based assays. Protease activity assays were chosen as a model assay format, as their aberrant activity is implicated in numerous diseases (*e.g.* cancers [477], arthritis [395], neurodegenerative conditions [394]) and the virulence of many pathogens (*e.g.* HIV [478], malaria [479]).

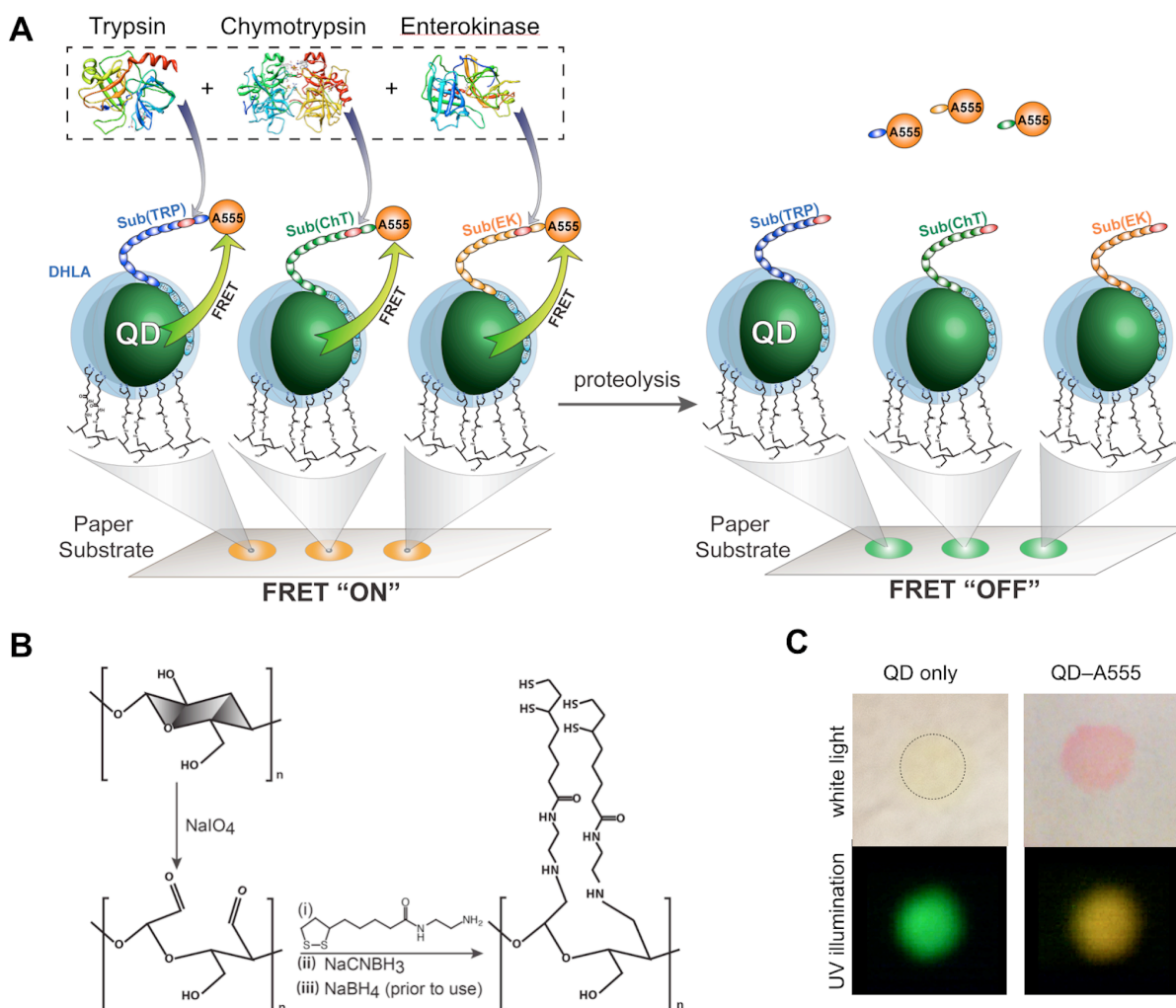


Figure 5.1 (A) Design of a paper-based assay to monitor protease activity via FRET with QD donors. Acceptor dye-labeled (A555) peptide substrates containing a cleavage site for trypsin (TRP), chymotrypsin (ChT), and enterokinase (EK) were assembled on immobilized QDs. Protease activity was measured through changes in the intensity and colour of PL from the spots of immobilized QDs and peptides. (B) Synthetic steps used for modification of cellulose paper fibers with bidentate thiol surface ligands for immobilization of QDs. (C) Colour images of paper-immobilized QDs and A555-labeled QD-Sub(TRP) peptide conjugates under white light and their PL under UV illumination.

5.2 Results and Discussion

5.2.1 FRET pair and LED excitation

Absorption and PL spectra for green-emitting alloyed QD525a and A555, and the LED emission spectrum, are shown in Figure 5.2. The spectral overlap integral and Förster distance for the QD-A555 FRET pair were calculated to be $6.1 \times 10^{-10} \text{ mol}^{-1} \text{ cm}^6$ and 3.9 nm, respectively. The Förster distance was calculated based on assumptions described in the Section 1.2.8.3 and the measured quantum yield of the QDs in solution (see Appendix II for details). However, as was reported in Chapter 4, there is a change in QD lifetime upon immobilization, indicating a concomitant change in the quantum yield of the QDs. TEM images of QD525a are shown in Figure 2.18 (page 106). The LED emission centered at 405 nm (input voltage = 3.3–4.5 V) was sufficient for QD excitation and no detectable direct excitation of A555 was observed.

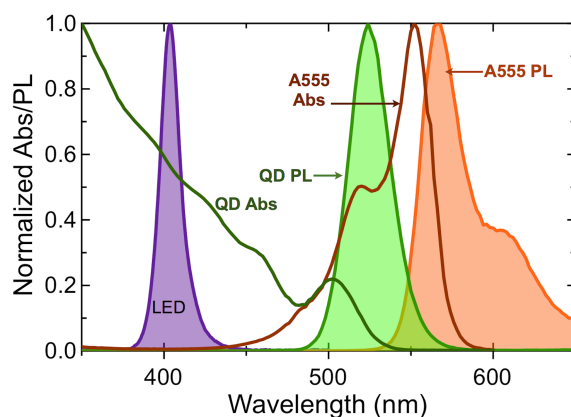


Figure 5.2 Normalized absorption and PL spectra for the QD and A555 FRET-pair. The emission profile for the LED excitation source is also shown.

5.2.2 Assay design and characterization

Figure 5.1B summarizes chemistry used to modify cellulose paper for the immobilization of QDs. As was described in Chapter 4, cellulose paper modified with lipoic amine ligands (see Scheme 4.3, page 179) was optimum from the standpoint of (i) the density of immobilized QDs,

(ii) enhancement of FRET efficiency (*cf.* solution FRET), and (iii) a minimal inhibitory effect on proteolytic activity. Water-soluble QDs coated with DHLA or GSH ligands readily immobilized on the modified paper substrates (< 1 h) as a result of the strong affinity between the thiol surface ligands and the inorganic ZnS shell of the QDs. Without modification of the paper, the QDs were easily washed away. Typical spot diameters for immobilized QDs were 3–4 mm. Spots with green emitting QDs (peak PL at 525 nm, QD525) had a faint yellow colour under room light and exhibited bright green PL under UV or violet illumination (Figure 5.1C). Confocal PL imaging, Figure 5.3A, indicated a relatively uniform distribution of QDs along the fibers of the paper.

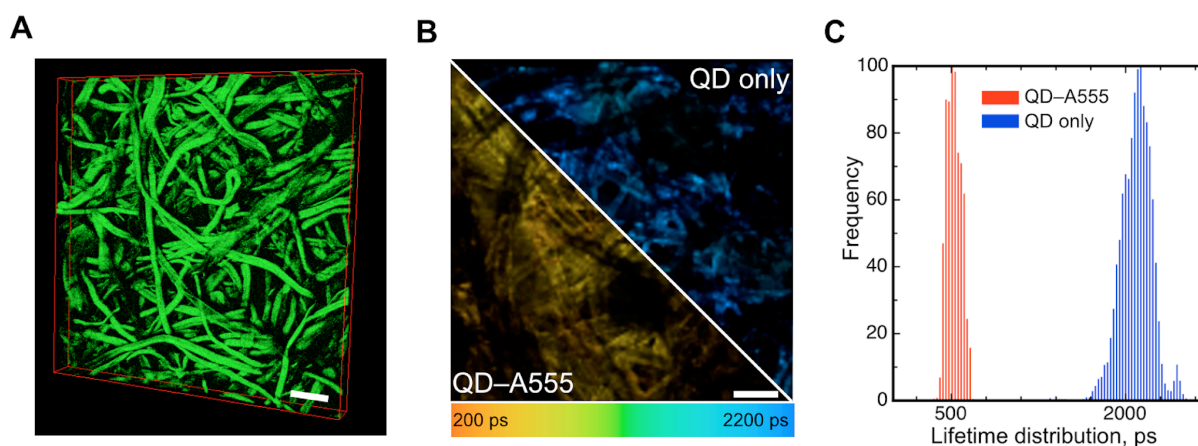


Figure 5.3 (A) Three-dimensional PL image of immobilized DHLA-coated QDs on cellulose paper fibers obtained using confocal microscopy. The image dimensions are $775 \times 775 \times 42 \mu\text{m}$. (B) Fluorescence lifetime images of paper substrates modified with green-emitting DHLA-coated QDs and QD-Sub_{TRP} conjugates (*i.e.* QD-A555). The scale bars in (A) and (B) are $100 \mu\text{m}$. (C) Fluorescence lifetime distributions for immobilized QDs and QD-Sub_{TRP} conjugates (*i.e.* QD-A555).

To demonstrate this paper-based assay format with QDs, assays were first carried out with TRP, its upstream activator, EK, and one of its downstream proteases, ChT, as model enzymes. This system was selected as a model for assays because these proteases are among the best characterized and most widely available members of the serine protease family [480, 481]. These proteases are implicated in diseases such as pancreatitis [482] and some types of cancers [483].

Immobilized QDs were self-assembled with dye-labeled peptide substrates for these proteases (see peptide sequences in Table 5.1, Section 5.4.1, page 209), each containing four modules along their sequence: (i) a hexahistidine tag for self-assembly with the QDs ($K_d \approx 1$ nM) [369]; (ii) a polyproline helix to extend the peptide away from the surface of the QD; (iii) a specific cleavage site for a protease of interest (Arg for TRP, Tyr for ChT, Asp₄-Lys for EK); and (iv) a terminal Cys residue for labeling with A555. Throughout this chapter, each peptide (see Table 5.1, page 209) is denoted as a substrate for a specific protease (*i.e.* Sub_{TRP}), where the identity of protease is written as the subscript; the identity of the dye, A555, was not included in the notation (*cf.* Chapter 3), as this was the only dye used for substrate labeling in this chapter. The sequences of the peptides were chosen to minimize cross-reactivity with non-target proteases. Self-assembly of peptides on spots of immobilized QDs produced bright pink spots under room light. Each spot contained *ca.* 4 pmol of QDs and an estimated 110–115 pmol of peptide Sub_{TRP}. Under UV/violet illumination, the spots exhibited bright yellow luminescence, indicative of FRET-sensitized A555 emission (Figure 5.1C). Fluorescence lifetime imaging (FLIM) of paper substrates indicated average PL lifetimes of 2.10 ± 0.14 ns and 0.53 ± 0.07 ns for immobilized QDs before and after modification with Sub_{TRP}, respectively (Figure 5.3B–C), corresponding to an apparent FRET efficiency of 75%.

5.2.3 Spectral validation of protease assays on paper substrates

The paper-based assay format was first tested with QD-Sub_{TRP} conjugates and a portable USB spectrometer under violet LED illumination. Representative PL spectra collected over 1 h of proteolytic activity are shown in Figure 5.4A for exposure to 430 nM (43 pmol) TRP. The apparent FRET efficiency, measured from the level of QD PL quenching, dropped from 80% to 15% over this time period. The initial value of 80% was in good agreement with that measured by FLIM, with the 5% discrepancy likely due to batch-to-batch variation or the steady-state efficiency calculation (see Section 5.4.5) not accounting for small changes in the quantum yield of the QD or A555 between the paper matrix and bulk solution. Increases in the concentration of TRP (0–860 nM) increased the rate of peptide digestion and loss of FRET as shown in the progress curves in Figure 5.4B. It is important to note that these progress curves are in terms of the normalized A555/QD PL ratio (see Section 5.4.5), which accounts for small changes in PL intensities over time in the absence of TRP (putatively due to photobrightening [212] of the

QDs), as well as variations between different paper substrates. The A555/QD PL ratio is directly proportional to changes in the average number of A555-labeled peptides per QD. After normalization, the abscissa can thus be read as the approximate fraction of substrate remaining.

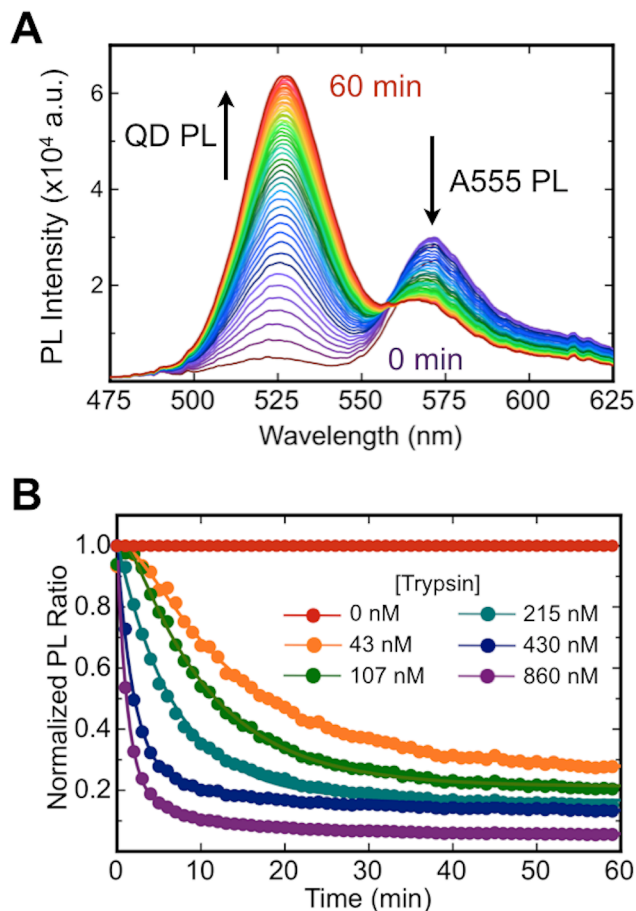


Figure 5.4 (A) Time-dependent PL spectra for paper-immobilized QD-Sub_{TRP} conjugates upon exposure to 430 nM TRP over 1 h. PL spectra were collected at 1 min intervals. Protease activity resulted in the simultaneous recovery of QD PL and loss of FRET-sensitized A555 PL. Residual A555 emission above the baseline is indicative of incomplete proteolysis or some limited adsorption of digested peptide fragments to the QDs. **(B)** Progress curves for the hydrolysis of QD-Sub_{TRP} conjugates catalyzed by different concentrations of TRP.

5.2.4 Proteolytic assays with digital colour imaging

5.2.4.1 Trypsin and chymotrypsin paper-based assays

Digital cameras generate colour images by placing a Bayer mosaic filter (or similar) over CCD or CMOS arrays, such that 2×2 sets of pixels are masked by red, green (2), and blue filters [386]. Data from each colour pixel are then interpolated to generate a colour image. Similar to the concept introduced in Chapter 3, where the emission colour of QDs was matched with red, green or blue channels, it was hypothesized here that the built-in colour filters in a digital camera could distinguish between the QD and A555 PL, and that such data could be obtained by breaking down colour images into composite red, green, and blue channels using image analysis software. It was expected that the QD PL would be observed in the green (G) channel and the FRET-sensitized A555 PL would be observed in the red (R) channel, permitting quantitative analysis through an R/G intensity ratio in place of the PL ratio, as shown in Figure 5.5A.

To investigate the above hypothesis, digital colour images of spots of QD-Sub_{TRP} conjugates at different stages of proteolytic digestion were imaged under violet LED illumination using a low-cost, educational-grade digital microscopy camera (henceforth, “digital camera”). A magnifying lens and long-pass filter were added in front of the camera lens. As shown in Figure 5.5B, the PL colour of a spot changed in appearance from yellow to green as proteolysis progressed, with the signal in the green channel intensifying and the signal in the red channel fading. The spectral response of the digital camera’s green and red channels is shown in Figure 5.5B, where it is seen that the green channel is most sensitive to the QD PL and the red channel is primarily sensitive to the A555 PL. While the green channel response appears, *a priori*, to be somewhat inclusive of A555 emission, this was not problematic in real experiments. To assess whether the R/G intensity ratio could provide the same quantitative information as the PL intensity ratio, the correlation between the PL ratio and the R/G ratio was determined experimentally by imaging and recording PL spectra for a set of QD-Sub_{TRP} conjugate samples. As shown in Figure 5.5C, the relationship was best described by an empirical power function, which permits conversion of the R/G ratio to more traditional parameters such as the PL ratio and FRET efficiency. The advantage of the R/G ratio, like the PL ratio, is that the ratiometric analysis is robust and better accounts for drift and variations in absolute PL intensities. Such variations are likely to be

encountered in paper-based assays because of both the nature of the paper substrate and the desire for minimal readout technology.

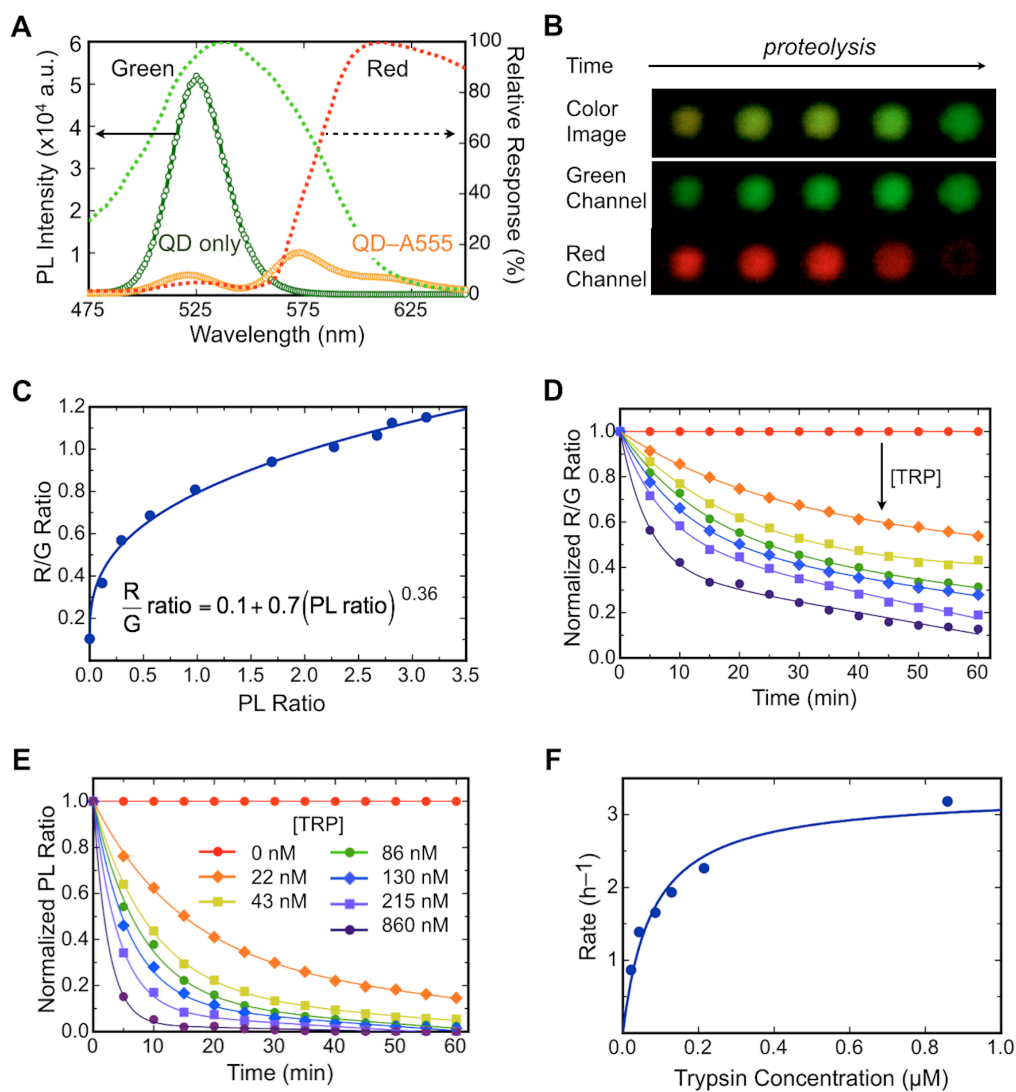


Figure 5.5 (A) PL spectra of immobilized DHLA-QDs and QD-Sub_{TRP} conjugates (*i.e.* QD-A555). Dotted lines show the relative spectral response of the digital camera (Moticam 1 [484]) in the G and R channels. (B) Colour digital images of immobilized QD-Sub_{TRP} at various time points of protease activity acquired with a digital camera and corresponding pseudo-coloured images in the green and red channel upon R-G-B splitting. (C) The empirical relationship between R/G ratio and PL ratio. (D) R/G progress curves obtained from colour images of immobilized QD-Sub_{TRP} spots upon exposure to different concentrations of TRP (see legend in panel E). (E) R/G progress curves in panel D converted to progress curves in terms of PL ratio using the data in panel C. (F) Calibration curve for measuring TRP activity based on the normalized initial rates of digestion. Normalized initial rates were reproducible within 10%.

The utility of the R/G ratio for monitoring proteolytic activity was next tested in a series of assays with TRP, using the digital camera and violet LED to make PL measurements. Paper samples with immobilized QD-Sub_{TRP} conjugates were exposed to increasing concentrations of TRP and colour images were acquired at 5 min intervals for 1 h. The mean spot intensities in the colour channels were used to calculate the R/G ratios for the progress curves in Figure 5.5D. Once again, a blank sample was measured in parallel and used as a reference point to normalize data to account for any non-proteolytic variations between spots. The progress curves in terms of R/G ratio (Figure 5.5D) were converted to progress curves in terms of PL ratio (Figure 5.5E) using the empirical relationship noted previously. The data in Figure 5.5E shows good correspondence with the spectrometer data in Figure 5.4B, confirming the efficacy of this readout format and validating the use of R/G ratio as an analytical parameter.

Initial rates of digestion were derived from the R/G progress curves at 5 min in Figure 5.5D to prepare a calibration plot as a function of TRP concentration, as shown in Figure 5.5F. The data was fit to eqn. 5.1,

$$v = \frac{a[E]}{b + [E]} \propto \frac{V_{\max} [E]}{K_{m,app} + [E]} \quad (5.1)$$

where a and b were constants from least squares regression and v was the initial rate of change in the R/G ratio. This equation is isomorphous with the excess enzyme form of the Michaelis-Menten equation [402], and the constants a and b were taken to be proportional to the maximum proteolytic velocity, V_{\max} , and the apparent Michaelis constant, $K_{m,app}$, respectively. The latter must be an *apparent* value for K_m since the conditions of the experiment do not meet the assumptions of the Michaelis-Menten model (*e.g.* homogeneous system). A value of $K_{m,app} = 77 \pm 16$ nM was derived for the paper-based TRP assay, which is orders of magnitude lower than K_m values reported for other peptidyl substrates for trypsin, including QD-peptide conjugates [485, 486], albeit higher than the value reported for an electroluminescent chip assay with QD-peptide conjugates [401]. Values of $K_{m,app}$ should be useful for comparisons between different substrates and proteases in paper-based assays. The limit of detection (LOD; defined as three standard deviations above the background) calculated from the initial rates was 1.3 nM (0.03 $\mu\text{g/mL}$) TRP. Initial rates were calculated at 5 min of digestion time, suggesting the potential for

rapid analyses. Reliable clinical screening of acute pancreatitis is routinely done with urinary trypsinogen-2 immunochromatographic test strips (Actim Pancreatitis, Medix Biochemica) with an LOD of 0.05 $\mu\text{g/mL}$ and assay time of 3–5 min [487, 488]. This proof-of-concept assay format well compares with commercialized product, albeit the latter uses more complex biological samples for analysis.

The assay format was further evaluated with ChT by self-assembling A555-labeled Sub_{ChT} peptides to a spot of immobilized QDs instead of Sub_{TRP}. Exposure of immobilized QD-Sub_{ChT} conjugates to increasing concentrations of ChT (0–2.0 μM) resulted in progress curves with incrementally faster decreases in R/G ratio, analogous to the experiments with TRP. Figure 5.6A-C shows raw R/G ratios for immobilized QD-Sub_{ChT} exposed to different concentrations of ChT. This data illustrates the conversion of raw data to processed data. In Figure 5.6E, raw R and G channel data is shown, which illustrates a small amount of non-ideal behavior typical of the paper assays with DHLA and GSH coated QDs. There is a small increase in the R/G ratio in the absence of protease (*i.e.* blank sample) over the course of the assay. Such behavior, as well as variability associated with paper substrates, was observed as slight differences in R/G ratio between spots and experiments. These factors, as well as any temporal fluctuations in instrumental response, were accounted for by normalizing the data according to eqn. 5.6 (see Section 5.4.5). These progress curves were analyzed to determine normalized initial rates of digestion and an apparent $K_{m,app} = 145 \pm 27$ nM was derived (see Figure 5.6D). This value is slightly lower than reported for a previous assay for ChT activity with QD-peptide conjugates [291]. The LOD was 1.8 nM (0.05 $\mu\text{g/mL}$) of ChT.

Variations in the normalized initial rates for assays performed on paper substrates from the same synthetic batch and same stock solution of enzyme were typically < 10%. Although proteolysis kinetics were tracked here, “snapshot” measurements could be made at a fixed time point and the difference in R/G ratio used for analysis (rather than the rate of change in R/G ratio).

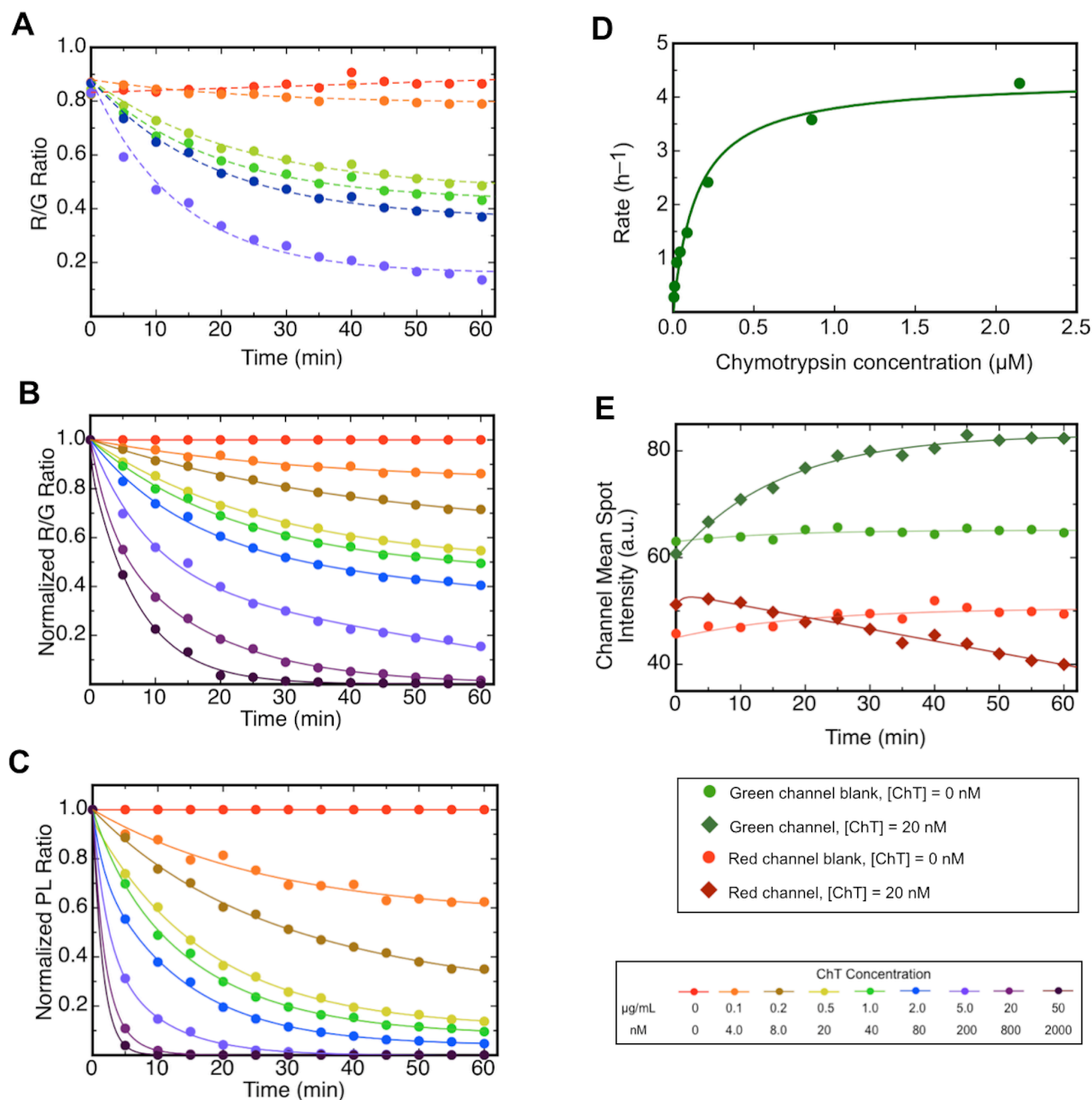


Figure 5.6 (A) Examples of raw R/G ratio progress curves obtained from colour images of immobilized QD-Sub_{ChT} spots upon exposure to different concentrations of ChT. (B) Normalized R/G progress curves derived from the data in panel A and additional data. (C) PL ratio progress curves derived from the data in panel B and the power relationship between R/G and PL ratios, using relationship shown in Figure 5.5C. (D) Calibration curve for ChT activity based on normalized initial rates derived from the progress curves in panel B. The curve was used to determine the apparent K_m . (E) Representative examples of changes in the mean intensity in the G and R channels for QD-Sub_{ChT} exposed to buffer (blank) and 20 nM ChT.

5.2.4.2 Aprotinin inhibition assays with digital colour imaging

Using DHLA coated QDs, an inhibition assay was demonstrated with TRP and aprotinin, a potent competitive inhibitor of many serine proteases and a drug formerly used to control bleeding during surgical procedures [489, 490]. Progress curves were obtained with 860 nM TRP at different concentrations of inhibitor (0.1, 1.0, 15 μM). Figure 5.7 shows R/G ratio progress curves with 860 nM TRP in the presence of different concentrations of aprotinin. In the presence of 0.1 μM aprotinin, the normalized initial rate of digestion decreased 40%, from 3.18 h^{-1} to 1.87 h^{-1} . Complete inhibition was observed at 1.0 and 15 μM aprotinin.

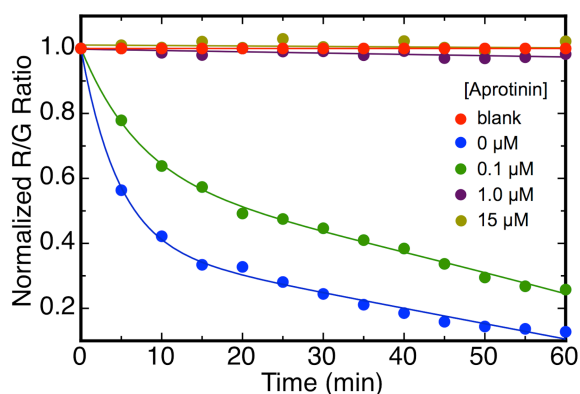


Figure 5.7 Progress curves showing the inhibition of TRP (860 nM, 20 $\mu\text{g}/\text{mL}$) activity by different concentrations of aprotinin.

5.2.4.3 Multiplexed proteolytic assays with digital colour imaging

To demonstrate multiplexed assays, an array of DHLA-QD spots on paper substrates was prepared, where each spot was modified with a different A555-labeled peptide substrate and interrogated using the LED and digital camera. The two-plex detection of TRP and ChT activity were evaluated first. Four paper spots were imaged: one spot with Sub_{TRP} and a second spot with Sub_{ChT} , both of which were exposed to a mixture of TRP and ChT; and two corresponding control spots exposed to buffer as a negative control (blank). Figure 5.8 shows progress curves obtained with three different mixtures of ChT and TRP. Corresponding raw data is shown in

Figure 5.9. A time series of colour digital images are shown in parallel with the R/G progress curves. In each case, the rate of change in the R/G ratio of an assay spot was proportional to the concentration of its target protease. The normalized initial rates of digestion for TRP in the two-plex assay (2.8 h^{-1} at 215 nM and 1.6 h^{-1} at 86 nM) were in relatively good agreement with those measured in the assay for TRP alone (2.3 h^{-1} and 1.6 h^{-1}). Similarly, the normalized initial rates of digestion for ChT in the mixture (0.5 h^{-1} at 8 nM, 1.7 h^{-1} at 80 nM, and 3.6 h^{-1} at 200 nM) were comparable to those measured for ChT alone (0.5 h^{-1} , 1.5 h^{-1} , and 2.4 h^{-1} , respectively).

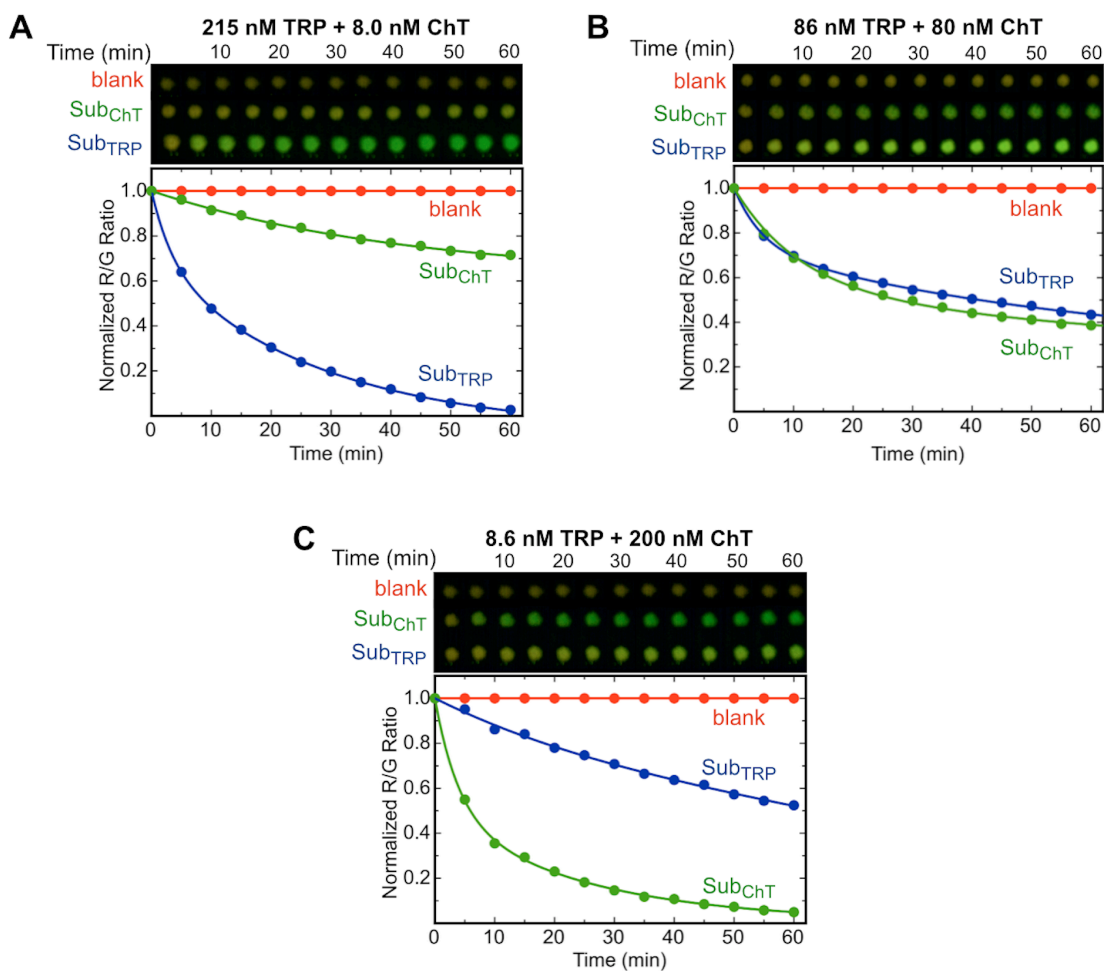


Figure 5.8 Two-plex assays of proteolytic activity. Progress curves and corresponding colour images acquired upon exposure of immobilized spots of QD-Sub_{TRP} and QD-Sub_{ChT} to protease mixtures containing (A) 215 nM (5 $\mu\text{g/mL}$) TRP and 8 nM (0.2 $\mu\text{g/mL}$) ChT, (B) 86 nM (2 $\mu\text{g/mL}$) TRP and 80 nM (2 $\mu\text{g/mL}$) ChT, and (C) 8.6 nM (0.2 $\mu\text{g/mL}$) TRP and 200 nM (5 $\mu\text{g/mL}$) ChT. Only the negative control spot with Sub_{TRP} is shown (blank).

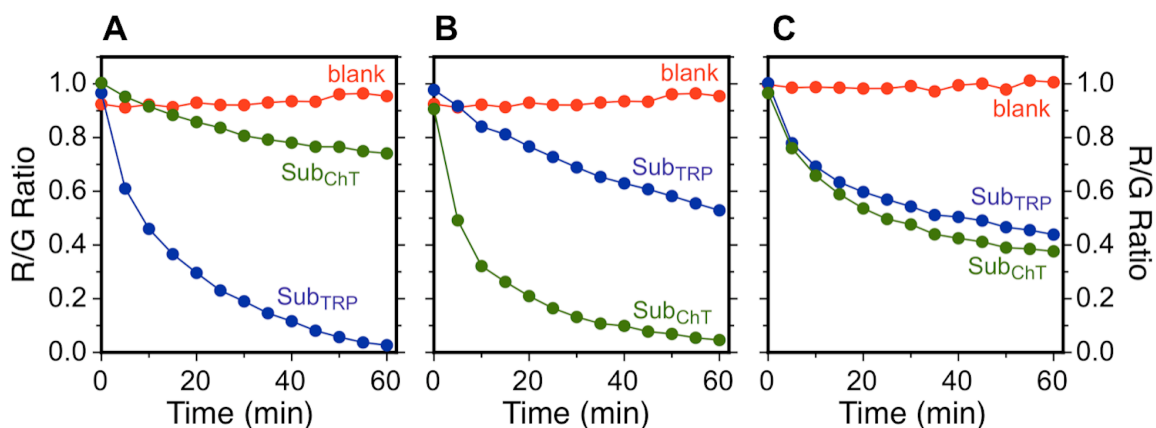


Figure 5.9 Non-normalized R/G ratio progress curves for exposure of immobilized spots of QD–Sub_{TRP} and QD–Sub_{ChT} to protease mixtures containing **(A)** 215 nM (5 $\mu\text{g}/\text{mL}$) TRP and 8 nM (0.2 $\mu\text{g}/\text{mL}$) ChT, **(B)** 86 nM (2 $\mu\text{g}/\text{mL}$) TRP and 80 nM (2 $\mu\text{g}/\text{mL}$) ChT, and **(C)** 8.6 nM (0.2 $\mu\text{g}/\text{mL}$) TRP and 200 nM (5 $\mu\text{g}/\text{mL}$) ChT. Only the negative control spot with Sub_{TRP} is shown (blank). The corresponding normalized data is shown in Figure 5.8.

As shown in Figure 5.10, a three-plex assay with a mixture of EK (7.6 nM), TRP (8.6 nM), and ChT (8.0 nM) was also possible. A mixture of proteases was applied to three paper spots modified with GSH-coated QDs and either Sub_{TRP}, Sub_{ChT}, or Sub_{EK}. Three replicate spots were used as negative controls (blanks). Measurements were made over 6 h because of the low proteolytic activity at these enzyme concentrations and buffer conditions, although initial rates of digestion (EK, 0.07 h^{-1} ; ChT, 0.16 h^{-1} ; TRP, 0.08 h^{-1}) were measurable at 30 min. In general, longer assay times will permit lower LODs and very sensitive assays.

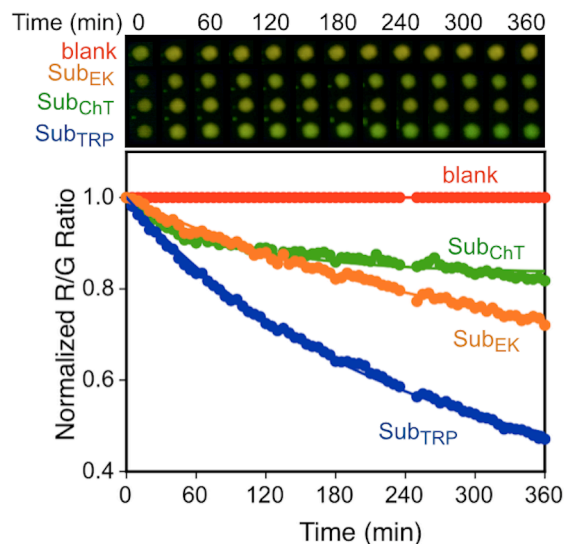


Figure 5.10 Progress curves and corresponding colour digital images for multiplexed protease assays. Spots of GSH-QDs functionalized with Sub_{TRP}, Sub_{ChT}, and Sub_{EK} were tested against a mixture containing TRP 8.6 nM (0.2 $\mu\text{g}/\text{mL}$), ChT 8.0 nM (0.2 $\mu\text{g}/\text{mL}$), and EK 7.6 nM (0.2 $\mu\text{g}/\text{mL}$). Only the negative control spot with Sub_{TRP} is shown.

5.2.4.4 Proteolytic activation assays with digital colour imaging

Given the success of the above multiplexed assays, next multiplexed pro-enzyme activation assays were tested with the paper substrates. The concept of this assay is illustrated in Figure 5.11A. All enzymes exist *in vivo* in its inactive form (*i.e.* pro-enzyme or zymogen) and activated as needed into its active form. For instance, TRP is the product of activation of pro-trypsin (pTRP) by EK, and ChT is an active form of pro-chymotrypsin (pChT), activated by trypsin. An initial experiment (Figure 5.11B) with activation of pChT (195 nM) by TRP (215 nM) revealed that, as expected, the normalized initial rate of digestion of Sub_{ChT} (1.3 h^{-1}) was much slower than assays with an equal amount of ChT (2.4 h^{-1}) because of the activation process. Note that digestion of Sub_{ChT} was a function of both the activation rate of pChT and the subsequent action of ChT on Sub_{ChT}. An interesting observation in these paper-based activation assays was the absence of a clear lag-time and inflection in the progress curve for activated pro-ChT. In prior solution phase assays, such features were observed and attributed to the transition

from pChT to ChT [388, 491]. The heterogeneous kinetics of the paper assay system appears to have obscured these details, albeit that net activation was clearly observed.

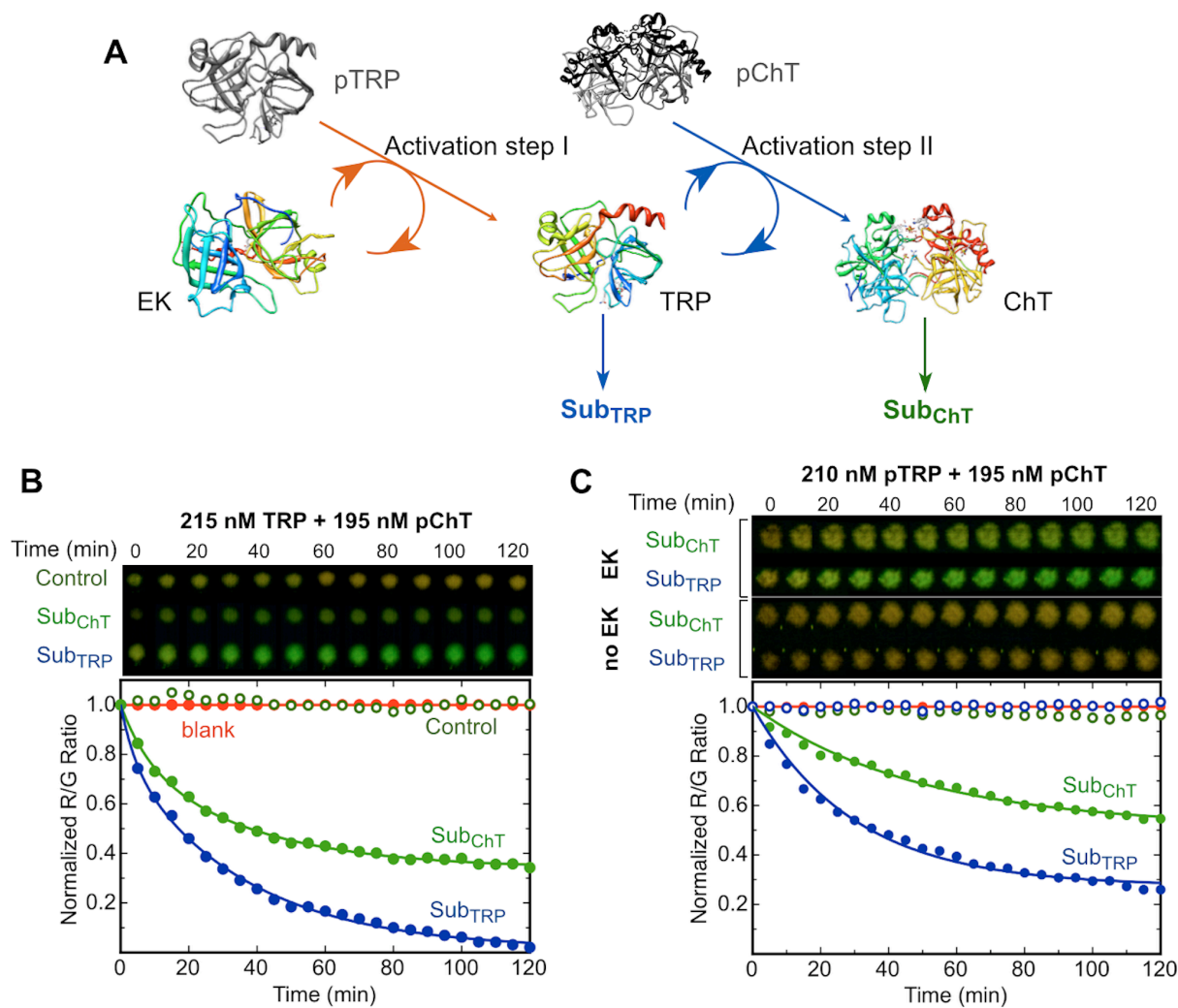


Figure 5.11 (A) Schematic of cascaded pro-enzyme activation: EK activates pTRP to TRP (step I), which then activates pChT to ChT (step II). The formation of active TRP and ChT is monitored with Sub_{TRP} and Sub_{ChT}, respectively. (B) Progress curves and corresponding colour digital images for direct activation of 195 nM pChT (5 µg/mL) by 215 nM TRP (5 µg/mL). Open circles correspond to the control samples containing only pChT at 5 µg/mL. (C) Progress curves and corresponding colour digital images for cascaded activation of 210 nM pTRP (5 µg/mL) and 195 nM pChT (5 µg/mL) initiated with EK (5 units). Open circles correspond to the control samples containing a mixture of pTRP and pChT at 5 µg/mL concentration each (no EK).

A further experiment assaying the two-step sequential activation of pTRP and pChT initiated by EK was done with the LED and digital camera system. Progress curves for the digestion of Sub_{TRP} and Sub_{ChT} with a mixture of pTRP (210 nM, 5 µg/mL), pChT (195 nM, 5 µg/mL), and EK (5 units) are shown in Figure 5.11C. The normalized initial rates of digestion of Sub_{TRP} and Sub_{ChT} were 1.2 h⁻¹ and 0.54 h⁻¹, respectively. Consistent with expectations, these rates were slower than those in the previous one-step activation assay (1.9 h⁻¹ and 1.3 h⁻¹, respectively). No significant digestion of Sub_{TRP} and Sub_{ChT} was observed with pTRP and pChT in the absence of EK. These results clearly demonstrated the utility of this simple paper-based QD-FRET format for complex protease activation assays.

5.2.5 Assays with a webcam and smartphone camera

To establish that paper-based QD-FRET assays were accessible with other devices, it was investigated if the digital camera could be substituted with a consumer webcam (USB connected) or a standalone smartphone camera (iPhone). The webcam is mass produced and the lowest cost detector that was evaluate in this chapter. The smartphone, as described in previous chapters, is an almost ideal standalone platform for both completing the assay and communicating the results [139], and has a distinct portability advantage. To this end, the digital camera, webcam, and smartphone camera were directly compared for multiplexed assays with TRP and ChT.

Figure 5.12 shows R/G ratio progress curves obtained from the images acquired with the digital camera, webcam, and an iPhone. For each device, the time required to reach 90% completion of the digestion reaction agreed within 14% (17 ± 2 min for TRP and 24 ± 3 min for ChT). Similarly, normalized initial rates of digestion (the change in R/G ratio) were found to agree within 7% (4.1 ± 0.2 h⁻¹ for TRP and 3.6 ± 0.3 h⁻¹ for ChT). Overall, the results suggest that R/G ratios from digital colour images can be used for paper-based QD-FRET assays with readout from almost any camera. Importantly, it was also possible to use the smartphone with a battery powered (4.5V; 3×AA cells) LED excitation source for complete portability. The simplicity and low-cost of the three camera setups for quantitative analysis compare favorably with the scanners used with noble metal nanoparticles assays [468, 471, 472] and the clinical reflectometers used with colourimetric small molecule substrate assays [492].

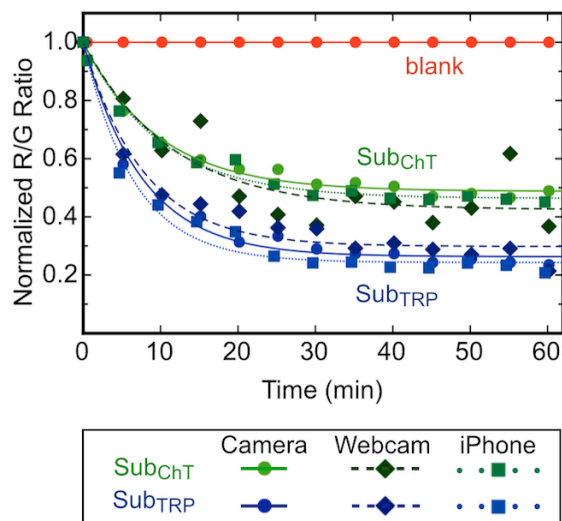


Figure 5.12 Comparison of R/G progress curves acquired with a digital camera, computer webcam, and iPhone (smartphone) upon exposure of spots of immobilized QD-Sub_{TRP} and QD-Sub_{ChT} to a mixture containing 215 nM TRP (5 μ g/mL) and 160 nM ChT (4 μ g/mL). The camera responses are almost indistinguishable.

5.3 Conclusions

This chapter has shown that QDs, in combination with FRET, are suitable for developing quantitative paper-based diagnostics with simple and relatively low-cost optical readout platforms. Paper-based diagnostics are very promising because of their low-cost and simplicity, which translates into potentially broad accessibility. Chemistry used for the immobilization of CdSeS/ZnS QDs on paper was based on modifying its cellulose fibers with thiol ligands that coordinated to the ZnS shell of the QDs. Dye-labeled peptide substrates were self-assembled to the immobilized QDs through polyhistidine metal-affinity coordination. In addition to enabling the assays, immobilization of QDs may help allay concerns about user or environmental exposure to QDs in practical applications. Future use of non-heavy metal QDs (*e.g.* InP/ZnS) may further address any such concerns. The QD-peptide conjugate-modified paper, which was characterized by steady-state and fluorescence lifetime imaging, exhibited highly efficient FRET between the QDs and dye ($\geq 75\%$). Colourimetric changes in PL occurred with protease-catalyzed digestion of the peptides as a result of changes in FRET efficiency: yellow FRET-

sensitized acceptor dye emission transitioned to unquenched green QD donor emission. A series of paper-based assays for proteolytic activity were demonstrated, including inhibition assays, multiplexed assays, and pro-enzyme activation assays. Changes in PL during the assays were visible by eye and quantitative measurements were possible with optical readout platforms that did not negate the accessibility advantages of the paper-based diagnostic concept. Most notably, a violet LED and colour digital imaging permitted robust quantitative detection of protease activity within 5 min and at levels as low as 1–2 nM TRP and ChT using an R/G ratio derived from colour image analysis. Through careful selection of the sequences of peptide substrates, it was possible to achieve high selectivity in multiplexed assays with TRP, ChT and EK. Complex mixtures where enzymes share substrate specificities or where high levels of non-specific protease activity are present will be more difficult to assay; however, this is a common challenge for activity-based assays [493]. The various detection systems, which included an educational-grade digital microscopy camera, consumer webcam, and smartphone camera, required only a USB connection to a computer (or nothing at all in the case of the smartphone) and had costs between a few hundreds of dollars and a few tens of dollars—orders of magnitude less than the cost of the sophisticated laboratory instrumentation currently used for *in vitro* assays with QDs. Although primary focus was on protease detection in this work because of the value of these enzymes as diagnostic and therapeutic targets, the myriad of FRET-based assay and biosensor designs reported in the literature [282, 381] suggest that this chemistry and these readout methods used will be adaptable to many other types of paper-based assays with QDs. Even greater utility will arise from patterning other reagent zones or channel structures on paper substrates to develop μ PADs, dip-strip assays, or lateral devices. Like their gold nanoparticle counterparts, QDs are valuable probes for developing a new generation of paper-based diagnostics.

5.4 Experimental Section

5.4.1 Materials and reagents

Lipoic acid (LA, $\geq 99\%$), *N,N'*-diisopropylcarbodiimide (DIC, $>98\%$), *N*-hydroxysuccinimide (NHS, 98%), ethylenediamine, tetramethylammonium hydroxide (TMAH) solution in methanol (25% w/v), sodium borohydride ($\geq 98\%$), sodium cyanoborohydride (95%), sodium (meta)periodate ($\geq 99\%$), and glutathione (GSH) were from Sigma-Aldrich (Oakville, ON,

Canada). Ammonium chloride and ammonium hydroxide (30% w/w) were from Fisher Scientific (Ottawa, ON, Canada).

Trypsin (TRP) from bovine pancreas (#T1426, TPCK treated, $\geq 10,000$ BAEE units/mg protein), α -chymotrypsin (ChT) from bovine pancreas (#C3412, TLCK treated, Type VII, ≥ 40 units/mg protein), trypsinogen (pTRP) from bovine pancreas (#T1143, $\geq 10,000$ BAEE units/mg protein after activation), α -chymotrypsinogen A (pChT) from bovine pancreas (#C4879, ≥ 40 units/mg solid after activation), and enterokinase (EK) from porcine intestine (#E0885, ≥ 100 units/mg protein) were from Sigma-Aldrich. Recombinant light chain bovine enterokinase (EK, P8070S) was from New England Biolabs (Whitby, ON, Canada).

CdSe_{1-x}S_x/ZnS core/shell nanocrystals (dispersed in toluene) with emission maxima at 525 nm (gQD) were from Cytodiagnosics (Burlington, ON, Canada). QDs were made water-soluble by coating with glutathione (GSH) or dihydrolipoic acid (DHLA) ligands as described in Chapter 2 and Chapter 4, respectively. Peptides were from Bio-Synthesis Inc. (Lewisville, TX, USA) and were labeled with Alexa Fluor 555 (A555) C2 maleimide dye (Life Technologies, Carlsbad, CA) as described previously [368]. The peptide sequences are shown in Table 5.1. Buffers were prepared with water purified by a Barnstead Nanopure water purification system (Thermo Scientific, Ottawa, ON, Canada) and sterilized by autoclaving prior to use. Buffers included borate buffer (50 mM, pH 9.2), borate buffer (10 mM, pH 8.5, 50 mM NaCl), Tris-HCl (20 mM, pH 7.6, 50 mM NaCl, 1 mM CaCl₂), and HEPES (100 mM, pH 7.0).

Table 5.1 Peptide substrate sequences.

Amino acid sequence (written N-terminal to C-terminal)^a	Abbreviation
HHHHHH SPPPPPPS GQGE GEGNSGR↓GGSGNG C(A555)	Sub _{TRP}
HHHHHH SPPPPPPS GQGE GEGNSAAY↓ASGNG C(A555)	Sub _{ChT}
HHHHHH SPPPPPPS GQGE GGN SDDDDK ↓SGNG C(A555)	Sub _{EK}

^a Protease recognition sites are indicated in bold and the cut position is indicated by the downwards arrow.

5.4.2 Preparation of paper substrates

Chromatography paper (Whatman, grade 4) was functionalized with a derivative of lipoic acid, *N*-(2-aminoethyl)-5-(1,2-dithiolan-3-yl)pentanamide, as described in Chapter 4, Section 4.4.2.2 (page 178). Prior to use, paper sheets were cut into 6 × 6 mm² squares for one-plex assays, 6 × 12 mm² for two-plex, and 6 × 15 mm² for three-plex assays. The disulfides were reduced in 50 mM aqueous sodium borohydride solution for 2–4 h, rinsed three times with water and once with ammonium acetate buffer (100 mM, pH 4.5). The paper substrates were then dried for 5 min. QDs (1 μL of 4 μM) were spotted on the paper in an array format necessary for a particular experiment and incubated for 1 h. The paper was then rinsed in borate buffer (50 mM, pH 9.2) and excess water drained. Next, 5 μL of 50 μM A555-labeled peptide substrate was spotted and incubated for 1 h in the dark. Paper was thoroughly rinsed with borate buffer (50 mM, pH 8.5).

5.4.3 Enzyme assays

TRP and ChT protease solutions were prepared in borate buffer (10 mM, pH 8.5, 50 mM NaCl) except when used with EK. Mixtures of TRP/ChT with EK were prepared in Tris buffer (20 mM Tris, pH 7.6, 50 mM NaCl, 1 mM CaCl₂). Protease activity was monitored by adding 100 μL of enzyme solution to paper substrates with one spot of QD-peptide conjugates, and 200–300 μL of enzyme solution to paper substrates with two or three spots (the solution covered all spots). Inhibition assays were done with 860 nM (20 μg/mL) TRP and varying concentrations of aprotinin (0.1–15 μM). Chymotrypsinogen (pChT) was substituted for ChT and trypsinogen (pTRP) was substituted for TRP in pro-enzyme activation assays. For three-plex assays, recombinant light-chain EK was used, whereas native EK was used for activation assays. PL spectra were measured at 1 min intervals and images were acquired every 5 min for 1–2 h unless otherwise indicated. Quantification of protease activity was done at 5 min.

5.4.4 Instrumentation and data acquisition

Paper samples were illuminated with a violet (405 nm) light-emitting diode (LED; VAOL-5GUV0T4, Visual Communications Company, Poway, CA, USA). The LED was controlled and powered using LabVIEW software (see Appendix III) and a USB-6008 data acquisition (DAQ) module (National Instruments, Austin, TX, USA) unless otherwise noted. For imaging experiments with an array of spots, it was necessary to use three LEDs connected in parallel (no

change in power requirements) to illuminate a sufficiently large area. In some experiments, a faint reflection of incompletely filtered LED light off the bubbles of solution on the paper substrates could be observed in images. These reflections were always away from the glowing spots of QDs and did not interfere with data analysis.

PL spectra were obtained from paper samples using a Green-Wave spectrometer (StellarNet, Tampa, FL, USA) coupled with an optical fiber (1000 μm diameter; M37L01, Thorlabs, Newton NJ, USA). A schematic of the setup is shown in Figure 5.13A. PL emission from a paper sample was collected using a 0.5" diameter aspheric condenser lens. A long-pass filter with a 450 nm cut-off (FEL0450, Thorlabs, Newton, NJ, USA) was placed after the lens to reject reflected light from the LED excitation source. A second lens was used to focus the collected PL emission into the optical fiber. Spectra acquisition with a Green-Wave spectrometer was done using LabVIEW software written in-house (see Appendix III).

PL images of paper samples were acquired using either (i) a Moticam 1 (Motic Instruments, Inc., Richmond, BC, Canada) low-cost, educational-grade digital camera, (ii) a C270 webcam (Logitech, Newark, CA, USA), or (iii) an iPhone 4S (Apple, Cupertino, CA, USA). A long-pass filter with a 500 nm cut-off (FEL0500, Thorlabs) was used to reject reflected LED light. A schematic of the setup shown in Figure 5.13. Image acquisition with the Moticam 1 digital camera was done using Motic Images Plus 2.0 software (Motic Instruments). Image acquisition with the C270 webcam was done using LabVIEW software written in-house. All image analysis was done using ImageJ software (National Institutes of Health, Bethesda, MD, USA).

For characterization, confocal fluorescence images were acquired with a Leica (Concord, ON, Canada) SP5 laser scanning confocal microscope equipped with an argon laser (excitation at 458 nm, emission bandwidth 470–740 nm). Images were processed in ImageJ using the Loci plug-in.

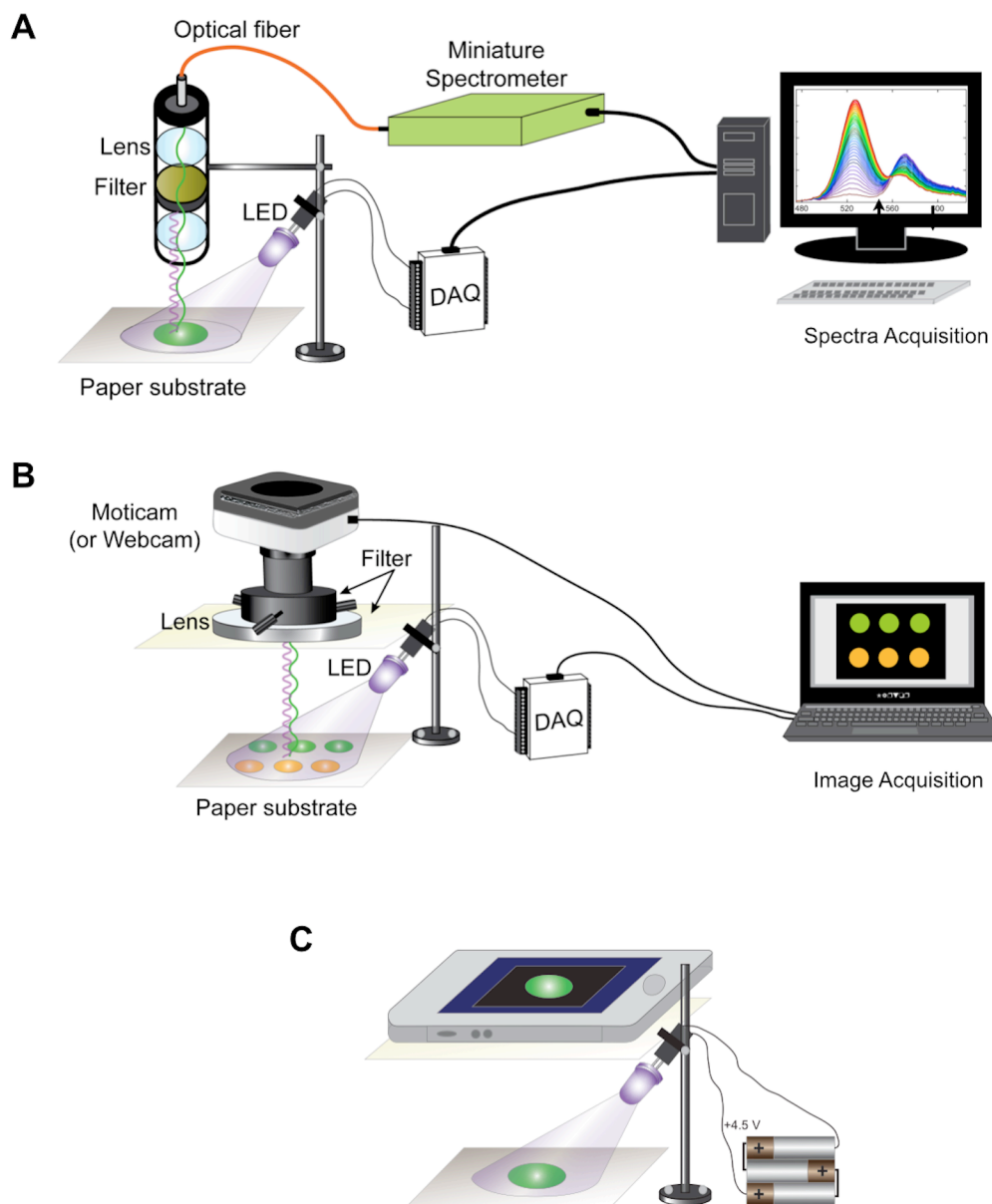


Figure 5.13 Schematics of the instrumental setups used for **(A)** acquisition of PL spectra, **(B)** colour digital PL images with either a low-cost digital microscopy camera (Moticam 1) or consumer webcam, and **(C)** colour digital PL images with a smartphone. For the smartphone imaging, the LED source was powered from three 1.5 V batteries (in series) instead of the USB connected DAQ module. Schematics are not to scale. In each case, a long-pass filter was used to block reflected LED light. The built-in colour filters of the cameras discriminated between QD and dye emission.

Fluorescence lifetime imaging microscopy (FLIM) was done on Zeiss LSM510 two-photon scanning confocal microscope equipped with fluorescence lifetime imaging module (Becker & Hickl GmbH, Berlin, Germany). Two-photon excitation (840 nm) was from a tunable Coherent Chameleon XR femtosecond laser. Data acquisition was done over 8 wavelength channels with an xy -resolution of 128×128 pixels and 256 time channels with data collection for 20-30 min. QD PL was detected in the 525 nm channel and the decay curve was fitted with a biexponential function. Solution phase PL spectra and absorbance spectra were acquired with an Infinite M1000 fluorescence plate reader (Tecan US, Inc., Morrisville, NC, USA).

^1H NMR spectra were acquired with a Bruker 400 MHz spectrometer (Bruker, Billerica, MA, USA). Electrospray ionization (ESI) mass spectra were obtained using a Waters ZQ mass spectrometer (Milford, MA, USA).

5.4.5 Data analysis

5.4.5.1 FRET parameters

The QD-A555 FRET pair was characterized using the Förster formalism as described in Chapter 1 (see Section 1.2.8). The Förster distance, R_0 , was calculated using eqn. 1.18, where the refractive index of the medium, n , was assumed to be 1.335, and the orientation factor, κ^2 , was assumed to be 2/3. The quantum yield of the QDs was measured as described in Appendix II and found to be $\Phi_D = 0.05$ (relative to fluorescein). The spectral overlap was calculated according to eqn. 1.19 and found to be $6.1 \times 10^{-10} \text{ mol}^{-1} \text{ cm}^6$. The *apparent* FRET efficiency, E , was calculated from the PL measurements using eqns. 1.24 and 5.2, as appropriate.

$$E = \frac{\Phi_D \left(\frac{F_{AD}}{F_{DA}} \right)}{\Phi_D \left(\frac{F_{AD}}{F_{DA}} \right) + \Phi_A} \quad (5.2)$$

where the terms F_D and F_{DA} are the fluorescence intensity of the QD donors (D) in the absence and presence of A555 acceptor (A), respectively. F_{AD} is the fluorescence intensity of the acceptor in the presence of donor. $\Phi_A = 0.09$ is the quantum yield of the A555 acceptor.

5.4.5.2 Analysis of spectral data

The relationship between the A555/QD PL ratio, F_{AD}/F_{DA} , and FRET efficiency is defined by eqn. 5.3, where R_0 is the Förster distance for the QD-dye FRET pair, r is the QD-dye separation distance, and n is the number of dye acceptors per QD donor.

$$\frac{F_{AD}}{F_{DA}} = \frac{E}{(1-E)} \left(\frac{\Phi_A}{\Phi_D} \right) = n \left(\frac{\Phi_A}{\Phi_D} \right) \left(\frac{R_0}{r} \right)^6 \quad (5.3)$$

A555/QD PL ratios were used for ratiometric data analysis and were calculated using eqn. 5.4 where $\gamma = 0.022$ is the correction factor calculated as PL(568 nm)/PL(525 nm) for a sample with only QDs using eqn. 1.30 (see Section 1.3.6.1).

$$PL \text{ Ratio} = \frac{PL(568 \text{ nm}) - \gamma PL(525 \text{ nm})}{PL(525 \text{ nm})} \quad (5.4)$$

Although eqn. 5.3 strictly requires a PL ratio in terms of peak areas rather than heights, the PL ratio calculated by eqn. 5.4 is still directly proportional to the right hand side of eqn. 5.3, which is all that is important for the purposes of the analysis.

5.4.5.3 Analysis of RGB data

The R/G ratio from digital colour images were calculated by splitting images into corresponding R-G-B channels, determining the mean intensity (I) of the spots in the red (R) and the green (G) channels, followed by use of eqn. 5.5.

$$\frac{R}{G} \text{ ratio} = \frac{\bar{I}(R)_{spot} - \bar{I}(R)_{background}}{\bar{I}(G)_{spot} - \bar{I}(G)_{background}} \quad (5.5)$$

5.4.5.4 Normalization of progress curves

All experiments were done in parallel with at least one control sample with no added protease(s) to account for any drift in the LED intensity or other sources of temporal variation, including potential photobrightening or photobleaching. At each time point, t , either the PL ratio (eqn. 5.4) or the R/G ratio (eqn. 5.5), $R_{t,[E]}$, was calculated. As shown in eqn. 5.6, each of these values for a

given enzyme concentration, $[E]$, were normalized to an initial value of unity by dividing by the ratio at $t = 0$, and all subsequent time points were then scaled to the control sample as a reference point.

$$R_{N,t} = \frac{R_{t,[E]}/R_{t=0,[E]}}{R_{t,[E]=0}} \quad (5.6)$$

5.4.5.5 Calculation of normalized initial rates

Normalized progress curves were fit with an exponential function in ProFit software (QuantumSoft, Bühlstr, Switzerland) using eqn. 5.7. Normalized initial rates were calculated at time point, $t = 5$ min, by taking the derivative of eqn. 5.7, as shown in eqn. 5.8. For clarity, the normalized initial rates are reported in the text as absolute values (*i.e.* non-negative).

$$\frac{R}{G} \text{Ratio} = 1 - a(1 - \exp(-bt)) \quad (5.7)$$

$$\frac{d}{dt} \left(\frac{R}{G} \text{Ratio} \right) = -ab \exp(-bt) \quad (5.8)$$

Chapter 6 Single-Step Bioassays in Serum and Whole Blood with a Smartphone, Quantum Dots and Paper-in-PDMS Chips

This chapter is an adaptation of published work, and is reproduced from Petryayeva, E.; Algar, W. R., Single-step bioassays in serum and whole blood with a smartphone, quantum dots and paper-in-PDMS chips. *Analyst* **2015**, *140*, 4037-4045, with permission from The Royal Society of Chemistry (Copyright 2015 The Royal Society of Chemistry).

6.1 Introduction

As described in Chapter 1, semiconductor quantum dots (QDs) are one of many promising nanoparticles for bioanalysis applications [6, 374, 375]. Advantages of these materials include their excellent brightness, broad absorption bands, narrow emission bands that can be spectrally tuned as a function of size and composition, superior resistance to photobleaching, and surface area that is amenable to both chemical and biological functionalization [222, 494]. Although fluorescent dyes and other nanoparticles can sometimes rival QDs in one of these aspects, the cumulative properties of QDs are a rare combination. Consequently, QDs have been widely used as labels for cellular imaging and single biomolecule tracking, encoders for suspension arrays, and probes for biological assays and sensing [222, 282, 473, 495, 496]. The latter applications, which include a myriad of Förster resonance energy transfer (FRET) probes, are especially interesting due to the large variety of methods that have been developed and their potential for *in vitro* diagnostics [421, 497]. While an exciting and promising area of research, current limitations of these methods include the frequent use of sophisticated laboratory instrumentation, and infrequent application with clinically relevant biological sample matrices.

In recent years, many research groups have sought to address the foregoing limitations, particularly the need for sophisticated laboratory instrumentation. Smartphones have emerged as promising consumer platforms for the optical readout of assays [157, 158, 345, 498, 499],

opening the door to prospective point-of-care diagnostic applications with QDs and other nanoparticles. The Ozcan Laboratory utilized QDs as fluorescent labels in a sandwich immunoassay for the detection of *Escherichia coli* O157:H7 using cell phone imaging [110]. The work described in this thesis demonstrated the use of smartphone imaging for multiplexed, QD-FRET-based detection of protease activity in solution (Chapter 3), and with sample application to paper test strips (Chapter 5). These examples demonstrate the significant potential of smartphone-based assays with QDs and highlight the need for their continued development. QD-based assays suitable for the direct analysis of analytes in serum matrices have been developed [379, 500], but represent a small subset of the total assays that have been developed and have required sophisticated instrumentation. Most other serum-compatible assays with QDs also use sophisticated instrumentation and further tend to be heterogeneous formats requiring washing steps [501-504]. Consequently, there is a need for assay platforms that permit direct, single-step analysis of serum and blood samples, while also utilizing a smartphone or other mass-produced consumer electronic devices for readout.

This chapter outlines design criteria and demonstrates proof-of-concept for an assay format that utilizes smartphone readout for the single-step, FRET-based detection of hydrolase activity in serum and whole blood, using thrombin as a model analyte. Thrombin plays a central role in thrombosis and haemostasis, with implications in many diseases including stroke and myocardial infarction based on its procoagulant and anticoagulant functions [505]. Although this study builds on the work described in Chapter 5 that demonstrated smartphone readout of QD-FRET-based test strips for proteolytic activity, a near complete redesign of the assay format was required to permit direct measurements in whole blood. Figure 6.1 summarizes the new assay format. A sample spot of immobilized QDs, conjugated with an Alexa Fluor 647 (A647)-labeled peptide substrate, responds to thrombin activity through loss of FRET between the QD and A647 with recovery of quenched QD photoluminescence (PL). The reference spot of QD-peptide conjugates is insensitive to thrombin and serves as an internal standard. The paper test strips are placed inside cells in a polydimethylsiloxane (PDMS)-on-glass sample chip, illuminated with an array of blue light-emitting diodes (LEDs), and changes in QD PL are imaged with a smartphone (or other CMOS camera device) to detect thrombin activity. In addition, the test strips can be adapted to a competitive binding FRET-assay format, such that the assay format may have potential utility beyond assays for the activity of proteases or other hydrolases. Each non-

smartphone component of this assay format was carefully designed or optimized to enable measurements in whole blood, including the LED illumination, the QD-dye FRET pair, the paper test strips, and the PDMS-on-glass sample chip. Overall, this study shows how consumer electronics and QDs can be integrated to permit assays in serum and whole blood in a format that will ultimately be suitable for many point-of-care diagnostic applications.

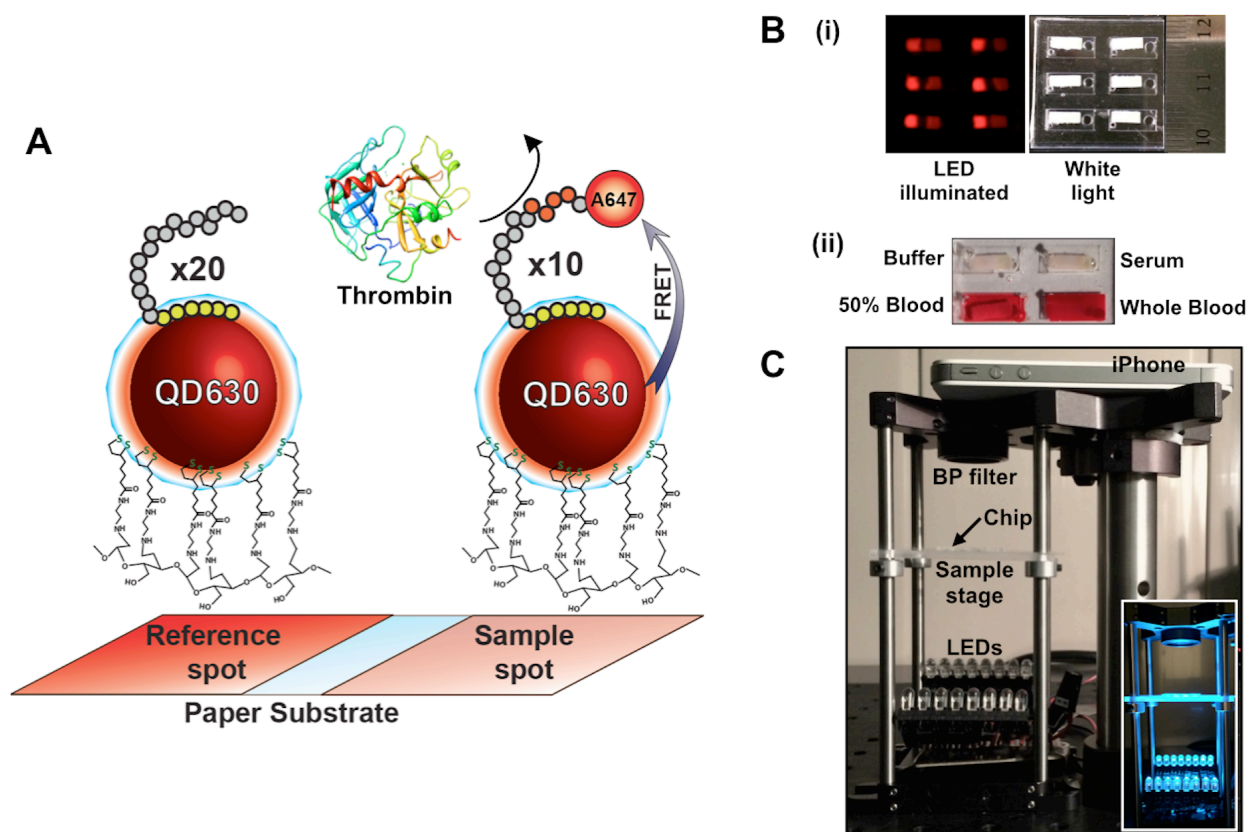


Figure 6.1 (A) Design of paper test strips to measure thrombin activity *via* FRET with immobilized QD donors and A647 acceptor dye-labeled peptide substrates containing a cleavage site recognized by thrombin. Protease activity was measured through the recovery QD PL with loss of FRET. (B) Paper test strips with sample and reference spots of immobilized QD-peptide conjugates were (i) enclosed within PDMS/glass sample cells that were then (ii) filled with a biological sample matrix such as serum, diluted blood or whole blood. Note the opacity of the whole blood. (C) Photograph of the setup used for smartphone readout of QD-FRET test strip assays with serum and blood samples. The inset shows the setup with the LED470 illuminating the PDMS/glass sample chip.

6.2 Results

6.2.1 Assay design: selection of QDs

As noted in the Introduction, several FRET-based assays with QDs have been developed for measuring proteolytic activity and other analytes, but have been rarely utilized with crude samples of biological fluids. Here, the challenge was to adapt the basic QD-FRET assay format to measurements in serum and blood while using low-cost LEDs ($\leq \$1$) and a smartphone or other CMOS camera for readout. It was important to use a readout format that was amenable to point-of-care settings, as that is where crude biological fluids are most likely to be assayed. As shown in Figure 6.2, blood exhibits strong absorption and scattering across most of the UV-visible spectrum, with the greatest optical transmission in the red and near-infrared (NIR) regions of the spectrum. For this reason, and recognizing that smartphones and most other consumer CMOS devices contain a built-in IR-blocking filter, CdSe/CdS/ZnS QDs with red emission were evaluated for assaying proteolytic activity in serum and blood.

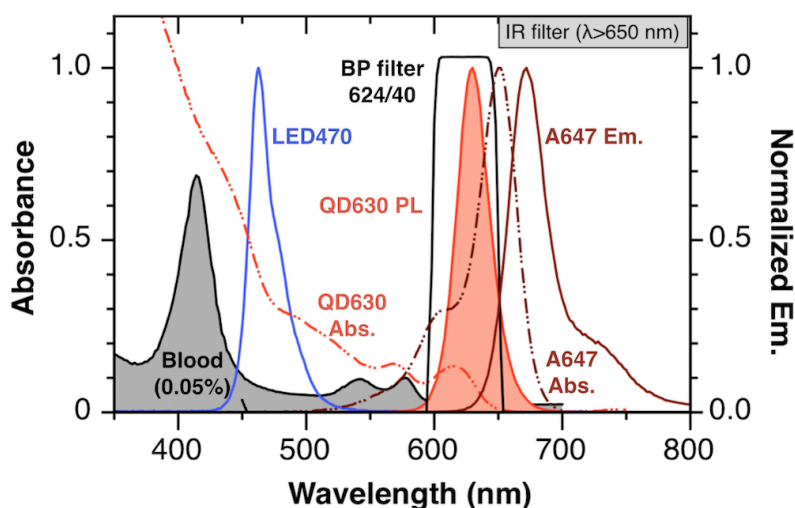


Figure 6.2 Spectra showing the absorption of a blood sample, the absorption (dashed line) and emission (solid line) spectra associated with the QD630-A647 FRET pair, and the emission spectrum of the LED470 excitation source. The fluorescence spectra are normalized for easy comparison. The absorbance spectra were measured for the following solutions: 0.27 μM QD630, 4.0 μM A647, and 0.05% v/v blood (1 cm path length). The transmission spectrum of a 624/40 bandpass filter used to isolate QD emission prior to the smartphone camera is also shown.

6.2.1.1 The effect of QD emission wavelength range

As shown in Figure 6.3, two candidate QDs had emission centered at 630 nm (QD630) and 650 nm (QD650). It was necessary to consider their excitation, emission, and FRET signaling properties. The absorption and emission spectra of QD630 and QD650 are shown in Figure 6.3. The broad and strong absorption of QDs from < 400 nm to *ca.* 600 nm permitted selection of an optimum excitation wavelength that was a compromise between minimizing the attenuation of excitation light by blood and the wavelength-dependent molar absorption coefficients of the QDs. Bandpass (BP) filters were used for imaging QDs with a smartphone (iPhone 5S) and USB-CMOS monochrome camera (the filter eliminated reflected and scattered excitation light). The transmission of the BP624/40 and BP650/40 filters (the numbers indicate the center wavelength/bandwidth for transmission) used with QD630 and QD650, respectively, are shown in Figure 6.3.

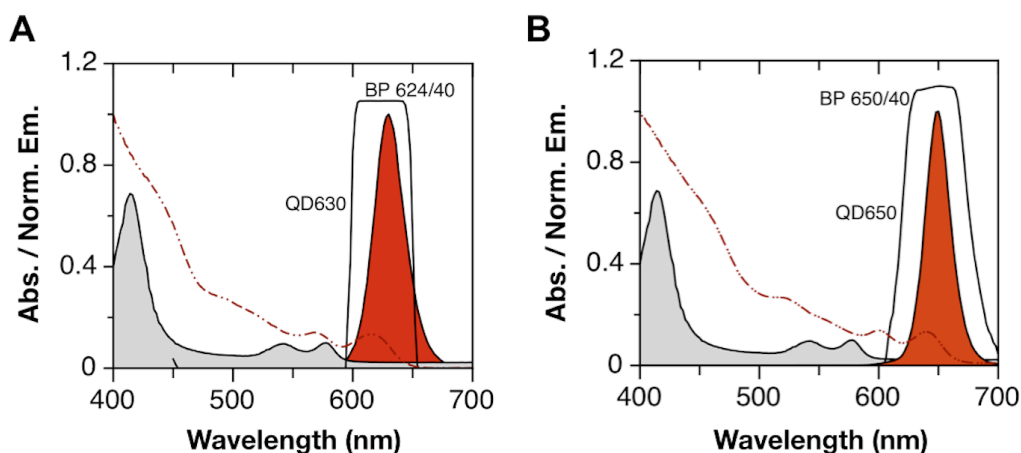


Figure 6.3 Normalized absorption and PL spectra for the (A) QD630 and (B) QD650. The transmission spectra of the bandpass filters are shown as solid black lines and the absorption spectrum of a 0.05% blood sample (path length = 1 cm) is shown as a shaded grey region.

6.2.1.2 The effect of QD excitation wavelength

The emission intensities from QD630 and QD650 spiked into serum and blood at equal concentrations were first compared, as a function of excitation wavelength, to those in a simple buffer solution, using a monochromator-based fluorescence plate reader. Figure 6.4B shows that

the QD emission intensities decreased by *ca.* 15–45% in serum and by *ca.* 82–98% in whole blood. The QD630 and QD650 had quantum yields of 0.77 and 0.25, respectively; however, the larger molar absorption coefficient of QD650 (dashed lines, Figure 6.4B) led to better overall brightness, and the longer emission wavelength of the QD650 provided slightly better retention of signal in serum and blood for excitation wavelengths between 350–570 nm. In buffer samples, a 1.4-fold higher signal was observed from the QD650 *via* smartphone imaging with optimized bandpass filters (624/40 and 650/40 for QD630 and QD650, respectively). The impact of the built-in IR filter associated with the smartphone camera was evident as the QD650 was 2.8-fold brighter than the QD630 when measured with a fluorescence plate reader.

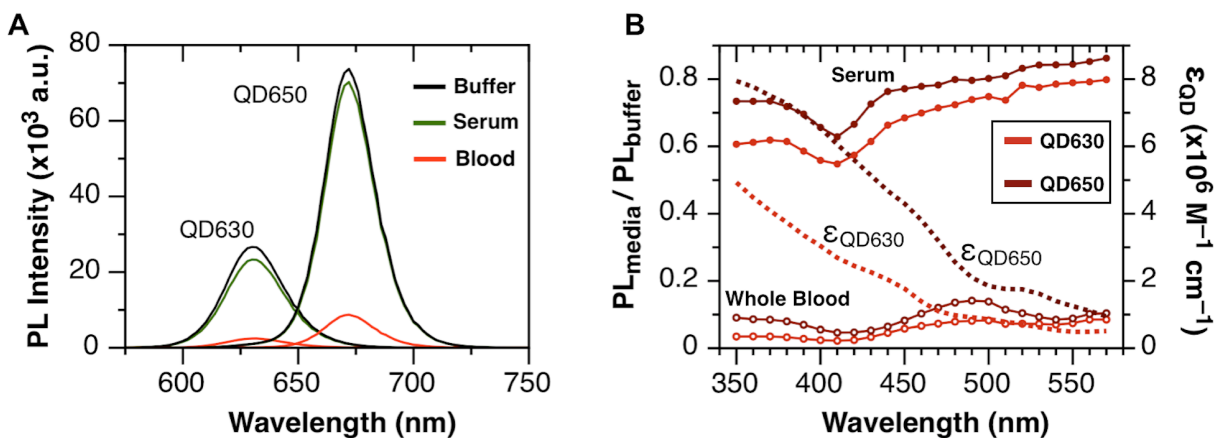


Figure 6.4 (A) Variation in the intensity of the QD630 and QD650 PL spectra as a function of sample matrix (excitation at 470 nm). (B) Excitation wavelength-dependent attenuation of the QD630 and QD650 PL in serum and whole blood (solid lines). The wavelength-dependent molar absorption coefficients of QD630 and QD650 are also shown (dashed lines). These measurements were done with a fluorescence plate reader.

6.2.1.3 Selection of FRET pair: QD630-A647 and QD650-A680

In addition to brightness, another important consideration was FRET for signaling proteolysis. The QD630 were paired with Alexa Fluor 647 (A647) and QD650 with Alexa Fluor 680 (A680). The absorption and emission spectra, and the spectral overlap integrals for each QD-dye FRET pair is shown in Figure 6.5 and photophysical parameters are summarized in Table 6.1. The Förster distances for the QD630-A647 and QD650-A680 FRET pairs were 7.8 nm and 6.2 nm, respectively. TEM images of QD630 and QD650 are shown in Figure 6.6.

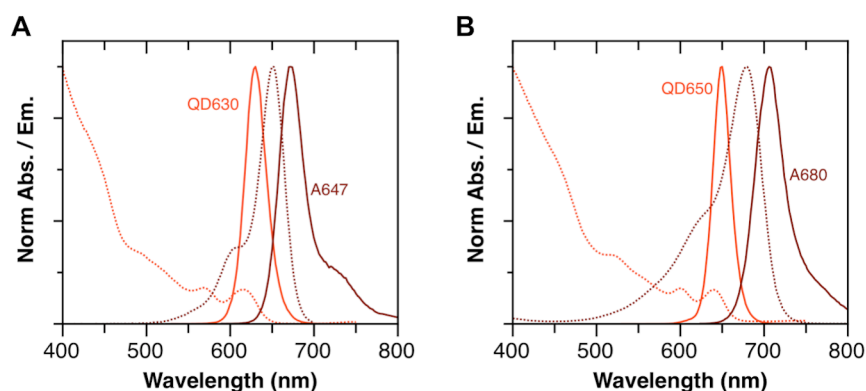


Figure 6.5 Normalized absorption and emission spectra for (A) the QD630-A647 FRET pair and (B) the QD650-A680 FRET pair. Absorption spectra are shown as dotted lines and emission spectra are shown as solid lines.

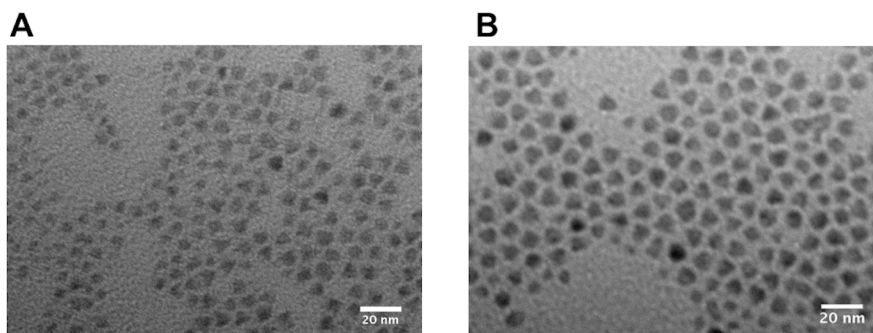


Figure 6.6 TEM images of (A) QD630 and (B) QD650.

Table 6.1 Photophysical parameters of QD630-A647 and QD650-A680 FRET pairs.

QD	$\lambda_{\max,em}^a$	FWHM ^b	Dye	$\epsilon_{A,\max}^c$	Φ_{QD}^d	\varnothing_{QD}^f (nm)	J (cm ⁶ mol ⁻¹) ^g	R_o (nm)	r (nm)
QD630	630	29	A647	250 000	0.77	5.4	2.3×10^{-9}	7.8	10.9
QD650	652	25	A680	175 000	0.25	7.8	2.0×10^{-9}	6.2	12.4

^a Maximum emission wavelength of QD; ^b full-width-at-half-maximum; ^c molar absorption coefficient of the dye at its absorption maximum; ^d quantum yield of the QD; ^f Average diameter of the QD nanocrystal based on the estimate from Figure 6.6; ^g spectral overlap integral.

Figure 6.7A-B shows that when QDs in bulk solution were assembled with increasing amounts of acceptor dye-labeled peptide substrate, Sub(A647) or Sub(A680), and energy transfer was measured in a fluorescence plate reader, the QD630-A647 pair was observed to be a more efficient FRET system. After correction for the Poisson distribution of acceptors per QD, [305] the QD630-FRET efficiency exceeded 70% with 20 acceptors per QD *versus* < 20% efficiency for the QD650-A680. This result was consistent with the smaller Förster distance for the QD650-A680 FRET pair and the larger radius of the QD650 (~3.9 nm *versus* ~2.7 nm for QD630), as can be seen from TEM images shown in Figure 6.6 which increased the effective donor-acceptor separation distance. The average diameter of QDs was calculated to be 5.4 ± 0.2 nm for QD630 and 7.8 ± 0.3 nm for QD650 (sample size > 200 nanocrystals). Despite the somewhat superior brightness of the QD650, the greater FRET efficiencies associated with the QD630-A647 FRET pair and the only somewhat better brightness of the QD650 (40% with smartphone imaging) made QD630 the preferred QD material, particularly since FRET efficiency is a key determinant of assay sensitivity.

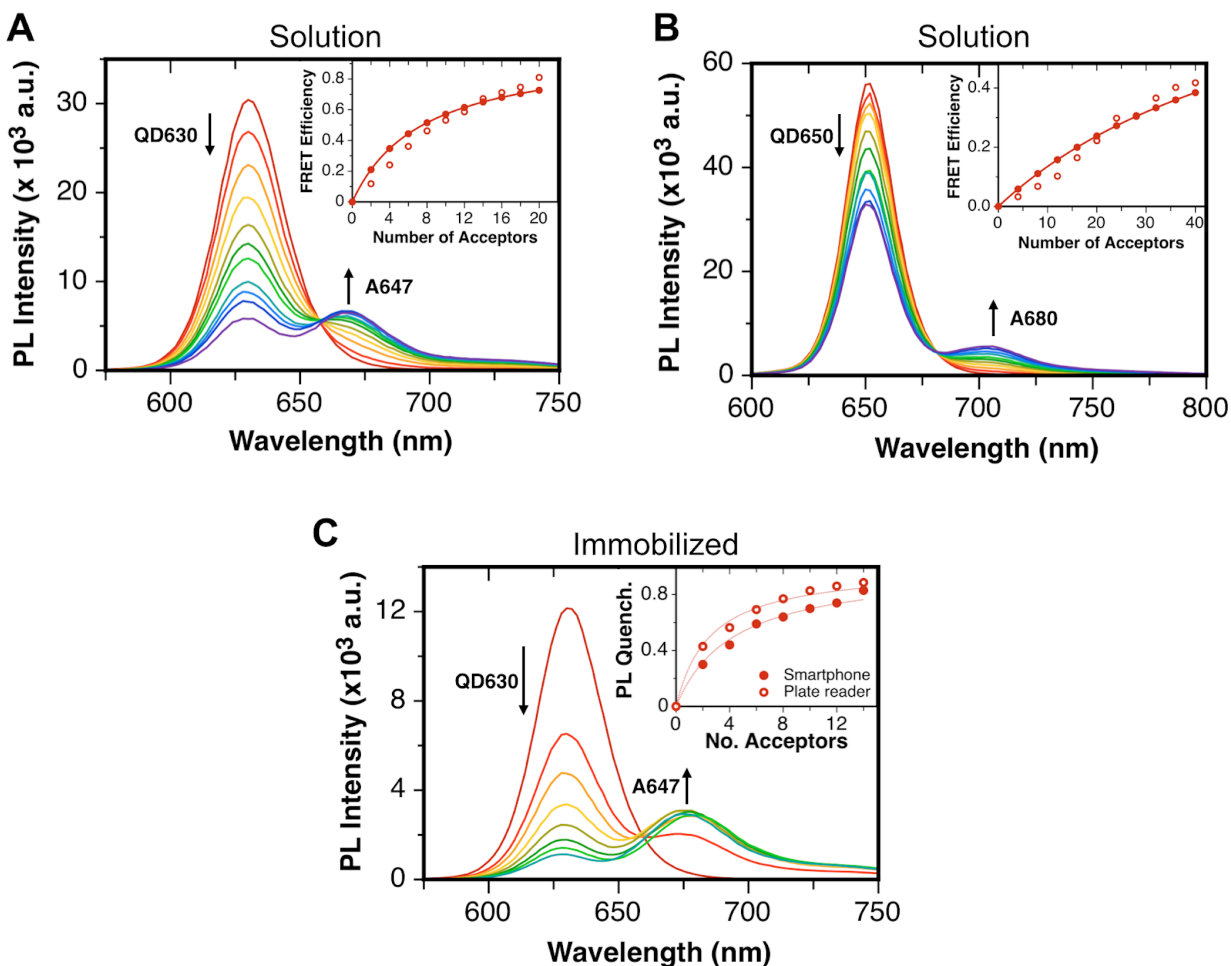


Figure 6.7 Comparison of FRET efficiency between (A) the QD630-A647 and (B) the QD650-A680 FRET pairs in bulk solution, measured with a fluorescence plate reader. Insets in (A) and (B) show the FRET efficiencies calculated from quenching of QD PL according to eqn. 1.24 as a function of the number of acceptors per QD (open circles, raw data; closed circles, Poisson corrected data). (C) PL spectra of paper-immobilized QD630-A647 peptide conjugates. The inset shows extent of QD PL quenching as a function of the number of acceptors, measured from spectra acquired with fluorescence plate reader (open circles) and digital images acquired with smartphone (closed circles).

6.2.2 Assay design: immobilization, reference spot, and sample chip

As Figure 6.1 illustrates, spots of substrate QD-peptide conjugates, QD630-Sub(A647), were immobilized on paper test strips alongside spots of non-substrate QD-peptide conjugates, QD630-Pep. The peptide sequences are given in Table 6.4 (Section 6.5.1, page 241). Typical

spot sizes were $2 \times 2.5 \text{ mm}^2$. The spots of QD630-Sub(A647) were sensitive to thrombin activity by virtue of the LVPRGS amino acid sequence in the substrate peptide. Figure 6.7C shows that assembly of an average of 10 Sub(A647) acceptors per QD630 resulted in *ca.* 70% PL quenching when immobilized on the paper test strip. The same conjugates in bulk solution exhibited *ca.* 50% PL quenching, which is consistent with previous observation of enhanced FRET efficiencies when QDs are immobilized within a paper matrix (Chapter 4). Recovery of QD630 PL from the sample spot was expected with thrombin activity and the resultant loss of FRET. Reference spots had unquenched QD PL that was, to a first approximation, insensitive to thrombin activity. These spots were used for ratiometric data analysis to mitigate fluctuations in excitation intensity, non-uniform illumination, and variations in PL collection efficiency. Sample spots contained 20 pmol of QD630 and 200 pmol of Sub(A647), whereas reference spots contained 5 pmol of QD630 and 100 pmol of Pep. The difference in the amount of QD630 between the sample and reference spots was necessary to ensure that QD PL intensity from both spots was within the dynamic range of digital images acquired with the smartphone (or other CMOS camera device).

In the case of blood samples, and despite the best efforts to optimize the selection of QDs, the biggest determinant of the observed QD PL signal was the path length through the blood. The maximum signal was observed for a path length of 250–300 μm , which was the shortest length that could be achieved with paper substrates and also the most relevant to the assay format because paper test strips had a thickness of *ca.* 200 μm . For path lengths of 1.2 mm and 450 μm , 80% and 50% reductions of QD630 PL, respectively, were observed relative to the shortest path length, as shown in Figure 6.8. Given the foregoing, the paper test strips functionalized with QDs were placed within $4 \times 9 \times 0.25 \text{ mm}^3$ PDMS cells (see Figure 6.1B) on a glass chip. Each cell required only 12 μL of sample, minimized drying of the sample during analysis, and ensured a reproducibly short path length (*ca.* 250 μm). This format was suitable for the analysis of buffer, serum, 50% blood, and whole blood samples.

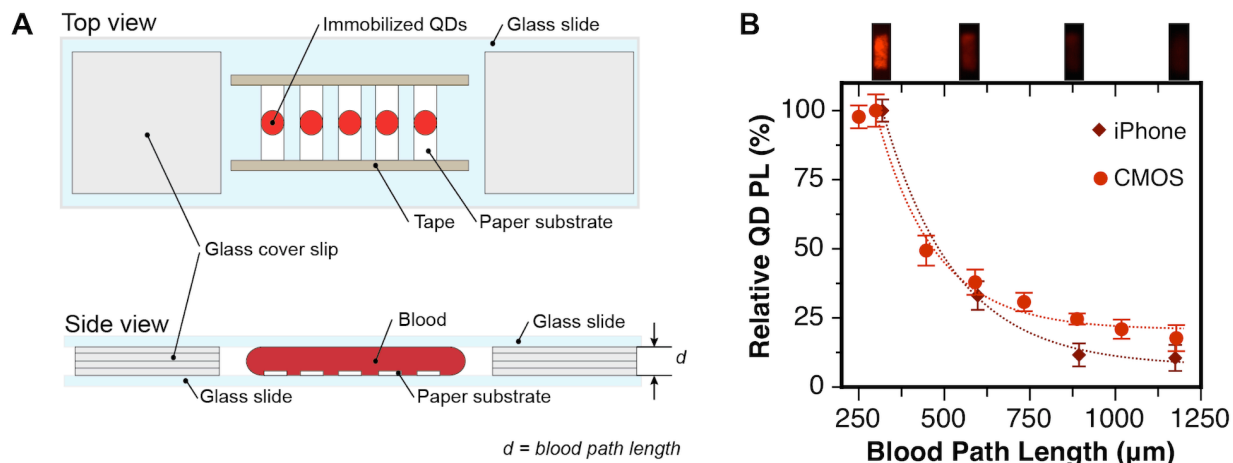


Figure 6.8 (A) Experimental design to determine effect of the optical path length through blood on measured PL intensity of immobilized QDs. The paper substrates were placed between two glass slides and distance separation was controlled by placing cover slips ($n = 1-8$) between them. **(B)** Effect of the optical path length through blood on attenuation of QD630 PL intensity from paper substrates measured with iPhone and CMOS monochrome camera.

Another factor that limited the brightness of QD630 PL was the intensity of excitation light that could be delivered. Trans-illumination of the spots of QD630 with LED470 light provided better signal-to-background ratios than epi-illumination. Although trans-illumination was more favorable than epi-illumination, the attenuation of excitation light by the paper test strip was nonetheless non-trivial. Only $\sim 5\%$ of the incident excitation was transmitted directly through a paper test strip, and an exponential decrease in transmission was observed with increasing paper thickness (*i.e.* paper layers in this experiment). It is important to note that the values in Figure 6.9 represent transmitted intensities. Since QDs were immobilized throughout the thickness of the paper, QDs near the face of the paper closest to the LED experienced much greater excitation intensity than those on the opposite face. With epi-illumination, in the case that the test strip was at the bottom of a blood sample with a non-trivial path length, the excitation light was attenuated by the blood before reaching the near face of the paper test strip, resulting in a lower average excitation intensity for the QDs than with trans-illumination. In addition, attenuation of excitation light by paper and blood in the trans-illumination configuration minimized the amount

of excitation light reaching the detection optics. The open space between the sample chip and detector was also more convenient for adding samples to the chip and running assays.

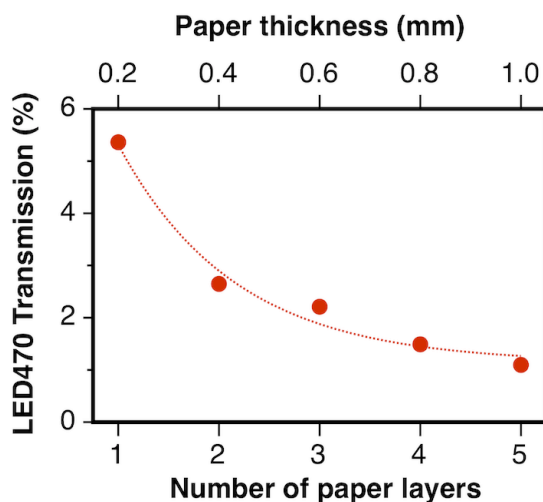


Figure 6.9 Effect of thickness of the paper on the intensity of LED470 light transmitted through chemically modified Whatman chromatography paper No. 4 soaked in buffer.

6.2.3 Assay design: readout platform

An array of 5 mm (T-1 ³/₄) LEDs was chosen to illuminate the sample chip and excite QD PL because of the compact size, low-cost, low-power requirements, and relatively wide illumination area of LEDs. To select the optimum LED for assays in whole blood, a variety of LED types and colours that were potentially suitable for excitation of QD630 (peak emission wavelengths within the range from *ca.* 385–585 nm; see Table 6.2, Section 6.2.3.1, page 229) were evaluated. Important considerations included:

- (1) the brightness of an LED,
- (2) the molar absorption coefficient of the QD630 at the LED emission wavelength,
- (3) the optical density of blood at the LED emission wavelength, and
- (4) crosstalk between the long-wavelength tail of the LED emission and the QD630 PL.

From the standpoint of the QD630, UV (385 nm) and violet (405 nm) LEDs were ideal because these wavelengths corresponded to the highest molar absorption coefficients, were spectrally well-separated from the QD630 emission, and had been used effectively in previous studies with QDs, as described in Chapter 5. Unfortunately, it is in this spectral region that serum and blood most strongly attenuated light. At longer wavelengths, yellow (565, 585 nm) and orange (605 nm) LEDs were found to have relatively low brightness that, when combined with the lower light absorption by the QD630 at these wavelengths, were poorly suited for measurements. Moreover, a significant issue was very large crosstalk with the QD630 PL from the red tail of the LED emission. Blue (470 nm) and green (500, 510, 525 nm) LEDs were found to be a good compromise between maximizing excitation of the QDs and maximizing transmission through blood samples, and were available with very bright emission. A blue LED (LED470) was ultimately found to be optimum because green LEDs had significantly greater crosstalk with QD630 PL, less efficient excitation of the QD630, and lower brightness (see Table 6.2, page 229). The emission spectrum of the LED470 is shown in Figure 6.2 relative to the absorption spectrum of blood, as well as the absorption and emission spectra of the QD630.

6.2.3.1 LED brightness

To detect QD630 PL, pulsed LED illumination was synched with image acquisition and used to minimize effects such as photobrightening of the QD630 and photobleaching of the A647, which were observed with time under continuous illumination. LEDs were turned on with the applied voltage indicated by the manufacturer (Table 6.2B). The LED spectra were collected with a portable spectrometer and the integrated emission intensities were calculated (Table 6.2B) to identify the brightest LEDs (LED No. 5, 7, 8, and 10). These results largely correlated with those obtained by measuring the LED output with an optical power meter (Table 6.2E).

Next, the ability of LEDs to excite QD630 and QD650 PL was evaluated. Aqueous samples of QDs were illuminated with an LED (see Figure 6.15, Section 6.5.7.2) and QD PL spectra were acquired with a portable spectrometer. The relative QD PL intensity between LED excitation sources was calculated according to eqn. 6.1. The results are summarized in (Table 6.2G, J).

$$PL_{QD} = \left(\frac{\int_{550}^{750} I_{QD}}{\left[\int_{550}^{750} I_{QD} \right]_{MAX}} \right) \times 100\% \quad (6.1)$$

The magnitude of integrated QD PL intensity was dependent on the brightness of an LED, the size of the QD molar absorption coefficient over the wavelength range of LED emission, and the quantum yield of the QD. The QD630 and QD650 molar absorption coefficients at the peak LED emission wavelengths are indicated (Table 6.2F, I). The strongest QD PL was observed with a blue LED470 (LED No. 5), followed by a green LED525 (LED No. 10), and a UV LED385 (LED No. 1).

Table 6.2 Characterization of LEDs as excitation sources for QD630 and QD650.

	(A)	(B)	(C)	(D)	(E)	(F)	(G)	(H)	(I)	(J)	(K)
LED	λ_{\max}	I_{LED} (%)	X_{LED} (%)	V_{appl}	Output (mW)	ϵ_{QD630} ($\times 10^5 \text{ cm}^{-1} \text{ M}^{-1}$)	PL_{QD630} (%)	$X_{\text{LED/QD630}}$ (%)	ϵ_{QD650} ($\times 10^5 \text{ cm}^{-1} \text{ M}^{-1}$)	PL_{QD650} (%)	$X_{\text{LED/QD650}}$ (%)
1	385	1.1	0.24	3.6 V	1.44	36.0	46.2	0.02	71.6	41.0	0.007
2	405	3.0	0.09	3.6 V	1.32	28.2	19.7	0.04	62.4	19.7	0.014
3	470	7.8	0.04	3.6 V	1.23	11.0	20.0	0.015	32.0	19.7	0.007
4	470	0.3	0.07	3.8 V	0.60	11.0	2.0	0.006	32.0	2.1	0.006
5	470	72.0	0.01	4.0 V	3.80	11.0	100.0	0.019	32.0	100	0.006
6	465	5.9	0.01	3.8 V	0.97	12.6	17.4	0.013	36.0	18.3	0.005
7	500	40.9	0.09	4.0 V	2.90	8.42	37.9	0.32	18.2	35.0	0.061
8	510	100.0	0.07	4.0 V	2.53	7.87	29.1	0.74	17.6	27.3	0.13
9	525	41.5	0.39	4.0 V	1.86	6.79	21.6	2.6	17.2	21.7	0.34
10	525	36.2	0.39	4.0 V	2.14	6.79	65.0	0.56	17.2	63.7	0.065
11	565	2.6	0.73	2.4 V	0.66	5.03	0.01	662	10.4	0.0	286
12	585	0.1	21.5	2.4 V	0.59	3.84	0.03	285	7.85	0.1	22

(A) λ_{\max} = wavelength of maximum emission; (B) I_{LED} = integrated intensity of LED relative to the LED with highest intensity; (C) X_{LED} = crosstalk of the LED in 600–650 nm spectral range (eqn. 6.2); (D) V_{appl} = applied LED voltage ; (E) light output from the LED at the specified voltage; (F, I) ϵ_{QD} = molar absorption coefficient of the QD at the peak LED emission wavelength; (G, J) PL_{QD} = relative QD PL with LED excitation calculated (eqn. 6.1); (H, K) $X_{\text{LED/QD}}$ = crosstalk of the LED relative to the QD PL (eqns. 6.3-6.4).

6.2.3.1 LED crosstalk

Another important factor in LED selection is the extent of crosstalk with the QD detection channel, as scattered excitation light was unavoidable in our assays and optical filters are imperfect. The relative LED crosstalk, X_{LED} , in the putative red channel for smartphone imaging (600–650 nm) was calculated according to eqn. 6.2 from spectrometer measurements (Table 6.2C). As expected, LEDs with emission in the green-yellow region of the spectrum had the greatest crosstalk from their emission tails.

$$X_{LED} = \left(\int_{600}^{650} I_{LED} / \int_{350}^{700} I_{LED} \right) \times 100\% \quad (6.2)$$

Furthermore, to evaluate LED crosstalk under conditions similar to the assay, LED spectra were acquired with a longpass filter (600 nm cutoff). The LED crosstalk relative to the QD PL intensity measured upon excitation with the same LED was calculated according to eqns. 6.3–6.4 (Table 6.2H,K).

$$X_{LED/QD630} = \left(\int_{604}^{644} I_{LED} / \int_{604}^{644} I_{QD630} \right) \times 100\% \quad (6.3)$$

$$X_{LED/QD650} = \left(\int_{630}^{670} I_{LED} / \int_{630}^{670} I_{QD650} \right) \times 100\% \quad (6.4)$$

All LEDs had negligible crosstalk in the QD650 channel (650/50 filter), whereas the largest crosstalk in QD630 channel (625/50 filter) was noted with yellow-emitting LEDs. This result was due to a combination of inefficient excitation of the QD (lower intensity LED, smaller absorption coefficient at those wavelengths) and an LED emission profile that tailed into the red region of the spectrum. Less than 1% crosstalk was calculated for the UV and blue-emitting LEDs. Although some of the crosstalk values may appear small, it is important to note that LED emission is many times brighter than QD PL.

6.2.3.2 LED emission attenuation by blood

Given the foregoing evaluation of candidate LEDs, and the efficiency of QD excitation and minimization of crosstalk, five LEDs emerged as leading candidates: a blue LED (No. 5), green LEDs (No. 7, 8 and 10), and a UV LED (No. 1). These five LEDs were further compared by exciting paper-immobilized QDs soaked in blood. No QD PL was observed upon excitation with the UV LED, primarily due to the strong absorption and scattering of these wavelengths by blood. Between the green LEDs and blue LED, excitation of immobilized QDs in a blood matrix with a blue LED provided a more than 8-fold better signal-to-background ratio (Table 6.2, LED No. 5). This result was due to both the spectral characteristics of the LED and its intensity level. Therefore, LED470 (No. 5) was used as the excitation source for all assays.

6.2.4 Thrombin assays

Samples containing various concentrations of thrombin (7.6–480 NIH units) were added to cells in the sample chip, where each cell contained a paper test strip with substrate and reference spots of QD-peptide conjugates. Changes in QD630 PL were monitored over time with either smartphone or USB-CMOS camera imaging. Buffer, serum and blood samples were tested. Mean spot intensities from reference and sample spots, measured *via* images, were used to calculate a signal ratio (eqn. 6.6, Section 6.5.7.2) that helped account for fluctuations and differences in illumination intensity between sample cells in the chip. A blank sample (*i.e.* sample and reference spot exposed to sample matrix only) was measured in parallel and used to normalize data (eqn. 6.7, Section 6.5.7.2) to account for non-proteolytic changes. Smartphone imaging-derived progress curves for the digestion of Sub(A647) by increasing concentrations of thrombin are shown in Figure 6.10 as a function of the normalized QD PL intensity. The progress curves were reduced to average hydrolysis rates for quantitative analysis.

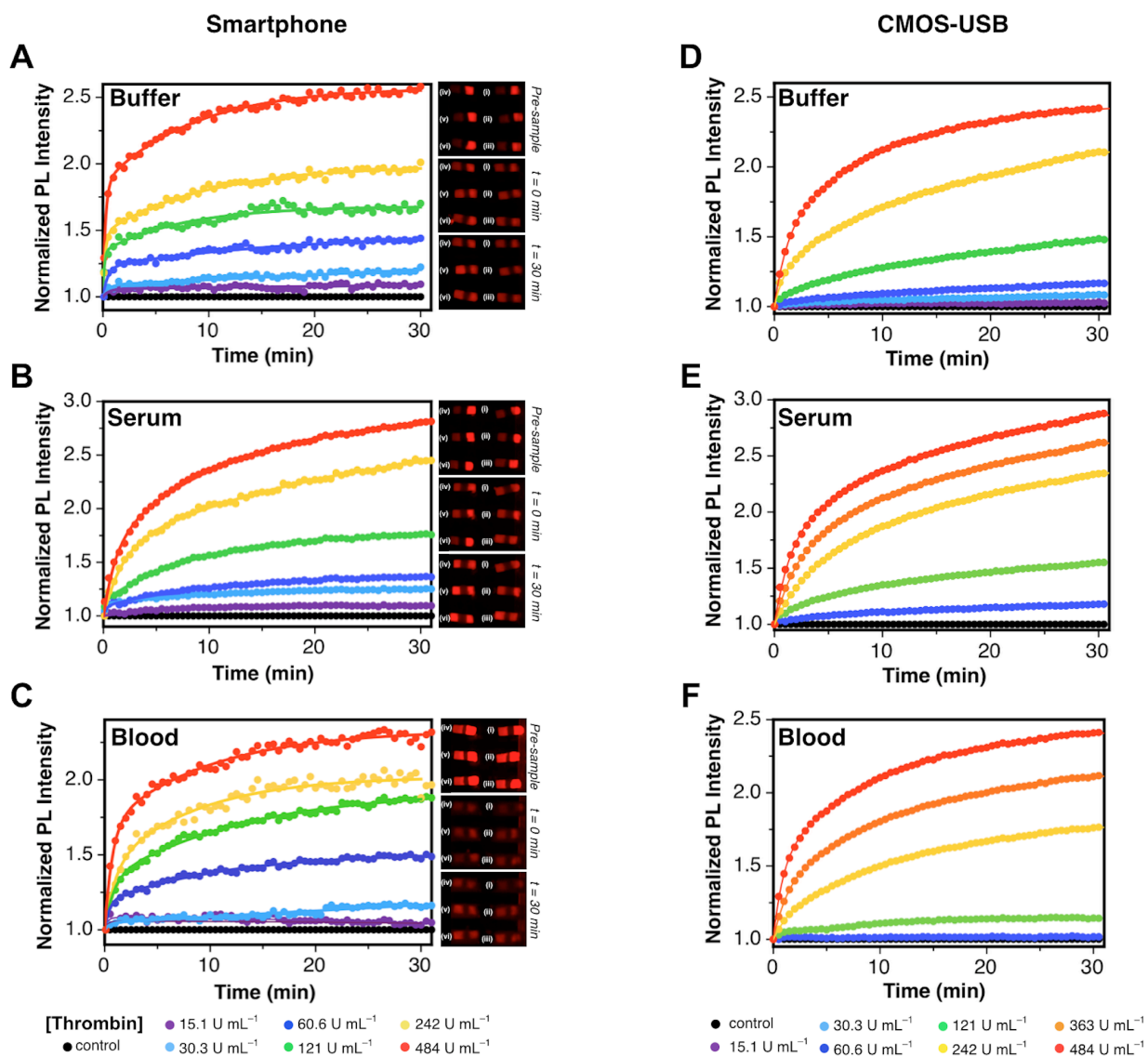


Figure 6.10 Normalized progress curves for thrombin activity in (A, D) buffer, (B, E) serum, and (C, F) whole blood samples, measured *via* smartphone imaging (A, B, C) and *via* a USB-CMOS camera (D, E, F). Representative smartphone images are shown for three points in the assays: prior to the addition of sample, immediately after adding sample, and after 30 min. In each image, the spiked thrombin concentrations were (i) 0, (ii) 15.1 NIH U mL⁻¹, (iii) 30.3 NIH U mL⁻¹, (iv) 121 NIH U mL⁻¹, (v) 242 NIH U mL⁻¹, and (vi) 484 NIH U mL⁻¹.

Some adjustment of acquisition parameters (*e.g.*, LED intensity, camera exposure; see Table 6.7, Section 6.5.6.3, page 250) was necessary for assaying different sample matrices. The average

rates obtained from progress curves were used for quantification of thrombin in the sample. For smartphone readout, Figure 6.10, the limit of detection (defined as three standard deviations above the average rate calculated for progress curves for negative controls samples) was *ca.* 12 NIH units mL^{-1} for thrombin in buffer and serum, and *ca.* 18 NIH units mL^{-1} for whole blood assays. Assays with the USB-CMOS camera readout yielded results that were similar to analogous assays with smartphone readout (see Figure 6.10D-F).

6.2.4.1 Blind assay for thrombin activity in blood

A set of blind assays was also done to confirm that calibrations of the type in Figure 6.10 could be used to determine unknown thrombin activities. Whole blood samples spiked with three concentrations of human thrombin were analyzed as five replicates in the sample chip. Normalized progress curves are shown in Figure 6.11 and Table 6.3 summarizes these results and, within the experimental uncertainty, shows good agreement between spiked thrombin concentrations (unknown to the assayer) and those determined from QD PL measurements and calibration data. Notably, the precision and accuracy decrease as the thrombin concentration increases and the rate of hydrolysis of $\text{Sub}_{\text{THR}}(\text{A647})$ increases; however, this limitation is common to all rate-based enzymatic activity assays and is not unique to the readout format.

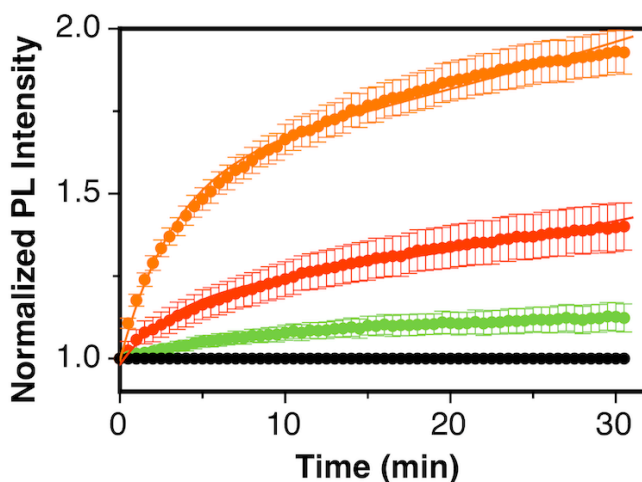


Figure 6.11 Progress curves for the detection of thrombin activity in blind samples. Error bars describe standard deviation ($n = 5$).

Table 6.3 Results of blind assays for thrombin in whole blood.

Blind Sample	Concentration of Thrombin (NIH U mL ⁻¹)		Relative Error (%)
	Measured	Spiked	
1	154 ± 34	157	1.9
2	96 ± 8	97	1.0
3	348 ± 85	291	20

6.2.5 Competitive binding assays

While activity-based assays for thrombin are analytically important [506, 507], there are many other prospective protein analytes in blood, many of which are not hydrolase enzymes. One of the most common approaches in biochemistry and clinical diagnostics to detect this type of analyte is *via* a binding experiment, where either two proteins can bind each other, or a protein binds to a nucleic acid. In a competitive binding assay, an analyte of interest competes for binding sites with a synthetic analyte labeled with a fluorescent reporter at a known concentration. Therefore, to evaluate the smartphone imaging platform with a competitive binding assay format, the well-established biotin-streptavidin interaction was studied as a model system. QD630 conjugated with biotinylated peptide, Pep(biotin), were immobilized within paper substrates and exposed to various amounts of A647-labeled streptavidin (SAv). Increasing the SAv-A647 equivalents per QD from zero to four resulted in parallel decreases in QD PL and increases in FRET-sensitized emission from A647, as shown in Figure 6.12A. The red channel response of colour images indicated that QD PL quenched up to *ca.* 60% (*cf.* 80% from PL spectra acquired with spectrofluorimeter). Despite the differences in the response between the two imaging methods, it can be seen in Figure 6.12B that the general trend was consistent within each method and that QD PL quenching increased with increasing number of SAv-A647. A competitive binding assay with QD630 and SAv-A647 was evaluated in buffer (Figure 6.12C) and 50% blood (Figure 6.12D) by spiking samples with various amounts of unlabeled streptavidin (SAv). As shown in Figure 6.12D, detection of streptavidin in 50% blood was

possible at levels between 200 nM–10 μ M. It should be possible to use this assay format with other more interesting protein analytes by substituting biotin with ligands for those proteins. Although preliminary, these results suggest that that QD-FRET signaling and LED/smartphone readout have the potential for broader applicability than hydrolase assays.

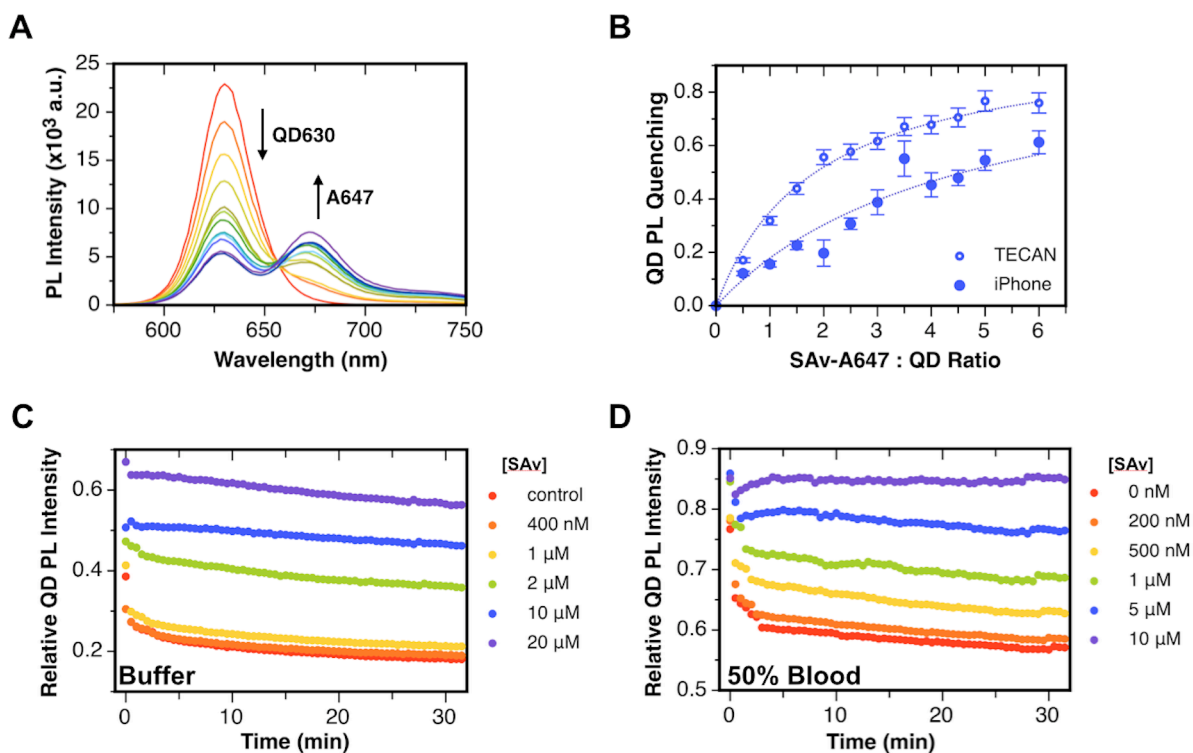


Figure 6.12 (A) PL emission spectra corresponding to the increasing number of SAV-A647 binding to immobilized QD630-Pep(biotin) conjugates. The number of SAV per QD were 0, 0.5, 1, 1.5, 2, 2.5, 3, 3.5, 4, 4.5, 5, and 6. (B) QD PL intensity corresponding to (A); spectral data is plotted in terms of the QD peak PL intensity and smartphone data is plotted as the red channel intensity. The other panels show data from paper-based competitive SAV assays in (C) buffer and (D) 50% blood. The data is the relative QD PL intensity as a function of time upon exposure to different concentrations of SAV (analyte) and a fixed concentration of SAV-A647 (competitor). For assays in buffer, the concentration of SAV-A647 was 2.0 μ M, whereas the concentration for assays in 50% blood was 1.0 μ M.

6.3 Discussion

There is a need for assay methods that can be applied directly in serum and, more ideally, whole blood, particularly in the context of point-of-care diagnostics. Among other criteria, these point-of-care diagnostics require simple and accessible platforms for readout of assays [35, 36]. Smartphones are highly promising candidates for assay readout because of their multitude of features, including high-quality built-in cameras, excellent storage capacity, wireless communication (LTE, WiFi, Bluetooth), and software applications (apps). Importantly, smartphones are also ubiquitous with more than 61% of mobile subscribers owning smartphones in the US as of 2014 (with similar ownership statistics in Canada and Europe) [71]. Smartphone imaging can also generate quantitative data from diagnostic tests that have typically been qualitative (*e.g.* colourimetric assays). This Chapter shows that a well-thought-out combination of quantum dots with smartphone imaging can offer direct, single-step and quantitative fluorescence-based detection of analytes in whole blood, in a manner that is very amenable to point-of-care applications.

Two of the major challenges faced in this work were the physical and chemical properties of whole blood. Physically, blood is a strongly absorbing, strongly scattering and autofluorescent sample matrix, often resulting in poor sensitivity in optical assays. Oxy-hemoglobin has absorption peaks centered at 541 and 577 nm, deoxyhemoglobin has an absorption peak at 555 nm, and both have strong UV absorption [508, 509]. NAD(P)H, vitamins A and B6, collagens, folic acid, and cholecalciferol fluoresce in the 300–450 nm region, and porphyrins fluoresce at 500 nm and 630 nm [508]. Blood cells are also good light scatterers [510]. Given these optical interferences, bright fluorophores with emission in the red or NIR region of the spectrum are typically used for measurement of blood and tissue specimens [511, 512]. Although, NIR wavelengths are most common and best suited to these measurements, this utility must be balanced against technical requirements in the context of prospective point-of-care diagnostics. Mass produced consumer smartphones are an ideal platform for measurements; however, their built-in IR filters preclude measurement of NIR fluorescence without custom modifications. It was for this reason that red-emitting QDs with emission maxima centered at 630 and 650 nm were evaluated throughout this chapter rather than NIR QDs. The advantages of using QDs for smartphone-based fluorescence measurements include (i) their excellent

brightness, which is better than that of most fluorescent dyes; (ii) the ability to tune their narrow emission spectra to align with the transmission bands of the built-in colour filters of CMOS camera chips; and (iii) their broad absorption spectra, which can afford excellent spectral separation between excitation and emission and permit the use of light sources such as LEDs without problematic crosstalk.

Chemically, blood is a very complex sample matrix with relatively high ionic strength, a high concentration of proteins, and a multitude of small molecules. These components all have the potential to affect the properties of nanoparticles or compromise their colloidal stability. Immobilization of QDs on a paper substrate or “test strip” avoids problems with colloidal stability because the QDs are physically prevented from aggregating. This format is also better suited for storage than QDs in bulk solution, where shelf life is an important consideration for prospective point-of-care use. Additionally, immobilization can improve signal magnitudes because the QDs remain concentrated in a defined zone and are not diluted by the addition of biological sample. The use of paper as an immobilization substrate was also advantageous because the porous, three-dimensional network of cellulose fibers allowed for immobilization of QDs at effective densities of *ca.* 4 pmol cm^{-2} , which improves signal levels when compared to immobilization on a substrate that only accommodates a monolayer of immobilized QDs (*e.g.* glass substrates, where *ca.* 0.8 pmol cm^{-2} are immobilized) [431]. This consideration is especially important when minimizing the technical requirements for readout, such as by using low-power LEDs as an excitation source and a smartphone camera for detection of emission.

The benefits of using LEDs as excitation sources are their compact size, low-cost, several choices for excitation wavelength (*i.e.* colour), and a relatively large area of illumination, the latter of which permits analysis of multiple samples simultaneously (whether for multiplexing or inclusion of control samples). Although laser diodes could provide more intense and monochromatic excitation, the small illumination area is not conducive to array-based multiplexing, and both unit cost and power consumption are greater. Nonetheless, LED illumination is not without its challenges; for example, the current method had to compensate for non-uniform illumination of the sample chip, as well as temporal variation in LED intensity. In Chapter 5 it was demonstrated that the ratiometric detection of FRET in the red and green channels of smartphone images can effectively mitigate variations in excitation intensity;

however, the requisite green fluorescence and violet excitation are poorly suited for a sample matrix of blood. The concept of a ratiometric or referenced measurement was therefore implemented in the present study using a two-spot system: (i) a sample spot that responded to our analyte; and (ii) a reference spot that was insensitive to the presence of analyte.

While all of the considerations discussed above were important for detection in whole blood, the optical path length through the blood remained one of the most critical factors. For this reason, a disposable PDMS/glass chip was designed that contained sample cells that housed paper test strips and provided a well-controlled optical path length of *ca.* 250 μm . Application of a drop of blood on test strips resulted in a much greater path length (millimeters) that significantly reduced signals. The chip and sample cells also offered greater containment of blood samples. Notably, the PDMS component was molded on a machined template and did not require lithographic techniques or a cleanroom. All of the components of this prototype system were low-cost and either easily obtained or easily fabricated. The recent increase in the availability of low-cost, desktop 3D printing will ultimately support further optimization, refinement and manufacturing of the non-optical components of our prototype system.

Considering the assay chemistry, the QD-FRET format was advantageous because no washing step was required, and the only manipulation was to add samples to a pre-prepared chip. This capability would not be possible with colourmetric assays, and most other non-QD fluorescent materials are not as suitable for integration with LED excitation and smartphone readout because of their lower brightness and small Stokes shifts (see Chapter 1 for additional detail). Although not all assays will be compatible with a FRET format, this chapter has presented preliminary data that suggests a competitive assay format is viable, thus representing a potential means for the FRET detection of non-hydrolase proteins through affinity rather than activity. Another binding assay format that could also be utilized is displacement of an A647-labeled oligonucleotide from an immobilized aptamer (*e.g.* thrombin binding aptamer), which is a strategy that has been shown to be effective in a variety of formats [513, 514]. Moreover, a multitude of different FRET-based assays for a wide variety of analytes has been cataloged in the literature, and many of these assays will be adaptable to this platform [282]. Here, human thrombin was used as a model bloodborne analyte of biomedical importance [506, 507]. It was spiked into bovine blood samples that did not have appreciable native thrombin activity as prepared. It was thus useful for

demonstrating that a disposable test chip, QDs and FRET could be combined to enable single-step bioassays in whole blood, using a smartphone readout platform amenable to point-of-care diagnostic applications. Nonetheless, the thrombin assay should neither be considered to represent the full scope of possibilities with this general assay platform, nor represent the best possible analytical performance that will be obtainable with further optimization.

6.4 Conclusions

In this chapter, it was shown that the combination of QDs, FRET and smartphone imaging is a viable and easily accessible platform for quantitative, single-step bioassays in serum and whole blood. Although further engineering and optimization is possible, the assay format and prototype design is highly amenable to point-of-care diagnostic settings because of its portability and the use of mass-produced, low-power consumer components. The major challenge overcome in this study was the optical properties of whole blood, which imposed significant design restrictions. The final assay design included the following components:

- a QD630-A647 FRET pair, which achieved a compromise between transmission of QD PL through blood and FRET-based signal changes upon proteolysis;
- a test strip with reference and sample spots of QDs, which permitted localization of PL signals and ratiometric measurements;
- a disposable PDMS/glass sample chip, which controlled the optical path length through blood and facilitated multiplexing;
- an LED470 excitation source that balanced brightness, transmission through blood, and minimization of crosstalk with QD630 PL.

The successful integration of these components was demonstrated with QD-FRET assays for thrombin activity in 12 μL of serum and whole blood, with detection limits of 12 and 18 NIH units mL^{-1} , respectively. The assay platform will also be applicable with the wide range of QD-FRET methods available for the detection other analytes, as demonstrated through a mock competitive binding assay. Overall, the optical properties of QDs provide new opportunities for

future point-of-care diagnostics by permitting single-step, FRET-based assays in serum and whole blood with smartphone readout.

6.5 Experimental Section

6.5.1 Materials and reagents

Lipoic acid (LA, $\geq 99\%$), *N,N'*-diisopropylcarbodiimide (DIC, $>98\%$), *N,N*-diisopropylethylamine (DIPEA, $\geq 99\%$) *N*-hydroxysuccinimide (NHS, 98%), succinic anhydride, ethylenediamine, tetramethylammonium hydroxide (TMAH) solution in methanol (25% w/v), sodium borohydride ($\geq 98\%$), sodium cyanoborohydride (95%), sodium (meta)periodate ($\geq 99\%$), glutathione (GSH), streptavidin (SA_v), and bovine serum (adult) were from Sigma-Aldrich (Oakville, ON, Canada). EZ-Link amine-PEG₃-biotin (biotinyl-3,6,9,-trioxaundecanediamine), ammonium acetate, sodium hydroxide, acetic acid, and boric acid were from Fisher Scientific (Ottawa, ON, Canada). A polydimethylsiloxane (PDMS, Sylgard 184) elastomer kit was obtained from Dow Corning (Midland, MI, USA). Defibrinated bovine blood was from Hemostat Laboratories (Dixon, CA, USA). Human alpha-thrombin was from Haematologic Technologies (Essex Junction, VT, USA).

GSH-capped water-soluble QDs were prepared as described in Section 2.4.4. Peptides were from Bio-Synthesis Inc. (Lewisville, TX, USA) and their sequences are listed in Table 6.4. Alexa Fluor 647 (A647) C2 maleimide dye, Alexa Fluor 680 (A680) C2 maleimide dye, and streptavidin Alexa Fluor 647 (SA_v-A647) conjugate were purchased from Life Technologies (Carlsbad, CA, USA). Buffers were prepared with water purified by a Barnstead Nanopure water purification system (Thermo Scientific, Ottawa, ON, Canada) and sterilized by autoclaving prior to use. Buffers included borate buffer (50 mM, pH 9.2 and 50 mM, pH 8.5), and phosphate buffered saline (PBS; 12 mM phosphate, 137 mM NaCl, 2.7 mM KCl, pH 7.4).

Table 6.4 Peptide substrate sequences.

Amino acid sequence (written N-terminal to C-terminal) ^{a,b,c}	Abbreviation	Assay ^d
(1) Ace-HHHHHHSPPPPPGSDGNESGLVPR↓GSGC(A647)	Sub(A647)	THR (sample spot)
(2) Ace-HHHHHHSPPPPSGNLGNDSGWDSGNDSGN	Pep	THR and SA _v (reference spot)
(3) Biotin-PEG ₃ -GSGP ₄ GSGHHHHHH-Am	Pep(Biotin)	SA _v (sample spot)

^a The protease recognition site is indicated in bold and the hydrolysis position is indicated by the downwards arrow; ^b Ace = acetylated; ^c PEG₃ = -NH-[CH₂-CH₂-O]₃-CH₂-CH₂-NH-; Am = amidated; ^d THR = thrombin, SA_v = streptavidin.

6.5.2 Peptide modifications

6.5.2.1 Dye-labeled peptides

Peptide **1** (see Table 6.4) with a terminal cysteine residue was labeled with Alexa Fluor 647 C2 maleimide dye (or Alexa Fluor 680 C2 maleimide) according to previously published protocols with slight modifications [368]. Briefly, 1.0 mg (0.33 μmol) of peptide was dissolved in 50 μL of 50% v/v MeCN:water, diluted with 350 μL of PBS and mixed with ~0.5 mg (0.4–0.5 μmol) of A647 (or A680) dye dissolved in 25 μL of DMSO. The reaction was placed on a mixer for 24 h at room temperature in the dark. Labeled peptide was separated from excess dye using nickel(II) nitrilotriacetic acid (Ni-NTA) agarose and subsequently desalted using Amberchrom CG300M chromatographic grade resin (Dow Chemical, Midland, MI, USA). Peptides were quantitated using UV-visible spectrophotometry. The peptide was aliquoted into 20 nmol fractions, dried under vacuum, and stored at -20 °C until needed.

6.5.2.2 Biotinylated peptide

The *N*-terminus of peptide **3** (see Table 6.4) was first reacted with succinic anhydride to convert it to a carboxylic acid group. Briefly, 1.0 mg (0.58 μmol) of peptide was dissolved in 100 μL of DMF and mixed with 100 μL of a 58 mM solution of succinic anhydride in DMF (5.8 μmol, 10 equiv.). Then, 5 μL of a 0.1 M solution of DIPEA in DMF was added and the reaction was mixed for 6 h at room temperature. Modified peptide was diluted with PBS buffer (2 mL) and

purified from excess reagents using a nickel(II) nitrilotriacetic acid (Ni-NTA) agarose cartridge, and desalted using Amberchrom CG300M resin. The purified peptide was dried *in vacuo*.

The succinic acid-modified peptide was dissolved in 200 μL of DMF and mixed with 45 μL of a 20 mM solution of NHS (0.9 μmol) in DMF, followed by the addition of 32 μL of a 20 mM solution of DIC (0.64 μmol) in DMF. The reaction was mixed for 4 h at room temperature, then 20 μL of 50 mM solution of EZ-Link-PEG₃-biotin (1.0 μmol) in DMF was added and the reaction left to mix overnight at room temperature. The modified peptide was diluted with PBS buffer (2 mL), purified and desalted as described above, then dried *in vacuo* and stored at $-20\text{ }^{\circ}\text{C}$ until needed.

6.5.3 Preparation of paper test strips

6.5.3.1 Sizing and chemical reduction of cellulose paper

Cellulose paper was modified with bidentate thiol ligands according to procedure described in Chapter 4, Section 4.4.4. Paper sheets modified with the lipoic acid derivative, *N*-(2-aminoethyl)-5-(1,2-dithiolan-3-yl)pentanamide, were cut into rectangles (2 \times 6 mm) or “test strips” using a paper punch (RecollectionsTM, Michaels Stores, Inc., Irving, TX, USA). The paper test strips were added to solution of 50 mM sodium borohydride for 1–2 h to reduce disulfide groups to dithiols. The test strips were then washed three times with water and once with ammonium acetate buffer (100 mM, pH 4.5). Excess buffer was removed by gently sandwiching paper substrates between dry sheets of lint-free tissues (Kimwipes, Kimberly Clark) three times and further air-drying for 5 min. Prolonged exposure to air (>20 min) prior to spotting QD solution was noted to produce less uniform QD immobilization, presumably due to reoxidation of the dithiols to disulfides.

6.5.3.2 Immobilization of QD-peptide conjugates

QD-peptide conjugates were prepared for sample and reference spots by mixing QD630 with the desired peptide at the desired concentration and ratio, as summarized in Table 6.5. All conjugates were prepared in borate buffer (50 mM, pH 9.2). The QD630–Pep(Biotin) and QD630–Pep (see Table 6.4) conjugates were prepared in advance and stored at room temperature for up to one week. The QD630–Sub(A647) were prepared prior to use. In a typical experiment, solutions of

QD630 and Sub(A647) were thoroughly mixed, incubated in the dark for 3–5 min. Next, 0.5 μL of this conjugate solution spotted directly on one end of the paper test strip placed in humid chamber, and the opposite end of paper test strip was then spotted with 0.5 μL of the reference conjugate, as illustrated in Figure 6.13. Test strips for thrombin assays were incubated inside the humid chamber for 5–10 min, rinsed with borate buffer (5 mM, pH 9.2), dried on lint-free tissues and enclosed within the sample cells of a PDMS/glass chip (see Section 6.5.4). Test strips for competitive-binding SAv assays were washed with borate buffer (50 mM, pH 8.5, 50 mM NaCl), rinsed with 0.1% bovine serum albumin (BSA) in borate buffer, and finally rinsed once with borate buffer (5 mM, pH 8.5). The finished test strips were dried on lint-free tissues and enclosed within the sample cells of a PDMS/glass chip.

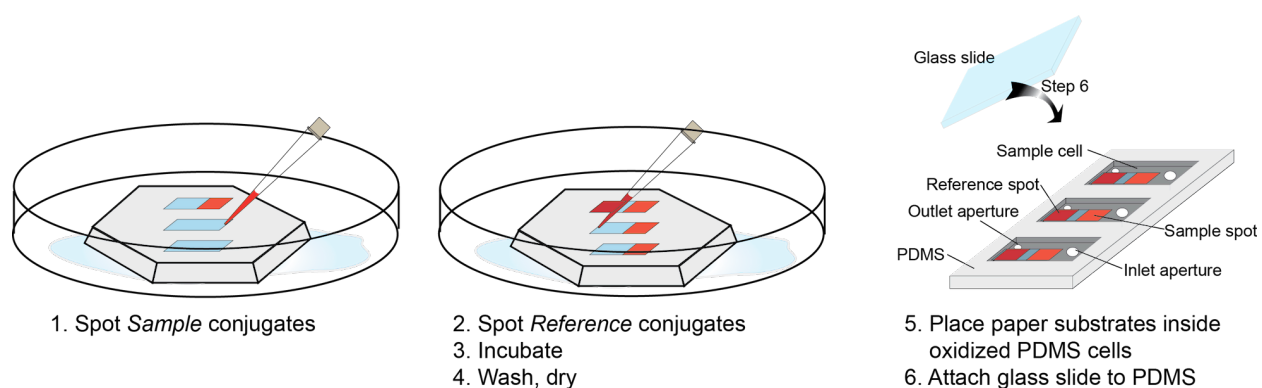


Figure 6.13 Preparation of paper substrates with immobilized QD-peptide conjugates and assembly of glass/PDMS chip containing paper substrate within sample cell.

Table 6.5 Spotted solutions of QD–peptide conjugates.

Assay	Sample Spot	Reference Spot
Thrombin activity assay	Sub(A647) ^a	Pep ^a
	QD:peptide Ratio 1:10	QD:peptide Ratio 1:20
	[QD630] = 4 μM	[QD630] = 1 μM
	[Sub(A647)] = 40 μM	[Pep] = 20 μM
	Volume spotted: 0.5 μL	Volume spotted: 0.5 μL
Competitive-binding SAv assay	Pep(Biotin) ^a	Pep ^a
	QD:peptide Ratio 1:20	QD:peptide Ratio 1:20
	[QD630] = 2 μM	[QD630] = 1 μM
	[Pep(Biotin)] = 40 μM	[Pep] = 20 μM
	Volume spotted: 0.5 μL	Volume spotted: 0.5 μL

^a Refer to Table 6.4 (p. 241) for the amino acid sequences of the peptides.

6.5.4 Fabrication of PDMS/glass chip

A positive-relief template for the sample cells and a holder for this template were fabricated from brass in-house (post-manufacture polishing is recommended). The template was the size of a standard glass microscope slide (~75 mm × 25 mm) and patterned 18 sample cells, each of which had dimensions of 4 mm × 9 mm × 250 μm ($l \times w \times h$). A schematic of the template is shown in Figure 6.14. PDMS chips were prepared from an elastomer kit by mixing elastomer base and curing agent in 10:1 w/w ratio. The mixture was degassed under vacuum for 40 min and *ca.* 3.0 g was poured over the template in its holder. PDMS was cured in the oven at 120 °C for 10 min, cooled, cut and peeled from the template. Cured PDMS was rinsed thoroughly with water and ethanol, then dried. Apertures were made at opposite ends of each sample cell with a 2 mm diameter punch (inlet for sample addition) and 1 mm diameter punch (outlet for air). The PDMS chip was placed upside down (recessed cells facing up) and air plasma oxidized for 60 s at 10.5 W. Finished test strips were then placed within the sample cells and a pre-cleaned (plasma

treated, 5 min, 10.5 W) glass slide was pressed against the PDMS to form the PDMS/glass chip. A photograph of a chip is shown in Figure 6.1 (p. 218).

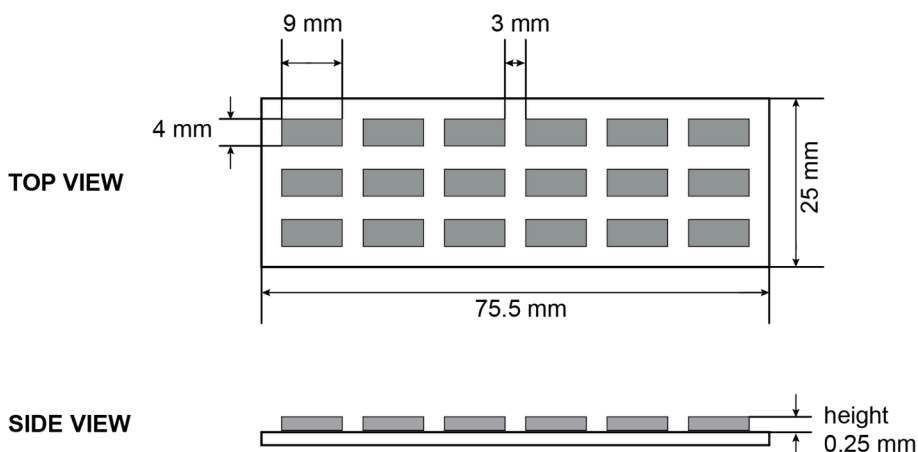


Figure 6.14 Drawing of a positive-relief template used to mould PDMS to form 18 sample cells on a microscope slide-sized chip.

6.5.5 Assay procedures

6.5.5.1 Thrombin assays

Human thrombin solutions were prepared in borate buffer (50 mM, pH 8.5), serum, 50% blood (prepared with borate buffer, pH 8.5), or whole blood. Thrombin stock solutions supplied by the vendor were typically in a concentration range 0.14–0.21 mM, so that even for the highest thrombin concentrations tested (*i.e.* $[\text{THR}] = 4.0 \mu\text{M}$), the content of the serum or whole blood in the sample was >96%. Protease activity was monitored by adding 12 μL of enzyme solution (7.6–480 NIH units, or 63 nM–4 μM for the particular lot of enzyme) to the sample well containing paper substrates. An image (smartphone or USB-CMOS camera) was acquired prior to sample addition (noted as *dry sample*) and then after sample addition at 30 s intervals for 30 min.

6.5.5.2 Competitive binding streptavidin assay

Six solutions were prepared in borate buffer (50 mM, pH 8.5, 50 mM NaCl) with 2.0 μM SAV-A647 and SAV at a concentration of 0, 0.4, 1.0, 2.0, 10, or 20 μM . These solutions (12 μL) were added to the sample wells containing paper tests strips. An image (smartphone) was acquired prior to sample addition (noted as *dry sample*) and then after sample addition at 30 s intervals for 30 min. For SAV detection in 50% blood, a 15 μL volume samples containing SAV-A647 and SAV were prepared as described above and mixed with 15 μL volume of whole blood. The final concentrations were 1.0 μM SAV-A647 and 0, 0.2, 0.5, 1.0, 5.0 or 10 μM SAV.

6.5.6 Instrumentation and data acquisition

6.5.6.1 Characterization of LEDs

Several LEDs, listed in Table 6.6, with emission maxima over the range 385–605 nm were evaluated as potential excitation sources. The LEDs were controlled and powered using LabVIEW software and a USB-6008 data acquisition (DAQ) module (National Instruments, Austin, TX, USA). LED emission spectra were obtained using a Green-Wave spectrometer (StellarNet, Tampa, FL, USA) coupled with an optical fiber (200 μm diameter; M25L01, Thorlabs, Newton NJ, USA) and LabView software, as described in Chapter 5 and Appendix III. A neutral density filter (OD 3.0, Thorlabs) was used to reduce the LED intensity for acquisition of spectra. LED crosstalk was determined by collecting LED spectra using a longpass filter with a cutoff wavelength of 600 nm (FEL600, Thorlabs). A schematic of the setups used for acquisition of LED spectra is shown in Figure 6.15A. LED power was measured with handheld laser power meter (Vega, Ophir-Spiricon LLC, North Logan, UT, USA).

Table 6.6 LEDs used for optimization experiments.

LED	Manufacturer / Supplier	Product number
1	Visual Communications Company, LLC	VAOL-5EUV8T4
2	Visual Communications Company, LLC	VAOL-5EUV0T4
3	Lee's Electronics	M506WCP
4	Lumex	LX509FT3U5BD
5	LEDtronics	LDF200-2PB-22
6	Lumex	LX9053UEGC
7	Everlight Electronics Co. Ltd.	EL-333-2UBGC/S400-A4
8	Fairchild Semiconductor Corp.	MV8G03
9	Kingbright	WP7143ZGC/G
10	Visual Communications Company, LLC	VAOL-5GDE4
11	Visual Communications Company, LLC	VAOL-5GCE4
12	Visual Communications Company, LLC	VAOL-5GSBY4

6.5.6.2 Absorbance, transmittance and fluorescence measurements

Solution-phase PL spectra and absorbance spectra were acquired with either an Infinite M1000 fluorescence plate reader (Tecan US, Inc., Morrisville, NC, USA) or, when using LED excitation, the Green-Wave spectrometer. A schematic of the latter setup is shown in Figure 6.15B. PL emission and absorption spectra of immobilized QDs and QD-conjugates (see Figure 6.7 and Figure 6.12) were obtained with an Infinite M1000 Pro by placing paper substrates between the windows of a NanoQuant plate (Tecan Ltd.).

PL images of paper samples were acquired using either (i) an iPhone 5S (Apple, Cupertino, CA, USA), or (ii) USB-CMOS monochrome camera (DCC1545; Thorlabs, Newton NJ, USA). For imaging experiments with PDMS/glass chip, two arrays of LEDs (VAOL-5GSBY4, 470 nm) connected in parallel (3.0–4.0 V applied, Table 6.7, 6.8) were used to illuminate the chip. A bandpass filter (624/40, center wavelength/bandwidth; Chroma, Bellows Falls, VT, USA) was used to isolate emission from QD630, and another bandpass filter (650/40, #FB650-40,

Thorlabs) was used to isolate emission from QD650. A photograph of this setup is shown in Figure 6.1 and a schematic is shown in Figure 6.15C. Image acquisition with the iPhone 5S was done using the Lapse It Pro application (Interactive Universe developer). Image acquisition with the USB-CMOS camera was done using micro-Manager software [515]. All image analysis was done using ImageJ software and the Time Series Analyzer 2.0 plug-in (National Institutes of Health, Bethesda, MD, USA).

The transmittance of LED light through paper substrates was measured on an inverted Olympus IX83 microscope (Olympus Canada Inc., ON, Canada) equipped with a sCMOS digital camera (ORCA-Flash 4.0, Hamamatsu) using a UV-transparent 96-well plate (Corning 3679). An increasing number of hydrated paper substrates (3 mm diameter) were placed in a well and an LED470 positioned for trans-illumination.

The effect of blood path length on the transmittance of light through blood was measured by pipetting a drop of blood between two glass slides separated by a defined distance using spacers (wetted cover slips with ~ 150 μm thickness). The bottom slide supported a test strip with immobilized QDs, held in place with tape. The path length was calculated from images acquired with $4\times$ magnification lens. The length scale calibration was done using a calibration slide (Motic Instruments Inc., Richmond, BC, Canada). For measurement of QD630 PL (LED470 excitation) as a function of path length, images were acquired with a smartphone (iPhone 5S) or USB-CMOS monochrome camera and the intensities analyzed in ImageJ.

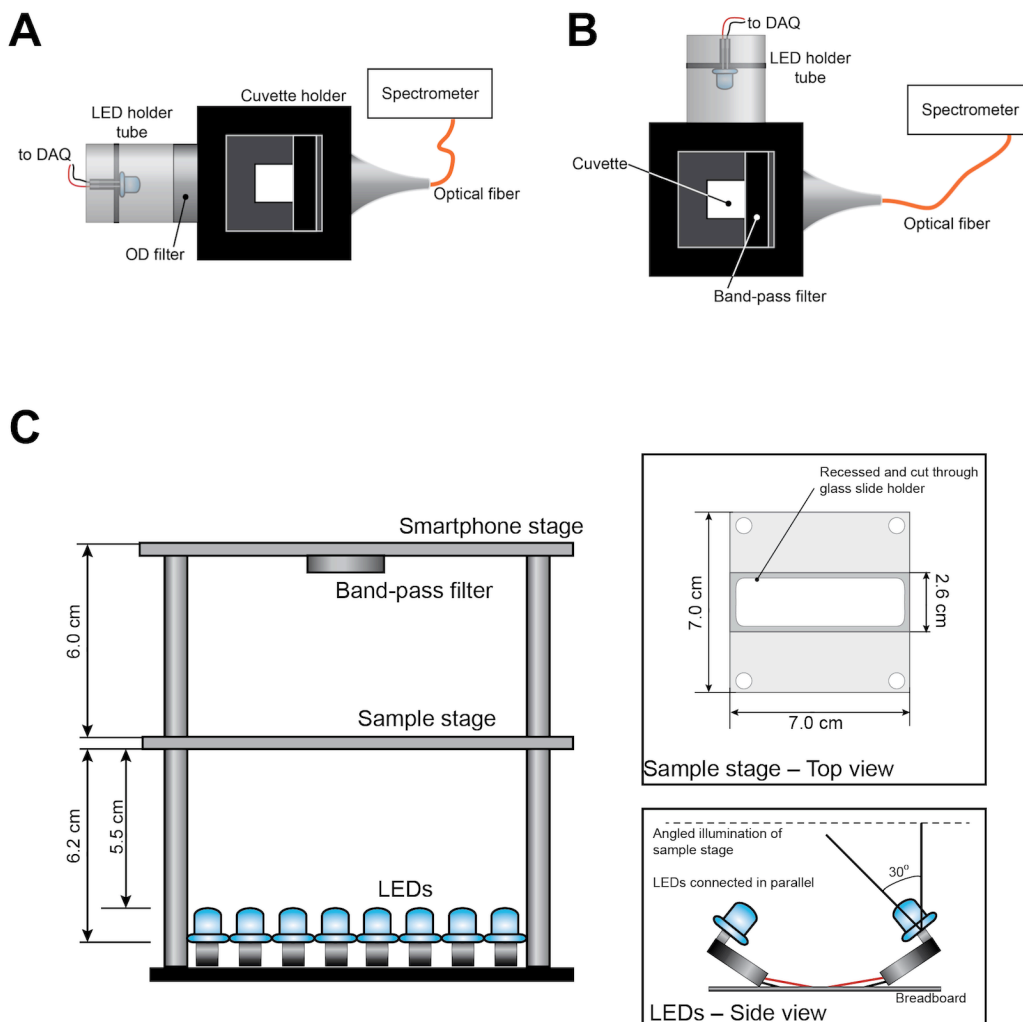


Figure 6.15 Schematics of the instrumental setups used for (A) acquisition of LED spectra, (B) solution-phase QD PL with LED excitation, and (C) colour digital PL images with a smartphone. For the smartphone imaging, the pulsed LED source was powered from the USB connected DAQ module. Schematics are not to scale. A bandpass filter was used to isolate QD PL and reject reflected LED light and FRET-sensitized emission from dye-acceptor.

6.5.6.3 Sample matrix-dependent image acquisition parameters

Table 6.7 and 6.8 summarize optimized parameters, including LED voltages and camera exposure times, used for QD PL imaging with either (i) an Apple iPhone 5S and the Lapse it Pro app, or (ii) a Thorlabs USB-CMOS monochrome camera and micro-Manager software.

Table 6.7 Acquisition parameters for iPhone and Lapse It Pro application.

Media	LED voltage (V)	Exposure	ISO	White Balance	Resolution
Buffer	3.0	1/60	544	0%	1080p
Serum	3.5	1/60	544	0%	1080p
50% blood	3.7	1/30	544	0%	1080p
Whole blood	4.0	1/20–1/15	544	0%	1080p

Table 6.8 Acquisition parameters for Thorlab CMOS camera and micro-Manager software.

Media	LED voltage (V)	Exposure	Gain
Buffer	3.5	10 ms	50
Serum	3.7	20 ms	50
50% blood	4.0	75 ms	50
Whole blood	4.0	100 ms	50

6.5.7 Data analysis

6.5.7.1 FRET parameters

The QD630-A647 and QD650-A680 FRET pairs were characterized using the Förster formalism as described in Chapter 1, Section 1.2.8. The Förster distance, R_0 , was calculated using eqn. 1.18 and the spectral overlap integral, J , was calculated according to eqn. 1.19. QD quantum yields were measured as described in Appendix II, using Rhodamine B in acidic ethanol ($\Phi = 0.49$, [516]) as a standard. The absorbance and fluorescence intensities of a series of concentrations of QD630 and QD650 were measured with the plate reader and the slopes of plots of PL *versus* absorbance were used to determine the QD quantum yields. The FRET efficiency, E , was calculated from the PL measurements using eqn. 1.24.

6.5.7.2 Image and RGB data analysis

Digital colour images acquired with the iPhone 5S were split into corresponding R-G-B channels, and the average spot intensity, I , in the red channel was used for analysis. Digital images acquired with the monochrome USB-CMOS camera were used directly to calculate the average spot intensity, I . At each time point, t , a ratio between the sample and reference spot, $R(t)$, was calculated according to eqn. 6.5, where the subscript S indicates the intensity of the sample spot, the subscript Ref indicates the intensity of the reference spot, and the notation *dry* refers to the images acquired prior to sample addition. For 50% blood and whole blood samples, dry images were acquired with the buffer acquisition parameters (see Tables 6.7 and 6.8).

$$R(t) = \frac{I_S(t)/I_S(\text{dry})}{I_{Ref}(t)/I_{Ref}(\text{dry})} \quad (6.5)$$

Thrombin assays were done with a control sample that had no added thrombin, $[E] = 0$. As shown in eqn. 6.6, each of the values of $R(t)$ (eqn. 6.5) for a given enzyme concentration, $[E]$, were normalized to an initial value of unity by dividing by the ratio at $t = 0$ (*i.e.* immediately after sample addition), and all subsequent time points were then scaled to the control sample.

$$R_N(t) = \frac{R_{[E]}(t)/R_{[E]}(0)}{R_{[E]=0}(t)/R_{[E]=0}(0)} \quad (6.6)$$

Normalized progress curves were fit with an exponential function in ProFit software (QuantumSoft, Bühlstr, Switzerland) using eqn. 6.7. Average rates were calculated according to eqn. 6.8.

$$R_{N,t} = A_2 \left(2 - (A_1 \exp(-k_1 x)) - ((2 - A_1) \exp(-k_2 x)) \right) + C \quad (6.7)$$

$$k_{av} = \frac{A_1 k_1 + (2 - A_1) k_2}{A_1 + (2 - A_1)} \quad (6.8)$$

Chapter 7 Conclusions and Future Work

7.1 Thesis Overview

The work in this thesis impacts the development of strategies for luminescence-based diagnostics suitable for point-of-care applications using a smartphone as a readout platform. These strategies are based on a platform that combines quantum dots with smartphone technology, thus integrating molecular diagnostics with a portable, low-cost and widely accessible device. First, the superiority of quantum dots for smartphone imaging is established *versus* traditional fluorophores and fluorescent proteins with regard to absorption and emission properties. QDs are renowned for their brightness, such that they were far more superior fluorescent materials for smartphone imaging. One of the challenges in developing a luminescence-based platform is that fluorescence imaging requires an excitation source and, as such, smartphone-based configurations have typically required additional component (*e.g.* laser diodes, LEDs, UV lamps). In this thesis (Chapter 2), it was demonstrated that the need for an external device can be eliminated by using the built-in LED photographic flash of the smartphone for imaging of fluorescence assays. A robust and compact 3D-printed prototype accessory enabled all-in-one smartphone excitation and imaging of PL, housing all necessary optical components.

Every smartphone camera offers a built-in, three-channel red-green-blue imaging. The spectrally narrow PL emission and strong, broad light absorption of QDs was combined with red-green-blue (RGB) digital colour imaging for quantitative, multiplexed homogeneous assays in Chapter 3. Importantly, this work shows that quantification of proteolytic rates is identical for smartphone based detection and sophisticated fluorescence plate reader. This work was recently highlighted by Stevens as an important contribution to nanoparticle based POC diagnostics [326], and, to date, remains the only report of smartphone digital imaging as a readout for multiplexed FRET-based assay with QD donors.

Building on the success of QD-smartphone imaging, the development of a paper-based assay was pursued, using as an inspiration, the simplicity of blood glucose meters and lateral flow assays that typically do not require additional sample pre-treatment steps. Different surface chemistries for modification of cellulose paper fibers were evaluated in Chapter 4 for efficient immobilization of QDs and QD-peptide bioconjugates. Each of the three evaluated chemistries

had a different effect on the optical properties of QDs, their photobleaching behaviour, their long-term stability monitored over five months, and the density of immobilized QDs. Interestingly, an enhancement in the rate and efficiency of FRET, and a decrease in the *effective* donor-acceptor distance between immobilized QDs and dye acceptors within a paper matrix was observed in comparison to the solution-phase FRET. The extent of enhancement in FRET efficiency was found to depend on the underlying immobilization chemistry of cellulose fibers.

The diagnostic utility of QD-modified paper substrates with digital imaging detection platform was demonstrated through a series of proteolytic assays based on FRET in Chapter 5. Solid substrates are heterogeneous in their nature, and paper is even more so. Therefore, a ratiometric approach that relied on simultaneous imaging of QD donor PL and FRET-sensitized acceptor PL was essential. A green-emitting QDs and Alexa Fluor 555 dye were optimal FRET-pair for simultaneous imaging in the green and red channels of digital colour images. Up to three-plex assays were demonstrated for detection of trypsin, chymotrypsin, and enterokinase proteases that belong to the pancreatic family of enzymes.

Finally, merging all the work, a paper-in-PDMS chip for a smartphone-based assay of a blood-borne protease was demonstrated directly in whole blood samples in Chapter 6. Overall, the results described in this thesis contribute to the areas of spectroscopy, nanotechnology, and bioanalysis with emphasis on multiplexed detection and measurements with biological sample matrices in smartphone-based fluorescence assays, as well as interfacial chemistry associated with chemical modification of cellulose. This research provides a framework for future work aimed at translating this proof-of-principle, point-of-care platform with consumer electronics to a stage where it would be suitable for a reliable detection of clinically-relevant biomarkers.

7.2 Significance

There is a critical need for point-of-care diagnostics in health care and in other sectors. Such technology could have a profoundly positive impact on health, wellness and quality-of-life in both the developed and developing worlds. Diagnostic technologies that are sufficiently simple, rapid, reliable and economical to be deployed in a physician's office or in patient's homes would be a tremendous step toward increasing the efficiency of health care in developed countries. In developing countries, large populations may have little or no access to even the basic health

services of the developed world due to financial limitations, a shortage of skilled personnel, and a lack of infrastructure. The lack of infrastructure is not only with respect to biomedical and clinical equipment, but may also include running water, refrigeration and electricity. In addition to basic medical tests and screening for chronic disease, affordable test kits for infectious diseases can be a life-saving intervention in many developing countries, where millions die every year due to inadequate diagnosis and these tests could help prevent epidemics from turning into pandemics.

Over the last five years, there has been a significant surge in the number of publications associated with cellphone or smartphone-based diagnostics. For the most part, this interest was driven by the wide availability of these mobile devices, which provide means for image capture, data storage, spatial mapping, temporal tracking, and wireless transmission of information. These devices have become an integral part of daily life. Thus, an important goal is to integrate these devices into healthcare and clinical use. The vast majority of the research work that aims to take advantage of smartphone technology has relied on the design of colorimetric assays, or by demonstrating validity of smartphone technology for quantitative analysis of commercially available lateral flow assays. The main difference of the work described in this thesis is the development of fluorescence-based multiplexed assays integrating quantum dots as a transduction component in smartphone-imaging. Two main challenges have been addressed in this thesis: (i) multiplexing and (ii) whole blood assay. The multiplexing problem was solved with the smartphone by taking advantage of its built-in RGB channels and matching them with blue, green, or red-emitting QDs. The assay response acquired with the smartphone platform was identical to the one obtained with laboratory plate reader. Importantly, the smartphone platform was only a fraction of the price and size of the plate reader. Moreover, this study describes a fluorescence-based quantitative assay directly in whole blood, using thrombin protease as a model enzyme and smartphone imaging for detection. Importantly, this design does not require any additional sample-handling steps, as measurements are possible with simple addition of a drop of blood to the sample chip. Assays performed in clinical settings often require measurements of samples taken from patients, which would include serum, plasma, and whole blood. A majority of bioassays reported in the literature are demonstrated in clean samples (*i.e.* buffers); however, there is a need to develop platform suitable for direct measurements in biological matrices (*i.e.* serum, whole blood). This thesis addresses the challenge of performing

optical measurements in whole blood by developing a luminescence-based assay using paper-in-PDMS chips compatible with smartphone imaging detection. This format provides an important framework for future development of point-of-care diagnostics.

7.3 Future Work

The results presented in this thesis have established a solid foundation for the development of luminescence-based diagnostic assays using smartphone imaging. Optimization and expansion of the scope of the proof-of-principle platforms developed in this thesis—with an ultimate goal of developing clinically relevant diagnostic device—will be the main focus of future work. Therefore, in order to identify direction for this future work, it is necessary to establish current limitations and challenges. In the context of smartphone-based luminescent bioassays, these limitations and challenges can be summarized into three main groups: (i) the poorer sensitivity of smartphone cameras in comparison to laboratory instrumentation; (ii) the non-universal nature of the smartphone platform; and (iii) the currently limited scope of analytes and assays. Important considerations arise for the development of QD-FRET proteolytic assays, particularly from the standpoint of improving our understanding of the complex interactions between nanoparticle interfaces and proteins. Further advancement of solid-phase assays, and paper-based assays in particular, requires evaluation and optimization of surface chemistry to gain a better understanding of the interplay between nanoparticles, biomolecules, and the solid substrate. Addressing some of the challenges noted above would contribute to the advancement of smartphone-based bioimaging, whereas investigating others, such as interactions between nanoparticles and proteases or paper substrates and biomolecules will provide insight into fundamental understanding of interactions at the interfaces. The latter would have an impact on a larger scale, providing tools for designing effective *in vitro* assays. Each of the factors listed in this paragraph is discussed in detail below, with emphasis on how to address them and how solving one challenge may require to take considerations of other factors.

7.3.1 Improving sensitivity

Fluorescence-based assays generally provide a significant advantage in terms of better limits of detection (LODs) and sensitivity in comparison to colorimetric assays that often resort to an enzyme-amplification step (*i.e.* horse radish peroxidase) or silver staining of gold nanoparticles

to achieve sufficient sensitivity. The integration of fluorescence-based detection with point-of-care assays is largely developed for lateral flow assays; fluorescence strip readers are available commercially. The implementation of smartphone for fluorescence imaging requires additional components (*e.g.* excitation source, enclosure from ambient light) but it offers intrinsic advantages associated with fluorescence-based assays. This format is particularly suitable for developing assays that measure an analyte that is not very abundant in the sample. Given the need to be able to detect analytes at lower concentration, there are few parameters that can be optimized to improve fluorescence signals.

As was shown in eqn. 1.13, a measured fluorescence intensity depends on (i) the power density of the excitation source, (ii) the collection and detection efficiency of the detector, (iii) the effective fluorophore concentration, (iv) the brightness of the fluorophore (*i.e.* product of the molar absorption coefficient and the quantum yield of a fluorophore), and (v) the sample path length. Each of these parameters is still valid and can be optimized in smartphone imaging. The power of the excitation source can be controlled by selecting from a range of low-cost, compact devices such as portable UV lamps, LEDs, or laser diodes. LEDs and UV lamps were used extensively throughout this thesis, where the UV lamp generates much brighter images of QDs when used as an excitation source in comparison to LEDs, but LEDs are much smaller, cheaper and easier to integrate. These light sources also provided large areas of illumination, as a result of the size (UV lamp) or dispersion of light (LEDs), such that multiple samples could be analyzed simultaneously over period of time to track kinetics. The trade-off in using light sources to illuminate larger area is that the intensity of the excitation light per unit area decreases. Since many assays only require one point measurement (*cf.* kinetics data), having point light source to achieve maximum excitation power would be an advantage. One such excitation source is laser diodes. They are small, compact, generate very narrow light beam, narrow bandwidth (< 3 nm) and available over wide range of powers (2 mW–1400 mW) and wavelengths.

The second aspect to consider is the collection and detection efficiency of emitted photons. Fluorescence is emitted in all directions and positioning the detector closer to the sample emitting light will result in capturing more photons. However, bringing the camera closer to the sample requires additional lenses to ensure that sample is in focus, and another trade-off is that

the imaging area will decrease as well. For instance, some preliminary tests indicated that the native minimum focal distance for a smartphone (iPhone 5S) is 5–7 cm and with additional magnification lens it reduces to ~2 cm. Measuring the same sample under those conditions using trans-illumination resulted in *ca.* 4-fold increase in fluorescence signal intensity. These modifications, however, require careful consideration for the positioning of the excitation source and may require selection of an appropriate filter to minimize excitation light reaching the detector. Low-cost alternatives for magnification and condenser lens are now available, including PDMS lenses [517] that can be fabricated directly in the lab, or ball lenses, where many transparent spherical materials can be used. The technology of CMOS sensors, as those used in consumer electronics is evolving very rapidly, which can, in turn, bring further improvements in camera sensitivity. Two decades ago CCD cameras were the only suitable choice for sensitive microscopy imaging, today scientific CMOS (sCMOS) cameras are offered by every leading supplier of digital microscope cameras.

A third factor that was noted to affect the measured PL intensity was the *effective* fluorophore concentration. In bioassays, one is interested in measuring the number of biorecognition events with target analyte that will provide the information about its concentration. The actual measurements are typically done using a labeled reporter that binds to the target analyte and provides the signal. Therefore, increasing the number of labels per reporter provides a means to generate a larger signal per binding event or to increase the *effective* concentration of the fluorescent label. As such, in order to overcome low signals associated with a single QD per one binding event, it would be better to use QD-doped nanobeads or microbeads (up to 1 μm in diameter) that carry tens to thousands of QDs per bead and thus binding event. A large variety of polystyrene beads modified with reactive functional groups (*i.e.* primary amine, aldehyde, and carboxylic acid groups) are available commercially and suitable for effective doping with hydrophobic QDs. Furthermore, impregnating QDs within a hydrophobic polystyrene matrix, generally leads to the retention of higher quantum yields of QDs—another parameter that can contribute to improving the assay sensitivity. The advantages of QD-doped beads have been demonstrated with QD optical barcode technology used for nucleic acid hybridization assays with flow cytometry [518] and, more recently, with smartphone imaging [325].

One last parameter that was indicated to affect measured fluorescence intensity was optical path length, which is likely one of the easiest parameters to modify and control. The sample chambers can be designed to still contain the same small sample volume but to ensure that the height of the sample is sufficient to accumulate signal. For instance, it was shown in Figure 2.3 that imaging of microfluidic channels with 300 μm height was successful with very high signal to noise ratio. In contrast, microfluidic channels with 100 μm height, containing 10 times higher concentration of QD could not be imaged. For solid phase assays, the same principle will apply if the sampling area is decreased. As a result, for the same amount of target analyte to be measured, QDs or QD-beads are concentrated over a smaller defined area.

Overall, this section highlights numerous ways, ranging from hardware engineering to the chemistry of nanomaterials that could be used to improve assay sensitivity.

7.3.2 Universal imaging platform for smartphones

From an engineering standpoint, developing a platform that would be suitable for every cellphone and smartphone is very challenging. Hundreds of device designs manufactured by different companies pose challenges in (i) adapting optical components to align with the position of the camera on the phone, as well as fitting the smartphone within a device, and (ii) accounting for differences in cameras, image quality, and built-in software used for image processing. In order to account for different locations of the camera lens with different smartphone models, a movable lens adaptor located outside of the device box can be designed as a direct clip-on to the smartphone, whereas an optical fiber will be used to deliver PL signal from the sample to the lens. Flexible optical fibers with inner diameter up to 1000 μm can be placed in close proximity to the sample which would also improve light capture as was noted above. Using multiple fibers to image multiple samples simultaneously—a concept that has been demonstrated recently by Ozcan laboratory [320]—could extend this configuration further.

Another challenge associated with the multitude of commercial smartphone devices is the proprietary image post-processing algorithms. When the raw RGB image is captured by the device, there is a built-in algorithm that processes each pixel and makes adjustments to generate the final processed image. One of the best approaches will be able to bypass the post-processing

step and get the raw image for analysis. Unfortunately, unlike digital DLSR cameras, not all smartphones provide an access to the raw image (although some do).

7.3.3 Scope of analytes and assays

There are numerous analytes that are clinically relevant and useful for the detection of various diseases. These analytes can further be detected using different transduction methods. What is more interesting is how FRET-based assays and non-FRET assays (*e.g.* binding assays such as immunoassays) compare in smartphone imaging. The vast majority of the work presented in this thesis is based on FRET, whereas examples of a direct binding assay (Chapter 2), and a competitive binding assay (Chapter 6) have also been presented. The major advantage of FRET-based assays, due to its strong distance-dependence, is the fact that no additional washing steps are required. In contrast, binding assays that use QDs as labels require washing steps to remove excess reagent, adding complexity and often greater challenges with non-specific adsorption. As a tradeoff, a larger dynamic range and often a greater sensitivity is observed in non-FRET binding assays. These assays can be further improved by integrating QD-doped nanobeads and microbeads as was described in Section 7.3.1. The complexity of non-FRET binding assays could range from simple dipstick-type assays to more sophisticated microfluidic platforms. Microfluidic platforms can be based on pressure-driven flow, electrokinetic flow, electroosmotic flow, or digital microfluidics [24, 519-521]. It offers numerous ways to control non-selective adsorption, and to achieve selectivity and multiplexing [520, 522]. The combination of miniaturized chip-based assays and an all-in-one smartphone imaging platform can potentiate development of sensitive assay, including those compatible with biological sample matrices (*i.e.* serum, blood).

7.3.4 Interaction between nanoparticles and proteases

Further improvement of protease activity-based assays will be dependent on the ability to evaluate the mechanism of the interaction between nanoparticles, their interface (*i.e.* ligand coating) and target proteases. It has been reported in the literature that there is an enhancement of proteolytic rates for substrates located at the QD interface due to a putative “hopping” mechanism that does not strictly follow a classic Michaelis-Menten kinetics model for isolated substrates [387]. The magnitude of the enhancement appears to be strongly dependent on the

charge and other properties of the ligands used to prepare water-soluble QDs, which determine their inhibitory effects [391]. These preliminary studies indicate that the interactions are rather complex and vary greatly between different proteases. Therefore, a systematic study that will correlate QD surface charge, ligand density, ligand size with the protease structure (*i.e.* charge, charge distribution, size) is necessary to gain a better understanding of the parameters that control protease activity. Some preliminary data shows that proteolytic activity towards QD-peptide conjugates is determined by a careful balance between the protease being attracted to QD interface to initiate hydrolysis of peptide substrates and too strong of attraction, such that protease adsorbs and its activity is inhibited. As shown in Figure 7.2, saturating a QD surface with peptide substrates actually leads to a net enhancement in the rate of proteolysis, despite the fact that there are many more substrates to be cleaved. This phenomenon is even more pronounced with proteases that exhibit stronger adsorption and inhibition (*e.g.* plasmin) or ligand coatings that promote adsorption on the QD (*e.g.* DHLA). Overall, these results indicate that non-specific inhibitory interactions between a protease and nanoparticle decrease as the nanoparticle surface begins to resemble a protein surface. Therefore, experimental studies of proteolytic rates as a function of the type, size, charge, and density of additive ligand (*i.e.* peptide, protein) need to be done. The charge of the peptide can be potentially controlled by introducing arginine-rich, aspartic acid-rich, or serine-rich amino acid sequences. The serine-rich peptide can provide a good reference point; as neutral peptide, it can offer passivation effect by physically blocking underlying ligands on the QD without inducing additional electrostatic interactions with proteases. Studies with proteins of various sizes, such as monomeric and tetrameric streptavidin, or other His-tag appended proteins can be used to investigate steric effects, as well as passivation effects. Furthermore, other biomolecules, including oligosaccharides and oligonucleotides can be introduced. Despite many reports in the literature regarding nanoparticle ligands and protein adsorption (*i.e.* corona), particularly upon exposure of nanoparticles to serum, whole blood or *in vivo*, there is very limited understanding of the factors that drive corona formation. The model with proteases is very useful to evaluate various parameters and to determine what influences those interactions.

The above studies would be ambitious and challenging work, and it is anticipated that many proteases and surface “coatings” will have to be evaluated before potential trends may become apparent. One of the anticipated challenges in this work will be quantitatively distinguishing

enhancements and decreases in proteolytic rates as a result of changes in proteases behaviour from apparent changes that may arise as a result of changes in optical properties of QDs. Many QDs exhibit non-linear relationship between PL ratio and the number of FRET acceptors, such that the deviation from linearity is dependent on the quantum yields of the QDs and the acceptors, which, in turn, can be influenced by the interface of the QD. To achieve reliable data analysis and data interpretation, it would be crucial to identify the mechanism of proteolysis in order to construct calibration curves. As was noted above, one of the proposed mechanisms is a “hopping mechanism” [387]. In this model, it is proposed that protease encounters a QD-peptide conjugate, cleaves all the peptides on its surface, and then moves away to the next one. The diffusion of protease from one QD to another is the rate-limiting step. Therefore, there is always a bimodal distribution that consists of QDs with either fully digested or non-digested peptides. This model is also plausible in the interpretation of the data shown in Figure 7.2, where an increase in the number of substrates per QD did not result in the decrease of proteolytic rates. However, given the discussion above and the data shown in Figure 7.2, it may also be suggested that the mechanism would depend on the underlying QD interface. If QDs promote protease adsorption, then protease may not be able to cleave all the peptides, and additional rates of protease adsorption and desorption may become significant.

Another level of complexity in studying proteolysis with QD conjugates is introduced by the fact that some proteases require divalent ions (*e.g.* Ca^{2+} , Zn^{2+}) to remain active, whereas many of the same ions can substantially affect optical and colloidal properties of some QDs. Overall, completion of the studies outlined in Section 7.3.4 is expected to provide a solid foundation for the design of protease-based assays for optimum sensitivity, as well as provide an empirical foundation for data analysis based on the identified mechanism of proteolysis in the systems with QD-substrate conjugates. Furthermore, it may offer guidance in designing smarter nanomaterials for cellular and *in vivo* studies.

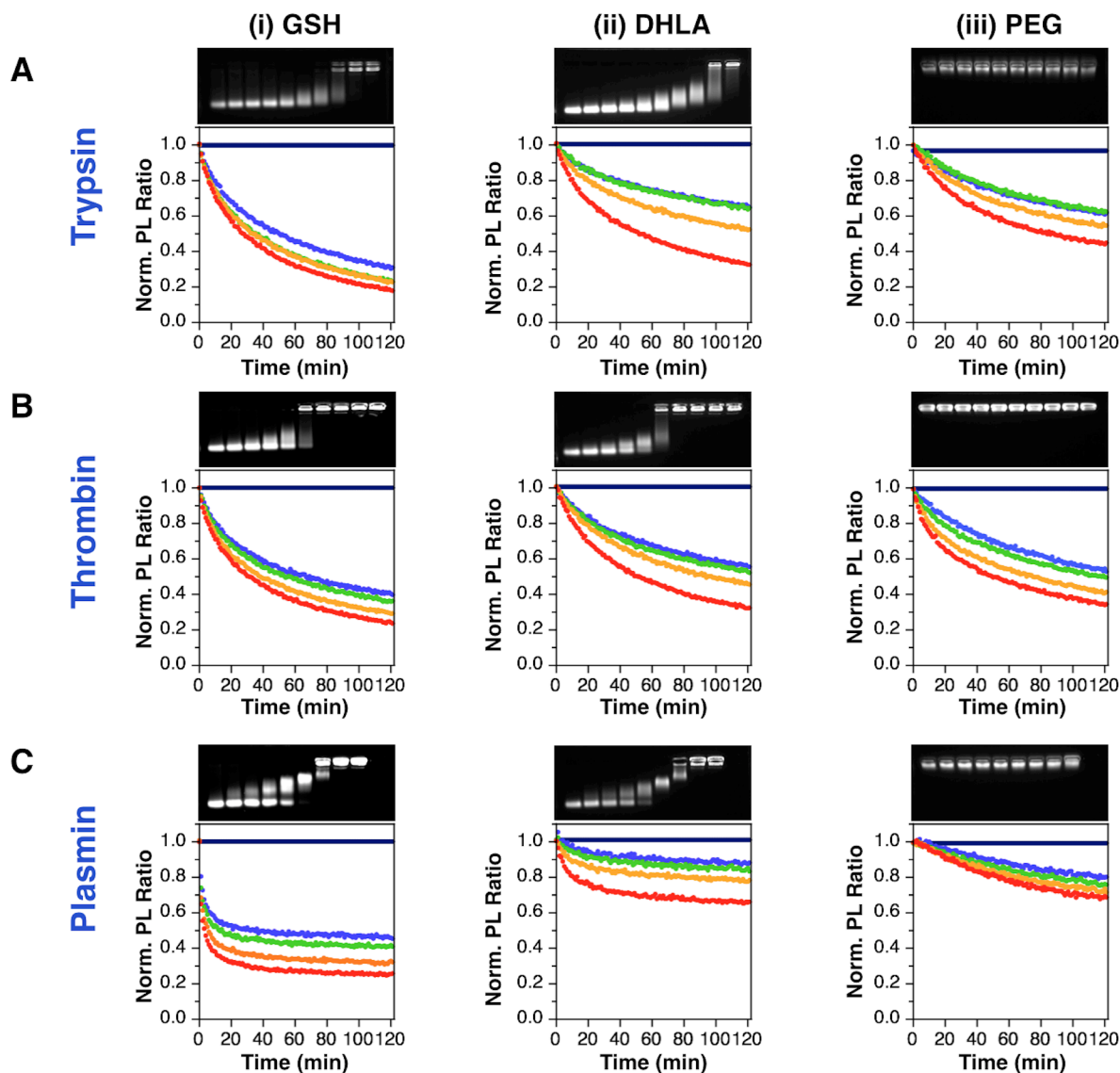


Figure 7.1 Representative data for proteolysis by (A) trypsin, (B) thrombin, and (C) plasmin on (i) GSH, (ii) DHLA, and (iii) PEG coated QDs as a function of additional peptide substrate assembled on QDs. A total number of peptides per QD is 10 (blue), 20 (green), 40 (orange), and (60) red on GSH (i) and DHLA (ii) capped QDs and 10 (blue), 20 (green), 30 (orange), and 40 (red) on PEG coated QDs. Maximum peptide loading on QD was determined using gel electrophoresis (data not shown): 60 peptides on GSH and DHLA capped QDs, and 40 peptides on PEG-coated QDs. Corresponding gel electrophoresis (0.7%, TB, pH 8.5) for QDs mixed with an increasing concentration of the protease are also shown; [QD] = 200 nM and protease concentration (from left to right on the image) 0, 0.1, 0.2, 0.4, 0.8, 1.6, 3.2, 6.4, 13, and 25 μ M.

7.3.5 Interaction between nanoparticles, proteases, and solid substrates

In addition to optimizing hardware and software components of devices to improve the sensitivity of smartphone imaging, future work also needs to focus on further evaluation of surface chemistry for solid-phase assays. Different types of chemical modification of cellulose fibers were introduced in Chapter 4 and served as a basis for the development of protease assays in whole blood. The impact of the interfacial chemistry was found to be two-fold: (i) it determined density of immobilized QDs and influenced the observed FRET efficiency; and (ii) it affected protease activity, as proteins can exhibit strong non-specific interactions with surfaces *via* hydrophobic and electrostatic interactions. Therefore, developing chemistries that will mitigate inhibitory effects on proteases are desirable for improving assay sensitivity. In addition to cellulose paper, alternative solid substrates should also be evaluated, as they may be advantageous for improving signal-to-noise ratio. Paper, despite its many advantages, exhibits weak green fluorescence when excited with UV and blue light. In contrast, glass substrates do not show same level of background and imaging of glass beads with immobilized QDs was shown in Chapter 2. Although, chemical modification of glass may be easily achieved using well-established silanization procedures in the literature, it has limited 2D surface area in comparison to cellulose fibers. In order to increase effective surface area for sufficient sensitivity of smartphone imaging, one could modify the glass surface with polymers or porous hydrogels. Natural biopolymers (gelatin, dextran) could minimize non-specific adsorption of proteins while substantially increasing ligand density for QD immobilization. Furthermore, these approaches are suitable for the development of binding assays, such as in immunoassays or aptamer binding assays, as was described in Section 7.3.3. Although, the main focus of this thesis was the development of QD-FRET assay for protease activity, the advantage of using QDs as labels in binding assay was also demonstrated in Chapter 2 and Chapter 6. As such, a higher surface area and density of functional groups suitable for bioconjugation with antibodies or aptamers will improve assay performance.

7.4 Concluding Remarks

This thesis has presented important contributions towards the development of a point-of-care platform for luminescent diagnostic applications using smartphones for optical readout. With future developments and improvements, such as outlined in Section 7.3, these platforms are anticipated to have the potential to evolve from proof-of-principle devices to viable commercial products. Some of these future directions include optimization of surface chemistry, integration of QD-doped beads and chip-based formats, tuning of optical and hardware components of smartphone imaging platform, and further insight into the interactions between nanomaterials and proteins. These studies will provide the tools necessary to improve sensitivity and expand the scope of the proof-of-principle smartphone assay platforms introduced in this thesis, and thereby facilitate development of clinically relevant assays on a smartphone, moving us closer to the achieving the goals of affordable and personalized medicine. Smartphones, as well as other portable devices (iPads, tablets), are almost ideal platforms that contain built-in sensors and provide means for wireless data communication *via* cloud-based applications and management systems. It is only a matter of time before these platforms will be successfully integrated with molecular diagnostics, empowering healthcare professionals to bring advanced health care to patients, wherever they are located. One can envision the future development and design of a unified and customizable app for monitoring health, administering regular tests, communicating with health professionals, and storing medical records. Such integrated capability would greatly reduce the cost of healthcare and offer patients much simpler ways to maintain, understand, and personalize their health-related records, treatments, and activities. Furthermore, the existence of such database can provide valuable information on the efficacy of treatments, which in turn (albeit with unavoidable privacy concerns) can offer a wealth of data for future development of therapies and interventions.

References

1. Vashist, S.; Mudanyali, O.; Schneider, E. M.; Zengerle, R.; Ozcan, A., Cellphone-based devices for bioanalytical sciences. *Anal. Bioanal. Chem.* **2014**, *406* (14), 3263-3277.
2. Ahmed, M. U.; Saaem, I.; Wu, P. C.; Brown, A. S., Personalized diagnostics and biosensors: a review of the biology and technology needed for personalized medicine. *Crit. Rev. Biotechnol.* **2014**, *34* (2), 180-196.
3. Boisselier, E.; Astruc, D., Gold nanoparticles in nanomedicine: preparations, imaging, diagnostics, therapies and toxicity. *Chem. Soc. Rev.* **2009**, *38* (6), 1759-1782.
4. Dreaden, E. C.; Alkilany, A. M.; Huang, X.; Murphy, C. J.; El-Sayed, M. A., The golden age: gold nanoparticles for biomedicine. *Chem. Soc. Rev.* **2012**, *41* (7), 2740-2779.
5. Saha, K.; Agasti, S. S.; Kim, C.; Li, X.; Rotello, V. M., Gold Nanoparticles in chemical and biological sensing. *Chem. Rev.* **2012**, *112* (5), 2739-2779.
6. Mattoussi, H.; Palui, G.; Na, H. B., Luminescent quantum dots as platforms for probing in vitro and in vivo biological processes. *Adv. Drug Deliv. Rev.* **2012**, *64* (2), 138-166.
7. Probst, C. E.; Zrazhevskiy, P.; Bagalkot, V.; Gao, X., Quantum dots as a platform for nanoparticle drug delivery vehicle design. *Adv. Drug Deliv. Rev.* **2013**, *65* (5), 703-718.
8. Doane, T. L.; Burda, C., The unique role of nanoparticles in nanomedicine: imaging, drug delivery and therapy. *Chem. Soc. Rev.* **2012**, *41* (7), 2885-2911.
9. Wang, F.; Liu, X. G., Recent advances in the chemistry of lanthanide-doped upconversion nanocrystals. *Chem. Soc. Rev.* **2009**, *38* (4), 976-989.
10. Haase, M.; Schafer, H., Upconverting nanoparticles. *Angew. Chem. Int. Ed.* **2011**, *50* (26), 5808-5829.
11. Chen, G. Y.; Qju, H. L.; Prasad, P. N.; Chen, X. Y., Upconversion nanoparticles: design, nanochemistry, and applications in theranostics. *Chem. Rev.* **2014**, *114* (10), 5161-5214.
12. DaCosta, M. V.; Doughan, S.; Han, Y.; Krull, U. J., Lanthanide upconversion nanoparticles and applications in bioassays and bioimaging: A review. *Anal. Chim. Acta* **2014**, *832*, 1-33.
13. Song, Y.; Huang, Y.-Y.; Liu, X., et al., Point-of-care technologies for molecular diagnostics using a drop of blood. *Trends Biotechnol.* **2014**, *32* (3), 132-139.
14. Lippa, P. B.; Müller, C.; Schlichtiger, A.; Schlebusch, H., Point-of-care testing (POCT): Current techniques and future perspectives. *TrAC, Trends Anal. Chem.* **2011**, *30* (6), 887-898.

15. Clerc, O.; Greub, G., Routine use of point-of-care tests: usefulness and application in clinical microbiology. *Clin. Microbiol. Infect.* **2010**, *16* (8), 1054-1061.
16. Gulley, M. L.; Morgan, D. R., Molecular oncology testing in resource-limited settings. *J. Mol. Diagn.* **2014**, *16* (6), 601-611.
17. Anfossi, L.; Baggiani, C.; Giovannoli, C.; D'Arco, G.; Giraudi, G., Lateral-flow immunoassays for mycotoxins and phycotoxins: a review. *Anal. Bioanal. Chem.* **2013**, *405* (2-3), 467-480.
18. Hu, J.; Wang, S.; Wang, L., et al., Advances in paper-based point-of-care diagnostics. *Biosens. Bioelectron.* **2014**, *54* (0), 585-597.
19. Yetisen, A. K.; Akram, M. S.; Lowe, C. R., Paper-based microfluidic point-of-care diagnostic devices. *Lab Chip* **2013**, *13* (12), 2210-2251.
20. Pelton, R., Bioactive paper provides a low-cost platform for diagnostics. *TrAC, Trends Anal. Chem.* **2009**, *28* (8), 925-942.
21. Liu, B.; Du, D.; Hua, X.; Yu, X. Y.; Lin, Y., Paper-based electrochemical biosensors: from test strips to paper-based microfluidics. *Electroanalysis* **2014**, *26* (6), 1214-1223.
22. Byrnes, S.; Thiessen, G.; Fu, E., Progress in the development of paper-based diagnostics for low-resource point-of-care settings. *Bioanalysis* **2013**, *5* (22), 2821-2836.
23. Posthuma-Trumpie, G.; Korf, J.; van Amerongen, A., Lateral flow (immuno)assay: its strengths, weaknesses, opportunities and threats. A literature survey. *Anal. Bioanal. Chem.* **2009**, *393* (2), 569-582.
24. Mark, D.; Haeberle, S.; Roth, G.; von Stetten, F.; Zengerle, R., Microfluidic lab-on-a-chip platforms: requirements, characteristics and applications. *Chem. Soc. Rev.* **2010**, *39* (3), 1153-1182.
25. Chin, C. D.; Linder, V.; Sia, S. K., Commercialization of microfluidic point-of-care diagnostic devices. *Lab Chip* **2012**, *12* (12), 2118-2134.
26. Ng, A. C.; Uddayasankar, U.; Wheeler, A., Immunoassays in microfluidic systems. *Anal. Bioanal. Chem.* **2010**, *397* (3), 991-1007.
27. Gorocs, Z.; Ozcan, A., Biomedical imaging and sensing using flatbed scanners. *Lab Chip* **2014**, *14* (17), 3248-3257.
28. Yu, H.-Z.; Li, Y.; Ou, L. M. L., Reading Disc-Based Bioassays with Standard Computer Drives. *Acc. Chem. Res.* **2012**, *46* (2), 258-268.
29. Morais, S.; Tortajada-Genaro, L.; Maquieira, Á., Array-on-a-disk? How Blu-ray technology can be applied to molecular diagnostics. *Expert Rev. Mol. Diagn.* **2014**, *14* (7), 773-775.

30. Preechaburana, P.; Suska, A.; Filippini, D., Biosensing with cell phones. *Trends Biotechnol.* **2014**, *32* (7), 351-355.
31. Erickson, D.; O'Dell, D.; Jiang, L., et al., Smartphone technology can be transformative to the deployment of lab-on-chip diagnostics. *Lab Chip* **2014**, *14* (17), 3159-3164.
32. Liu, X.; Lin, T. Y.; Lillehoj, P., Smartphones for Cell and Biomolecular Detection. *Ann. Biomed. Eng.* **2014**, 1-13.
33. Goryacheva, I. Y.; Lenain, P.; De Saeger, S., Nanosized labels for rapid immunotests. *TrAC, Trends Anal. Chem.* **2013**, *46* (0), 30-43.
34. Sun, J.; Xianyu, Y.; Jiang, X., Point-of-care biochemical assays using gold nanoparticle-implemented microfluidics. *Chem. Soc. Rev.* **2014**, *43* (17), 6239-6253.
35. Yager, P.; Domingo, G. J.; Gerdes, J., Point-of-care diagnostics for global health. *Annu. Rev. Biomed. Eng.* **2008**, *10*, 107-144.
36. Martinez, A. W.; Phillips, S. T.; Whitesides, G. M.; Carrilho, E., Diagnostics for the Developing World: Microfluidic Paper-Based Analytical Devices. *Anal. Chem.* **2010**, *82* (1), 3-10.
37. Wu, G.; Zaman, M. H., Low-cost tools for diagnosing and monitoring HIV infection in low-resource settings. *Bulletin of the World Health Organization* **2012**, *90*, 914-920. www.who.int/bulletin/volumes/90/12/12-102780/en/.
38. <http://data.worldbank.org/indicator/SH.XPD.PUBL.ZS> (accessed November 6, 2014).
39. <http://www.standardandpoors.com/ratings/articles/en/eu/?articleType=HTML&assetID=1245328578642> (accessed November 10, 2014).
40. Canada Health Act Annual Report 2010-2011. www.hc-sc.gc.ca/hcs-sss/pubs/cha-lcs/2011-cha-lcs-ar-ra/index-eng.php#nu (accessed November 10, 2014).
41. Centers for Disease Control and Prevention. Cholera - *Vibrio cholerae* infection. www.cdc.gov/cholera/general/ (accessed November 10, 2014).
42. Cameron, J.; Jagals, P.; Hunter, P. R.; Pedley, S.; Pond, K., Economic assessments of small-scale drinking-water interventions in pursuit of MDG target 7C. *Sci. Total Environ.* **2011**, *410-411* (0), 8-15.
43. Diarrhoea: Why children are still dying and what can be done. www.whqlibdoc.who.int/publications/2009/9789241598415_eng.pdf. (accessed November 16, 2014).
44. Concoran, E.; Nellesmann, C.; Baker, E., et al. United Nations Environment Programme. Sick Water? The central role of waste- water management in sustainable development. http://www.unep.org/pdf/SickWater_screen.pdf (accessed October 2014).

45. Whitesides, G. A lab the size of a postage stamp. TEDX Boston 2009. http://www.ted.com/talks/george_whitesides_a_lab_the_size_of_a_postage_stamp.
46. Durner, J., Clinical chemistry: challenges for analytical chemistry and the nanosciences from medicine. *Angew. Chem. Int. Ed.* **2010**, *49* (6), 1026-1051.
47. RCSB protein data bank. www.rcsb.org/pdb/home/home.do (accessed November 8, 2014).
48. Protein database for biomedical research. www.proteomicsdb.org (accessed November 8, 2014).
49. Wilhelm, M.; Schlegl, J.; Hahne, H., et al., Mass-spectrometry-based draft of the human proteome. *Nature* **2014**, *509* (7502), 582-587.
50. Kim, M. S.; Pinto, S. M.; Getnet, D., et al., A draft map of the human proteome. *Nature* **2014**, *509* (7502), 575-581.
51. Human Proteome Map. <http://www.humanproteomemap.org> (accessed November 16, 2014).
52. Keefe, A. D.; Pai, S.; Ellington, A., Aptamers as therapeutics. *Nat. Rev. Drug Discov.* **2010**, *9*, 537-550.
53. Jayasena, S. D., Aptamers: An emerging class of molecules that rival antibodies in diagnostics. *Clin. Chem.* **1999**, *45*, 1628-1650.
54. National Center for Biotechnology Information. Resources. www.ncbi.nlm.nih.gov/genome (accessed October 29, 2014).
55. Ezkurdia, I.; Juan, D.; Rodriguez, J. M., et al., Multiple evidence strands suggest that there may be as few as 19 000 human protein-coding genes. *Hum. Mol. Gen.* **2014**, *23* (22), 5866-5878.
56. Walker, F. M.; Ahmad, K. M.; Eisenstein, M.; Soh, H. T., Transformation of personal computers and mobile phones into genetic diagnostic systems. *Anal. Chem.* **2014**, *86* (18), 9236-9241.
57. Ren, M.; Xu, H.; Huang, X., et al., Immunochromatographic assay for ultrasensitive detection of aflatoxin B1 in maize by highly luminescent quantum dot beads. *ACS Appl. Mater. Interfaces* **2014**, *6* (16), 14215-14222.
58. Wishart, D. S.; Jewison, T.; Guo, A. C., et al., HMDB 3.0—The Human Metabolome Database in 2013. *Nucleic Acids Res.* **2013**, *41* (D1), D801-D807.
59. The human metabolome database. www.hmdb.ca (accessed October 15, 2014).
60. Mabey, D.; Peeling, R. W.; Ustianowski, A.; Perkins, M. D., Tropical infectious diseases: Diagnostics for the developing world. *Nat. Rev. Microbiol.* **2004**, *2* (3), 231-240.

61. BBC News. Ebola: mapping the outbreak. <http://www.bbc.com/news/world-africa-28755033> (accessed November 17, 2014).
62. <http://www.foodsafetynews.com/sections/foodborne-illness-outbreaks/#.VFE80b5A8ZY> (accessed October 26, 2014).
63. BBC News. Denmark links 12 listeria deaths to pork sausage. www.bbc.com/news/world-europe-28761463 (accessed October 26, 2014).
64. Oyarzabal, O. A.; Backert, S., *Microbial Food Safety: An Introduction*. Springer: 2011.
65. FDA: Environmental chemical contaminants and pesticides. <http://www.fda.gov/downloads/Food/GuidanceRegulation/UCM252404.pdf> (accessed November 16, 2014).
66. Monteiro, M. R.; Ambrozini, A. R. P.; Lião, L. M.; Ferreira, A. G., Critical review on analytical methods for biodiesel characterization. *Talanta* **2008**, *77* (2), 593-605.
67. Hoekman, S. K.; Broch, A.; Robbins, C.; Cenicerros, E.; Natarajan, M., Review of biodiesel composition, properties, and specifications. *Renew. Sustainable Energy Rev.* **2012**, *16* (1), 143-169.
68. Liron, Z.; Bromberg, A.; Fisher, M., *Novel Approaches in Biosensors and Rapid Diagnostic Assays*. Springer US: 2001.
69. Ngom, B.; Guo, Y. C.; Wang, X. L.; Bi, D. R., Development and application of lateral flow test strip technology for detection of infectious agents and chemical contaminants: a review. *Anal. Bioanal. Chem.* **2010**, *397* (3), 1113-1135.
70. Wong, R.; Tse, H., *Lateral Flow Immunoassay*. Humana: 2008.
71. Dugan, A. Americans' Tech Tastes Change With Times. <http://www.gallup.com/poll/166745/americans-tech-tastes-change-times.aspx> (accessed November 15, 2014).
72. Chan, W. C. W.; Nie, S. M., Quantum Dot Bioconjugates for Ultrasensitive Nonisotopic Detection. *Science* **1998**, *281* (5385), 2016-2018.
73. Peter, H. All-TIME 100 Gadgets 2010. http://content.time.com/time/specials/packages/article/0,28804,2023689_2026196_2026194,00.html.
74. ICT Data and Statistics Division. Telecommunication Development Bureau. The World in 2014. www.itu.int/en/ITU-D/Statistics/Documents/facts/ICTFactsFigures2014-e.pdf (accessed November 10, 2014).
75. Auffan, M.; Rose, J.; Bottero, J.-Y., et al., Towards a definition of inorganic nanoparticles from an environmental, health and safety perspective. *Nat. Nano* **2009**, *4* (10), 634-641.

76. Petryayeva, E.; Krull, U. J., Localized surface plasmon resonance: nanostructures, bioassays and biosensing-A review. *Anal. Chim. Acta* **2011**, *706* (1), 8-24.
77. Taton, T. A.; Mirkin, C. A.; Letsinger, R. L., Scanometric DNA array detection with nanoparticle probes. *Science* **2000**, *289* (5485), 1757-1760.
78. Posthuma-Trumpie, G.; Wichers, J.; Koets, M.; Berendsen, L. J. M.; van Amerongen, A., Amorphous carbon nanoparticles: a versatile label for rapid diagnostic (immuno)assays. *Anal. Bioanal. Chem.* **2012**, *402* (2), 593-600.
79. Lee, S.; Oncescu, V.; Mancuso, M.; Mehta, S.; Erickson, D., A smartphone platform for the quantification of vitamin D levels. *Lab Chip* **2014**, *14* (8), 1437-1442.
80. Lu, Y.; Shi, W.; Qin, J.; Lin, B., Low cost, portable detection of gold nanoparticle-labeled microfluidic immunoassay with camera cell phone. *Electrophoresis* **2009**, *30* (4), 579-582.
81. Luckham, R. E.; Brennan, J. D., Bioactive paper dipstick sensors for acetylcholinesterase inhibitors based on sol-gel/enzyme/gold nanoparticle composites. *Analyst* **2010**, *135* (8), 2028-2035.
82. Choi, D. H.; Lee, S. K.; Oh, Y. K., et al., A dual gold nanoparticle conjugate-based lateral flow assay (LFA) method for the analysis of troponin I. *Biosens. Bioelectron.* **2010**, *25* (8), 1999-2002.
83. Chiu, R. Y. T.; Jue, E.; Yip, A. T., et al., Simultaneous concentration and detection of biomarkers on paper. *Lab Chip* **2014**, *14* (16), 3021-3028.
84. Warren, A. D.; Kwong, G. A.; Wood, D. K.; Lin, K. Y.; Bhatia, S. N., Point-of-care diagnostics for noncommunicable diseases using synthetic urinary biomarkers and paper microfluidics. *Proc. Natl. Acad. Sci. U.S.A.* **2014**, *111* (10), 3671-3676.
85. Gong, M. M.; MacDonald, B. D.; Nguyen, T. V.; Van Nguyen, K.; Sinton, D., Lab-in-a-pen: a diagnostics format familiar to patients for low-resource settings. *Lab Chip* **2014**, *14* (5), 957-963.
86. Anfossi, L.; Calderara, M.; Baggiani, C., et al., Development and application of a quantitative lateral flow immunoassay for fumonisins in maize. *Anal. Chim. Acta* **2010**, *682* (1-2), 104-109.
87. Anfossi, L.; D'Arco, G.; Calderara, M., et al., Development of a quantitative lateral flow immunoassay for the detection of aflatoxins in maize. *Food Addit. Contam. Part A-Chem. Anal. Control Expo. Risk Assess.* **2011**, *28* (2), 226-234.
88. Zhou, G.; Mao, X.; Juncker, D., Immunochromatographic assay on thread. *Anal. Chem.* **2012**, *84* (18), 7736-7743.
89. Rohrman, B. A.; Leautaud, V.; Molyneux, E.; Richards-Kortum, R. R., A Lateral flow assay for quantitative detection of amplified HIV-1 RNA. *PLoS One* **2012**, *7* (9), e45611.

90. Shi, X.; Wen, J.; Li, Y., et al., DNA molecular beacon-based plastic biochip: a versatile and sensitive scanometric detection platform. *ACS Appl. Mater. Interfaces* **2014**, *6* (24), 21788-21797.
91. Pallapa, M.; Ou, L. M. L.; Parameswaran, M.; Yu, H. Z., Software-based quantitation of bioassays on CD. *Sensor Actuat. B-Chem.* **2010**, *148* (2), 620-623.
92. Li, Y.; Ou, L. M. L.; Yu, H. Z., Digitized molecular diagnostics: reading disk-based bioassays with standard computer drives. *Anal. Chem.* **2008**, *80* (21), 8216-8223.
93. Morais, S.; Tortajada-Genaro, L. A.; Arnandis-Chover, T.; Puchades, R.; Maquieira, A., multiplexed microimmunoassays on a digital versatile disk. *Anal. Chem.* **2009**, *81* (14), 5646-5654.
94. Morais, S.; Tamarit-Lopez, J.; Puchades, R.; Maquieira, A., Determination of microcystins in river waters using microsensor arrays on disk. *Environ. Sci. Technol.* **2010**, *44* (23), 9024-9029.
95. Wang, H.; Ou, L. M. L.; Suo, Y.; Yu, H.-Z., Computer-readable DNAzyme assay on disc for ppb-level lead detection. *Anal. Chem.* **2011**, *83* (5), 1557-1563.
96. Li, X.; Shi, M.; Cui, C.; Yu, H.-Z., Inkjet-printed bioassays for direct reading with a multimode dvd/blu-ray optical drive. *Anal. Chem.* **2014**, *86* (18), 8922-8926.
97. Arnandis-Chover, T.; Morais, S.; González-Martínez, M. Á.; Puchades, R.; Maquieira, Á., high density MicroArrays on Blu-ray discs for massive screening. *Biosens. Bioelectron.* **2014**, *51*, 109-114.
98. Li, X.; Wang, S.; Ge, B.; Yao, Z.; Yu, H. Z., DVD technology-based molecular diagnosis platform: quantitative pregnancy test on a disc. *Lab Chip* **2014**, *14*, 1686-1694.
99. Xu, H.; Chen, J.; Birrenkott, J., et al., Gold-nanoparticle-decorated silica nanorods for sensitive visual detection of proteins. *Anal. Chem.* **2014**, *86* (15), 7351-7359.
100. Rivas, L.; Medina-Sanchez, M.; de la Escosura-Muniz, A.; Merkoci, A., Improving sensitivity of gold nanoparticle-based lateral flow assays by using wax-printed pillars as delay barriers of microfluidics. *Lab Chip* **2014**, *14* (22), 4406-4414.
101. Xu, H.; Mao, X.; Zeng, Q., et al., Aptamer-functionalized gold nanoparticles as probes in a dry-reagent strip biosensor for protein analysis. *Anal. Chem.* **2008**, *81* (2), 669-675.
102. Chen, J.; Zhou, S.; Wen, J., Disposable strip biosensor for visual detection of Hg²⁺ based on Hg²⁺-triggered toehold binding and Exonuclease III-assisted signal amplification. *Anal. Chem.* **2014**, *86* (6), 3108-3114.
103. Juntunen, E.; Myyryläinen, T.; Salminen, T.; Soukka, T.; Pettersson, K., Performance of fluorescent europium(III) nanoparticles and colloidal gold reporters in lateral flow bioaffinity assay. *Anal. Biochem.* **2012**, *428* (1), 31-38.

104. Song, X.; Knotts, M., Time-resolved luminescent lateral flow assay technology. *Anal. Chim. Acta* **2008**, *626* (2), 186-192.
105. Li, X.; Li, W.; Yang, Q., et al., Rapid and quantitative detection of prostate specific antigen with a quantum dot nanobeads-based immunochromatography test strip. *ACS Appl. Mater. Interfaces* **2014**, *6* (9), 6406-6414.
106. Lönnberg, M.; Drevin, M.; Carlsson, J., Ultra-sensitive immunochromatographic assay for quantitative determination of erythropoietin. *J. Immunol. Methods* **2008**, *339* (2), 236-244.
107. Blažková, M.; Mičková-Holubová, B.; Rauch, P.; Fukal, L., Immunochromatographic colloidal carbon-based assay for detection of methiocarb in surface water. *Biosens. Bioelectron.* **2009**, *25* (4), 753-758.
108. Lönnberg, M.; Carlsson, J., Membrane assisted isoform immunoassay: a rapid method for the separation and determination of protein isoforms in an integrated immunoassay. *J. Immunol. Methods* **2000**, *246* (1-2), 25-36.
109. Linares, E. M.; Kubota, L. T.; Michaelis, J.; Thalhammer, S., Enhancement of the detection limit for lateral flow immunoassays: evaluation and comparison of bioconjugates. *J. Immunol. Methods* **2012**, *375* (1-2), 264-270.
110. Zhu, H. Y.; Sikora, U.; Ozcan, A., Quantum dot enabled detection of Escherichia coli using a cell-phone. *Analyst* **2012**, *137* (11), 2541-2544.
111. Zou, Z.; Du, D.; Wang, J., et al., Quantum dot-based immunochromatographic fluorescent biosensor for biomonitoring trichloropyridinol, a biomarker of exposure to chlorpyrifos. *Anal. Chem.* **2010**, *82* (12), 5125-5133.
112. Li, Z.; Wang, Y.; Wang, J., et al., Rapid and sensitive detection of protein biomarker using a portable fluorescence biosensor based on quantum dots and a lateral flow test strip. *Anal. Chem.* **2010**, *82* (16), 7008-7014.
113. Wang, L.; Chen, W.; Ma, W., et al., Fluorescent strip sensor for rapid determination of toxins. *Chem. Commun.* **2011**, *47* (5), 1574-1576.
114. Zhao, P.; Wu, Y.; Zhu, Y., et al., Upconversion fluorescent strip sensor for rapid determination of *Vibrio anguillarum*. *Nanoscale* **2014**, *6* (7), 3804-3809.
115. van Dam, G. J.; de Dood, C. J.; Lewis, M., et al., A robust dry reagent lateral flow assay for diagnosis of active schistosomiasis by detection of *Schistosoma* circulating anodic antigen. *Exp. Parasitol.* **2013**, *135* (2), 274-282.
116. Bobosha, K.; Fat, E.; van den Eeden, S. J. F., et al., Field-evaluation of a new lateral flow assay for detection of cellular and humoral immunity against *Mycobacterium leprae*. *PLoS Negl. Trop. Dis.* **2014**, *8* (5), e2845.

117. Song, C.; Zhi, A.; Liu, Q., et al., Rapid and sensitive detection of β -agonists using a portable fluorescence biosensor based on fluorescent nanosilica and a lateral flow test strip. *Biosens. Bioelectron.* **2013**, *50*, 62-65.
118. Adhikari, M.; Dhamane, S.; Hagstrom, A. E. V., et al., Functionalized viral nanoparticles as ultrasensitive reporters in lateral-flow assays. *Analyst* **2013**, *138* (19), 5584-5587.
119. Li, Z.; Barnes, J. C.; Bosoy, A.; Stoddart, J. F.; Zink, J. I., Mesoporous silica nanoparticles in biomedical applications. *Chem. Soc. Rev.* **2012**, *41* (7), 2590-2605.
120. Montalti, M.; Prodi, L.; Rampazzo, E.; Zaccheroni, N., Dye-doped silica nanoparticles as luminescent organized systems for nanomedicine. *Chem. Soc. Rev.* **2014**, *43* (12), 4243-4268.
121. Burns, A.; Ow, H.; Wiesner, U., Fluorescent core-shell silica nanoparticles: towards "Lab on a Particle" architectures for nanobiotechnology. *Chem. Soc. Rev.* **2006**, *35* (11), 1028-1042.
122. Elsabahy, M.; Wooley, K. L., Design of polymeric nanoparticles for biomedical delivery applications. *Chem. Soc. Rev.* **2012**, *41* (7), 2545-2561.
123. Tong, R.; Tang, L.; Ma, L., et al., Smart chemistry in polymeric nanomedicine. *Chem. Soc. Rev.* **2014**, *43* (20), 6982-7012.
124. Yildiz, I.; Shukla, S.; Steinmetz, N. F., Applications of viral nanoparticles in medicine. *Curr. Opin. Biotechnol.* **2011**, *22* (6), 901-908.
125. Fischlechner, M.; Donath, E., Viruses as Building blocks for materials and devices. *Angew. Chem. Int. Ed.* **2007**, *46* (18), 3184-3193.
126. Algar, W. R.; Susumu, K.; Delehanty, J. B.; Medintz, I. L., Semiconductor quantum dots in bioanalysis: crossing the valley of death. *Anal. Chem.* **2011**, *83* (23), 8826-8837.
127. Wang, F.; Liu, X., Upconversion multicolor fine-tuning: visible to near-infrared emission from lanthanide-doped NaYF₄ nanoparticles. *J. Am. Chem. Soc.* **2008**, *130* (17), 5642-5643.
128. Jacobs, C. B.; Peairs, M. J.; Venton, B. J., Review: Carbon nanotube based electrochemical sensors for biomolecules. *Anal. Chim. Acta* **2010**, *662* (2), 105-127.
129. De Volder, M. F. L.; Tawfick, S. H.; Baughman, R. H.; Hart, A. J., Carbon nanotubes: present and future commercial applications. *Science* **2013**, *339* (6119), 535-539.
130. Zhu, Y. W.; Murali, S.; Cai, W. W., et al., Graphene and graphene oxide: synthesis, properties, and applications. *Adv. Mater.* **2010**, *22* (35), 3906-3924.
131. Loh, K. P.; Bao, Q. L.; Eda, G.; Chhowalla, M., Graphene oxide as a chemically tunable platform for optical applications. *Nat. Chem.* **2010**, *2* (12), 1015-1024.

132. Baker, S. N.; Baker, G. A., Luminescent carbon nanodots: emergent nanolights. *Angew. Chem. Int. Ed.* **2010**, *49* (38), 6726-6744.
133. Shen, J. H.; Zhu, Y. H.; Yang, X. L.; Li, C. Z., Graphene quantum dots: emergent nanolights for bioimaging, sensors, catalysis and photovoltaic devices. *Chem. Commun.* **2012**, *48* (31), 3686-3699.
134. Mochalin, V. N.; Shenderova, O.; Ho, D.; Gogotsi, Y., The properties and applications of nanodiamonds. *Nat. Nanotechnol.* **2012**, *7* (1), 11-23.
135. Schirhagl, R.; Chang, K.; Loretz, M.; Degen, C. L., Nitrogen-vacancy centers in diamond: nanoscale sensors for physics and biology. *Annu. Rev. Phys. Chem.* **2014**, *65*, 83-105.
136. Wu, C.; Chiu, D. T., Highly fluorescent semiconducting polymer dots for biology and medicine. *Angew. Chem. Int. Ed.* **2013**, *52* (11), 3086-3109.
137. Feng, S.; Caire, R.; Cortazar, B., et al., Immunochromatographic diagnostic test analysis using google glass. *ACS Nano* **2014**, *8* (3), 3069-3079.
138. Durini, D., *High Performance Silicon Imaging: Fundamentals and Applications of CMOS and CCD sensors*. Elsevier Science: 2014.
139. Martinez, A. W.; Phillips, S. T.; Carrilho, E., et al., Simple telemedicine for developing regions: Camera phones and paper-based microfluidic devices for real-time, off-site diagnosis. *Anal. Chem.* **2008**, *80* (10), 3699-3707.
140. iHealthLabs Inc. . www.ihealthlabs.com (accessed October 8, 2014).
141. Kardia Mobile by AliveCor Inc. www.alivecor.com (accessed October 8, 2014).
142. CellScope app to monitor skin and ear condition. www.cellscope.com (accessed October 8, 2014).
143. SkinVision - skin health mobile app. www.skinvision.com (accessed October 8, 2014).
144. Wolf, J. A.; Moreau, J. F.; Akilov, O.; et al., Diagnostic inaccuracy of smartphone applications for melanoma detection. *JAMA Dermatol.* **2013**, *149* (4), 422-426.
145. Bond, D. S.; Thomas, J. G.; Raynor, H. A., et al., B-MOBILE - A smartphone-based intervention to reduce sedentary time in overweight/obese individuals: a within-subjects experimental trial. *PLoS One* **2014**, *9* (6), e100821.
146. Recio-Rodriguez, J. I.; Martin-Cantera, C.; Gonzalez-Viejo, N., et al., Effectiveness of a smartphone application for improving healthy lifestyles, a randomized clinical trial (EVIDENT II): study protocol. *BMC Public Health* **2014**, *14* (254), 1-13.

147. Wang, S.; Zhao, X.; Khimji, I., et al., Integration of cell phone imaging with microchip ELISA to detect ovarian cancer HE4 biomarker in urine at the point-of-care. *Lab Chip* **2011**, *11* (20), 3411-3418.
148. McGeough, C. M.; O'Driscoll, S., Camera phone-based quantitative analysis of C-reactive protein ELISA. *IEEE Trans. Biomed. Circuits. Syst.* **2013**, *7* (5), 655-659.
149. López-Muedano, C.; Kirton, R. S.; Kumble, K. D.; Taberner, A. J., Inexpensive optical system for microarray ELISA. *Talanta* **2012**, *100*, 405-409.
150. Fronczek, C. F.; Park, T. S.; Harshman, D. K.; Nicolini, A. M.; Yoon, J.Y., Paper microfluidic extraction and direct smartphone-based identification of pathogenic nucleic acids from field and clinical samples. *RSC Adv.* **2014**, *4* (22), 11103-11110.
151. Oncescu, V.; Mancuso, M.; Erickson, D., Cholesterol testing on a smartphone. *Lab Chip* **2014**, *14* (4), 759-763.
152. Coskun, A. F.; Wong, J.; Khodadadi, D., et al., A personalized food allergen testing platform on a cellphone. *Lab Chip* **2013**, *13* (4), 636-640.
153. Thom, N. K.; Lewis, G. G.; Yeung, K.; Phillips, S. T., Quantitative fluorescence assays using a self-powered paper-based microfluidic device and a camera-equipped cellular phone. *RSC Adv.* **2014**, *4* (3), 1334-1340.
154. Oncescu, V.; O'Dell, D.; Erickson, D., Smartphone based health accessory for colorimetric detection of biomarkers in sweat and saliva. *Lab Chip* **2013**, *13* (16), 3232-3238.
155. Hong, J. I.; Chang, B. Y., Development of the smartphone-based colorimetry for multi-analyte sensing arrays. *Lab Chip* **2014**, *14* (10), 1725-1732.
156. Wu, T. F.; Yen, T. M.; Han, Y., et al., A light-sheet microscope compatible with mobile devices for label-free intracellular imaging and biosensing. *Lab Chip* **2014**, *14* (17), 3341-3348.
157. Wei, Q.; Qi, H.; Luo, W., et al., Fluorescent imaging of single nanoparticles and viruses on a smart phone. *ACS Nano* **2013**, *7* (10), 9147-9155.
158. Yu, H.; Tan, Y.; Cunningham, B. T., Smartphone fluorescence spectroscopy. *Anal. Chem.* **2014**, *86* (17), 8805-8813.
159. Scheeline, A., Teaching, learning, and using spectroscopy with commercial, off-the-shelf technology. *Appl. Spectrosc.* **2010**, *64* (9), 256A-268A.
160. Ayas, S.; Cupallari, A.; Ekiz, O. O.; Kaya, Y.; Dana, A., Counting molecules with a mobile phone camera using plasmonic enhancement. *ACS Photonics* **2014**, *1* (1), 17-26.
161. Preechaburana, P.; Gonzalez, M. C.; Suska, A.; Filippini, D., Surface plasmon resonance chemical sensing on cell phones. *Angew. Chem. Int. Ed.* **2012**, *51* (46), 11585-11588.

162. Deiss, F.; Funes-Huacca, M. E.; Bal, J.; Tjhung, K. F.; Derda, R., Antimicrobial susceptibility assays in paper-based portable culture devices. *Lab Chip* **2014**, *14* (1), 167-171.
163. Broekaert, J. A. C., Inductively coupled plasma spectrometry. In *Handbook of Spectroscopy*, Wiley-VCH Verlag GmbH & Co. KGaA: 2014; pp 583-646.
164. Lakowicz, J. R., *Principles of Fluorescence Spectroscopy*. 3rd ed.; Plenum Press: New York, 2006.
165. Valeur, B., *Molecular Fluorescence: Principles and Applications*. Wiley-VCH Verlag GmbH: Toronto, 2001.
166. Atkins, P.; de Paula, J., *Physical Chemistry*. 8th ed.; W. H. Freeman and Company: New York, 2006.
167. Douglas, P.; Burrows, H. D.; Evans, R. C., Foundation of Photochemistry: A background on the interactions between light and molecules. In *Applied Photochemistry*, Evans, R. C.; Douglas, P.; Burrow, H. D., Eds. Springer Science & Business Media: 2014.
168. Sauer, M.; Hofkens, J.; Enderlein, J., Basic principles of fluorescence spectroscopy. In *Handbook of Fluorescence Spectroscopy and Imaging*, Wiley-VCH Verlag GmbH & Co. KGaA: 2011; pp 1-30.
169. Klaus, S., Photophysics of fluorescence. In *Fluorescence Lifetime Spectroscopy and Imaging*, CRC Press: 2014; pp 23-46.
170. Klán, P.; Wirz, J., A crash course in photophysics and a classification of primary photoreactions. In *Photochemistry of Organic Compounds*, John Wiley & Sons, Ltd: 2009; pp 25-72.
171. Diaspro, A.; Chirico, G.; Usai, C.; Ramoino, P.; Dobrucki, J., Photobleaching. In *Handbook Of Biological Confocal Microscopy*, Pawley, B. J., Ed. Springer US: Boston, MA, 2006; pp 690-702.
172. Berezin, M. Y.; Achilefu, S., Fluorescence lifetime measurements and biological imaging. *Chem. Rev.* **2010**, *110* (5), 2641-2684.
173. Muskens, O. L.; Giannini, V.; Sánchez-Gil, J. A.; Gómez Rivas, J., Strong enhancement of the radiative decay rate of emitters by single plasmonic nanoantennas. *Nano Lett.* **2007**, *7* (9), 2871-2875.
174. Schuller, J. A.; Barnard, E. S.; Cai, W., et al., Plasmonics for extreme light concentration and manipulation. *Nat. Mater.* **2010**, *9* (3), 193-204.
175. Sjöback, R.; Nygren, J.; Kubista, M., Absorption and fluorescence properties of fluorescein. *Spectrochim. Acta Mol. Biomol. Spectrosc.* **1995**, *51* (6), L7-L21.

176. Skoog, D. A., *Principles of instrumental analysis*. Fourth edition. Fort Worth : Saunders College Pub.: 1992.
177. Becker, W.; Bergmann, A.; Biscotti, G., et al. In *High-speed FLIM data acquisition by time-correlated single-photon counting*, 2004; pp 27-35.
178. Waters, J. C., Accuracy and precision in quantitative fluorescence microscopy. *J. Cell Biol.* **2009**, *185* (7), 1135-1148.
179. Munoz-Losa, A.; Curutchet, C.; Krueger, B. P.; Hartsell, L. R.; Mennucci, B., Fretting about FRET: failure of the ideal dipole approximation. *Biophys. J.* **2009**, *96* (12), 4779-4788.
180. Dale, R. E.; Eisinger, J.; Blumberg, W. E., Orientational freedom of molecular probes - orientation factor in intra-molecular energy-transfer. *Biophys. J.* **1979**, *26* (2), 161-193.
181. Dosremedios, C. G.; Moens, P. D. J., Fluorescence resonance energy-transfer spectroscopy is a reliable ruler for measuring structural-changes in proteins - dispelling the problem of the unknown orientation factor. *J. Struct. Biol.* **1995**, *115* (2), 175-185.
182. Yan, Y.; Marriott, G., Analysis of protein interactions using fluorescence technologies. *Curr. Opin. Chem. Biol.* **2003**, *7* (5), 635-640.
183. Sekar, R. B.; Periasamy, A., Fluorescence resonance energy transfer (FRET) microscopy imaging of live cell protein localizations. *J. Cell Biol.* **2003**, *160* (5), 629-633.
184. Schuler, B.; Eaton, W. A., Protein folding studied by single-molecule FRET. *Curr. Opin. Struct. Biol.* **2008**, *18* (1), 16-26.
185. Hildebrandt, N.; Spillmann, C. M.; Algar, W. R., et al., Energy transfer with semiconductor quantum dot bioconjugates: a versatile platform for biosensing, energy harvesting, and other developing applications. *Chem. Rev.* **2016**, DOI:10.1021/acs.chemrev.6b00030.
186. van der Meer, B. W., Förster Theory. In *FRET – Förster Resonance Energy Transfer*, Wiley-VCH Verlag GmbH & Co. KGaA: 2013; pp 23-62.
187. Aartsma, T. J.; Köhler, J., Optical spectroscopy of individual light-harvesting complexes. In *Biophysical Techniques in Photosynthesis*, Aartsma, T. J.; Matysik, J., Eds. Springer Netherlands: Dordrecht, 2008; pp 241-266.
188. Loura, L. M. S., Simple estimation of Förster resonance energy transfer (FRET) orientation factor distribution in membranes. *Int. J. Mol. Sci.* **2012**, *13* (11), 15252-15270.
189. Cheung, H. C., Resonance energy transfer. In *Topics in Fluorescence Spectroscopy*, Lakowicz, J. R., Ed. Plenum Press: New York, 1991; Vol. 2, pp 127-176.

190. Moog, R. S.; Kuki, A.; Fayer, M. D.; Boxer, S. G., Energy transport and trapping in a synthetic chlorophyllide substituted hemoglobin: orientation of the chlorophyll S1 transition dipole. *Biochemistry* **1984**, *23* (7), 1564-1571.
191. Knox, R. S.; van Amerongen, H., Refractive index dependence of the Förster resonance excitation transfer rate. *J. Phys. Chem. B* **2002**, *106* (20), 5289-5293.
192. Wouters, F. S., Förster resonance energy transfer and fluorescence lifetime imaging. In *Fluorescence Microscopy*, Wiley-VCH Verlag GmbH & Co. KGaA: 2013; pp 245-291.
193. Smith, A. M.; Nie, S., Semiconductor nanocrystals: structure, properties, and band gap engineering. *Acc. Chem. Res.* **2009**, *43* (2), 190-200.
194. Zhong, X.; Han, M.; Dong, Z.; White, T. J.; Knoll, W., Composition-tunable $Zn_xCd_{1-x}Se$ nanocrystals with high luminescence and stability. *J. Am. Chem. Soc.* **2003**, *125* (28), 8589-8594.
195. Larson, D. R.; Zipfel, W. R.; Williams, R. M., et al., Water-soluble quantum dots for multiphoton fluorescence imaging *in vivo*. *Science* **2003**, *300* (5624), 1434-1436.
196. Helmchen, F.; Denk, W., Deep tissue two-photon microscopy. *Nat. Methods* **2005**, *2* (12), 932-940.
197. Na, R. H.; Stender, I. M.; Ma, L. X.; Wulf, H. C., Autofluorescence spectrum of skin: component bands and body site variations. *Skin Res. Technol.* **2000**, *6* (3), 112-117.
198. Medintz, I. L.; Uyeda, H. T.; Goldman, E. R.; Mattoussi, H., Quantum dot bioconjugates for imaging, labelling and sensing. *Nat. Mater.* **2005**, *4* (6), 435-446.
199. Kim, S.; Fisher, B.; Eisler, H. J.; Bawendi, M., Type-II quantum dots: CdTe/CdSe (core/shell) and CdSe/ZnTe (core/shell) heterostructures. *J. Am. Chem. Soc.* **2003**, *125* (38), 11466-11467.
200. Blackman, B.; Battaglia, D.; Peng, X., Bright and water-soluble near IR-emitting CdSe/CdTe/ZnSe Type-II/Type-I nanocrystals, tuning the efficiency and stability by growth. *Chem. Mater.* **2008**, *20* (15), 4847-4853.
201. Xie, R.; Peng, X., Synthetic scheme for high-quality InAs nanocrystals based on self-focusing and one-pot synthesis of InAs-based core-shell nanocrystals. *Angew. Chem. Int. Ed.* **2008**, *47* (40), 7677-7680.
202. Xie, R.; Peng, X., Synthesis of Cu-doped InP nanocrystals (d-dots) with ZnSe diffusion barrier as efficient and color-tunable NIR emitters. *J. Am. Chem. Soc.* **2009**, *131* (30), 10645-10651.
203. Kim, S. W.; Zimmer, J. P.; Ohnishi, S., et al., Engineering $InAs_xP_{1-x}/InP/ZnSe$ III-V alloyed core/shell quantum dots for the near-infrared. *J. Am. Chem. Soc.* **2005**, *127* (30), 10526-10532.

204. Xie, R. G.; Chen, K.; Chen, X. Y.; Peng, X. G., InAs/InP/ZnSe core/shell/shell quantum dots as near-infrared emitters: bright, narrow-band, non-cadmium containing, and biocompatible. *Nano Res.* **2008**, *1* (6), 457-464.
205. Zhong, X.; Xie, R.; Zhang, Y.; Basché, T.; Knoll, W., High-quality violet- to red-emitting ZnSe/CdSe core/shell nanocrystals. *Chem. Mater.* **2005**, *17* (16), 4038-4042.
206. Kim, S.; Park, J.; Kim, T., et al., Reverse Type-I ZnSe/InP/ZnS core/shell/shell nanocrystals: cadmium-free quantum dots for visible luminescence. *Small* **2011**, *7* (1), 70-73.
207. Smith, A. M.; Mohs, A. M.; Nie, S., Tuning the optical and electronic properties of colloidal nanocrystals by lattice strain. *Nat. Nanotechnol.* **2009**, *4* (1), 56-63.
208. Galland, C.; Ghosh, Y.; Steinbruck, A., et al., Two Types of luminescence blinking revealed by spectroelectrochemistry of single quantum dots. *Nature* **2011**, *479* (7372), 203-U75.
209. Clarke, S.; Pinaud, F.; Beutel, O., et al., Covalent monofunctionalization of peptide-coated quantum dots for single-molecule assays. *Nano Lett.* **2010**, *10* (6), 2147-2154.
210. Ehrensperger, M. V.; Hanus, C.; Vannier, C.; Triller, A.; Dahan, M., Multiple association states between glycine receptors and gephyrin identified by SPT analysis. *Biophys. J.* **2007**, *92* (10), 3706-3718.
211. Dertinger, T.; Colyer, R.; Iyer, G.; Weiss, S.; Enderlein, J., Fast, background-free, 3D super-resolution optical fluctuation imaging (SOFI). *Proc. Natl. Acad. Sci. U.S.A.* **2009**, *106* (52), 22287-22292.
212. Lee, S. F.; Osborne, M. A., Brightening, blinking, bluing and bleaching in the life of a quantum dot: friend or foe? *ChemPhysChem* **2009**, *10* (13), 2174-2191.
213. Hay, K. X.; Waisundara, V. Y.; Zong, Y.; Han, M.-Y.; Huang, D., CdSe nanocrystals as hydroperoxide scavengers: a new approach to highly sensitive quantification of lipid hydroperoxides. *Small* **2007**, *3* (2), 290-293.
214. Javier, A.; Strouse, G. F., Activated and intermittent photoluminescence in thin CdSe quantum dot films. *Chem. Phys. Lett.* **2004**, *391* (1-3), 60-63.
215. Sutter, J. U.; Birch, D. J. S.; Rolinski, O. J., The effect of intensity of excitation on CdSe/ZnS quantum dots: opportunities in luminescence sensing. *Appl. Phys. Lett.* **2011**, *98* (2), 021108.
216. Yao, J.; Larson, D. R.; Vishwasrao, H. D.; Zipfel, W. R.; Webb, W. W., Blinking and nonradiant dark fraction of water-soluble quantum dots in aqueous solution. *Proc. Natl. Acad. Sci. U.S.A.* **2005**, *102* (40), 14284-14289.

217. Pons, T.; Medintz, I. L.; Farrell, D., et al., Single-molecule colocalization studies shed light on the idea of fully emitting versus dark single quantum dots. *Small* **2011**, *7* (14), 2101-2108.
218. Durisic, N.; Wiseman, P. W.; Grutter, P.; Heyes, C. D., A common mechanism underlies the dark fraction formation and fluorescence blinking of quantum dots. *ACS Nano* **2009**, *3* (5), 1167-1175.
219. Medintz, I. L.; Clapp, A. R.; Mattoussi, H., et al., Self-assembled nanoscale biosensors based on quantum dot FRET donors. *Nat. Mater.* **2003**, *2* (9), 630-638.
220. Hines, M. A.; Guyot-Sionnest, P., Synthesis and characterization of strongly luminescing ZnS-capped CdSe nanocrystals. *J. Phys. Chem.* **1996**, *100* (2), 468-471.
221. Dabbousi, B. O.; RodriguezViejo, J.; Mikulec, F. V., et al., (CdSe)ZnS core-shell quantum dots: synthesis and characterization of a size series of highly luminescent nanocrystallites. *J. Phys. Chem. B* **1997**, *101* (46), 9463-9475.
222. Rosenthal, S. J.; Chang, J. C.; Kovtun, O.; McBride, J. R.; Tomlinson, I. D., Biocompatible quantum dots for biological applications. *Chem. Biol.* **2011**, *18* (1), 10-24.
223. Wang, X. Y.; Ren, X. F.; Kahen, K., et al., Non-blinking semiconductor nanocrystals. *Nature* **2009**, *459* (7247), 686-689.
224. McBride, J.; Treadway, J.; Feldman, L. C.; Pennycook, S. J.; Rosenthal, S. J., Structural Basis for near unity quantum yield core/shell nanostructures. *Nano Lett.* **2006**, *6* (7), 1496-1501.
225. Talapin, D. V.; Mekis, I.; Gotzinger, S., et al., CdSe/CdS/ZnS and CdSe/ZnSe/ZnS core-shell-shell nanocrystals. *J. Phys. Chem. B* **2004**, *108* (49), 18826-18831.
226. Xie, R. G.; Kolb, U.; Li, J. X.; Basche, T.; Mews, A., Synthesis and characterization of highly luminescent CdSe-Core CdS/Zn_{0.5}Cd_{0.5}S/ZnS multishell nanocrystals. *J. Am. Chem. Soc.* **2005**, *127* (20), 7480-7488.
227. Regulacio, M. D.; Han, M. Y., Composition-tunable alloyed semiconductor nanocrystals. *Acc. Chem. Res.* **2010**, *43* (5), 621-630.
228. Al-Salim, N.; Young, A. G.; Tilley, R. D.; McQuillan, A. J.; Xia, J., Synthesis of CdSeS nanocrystals in coordinating and noncoordinating solvents: solvent's role in evolution of the optical and structural properties. *Chem. Mater.* **2007**, *19* (21), 5185-5193.
229. Swafford, L. A.; Weigand, L. A.; Bowers, M. J., et al., Homogeneously alloyed CdS_xSe_{1-x} nanocrystals: synthesis, characterization, and composition/size-dependent band gap. *J. Am. Chem. Soc.* **2006**, *128* (37), 12299-12306.
230. Bailey, R. E.; Nie, S., Alloyed semiconductor quantum dots: tuning the optical properties without changing the particle size. *J. Am. Chem. Soc.* **2003**, *125* (23), 7100-7106.

231. Zhong, X.; Feng, Y.; Knoll, W.; Han, M., Alloyed ZnxCd1-xS Nanocrystals with Highly Narrow Luminescence Spectral Width. *J. Am. Chem. Soc.* **2003**, *125* (44), 13559-13563.
232. Micic, O. I.; Ahrenkiel, S. P.; Nozik, A. J., Synthesis of extremely small InP quantum dots and electronic coupling in their disordered solid films. *Appl. Phys. Lett.* **2001**, *78* (25), 4022-4024.
233. Battaglia, D.; Peng, X., Formation of high quality InP and InAs nanocrystals in a noncoordinating solvent. *Nano Lett.* **2002**, *2* (9), 1027-1030.
234. Shiohara, A.; Prabakar, S.; Faramus, A., et al., Sized controlled synthesis, purification, and cell studies with silicon quantum dots. *Nanoscale* **2011**, *3* (8), 3364-3370.
235. Erogbogbo, F.; Yong, K. T.; Roy, I., et al., *In vivo* targeted cancer imaging, sentinel lymph node mapping and multi-channel imaging with biocompatible silicon nanocrystals. *ACS Nano* **2011**, *5* (1), 413-423.
236. Chou, L. Y. T.; Chan, W. C. W., Nanotoxicology no signs of illness. *Nat. Nanotechnol.* **2012**, *7* (7), 416-417.
237. Ghaderi, S.; Ramesh, B.; Seifalian, A. M., Fluorescence nanoparticles "quantum dots" as drug delivery system and their toxicity: a review. *J. Drug Target.* **2011**, *19* (7), 475-486.
238. Winnik, F. M.; Maysinger, D., Quantum dot cytotoxicity and ways to reduce it. *Acc. Chem. Res.* **2012**, *46* (3), 672-680.
239. Xu, S.; Ziegler, J.; Nann, T., Rapid synthesis of highly luminescent InP and InP/ZnS nanocrystals. *J. Mater. Chem.* **2008**, *18* (23), 2653-2656.
240. Greco, T.; Ippen, C.; Wedel, A., InP/ZnSe/ZnS Core-Multishell Quantum Dots for Improved Luminescence Efficiency. *Proc. SPIE* **2012**, *8424*, 842439.
241. Choi, H. S.; Liu, W.; Misra, P., et al., Renal clearance of quantum dots. *Nat. Biotechnol.* **2007**, *25* (10), 1165-1170.
242. Park, J.; Dvoracek, C.; Lee, K. H., et al., CuInSe/ZnS core/shell NIR quantum dots for biomedical imaging. *Small* **2011**, *7* (22), 3148-3152.
243. Peng, Z. A.; Peng, X. G., Formation of high-quality CdTe, CdSe, and CdS nanocrystals using CdO as precursor. *J. Am. Chem. Soc.* **2001**, *123* (1), 183-184.
244. Qu, L. H.; Peng, Z. A.; Peng, X. G., Alternative routes toward high quality CdSe nanocrystals. *Nano Lett.* **2001**, *1* (6), 333-337.
245. Yu, W. W.; Peng, X. G., Formation of high-quality CdS and other II-VI semiconductor nanocrystals in noncoordinating solvents: Tunable reactivity of monomers. *Angew. Chem. Int. Ed.* **2002**, *41* (13), 2368-2371.

246. Zhang, W. J.; Chen, G. J.; Wang, J.; Ye, B. C.; Zhong, X. H., Design and synthesis of highly luminescent near-infrared-emitting water-soluble CdTe/CdSe/ZnS core/shell/shell quantum dots. *Inorg. Chem.* **2009**, *48* (20), 9723-9731.
247. Deng, Z. T.; Schulz, O.; Lin, S., et al., Aqueous synthesis of zinc blende CdTe/CdS magic-core/thick-shell tetrahedral-shaped nanocrystals with emission tunable to near-infrared. *J. Am. Chem. Soc.* **2010**, *132* (16), 5592.
248. Yuan, Z. M.; Ma, Q.; Zhang, A. Y., et al., Synthesis of highly luminescent CdTe/ZnO core/shell quantum dots in aqueous solution. *J. Mater. Sci.* **2012**, *47* (8), 3770-3776.
249. Parak, W. J.; Pellegrino, T.; Plank, C., Labelling of cells with quantum dots. *Nanotechnology* **2005**, *16* (2), R9-R25.
250. Algar, W. R.; Prasuhn, D. E.; Stewart, M. H., et al., The controlled display of biomolecules on nanoparticles: a challenge suited to bioorthogonal chemistry. *Bioconjugate Chem.* **2011**, *22* (5), 825-858.
251. Sapsford, K. E.; Algar, W. R.; Berti, L., et al., Functionalizing nanoparticles with biological molecules: developing chemistries that facilitate nanotechnology. *Chem. Rev.* **2012**, *113* (3), 1904-2074.
252. Sapsford, K. E.; Tyner, K. M.; Dair, B. J.; Deschamps, J. R.; Medintz, I. L., Analyzing nanomaterial bioconjugates: a review of current and emerging purification and characterization techniques. *Anal. Chem.* **2011**, *83* (12), 4453-4488.
253. Medintz, I., Universal tools for biomolecular attachment to surfaces. *Nat. Mater.* **2006**, *5* (11), 842-842.
254. Jorge, P. A. S.; Martins, M. A.; Trindade, T.; Santos, J. L.; Farahi, F., Optical fiber sensing using quantum dots. *Sensors* **2007**, *7* (12), 3489-3534.
255. Susumu, K.; Uyeda, H. T.; Medintz, I. L., et al., Enhancing the stability and biological functionalities of quantum dots *via* compact multifunctional ligands. *J. Am. Chem. Soc.* **2007**, *129* (45), 13987-13996.
256. Susumu, K.; Mei, B. C.; Mattoussi, H., Multifunctional ligands based on dihydrolipoic acid and polyethylene glycol to promote biocompatibility of quantum dots. *Nat. Protoc.* **2009**, *4* (3), 424-436.
257. Mei, B. C.; Susumu, K.; Medintz, I. L., et al., Modular poly(ethylene glycol) ligands for biocompatible semiconductor and gold nanocrystals with extended pH and ionic stability. *J. Mater. Chem.* **2008**, *18* (41), 4949-4958.
258. Liu, W.; Howarth, M.; Greytak, A. B., et al., Compact biocompatible quantum dots functionalized for cellular imaging. *J. Am. Chem. Soc.* **2008**, *130* (4), 1274-1284.

259. Muro, E.; Pons, T.; Lequeux, N., et al., Small and stable sulfobetaine zwitterionic quantum dots for functional live-cell imaging. *J. Am. Chem. Soc.* **2010**, *132* (13), 4556.
260. Susumu, K.; Oh, E.; Delehanty, J. B., et al., Multifunctional compact zwitterionic ligands for preparing robust biocompatible semiconductor quantum dots and gold nanoparticles. *J. Am. Chem. Soc.* **2011**, *133* (24), 9480-9496.
261. Zhang, Y. J.; Clapp, A., Overview of stabilizing ligands for biocompatible quantum dot nanocrystals. *Sensors* **2011**, *11* (12), 11036-11055.
262. Liu, D.; Snee, P. T., Water-soluble semiconductor nanocrystals cap exchanged with metalated ligands. *ACS Nano* **2011**, *5* (1), 546-550.
263. Zhang, Y. J.; Schnoes, A. M.; Clapp, A. R., Dithiocarbamates as capping ligands for water-soluble quantum dots. *ACS Appl. Mater. Interfaces* **2010**, *2* (11), 3384-3395.
264. Zhou, D. J.; Li, Y.; Hall, E. A. H.; Abell, C.; Klenerman, D., A chelating dendritic ligand capped quantum dot: preparation, surface passivation, bioconjugation and specific DNA detection. *Nanoscale* **2011**, *3* (1), 201-211.
265. Lees, E. E.; Nguyen, T. L.; Clayton, A. H. A.; Mulvaney, P.; Muir, B. W., The preparation of colloidally stable, water-soluble, biocompatible, semiconductor nanocrystals with a small hydrodynamic diameter. *ACS Nano* **2009**, *3* (5), 1121-1128.
266. Yu, W. W.; Chang, E.; Falkner, J. C., et al., Forming biocompatible and nonaggregated nanocrystals in water using amphiphilic polymers. *J. Am. Chem. Soc.* **2007**, *129* (10), 2871-2879.
267. Pellegrino, T.; Manna, L.; Kudera, S., et al., Hydrophobic nanocrystals coated with an amphiphilic polymer shell: a general route to water soluble nanocrystals. *Nano Lett.* **2004**, *4* (4), 703-707.
268. Luccardini, C.; Tribet, C.; Vial, F.; Marchi-Artzner, V.; Dahan, M., Size, charge, and interactions with giant lipid vesicles of quantum dots coated with an amphiphilic macromolecule. *Langmuir* **2006**, *22* (5), 2304-2310.
269. Janczewski, D.; Tomczak, N.; Han, M. Y.; Vancso, G. J., Synthesis of functionalized amphiphilic polymers for coating quantum dots. *Nat. Protoc.* **2011**, *6* (10), 1546-1553.
270. Yildiz, I.; McCaughan, B.; Cruickshank, S. F.; Callan, J. F.; Raymo, F. i. M., Biocompatible CdSe-ZnS core-shell quantum dots coated with hydrophilic polythiols. *Langmuir* **2009**, *25* (12), 7090-7096.
271. Liu, W. H.; Greytak, A. B.; Lee, J., et al., Compact biocompatible quantum dots via RAFT-mediated synthesis of imidazole-based random copolymer ligand. *J. Am. Chem. Soc.* **2010**, *132* (2), 472-483.

272. Oh, J. K., Surface modification of colloidal CdX-based quantum dots for biomedical applications. *J. Mater. Chem.* **2010**, *20* (39), 8433-8445.
273. Wu, X. Y.; Liu, H. J.; Liu, J. Q., et al., Immunofluorescent labeling of cancer marker Her2 and other cellular targets with semiconductor quantum dots. *Nat. Biotechnol.* **2003**, *21* (1), 41-46.
274. Jennings, T. L.; Becker-Catania, S. G.; Triulzi, R. C., et al., Reactive semiconductor nanocrystals for chemoselective biolabeling and multiplexed analysis. *ACS Nano* **2011**, *5* (7), 5579-5593.
275. Prasuhn, D. E.; Blanco-Canosa, J. B.; Vora, G. J., et al., Combining chemoselective ligation with polyhistidine-driven self-assembly for the modular display of biomolecules on quantum dots. *ACS Nano* **2010**, *4* (1), 267-278.
276. Han, H. S.; Devaraj, N. K.; Lee, J., et al., Development of a bioorthogonal and highly efficient conjugation method for quantum dots using tetrazine-norbornene cycloaddition. *J. Am. Chem. Soc.* **2010**, *132* (23), 7838.
277. Bernardin, A.; Cazet, A.; Guyon, L., et al., Copper-free click chemistry for highly luminescent quantum dot conjugates: application to *in vivo* metabolic imaging. *Bioconjugate Chem.* **2010**, *21* (4), 583-588.
278. Prasuhn, D. E.; Feltz, A.; Blanco-Canosa, J. B., et al., Quantum dot peptide biosensors for monitoring caspase 3 proteolysis and calcium ions. *ACS Nano* **2010**, *4* (9), 5487-5497.
279. Boeneman, K.; Deschamps, J. R.; Buckhout-White, S., et al., Quantum dot DNA bioconjugates: attachment chemistry strongly influences the resulting composite architecture. *ACS Nano* **2010**, *4* (12), 7253-7266.
280. Dennis, A. M.; Sotto, D. C.; Mei, B. C., et al., Surface ligand effects on metal-affinity coordination to quantum dots: implications for nanoprobe self-assembly. *Bioconjugate Chem.* **2010**, *21* (7), 1160-1170.
281. Algar, W. R.; Wegner, D.; Huston, A. L., et al., Quantum dots as simultaneous acceptors and donors in time-gated Förster resonance energy transfer relays: characterization and biosensing. *J. Am. Chem. Soc.* **2012**, *134* (3), 1876-1891.
282. Algar W.R.; Tavares A.J.; Krull U.J., Beyond labels: a review of the application of quantum dots as integrated components of assays, bioprobes, and biosensors utilizing optical transduction. *Anal. Chim. Acta* **2010**, *673* (1), 1-25.
283. Resch-Genger, U.; Grabolle, M.; Cavaliere-Jaricot, S.; Nitschke, R.; Nann, T., Quantum dots versus organic dyes as fluorescent labels. *Nat. Methods* **2008**, *5* (9), 763-775.
284. Geissler, D.; Charbonniere, L. J.; Ziessel, R. F., et al., Quantum dot biosensors for ultrasensitive multiplexed diagnostics. *Angew. Chem. Int. Ed.* **2010**, *49* (8), 1396-1401.

285. Morgner, F.; Stufler, S.; Geissler, D., et al., Terbium to quantum dot FRET bioconjugates for clinical diagnostics: influence of human plasma on optical and assembly properties. *Sensors* **2011**, *11* (10), 9667-9684.
286. Wu, C. S.; Oo, M. K. K.; Fan, X. D., Highly sensitive multiplexed heavy metal detection using quantum-dot-labeled DNazymes. *ACS Nano* **2010**, *4* (10), 5897-5904.
287. Freeman, R.; Li, Y.; Tel-Vered, R., et al., Self-assembly of supramolecular aptamer structures for optical or electrochemical sensing. *Analyst* **2009**, *134* (4), 653-656.
288. Goldman, E. R.; Medintz, I. L.; Whitley, J. L., et al., A hybrid quantum dot-antibody fragment fluorescence resonance energy transfer-based TNT sensor. *J. Am. Chem. Soc.* **2005**, *127* (18), 6744-6751.
289. Sapsford, K. E.; Granek, J.; Deschamps, J. R., et al., Monitoring botulinum neurotoxin A activity with peptide-functionalized quantum dot resonance energy transfer sensors. *ACS Nano* **2011**, *5* (4), 2687-2699.
290. Lee, K. R.; Kang, I.-J., Effects of dopamine concentration on energy transfer between dendrimer-QD and dye-labeled antibody. *Ultramicroscopy* **2009**, *109* (8), 894-898.
291. Medintz, I. L.; Clapp, A. R.; Brunel, F. M., et al., Proteolytic activity monitored by fluorescence resonance energy transfer through quantum-dot-peptide conjugates. *Nat. Mater.* **2006**, *5* (7), 581-589.
292. Boeneman, K.; Mei, B. C.; Dennis, A. M., et al., Sensing caspase 3 activity with quantum dot-fluorescent protein assemblies. *J. Am. Chem. Soc.* **2009**, *131* (11), 3828.
293. Huang, S.; Xiao, Q.; He, Z. K., et al., A high sensitive and specific QDs FRET bioprobe for MNase. *Chem. Commun.* **2008**, (45), 5990-5992.
294. Suzuki, M.; Husimi, Y.; Komatsu, H.; Suzuki, K.; Douglas, K. T., Quantum dot FRET biosensors that respond to pH, to proteolytic or nucleolytic cleavage, to DNA synthesis, or to a multiplexing combination. *J. Am. Chem. Soc.* **2008**, *130* (17), 5720-5725.
295. Bailey, V. J.; Easwaran, H.; Zhang, Y., et al., MS-qFRET: a quantum dot-based method for analysis of DNA methylation. *Genome Res.* **2009**, *19* (8), 1455-1461.
296. Algar, W. R.; Krull, U. J., Towards multi-colour strategies for the detection of oligonucleotide hybridization using quantum dots as energy donors in fluorescence resonance energy transfer (FRET). *Anal. Chim. Acta* **2007**, *581* (2), 193-201.
297. Kattke, M. D.; Gao, E. J.; Sapsford, K. E.; Stephenson, L. D.; Kumar, A., FRET-based quantum dot immunoassay for rapid and sensitive detection of *Aspergillus amstelodami*. *Sensors* **2011**, *11* (6), 6396-6410.
298. Dennis, A. M.; Rhee, W. J.; Sotto, D.; Dublin, S. N.; Bao, G., Quantum dot-fluorescent protein FRET probes for sensing intracellular pH. *ACS Nano* **2012**, *6* (4), 2917-2924.

299. Somers, R. C.; Lanning, R. M.; Snee, P. T., et al., A Nanocrystal-based ratiometric pH sensor for natural pH ranges. *Chem. Sci.* **2012**, *3* (10), 2980-2985.
300. Clapp, A. R.; Medintz, I. L.; Mauro, J. M., et al., Fluorescence resonance energy transfer between quantum dot donors and dye-labeled protein acceptors. *J. Am. Chem. Soc.* **2004**, *126* (1), 301-310.
301. Allan, G.; Delerue, C., Energy transfer between semiconductor nanocrystals: validity of Förster's theory. *Phys. Rev. B* **2007**, *75* (19), 195311.
302. Curutchet, C.; Franceschetti, A.; Zunger, A.; Scholes, G. D., Examining Förster energy transfer for semiconductor nanocrystalline quantum dot donors and acceptors. *J. Phys. Chem. C* **2008**, *112* (35), 13336-13341.
303. Pons, T.; Medintz, I. L.; Sapsford, K. E., et al., On the quenching of semiconductor quantum dot photoluminescence by proximal gold nanoparticles. *Nano Lett.* **2007**, *7* (10), 3157-3164.
304. Medintz, I. L.; Sapsford, K. E.; Clapp, A. R., et al., Designer variable repeat length polypeptides as scaffolds for surface immobilization of quantum dots. *J. Phys. Chem. B* **2006**, *110* (22), 10683-10690.
305. Pons, T.; Medintz, I. L.; Wang, X.; English, D. S.; Matoussi, H., Solution-phase single quantum dot fluorescence resonance energy transfer. *J. Am. Chem. Soc.* **2006**, *128*, 15324-15331.
306. Patra, D.; Gregor, I.; Enderlein, J.; Sauer, M., Defocused imaging of quantum-dot angular distribution of radiation. *Appl. Phys. Lett.* **2005**, *87* (10), 101103.
307. Chung, I. H.; Shimizu, K. T.; Bawendi, M. G., Room temperature measurements of the 3D orientation of single CdSe quantum dots using polarization microscopy. *Proc. Natl. Acad. Sci. U.S.A.* **2003**, *100* (2), 405-408.
308. Cyphersmith, A.; Early, K.; Maksov, A., et al., Disentangling the role of linear transition dipole in band-edge emission from single CdSe/ZnS quantum dots: Combined linear anisotropy and defocused emission pattern imaging. *Appl. Phys. Lett.* **2010**, *97* (12), 121915.
309. Fisher, B. R.; Eisler, H. J.; Stott, N. E.; Bawendi, M. G., Emission intensity dependence and single-exponential behavior in single colloidal quantum dot fluorescence lifetimes. *J. Phys. Chem. B* **2004**, *108* (1), 143-148.
310. Schlegel, G.; Bohnenberger, J.; Potapova, I.; Mews, A., Fluorescence decay time of single semiconductor nanocrystals. *Phys. Rev. Lett.* **2002**, *88* (13), 137401.
311. Spence, M. T. Z.; Johnson, I. D., *The Molecular Probes Handbook: A Guide to Fluorescent Probes and Labeling Technologies*. Live Technologies Corporation: 2010.

312. Noor, M. O.; Krull, U. J., Camera-based ratiometric fluorescence transduction of nucleic acid hybridization with reagentless signal amplification on a paper-based platform using immobilized quantum dots as donors. *Anal. Chem.* **2014**, *86* (20), 10331-10339.
313. Noor, M. O.; Hrovat, D.; Moazami-Goudarzi, M.; Espie, G. S.; Krull, U. J., Ratiometric fluorescence transduction by hybridization after isothermal amplification for determination of zeptomole quantities of oligonucleotide biomarkers with a paper-based platform and camera-based detection. *Anal. Chim. Acta* **2015**, *885*, 156-165.
314. Breslauer, D. N.; Maamari, R. N.; Switz, N. A.; Lam, W. A.; Fletcher, D. A., Mobile phone based clinical microscopy for global health applications. *PLoS One* **2009**, *4* (7), e6320.
315. Zhu, H.; Mavandadi, S.; Coskun, A. F.; Yaglidere, O.; Ozcan, A., Optofluidic fluorescent imaging cytometry on a cell phone. *Anal. Chem.* **2011**, *83* (17), 6641-6647.
316. Zhu, H.; Yaglidere, O.; Su, T.-W.; Tseng, D.; Ozcan, A., Cost-effective and compact wide-field fluorescent imaging on a cell-phone. *Lab Chip* **2011**, *11* (2), 315-322.
317. Zhu, H.; Sencan, I.; Wong, J., et al., Cost-effective and rapid blood analysis on a cell-phone. *Lab Chip* **2013**, *13* (7), 1282-1288.
318. Shen, L.; Hagen, J. A.; Papautsky, I., Point-of-care colorimetric detection with a smartphone. *Lab Chip* **2012**, *12* (21), 4240-4243.
319. Vashist, S. K.; van Oordt, T.; Schneider, E. M., et al., A smartphone-based colorimetric reader for bioanalytical applications using the screen-based bottom illumination provided by gadgets. *Biosens. Bioelectron.* **2015**, *67*, 248-255.
320. Berg, B.; Cortazar, B.; Tseng, D., et al., Cellphone-based hand-held microplate reader for point-of-care testing of enzyme-linked immunosorbent assays. *ACS Nano* **2015**, *9* (8), 7857-66.
321. Rodriguez-Manzano, J.; Karymov, M. A.; Begolo, S., et al., Reading out single-molecule digital RNA and DNA isothermal amplification in nanoliter volumes with unmodified camera phones. *ACS Nano* **2016**, *10* (3), 3102-3113.
322. Wei, Q.; Nagi, R.; Sadeghi, K., et al., Detection and spatial mapping of mercury contamination in water samples using a smart-phone. *ACS Nano* **2014**, *8* (2), 1121-1129.
323. Lee, S.; O'Dell, D.; Hohenstein, J., et al., NutriPhone: a mobile platform for low-cost point-of-care quantification of vitamin B12 concentrations. *Sci. Rep.* **2016**, *6*, 28237.
324. Veigas, B.; Fortunato, E.; Baptista, P. V., Mobile based gold nanoprobe TB diagnostics for point-of-need. In *Mobile Health Technologies: Methods and Protocols*, Rasooly, A.; Herold, E. K., Eds. Springer New York: New York, NY, 2015; pp 41-56.

325. Ming, K.; Kim, J.; Biondi, M. J., et al., Integrated quantum dot barcode smartphone optical device for wireless multiplexed diagnosis of infected patients. *ACS Nano* **2015**, *9* (3), 3060-3074.
326. Howes, P. D.; Chandrawati, R.; Stevens, M. M., Colloidal nanoparticles as advanced biological sensors. *Science* **2014**, *346* (6205).
327. Dhalla, I., Canada's health care system and the sustainability paradox. *Can. Med. Assoc. J.* **2007**, *177* (1), 51-53.
328. Pentecost, M. J., Health care in America: sustainable path or collision course? *J. Am. Coll. Radiol.* **2005**, *2* (2), 114-117.
329. Erickson, D.; O'Dell, D.; Jiang, L., et al., Smartphone technology can be transformative to deployment of lab-on-chip diagnostics. *Lab Chip* **2014**, *14*, 3159-3164.
330. Laksanasopin, T.; Guo, T. W.; Nayak, S., et al., A smartphone dongle for diagnosis of infectious diseases at the point of care. *Sci. Transl. Med.* **2015**, *7* (273), 273re1.
331. Mancuso, M.; Cesarman, E.; Erickson, D., Detection of Kaposi's sarcoma associated herpesvirus nucleic acids using a smartphone accessory. *Lab Chip* **2014**, *14* (19), 3809-3816.
332. Nemiroski, A.; Christodouleas, D. C.; Hennek, J. W., et al., Universal mobile electrochemical detector designed for use in resource-limited applications. *Proc. Natl. Acad. Sci. U.S.A.* **2014**, *111* (33), 11984-11989.
333. Long, K. D.; Yu, H.; Cunningham, B. T., Smartphone instrument for portable enzyme-linked immunosorbent assays. *Biomed. Opt. Express* **2014**, *5* (11), 3792-3806.
334. Nie, H.; Wang, W.; Li, W.; Nie, Z.; Yao, S., A colorimetric and smartphone readable method for uracil-DNA glycosylase detection based on the target-triggered formation of G-quadruplex. *Analyst* **2015**, *140* (8), 2771-2777.
335. Guo, J.; Wong, J. X. H.; Cui, C.; Li, X.; Yu, H.-Z., A smartphone-readable barcode assay for the detection and quantitation of pesticide residues. *Analyst* **2015**, *140* (16), 5518-5525.
336. Veigas, B.; Jacob, J. M.; Costa, M. N., et al., Gold on paper-paper platform for Au-nanoprobe TB detection. *Lab Chip* **2012**, *12* (22), 4802-4808.
337. Wong, J. X. H.; Li, X.; Liu, F. S. F.; Yu, H.-Z., Direct reading of bona fide barcode assays for diagnostics with smartphone apps. *Sci. Rep.* **2015**, *5*, 11727.
338. Gallegos, D.; Long, K. D.; Yu, H., et al., Label-free biodetection using a smartphone. *Lab Chip* **2013**, *13* (11), 2124-2132.

339. Im, H.; Castro, C. M.; Shao, H., et al., Digital diffraction analysis enables low-cost molecular diagnostics on a smartphone. *Proc. Natl. Acad. Sci. U.S.A.* **2015**, *112* (18), 5613-5618.
340. Rajendran, V. K.; Bakthavathsalam, P.; Ali, B. M. J., Smartphone based bacterial detection using biofunctionalized fluorescent nanoparticles. *Microchim. Acta* **2014**, *181* (15-16), 1815-1821.
341. Jiang, L.; Mancuso, M.; Lu, Z., et al., Solar thermal polymerase chain reaction for smartphone-assisted molecular diagnostics. *Sci. Rep.* **2014**, *4*, 4137.
342. Shu, B.; Zhang, C.; Xing, D., A handheld flow genetic analysis system (FGAS): towards rapid, sensitive, quantitative and multiplex molecular diagnosis at the point-of-care level. *Lab Chip* **2015**, *15* (12), 2597-2605.
343. Hempstead, J.; Jones, D. P.; Ziouche, A., et al., Low-cost photodynamic therapy devices for global health settings: Characterization of battery-powered LED performance and smartphone imaging in 3D tumor models. *Sci. Rep.* **2015**, *5*, 10093.
344. Koydemir, H. C.; Gorocs, Z.; Tseng, D., et al., Rapid imaging, detection and quantification of Giardia lamblia cysts using mobile-phone based fluorescent microscopy and machine learning. *Lab Chip* **2015**, *15* (5), 1284-1293.
345. Wei, Q.; Luo, W.; Chiang, S., et al., Imaging and Sizing of Single DNA Molecules on a Mobile Phone. *ACS Nano* **2014**, *8* (12), 12725-12733.
346. Balsam, J.; Bruck, H. A.; Rasooly, A., Capillary array waveguide amplified fluorescence detector for mHealth. *Sensor Actuat. B-Chem.* **2013**, *186*, 711-717.
347. Hossain, M. A.; Canning, J.; Ast, S., et al., Combined "dual" absorption and fluorescence smartphone spectrometers. *Opt. Lett.* **2015**, *40* (8), 1737-1740.
348. Umberger, J. Q.; LaMer, V. K., The kinetics of diffusion controlled molecular and ionic reactions in solution as determined by measurements of the quenching of fluorescence. *J. Am. Chem. Soc.* **1945**, *67*, 1099-1109.
349. Oi, V. T.; Glazer, A. N.; Stryer, L., Fluorescent phycobiliprotein conjugates for analyses of cells and molecules. *J. Cell. Biol.* **1982**, *93*, 981-986.
350. Pommier, A. J. C.; Shaw, R.; Spencer, S. K. M., et al., Serum protein profiling reveals baseline and pharmacodynamic biomarker signatures associated with clinical outcome in mCRC patients treated with chemotherapy ± cediranib. *British J. Cancer* **2014**, *111*, 1590-1604.
351. Pansare, V.; Hejazi, S.; Faenza, W.; Prud'homme, R. K., Review of long-wavelength optical and NIR imaging materials: contrast agents, fluorophors and multifunctional nano carriers. *Chem. Mater.* **2012**, *24*, 812-827.

352. Szollosi, J.; Damjanovich, S.; Matyus, L., Application of fluorescence resonance energy transfer in the clinical laboratory: Routine and research. *Cytometry* **1998**, *34*, 159-179.
353. Brown, M.; Wittwer, C., Flow Cytometry: Principles and clinical applications in hematology. *Clin. Chem.* **2000**, *46*, 1221-1229.
354. Batard, P.; Szollosi, J.; Luescher, I., et al., Use of phycoerythrin and allophycocyanin for fluorescence resonance energy transfer analyzed by flow cytometry: advantages and limitations. *Cytometry* **2002**, *48*, 97-105.
355. ThermoFisher Scientific R-phycoerythrin (R-PE). <https://www.thermofisher.com/ca/en/home/life-science/cell-analysis/fluorophores/r-phycoerythrin.html> (accessed 17 October 2015).
356. ThermoFisher Scientific Fluorescein (FITC). <https://www.thermofisher.com/ca/en/home/life-science/cell-analysis/fluorophores/fluorescein.html> (accessed 17 October 2015).
357. Song, L.; Hennink, E. J.; Young, I. T.; Tanke, H. J., Photobleaching kinetics of fluorescein in quantitative fluorescence microscopy. *Biophys J.* **1995**, *68*, 2588-2600.
358. Bünzli, J. C. G., On the design of highly luminescent lanthanide complexes. *Coord. Chem. Rev.* **2015**, *293-294*, 19-47.
359. Park, Y. I.; Lee, K. T.; Suh, Y. D.; Hyeon, T., Upconverting nanoparticles: a versatile platform for wide-field two-photon microscopy and multi-modal *in vivo* imaging. *Chem. Soc. Rev.* **2015**, *44*, 1302-1317.
360. Wang, F.; Liu, X., Recent advances in the chemistry of lanthanide-doped upconversion nanocrystals. *Chem. Soc. Rev.* **2009**, *38*, 976-989.
361. Chen, L. Y.; Wang, C. W.; Yuan, Z.; Chang, H. T., Fluorescent gold nanoclusters: recent advances in sensing and imaging. *Anal. Chem.* **2015**, *87*, 216-229.
362. Yu, P.; Wen, X.; Toh, Y. R.; Ma, X.; Tang, J., Fluorescent metallic nanoclusters: electron dynamics, structure, and applications. *Part. Part. Syst. Character.* **2015**, *32*, 142-163.
363. Luo, P. G.; Yang, F.; Yang, S. T., et al., Carbon-based quantum dots for fluorescence imaging of cells and tissues. *RSC Adv.* **2014**, *4*, 10791-10807.
364. Yan, J.; Estévez, M. C.; Smith, J. E., et al., Dye-doped nanoparticles for bioanalysis. *Nano Today* **2007**, *2*, 44-50.
365. Massey, M.; Wu, M.; Conroy, E. M.; Algar, W. R., Mind your P's and Q's: the coming of age of semiconducting polymer dots and semiconductor quantum dots in biological applications. *Curr. Opin. Biotechnol.* **2015**, *34*, 30-40.
366. Wu, C. F.; Chiu, D. T., Highly fluorescent semiconductor polymer dots for biology and medicine. *Angew. Chem. Int. Ed.* **2013**, *52*, 3086-3109.

367. Li, J. J.; Wang, Y. A.; Guo, W. Z., et al., Large-scale synthesis of nearly monodisperse CdSe/CdS core/shell nanocrystals using air-stable reagents *via* successive ion layer adsorption and reaction. *J. Am. Chem. Soc.* **2003**, *125*, 12567-12575.
368. Algar, W. R.; Blanco-Canosa, J. B.; Manthe, R. L., et al., Synthesizing and modifying peptides for chemoselective ligation and assembly into quantum dot-peptide bioconjugates. *Methods Mol. Biol.* **2013**, *1025*, 47-73.
369. Sapsford, K. E.; Pons, T.; Medintz, I. L., et al., Kinetics of metal-affinity driven self-assembly between proteins or peptides and CdSe-ZnS quantum dots. *J. Phys. Chem. C* **2007**, *111*, 11528-11538.
370. Aldeek, F.; Safi, M.; Zhan, N. Q.; Palui, G.; Mattoussi, H., Understanding the self-assembly of proteins onto gold nanoparticles and quantum dots driven by metal-histidine coordination. *ACS Nano* **2013**, *7*, 10197-10210.
371. Yu, W. W.; Qu, L.; Guo, W.; Peng, X., Experimental determination of the extinction coefficient of CdTe, CdSe, and CdS nanocrystals. *Chem. Mater.* **2003**, *15* (14), 2854-2860.
372. Uddayasankar, U.; Shergill, R. T.; Krull, U. J., Evaluation of nanoparticle–ligand distributions to determine nanoparticle concentration. *Anal. Chem.* **2015**, *87* (2), 1297-1305.
373. Magde, D.; Rojas, G. E.; Seybold, P. G., Solvent dependence of the fluorescence lifetimes of xanthene dyes. *Photochem. Photobiol.* **2008**, *70*, 737-744.
374. Zrazhevskiy, P.; Sena, M.; Gao, X. H., Designing multifunctional quantum dots for bioimaging, detection, and drug delivery. *Chem. Soc. Rev.* **2010**, *39*, 4326-4354.
375. Jin, Z.; Hildebrandt, N., Semiconductor quantum dots for *in vitro* diagnostics and cellular imaging. *Trends Biotechnol.* **2012**, *30*, 394-403.
376. Freeman, R.; Liu, X.; Willner, I., Amplified multiplexed analysis of DNA by the Exonuclease III-catalyzed regeneration of the target DNA in the presence of functionalized semiconductor quantum dots. *Nano Lett.* **2011**, *11*, 4456-4461.
377. Zhang, C. Y.; Johnson, L. W., Single quantum-dot-based aptameric nanosensor for cocaine. *Anal. Chem.* **2009**, *81*, 3051-3055.
378. Wang, S.; han, M. Y.; Huang, D., Nitric oxide switches on the photoluminescence of molecularly engineered quantum dots. *J. Am. Chem. Soc.* **2009**, *131*, 11692-11694.
379. Wegner, K. D.; Jin, Z.; Lindén, S.; Jennings, T. L.; Hildebrandt, N., Quantum-dot-based Förster resonance energy transfer immunoassay for sensitive clinical diagnostics of low-volume serum samples. *ACS Nano* **2013**, *7*, 7411-7419.
380. Freeman, R.; Finder, T.; Gill, R.; Willner, I., Probing protein kinase (CK2) and alkaline phosphatase with CdSe/ZnS quantum dots. *Nano Lett.* **2010**, *10* (6), 2192-2196.

381. Medintz, I. L.; Mattoussi, H., Quantum dot-based resonance energy transfer and its growing application in biology. *Phys. Chem. Chem. Phys.* **2009**, *165*, 17-45.
382. Yong, K. T.; Law, W. C.; Roy, I., et al., Aqueous phase synthesis of CdTe quantum dots for biophotonics. *J. Biophotonics* **2011**, *4*, 9-20.
383. Palui, G.; Avellini, T.; Zhan, N. Q., et al., Photoinduced phase transfer of luminescent quantum dots to polar and aqueous media. *J. Am. Chem. Soc.* **2012**, *134*, 16370-16378.
384. Chang, E.; Miller, J. S.; Sun, J., et al., Protease-activated quantum dot probes. *Biochem. Biophys. Res. Commun.* **2005**, *334*, 1317-1321.
385. Shi, L. F.; De Paoli, V.; Rosenzweig, N.; Rosenzweig, Z., Synthesis and application of quantum dots FRET-based protease sensors. *J. Am. Chem. Soc.* **2006**, *128* (32), 10378-10379.
386. Spring, K. R., Cameras for digital microscopy. In *Digital Microscopy: Methods in Cell Biology*, Sluder, G.; Wolf, D. E., Eds. Academic Press: 2007; pp 171-187.
387. Algar, W. R.; Malonoski, A.; Deschamps, J. R., et al., Proteolytic activity at quantum dot-conjugates: kinetic analysis reveals enhanced enzyme activity and localized interfacial "hopping". *Nano Lett.* **2012**, *12* (7), 3793-3802.
388. Algar, W. R.; Malanoski, A. P.; Susumu, K., et al., Multiplexed tracking of protease activity using a single color of quantum dot vector and a time-gated Förster resonance energy transfer relay. *Anal. Chem.* **2012**, *84*, 10136-10146.
389. You, C. C.; De, M.; Rotello, V. M., Monolayer-protected nanoparticle-protein interactions. *Curr. Opin. Chem. Biol.* **2005**, *9*, 639-646.
390. Lynch, I.; Dawson, K. A., Protein-nanoparticle interactions. *Nano Today* **2008**, *3*, 40-47.
391. Wu, M.; Algar, W. R., Acceleration of proteolytic activity associated with selection of thiol ligand coatings on quantum dots. *ACS Appl. Mater. Interfaces* **2015**, *7* (4), 2535-2545.
392. Knudsen, B. R.; Jepsen, M. L.; Ho, Y. P., Quantum dot-based nanosensors for diagnosis via enzyme activity measurement. *Expert Rev. Mol. Diagn.* **2013**, *13*, 367-375.
393. Folgueras, A. R.; Pendas, A. M.; Sanchez, L. M.; López-Otín, C., Matrix metalloproteinases in cancer: from new functions to improved inhibition strategies. *Int. J. Develop. Biol.* **2004**, *48*, 411-424.
394. Rosenberg, G. A., Matrix metalloproteinases and their multiple roles in neurodegenerative diseases. *Lancet Neurol.* **2009**, *8* (2), 205-216.
395. Yasuda, Y.; Kaleta, J.; Bromme, D., The role of cathepsins in osteoporosis and arthritis: Rationale for the design of new therapeutics. *Adv. Drug Deliv. Rev.* **2005**, *57* (7), 973-993.

396. Scott, C. J.; Taggart, C. C., Biologic protease inhibitors as novel therapeutic agents. *Biochimie* **2010**, *92*, 1681-1688.
397. Freeman, R.; Bahshi, L.; Finder, T.; Gill, R.; Willner, I., Competitive analysis of saccharides or dopamine by boronic acid-functionalized CdSe-ZnS quantum dots. *Chem. Commun.* **2009**, 764-766.
398. Chen, L.; Zhang, X.; Zhou, G., et al., Simultaneous determination of Human Enterovirus 71 and Coxsackievirus B3 by dual-color quantum dots and homogeneous immunoassay. *Anal. Chem.* **2012**, *84*, 3200-3207.
399. Medintz, I. L.; Pons, T.; Trammell, S. A., et al., Interactions between redox complexes and semiconductor quantum dots coupled via a peptide bridge. *J. Am. Chem. Soc.* **2008**, *130* (49), 16745-16756.
400. Sandros, M. G.; Shete, V.; Benson, D. E., Selective, reversible, reagentless maltose biosensing with core-shell semiconducting nanoparticles. *Analyst* **2006**, *131* (2), 229-235.
401. Sapsford, K. E.; Farrell, D.; Sun, S., et al., Monitoring of enzymatic proteolysis on a electroluminescent-CCD microchip platform using quantum dot-peptide substrates. *Sensor Actuat. B-Chem.* **2009**, *139*, 13-21.
402. Michaelis-Menten Kinetics. In *The Gold Book. IUPAC Compendium of Chemical Terminology*, 2nd ed.; McNaught, A. D.; Wilkinson, A., Eds. Blackwell Scientific Publications: Oxford, 1997; p doi:10.1351/goldbook.
403. Sicard, C.; brennan, J. D., Bioactive paper: biomolecule immobilization methods and applications in environmental monitoring. *MRS Bull.* **2013**, *38*, 331-334.
404. Credou, J.; Berthelot, T., Cellulose: from biocompatible to bioactive material. *J. Mater. Chem. B* **2014**, *2* (30), 4767-4788.
405. Govindarajan, A. V.; Ramachandran, S.; Vigil, G. D.; Yager, P.; Bohringer, K. F., A low cost point-of-care viscous sample preparation device for molecular diagnosis in the developing world; an example of microfluidic origami. *Lab Chip* **2012**, *12* (1), 174-181.
406. Derda, R.; Tang, S. K. Y.; Laromaine, A., et al., Multizone paper platform for 3D cell cultures. *PLoS One* **2011**, *6* (5), e18940.
407. Fenton, E. M.; Mascarenas, M. R.; López, G. P.; Sibbett, S. S., Multiplex lateral-flow test strips fabricated by two-dimensional shaping. *ACS Appl. Mater. Interfaces* **2009**, *1* (1), 124-129.
408. Vella, S. J.; Beattie, P.; Cademartiri, R., et al., Measuring markers of liver function using a micropatterned paper device designed for blood from a fingerstick. *Anal. Chem.* **2012**, *84* (6), 2883-2891.

409. Hossain, S. M. Z.; Brennan, J. D., beta-Galactosidase-based colorimetric paper sensor for determination of heavy metals. *Anal. Chem.* **2011**, *83* (22), 8772-8778.
410. Hossain, S. M. Z.; Luckham, R. E.; McFadden, M. J.; Brennan, J. D., Reagentless bidirectional lateral flow bioactive paper sensors for detection of pesticides in beverage and food samples. *Anal. Chem.* **2009**, *81* (21), 9055-9064.
411. Hossain, S. M. Z.; Ozimok, C.; Sicard, C., et al., Multiplexed paper test strip for quantitative bacterial detection. *Anal. Bioanal. Chem.* **2012**, *403* (6), 1567-1576.
412. Martinez, A. W.; Phillips, S. T.; Butte, M. J.; Whitesides, G. M., Patterned paper as a platform for inexpensive, low-volume, portable bioassays. *Angew. Chem. Int. Ed.* **2007**, *46* (8), 1318-1320.
413. Pollock, N. R.; Rolland, J. P.; Kumar, S., et al., A paper-based multiplexed transaminase test for low-cost, point-of-care liver function testing. *Sci. Transl. Med.* **2012**, *4* (152).
414. John, M. J.; Anandjiwala, R. D., Recent developments in chemical modification and characterization of natural fiber-reinforced composites. *Polym. Compos.* **2008**, *29* (2), 187-207.
415. Ju, Q.; Noor, M. O.; Krull, U. J., Paper-based biodetection using luminescent nanoparticles. *Analyst* **2016**, *141* (10), 2838-2860.
416. Parolo, C.; Merkoci, A., Paper-based nanobiosensors for diagnostics. *Chem. Soc. Rev.* **2013**, *42* (2), 450-457.
417. Berlina, A. N.; Taranova, N. A.; Zherdev, A. V.; Vengerov, Y. Y.; Dzantiev, B. B., Quantum dot-based lateral flow immunoassay for detection of chloramphenicol in milk. *Anal. Bioanal. Chem.* **2013**, *405* (14), 4997-5000.
418. Zheng, G.; Kaefer, K.; Mourdikoudis, S., et al., Palladium nanoparticle-loaded cellulose paper: a highly efficient, robust, and recyclable self-assembled composite catalytic system. *J. Phys. Chem. Lett.* **2015**, *6* (2), 230-238.
419. Bodelón, G.; Mourdikoudis, S.; Yate, L., et al., Nickel nanoparticle-doped paper as a bioactive scaffold for targeted and robust immobilization of functional proteins. *ACS Nano* **2014**, *8* (6), 6221-6231.
420. Durán, G. M.; Benavidez, T. E.; Ríos, Á.; García, C. D., Quantum dot-modified paper-based assay for glucose screening. *Microchim. Acta* **2016**, *183* (2), 611-616.
421. Algar, W. R.; Kim, H.; Medintz, I. L.; Hildebrandt, N., Emerging non-traditional Förster resonance energy transfer configurations with semiconductor quantum dots: investigations and applications. *Coord. Chem. Rev.* **2014**, *263-264*, 65-85.
422. Jares-Erijman, E. A.; Jovin, T. M., FRET imaging. *Nat. Biotechnol.* **2003**, *21*, 1387-1395.

423. Kim, Y.-P.; Oh, Y.-H.; Oh, E., et al., Energy transfer-based multiplexed assay of proteases by using gold nanoparticle and quantum dot conjugates on a surface. *Anal. Chem.* **2008**, *80* (12), 4634-4641.
424. Algar, W. R.; Krull, U. J., Toward a multiplexed solid-phase nucleic acid hybridization assay using quantum dots as donors in fluorescence resonance energy transfer. *Anal. Chem.* **2009**, *81* (10), 4113-4120.
425. Noor, M. O.; Tavares, A. J.; Krull, U. J., On-chip multiplexed solid-phase nucleic acid hybridization assay using spatial profiles of immobilized quantum dots and fluorescence resonance energy transfer. *Anal. Chim. Acta* **2013**, *788*, 148-157.
426. Petryayeva, E.; Algar, W. R.; Krull, U. J., Adapting fluorescence resonance energy transfer with quantum dot donors for solid-phase hybridization assays in microtiter plate format. *Langmuir* **2013**, *29* (3), 977-987.
427. Noor, M. O.; Shahmuradyan, A.; Krull, U. J., Paper-based solid-phase nucleic acid hybridization assay using immobilized quantum dots as donors in fluorescence resonance energy transfer. *Anal. Chem.* **2013**, *85*, 1860-1867.
428. Blanco-Canosa, J. B.; Wu, M.; Susumu, K., et al., Recent progress in the bioconjugation of quantum dots. *Coord. Chem. Rev.* **2014**, *263-264*, 101-137.
429. Bilan, R.; Fleury, F.; Nabiev, I.; Sukhanova, A., Quantum Dot Surface Chemistry and Functionalization for Cell Targeting and Imaging. *Bioconjugate Chem.* **2015**, *26* (4), 609-624.
430. Algar, W. R.; Krull, U. J., Interfacial chemistry and the design of solid-phase nucleic acid hybridization assays using immobilized quantum dots as donors in fluorescence resonance energy transfer. *Sensors* **2011**, *11* (6), 6214-6236.
431. Petryayeva, E.; Krull, U. J., Quantum dot and gold nanoparticle immobilization for biosensing applications using multidentate imidazole surface ligands. *Langmuir* **2012**, *28* (39), 13943-13951.
432. Chen, L.; Algar, W. R.; Tavares, A. J.; Krull, U. J., Toward a solid-phase nucleic acid hybridization assay within microfluidic channels using immobilized quantum dots as donors in fluorescence resonance energy transfer. *Anal. Bioanal. Chem.* **2011**, *399* (1), 133-141.
433. Goldman, E. R.; Balighian, E. D.; Kuno, M. K., et al., Luminescent quantum dot-adaptor protein-antibody conjugates for use in fluoroimmunoassays. *Phys. Stat. Sol. (B)* **2002**, *229* (1), 407-414.
434. Sapsford, K. E.; Medintz, I. L.; Golden, J. P., et al., Surface-immobilized self-assembled protein-based quantum dot nanoassemblies. *Langmuir* **2004**, *20* (18), 7720-7728.

435. Tavares, A. J.; Noor, M. O.; Vannoy, C. H.; Algar, W. R.; Krull, U. J., On-chip transduction of nucleic acid hybridization using spatial profiles of immobilized quantum dots and fluorescence resonance energy transfer. *Anal. Chem.* **2012**, *84* (1), 312-319.
436. Sun, M.; Yang, L.; Jose, P.; Wang, L.; Zweit, J., Functionalization of quantum dots with multidentate zwitterionic ligands: impact on cellular interactions and cytotoxicity. *J. Mater. Chem. B* **2013**, *1* (44), 6137-6146.
437. Sapieha, S.; Inoue, M.; Lepoutre, P., Conductivity and water sorption in paper. *J. Appl. Polym. Sci.* **1985**, *30* (3), 1257-1266.
438. Johansson, L. S.; Campbell, J. M., Reproducible XPS on biopolymers: cellulose studies. *Surf. Interface Anal.* **2004**, *36* (8), 1018-1022.
439. ATR – Theory and Applications. <http://www.piketech.com/files/pdfs/ATRAN611.pdf> (accessed May 16, 2016).
440. Koga, H.; Kitaoka, T.; Isogai, A., In situ modification of cellulose paper with amino groups for catalytic applications. *J. Mater. Chem.* **2011**, *21* (25), 9356-9361.
441. Lecoq, E.; Duday, D.; Bulou, S., et al., Plasma polymerization of APTES to elaborate nitrogen containing organosilicon thin films: influence of process parameters and discussion about the growing mechanisms. *Plasma Process Polym.* **2013**, *10* (3), 250-261.
442. Aneja, K. S.; Bohm, S.; Khanna, A. S.; Bohm, H. L. M., Graphene based anticorrosive coatings for Cr(vi) replacement. *Nanoscale* **2015**, *7* (42), 17879-17888.
443. Orelma, H.; Teerinen, T.; Johansson, L.-S.; Holappa, S.; Laine, J., CMC-modified cellulose biointerface for antibody conjugation. *Biomacromolecules* **2012**, *13* (4), 1051-1058.
444. Credou, J.; Faddoul, R.; Berthelot, T., Photo-assisted inkjet printing of antibodies onto cellulose for the eco2-friendly preparation of immunoassay membranes. *RSC Adv.* **2015**, *5* (38), 29786-29798.
445. Ye, C.; Wu, Y.; Wang, Z., Modification of cellulose paper with polydopamine as a thin film microextraction phase for detection of nitrophenols in oil samples. *RSC Adv.* **2016**, *6* (11), 9066-9071.
446. Przybylak, M.; Maciejewski, H.; Dutkiewicz, A.; Dąbek, I.; Nowicki, M., Fabrication of superhydrophobic cotton fabrics by a simple chemical modification. *Cellulose* **2016**, *23* (3), 2185-2197.
447. Mattson, A. M.; Jensen, C. O., Colorimetric Determination of Reducing Sugars with Triphenyltetrazolium Chloride. *Anal. Chem.* **1950**, *22* (1), 182-185.
448. Strlic, M.; Pihlar, B., Determination of reducing carbonyl groups in cellulose in the solvent system LiCl/*N,N*-dimethylacetamide. *Fresenius J. Anal. Chem.* **1997**, *357* (6), 670-675.

449. Kaiser, E.; Colescott, R. L.; Bossinger, C. D.; Cook, P. I., Color test for detection of free terminal amino groups in the solid-phase synthesis of peptides. *Anal. Biochem.* **1970**, *34* (2), 595-598.
450. Sarin, V. K.; Kent, S. B. H.; Tam, J. P.; Merrifield, R. B., Quantitative monitoring of solid-phase peptide synthesis by the ninhydrin reaction. *Anal. Biochem.* **1981**, *117* (1), 147-157.
451. Soto-Cantu, E.; Cueto, R.; Koch, J.; Russo, P. S., Synthesis and rapid characterization of amine-functionalized silica. *Langmuir* **2012**, *28* (13), 5562-5569.
452. Jarre, G.; Heyer, S.; Memmel, E.; Meinhardt, T.; Krueger, A., Synthesis of nanodiamond derivatives carrying amino functions and quantification by a modified Kaiser test. *Beilstein J. Org. Chem.* **2014**, *10*, 2729-2737.
453. Eyer, P.; Worek, F.; Kiderlen, D., et al., Molar absorption coefficients for the reduced Ellman reagent: reassessment. *Anal. Biochem.* **2003**, *312* (2), 224-227.
454. Wuister, S. F.; de Mello Donegá, C.; Meijerink, A., Influence of thiol capping on the exciton luminescence and decay kinetics of CdTe and CdSe quantum dots. *J. Phys. Chem. B* **2004**, *108* (45), 17393-17397.
455. Pong, B.-K.; Trout, B. L.; Lee, J.-Y., Modified ligand-exchange for efficient solubilization of CdSe/ZnS quantum dots in water: a procedure guided by computational studies. *Langmuir* **2008**, *24* (10), 5270-5276.
456. Algar, W. R.; Krull, U. J., Multidentate surface ligand exchange for the immobilization of CdSe/ZnS quantum dots and surface quantum dot-oligonucleotide conjugates. *Langmuir* **2008**, *24* (10), 5514-5520.
457. Schapotschnikow, P.; Hommersom, B.; Vlugt, T. J. H., Adsorption and binding of ligands to CdSe nanocrystals. *J. Phys. Chem. C* **2009**, *113* (29), 12690-12698.
458. Jeong, S.; Achermann, M.; Nanda, J., et al., Effect of the thiol–thiolate equilibrium on the photophysical properties of aqueous CdSe/ZnS nanocrystal quantum dots. *J. Am. Chem. Soc.* **2005**, *127* (29), 10126-10127.
459. Kakiuchi, T.; Iida, M.; Imabayashi, S.-i.; Niki, K., Double-layer-capacitance titration of self-assembled monolayers of ω -functionalized alkanethiols on Au(111) surface. *Langmuir* **2000**, *16* (12), 5397-5401.
460. Leopold, M. C.; Bowden, E. F., Influence of gold substrate topography on the voltammetry of cytochrome c adsorbed on carboxylic acid terminated self-assembled monolayers. *Langmuir* **2002**, *18* (6), 2239-2245.
461. Wang, D.; Nap, R. J.; Lagzi, I., et al., How and why nanoparticle's curvature regulates the apparent pKa of the coating ligands. *J. Am. Chem. Soc.* **2011**, *133* (7), 2192-2197.

462. Mancini, M. C.; Kairdolf, B. A.; Smith, A. M.; Nie, S., Oxidative quenching and degradation of polymer-encapsulated quantum dots: new insights into the long-term fate and toxicity of nanocrystals *in vivo*. *J. Am. Chem. Soc.* **2008**, *130* (33), 10836-10837.
463. Wu, M.; Petryayeva, E.; Medintz, I. L.; Algar, W. R., Quantitative measurement of proteolytic rates with quantum dot-peptide substrate conjugates and Förster resonance energy transfer. *Methods Mol. Biol.* **2014**, *1199*, 215-239.
464. Elghanian, R.; Storhoff, J. J.; Mucic, R. C.; Letsinger, R. L.; Mirkin, C. A., Selective colorimetric detection of polynucleotides based on the distance-dependent optical properties of gold nanoparticles. *Science* **1997**, *277* (5329), 1078-1081.
465. Zhang, C. Y.; Yeh, H. C.; Kuroki, M. T.; Wang, T. H., Single-quantum-dot-based DNA nanosensor. *Nat. Mater.* **2005**, *4* (11), 826-831.
466. Besteman, K.; Lee, J. O.; Wiertz, F. G. M.; Heering, H. A.; Dekker, C., Enzyme-coated carbon nanotubes as single-molecule biosensors. *Nano Lett.* **2003**, *3* (6), 727-730.
467. Saleh, O. A.; Sohn, L. L., An artificial nanopore for molecular sensing. *Nano Lett.* **2003**, *3* (1), 37-38.
468. Kim, D.; Daniel, W. L.; Mirkin, C. A., Microarray-based multiplexed scanometric immunoassay for protein cancer markers using gold nanoparticle probes. *Anal. Chem.* **2009**, *81* (21), 9183-9187.
469. Braun, G.; Lee, S. J.; Dante, M., et al., Surface-enhanced raman spectroscopy for DNA detection by nanoparticle assembly onto smooth metal films. *J. Am. Chem. Soc.* **2007**, *129* (20), 6378-6379.
470. Maxwell, E. J.; Mazzeo, A. D.; Whitesides, G. M., Paper-based electroanalytical devices for accessible diagnostic testing. *MRS Bull.* **2013**, *38* (4), 309-314.
471. Alhasan, A. H.; Kim, D. Y.; Daniel, W. L., et al., Scanometric microRNA array profiling of prostate cancer markers using spherical nucleic acid-gold nanoparticle conjugates. *Anal. Chem.* **2012**, *84* (9), 4153-4160.
472. Lee, J. S.; Mirkin, C. A., Chip-based scanometric detection of mercuric ion using DNA-functionalized gold nanoparticles. *Anal. Chem.* **2008**, *80* (17), 6805-6808.
473. Freeman, R.; Willner, I., Optical molecular sensing with semiconductor quantum dots (QDs). *Chem. Soc. Rev.* **2012**, *41*, 4067-4085.
474. Bai, Y.; Tian, C.; Wei, X., et al., A sensitive lateral flow test strip based on silica nanoparticle/CdTe quantum dot composite reporter probes. *RSC Adv.* **2012**, *2*, 1778-1781.
475. Yuan, J.; Gaponik, N.; Eychmüller, A., Application of polymer quantum dot-enzyme hybrids in the biosensor development and test paper fabrication. *Anal. Chem.* **2012**, *84*, 5047-5052.

476. Serim, S.; Haedke, U.; Verhelst, S. H. L., Activity-based probes for the study of proteases: recent advances and developments. *ChemMedChem* **2012**, *7* (7), 1146-1159.
477. Overall, C. M.; Kleifeld, O., Validating Matrix Metalloproteinases as drug targets and anti-targets for cancer therapy. *Nat. Rev. Cancer* **2006**, *6* (3), 227-239.
478. Katz, R. A.; Skalka, A. M., The retroviral enzymes. *Annu. Rev. Biochem* **1994**, *63*, 133-173.
479. Rosenthal, P. J., Cysteine proteases of malaria parasites. *Int. J. Parasitol.* **2004**, *34* (13-14), 1489-1499.
480. Sharma, S. K.; Hopkins, T. R., Recent developments in the activation process of bovine chymotrypsinogen A. *Bioorg. Chem.* **1981**, *10* (4), 357-374.
481. Light, A.; Janska, H., Enterokinase (enteropeptidase): comparative aspects. *Trends Biochem. Sci* **1989**, *14* (3), 110-112.
482. Hirota, M.; Ohmuraya, M.; Baba, H., The role of trypsin, trypsin inhibitor, and trypsin receptor in the onset and aggravation of pancreatitis. *J. Gastroenterol.* **2006**, *41*, 832-836.
483. Nyberg, P.; Ylipalosaari, M.; Sorsa, T.; Salo, T., Trypsins and their role in carcinoma growth. *Exper. Cell Res.* **2006**, *312*, 1219-1228.
484. Moticam 1 digital camera spectral response. http://www.tedpella.com/cameras_html/camera1.htm (accessed November 20, 2016).
485. Neff, P. A.; Serr, A.; Wunderlich, B. K.; Bausch, A. R., Label-free electrical determination of trypsin activity by a silicon-on-insulator based thin film resistor. *ChemPhysChem* **2007**, *8* (14), 2133-2137.
486. Coombs, G. S.; Rao, M. S.; Olson, A. J.; Dawson, P. E.; Madison, E. L., Revisiting catalysis by chymotrypsin family serine proteases using peptide substrates and inhibitors with unnatural main chains. *J. Biol. Chem.* **1999**, *274*, 24074-24079.
487. Hedstrom, J.; Korvuo, A., Urinary trypsinogen-2 test strip for acute pancreatitis. *Lancet* **1996**, *347* (9003), 729.
488. Chang, K.; Lu, W.; Zhang, K., et al., Rapid urinary trypsinogen-2 test in the early diagnosis of acute pancreatitis: A meta-analysis. *Clin. Biochem.* **2012**, *45* (13-14), 1051-1056.
489. Kuepper, F.; Dangas, G.; Mueller-Chorus, A., et al., Fibrinolytic activity and bleeding after cardiac surgery with cardiopulmonary bypass and low-dose aprotinin therapy. *Blood Coagul. Fibrinolysis* **2003**, *14* (2), 147-153.
490. Smith, M.; Kocher, H. M.; Hunt, B. J., Aprotinin in severe acute pancreatitis. *Int. J. Clin. Pract.* **2010**, *64* (1), 84-92.

491. Algar, W. R.; Ancona, M. G.; Malanoski, A. P.; Susumu, K.; Medintz, I. L., Assembly of a concentric Förster resonance energy transfer relay on a quantum dot scaffold: characterization and application to multiplexed protease sensing. *ACS Nano* **2012**, *6* (12), 11044-11058.
492. Pugia, M. J.; Takemura, T.; Kuwajima, S., et al., Clinical utility of a rapid test for uristatin. *Clin. Biochem.* **2002**, *35* (2), 105-110.
493. Deu, E.; Verdoes, M.; Bogoyo, M., New approaches for dissecting protease functions to improve probe development and drug discovery. *Nat. Struct. Mol. Biol.* **2012**, *19* (1), 9-16.
494. Biju, V.; Itoh, T.; Ishikawa, M., Delivering quantum dots to cells: bioconjugated quantum dots for targeted and nonspecific extracellular and intracellular imaging. *Chem. Soc. Rev.* **2010**, *39* (8), 3031-3056.
495. Delehanty, J. B.; Susumu, K.; Manthe, R. L.; Algar, W. R.; Medintz, I. L., Active cellular sensing with quantum dots: Transitioning from research tool to reality; a review. *Anal. Chim. Acta* **2012**, *750*, 63-81.
496. Agasti, S. S.; Rana, S.; Park, M. H., et al., Nanoparticles for detection and diagnosis. *Adv. Drug Deliv. Rev.* **2010**, *62* (3), 316-328.
497. Hildebrandt, N.; Wegner, K. D.; Algar, W. R., Luminescent terbium complexes: Superior Förster resonance energy transfer donors for flexible and sensitive multiplexed biosensing. *Coord. Chem. Rev.* **2014**, *273*, 125-138.
498. Roda, A.; Michelini, E.; Cevenini, L., et al., Integrating biochemiluminescence detection on smartphones: mobile chemistry platform for point-of-need analysis. *Anal. Chem.* **2014**, *86* (15), 7299-7304.
499. Zhu, H.; Isikman, S. O.; Mudanyali, O.; Greenbaum, A.; Ozcan, A., Optical imaging techniques for point-of-care diagnostics. *Lab Chip* **2013**, *13* (1), 51-67.
500. Wegner, K. D.; Linden, S.; Jin, Z. W., et al., Nanobodies and nanocrystals: highly sensitive quantum dot-based homogeneous FRET Immunoassay for serum-based EGFR detection. *Small* **2014**, *10*, 734-740.
501. Liu, D.; Wu, F.; Zhou, C., et al., Multiplexed immunoassay biosensor for the detection of serum biomarkers - beta-HCG and AFP of down syndrome based on photoluminescent water-soluble CdSe/ZnS quantum dots. *Sensor Actuat. B-Chem.* **2013**, *186*, 235-243.
502. Yu, X.; Xia, H. S.; Sun, Z. D., et al., On-chip dual detection of cancer biomarkers directly in serum based on self-assembled magnetic bead patterns and quantum dots. *Biosens. Bioelectron.* **2013**, *4*, 129-136.
503. Hu, M.; Yan, J.; He, Y., et al., Ultrasensitive, multiplexed detection of cancer biomarkers directly in serum by using a quantum dot-based microfluidic protein chip. *ACS Nano* **2010**, *4*, 488-494.

504. Jokerst, J. V.; Raamanathan, A.; Christodoulides, N., et al., Nano-bio-chips for high performance multiplexed protein detection: Determinations of cancer biomarkers in serum and saliva using quantum dot bioconjugate labels. *Biosens. Bioelectron.* **2009**, *24*, 3622-3629.
505. Coughlin, S. R., Thrombin signalling and protease-activated receptors. *Nature* **2000**, *407* (6801), 258-264.
506. Lin, K. Y.; Kwong, G. A.; Warren, A. D.; Wood, D. K.; Bhatia, S. N., Nanoparticles that sense thrombin activity as synthetic urinary biomarkers of thrombosis. *ACS Nano* **2013**, *7*, 9001-9009.
507. Lancé, M. D., A general review of major global coagulation assays: thrombelastography, thrombin generation test and clot waveform analysis. *Thrombosis J.* **2015**, *13*, 1.
508. Swanson, C.; D'Andrea, A., Lateral flow assay with near-infrared dye for multiplex detection. *Clin. Chem.* **2013**, *59* (4), 641-648.
509. Zijlstra, W. G.; Buursma, A.; Meeuwse-van der Roest, W. P., Absorption spectra of human fetal and adult oxyhemoglobin, de-oxyhemoglobin, carboxyhemoglobin, and methemoglobin. *Clin. Chem.* **1991**, *37* (9), 1633-8.
510. Faber, D. J.; Aalders, M. C. G.; Mik, E. G., et al., Oxygen saturation-dependent absorption and scattering of blood. *Phys. Rev. Lett.* **2004**, *93* (2), 028102.
511. Luo, S.; Zhang, E.; Su, Y.; Cheng, T.; Shi, C., A review of NIR dyes in cancer targeting and imaging. *Biomaterials* **2011**, *32* (29), 7127-7138.
512. Gioux, S.; Choi, H. S.; Frangioni, J. V., Image-guided surgery using invisible near-infrared light: fundamentals of clinical translation. *Mol. Imaging* **2010**, *9* (5), 237-255.
513. Deng, B.; Lin, Y.; Wang, C., et al., Aptamer binding assays for proteins: the thrombin example-a review. *Anal. Chim. Acta* **2014**, *837*, 1-15.
514. Nutiu, R.; Li, Y., Structure-switching signaling aptamers: transducing molecular recognition into fluorescence signaling. *Chem. Eur. J.* **2004**, *10*, 1868-1876.
515. Edelstein, A. D.; Tsuchida, M. A.; Amodaj, N., et al., Advanced methods of microscope control using μ Manager software. *J. Biol. Methods* **2014**, *1*, e10.
516. Casey, K. G.; Quitevis, E. L., Effect of solvent polarity on nonradiative processes in xanthene dyes: rhodamine b in normal alcohols. *J. Phys. Chem.* **1988**, *92*, 6590-6594.
517. Lee, W. M.; Upadhy, A.; Reece, P. J.; Phan, T. G., Fabricating low cost and high performance elastomer lenses using hanging droplets. *Biomed. Opt. Express* **2014**, *5* (5), 1626-1635.

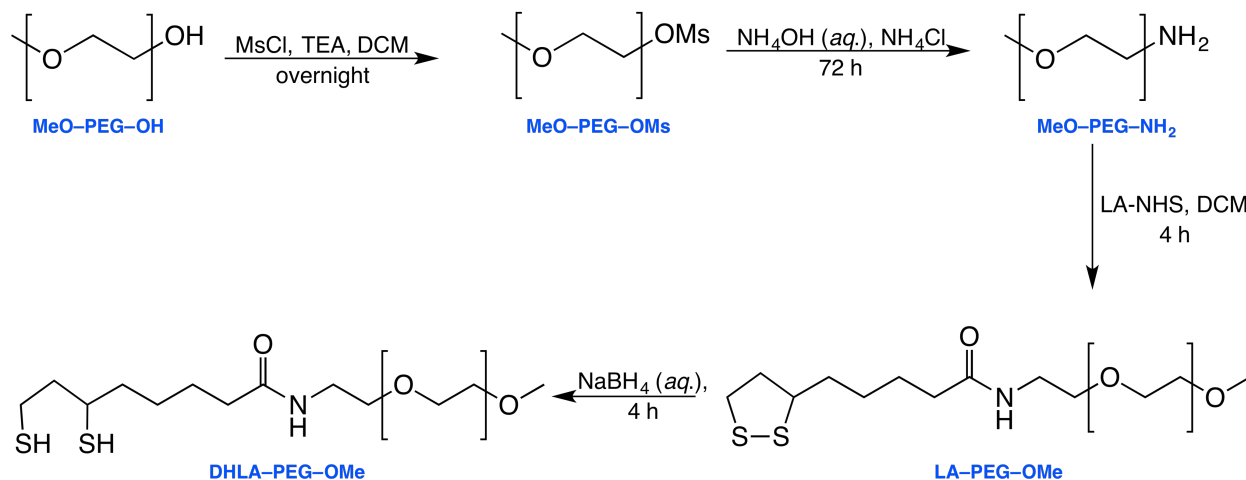
518. Giri, S.; Sykes, E. A.; Jennings, T. L.; Chan, W. C. W., Rapid screening of genetic biomarkers of infectious agents using quantum dot barcodes. *ACS Nano* **2011**, *5* (3), 1580-1587.
519. Haeberle, S.; Zengerle, R., Microfluidic platforms for lab-on-a-chip applications. *Lab Chip* **2007**, *7* (9), 1094-1110.
520. Choi, K.; Ng, A. H. C.; Fobel, R.; Wheeler, A. R., Digital microfluidics. *Annu. Rev. Anal. Chem.* **2012**, *5* (1), 413-440.
521. Samiei, E.; Tabrizian, M.; Hoorfar, M., A review of digital microfluidics as portable platforms for lab-on a-chip applications. *Lab Chip* **2016**, *16* (13), 2376-2396.
522. Addae-Mensah, K. A.; Wang, Z.; Parsa, H., et al., Fundamentals of microfluidics devices. In *Microfluidic Devices in Nanotechnology*, John Wiley & Sons, Inc.: 2010; pp 1-38.
523. Park, J.; Nam, J.; Won, N., et al., Compact and stable quantum dots with positive, negative, or zwitterionic surface: specific cell interactions and non-specific adsorptions by the surface charges. *Adv. Funct. Mater.* **2011**, *21* (9), 1558-1566.
524. Zhan, N.; Palui, G.; Grise, H., et al., Combining ligand design with photoligation to provide compact, colloidally stable, and easy to conjugate quantum dots. *ACS Appl. Mater. Interfaces* **2013**, *5* (8), 2861-2869.

Appendix I

Preparation of DHLA-PEG coated QDs

1. Synthesis of DHLA-PEG ligands

DHLA-PEG ligands were synthesized according to Scheme A1.



Scheme A1 Synthesis of DHLA-PEG ligands.

Synthesis of MeO-PEG-OMs. PEG (average MW ~750, 10 g, 13 mmol) was placed in a dry round bottom flask equipped with a magnetic stir bar and dried under vacuum at 50 °C overnight. Dried PEG was diluted with 50 mL of DCM and 2.1 mL (16 mmol) of methanesulfonyl chloride was added. Excess of TEA (5.6 mL, 40 mmol) was added to an addition funnel, the reaction was purged with argon and cooled on ice bath. The TEA was added dropwise (~ 2 h) with stirring, and the reaction was brought to room temperature and left overnight. The reaction mixture was concentrated in *vacuo*, and the crude product was precipitated with the addition of cold diethyl ether and collected by filtration. The recovered crude product was of sufficient purity to proceed to the next step without additional purification. Yield >90%. Thin layer chromatography: 10:1 (v/v) CHCl₃:MeOH, R_f (MeO-PEG-OH) = 0.35, R_f (MeO-PEG-OMs) = 0.48. TLC plates were developed with iodine.

Synthesis of MeO-PEG-NH₂. Activated MeO-PEG-OMs was dissolved in 150 mL of ammonium hydroxide (30% w/w) and 4 g of ammonium chloride was added to the reaction. The flask was capped but not sealed (to prevent pressure build-up) and allowed to react for 72 h. The product was extracted three times with 50 mL of DCM, dried over sodium sulphate, and the solvent evaporated using a rotary evaporator. The typical product yield was 60–80%. Thin layer chromatography: 10:1 (v/v) CHCl₃:MeOH, R_f (MeO-PEG-NH₂) = 0.02, R_f (MeO-PEG-OMs) = 0.48. TLC plates were developed with iodine and the presence of a primary amine was confirmed with the ninhydrin test. ESI⁺ MS (MeOH): m/z 780.8 (MH⁺, M=H₂N-(CH₂-CH₂-O)₁₆-OCH₃), 824.8 (MH⁺, M=H₂N-(CH₂-CH₂-O)₁₇-OCH₃).

Synthesis of MeO-PEG-LA. Lipoic acid-NHS (0.6 g, 2 mmol) (see synthesis procedure in Chapter 4, Section 4.4.2.3) and MeO-PEG-NH₂ were dissolved in 50 mL of DCM in a round bottom flask equipped with a magnetic stir bar. The flask was purged with argon and left to react overnight. Crude product was concentrated using a rotary evaporator and purified by column chromatography on silica gel with 20:1 (v/v) CHCl₃:MeOH as the eluent. Fractions containing pure product were combined and dried under vacuum to give a light yellow waxy solid. Thin layer chromatography: 10:1 (v/v) CHCl₃:MeOH, R_f (MeO-PEG-NH₂) = 0.02, R_f (LA-NHS) = 0.92, R_f (MeO-PEG-LA) = 0.64. NMR ¹H (CDCl₃): 1.45 ppm (m, 2H, **5**), 1.65 ppm (m, 2H, **4**), 1.85 ppm (m, 2H, **6**), 2.15 ppm (t, 2H, **7**), 2.45 ppm (m, 2H, **2**), 3.15 ppm (m, 1H, **3**), 3.35 ppm (s, 3H, **11**), 3.42 ppm (m, 2H, **1**), 3.52 ppm (m, 4H, **8,9**), 3.62 ppm (s, 64H, **10**), 6.2 ppm (s, broad, 1H).

Synthesis of MeO-PEG-DHLA. MeO-PEG-LA (1.4 g, 1.5 mmol) was dissolved in 50 mL water with stirring and cooled in an ice bath. Separately, 1.5 g (40 mmol) of sodium borohydride was dissolved in 100 mL of water and added in portions to the reaction mixture. The reaction was left for 4 h, diluted with 100 mL of water, and excess sodium borohydride was quenched with 12 M HCl (aq.) in an ice bath until pH 1–2 was reached. The reduced product was extracted with four portions of 50 mL DCM. The extracts were combined, dried over sodium sulphate, and the solvent removed using a rotary evaporator to yield a white waxy solid. The product was stored under argon at –20°C until further use. Thin layer chromatography: 10:1 (v/v) CHCl₃:MeOH, R_f (MeO-PEG-DHLA) = 0.62, R_f (MeO-PEG-LA) = 0.64.

2. QD Ligand Exchange with DHLA-PEG

Organic QDs capped with hexadecylamine (HDA) or oleic acid ligands, 100 μL (10–20 μM in toluene) were precipitated from toluene with ethanol by centrifugation (4800 rcf, 4 min) and redissolved in *ca.* 100 μL of chloroform (CHCl_3). QDs were then transferred into a 10 mL round bottom flask and the solvent removed by flushing with argon. DHLA-PEG (*ca.* 200 mg) and a stir bar were added to the QD residue, the flask was sealed, purged with nitrogen, and placed in an oil bath set to 80 $^\circ\text{C}$. Once DHLA-PEG melted, the mixture was gently mixed for 4–6 h to ensure the QDs were completely dispersed. To purify DHLA-PEG coated QDs from excess ligand, the mixture was diluted with a 15:10:1 (v/v) mixture of hexanes, ethanol, and CHCl_3 as described previously [256]. First, 0.2 mL ethanol was added to the QD solution, which was mixed and transferred to a 50 mL falcon tube, then hexanes was added until turbidity, a drop of CHCl_3 was added (solution turns clear), and once again hexanes was added until the solution turned cloudy. QDs were then pelleted by centrifugation (4800 rcf, 8 min). At this point, if the pellet appeared solid, 10 mL of Milli-Q water was added. If the precipitate appeared as an oil phase, the supernatant was discarded and 1 mL of CHCl_3 was added, followed by addition of diethyl ether (*ca.* 20 mL), and the QDs were pelleted once again by centrifugation. Pelleted QDs were dissolved in 10 mL of Milli-Q water, filtered through a 0.22 μm syringe filter (Millex-GP, PES membrane, EMD Millipore) and further purified three times with Milli-Q water using a 30 kDa centrifugal filter (Macrosep Advance, Pall Corporation). A final wash was done using borate buffer (pH 8.5, 50 mM), the residual \sim 2 mL QD solution was transferred to a clean vial (see note below) and purified QDs were stored at 4 $^\circ\text{C}$.

Note. Some batches of QDs were not sufficiently purified at this stage, as was observed through slight mobility shifts in gel electrophoresis and experimentally observed longer assembly times with His-tag appended peptides. Such QDs were further purified using an additional step. The ionic strength of the QD solution (*i.e.* 4 mL, borate buffer, pH 8.5, 50 mM) was adjusted to 1 M NaCl and 1 mL of CHCl_3 added. The biphasic mixture was thoroughly mixed and let stand for \sim 1 h for the layers to separate. DHLA-PEG-coated QDs in CHCl_3 were carefully transferred to a clean glass vial, and the solvent was removed by flowing nitrogen through at 50 $^\circ\text{C}$ for 2 h. The resulting dry QD pellet was cooled to room temperature and mixed with 1 mL of borate buffer (pH 8.5, 50 mM). QDs were allowed to stand for 1 h with occasional mixing, then QDs were

filtered through 0.22 μm syringe filter (Millex-GP, PES membrane, EMD Millipore) and stored at 4 $^{\circ}\text{C}$.

3. QD Ligand Exchange with mercaptopropionic (MPA) ligands

Organic QDs capped with hexadecylamine (HDA) or oleic acid ligands, 100 μL (10–20 μM in toluene) were added to 0.5 mL of CHCl_3 in a glass culture tube, followed by addition of 200 μL of mercaptopropionic acid. The mixture was purged with argon and placed on ice for 10 min. A volume of 300 μL of cold DIPEA was added, the tube was sealed and incubated at 70 $^{\circ}\text{C}$ for 4 h under argon. To purify QDs from excess ligand, the QD mixture was cooled on ice for 10 min, followed by sequential addition of 2 mL of cold CHCl_3 , 200 μL of cold tetramethylammonium hydroxide solution in methanol (TMAH, 25% w/v), and 300 μL of borate buffer (BB, pH 9.2, 50 mM, 250 mM NaCl). The mixture was thoroughly mixed by pipetting up and down few times and let stand until layers separated. The MPA-coated QDs in aqueous layer were transferred to 1.7 mL microcentrifuge tubes (200–300 μL per tube) and \sim 1 mL of ethanol added to each tube. The solution was vortexed, and QDs were then pelleted by centrifugation (4800 rcf, 4 min). The supernatant was discarded and the QDs were redissolved in 200 μL of BB. Three additional washes by precipitation with ethanol and redispersion with BB were done. After the final wash, QDs were redispersed in borate buffer (pH 9.2, 50 mM, no salt) and stored at 4 $^{\circ}\text{C}$ until needed.

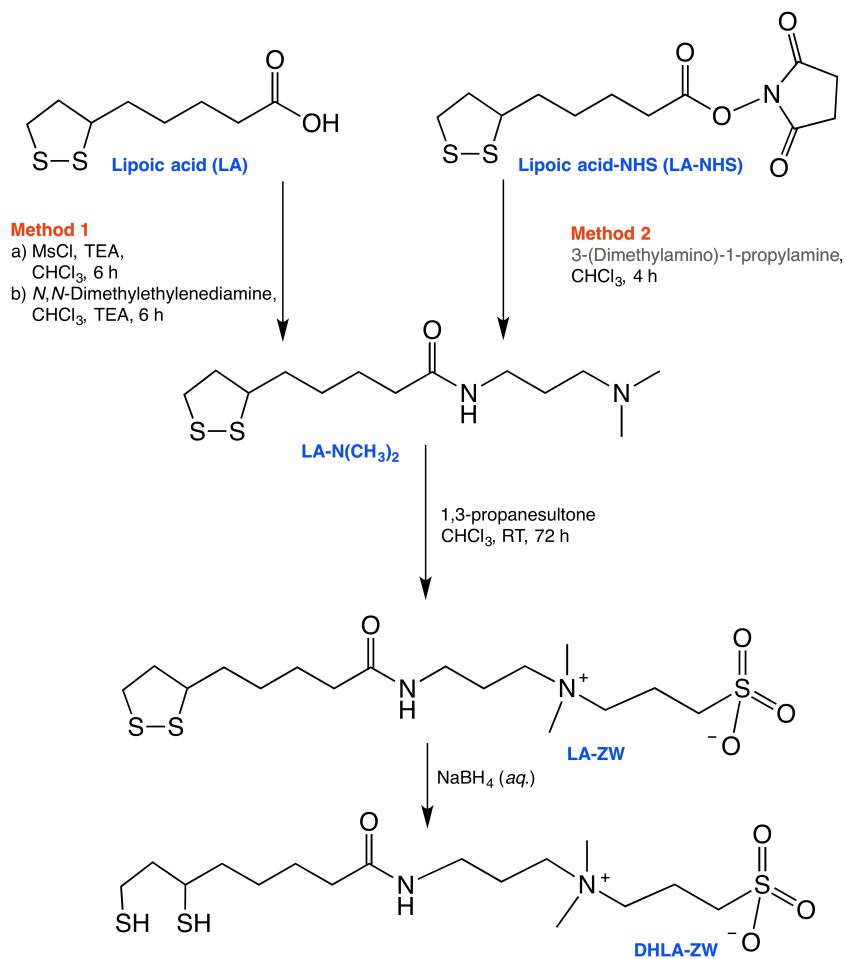
4. QD Ligand Exchange with cysteine (Cys) ligands

The procedure for the preparation of Cys-capped QDs is similar to the one used to prepare GSH-capped QDs (see Section 2.5.2). Organic QDs capped with hexadecylamine (HDA) or oleic acid ligands (100 μL , \sim 20 μM in toluene) were precipitated from toluene with ethanol by centrifugation (4800 rcf, 4 min) and redispersed in *ca.* 1000 μL of CHCl_3 . Separately, a solution of cysteine (120 mg, 1 mmol) was prepared in 300 μL of 25% w/v TMAH in methanol, and then added to the solution of QDs. This mixture was vortexed and allowed to stand for 2 h. Cys-coated QDs were then extracted into 200 μL of borate buffer (pH 9.2, 50 mM, 250 mM NaCl),

the organic layer discarded, and the QDs were washed by precipitation with ethanol and centrifugation (4800 rcf, 4 min). QDs were redispersed in 200 μL of buffer and washed twice more with ethanol. After the final wash, QDs were dissolved in borate buffer (pH 8.5, 50 mM) and stored at 4 $^{\circ}\text{C}$.

5. Synthesis of DHLA-zwitterionic (ZW) ligands

A lipoic acid-based ligand appended with a sulfobetaine zwitterion was synthesized using two methods, as shown in Scheme A2, following procedures described previously [523, 524] with a few modifications.



Scheme A2 Synthesis of DHLA-zwitterionic (ZW) ligands.

Synthesis of LA-N(CH₃)₂.

Method 1. Lipoic acid (2 g, ~10 mmol) and triethylamine (1.5 g, ~15 mmol) were added to 30 mL of CHCl₃ in three-neck round bottom flask. The mixture was placed in an ice bath for 20 min under argon with stirring. Methanesulfonyl chloride (1.15 g, ~10 mmol) was added dropwise, then the reaction mixture was brought to room temperature and left to react for 6 h. A solution of 3-(dimethylamino)-1-propylamine (0.92 g, ~9 mmol) and triethylamine (0.5 g, ~5 mmol) in 10 mL of CHCl₃ was added dropwise to the reaction mixture and left for 6 h under an argon atmosphere. The crude product was washed with one 60 mL portion of water, three 60 mL portions of brine, followed by three 50 mL portions of aqueous NaOH (1 M). The organic layer was dried over sodium sulfate, filtered, and the solvent removed using a rotary evaporator to give a yellow oil. This layer chromatography: 10:1 (v/v) DCM:MeOH, R_{f(LA)} = 0.48, R_{f(LA-N(CH₃)₂)} = 0.08. ESI⁺ MS (MeOH): m/z 413.2 (MH⁺).

Method 2. Lipoic acid-NHS (see Section 4.4.2.3, Scheme 4.3 for synthesis; 3 g, ~10 mmol) was dissolved in 50 mL of CHCl₃, and cooled in an ice bath for 20 min under argon. A solution of 3-(dimethylamino)-1-propylamine (1.53 g, ~15 mmol) in 10 mL of CHCl₃ was added dropwise to the reaction mixture and left to react for 4 h under an argon atmosphere. Crude product was purified by extraction with one 60 mL portion of water, three 60 mL portions of brine, and three 50 mL portions of aqueous NaOH (1 M). The organic layer was dried over sodium sulfate, filtered, and the solvent removed using a rotary evaporator to give yellow oil.

Synthesis of LA-ZW. Compound LA-N(CH₃)₂ (2.76 g, ~10 mmol) was dissolved in 30 mL of CHCl₃ and purged with argon for 20 min. 1,3-propanesultone (1.34 g, ~11 mmol) was added and reaction stirred at room temperature for 72 h (or alternatively at 60 °C for 24 h). As the reaction proceeded, the product LA-ZW precipitated from the solution. After the reaction was complete, the yellow precipitate was collected, washed with three portions of CHCl₃ and dried under vacuum to give yellow foamy solid. ESI⁺ MS (MeOH): m/z 413.2 (MH⁺), 447.3 (MNa⁺).

6. QD Ligand Exchange with DHLA-ZW ligands

NaBH₄ (23 mg, ~0.6 mmol) was dissolved in 0.5 mL Milli-Q water and added dropwise to the solution of LA-ZW (120 mg, ~0.3 mmol) in 1 mL of water. The mixture was stirred under an argon atmosphere for 2 h. The solution of DHLA-ZW ligand was filtered through 0.22 μm syringe filter (Millex-GP, PES membrane, EMD Millipore) into a clean glass vial and excess of NaBH₄ was quenched with 3 M HCl (~150 μL) until pH 1–2 was reached. Then, 400 μL of tris-borate buffer (200 mM, pH 7.4) was added, followed by addition of 5 M NaOH until pH ~7 was reached. Organic QDs (~3 nmol) were precipitated with ethanol by centrifugation (4800 rcf, 4 min), redissolved in 1 mL of CHCl₃ and added to the aqueous solution of DHLA-ZW. The biphasic mixture was purged with argon, vigorously stirred at 60 °C for 1 h, and subsequently left to stand overnight at 50 °C. The aqueous layer containing DHLA-ZW ligand-capped QDs was transferred to a clean glass vial, filtered through a 0.22 μm syringe filter (Millex-GP, PES membrane, EMD Millipore) and further purified three times with Milli-Q water using a 30 kDa centrifugal filter (Macrosep Advance, Pall Corporation). A final wash was done using borate buffer (pH 8.5, 50 mM), and the residual ~2 mL QD solution was transferred to a clean vial and the purified QDs were stored at 4 °C.

Appendix II

Quantum yield measurements

Quantum yields were calculated relative to standard dyes according to eqn. A1, where $A(\lambda_{exc})$ is a measured absorbance at the excitation wavelength, $\int I(\lambda_{em})d\lambda$ is an integrated emission intensity across all emission wavelengths, η is the solvent refractive index, Φ is a quantum yield, and the subscripts x and std refer to an unknown and a reference standard, respectively. A series of concentrations was measured for each emitter and the slopes of plots of PL *versus* absorbance were used for calculations. Standard dyes were fluorescein in 0.1 M NaOH ($\Phi = 0.79$) and rhodamine B in water ($\Phi = 0.31$) [348, 373]. QDs with an emission maximum located between 520–580 nm were measured relative to fluorescein, using an excitation wavelength of 460 nm and integrating the PL intensity over 470–750 nm. QDs with an emission maxima located between 590–650 nm were measured relative to rhodamine B, using an excitation wavelength 510 nm and integrating the PL intensity over 520–750 nm. Representative plots of absorbance *versus* fluorescence are shown in Figure A1. The quantum yield of QDs was calculated from the experimentally determined slopes (such as those shown in Figure A1) according to eqn. A2.

$$\frac{\int I_x(\lambda_{em})d\lambda}{\int I_{std}(\lambda_{em})d\lambda} = \frac{A_x(\lambda_{exc})}{A_{std}(\lambda_{exc})} \left(\frac{\Phi_x}{\Phi_{std}} \right) \left(\frac{\eta_{std}^2}{\eta_x^2} \right) \quad (A1)$$

$$\Phi_x = \frac{\Phi_{std} \times slope_x}{slope_{std}} \quad (A2)$$

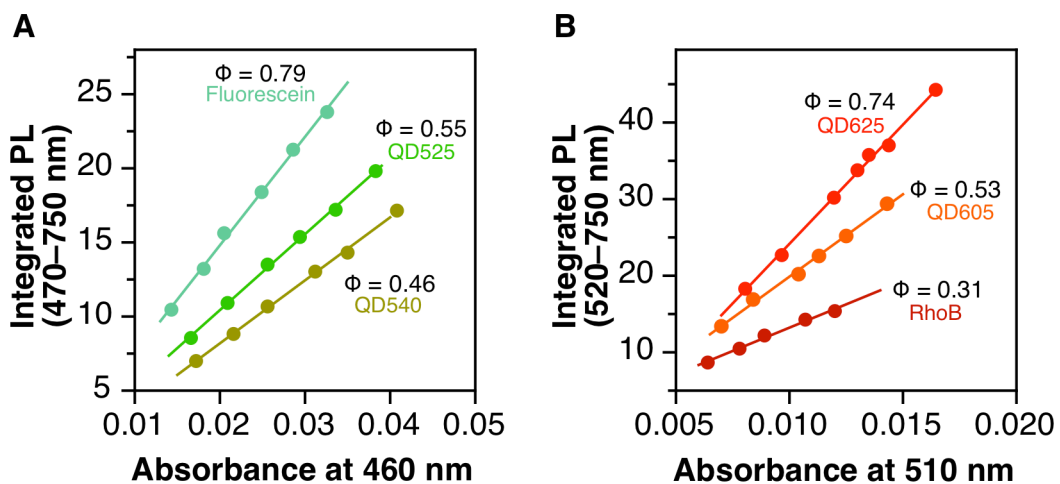


Figure A1 (A) Determining the quantum yields of green-emitting QD525 and QD540 relative to fluorescein, and (B) determining the quantum yields of red-emitting QD605 and QD625 relative to rhodamine B.

Appendix III

Custom LabVIEW software for LED control

Two LabVIEW programs were coded to turn LEDs on and off to collect data shown in Chapter 5 and 6. In both programs, the user could define the voltage output. The primary difference between these two programs was the continuity of illumination. In Chapter 5, the FRET pair was QD525-A555, where the A555 dye was very resistant to photobleaching under continuous illumination with LEDs. Therefore, the program was written for continuous light output from the LED. In Chapter 6, the FRET pair was chosen to be QD630-A647, where A647 was found to be susceptible to photobleaching under continuous illumination. To mitigate this problem, the LabVIEW program was modified to turn the LED on and off during data acquisition. Typically, data was acquired at 30 s intervals and the LED was on for 2 s and off for 28 s. A screenshot of the program is shown in Figure A2.

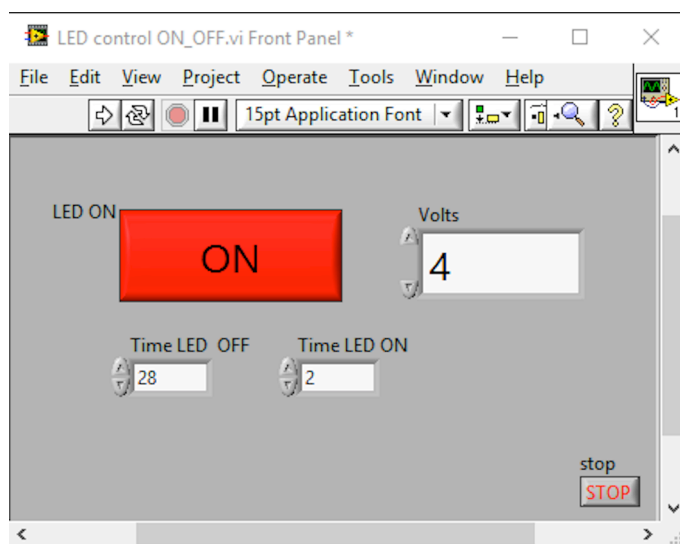


Figure A2 Screenshot of the custom LabVIEW program used to control LEDs.

Custom LabVIEW software for data acquisition

Time-based spectral acquisition with the Green-Wave spectrometer (StellarNet), presented in Chapter 4 and 5, was done using a custom LabVIEW program. The program was written to allow the user to define an acquisition rate/interval and the number of spectra to collect, as well as spectrometer parameters such as the integration time, optical smoothing level, and the number of scans to average. All acquired spectra were saved as an Excel file at the user specified location on the hard drive, where first column was the wavelength (nm) and all subsequent columns corresponded to PL spectra acquired at the pre-defined time interval. This program also allowed optional LED control with on and off illumination. A screenshot of this program is shown in Figure A3.

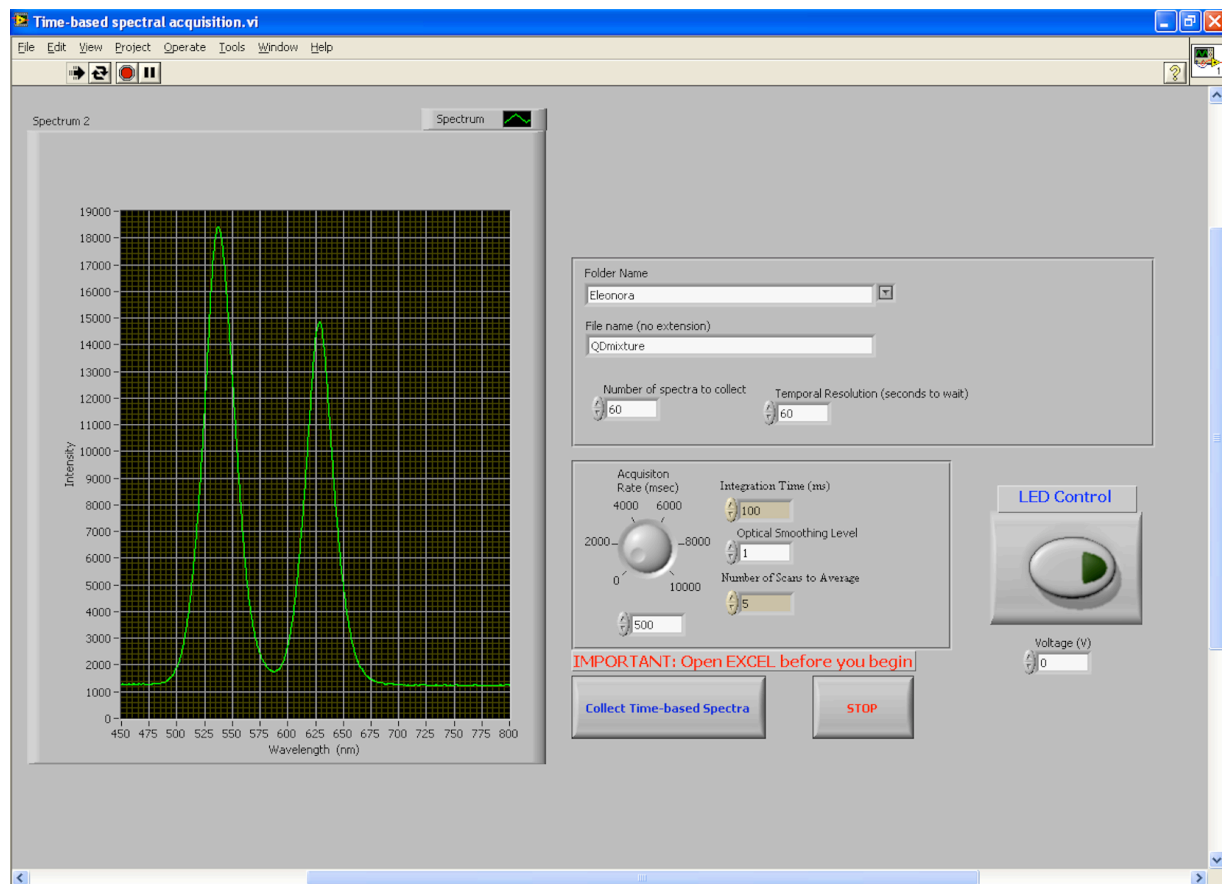


Figure A3 Screenshot of the custom LabVIEW program used to acquire time-based spectra with Green-Wave spectrometer (StellarNet).

Copyright Acknowledgements

Portions of this thesis have been reproduced in part and from the references with permission, as indicated in the Preface (page iv) and at the beginning of each chapter.

Copyright 2013, 2014: The American Chemical Society.

Copyright 2013: Creative Commons Attribution-NonCommercial 4.0 International licence.

Copyright 2014, 2015: The Royal Society of Chemistry.

Copyright 2016: Springer.

Copyright 2014: IEEE